A study of the kinetics and microstructure evolution during reactions of niobium/aluminum and titanium/aluminum multilayer thin-films.

INFORMATION TO USERS

This manuscript has been reproduced from the microfilm master. UMI films the text directly from the original or copy submitted. Thus, some thesis and dissertation copies are in typewriter face, while others may be from any type of computer printer.

The quality of this reproduction is dependent upon the quality of the copy submitted. Broken or indistinct print, colored or poor quality illustrations and photographs, print bleedthrough, substandard margins, and improper alignment can adversely affect reproduction.

In the unlikely event that the author did not send UMI a complete manuscript and there are missing pages, these will be noted. Also, if unauthorized copyright material had to be removed, a note will indicate the deletion.

Oversize materials (e.g., maps, drawings, charts) are reproduced by sectioning the original, beginning at the upper left-hand corner and continuing from left to right in equal sections with small overlaps.

Photographs included in the original manuscript have been reproduced xerographically in this copy. Higher quality 6" x 9" black and white photographic prints are available for any photographs or illustrations appearing in this copy for an additional charge. Contact UMI directly to order.

Bell & Howell Information and Learning
300 North Zeeb Road, Ann Arbor, MI 48106-1346 USA

UMI®
800-521-0600

A Study of the Kinetics and Microstructure Evolution during Reactions of Niobium/Aluminum and Titanium/Aluminum Multilayer Thin-Films

by

Gene A. Lucadamo

Presented to the Graduate and Research Committee

of Lehigh University

in Candidacy for the Degree of

Doctor of Philosophy

in

Materials Science and Engineering

Lehigh University

November 23, 1999

Approved and recommended for acceptance as a dissertation in partial fulfillment of the requirements for the degree of Doctor of Philosophy

11/23/99
Date

Dr. Katayun Barmak
Dissertation Advisor

12/7/99
Accepted Date

Committee Members:

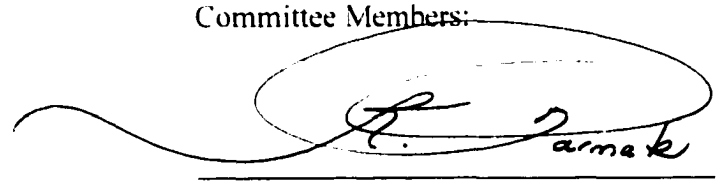

Dr. Katayun Barmak
Committee Chair

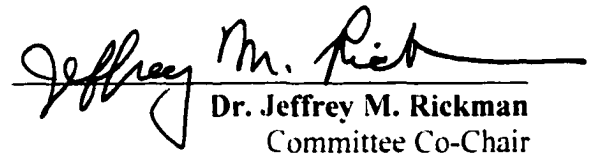

Dr. Jeffrey M. Rickman
Committee Co-Chair

Dr. David B. Williams
Committee Member

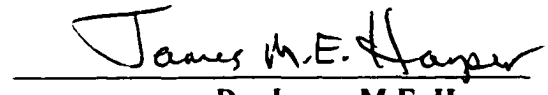

Dr. James M.E. Harper
Committee Member

Acknowledgements

Often it is said that life is a journey, not a destination. I think this statement can be applied equally to my progress in attaining this degree. I would like to express my sincere gratitude to Prof. Katy Barmak for providing me with the means and motivation (excellent labs, equipment, and consistent financial support) to complete what has been both an intellectually rewarding and a challenging endeavor. Prof. Barmak has been an outstanding mentor and guide over the course of my graduate research experience.

I would also like to thank my distinguished research committee: Co-chair Prof. Jeffrey M. Rickman and members Prof. David B. Williams and Prof. James M.E. Harper for their necessary and highly-valued advice and support.

There are many other researchers and friends whom I have met and interacted with along this sojourn; I will do my best to recognize their contributions.

I would like to thank Dr. James (Jim) Harper (again), Cyril Cabral, Jr., Dr. Christian Lavoie, and Dr. Jean Jordan-Sweet for their generosity and help with the synchrotron X-ray experiments. I also extend my appreciation for a truly rewarding research experience at the T.J. Watson Research Center over the summer of 1999. I felt it a great privilege to be offered the opportunity to learn from and collaborate with such distinguished scientists in what is indisputably a world-class facility. I would also like to thank Dr. Kenneth (Ken) P. Rodbell also of IBM Research for his invaluable assistance and expertise with the pole figure measurements.

I gratefully acknowledge the many contributions over the past five years of Herr Doktor Carsten (Casi) Michaelsen at the GKSS Research Center in Geesthacht, Germany. His knowledge and expertise of the reactions in the Ti/Al system and his excellent

previous research in the field formed a solid foundation on which much of the Ti/Al work that appears in this thesis was built. Dr. Michalesen also provided the rocking curve measurements of texture as well as assisting with their interpretation. He is a model of efficiency and organization.

The analytical electron microscopy work would not have been possible without the necessary assistance and instruction of Dr. Masashi Watanabe and Dr. Derrick Carpenter. Their skill and knowledge in these techniques was evident in the exceptional quality of the results that we obtained with the HB 603 STEM.

I would also like to thank former and current students of Prof. Barmak including Jihwan Kim and Dr. Roger Ristau for helping to keep the sputtering system working in peak condition. I also thank them for countless hours of discussion and laboratory assistance. I acknowledge the help offered by Ellen Youngblood and Dr. Saikumar Vivekanand who were the first to master the art of tripod polishing for cross section TEM sample preparation. I thank Seungmin Hyun for the excellent maintenance and calibration of the DSC 7 instrument. Finally, I thank work-study students Joleen Codner and Sarah Philips for their diligence and assistance with the grain size measurements and cross-sectional TEM sample preparation, respectively.

I extend grateful appreciation to the talents of Dave Ackland and Kathy Repa who kept the electron microscopes operating and exceeding specifications, and for making sure that sample preparation, not instrumentation, was the limiting factor for my electron microscopy studies. I also thank them for providing on-the-job training for many of the techniques learned about in class. Special thanks to Kathy Repa for performing the

EPMA analysis. Thanks also to Arlen Benscoter for running a tight (metallography) ship.

Other thanks go to Dr. Jerry Floro and Dr. Eric Chason (now at Brown U.) at Sandia National Laboratories in Albuquerque, NM for providing me with another excellent excuse to take a vacation from Whitaker Laboratory over the summer of 1997. I enjoyed the research with SiGe heteroepitaxy immensely and found it to be a very refreshing change from polycrystalline materials. The same was true of the New Mexico environment compared to the Lehigh Valley - I have not looked at South Mountain the same way since.

Finally, I come to those who have made this journey more than just a research experience and who have provided me with the necessary rest stops. Dr. Derrick Carpenter (before he was married), Dr. Anthony DiGiovanni, Brian Schorr, Gary Thompson, and Dr. Matt Watson for providing an interesting and diverse living experience. Thanks to all the fellow wanderers in the department for their advice and friendship. Special thanks to Michele Straka who has been my close companion for the majority of my post-high school education.

Lastly, I thank my parents and family for their unconditional support and encouragement.

I dedicate this work to those who have made the final and greatest journey and it is in their spirit that I continue my wondrous expedition.

Funding for this work was generously provided through NSF DMR-9713439, DMR-941116, and DMR-9458000. The support of KLA-Tencor and Perkin Elmer is acknowledged for partial contributions towards the purchase of the profiler and DSC 7, respectively. The synchrotron XRD experiments were conducted under DOE contract DE-AC02-76CH-00016.

Table of Contents

List of Tables

List of Figures

List of Abbreviations

AEM	Analytical electron microscopy
BEOL	Back end of line
BF	Bright field
CDF	Centered-dark field
CMOS	Complementary metal oxide silicon
DRAM	Dynamic random access memory
DSC	Differential scanning calorimeter
DTA	Differential thermal analysis (or analyzer)
EDX	Energy dispersive X-ray (spectroscopy)
HRTEM	High resolution transmission electron microscopy
IC	Integrated circuit
MFC	Mass flow controller
OIM	Orientation imaging microscopy
PVD	Physical vapor deposition
RBS	Rutherford backscattering spectrometry
SAD	Selected area diffraction
SEM	Scanning electron microscopy
SIMS	Secondary ion mass spectroscopy
SZM	Structure zone model
TEM	Transmission electron microscopy
UHV	Ultra-high vacuum
WDS	Wavelength dispersive (X-ray) spectroscopy
XRD	X-ray diffraction

Abstract

The study of phase formation kinetics and concurrent microstructure evolution in thin films is important to the development of interconnects for integrated circuits. The present work used differential scanning calorimetry (DSC), X-ray diffraction (XRD), and transmission electron microscopy (TEM) to examine aluminide formation in Nb/Al and Ti/Al thin-film multilayers with a fixed overall composition of XAl_3 (X = Nb,Ti). The effects of bilayer thickness (Λ) and composition on reaction kinetics and microstructure were investigated in films with Λ = 10 nm – 333 nm composed of Al, Al-0.5 wt.% Cu and Al-1.0 wt.% Cu layers.

DSC results indicated that solute Cu was did not effect the activation energy of the formation of $NbAl_3$. However, 1.0 wt.%Cu increased the activation energy for formation of the metastable, cubic superlattice structure of $TiAl_3$. The Avrami exponents associated with $NbAl_3$ and $TiAl_3$ formation suggested the possibility of heterogeneous product phase nucleation. Finally, analysis of DSC data indicated that the formation enthalpy of $NbAl_3$ and $TiAl_3$ was unchanged by the presence of Cu.

XRD showed that the multilayers exhibited Al <111>/Nb <110> or Al <111>/Ti <0002> fiber texture. The fiber plot pole intensity and peak width depended on layer thickness and Cu concentration. The presence of Cu reduced the fiber texture in both types of multilayers. *In situ* synchrotron XRD was used to study the formation kinetics of $TiAl_3$ and $NbAl_3$. Using this approach, the effective activation energies for the formation of $NbAl_3$ as well as the metastable and equilibrium structures of $TiAl_3$ were determined.

Cross-section TEM was used to examine the microstructures of as-deposited multilayers and samples that were annealed to different stages of the reaction. This provided a comparison with predictions of existing models of two-stage reaction kinetics. Analytical electron microscopy was used to determine the elemental distributions during the early stages of the Nb/Al reaction. Enhanced diffusion was observed at the intersections of Al grain boundaries with the Nb layer.

1 Introduction

1.1 Motivation

1.1.1 Microelectronics Manufacturing and Microstructure Control

One means to lower the cost of integrated circuits (IC) is to augment the functionality of the design by increasing the number of components per unit area. Consequently, the metallic interconnections between devices have been scaled down to smaller dimensions. As shown in Figure 1. 1, designs now incorporate several layers of metallization to connect the increased number of devices.

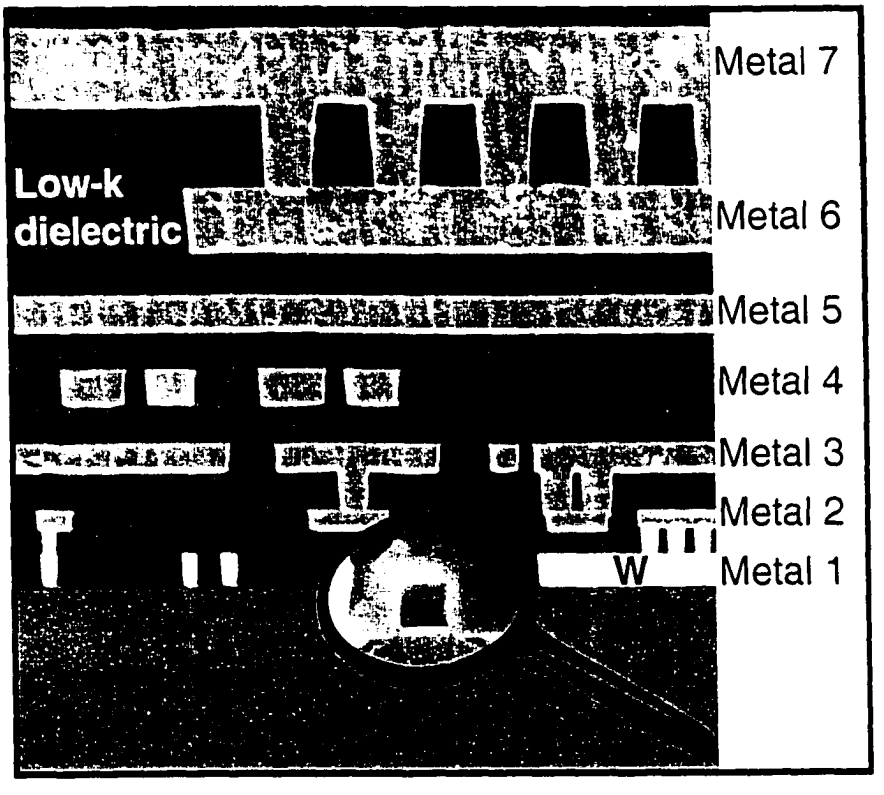

Figure 1. 1: SEM cross-section of an advanced CMOS design utilizing Cu with dual-damascene processing and seven layers of metallization. Magnified area shows a region around a transistor (from IBM Corp. website).

The reduced interconnect dimensions have resulted in increasing importance of microstructure control in semiconductor metallization.

There are many parameters that can be optimized in a typical thin-film microstructure deposited by a physical vapor deposition (PVD) process. These include, but are not limited to: grain size, grain texture (fiber texture), surface/interface roughness, composition (including the distribution of solute elements), and electrical properties (i.e., resistivity). If the scope is expanded to include magnetic thin films used in read/write heads or storage media, the magnetic properties such as: coercivity, saturation magnetization, and magnetic domain size can be included.

The microelectronics industry has long recognized the importance of controlling the microstructure and chemistry of thin films. In the 1960's, the addition of small amounts of Cu to Al was found to have a major impact on electromigration resistance in integrated circuits (Ames et al. 1970). Later, experiments investigating the effect of linewidth and texture in patterned thin films revealed a correlation with grain structure and electromigration resistance. Lines containing grain boundaries predominantly perpendicular to the line direction, the "bamboo" morphology, showed improved electromigration resistance (Vaidya and Sinha 1980). The Al grains in the bamboo lines also showed increased <111> fiber texture. Subsequent studies developed a correlation between grain size, grain size distribution, the degree of <111> texture and electromigration resistance (Vaidya et al. 1981). Later investigations refined the description of texture by incorporating not only the volume of <111>-oriented grains, but the distribution of the <111> orientations (Knorr 1991; Knorr and Rodbell 1992; Knorr 1993; Knorr and Rodbell 1996). Recent work using orientation imaging microscopy (OIM) has measured the texture of grains adjacent to failure sites in order to correlate these areas with localized changes in grain orientations (Keller et al. 1999).

The presence of underlayers has also been shown to have a significant effect on texture. For example, Al or Al(Cu) films show an improvement in the texture distribution when deposited on Ti underlayers that also have a narrow texture distribution (texture inheritance) (Tracy et al. 1994, Adamik, et al. 1997, Hurd et al. 1998, Adamik et al. 1998). The effects of texture and grain size on electromigration performance have spawned efforts to understand the evolution of texture based on processing parameters (Grovenor et al. 1984, Thompson 1993, Adamik et al. 1994, Thompson and Carel 1995, Thompson and Carel 1996). As logic and memory devices have continued to increase in speed and processing power while decreasing in size, processing steps involving microstructure control have been continually addressed and have taken on greater importance (Licata et al. 1995; Harper and Rodbell 1997).

There are other types of microstructures that are prevalent in microelectronic metallization schemes. These microstructures are the direct result of a chemical reaction of two (or more) elements or alloys resulting in a new compound with a different composition. In microelectronics, these reactions are classified into two main types: silicon-transition metal reactions forming silicides and, where aluminum metallization is employed, aluminum-transition metal reactions leading to the formation of aluminides. At this time, both types of reactions have been investigated using a range of analytical techniques. Silicides involve the reaction of a polycrystalline metal film with single crystal Si or polycrystalline Si (polysilicon) as would be found in the contact to the source, drain, or gate of a complementary metal oxide semiconductor (CMOS) field effect transistor (FET) shown in Figure 1. 2.

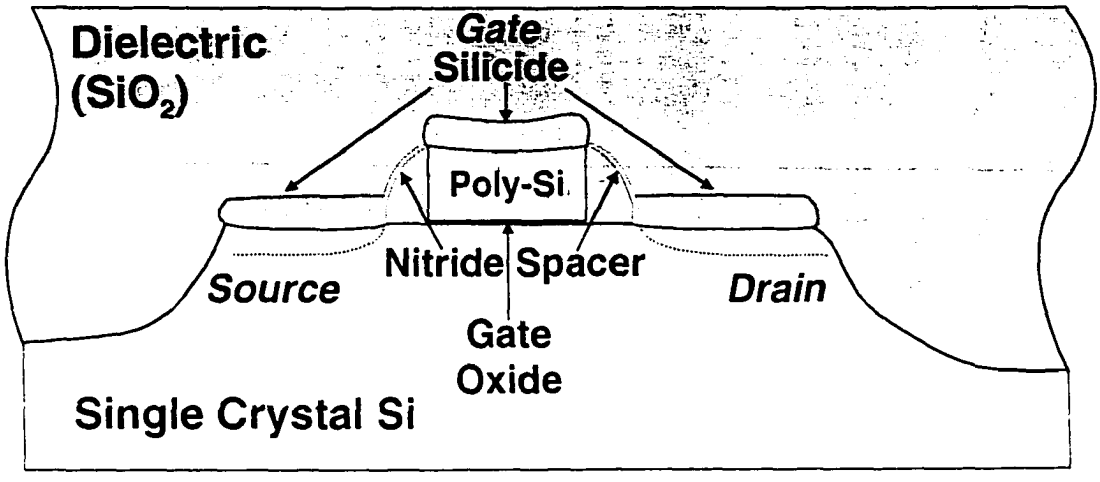

Figure 1. 2: Schematic illustration of a CMOS FET.

Silicides must be thermodynamically stable under normal operating conditions, i.e., the reaction should not proceed under operating conditions. Additionally, the compound formed should possess as low a resistivity as possible to maintain compatibility with circuit design rules and to reduce power requirements. A particularly good example of the control of microstructure evolution and kinetics to optimize properties is found in the use of $TiSi_2$ for current CMOS technology.

1.1.1.1 Titanium Silicide

$TiSi_2$ is used in current microelectronic contact metallurgy schemes and is formed by the self-aligned silicide (salicide) process (Mann et al. 1995). In this process, the polysilicon gate is patterned and sidewall spacers are added between the gate and doped source and drain regions. The Ti is then deposited and reacted with the exposed Si regions to form the silicide. Finally, the remaining unreacted Ti is removed by a selective etch process. Usually, a second anneal is then performed to form the desired, low resistivity disilicide phase. The $TiSi_2$ phase can exist in two structures: a metastable, base-centered orthorhombic C49 structure with a high resistivity (60-70 $\mu\Omega$-cm) and a

face-centered orthorhombic C54 structure with a low resistivity (15-20 μΩ-cm) (Beyers and Sinclair 1985). Under typical conditions, the transformation of C49 to C54 occurs at high temperatures (> 700 °C). Therefore, the C54 is the desired structure due to its significantly lower resitivity, however, the high temperatures required for its formation place stringent demands on processing (Mann and Clevenger 1994). At such high temperatures, diffusion rates can lead to the undesirable agglomeration of the silicide (Lasky et al. 1991). Initially, C49 nucleates in the interface and grows laterally and vertically to form a continuous layer (Ma et al. 1993). Later investigations revealed that the C54 phase then nucleated heterogeneously at grain boundary triple junctions (Ma et al. 1995). Previous experiments had indicated that growth of the silicide was dominated by grain boundary diffusion (Corcoran et al. 1990). The importance of nucleation was also emphasized in studies on the effect of linewidth on the C49-C54 transformation temperature (Lasky et al. 1991; Privitera et al. 1998). Experiments using different widths of patterned Si lines found that the wider lines transformed at lower temperatures (Lasky et al. 1991) or in shorter times (Privitera et al. 1998) than thinner lines. The authors concluded that the thinner lines contained less potential nucleation sites (such as grain boundary triple junctions), and therefore, required higher temperatures or longer times to nucleate the $TiSi_2$ phase. Thicker lines, on the other hand, possessed a proportionally larger number of nucleation sites, thus allowing the transformation to proceed more rapidly at lower temperatures.

Due to the high temperatures necessary to form the low resistivity C54 $TiSi_2$, a new processing method was desired to induce the C54 transformation at lower temperatures. Thus, the goals of recent research efforts have been to reduce the

temperature required for C54 formation and to expand the process window for its formation. A solution was found in alloying the Ti with another element to influence the nucleation kinetics of the two phases. By adding a small amount of Mo by ion implantation (Mann et al. 1995), as a separate layer (Mouroux et al. 1996; Cabral, Jr. et al. 1997, Cabral Jr. et al. 1997a) or by co-deposition (Cabral, Jr. et al. 1997b), the nucleation barrier for C54 $TiSi_2$ was reduced and allowed the C49 phase to transform at lower temperatures. The reduction in transformation temperature was attributed to a refinement in the C49 grain size resulting in an increased density of nucleation sites for C54 (Mann et al. 1995; Cabral, Jr. et al. 1997; Cabral Jr. et al. 1997a; Cabral, Jr. et al. 1997b), or the presence of a $(Ti,Mo)Si_2$ compounds with a C40 structure that act as structural templates for the C54 (Mouroux et al. 1996; Kittl et al. 1998; Zhang et al. 1999; Mouroux and Zhang 1999) . The C40 structure of the $(Ti,Mo)Si_2$ more closely matches the C54 structure than the C49 $TiSi_2$ and can therefore reduce the nucleation barrier and lower the transformation temperature.

The examples of silicide formation and the C49-C54 transformation of $TiSi_2$ highlight several important aspects of thin-film transformations. First, often a distinct and immutable reaction sequence resulting from the selection of certain phases is observed, in this case, the formation of an amorphous silicide followed by the nucleation and lateral growth of C49 $TiSi_2$, then a polymorphous transformation from C49 to C54. Second, is the importance of obtaining accurate information on the crystal structures of the phases that are forming during the reaction. Without the use of diffraction techniques, the reason for the high resistance $TiSi_2$ could have been attributed to different causes and not the presence of a different crystal structure. Clearly, an analysis that

measures composition distributions such as Rutherford backscatter spectrometry (RBS) or secondary ion mass spectrometry (SIMS) would not provide an accurate result. Third, the C49-C54 transformation emphasizes the importance of nucleation in phase selection. The presence of nucleation barriers leading to the selection of a particular phase has been observed in other Si systems including Ni/ amorphous Si (Clevenger et al. 1988) Clevenger and Thompson 1990) and V/amorphous Si (Clevenger et al. 1990a). Nucleation selection is distinctly different from models that use growth kinetics to predict phase formation (Gösele and Tu 1982, Gösele and Tu 1989). A nucleation model can explicitly incorporate microstructure parameters such as nucleation site density or grain size. The relative effects of interface and surface energies in addition to grain boundary diffusion and changing composition gradients can be included as well (Coffey et al. 1989; Barmak and Coffey 1993; Coffey and Barmak 1994; Coffey and Barmak 1994b). These factors play a prominent role in phase transformations in thin films structures. Therefore, nucleation-selected phase formation should be considered before applying a model based on growth kinetics alone. Lastly, the case of $TiSi_2$ formation highlights the importance of as-deposited and reacted film microstructures when considering phase transformations in thin films. This is analogous to the effect of grain size on electromigration where a particular grain structure enhanced electromigration lifetimes. In the case of $TiSi_2$ formation, a certain type of grain structure or composition catalyzes the formation of the C54 structure.

1.1.1.2 Aluminide Reactions

There is another class of reactions extensively employed in semiconductor metallization. These reactions involve the patterned sub-micron wires that connect the

discrete devices on a chip (back-end-of-line (BEOL) technology). Until recently, Al was used exclusively as the conducting material in CMOS and dynamic random access memory (DRAM) products. New designs have begun to implement Cu as the interconnect material, but Al has persisted due to its process compatibility and the installed infrastructure of design and process tools available. The reaction products of Al with other metals, termed aluminides, have attracted significant interest due to their improvement of the reliability of integrated circuits (Howard et al. 1978; Estabil et al. 1991). A review of aluminide formation in several transition metal systems prior to 1990 has been provided by Colgan (1990).

Researchers discovered that by adding a thin layer of Ti either below or above the Al line, electromigration resistance could be significantly increased as shown in Figure 1. 3. This effect was attributed to the presence of a thin layer of $TiAl_3$ intermetallic that formed during process anneals at temperatures < 400 °C (Howard et al. 1978; Estabil et al. 1991, Guthrie et al. 1992). The $TiAl_3$ layer was found to serve as a current shunt in case of void formation in the primary Al conductor. The Ti underlayer also provided benefits of improved adhesion to the dielectric material (SiO_2) isolating the different metallization levels. In addition, it improved the texture of the deposited Al film which was later found to be another important factor in the improvement of electromigration resistance, as previously mentioned.

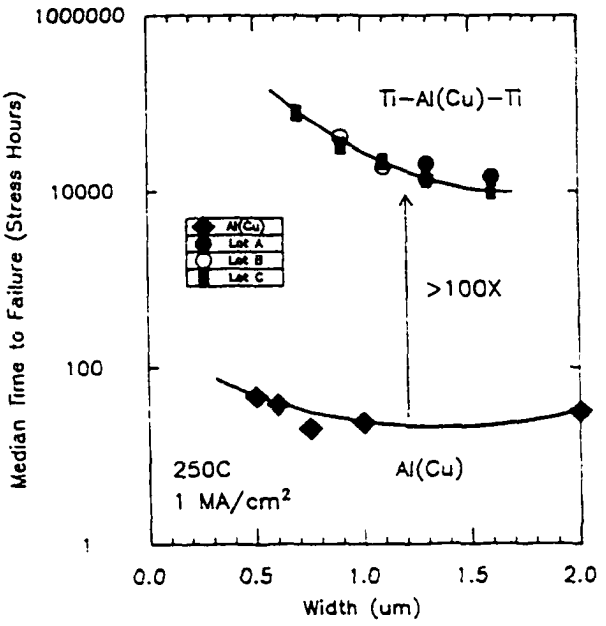

Figure 1. 3: Comparison of electromigration data with Ti/Al(Cu)/Ti metallization and Al(Cu) (from Estabil et al. 1991).

The disadvantage of the intermetallic compound was the increase in resistance caused by its presence shown in Figure 1. 4. Therefore, processing needed to be carefully controlled so as to provide the amount of intermetallic that would provide the maximum benefit to electromigration resistance while maintaining a sufficiently low line resistivity to meet performance requirements (Sullivan 1994).

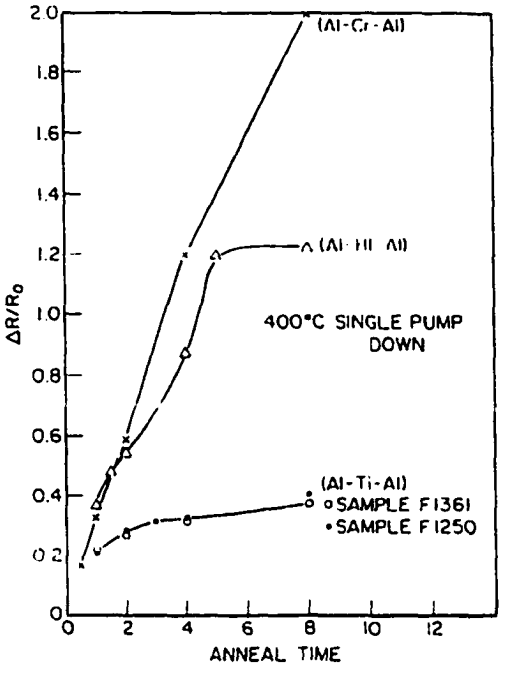

Figure 1. 4: Graph showing fractional increase in sheet resistance of Al-Ti, Al-Hf, and Al-Cr couples as a function of annealing time at 400 °C (from Howard et al. 1978).

As a result of the need to obtain the optimum aluminide thickness, many early studies of both aluminide (and silicide) reactions focused almost exclusively on the growth kinetics of compound formation. Data acquired included activation energies for compound growth and exponential prefactors to be used to calculate diffusivities at a given temperature. The effects of impurities (such as oxygen) on compound growth kinetics were also investigated. The diffusion data could be used to determine the time necessary to form a particular thickness of the product phase at a given temperature. This information could then be used in processing the interconnects. The majority of this early kinetic data was provided by "area averaging" techniques such as RBS. The commensurate descriptions of microstructural evolution were sparse, often lagged behind the kinetic studies, and were not as broad in scope. However, as stated earlier, with device and interconnect dimensions becoming comparable to microstructural length

scales, the grain structure acquires a greater importance in controlling the performance and reliability of IC's. In addition, new circuit materials and processes will impact film microstructures and the resulting resistance of the lines to electromigration. The use of improved conductor, diffusion barrier, and contact materials need to be actively researched to attain the performance goals for forthcoming device generations. The trends for decreasing circuit sizes while increasing computing power are forecasted to continue into the next millennium (National Roadmap for Semiconductors 1997). Further understanding of reaction kinetics on the nanometer length scale requires the direct observation of the microstructural changes during the transformation. Systematic investigations using techniques such as transmission electron microscopy (TEM) or orientation imaging microscopy (OIM) are necessary to advance the understanding of thin film reactions. This approach serves to complement kinetic data obtained through calorimetry and texture information obtained from X-ray diffraction (XRD).

The work described in this thesis applies this investigative approach to the study of phase transformations in Nb/Al and Ti/Al thin films. While both display qualitatively similar kinetics during the formation of the first phase XAl_3 (X = Nb,Al), Ti/Al is found to be more complex due to the formation of two metastable superlattice structures of $TiAl_3$ during phase formation. The presence of these superlattices complicates microstructure interpretation and the measurement of reaction kinetics.

By contrast to Ti/Al, the Nb/Al system was found to be an example of ideal two-stage kinetic behavior (discussed below) that involves no metastable phases. This allows for a more definitive description of the underlying microstructure evolution that occurs

during the reaction. As mentioned earlier, Ti/Al is also of interest technologically for use in integrated circuits employing Al metallization.

Several aluminide systems have been observed to exhibit unique kinetic behavior. This has been reported predominantly from DSC experiments involving the reaction of multilayer thin-films. These kinetics are characterized by presence of two, separated exothermic peaks found during constant heating rate experiments. *Ex situ* characterization methods such as XRD and TEM have found that both of the exothermic peaks can be attributed to one phase. However, the temporal evolution of the microstructure during the transformation has not been extensively studied. Note that in thin-film aluminide reactions the first phase that forms is usually the most aluminum-rich, and typically of the stoichiometry XAl_3 (Colgan 1990).

Observation of this two-stage reaction behavior has become somewhat common for the formation of the first phase in aluminide systems and to date has been observed in: Ag/Al → Ag_2Al (Baglin et al. 1978, Roy and Sen 1992), Nb/Al → $NbAl_3$ (Coffey et al. 1989, Coffey et al. 1992, Barmak et al. 1998, Lucadamo et al. 1999a), Ni/Al → $NiAl_3$ (Ma et al. 1991, Barmak et al. 1996, Barmak et al. 1997), Ti/Al → $TiAl_3$ (Michaelsen et al. 1996, Wöhlert 1995), and Co/Al → Co_2Al_9 (Emeric et al. 1998). Some of the characteristic constant-heating-rate DSC data is shown in Figure 1. 5. A detailed discussion of the Ti/Al and Nb/Al data will be presented in Chapter 4.

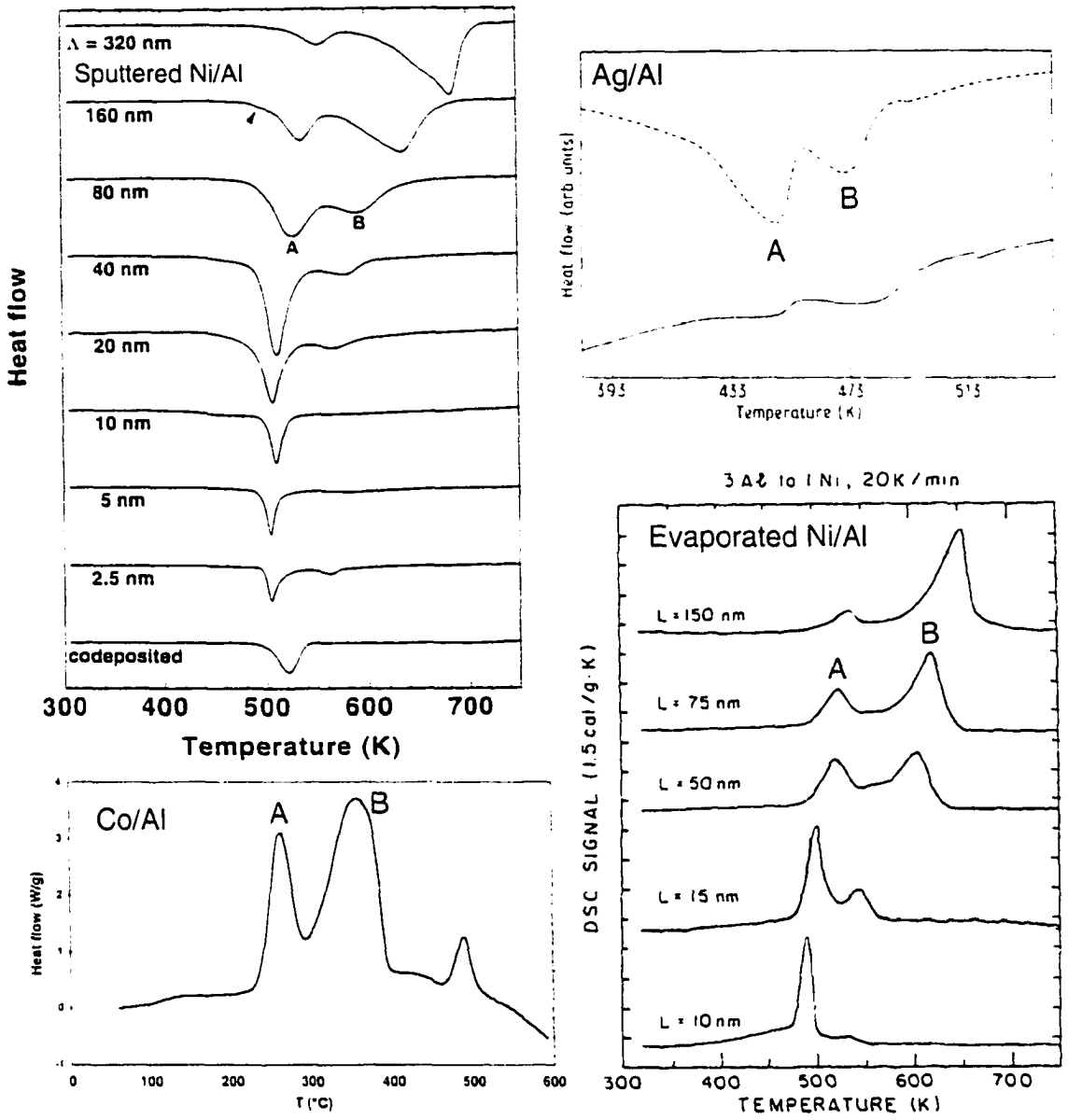

Figure 1. 5: Data from the literature showing two-stage reactions in several transition metal aluminide systems (see text for references). Note that the direction of exothermic heat flow is down for sputtered Ni/Al and Ag/Al, while it is up for Co/Al and evaporated Ni/Al.

In addition, two stage reactions have been observed in silicide systems shown in Figure 1. 6 including Ni/amorphous-Si →$NiSi_2$ (Clevenger et al. 1988, Clevenger and Thompson 1990) and V/amorphous-Si → VSi_2 (Clevenger et al.1990a).

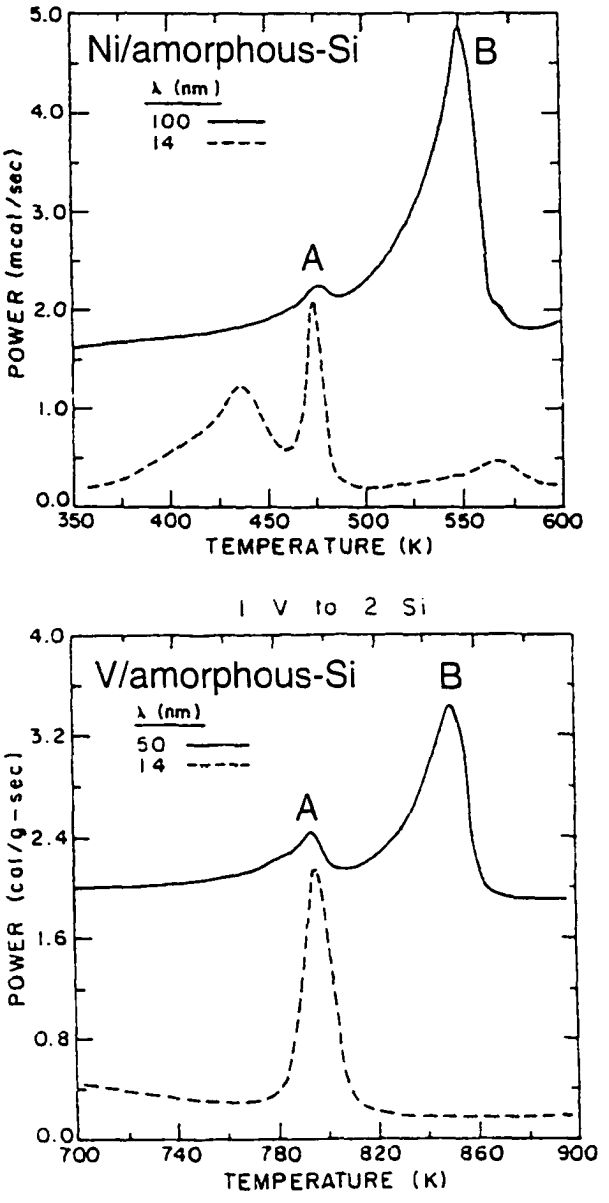

Figure 1. 6: Data from the literature showing two-stage reactions for two amorphous-Si thin-film systems (see text for references). Note the exothermic direction is up.

The prevalence of this phenomenon in technologically important thin-film materials systems where microstructure control is paramount to obtaining the optimum properties underscores the importance of a clear understanding of the underlying reaction mechanisms and causes for the observed behavior.

1.2 Research Objectives

Despite the ability of the model of Coffey et al. (1989) to provide a description of a two-stage reaction mechanism, verification of the assumptions of the model has not been accomplished. In addition, existing literature on the effects of dilute Cu additions on as-deposited film texture and the activation energies of the formation of $NbAl_3$ and $TiAl_3$ is incomplete. Many studies have reported kinetic results from only one or two Cu concentrations for bilayer films of a single thickness with limited microstructural observations to augment the kinetic studies. Activation energies have been determined using a range of techniques on films deposited using different methods. However, cross-comparison of existing data to identify underlying kinetic trends is difficult.

In light of these inconsistencies, the objectives of the research presented here are as follows: Experiments will be designed to provide a systematic and quantitative description of the reaction kinetics of Nb/Al and Ti/Al *multilayer* thin-films as a function of layer thickness and Cu concentration, as well as providing critical evidence of microstructure evolution during $NbAl_3$ formation to compare with the predictions of the Coffey et al. model. Reaction kinetics, including activation energies and Avrami exponents, will be quantified by DSC and *in situ* XRD experiments. Microstructure and texture data will be obtained by TEM and XRD. The microscopy results will focus primarily on the formation of $NbAl_3$ from Nb and pure Al multilayers since this system exhibits nominally model behavior. It is postulated that this experimental methodology in combination with the complementary analytical techniques listed above will provide a more complete and unambiguous description of solid state phase formation in the Nb/Al and Ti/Al thin-film systems.

2 Background

2.1 The Nb-Al System

The Nb-Al phase diagram contains three intermetallic phases: Nb_3Al, Nb_2Al, and $NbAl_3$ (Lundin and Yamamoto 1966, Jorda et al. 1980, ASM Handbook 1992) as shown in Figure 2. 1. No metastable phases or polymorphous transformations have been reported during the annealing of Nb/Al thin-films or alloys.

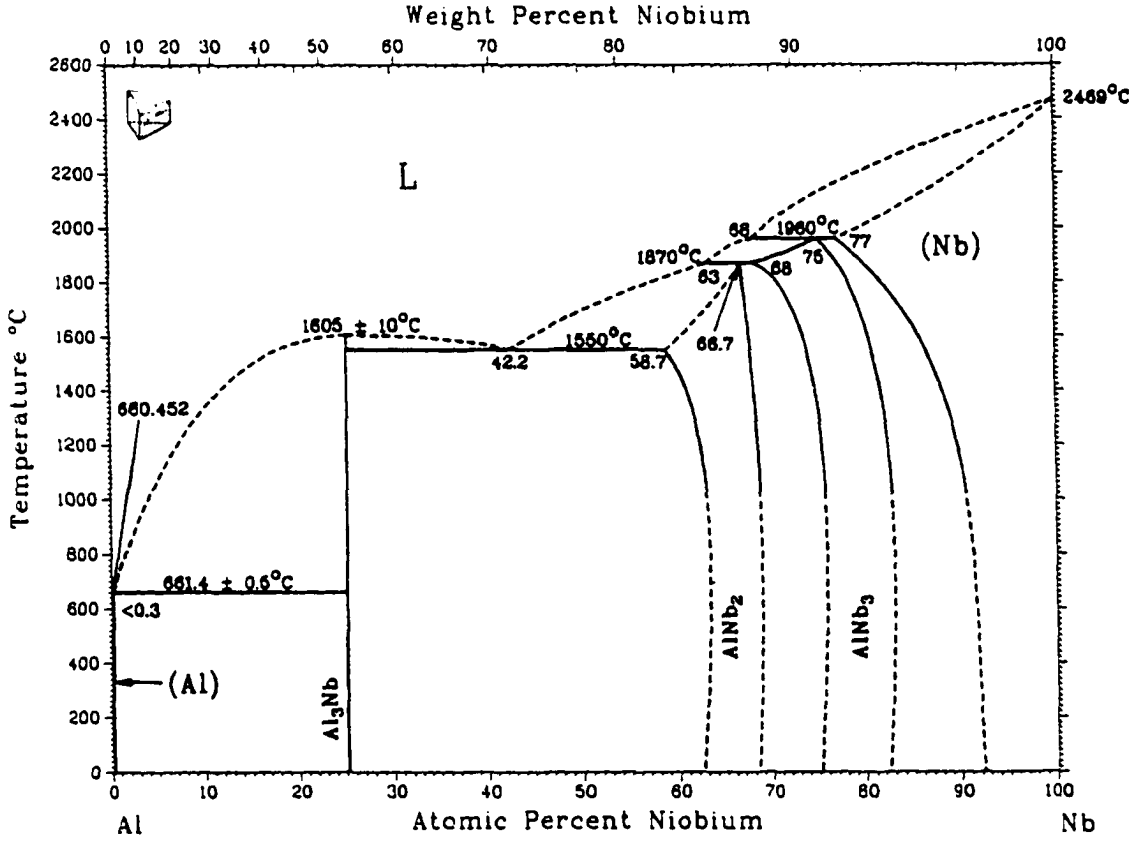

Figure 2. 1: The equilibrium Nb-Al phase diagram (from ASM Handbook 1992).

Initial interest in Nb/Al thin-film reactions resulted from the potential use of Nb_3Al wire in high temperature superconducting magnets (Im et al. 1988, Im and Morris 1988b, Barmak et al. 1990, Coffey et al. 1992). Experiments using bulk samples revealed that the equilibrium phase, $NbAl_3$, formed first (Ogurtani 1972). The selection

of $NbAl_3$ and the subsequent formation of other Nb-Al phases was investigated later in more detail using vacuum-deposited thin-films (Im et al. 1988, Im and Morris 1988b, Barmak et al. 1990). The $NbAl_3$ phase is essentially a line compound with a narrow composition range. For films with excess Nb, the complete sequence of phases was observed (Barmak et al. 1990):

$$Nb + Al \rightarrow NbAl_3 + Nb \rightarrow$$

$$Nb + NbAl_3 \rightarrow Nb + Nb_3Al + Nb_2Al + NbAl_3 \quad *$$

* phase(s) determined by overall stoichiometry and multilayer periodicity.

The equilibrium Nb-Al intermetallic phases and their crystal structures are listed in Table 2. I.

Table 2. I: Equilibrium Intermetallic Phases in the Nb-Al system.

Phase	Composition (at.% Nb)	Lattice Parameter [nm]	Pearson Symbol	Space Group	Structur-bericht
(Al)	< 0.3		*cF*4	*Fm*3*m*	*A*1
Al_3Nb	25	3.845 PDF 13-0146	*tI*8	*I*4/*mmm*	$D0_{22}$
$AlNb_2$	58.7 to 68		*tP*30	$P4_2/mnm$	*D*8b
$AlNb_3$	68 to 82	5.184 PDF 12-0085	*cI*2	*Pm*3*n*	*A*15
(Nb)	77 to 100		*cI*2	*Im*3*m*	*I*2

As mentioned previously, $NbAl_3$ formation exhibits two stages. The activation energies and the effect of dilute Cu additions will be presented in Chapters 4 and 5. The concurrent microstructural development during these two stages will be described in Chapter 6.

2.2 The Ti-Al System

As seen in the Ti-Al phase diagram shown in Figure 2. 4, the Ti-Al system consists of four intermetallic phases that include Ti_3Al, TiAl, $TiAl_2$, and $TiAl_3$. Also indicated on the phase diagram are the metastable superlattice structures of $TiAl_3$. The crystal structures for the different Ti/Al compounds are listed in Table 2. II.

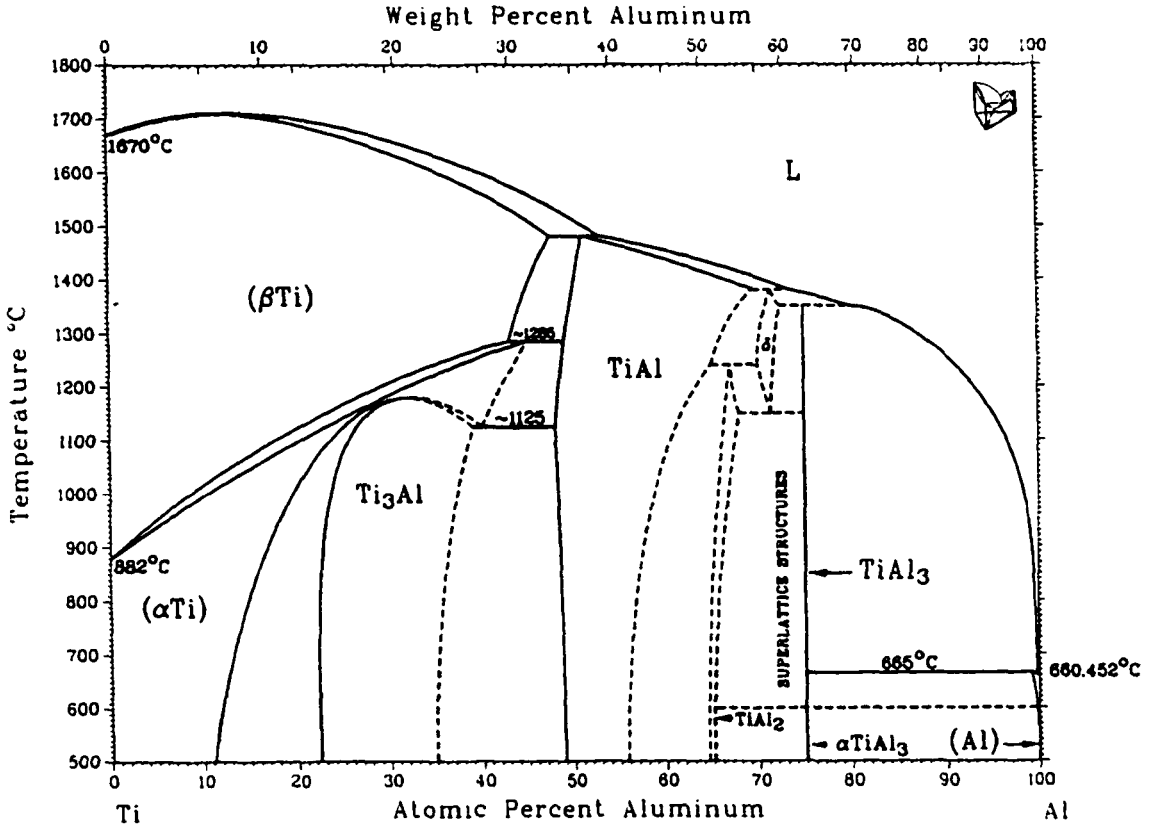

Figure 2. 2: Equilibrium phase diagram for the Ti-Al system (ASM Handbook 1992).

Table 2. II: Crystal structures for metastable and equilibrium intermetallic compounds found in the Ti/Al system (* indicates a metastable phase or structure).

Phase	Pearson Symbol	Space Group	Strukturbericht
Al_3Ti	*tI*8	*I*4/*mmm*	$D0_{22}$
Al_3Ti^*	*tI*16	*I*4/*mmm*	$D0_{23}$
Al_3Ti^*	*cP*4	*Pm*3*m*	$L1_2$
$Al_{23}Ti_9$	*tI*32	*I*	
Al_2Ti	*tI*24	$I4_1/amd$	
Ti_3Al_5 *	*tP*32	*I*4/*mbm*	
TiAl	*tP*4	*P*4/*mmm*	$L1_0$
Ti_3Al	*hP*8	$P6_3/mmc$	$D0_{19}$

The compounds of Ti and Al have attracted interest due to their low density and high temperature resistance for use in applications such as aircraft engines. Ti-Al compounds are also featured prominently in Al metallization for integrated circuits as described in chapter 1. Research into reactions of Ti/Al thin-films is closely related to the latter application and is of interest to the work here. Typically, the temperatures and compositions (Al-rich) involved in semiconductor processing lead to the formation of the $TiAl_3$ phase in one of its structural variants. Experiments have shown that, as in Nb-Al, the tri-aluminide phase, $TiAl_3$, forms first in both bulk (van Loo and Rieck 1973) and thin-film systems (Bower 1973). Recent experiments have indicated that the $TiAl_3$ will grow at the expense of preexisting Ti_3Al or TiAl phases in contact with Al, indicating its high kinetic stability in thin film reactions (Wöhlert 1995; Wöhlert et al. 1997; Wöhlert and Bormann 1999).

XRD and electron diffraction experiments have identified three polymorphous forms of $TiAl_3$ Figure 2. 3. The structures were identified (in order of temperature of

formation) as $L1_2$ (cubic superlattice), a tetragonal superlattice structure which has been observed to form with a DO_{23} structure, and the equilibrium DO_{22} (tetragonal) structure.

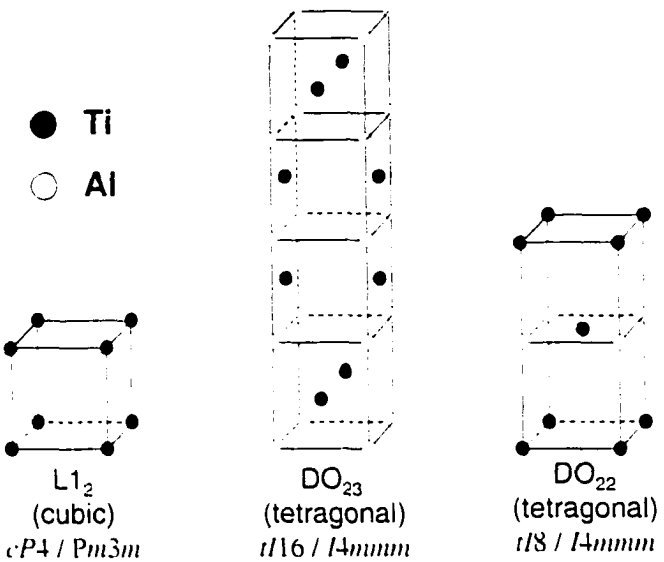

Figure 2. 3: Schematic illustration of the different crystal structures reported for the $TiAl_3$ phase.

Using ion beam mixing and thermal annealing of co-evaporated, multilayer, and bilayer samples, the formation of a cubic, $L1_2$ phase with a lattice parameter of 3.98 Å was first observed by Hong et al. (1988). The authors reported that the phase was stable until 450 °C whereupon it transformed directly to the equilibrium DO_{22} structure of the $TiAl_3$ phase. The formation of this metastable structure was attributed to a lower nucleation barrier to its formation (i.e., nucleation selection). Indeed, first-principles studies of phase formation in the Ti-Al system found a difference of only ~2.6 kJ/mol in the volume formation energy between DO_{22} and $L1_2$ with the DO_{22} structure slightly more stable as shown in Figure 2. 4 (Asta et al. 1992). Later isothermal and constant-heating-rate DSC studies found that a nucleation and growth process best described the formation of the $L1_2$ structure of $TiAl_3$ (Michaelsen et al.1996).

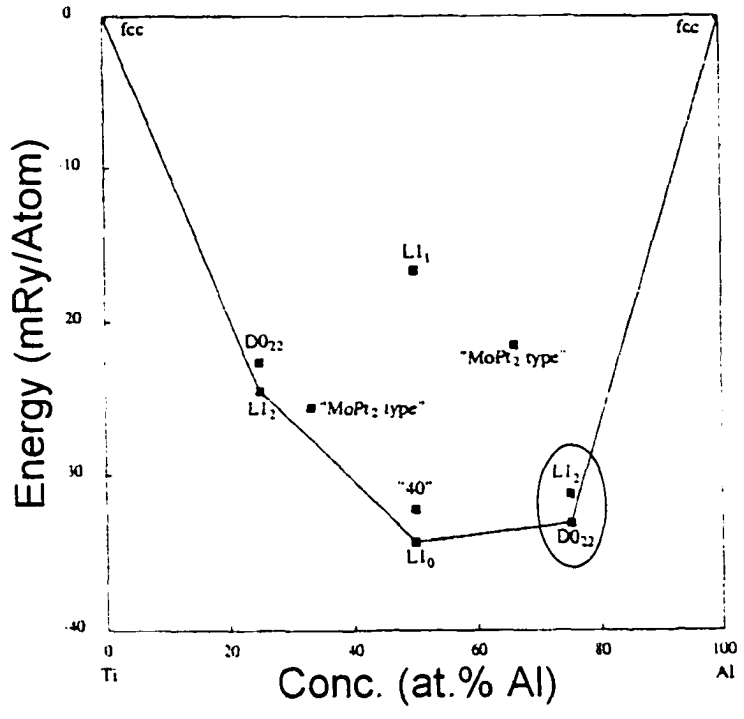

Figure 2. 4: Formation energies of Ti-Al intermetallic compounds as calculated by the full potential-linear muffin tin orbital method vs. the atomic concentration of Al. The solid lines connect the energetically stable structures (from Asta et al. 1992). Note: 1 mRy/atom = 1.312 kJ/mol.

The metastable $L1_2$ structure was also observed in annealing experiments conducted on mechanically alloyed powders produced by high-energy ball-milling (Srinivasan et al.1991). Using XRD analysis, the authors found that the structure was stable up to ~450 °C in agreement with the previous work. The measured lattice parameter of 3.967 Å was slightly smaller than that reported by Hong et al. (1988). The resulting d-spacings for the two measurements are listed in Table 2. III.

Table 2. III: d-spacings for the experimentally measured values of the lattice constant of the $L1_2$ structure of $TiAl_3$.

	Hong et al. (1988) (a = 3.98 Å)	Srinivasan et al. (1991) (a = 3.967 Å)
hkl	d (Å)	d (Å)
100	3.986	3.967
110	2.810	2.805
111	2.294	2.290
200	1.986	1.984
210	1.778	1.774
211	1.665	1.620
220	1.405	1.403
221	1.324	1.322
310	1.257	1.254
311	1.199	1.196
222	1.148	1.145

Unlike the previous work, the authors also observed an intermediate metastable DO_{23} phase before the transformation to DO_{22}. The phase was found to exist until ~800 °C when it was transformed to the equilibrium structure. Figure 2. 5 shows the limits of metastability of the $L1_2$ and DO_{23} structures of $TiAl_3$. In this case, an argument for metastability of a DO_{23} structure was presented based on the lattice mismatch to Al. The authors calculated an increasing mismatch of 2.0 %, 3.9 %, and 5.4 % for the $L1_2$, DO_{23}, and DO_{22} phases, respectively.

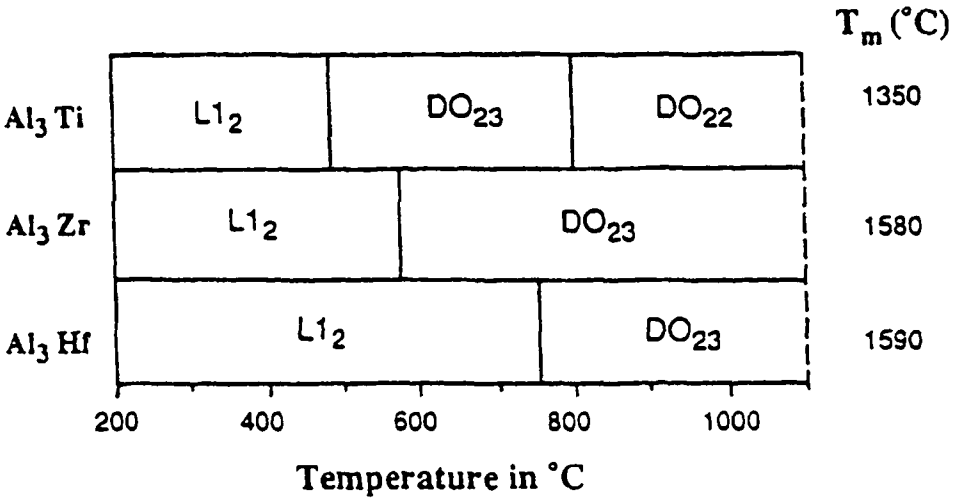

Figure 2. 5: Thermal stability of the metastable and stable phases in mechanically alloyed Al_3X (X = Ti, Zr, and Hf). (From Srinivasan et al. 1991)

The formation of the DO_{23} phase was also later reported in multilayer thin film annealing experiments and detected by XRD (Michaelsen et al. 1996) and electron diffraction (Wöhlert 1995). In these cases, the DO_{23} phase found to form at ~475 °C and transformed to DO_{22} between ~527 and ~727 °C. Since *ex situ* XRD measurements were used to characterize the structure and no measurable heat release was observed in the calorimeter, the exact temperature range of metastability of the DO_{23} structure could not be ascertained. The lower transformation temperature for the $DO_{23} \rightarrow DO_{22}$ in the thin film experiments compared with the ball milling could be due to the short diffusion distances present in the deposited films. There is also the possibility of a larger fraction of high diffusivity paths, especially grain boundaries, that could facilitate phase formation. Also, note that the DO_{23} and DO_{22} phases could co-exist in a small temperature regime, thus demarcation of a specific temperature could be somewhat arbitrary depending on the experimenter. The DO_{23} phase closely resembles the Ti_8Al_{24} structure first reported by van Loo and Rieck (1973). This structure has been observed in

sputtered bilayers with thicknesses of 6 nm Al and 4 nm Ti annealed for 30 min at 380 °C (Han et al. 1985). At lower Al thicknesses another tetragonal compound was formed, but could not be identified. The authors suspected it to be a ternary Al-Ti-Si compound, formed as a result of the reaction with the Si substrate.

Still other studies of Ti/Al thin-film reactions discovered the formation of the body-centered-tetragonal Ti_9Al_{23} phase first observed in high temperature anneals (730 °C) of bulk alloys with a composition of $Ti_{28}Al_{72}$ (Raman and Schubert 1965). Early thin film investigations identified this phase in evaporated Ti/Al bilayers and trilayers where it was stable from 325-440 °C (Howard et al. 1976). Later, Ti_9Al_{23} was observed in sputtered multilayers and found to be stable up to at least 550 °C (Ball and Todd 1987). This phase was also observed using electron diffraction in RF sputtered Ti/evaporated Al bilayers after annealing to 400 °C (Fujimura et al. 1989). Above 500 °C, a mixture of Ti_9Al_{23} and DO_{22} $TiAl_3$ was observed. The Ti_9Al_{23} phase was again identified in more recent studies by XRD and TEM in Ti/Al electron beam evaporated multilayers deposited at elevated temperatures, but was notably absent in similar films that were sputtered (Rodbell et. al 1991; Rodbell 1992).

The slight differences in structure may lead to discrepancies in the literature when identifying the DO_{23} structure of $TiAl_3$ or the Ti_9Al_{23} phase. The similarity is evident when comparing the lattice parameter and unit cell dimensions of the three studies of the superlattices in the literature (Table 2. IV). The reason for the selection of one superlattice structure/composition over another is still unclear. The results suggest that overall sample stoichiometry may have a significant effect on which superlattice structure will form as surmised by van Loo and Rieck (1973). If excess Ti is present, the Ti_9Al_{23}

phase will form prior to DO_{22} $TiAl_3$. However, if the sample is fabricated at the correct stoichiometry or with excess Al, the Ti_8Al_{24} phase with essentially a DO_{23} structure will form. The second postulate is borne out by experiments where alloy powder mixtures with excess Al resulted in DO_{23} $TiAl_3$ during subsequent annealing (Srinivasan et al. 1991).

Table 2. IV: Summary of the lattice parameters of the tetragonal superlattice phases observed in the Ti-Al system.

Reference	Composition	a (Å)	c (Å)	c/a	Temp. Range (°C)
Raman and Schubert (1965)	Ti_9Al_{23}	3.85	33.46	8.692	up to 780
van Loo and Rieck (1973)	Ti_8Al_{24}	3.875	33.84	8.732	585 - 638
Srinivasan et al. (1991)	Ti_8Al_{24}	3.890	33.64	8.649	500 - 750

A comparison of the d-spacings used to identify the different compounds is shown in Table 2. V.

It is interesting to note that, electromigration experiments performed on patterned lines revealed that particular type of Ti/Al intermetallic can affect lifetimes (Rodbell et al. 1991, Gupta et al. 1993). For samples without any measured Ti_9Al_{23}, the mean time to failure (T_{50}) was ~12,000 hours with a low standard deviation, σ. However, when samples were over-annealed resulting in the formation of Ti_9Al_{23}, the mean time to failure dropped to only 339 hours and σ doubled. This difference was attributed to the presence of the Ti_9Al_{23} phase formed by the extended anneal. The resulting electromigration measurements are shown in Figure 2. 6.

Table 2. V: d-spacings for the different $TiAl_3$ phases with a tetragonal structure.

d($TiAl_3$) DO_{22} JCPDS 37-1449 a = 3.8537 c = 8.5839	d(Ti_9Al_{23}) JCPDS 18-0069 a = 3.85 c = 33.46	d(Ti_8Al_{24}) van Loo and Rieck (1973) a = 3.875 c = 33.84	d($TiAl_3$) DO_{23}* Srinivasan et al. (1991) a = 3.890 c = 16.822
4.29 (002)			
	4.2 (008)	4.23 (008)	4.21 (004)
		3.86 (101)	
			3.79 (101)
	3.62 (013)	3.67 (103)	
3.52 (111)			
	3.34 (0010)	3.37 (105)	
			3.20 (103)
		3.03 (107)	
2.72 (200)	2.72 (110)	2.74 (110)	2.75 (110)
	2.57 (0013)		2.55 (105)
		2.41 (1011)	
	2.38 (1011)		
2.30 (113, 202)	2.28 (118)	2.30 (118)	2.30 (114)
2.15 (004)			
	2.09 (0016)	2.12 (0016)	2.10 (008)
1.93 (220)	1.92 (200)	1.94 (200)	1.95 (200)
1.75 (222)		1.76 (208)	1.77 (204)
		1.71 (213)	1.73 (211)
1.69 (204,311)	1.69	1.68 (1116)	1.68 (0010)
			1.662 (213)
		1.62 (1019)	
1.57 (115)			1.56 (215)
		1.51 (2014)	
1.48 (313)			
1.43 (006,224)	1.41 (1022)	1.43 (2016)	1.43 (208)
1.36 (400)	1.36 (220)	1.37 (220)	1.38 (220)
			1.31 (224)
			1.29 (301)
1.27 (116)		1.26 (1124)	1.27 (2010)
			1.25 (1112)
			1.22 (312)
			1.21 (305)
1.17 (303,312)	1.17 (318)	1.18 (318)	1.18 (314)

$ZrAl_3$ prototype JCPDS 02-1093

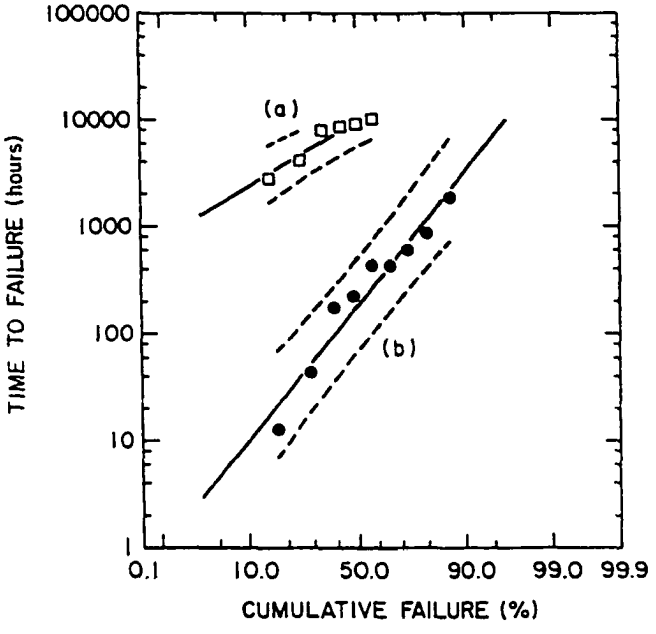

Figure 2. 6: A log-normal cumulative failure distribution of 1.1 μm wide 25 nm Ti/ 950 nm Al-0.5 wt.% Cu/25 nm Ti/ 25 nm Al-0.5 wt.% Cu samples at 250 °C, 2.5 x10^6 A/cm^2: (a) annealed at 400 °C for 1 hour in 90% N_2-10% H_2 with T_{50} = 12744 hrs, σ = 1.0 and (b) over-annealed (22-550 °C at 3 °C/min in He) with T_{50} = 339 hours, σ = 2.1. XRD of the over-annealed sputtered samples indicated the presence of Ti_9Al_{23}.

The authors postulated that a larger point defect density would be expected in Ti-Al superlattices than in the stoichiometric $TiAl_3$ compound. This would then lead to increased diffusivity of Al through the superlattice layers resulting in decreased resistance to electromigration (Gupta et al. 1993). Thus, the determination of the expected phase based on a particular layer thickness and heat treatment would be important to obtain the maximum resistance to electromigration when using Ti-Al metallurgy.

In summary, experimental results have shown that in thin-film and bulk alloyed systems the formation of $TiAl_3$ was complicated by the presence of two metastable structures and possibly the formation of a Ti_9Al_{23} phase, which is also a superlattice. Although the formation of $L1_2$ and DO_{23} are detectable by calorimetry, the formation of

the equilibrium DO_{22} phase was only observed by X-ray or electron diffraction experiments. Further, the range of stability of the DO_{23} phase may be less than 200 °C making its observation difficult with techniques such as *in situ* TEM.

3 Experiment

3.1 Film Deposition

3.1.1 EPI Systems Ultra-high Vacuum Sputtering System

All films were sputter-deposited using a load-locked ultra-high vacuum (UHV) sputtering system custom manufactured by EPI Systems Inc. (White Bear Lake, MN). A schematic diagram featuring the primary aspects of the system is shown in Figure 3. 1.

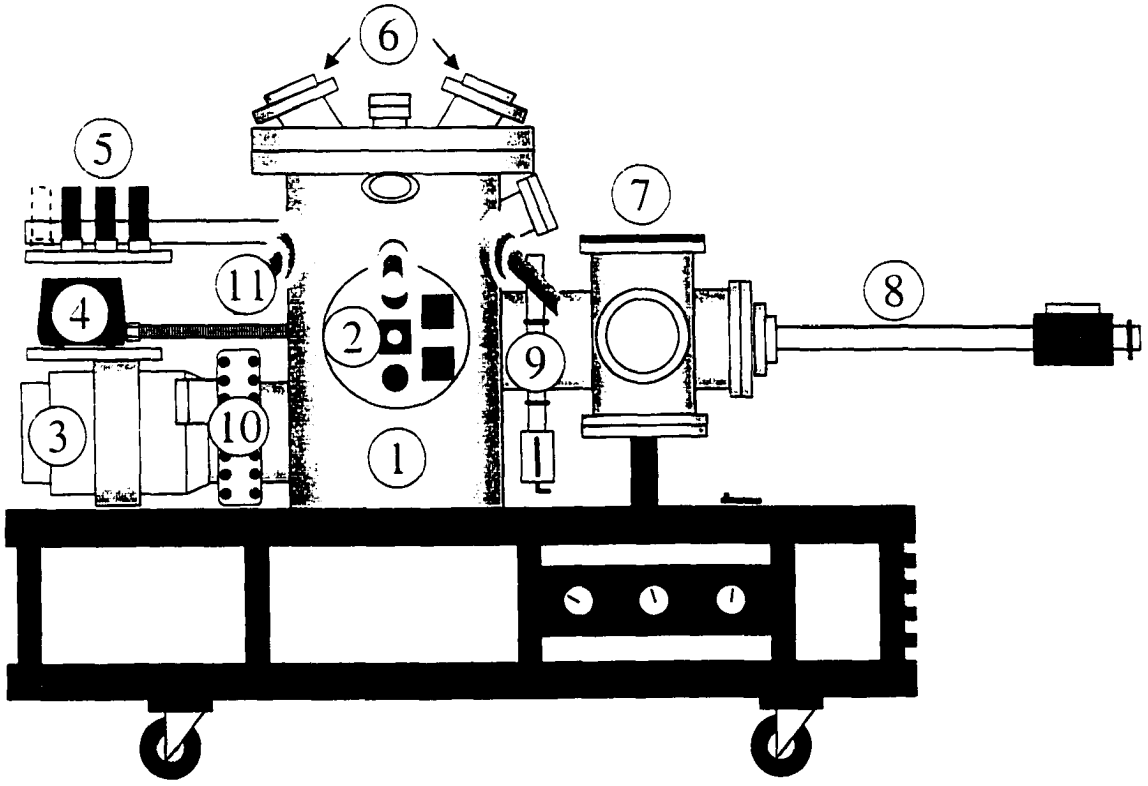

Figure 3. 1: Schematic illustration of the EPI UHV sputtering system used to deposited the films for study.

All seals on the deposition chamber were made using conflat flanges and OFHC Cu gaskets. Gas feed-throughs were connected using VCR (Swagelok Inc., Solon, OH) fittings. The loading flange on the load lock chamber was sealed using an O-ring.

The deposition system consists of primarily two chambers joined by a short connecting tunnel. The larger chamber [**1**] was used for deposition, the second chamber [**7**] was the load lock and was designed to accept three 3" wafers positioned on Mo or Cu transfer rings. The rings were manipulated by an elevator and placed into the chamber using a magnetically coupled arm [**8**]. Ultrahigh vacuum levels were obtained using two turbo molecular pumps located on the load lock chamber (not shown) and the main work chamber [**3**]. These pumps are backed by diaphragm pumps (not shown), thus providing a completely oil-free pumping system. The deposition chamber turbo molecular pump has additional backing provided by a molecular drag pump. Pumping at low base pressures was also available through the use of a Ti-sublimation pump (not shown). The deposition chamber was water-jacketed to improve vacuum conditions by reducing residual gases during sputtering. After venting the system for target changes or maintenance, a system bake was performed for 36 hours at 150 ^{o}C to reduce the amount of adsorbed gases, especially water. After the bake, base pressures in the deposition chamber were reduced to ~3-4 x 10^{-9} Torr.

When the vacuum in the load lock reached an acceptable level, the substrates were transferred into the deposition chamber through the interchamber gate valve [**9**]. Note that sufficient vacuum levels had to have been achieved in the load lock (<10^{-7} Torr), to permit transfer of the substrates into the deposition chamber. Typically, the load lock was allowed to pump down for at least three hours before transferring substrates. If time allowed, the load lock was pumped overnight before opening the gate valve.

Once placed onto the stage [**2**], the substrates could be either heated, cooled using liquid nitrogen, rotated, or electrically biased during deposition. The system had four

magnetron sputter sources (two shown) arranged symmetrically and mounted in the top flange of the work chamber [**6**]. These sources were manufactured by U.S. Guns (CA) and accepted a variety of 3" diameter targets of thicknesses ranging from 1/16"-0.5". Three of the guns were operated by Advanced Energy (Fort Collins, CO) DC sources (2 - 1.5 kW, 1 - 1 kW). The fourth gun was connected to an Advanced Energy RF source (600 W) that was used for sputtering electrically insulating materials as well as conductive materials. Each gun had a shutter blade to control the deposition flux onto the substrate [**11**]. The shutter blade was linearly actuated by a pneumatic cylinder operated with compressed nitrogen. This nitrogen also actuated the valves for process gases and was used to vent the deposition and load lock chambers.

Gas flow and deposition pressure could be independently controlled by values set in the run recipe. Gas flow was set by a mass flow controller (MFC) (MKS Inc., Andover, MA). Three MFCs are mounted on the system with the space to add a fourth if needed [**5**]. Sputtering pressure was measured by a Baratron® capacitance manometer [**4**] (MKS, Andover, MA) and was controlled through a feedback loop connected to a stepper-motor driven gate valve [**10**] between the deposition chamber turbo molecular pump and the deposition chamber. Process gases were transported to the mass flow controllers using electropolished stainless steel tubing. The tubing was valved to allow for line purging before starting a run. One of the gas lines (Ar) was routed through a Gate-Keeper purifier (Aeronex, Inc. San Diego, CA) immediately before entering the MFC. The purifier reduced the amount of H_2O, O_2, CO, CO_2, and H_2 present in the sputtering gas. Ultra-high purity Ar (99.9995%) was used as the sputtering gas for the runs described in this work.

All deposition parameters were specified in a Microsoft Excel spreadsheet (recipe) and downloaded to the sputtering system automation controller. This module contained a microprocessor that executed the recipe through several analogue and digital outputs. Gun power, gas flow, gas pressure, substrate rotation, and shutter actuation were all automated over the course of the run. An automatic data logging system periodically recorded relevant deposition parameters during processing.

Deposition rates were calibrated by measuring the thickness of calibration films using a Tencor P-2 (KLA-Tencor, Inc. San Jose, CA) contact profilometer. Prior to deposition, a coarse grid pattern was drawn on the surface of a Si wafer using a fine point Sharpie® permanent marker. Films of different elements were deposited for a fixed length of time (usually 15 min) using the specified sputter parameters onto the patterned wafer. After deposition, the wafers were placed in a beaker of acetone to dissolve the ink and ultrasonically cleaned for ~10 min. The wafers were then removed and rinsed using a stream of ethyl or isopropyl alcohol and placed into a second beaker containing either ethyl or isopropyl alcohol. The wafers were sonicated for another 10 min and allowed to dry in a laminar flow hood. Ultrasonic cleaning was necessary to completely remove the marker residue and unwanted film from the Si surface. The deposition rate was determined from the average of 16 independent thickness measurements distributed over the surface of the wafer depicted in Figure 3. 2. Each value was obtained from an average of five scans with a scan-to-scan reproducibility of ± 1 nm. Uniformity was calculated by dividing the standard deviation of the measurement by the average thickness. Scans used a stylus force of 4 mg and a scan length of 500-1500 μm depending on the roughness of the films. Generally, a shorter scan was necessary to

clearly identify the step edges on less uniform or thinner films. Several single "test" scans were used to identify an area containing a clean step. All scans were performed from the substrate surface to the film surface (up step). This necessitated rotating the wafer by 180° for half of the scans. Due to the relatively low deposition power and gas pressure, as well as the long source-to-substrate distance (~25 cm), deposition rates for the elements used in this study did not exceed 0.2 nm/s. The exception to this was Cu that has a high sputtering yield and was deposited at higher power to give a deposition rate as high as 0.4 nm/s.

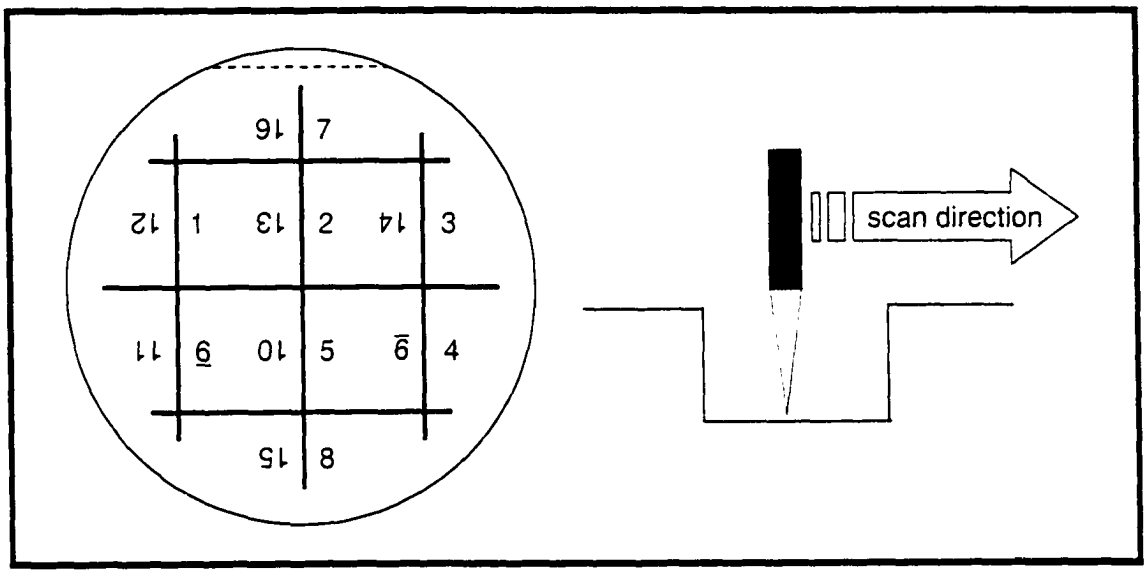

Figure 3. 2: Schematic of pattern and order of measurements used to calibrate the deposition rates for the various targets. Wafer was rotated 180° for half of the measurements to maintain an "up step" scan.

Using the measured deposition rates, deposition times for a 1-1.5 μm-thick multilayer ranged from 3-5 hours depending on the periodicity (number of shutter actuations) and the total thickness. The deposition rate of the targets tended to decrease with time, and needed to be recalibrated every 4-5 multilayer runs. The constantly decreasing deposition rate, coupled with long deposition and errors in thickness

measurements comprised the error in the overall stoichiometry of the multilayer. Sputtering targets were obtained from Pure Tech Inc. (Carmel, NY) and Target Materials Inc. (Columbus, OH). Respective target compositions, manufacturers, thicknesses, average deposition rate and uniformity are listed in Table 3. II. Uniformity and deposition rate decreased with increasing target erosion. For the Al and Al-Cu targets significant changes were noticed after 3-4 deposition runs (~12 hours of deposition). Note that the deposition rates of the Ti and Nb did not significantly change for longer times.

Table 3. I: Sputtering Targets and Deposition Parameters

Element	Purity [%]	Manufacturer	Thickness [in]	Ave.Dep.Rate [Å/s]	Uniformity [%]
Al	99.999	Pure Tech	0.25	1.08 ± 0.09	3.4
Al-0.5 wt.% Cu	99.999 each	Target Materials Inc.	1.0	1.45 ± 0.06	1.3
Al-1.0 wt.% Cu	99.999 each	Target Materials Inc.	1.0	1.39 ± 0.07	2.0
Cu	99.999	Pure Tech	0.25	4.2 (400 W)	2.0
Nb	99.95	Pure Tech	0.25	0.90 ± 0.08	2.3
Ti	99.995	Pure Tech	0.25	0.63 ± 0.06	3.0

Films were deposited under similar conditions to minimize any differences in as-deposited microstructures. The deposition parameters are listed in Table 3. II.

Table 3. II: Multilayer Deposition Parameters

Sputtering Gas:	Ar (99.9995%)
Flow Rate:	20 sccm
Gas Pressure:	2-3 mTorr*
Rotation:	10-16 RPM**
Power:	250 W DC
	(Cu 500 W DC)
Heating:	None***

*Slightly better uniformity was measured using 3 mTorr
**Higher rotation speeds were found detrimental to the life of the feed-through bearing assembly.
***Temperature estimated to be ~30-80 °C during deposition.

Silicon substrates with a (100) orientation were obtained from Wafernet Inc. (San Jose, CA). The substrates were ~450 μm thick and 3" (75 mm) in diameter with one side polished. Some of the wafers were thermally oxidized at the Fairchild Center at Lehigh University. The nominal oxide thickness was 100 nm. The presence of an oxide layer was necessary to prevent interdiffusion between Al and Si during *ex situ* annealing experiments for TEM and *in situ* XRD analyses. No special chemical cleaning procedure was employed before loading the substrates into the system. All substrates were cleaned with filtered, ionized N_2 (pre-purified grade) immediately before loading to remove particulates. Prior to deposition, substrates were degassed at 150 °C for 30 min. to remove any adsorbed water or gases. The base pressure typically increased by a decade during the degassing procedure, then rapidly recovered to its original level. Substrates were then allowed to cool to < 40 °C as measured by the stage thermocouple before deposition commenced. Targets were precleaned at the deposition power with the shutters closed for 2-5 minutes prior to deposition. When the target was not being used

to deposit a film, the power was reduced to 20 W to limit excess buildup of material on the source shutter while maintaining the plasma.

Films of various bilayer thicknesses, Λ, were deposited using the above procedure. The total thickness of the bilayer varied over the course of the study. Early depositions were 1.5 μm thick, later the thickness was reduced to 1 μm to reduce flake build-up in the system and to conserve consumable materials. For the films prepared specifically for synchrotron X-ray studies, a total thickness of 0.5 μm was used (even this was more than sufficient for the diffracted intensity). The total thickness was controlled simply by varying the number of times the bilayer was repeated. The individual layer thicknesses for film with a 1Nb/3Al stoichiometry are listed in Table 3. III.

Table 3. III: Bilayer period, Λ, and nominal thickness of the individual layers for the 1Nb/3Al and 1Nb/3Al(Cu) films used in this study.

Λ [nm]	d_{Al} [nm]	d_{Nb} [nm]
10	7.3	2.7
20	14.7	5.3
23.2	17	6.2
30	22	8
54.5	40	14.5
72	53	19
143	105	38
240	176	64
333	245	88

A similar approach was used for the 1Ti/3Al and 1Ti/3Al(Cu) samples. These multilayers were either 0.5 μm or 1.0 μm thick. The layer thicknesses are listed in Table 3. IV.

Table 3. IV: Bilayer period, Λ, and nominal thickness of the individual layers for the 1Ti/3Al and 1Ti/3Al(Cu) films used in this study.

Λ [nm]	d_{Al} [nm]	d_{Ti} [nm]
10	7.4	2.6
20	14.8	5.2
30	22.1	7.9
72	53.2	18.8
143	105.5	37.5
333	245.8	87.2

The overall composition of several multilayer samples was measured using a JEOL 733 Superprobe EPMA using wavelength dispersive spectroscopy (WDS). Pure element standards were used and characteristic X-ray intensities were obtained for the elements in the multilayer. A piece of wafer was diced from the center of the substrate. Al-K_{α} X-rays were collected using a TAP crystal with the Nb-L_{α} or Ti-K_{α} X-rays collected using a PET crystal. The accelerating voltage was limited to 15 kV in order to reduce the size of the interaction volume. No significant signal was detected for Si, indicating that the interaction volume was contained within the multilayer film (< 1μm). X-ray intensities were corrected using a $\phi(\rho z)$ program. Typically five points were taken from different areas on each specimen to provide an average concentration. The resulting films were found to be within 4 at.% or better of the desired stoichiometry of 75 at.% Al. The individual results obtained from these experiments are listed in Table 3. V and Table 3. VI.

Table 3. V: Results of EPMA analysis of selected sputtered Nb/Al multilayer films with thicknesses of 1 μm showing measured stoichiometry, the deviation from desired stoichiometry, and molar ratio of Al/Nb.

Run ID	Δ	Average	σ	Δ	Ratio
	23 nm				
021098a	Al at.%	72.79	0.24	-2.2	2.7
	Nb at. %	27.21	0.24	+2.2	
	54.5 nm				
020998a	Al at.%	72.21	0.13	-2.8	2.6
	Nb at. %	27.79	0.13	+2.8	
	72 nm				
031097a	Al at.%	75.13	0.20	0.1	3.0
	Nb at. %	25.13	0.64	0.1	
020798a	Al at.%	72.60	0.23	-2.4	2.7
	Nb at. %	27.40	0.23	+2.4	
	143 nm				
031397a	Al at.%	74.33	0.22	-0.7	2.9
	Nb at. %	25.67	0.22	+0.7	
021098b	Al at.%	71.52	0.13	-3.5	2.5
	Nb at. %	28.48	0.13	+3.5	
	240 nm				
020898a	Al at.%	70.60	0.04	-4.4	2.4
	Nb at. %	29.40	0.04	+4.4	
	333 nm				
100597a	Al at.%	72.77	0.26	-2.2	2.7
	Nb at. %	27.23	0.26	+2.2	

Table 3. VI: Results of EPMA analysis of selected sputtered Ti/Al multilayer films with thicknesses of 1 μm showing measured stoichiometry, deviation from desired stoichiometry, and molar ratio of Al/Ti.

Run ID	Δ	Average	σ	Δ	Ratio
	72 nm				
052198a	Al at.%	76.52	0.15	-1.5	**3.3**
	Ti at. %	23.48	0.15	+1.5	
	143 nm				
052298a	Al at.%	78.47	0.05	-3.5	**3.6**
	Ti at. %	21.53	0.05	+3.5	
	333 nm				
052498a	Al at.%	75.01	0.12	0.0	**3.0**
	Ti at. %	24.99	0.12	0.0	

4 Differential Scanning Calorimetry (DSC)

4.1 Introduction

The study of solid state reactions in thin-film transition metal aluminide and silicide systems continues to attract considerable interest. This interest is a result of the prevalence of thin-film reactions in microelectronics metallization that requires detailed knowledge of thermodynamic and kinetic reaction parameters in order to determine optimum processing conditions such as annealing temperatures and times. Differential scanning calorimetry (DSC) has proven to be an effective technique to obtain the relevant kinetic and thermodynamic information for solid-state thin-film reactions.

A power-compensated DSC consists of two isolated furnaces. The sample furnace holds a small amount of the material of interest while the reference furnace can be left empty or filled with an inert material (Michalesen et al. 1998). The furnaces are then heated or cooled using a specific temperature program involving a constant heating-rate or a constant temperature (isothermal). This can induce a transformation in the sample material such as melting, solid-state reaction, grain growth, etc. The change in sample temperature caused by the transformation is measured by a thermocouple in the furnace and fed into an analyzer. The analyzer then compares this temperature with the reference furnace temperature and adjusts the power to the reference furnace so that the two temperatures remain equal (i.e., $\Delta T = 0$). By operating in this mode, the DSC is able to directly measure the *rate* of heat release from an exothermic reaction given a known baseline. To reiterate, order to quantify the heat release, a baseline for the instrument must be established. For irreversible reactions, the baseline can be obtained by running the temperature program a second time. For reversible reactions the DSC must be run

with the furnaces empty, or with an inert substance in both furnaces that matches the heat capacity of the material of interest.

Several types of kinetic and thermodynamic information can be obtained by analyzing the output of the DSC. The total enthalpy released during the reaction is found by integrating the area bounded by the heat signal and baseline. The value for enthalpy must be normalized by the sample mass. This emphasizes the need for both accurate and precise weight measurements for the sample. By measuring peak onsets, the melting (or freezing) points of materials can be identified.

Depending on the type of transformation, kinetic information such as the Avrami exponent (Avrami 1939; Johnson and Mehl 1939) or activation energies can also be determined by using well-established methodologies (Kissinger 1957, Henderson 1979). These quantities are particularly useful in the study of solid-state reactions and require some additional data analysis. They will be discussed in detail in subsequent sections.

4.2 Background

4.2.1 Nb/Al Calorimetry

To date, several studies of the Nb/Al reaction using calorimetry techniques have been reported in the literature. The earliest reported work was performed by Ball and Todd (1987) on magnetron sputtered Nb/Al multilayers. The multilayers were composed of 9 layers: five layers of Al (400 nm thick) and 4 layers of Nb (40-120 nm thick). The actual thickness of the Nb layer shown in the DSC data was not specified in the paper. The films were studied in the temperature range of 250 °C to 600 °C. The results indicated two separated, exothermic peaks occurring at 383 °C and 569 °C, respectively Figure 4. 1. The authors attributed the first peak to the formation of $NbAl_3$, but could not

explain the formation of the second peak. Using the Kissinger analysis, the authors determined the activation energy for peak A and found it to be 1.56 eV.

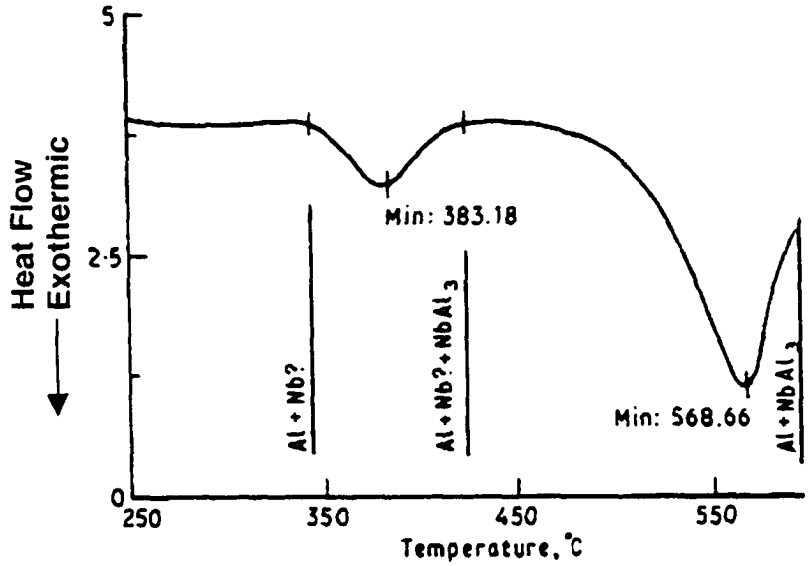

Figure 4. 1: DSC scan of a Nb/Al multilayer taken at 20°C/min (from Ball and Todd 1987).

The subject of Nb/Al reactions later gained attention for the potential use of Nb-aluminides in high temperature superconducting magnets. Understanding the kinetics of the solid state reactions was essential in order to form the stoichiometric superconducting Nb_3Al phase. Studies by Coffey et al. (1989, 1992) and Barmak et al. (1990) using differential thermal analysis (DTA) sought to clarify the kinetics of Nb-Al formation in thin films. Multilayer films were thermally evaporated with different bilayer thicknesses and overall compositions. In this case, the authors reported several important findings. Depending on the layer thickness and stoichiometry, one, two, or three peaks (A, B, and C) were observed as shown in Figure 4. 2.

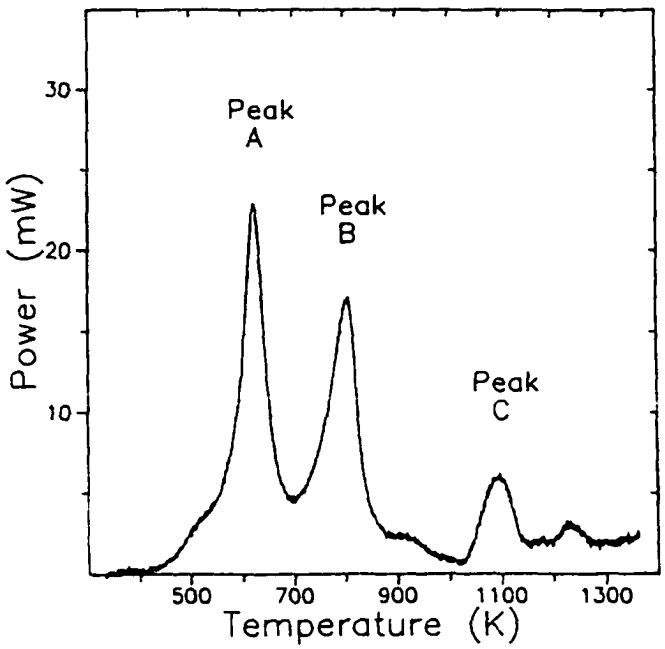

Figure 4. 2: Scanning calorimetry results from an evaporated 3Nb/1Al multilayer taken at a heating rate of 20 K/min. Peaks A and B are both stages of $NbAl_3$ formation. Peak C is the first stage of the formation of the A15 Nb_3Al phase (from Coffey et al. 1992).

As in the work of Ball and Todd (1987), two peaks (A and B) were observed in constant heating rate traces in films deposited with a molar ratio of 1Nb/3Al. Using *ex situ* XRD measurements at different points in the reaction, the authors concluded that both peaks (A and B were due to the formation of $NbAl_3$. A kinetic model describing how the formation of the two peaks could result from the presence of nucleation barriers in the interface was then developed by Coffey et al. (1989).

The model noted that the intermediate reduction in reaction rate could not be explained by a changeover from interface controlled growth where product thickness is directly proportional to time, to diffusion controlled growth, where the product layer thickness is proportional to $t^{0.5}$. Instead, it was necessary to invoke two distinct stages of phase formation that involved a change in the primary growth directions. Stage one was

due to the formation of product phase grains at isolated sites in the interlayer interface. These grains then grew predominantly in the plane of the interface (2-D) and formed a continuous product phase layer. The second peak arose from the 1-D thickening of the product phase normal to the interface. The stages of phase formation proposed in the model are shown schematically in Figure 4. 3.

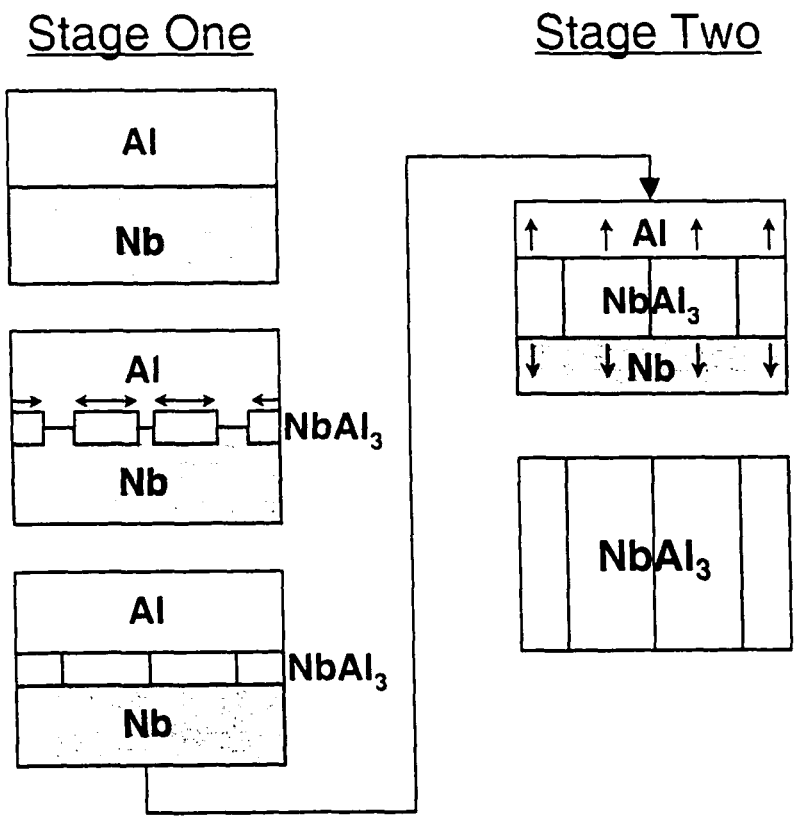

Figure 4. 3: Schematic illustration of stages one and two for thin film reactions, using the example of $NbAl_3$ formation in Nb/Al multilayer films.

The details of the kinetic model as developed by Coffey et al. (1989) are as follows. The first stage of the reaction (Peak A) was modeled by assuming that nucleation occurred from a fixed areal density (n) of nucleation sites in the interface. To simplify the modeling, the shape of the nuclei were chosen to be cylinders with height z_0

and radius r, with the radius in the plane of the interface. The growth rate of the nuclei in the plane of the interface was modeled as being interface limited:

$$\frac{dr}{dt} = K_{i0} \exp\left(-\frac{Q_i}{kT} \right). \qquad 4.1$$

Where K_{i0} and Q_i are the interface-limited growth prefactor and activation energy, respectively. The growth was assumed to occur two-dimensionally until the interface area had been consumed (i.e., the formation of a coalesced layer). For a random distribution of nuclei, the area fraction of the interface transformed can be described by a Johnson-Mehl-Avrami (JMA) expression. If the total area reacted without considering impingement of neighboring nuclei would be $n\pi r^2$, then the actual reacted area fraction, X_A, would then be described by

$$X_A = 1\text{-}\exp(-n\pi r^2). \qquad 4.2$$

Peak B of the constant-heating-rate traces was modeled as the diffusion-controlled thickening of the coalesced product layer. The product layer thickness, z, assuming an interdiffusivity with an Arrhenius temperature dependence could then be described by

$$\frac{dz}{dt} = \left(\frac{K_{d0}}{z} \right) \exp\left(-\frac{Q_d}{kT} \right). \qquad 4.3$$

where K_{d0} and Q_d are the diffusion-limited growth prefactor and activation energy, respectively.

The results of the interface-controlled and diffusion-controlled growth mechanisms in eqs. 4.1, 4.2, and 4.3 were then combined to produce a single equation describing product phase growth providing the volume fraction X_v transformed as a function of time.

$$\frac{dX_V}{dt} = \left(\frac{dX_A}{dt}\right)\left(\frac{z}{z_{max}}\right) + X_A\left(\frac{dz}{dt}\right)\frac{1}{z_{max}}. \qquad 4.4$$

where,

$$\frac{dX_A}{dt} = 2\pi r^2\left(\frac{dr}{dt}\right)\exp(-n\pi r^2) \qquad 4.5$$

and the thickness of the product layer, z starts from z_0 and grows until the reactants are consumed at z_{max}. A comparison of experimental DSC traces and the output from the model are reproduced in Figure 4. 4. The corresponding model parameters are listed in Table 4. 1.

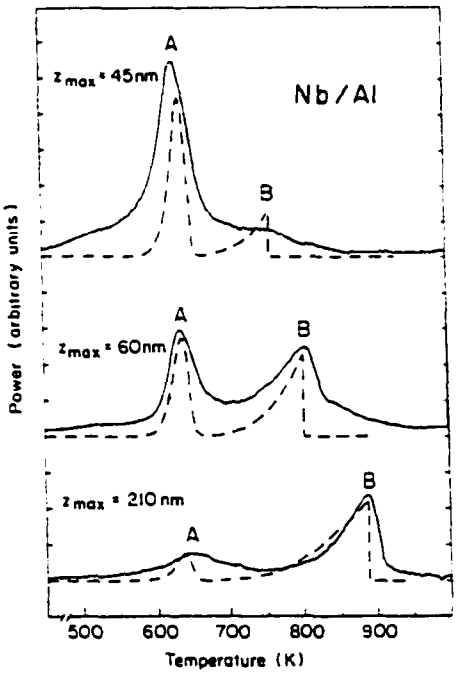

Figure 4. 4: Experimental calorimetry curves (solid line) calculated from differential thermal analysis of Nb/Al multilayer films heated at 50°K/min. Also shown are curves calculated using Equation 4.6 and the model parameters in Table 4. 1.

Table 4. I: Values of the model parameter used in conjunction with Equation 2.5 to describe the reaction kinetics of the Nb/Al system.

z_0 [nm]	nK_{i0}^2 [s^{-2}]	Q_i [eV]	K_{g0} [cm^2/s]	Q_g [eV]
30	3×10^{20}	1.5	10^{-3}	1.5

Despite assumptions of simplified grain shape and areal nucleation density, the model has been able to reproduce the main features of the calorimetry traces (peak height and positions). Note that the nucleation site density, n, could not be separated from the composite parameter nK_{i0}^2 (i.e., n could not be obtained from DSC measurements). Other assumptions included the radial growth of an existing population of cylinders with a fixed height with linear growth kinetics followed by diffusion controlled thickening of the product layer normal to the interface. Note that the second stage concluded when the initial reactants were consumed.

For multilayers with a stoichiometry of 50 at.% Al, 33 at.% Al, and 25 at.% Al, additional reaction stages were observed. Thermally, this meant that *three* exothermic peaks were observed for these multilayers. XRD experiments associated the third peak with the formation of the superconducting A15 phase, Nb_3Al. Separate TEM investigations also revealed the presence of the σ-Nb_2Al phase over the temperature range associated with peak C in the Nb-rich samples (Barmak et al.1990). The effective activation energies were determined using the Kissinger analysis. The results indicated that the activation energies for the first (A), second (B), and third (C) peaks were 1.5 ± 0.2 eV, 1.4 ± 0.3, and 6 ± 1 eV, respectively.

The study also examined the dependence of the peak temperature on reactant layer thickness. The first peak remained relatively constant with bilayer thickness and

occurred at a temperature of ~300 °C. The second peak shifted to slightly higher temperatures as the bilayer thickness increased and range from ~450 °C to 625 °C. The temperature of the third peak was independent of reactant layer thickness and occurred at ~825 °C. The Al layer thickness was plotted vs. peak temperature in Figure 4. 5.

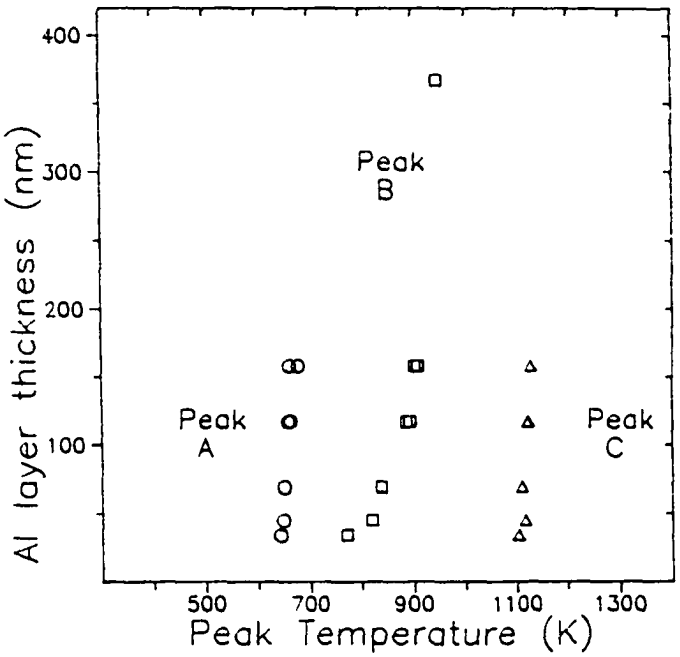

Figure 4. 5: Variation in the temperatures at which peaks A, B, and C occurred as a function of the thickness of the deposited Al layer for 50 K/min heating rates (from Coffey et al. 1992).

The study of $NbAl_3$ kinetics in sputter-deposited multilayers was again addressed in several of papers by Barmak et al. (1996,1997,1998). In these experiments, multilayers were again prepared with varying bilayer thickness (10-333 nm) and molar ratios of 25 at.%, 33 at.%, 50 at.% and 75 at.% Al with an emphasis on the transformation of the 75 at.% Al samples. The samples were studied using both DSC and DTA. As with the previous two studies, two separated, exothermic peaks were evident in films with $\Lambda >$ ~20 nm as seen in Figure 4. 6. As the reactant layer thickness decreased below 20 nm, the reaction associated with peak A became dominant. From the

disappearance of peak B, an estimate of ~8 nm (1/2 the thickness of the period where peak B is absent) was made for the coalescence thickness (z_0) assumed in the Coffey model.

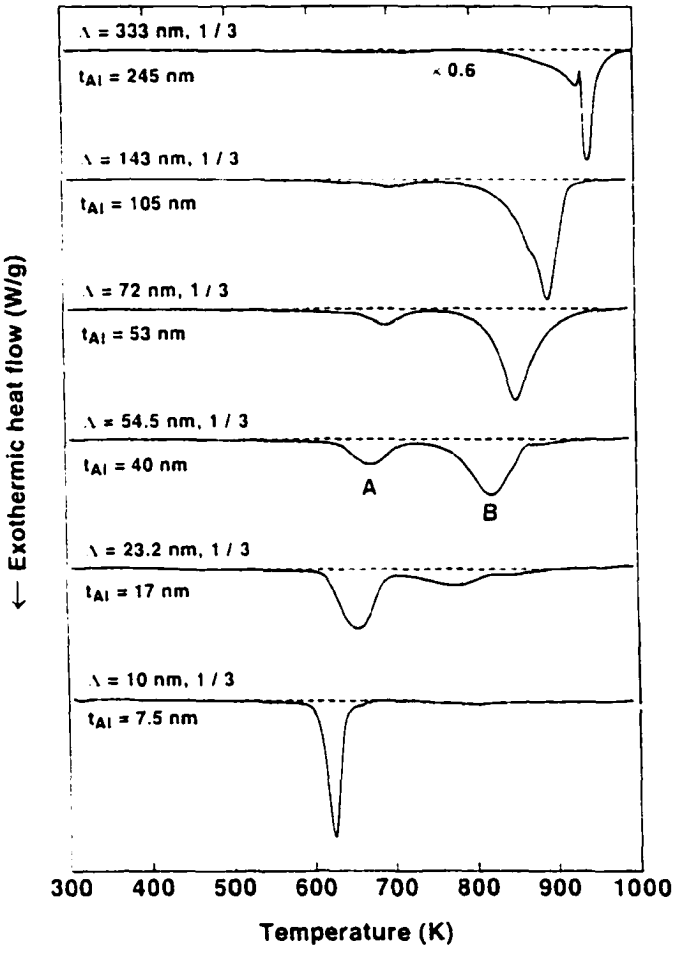

Figure 4. 6: Power compensated DSC traces for a series of 1Nb/3Al multilayer films annealed at 40 K/min. The period, Λ, the Al layer thickness, and the Nb/Al ratio are listed on each trace (from Barmak et al. 1998).

Furthermore, the results indicated a similar peak shift behavior with Al layer thickness similar to that observed by Coffey et al. (1992). The peak temperature in the sputter-deposited films occurred at higher temperatures as compared with electron beam evaporated films (Figure 4. 7).

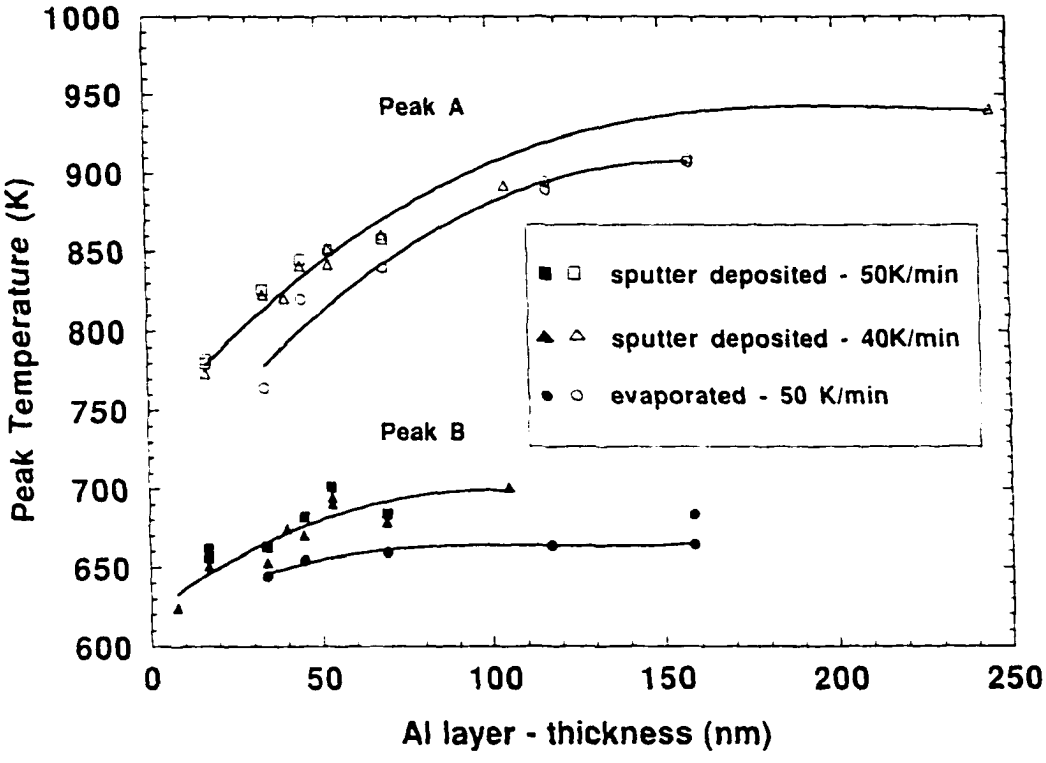

Figure 4. 7: Variation in peak temperatures as a function of deposited Al layer thickness for constant-heating-rate DSC traces. The lines have been drawn to guide the eye (from Barmak et al. 1998).

Activation energies for peak A were determined using the Kissinger approach. Results indicated activation energies of 1.6 ± 0.2 and 1.8 ± 0.1 eV from the heat-flux calorimeter and power compensated DSC results, respectively. Values for the second peak were 2.5 ± 0.6 eV and 2.5 ± 0.1 eV from the heat flux calorimeter and the power compensated DSC experiments, respectively. Note that the activation energies of Peak B are significantly higher than those reported by Coffey et al. (1992). This difference was attributed to the different deposition processes used in the two studies (Barmak et al. 1998). The results from the activation energy studies are summarized in Table 4. II. Included in the table are activation energies for the formation of $NbAl_3$ from "bulk"

processes such as hot dipping. In the latter cases, the activation energy was determined by measuring the thickness of the $NbAl_3$ layer at different times for a given temperature.

Table 4. II: Values of activation energies for the formation of $NbAl_3$ listed in the literature.

Sample	Deposition Technique	Analysis Tech.	Phase	Q [eV]	Temp. [°C]	Reference
Nb/Al (bulk)	hot-dip/ pack cement.	LOM	$NbAl_3$	1.13	1000 – 1400	Slama and Vignes (1972)
Nb/Al (bulk)	hot-dip	LOM	$NbAl_3$	1.58 ± 0.02	800 – 1300	Ogurtani (1972)
Nb/Al multi.	sputtered	DSC	$NbAl_3$	1.50 (A)	340 – 600	Ball and Todd (1987)
Nb/Al multi.	e-beam	DTA	$NbAl_3$	1.5 ± 0.2 (A) 1.4 ± 0.3 (B)	100 – 1100	Coffey et al. (1992)
Nb/Al multi.	magnetron sputtered	DSC	$NbAl_3$	1.8 ± 0.1 (A) 2.5 ± 0.1 (B)	30 – 700	Barmak et al. (1996) Barmak et al. (1997)
Nb/Al multi.	magnetron sputtered	DTA	$NbAl_3$	1.7 ± 0.2 (A) 2.5 ± 0.6 (B)	30 – 700	Barmak et al. (1998)

Prior to the present study, the only data concerning the effects of 4 wt.% Cu on the activation energy of $NbAl_3$ was provided by Ball and Todd (1987) and is summarized in Table 4. III. No significant difference was observed in the activation energy.

Table 4. III: Value of activation energy for the formation of $NbAl_3$ from an Nb/Al(Cu) multilayer listed in the literature.

Sample	Deposition Technique	Analysis Tech.	Phase	Q [eV]	Temp. [°C]	Reference
Nb/Al-4 wt.% Cu	sputtered	DSC	$NbAl_3$	1.54	340 – 600	Ball and Todd (1987)

Barmak et al. (1998) also performed isothermal DSC experiments to examine the transformation associated with peak A in more detail. The runs showed a bell-shaped peak that was indicative a JMA type nucleation and growth process (Figure 4. 8).

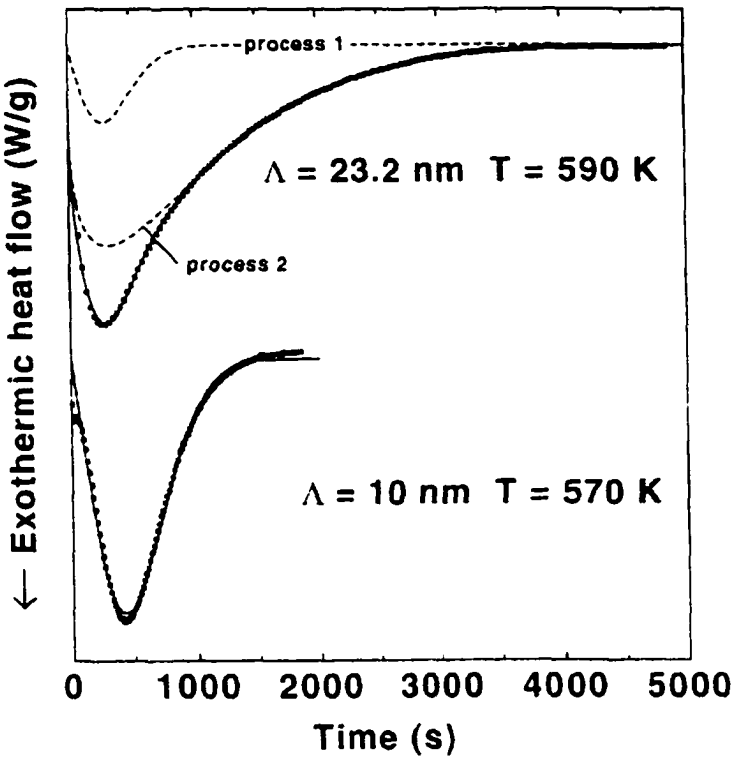

Figure 4. 8: Isothermal DSC measurements for 1Nb/3Al multilayer films with periodicities of 10 and 23.2 nm at 570 and 590 K, respectively. The solid line is the best fit to eq. 4.7 (from Barmak et al. 1996, Barmak et al. 1998).

Assuming that the heat released is proportional to the transformed volume fraction of the sample, such curves can be fit an equation of the form

$$X(t) = 1 - \exp[-(kt)^n], \qquad 4.6$$

where $X(t)$ is the volume fraction transformed as a function of time, $k = k(T)$ is a temperature dependent constant incorporating nucleation and growth rates and n is the Avrami exponent. In order to fit an isothermal DSC trace directly, eq. 4.6 can differentiated to describe the *rate* of transformation

$$\Delta H(t) \propto \frac{dX}{dt} = nkt^{n-1} \exp(-kt^n), \qquad 4.7$$

This equation can be fit using n and k as free parameters. Depending on the value of n, different characteristics can be attributed to the reaction.

By fitting the traces using the above kinetic equation, values of n were found to be ~2 for a 10 nm multilayer film with stoichiometry of 1Nb/3Al. The Avrami exponent was found to decrease with increasing periodicity. This was attributed to possible deviations from spatial randomness of nucleation (i.e., heterogeneous nucleation on grain boundaries). This has been the subject of numerical simulation work by Rickman et al. 1997. Results indicated that the shape of the peak of a nucleation and growth transformation from a fixed initial population of nuclei depended on the degree of heterogeneity of the transformation. It followed that boundary nucleation produced a much broader peak than a homogeneous distribution of nuclei as seen in Figure 4. 9. A broader peak would correspond to a lower Avrami exponent.

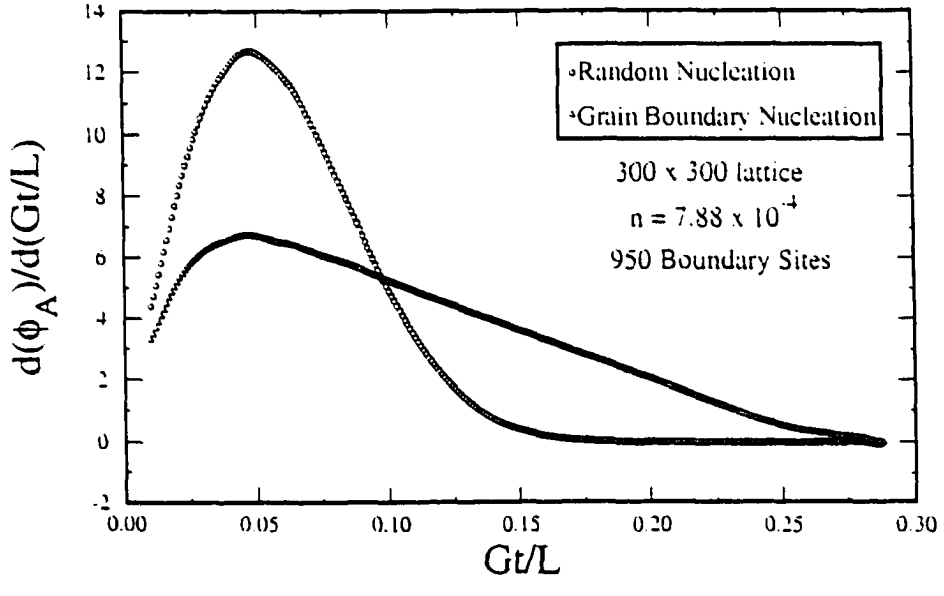

Figure 4. 9: The time dependence of the area fraction transformed (Φ_A) for cases of both homogeneous and heterogeneous nucleation. Clearly, the width of the peak depends on the nature of the nucleation process (from Rickman et al. 1996).

4.2.2 Ti/Al Calorimetry

Despite its prominence in Al-metallization metallurgy, until recently, the study of Ti/Al reactions using calorimetry was not pursued. Early investigations into the activation energy of $TiAl_3$ formation relied exclusively on isothermal anneals and RBS measurements. This provided an overall activation energy for $TiAl_3$ formation, but could not identify the metastable polymorphous transformations that were occurring simultaneously as the reaction proceeded. Ball and Todd (1987) provided the first calorimetric data on $TiAl_3$ formation. A constant-heating-rate DSC trace taken from a multilayer with a relatively thick bilayer thickness exhibited a single exothermic peak at 419 °C shown in Figure 4. 10. This was attributed to the formation of $TiAl_3$ and the superlattice Ti_8Al_{24} (van Loo and Rieck 1973).

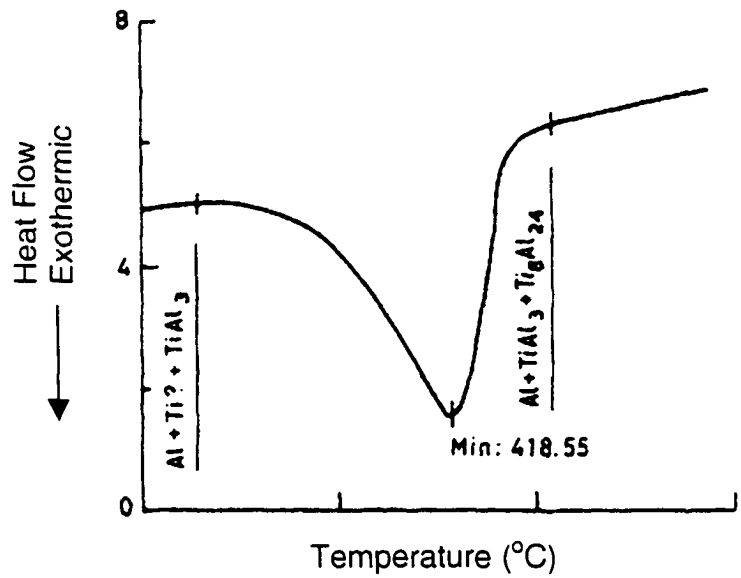

Figure 4. 10: DSC trace from a sputter-deposited Ti/Al multilayer heated at 20 °C/min (from Ball and Todd 1987).

The authors did not report any reaction prior to 300 °C. Using the Kissinger analysis they reported a wide range of activation energies ~0.60-1.80 eV and noted a non-linear behavior in the Kissinger plot.

Recently, the Ti/Al reaction was investigated using a more systematic approach using constant-heating-rate DSC with free-standing multilayers and various bilayer periods ranging from 5 nm to 40 nm (Michaelsen et al. 1996). Both calorimetry Figure 4. 11 and *ex situ* XRD were used to examine $TiAl_3$ formation in films with overall stoichiometry of 1Ti/3Al. For films with $\Lambda < 30$ nm two separated, exothermic peaks were again observed. The XRD data provided clear evidence for the formation of a metastable $L1_2$ structure of $TiAl_3$ which formed at temperatures as low as ~250 °C for films with $\Lambda = 5$ nm. This transformation is labeled as peak A in Figure 4. 10. The formation temperature of the $TiAl_3$ with the $L1_2$ structure was observed to shift to higher temperatures as Λ increased.

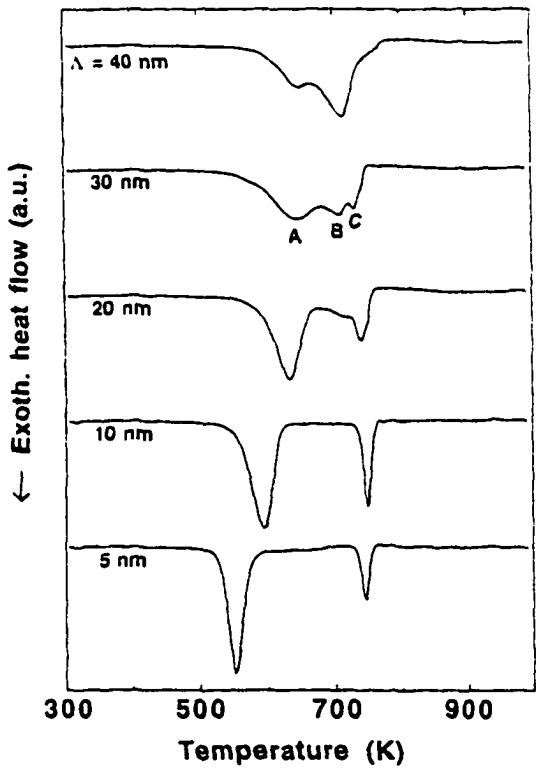

Figure 4. 11: DSC traces of 1Ti/3Al multilayer films with various periodicities taken at a heating rate of 40 K/min (from Michaelsen et al. 1996).

Ex situ XRD also determined that further annealing produced another metastable superlattice of $TiAl_3$ with a DO_{23} structure at ~530 °C. This transformation was associated with peak C. Finally, the equilibrium DO_{22} structure was formed from ~550-700 °C. This was evidenced in XRD by a slight increase in tetragonality. This point will be examined in more detail in Chapter 5. Observe that peak B, associated with the formation of $TiAl_3$ with the $L1_2$ structure was not observed until Λ = 20-30 nm. This was similar to the period in which peak B was seen in Nb/Al multilayers. Peak B merged with peak C in the sample with Λ = 40 nm.

Although the $L1_2$ and DO_{23} structure involved a measurable amount of heat, the final $DO_{23} \rightarrow DO_{22}$ transformation was not characterized by a significant heat flow. The Kissinger analysis was applied to the peaks corresponding to $L1_2$ and DO_{23} structures of $TiAl_3$ revealing activation energies of 1.6 ± 0.1 eV and 2.0 ± 0.2 eV, respectively. The study also measured the heat of formation of $TiAl_3$ from the DSC data and found it to be 34.7 ± 0.3 kJ/g-atom.

Isothermal and constant-heating-rate DSC runs of the reaction associated with the formation of $L1_2$ $TiAl_3$ (peak A) revealed a bell-shaped peak indicative of a nucleation and growth process for the formation of this phase as shown in Figure 4. 12 and Figure 4. 13 (Michaelsen et al. 1996). The values of n, the Avrami exponent, were found to be ~1 for a 10 nm multilayer film with a stoichiometry of 1Ti/3Al. A unique description of the origin value of n could not be obtained, but spatially-biased nucleation of the product phase can again provide a possible explanation for the low values.

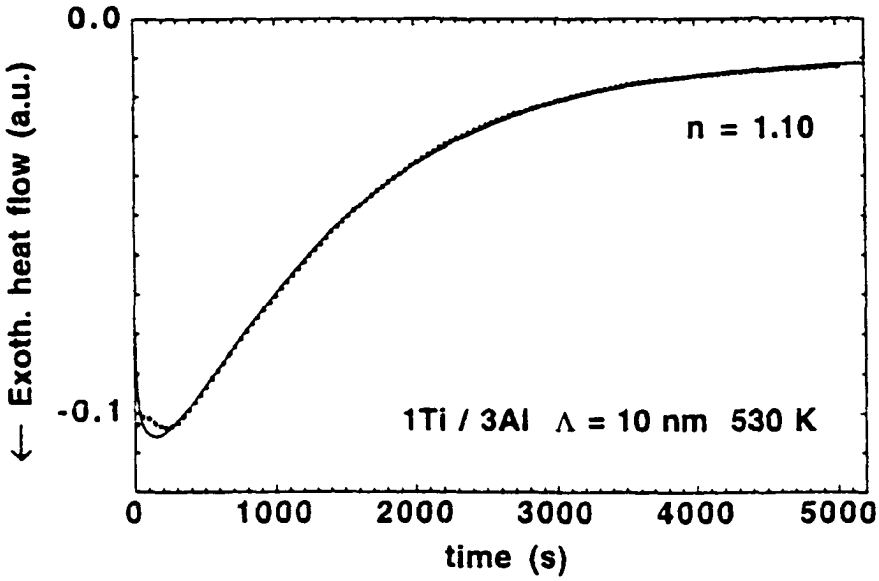

Figure 4. 12: Isothermal DSC trace of the transformation of associated with peak A at a temperature of 530 K obtained from a 1Ti/3Al multilayer film with Λ = 10 nm. The solid line is the best fit to eq. 4.7 (from Michaelsen et al. 1996).

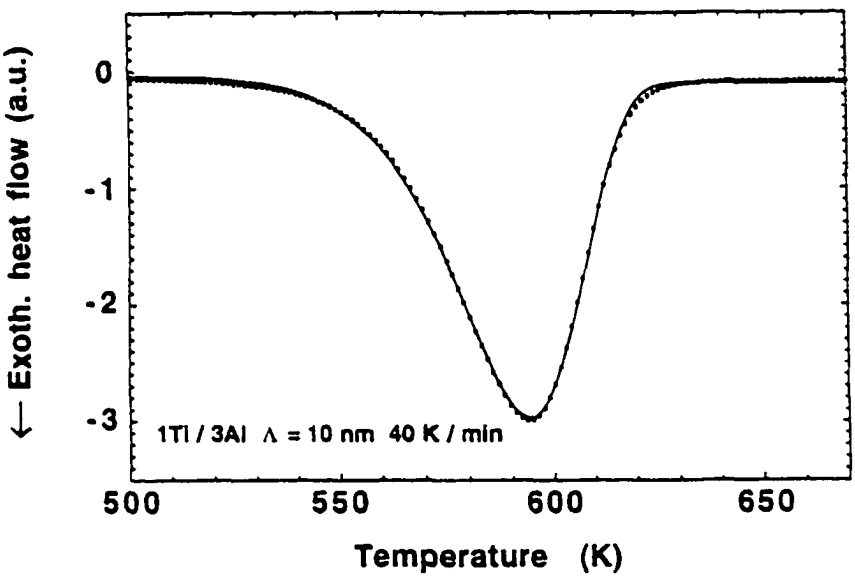

Figure 4. 13: Scanning DSC trace of 1Ti/3Al multilayer film with Λ = 10 nm at a heating rate of 40 K/min. The solid line is the best fit by a modified JMA equation used to determine the Avrami exponent (from Michaelsen et al. 1996).

The complexity of the $TiAl_3$ reaction was evident in the series of DSC traces with from multilayer films a broader range of bilayer thicknesses shown in Figure 4. 14. Peak

A simultaneously shifted to higher temperatures and decreased in amplitude with increasing Λ, while peak C remained at a relatively constant temperature. Peak B, evident in samples with Λ > 30 nm increased in amplitude engulfing peak C and shifted to higher temperatures with increasing Λ. Finally, where visible, peak C showed little or no systematic dependence on Λ. This created a series of overlaps involving two or three of the exothermic peaks beginning with peak A and B, followed by peak B and C, and eventually ending with a trace dominated by peak B (although the DO_{23} reaction still occurs) as shown in Figure 4. 14.

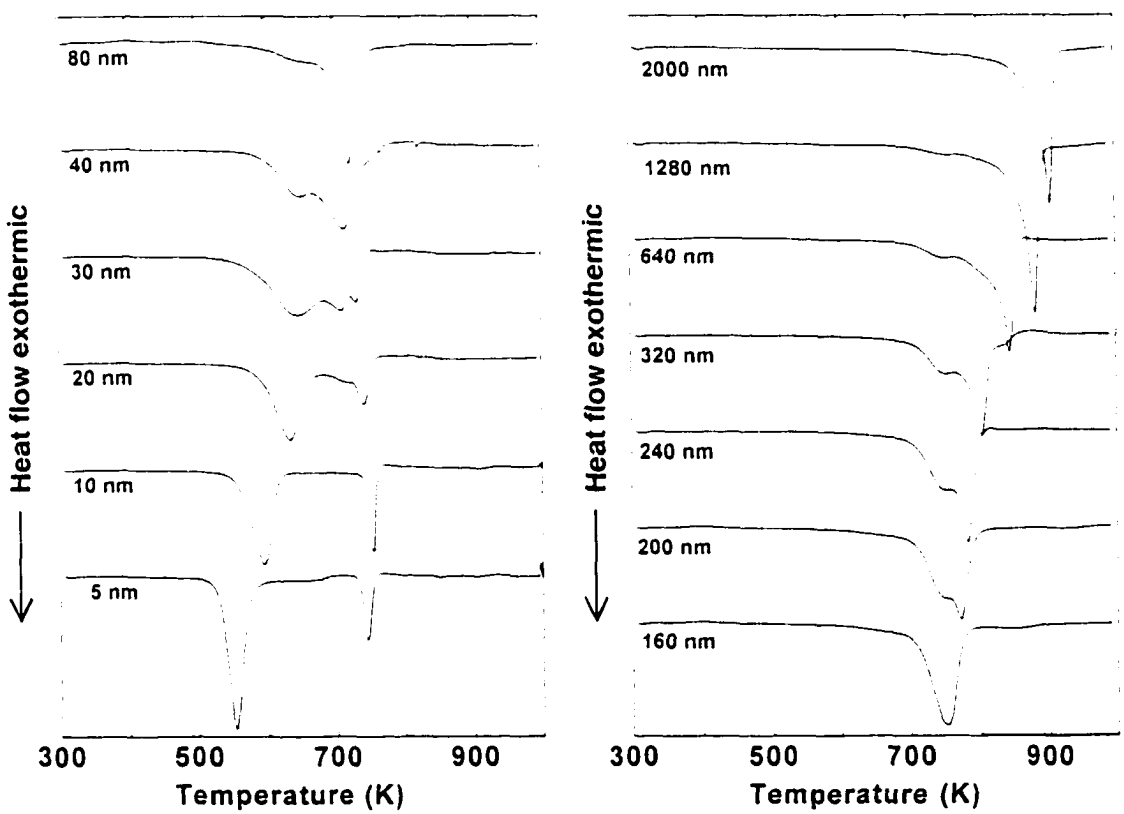

Figure 4. 14: Constant-heating-rate DSC traces taken at 40 °C/min for a range of Ti/Al multilayer films showing the evolution of peak height and temperature as a function of periodicity (courtesy of C. Michaelsen).

These showed that for thicker films the growth of the equilibrium DO_{22} structure of $TiAl_3$ will comprise a larger fraction of the total heat released during the reaction. Conversely, as the layer thicknesses decrease, the presence of the metastable $L1_2$ and DO_{23} phases will constitute the larger fraction of the measured enthalpy change. A summary of $TiAl_3$ activation energies reported in the literature (including those obtained by RBS or other techniques) is listed in Table 4.IV.

Table 4.IV: Listing of activation energies reported in the literature for $TiAl_3$ formation.

Sys.	Dep. Tech.	Analysis Tech.	Phase	Q [eV]	Temp. Range [°C]	Reference
Ti/Al (bulk)	various	LOM	$TiAl_3$	1.86 ± 0.06	580 – 640	van Loo and Rieck (1973)
Ti/Al	e-beam	RBS	$TiAl_3$	~1.85	350 – 475	Bower (1973)
Ti/Al	e-beam	RBS	$TiAl_3$	1.8	450 – 550	Nakamura et al. (1976)
Ti/Al	e-beam	Resistivity	$TiAl_3$	1.6	325 – 450	Huang and Wittmer (1984)
Ti/Al	not specified	RBS	$TiAl_3$	1.8 ± 0.1	300 – 500	Krafcsik et al. (1985)
Ti/Al	e-beam	RBS Resistivity	$TiAl_3$	1.6 ± 0.1RBS 1.5 ± 0.1Res.	375 – 450	Wittmer et al. (1985)
Ti/Al	e-beam	RBS	$TiAl_3$	1.72 ± 0.1	350 – 500	Tardy and Tu (1985)
Ti/Al	sputtered	DSC	$TiAl_3$	0.6-1.80	300 – 500	Ball and Todd (1987)
Ti/Al	sputtered	Resistivity	$TiAl_3$	1.76	400 – 450	Nahar et al. (1987) Nahar et al. (1988)
Ti/Al	e-beam	RBS	$TiAl_3$	1.9 ± 0.1	460 – 515	Zhao et al. (1988)
Ti/Al	sputtered	DSC	$TiAl_3$	1.6 ± 0.1 (A) 2.0 ± 0.2 (B) 2.0 ± 0.2 (C)	20 – 700	Michaelsen et al. (1996)
Ti/Al	sputtered	DSC	$TiAl_3$	2.0 ± 0.2	350 – 500	Federspiel et al. (1998)

Due to the ubiquitous use of Al(Cu) interconnects in microelectronics, there were slightly more studies performed on thin film reactions of Ti with Al(Cu) alloys compared

to Nb/Al(Cu) involving a range of Cu concentrations. The results from these studies are listed in Table 4. V

Table 4. V: Listing of literature values of the activation energy for the formation of $TiAl_3$ from Ti/Al(Cu) thin-films.

System	Dep. Techn.	Analysis Technique	Q [eV]	Temp. Range (°C)	Reference
Ti/Al-1 wt.% Cu	e-beam	Resistivity	2.2	325 – 450	Huang and Wittmer (1984)
Ti/Al-6.8 wt.% Cu	not specified	RBS	2.4 ± 0.1	300 – 500	Krafcsik et al. (1985)
Ti/Al-1 wt.% Cu	e-beam	RBS/ Resistivity	2.05 ± 0.1 RBS 2.00 ± 0.1 Res.	375 – 450	Wittmer et al. (1985)
Ti/Al-4.5 wt.% Cu	e-beam	RBS/ Resistivity	2.05 ± 0.1 RBS 2.00 ± 0.1 Res.	375 – 450	Wittmer et al. (1985)
Ti/Al-0.59 wt.% Cu	e-beam	RBS	2.05 ± 0.1	350 – 500	Tardy and Tu (1985)
Ti/Al-4 wt.%Cu	sputtered	DSC	1.93	300 – 500	Ball and Todd (1987)
Ti/Al-0.12 wt.% Cu	sputtered	Resistivity	2.01± 0.16	350 – 500	Rodbell et al. (1992)
Ti/Al-0.67 wt.% Cu	e-beam	Resistivity	2.13 ± 0.15	350 – 500	Rodbell et al. (1992)
Ti/Al-4 wt.% Cu	e-beam	Resistivity	2.06 ± 0.16	350 – 500	Rodbell et al. (1992)

In general, the activation energies for $TiAl_3$ formation in the presence of Cu were slightly higher ~0.1-0.4 eV than samples with pure Al and were ~2.0 eV. The activation energy was not found to be a strong function of Cu concentration.

4.3 Experimental Procedure

Free-standing films for DSC experiments were obtained from Cu-coated glass slides prepared in the following manner. The glass slides were first cleaned in acetone and ethanol for ~ 5-10 minutes and allowed to dry. Then a square substrate was prepared

by joining three slides together using Scotch tape. A fourth slide was cut and attached to the bottom of the other slides using double stick tape for support and alignment. Note that the fourth slide needed to be shortened by ~ 5 mm to allow it to fit into the transfer rings of the sputtering system. A schematic diagram of the final configuration is shown in Figure 4. 15.

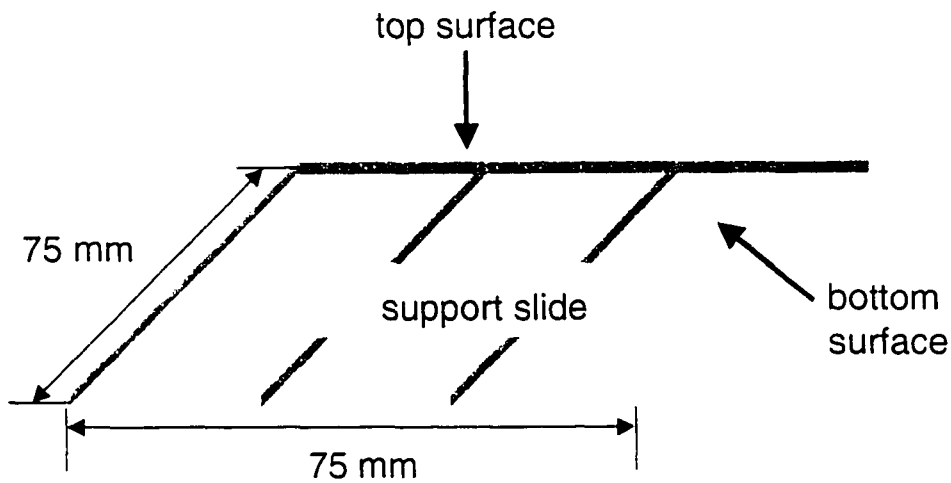

Figure 4. 15: Schematic illustration of the substrates fabricated for deposition of films for the DSC studies.

After this step, the substrates could be loaded into the system for deposition of the 200 nm Cu film as described in Chapter 3. After the deposition of this Cu layer, the substrates were removed from the deposition chamber and exposed to air. This step is critical as it significantly decreased the amount of time necessary to dissolve the Cu once it has become the underlayer for the multilayers. During the exposure of the Cu to air, a surface oxide is formed. Presumably, this oxide reduced the adhesion of the first deposited Al layer thus accelerating multilayer removal.

After the multilayer films were deposited as described in Chapter 3, films were removed from the substrate for DSC analysis by dissolving the Cu underlayer. To

decrease the time required to dissolve the underlayer, the films were first cut into ~2.5 cm x 2.5 cm sections using a scribe and placed in a 9:1 solution of HNO_3 and distilled water. Corrosion data obtained from studies of Al alloys revealed that this high concentration reduced the Al attack by more than a factor of 10 when compared to a 1:1 solution as shown in Figure 4. 16 (Uhlig and Revie 1985).

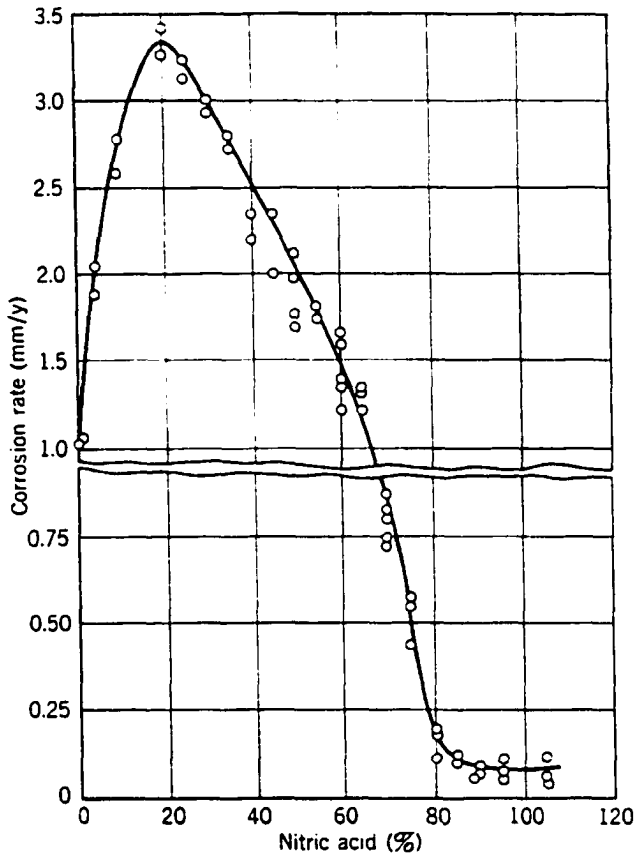

Figure 4. 16: Effect of concentration of nitric acid solutions at room temperature on the corrosion rate of 1100-H14 alloy (from Uhlig and Revie 1985).

Using this procedure, the Cu layer was completely dissolved within 10-20 min. The films were then successively rinsed for several minutes in three separate beakers containing distilled or deionized water. The free-standing films were then placed in a fourth beaker with distilled or deionized water for ~3 hours after which they were

transferred immediately to a beaker containing ethanol. The films were removed and allowed to dry for ~ 12 hours. After removal, the films retained a highly reflective surface. If the multilayer films were attacked by the acid, the surface acquired a dark gray color. Note that if a 1:1 ratio of acid to water is used (Coffey et al. 1992), dissolution of the Cu underlayer can take several hours, significantly prolonging exposure of the multilayer to the acid. This could lead to incorporation of hydrogen into the Nb layers and influence the enthalpy of the reaction.

Calorimetry was performed using a Perkin-Elmer DSC 7. The instrument was calibrated to ensure a reproducible and constant baseline response and to correct for temperature, thermal-lags and enthalpy release. The base line was adjusted to maintain an approximately linear heat signal over the temperature interval of the reactions of interest (200-900 °C). This is the most difficult and critical adjustment necessary for obtaining accurate reaction enthalpies due to the large temperature range needed to encompass the entire range of $NbAl_3$ or $TiAl_3$ formation.

The temperature calibration was performed by measuring the melting onset temperature of In and Zn. Three different tangent constructions were used to determine an average onset temperature. The thermal-lag factor for the instrument was determined by running a Zn sample at 10, 40, and 80 °C/min. Zn was used for this calibration since its melting point of 419 °C is closest to the reaction temperatures of Nb and Al. This resulted in a maximum deviation in temperature of +1.8 °C at 80 °C/min. Zn was also used to calibrate the enthalpy measurements. An average enthalpy of 108.78 ± 0.18 J/g was determined from the melting of the Zn calibration sample. This value is in excellent

agreement with the theoretical enthalpy of 108.37 J/g. Finally, a Pb sample was run to verify the temperature and enthalpy calibration.

For the next step, the dried, free-standing films were placed in an envelope made by folding a 10 mm x 10 mm x 0.025 mm piece Pt foil (99.99%) (Sigma-Aldrich, St. Louis, MO). The foil was first weighed using a calibrated balance to the nearest 10^{-5} g. Averages of at least three measurements were used to determine the weight and in most cases the average of five successive weight measurements were used. Approximately 2-3 mg of film was then added and the foil and film were re-weighed. Again, the actual weight was determined from an average of five separate measurements. A reference piece of Pt foil was prepared and its weight matched to within 0.1 mg of the first Pt foil (without film). The envelopes were carefully sealed by folding and flattened to ensure good thermal contact with the DSC furnace; this step resulted in a final sample size of ~ 4 mm x 4 mm. Figure 4. 17 shows the procedure for making the envelopes.

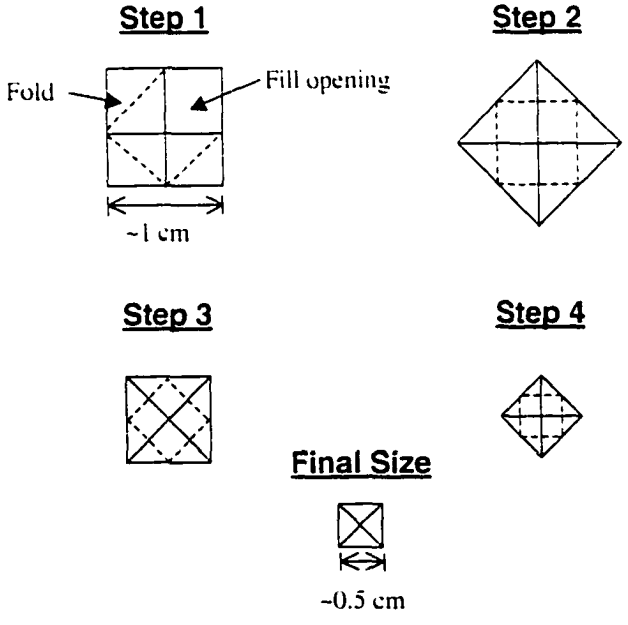

Figure 4. 17: Illustration of the procedure used to fabricate the Pt foil envelopes used for holding the free-standing films for use in the DSC.

Films were loaded into the calorimeter furnaces that were evacuated using a rotary vacuum pump for ~ 30 min. The furnaces were then purged with ultra high purity Ar (99.9995%) four times. The Ar gas was then permitted to flow through the furnaces for 10 min while the DSC signal stabilized. The flow rate of the Ar was controlled by an upstream flow meter to 20 ml/min. The specimen was ramped to 50 °C and held for 1 minute to allow the calorimeter to stabilize. The specimen was then heated from 50 °C to 700-720 °C at heating rates of 20 - 80 °C/min. After the particular run was completed, the DSC was allowed to stabilize for ~30 min before initiating the baseline scan. In the Nb/Al and Ti/Al systems, the reactions are irreversible. Therefore, the baseline was established by running the identical heating program a second time without disturbing the samples or reference. By subtracting this "null" signal, integrating the net area over the entire trace, and dividing by the mass of the sample, the enthalpy of the reaction was determined.

Information on reaction kinetics can also be obtained from the DSC traces. For thermally activated processes, an analysis originally developed by Kissinger (1957) can be used to determine an activation energy for the process being measured. A plot is constructed using calorimetry data acquired with a series of heating rates. Higher heating rates will cause the maxima in the calorimetry traces to shift to higher temperatures. The shift in peak position is related to the activation energy of the corresponding kinetic process or processes. The slope of the Arrhenius plot of $\ln(\beta/T_p^2)$ vs. $1/k_B T_p$, where β is the heating rate in K/s, T_p is the peak temperature and k_B is Boltzmann's constant in eV/K, is then $-Q$ in eV. In the case of the Nb/Al and Ti/Al reactions, a unique kinetic

mechanism is not known for each stage. The measured value was therefore an effective activation energy for the kinetic processes that are associated with the peak.

Further analysis of the peak shape can yield other kinetic parameters than can be used to describe the kinetics. For nucleation and growth type transformations the Avrami exponent, n, and rate constant, k, can be obtained from isothermal DSC traces. The value of n typically varies from 0.5 to 4 and can be interpreted to describe the time dependence and spatial distribution of nucleation as well as the dimensionality of growth. The rate constant is a temperature dependent parameter that describes the transformation velocity. Typically, these parameters are derived from curve fitting to isothermal calorimetry experiments. However, recently an analytical approach has been developed that allows the determination of these kinetic parameters from constant heating-rate experiments (Michaelsen and Dahms 1996). This approach allows the constant-heating- rate curves to be fit by the following expression:

$$\frac{dX_v}{dT} \approx n\left(\frac{\nu}{\beta}\right)^n \exp\left(-\frac{nE_a}{k_B T}\right)\cdot\left(\frac{k_B T^2}{E_a}\right)^{n-1}\cdot\exp\left[-\left(\frac{\nu}{\beta}\right)^n \exp\left(-\frac{nE_a}{k_B T}\right)\cdot\left(\frac{k_B T^2}{E_a}\right)^n\right]. \quad 4.8$$

where dX_v/dT is the rate of the volume transformed and proportional to the heat signal measured from the DSC, n is the Avrami exponent, ν is the frequency factor, E_a is the activation energy in eV of the peak of interest, k_B is Boltzmann's constant, T is temperature, and β is the heating rate in K/s.

The details of the derivation and the assessment of the validity of this equation will not be discussed here, as they be found in the original reference of Michaelsen and

Dahms (1996). The activation energy and frequency factor can be obtained experimentally from the Kissinger analysis described previously.

$$\ln\left(\frac{\beta}{T_p^2}\right) \approx \ln\left(\nu \frac{k_b}{E_a}\right) - \frac{E_a}{k_B T_p}. \qquad 4.9$$

where T_p is the peak temperature at a given heating rate. The frequency factor can be calculated using the y-intercept of the Kissinger plot, then the only remaining fit parameter is n. The error from the approximations used in the analytical fit is typically less than 5%. Note also that the error in the determination of n transfers linearly from the error for E_a.

The fit of eq. 4.8 also requires a flat baseline (i.e., the heat flow must match at the onset and end of the peak of interest. This was corrected following the approach by Michaelsen and Dahms (1996) by assuming the baseline change was proportional to the volume fraction transformed.

$$\text{baseline} = b_-(1-X_v) + b_+X_v, \qquad 4.10$$

where b_- and b_+ are the values of the baseline before and after the peak, respectively. This equation can then be added to eq. 4.8 or subtracted from the raw DSC data prior to fitting.

4.4 Results

4.4.1 Nb/Al-0 wt.% Cu, Nb/Al-0.5 wt.% Cu, and Nb/Al-1.0 wt.% Cu

4.4.1.1 Effect of Layer Thickness on Overall Reaction Kinetics

The baseline-subtracted, normalized heat flow of the Nb/Al-0 wt.% Cu films heated at 40 °C/min to 700 °C is plotted versus temperature in Figure 4.18.

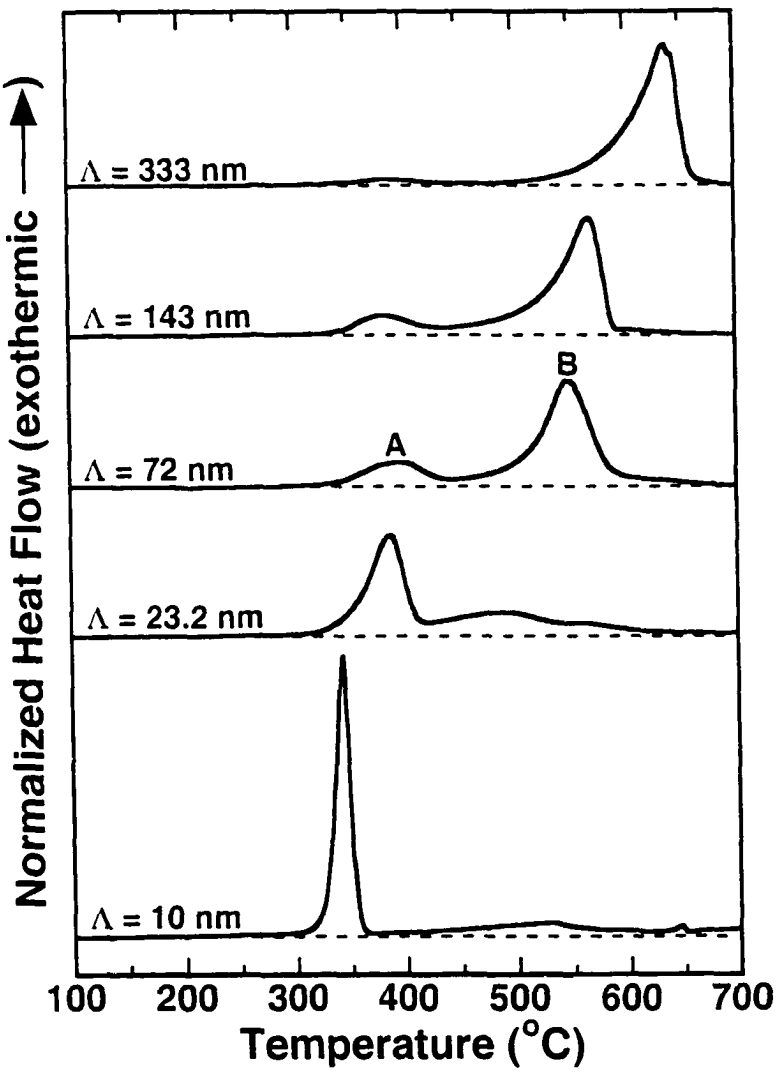

Figure 4.18: Baseline-subtracted, constant heating rate DSC traces obtained from a series of 1Nb/3Al multilayers heated at 40 °C/min to 700 °C. Both peaks A and B correspond to the formation of $NbAl_3$.

The traces contained two exothermic peaks labeled A and B for $\Lambda > 10$ nm. These peaks were due to the two-stage formation of $NbAl_3$ as discussed in Section 4.3 Peak A was observed to shift to slightly higher temperatures from $\Lambda = 10$ nm to 72 nm. For films with $\Lambda > 72$ nm the position of peak A remained nearly constant. Peak B also moved to higher temperatures as Λ increased. The magnitude of this shift decreased with increasing Λ. This peak-shift behavior was observed previously by Barmak et al. 1998. The peak temperatures from samples heated at 40 °C/min are listed in Table 4 .VI. Considering the general shape of the traces, the slight slope on the rightmost edge of the second peak results from the gradual completion of the reaction, in part due to roughness at the growing interface between $NbAl_3$ and Al. The foot evident in some traces on the high temperature side of Peak B is most likely due to the transformation of pockets of unreacted Nb and Al. Evidence for this was observed in cross-sectional electron microscopy results and will be discussed further in Chapter 6. Isolated regions of unreacted material may also be the cause of the exotherm at ~ 525 °C in the $\Lambda = 10$ nm film. Alternatively, this exotherm could be due to growth of the $NbAl_3$ grains which would be expected at ~800 °C ($> 0.5\ T_m$). Note the decrease in the height of peak A and the increase in height of peak B with increasing Λ. This variation in the relative height of the two peaks is a result of the two-stage phase formation in this system, with a larger volume of sample being transformed by growth normal to the original interlayer interfaces as Λ increases. In other words, the relative height of Peak B is governed by the amount of material that is not consumed during the transformation of the interfacial region and will increase proportionally with reactant layer thickness. By contrast, the

absolute height of peak A will be determined primarily by the number of interfaces in the sample and will therefore be larger at lower periodicities (for a constant multilayer thickness).

Table 4.VI: DSC peak temperatures for 1Nb/3Al multilayers heated at 40 °C/min to 700 °C.

sample ID	Λ [nm]	Peak A [°C]	Peak B [°C]
10smh0798a1	10	344	-
1Nb3Al231030	23.2	373	479
1Nb3Al721020	72	396	549
1Nb3Al143092998	143	382	567
1Nb3Al33308098	333	388	637

The baseline-subtracted, normalized heat flow of the Nb/Al-0.5 wt.% Cu films heated at 40 °C/min to 700 °C is plotted versus temperature in Figure 4. 19. Again, two peaks were evident in the traces with $\Lambda < 333$ nm and were found to correspond to the formation of $NbAl_3$. No significant changes in the peak positions or shape were evident. However, peak A was less distinct and did not show a clear maximum for the $\Lambda = 333$ nm sample. Peak temperatures are listed in Table 4.VII.

Table 4.VII: DSC peak temperatures for 1Nb/3Al-0.5 wt.% Cu multilayers heated at 40 °C/min to 700 °C.

Sample ID	Λ [nm]	Peak A [°C]	Peak B [°C]
102998a2	10	349	523
102998b1	20	366	485
102898b1	72	380	538
110698b1	143	391	578
111998b1	333	444	625

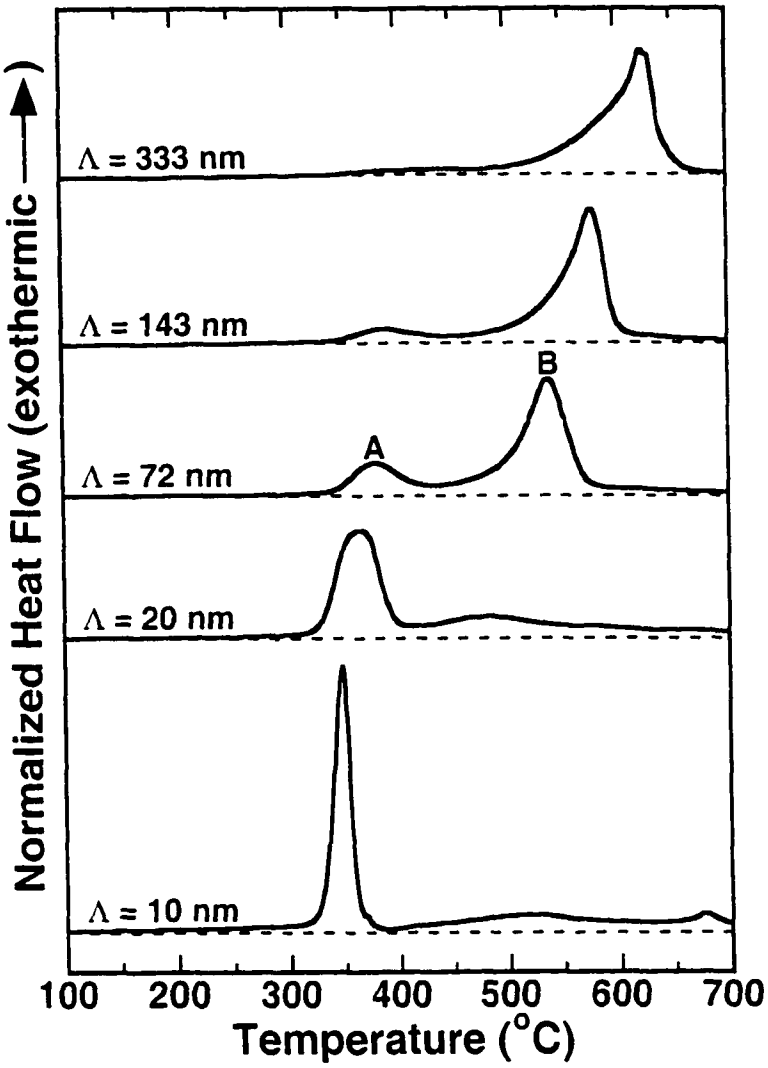

Figure 4. 19: Baseline-subtracted, constant heating rate DSC traces obtained from a series of 1Nb/3Al-0.5 wt.% Cu multilayers heated at 40 °C/min to 700 °C. Both peaks A and B correspond to the formation of $NbAl_3$.

The baseline-subtracted, normalized heat flow of the Nb/Al-1.0 wt.% Cu films heated at 40 °C/min to 700 °C is plotted versus temperature in Figure 4. 20. The results qualitatively resemble the previous traces, however, as in the 0.5 wt.% Cu samples, the Λ = 143 and 333 films exhibited a slight increase in the measured heat release between peaks A and B. This caused peak A to become less defined and signifies a less-abrupt transition between the two stages of $NbAl_3$ growth. This effect was not noted in the DSC

results from lower period films and may indicate a microstructural cause since the grain sizes of individual layers scale with periodicity. Peak temperatures for the plots in Figure 4. 20 are listed in Table 4.VIII.

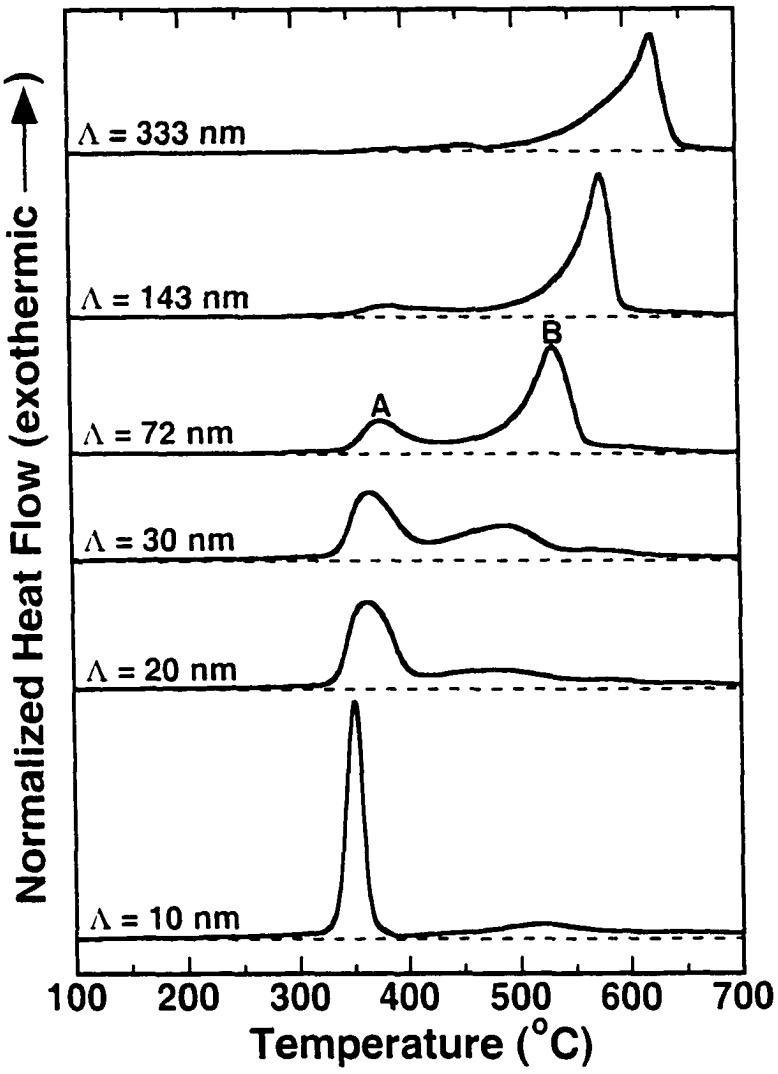

Figure 4. 20: Baseline-subtracted, constant heating rate DSC traces obtained from a series of 1Nb/3Al-1.0 wt.% Cu multilayers heated at 40 °C/min to 700 °C. Both peaks A and B correspond to the formation of $NbAl_3$.

Table 4.VIII: DSC peak temperatures for 1Nb/3Al-1.0 wt.% Cu multilayers heated at 40 °C/min to 700 °C.

Sample ID	Λ [nm]	Peak A [°C]	Peak B [°C]
101398a1	10	352	518
101498b2	20	364	478
101598a1	30	366	488
101598c1	72	378	534
101798b1	143	387	578
010699c1	333	452	626

4.4.1.2 Activation Energy

Due to the several studies of the Nb/Al activation energies extant in the literature, extensive experiments to determine the activation energies of the two peaks in the present DSC traces were not performed for the Al-0 wt.% Cu samples. For comparison with previous work on the formation of $NbAl_3$, activation energies were determined for peaks A and B for a 23.2 nm film. Four heating rates were used: 10, 20, 40, and 80 °C/min. The resulting Kissinger plot and fitting results are shown Figure 4. 14 and Table 4.IX, respectively. Measurement errors result primarily from the linear fitting routine, since the errors in temperature and heating rate are negligible for the DSC setup (error bars are less than the width of a data point). Values are reported with a 98% confidence level (2σ).

Table 4.IX: Results from Kissinger analysis of DSC data for a 1Nb/3Al multilayer film with Λ = 23.2 nm

1Nb/3Al- 0 wt.% Cu; Λ = 23.2 nm					
Peak	Q [eV]	Error (98% conf.)	y-int. [$K^{-1}s^{-1}$]	Error (98% conf.)	Freq. Factor (ν) [s^{-1}]
A	1.7	0.1	16.95	1.70	4.58E+11
B	2.1	0.2	18.84	3.34	3.74E+12

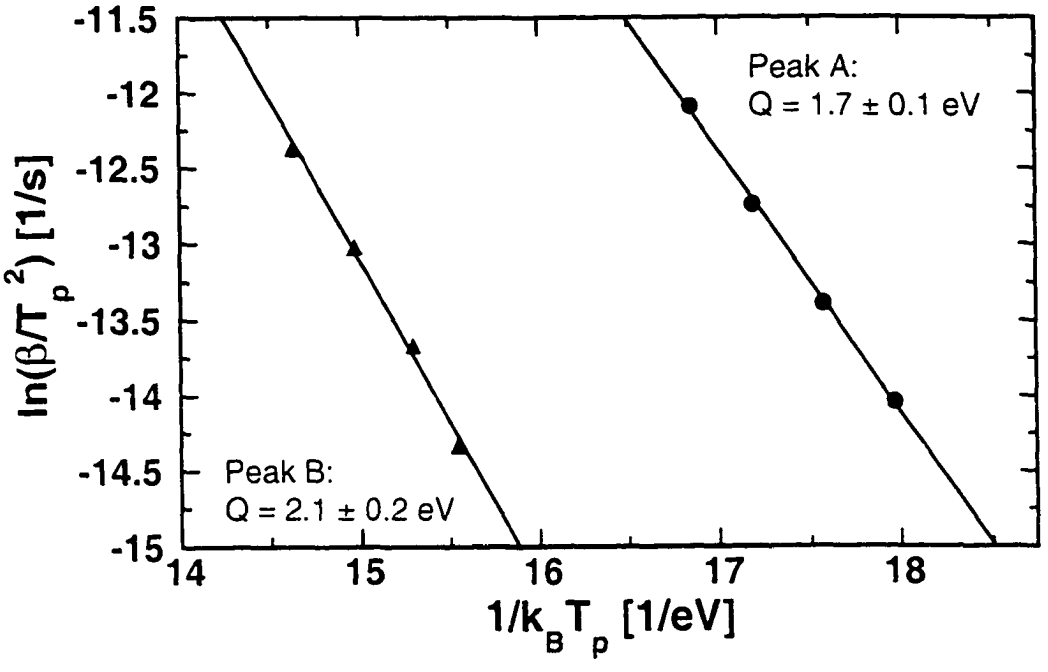

Figure 4.21: Kissinger plot showing activation energies for peaks A and B from a 1Nb/3Al, Λ = 23.2 nm multilayer thin-film.

The resulting values for peak A agreed quite well with those reported in prior investigations. However, as with the measurements of Barmak et al. (1998), the activation energies for peak B are significantly larger than those obtained by Coffey et al. (1992) in evaporated films.

To determine the effect of Cu on the transformation kinetics, activation energies were determined for 1Nb/3Al-0.5 wt.% Cu films with Λ = 72 nm and Λ = 143 nm. These values of Λ were chosen due to the clear presence of both peaks A and B. Also, peak B reached a maximum at a temperature well below the maximum operating limit of the DSC. Three heating rates, 20 °C/min, 40 °C/min, and 80 °C/min were run for both samples. The resulting Kissinger plot is shown in Figure 4. 22.

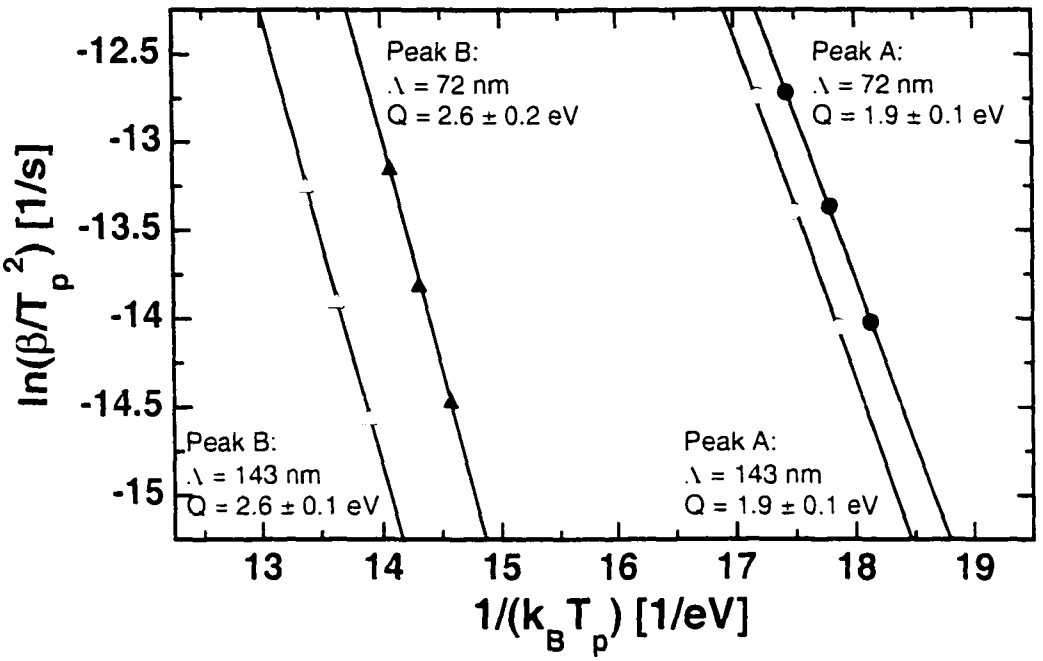

Figure 4. 22: Kissinger plot showing activation energies for peaks A and B from 1Nb/3Al-0.5 wt.% Cu, Λ = 72 nm and Λ = 143 nm multilayer thin-films.

The results obtained from the linear fit to the data are listed in Table 4.X. Within the precision of the measurement, the presence of Cu in the Al was not observed to have a measurable effect on the activation energies associated with peaks A and peak B when compared with the values in the literature (see Table 4. V). Recall that a similar observation was made by Ball and Todd (1987) for samples containing Al-4 wt.% Cu.

Table 4.X: Results of Kissinger analyses of DSC data for 1Nb/3Al-0.5 wt.% Cu multilayer films with Λ = 72 nm and 143 nm

Peak	Q [eV]	Error (98% conf.)	y-int. [$K^{-1}s^{-1}$]	Error (98% conf.)	Freq. Factor (ν) [s^{-1}]
1Nb/3Al- 0.5 wt.% Cu; Λ = 72 nm (102898b)					
A	1.9	0.1	19.62	0.90	7.16E+12
B	2.6	0.2	23.97	2.80	7.89E+14
1Nb/3Al- 0.5 wt.% Cu; Λ = 143 nm (110698b)					
A	1.9	0.3	20.35	4.82	1.55E+13
B	2.6	0.1	21.12	0.26	4.44E+13

Activation energies were also determined for 1Nb/3Al-1.0 wt.% Cu multilayers with Λ = 72 nm and 143 nm. Heating rates of 20 °C/min, 40 °C/min, and 80 °C/min were used. A linear equation was used to fit the data. The resulting plot obtained from the Kissinger analysis is shown in Figure 4. 23.

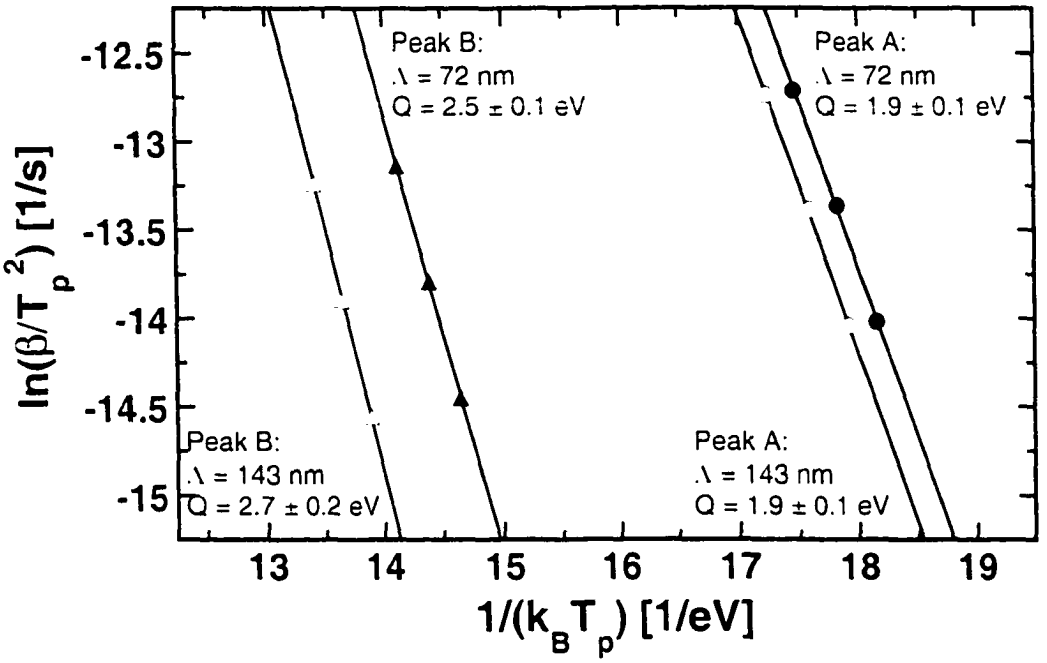

Figure 4. 23: Kissinger plot showing activation energies for peaks A and B from 1Nb/3Al-1.0 wt.% Cu, Λ = 72 nm and Λ = 143 nm multilayer thin-films.

The output from the fitting routine including the value of v, calculated from the y-intercept is listed in Table 4.XI.

Table 4.XI: Results of Kissinger analyses of DSC data for 1Nb/3Al-1.0 wt.% Cu multilayer films with Λ = 72 nm and 143 nm

Peak	Q [eV]	Error (98% conf.)	y-int. [$K^{-1}s^{-1}$]	Error (98% conf.)	Freq. Factor (v) [s^{-1}]
1Nb/3Al- 1.0 wt.% Cu; Λ = 72 nm (101598c)					
A	1.9	0.1	20.47	2.14	1.72E+13
B	2.5	0.1	22.08	1.36	1.13E+14
1Nb/3Al- 1.0 wt.% Cu; Λ = 143 nm (101798b)					
A	1.9	0.1	20.25	2.62	1.39E+13
B	2.7	0.2	23.36	2.20	4.42E+14

4.4.1.3 Reaction Order (Avrami Exponent)

Using the temperature dependent form of the JMA equation adapted by Michaelsen and Dahms (1996), the JMA exponent was determined for a 1Nb/3Al film with Λ = 10 nm heated at 40 K/min. This periodicity was chosen due to the absence of peak B. The presence of the second exothermic reaction peak and its relatively close proximity to the first peak, prevent accurate fitting. This is due to an inability to determine the baseline on the high temperature side of the first peak due to the interference of peak B.

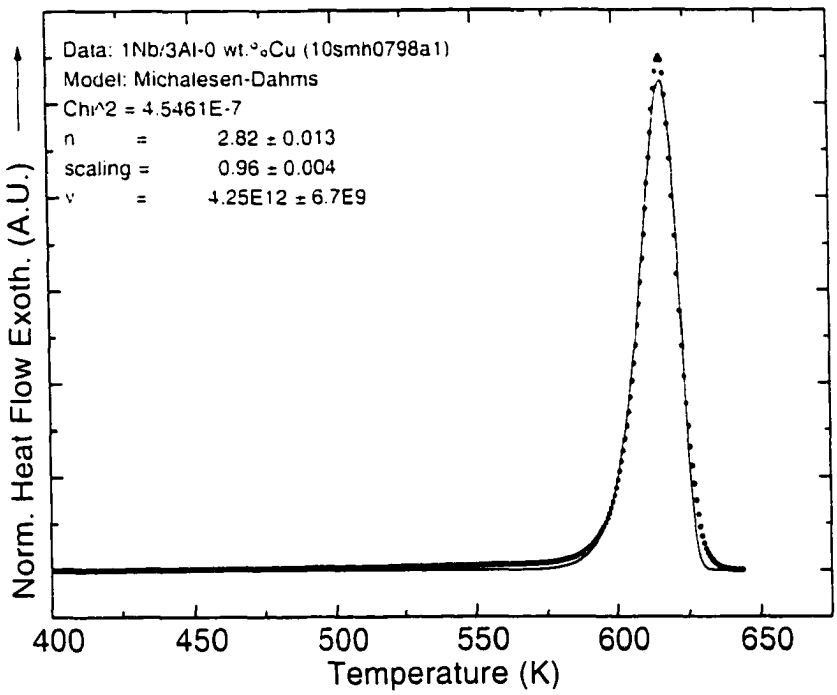

Figure 4. 24: DSC trace of a 1Nb/3Al multilayer film with Λ = 10 nm, taken at a heating rate of 40 K/min. The full line is the best fit of a JMA process to the measurement using eq. 4.8.

The results of a least squares fit of eq. 4.8 to the experimental data is shown in Figure 4. 24. The equation provides a good fit to the data and yields a value of $n \sim 2.8$. The error in this value was estimated to be ± 5-6% due to the errors in the Kissinger analysis. For this fit three parameters were used: the Avrami exponent, n, the frequency

factor, ν, and a multiplicative scaling factor. The scaling factor was included since the precise normalization procedure for the DSC result was not known. The activation energy for peak A was taken to be equal to the activation energy for peak A determined by the Kissinger analysis for the 1Nb/3Al, 23.2 nm film. However, since the 10 nm film was not used for activation energy determination, the value of ν could not be explicitly determined. Therefore, it was left as a free parameter.

The approach developed by Michaelsen and Dahms (1996) was used to fit the constant heating rate DSC trace obtained for a 1Nb/3Al-0.5 wt.% Cu, Λ = 10 nm multilayer. The results from the fit are shown in Figure 4. 25.

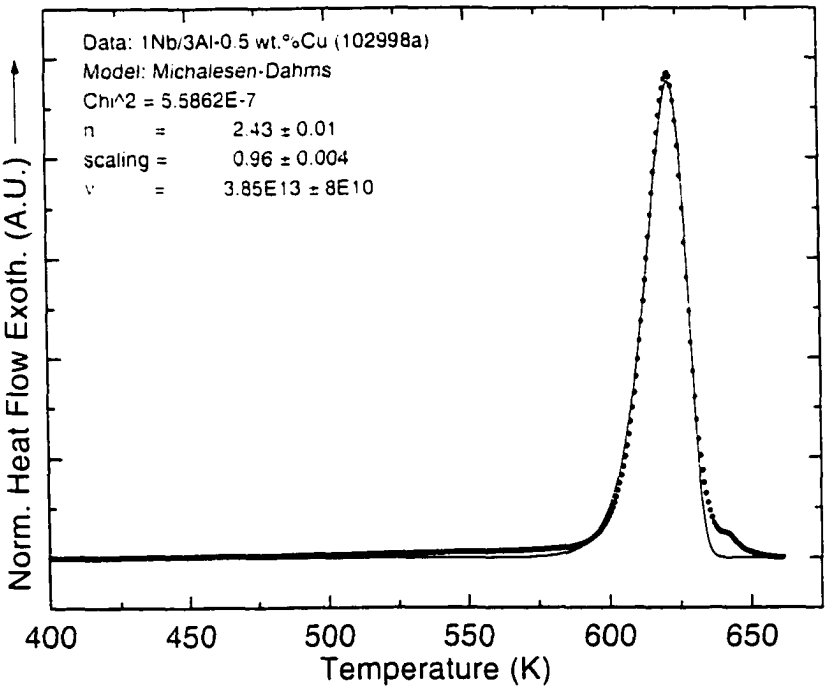

Figure 4. 25: DSC trace of a 1Nb/3Al-0.5 wt.%Cu multilayer film with Λ = 10 nm, taken at a heating rate of 40 °C/min. The full line is the best fit of a JMA process to the measurement using eq. 4.8.

In this case, the activation energy for peak A was taken to be equal to the 1Nb/3Al-0.5 wt.% Cu film with Λ = 72 nm. The frequency factor was again left as a fit parameter since it was not known in this case. The Avrami exponent was determined to

be ~ 2.4. The value for v was found to be within two orders of magnitude of the result for the Al-0 wt.% Cu multilayer.

Following the procedure for the previous two samples, peak A from a 1Nb/3Al-1.0 wt.% Cu sample with Λ = 10 nm heated at 40 °C/min was fit using Eq. 4.8 and shown in Figure 4. 26. The activation energy used in the fit was taken to be equal to the value obtained from a Λ = 72 nm film with the same composition. The frequency factor was left as a free parameter. The equation provided a reasonable fit to the data yielding a value of ~2.5 for the value of n. The value of v provided by the fit was within two orders of magnitude of the values obtained from the pure Al and Al-0.5 wt.% Cu samples.

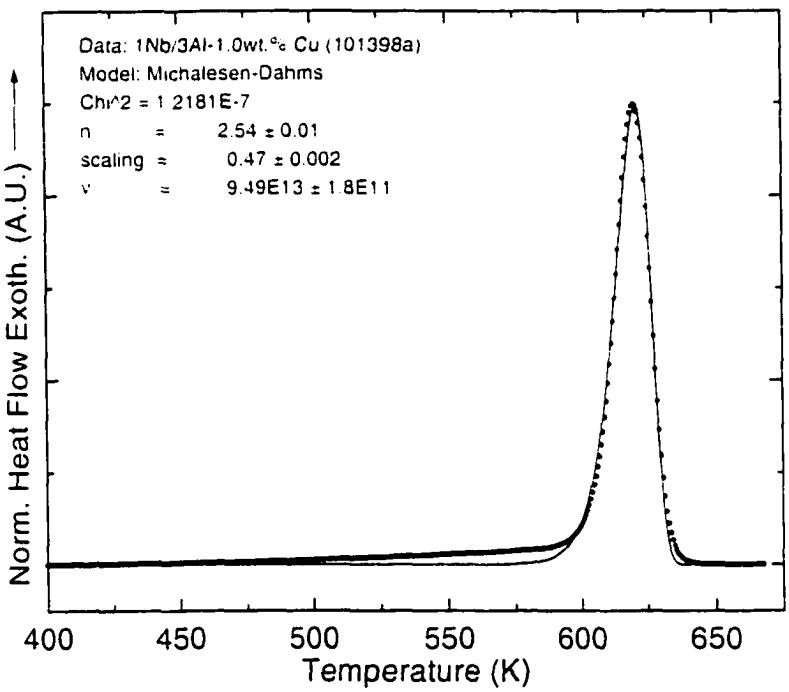

Figure 4. 26: DSC trace of a 1Nb/3Al-1.0 wt.% Cu multilayer film with Λ = 10 nm, taken at a heating rate of 40 °C/min. The full line is the best fit of a JMA process to the measurement using eq. 4.8.

4.4.1.4 Reaction Enthalpy ($NbAl_3$)

The DSC data from the constant heating-rate scans was also used to determine the enthalpy of $NbAl_3$ formation. Besides a precise weight measurement, the accurate determination of the heat of formation requires a repeatable baseline that matches the evolved heat signal at the beginning and end of the measurement. Figure 4. 27 shows a series of baseline-subtracted DSC curves obtained from free-standing 1Nb/3Al multilayer samples with Λ = 333 nm heated at 40 °C/min. In (a) the photoresist was dissolved and the film rinsed as described above. Although good matching between the baseline and heat signal was observed at low temperatures, the baseline deviated significantly from the heat signal at the high temperature portion of the reaction (~627 °C) resulting in an apparently larger heat release. Another sample from the same wafer was rinsed as before and then cleaned using ozone ashing (b). Although some improvement is noted, the result still does not permit accurate determination of the enthalpy of the formation of $NbAl_3$. A sample obtained using a Cu underlayer is shown in (c). In this case, the signal and baseline match at both the low and high temperature portions of the reaction.

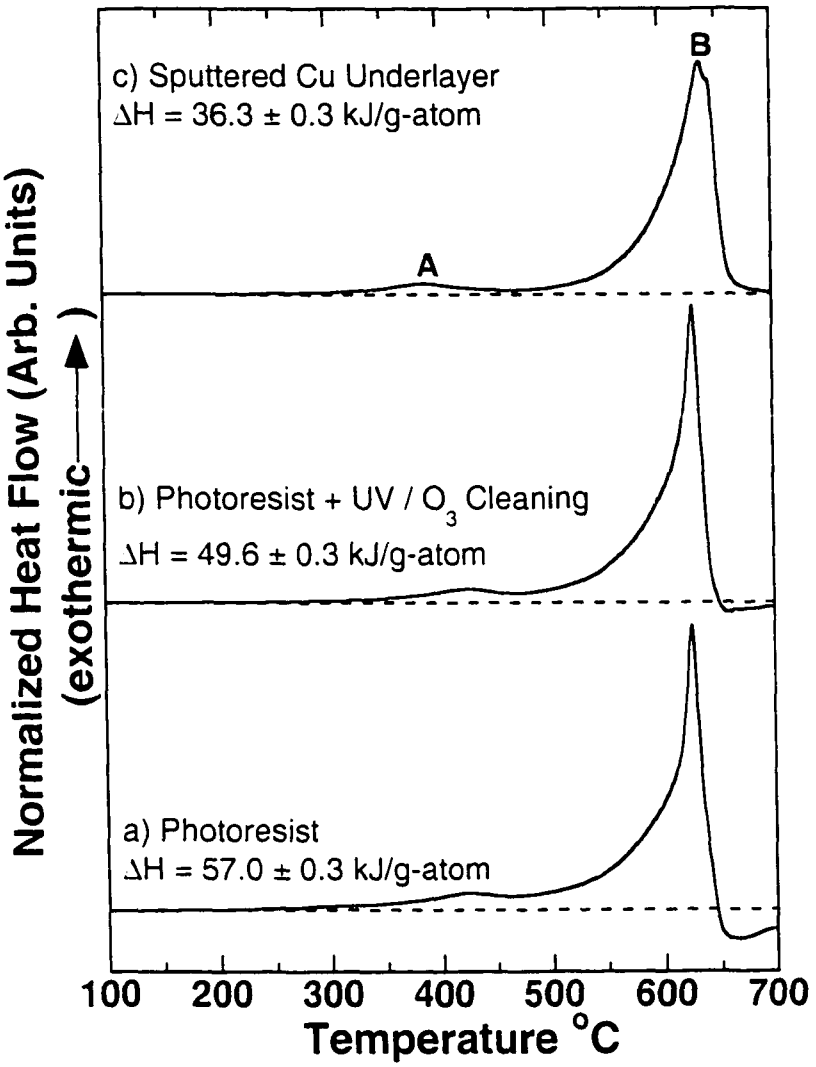

Figure 4. 27: Series of baseline-subtracted DSC curves taken from free-standing, Λ = 333 nm period 1Nb/3Al multilayers heated at 40 °C/min. (a) Photoresist underlayer removed by using photoresist stripper. Note discrepancy between signal and baseline at high temperatures (b) Same sample as (a) run after UV/O_3 cleaning. Baseline deviation still does not permit accurate determination of the heat of reaction. (c) DSC curve from a film obtained by dissolving a Cu underlayer in 9 HNO_3:1 H_2O providing good matching between the baseline and signal at low and high temperatures.

Despite repeated attempts to use photoresist as an underlayer material, a reproducible baseline was never obtained. This was presumably due to the inability to completely remove residual photoresist from the films. As a result, additional samples with various Λ deposited on Cu films were used to measure the enthalpy of $NbAl_3$ formation. The temperature range was taken from the point at which the heat signal

began to deviate from the baseline to the temperature where the baseline and heat signal rejoined at the completion of the reaction. Net areas were calculated using the analysis software provided with the calorimeter. The results of these measurements are listed in Table 4.XII.

Table 4.XII: Table of values for the enthalpy of formation of $NbAl_3$ determined by DSC measurements of free standing multilayer films.

Period [nm]	Run ID	Range [°C]	ΔH (Ave) [kJ g-atom^{-1}]	ΔH (σ) [kJ g-atom^{-1}]	ΔH (Ave) [kJ mol^{-1}]	ΔH (σ) [kJ mol^{-1}]
23.2	231030	280-700	38.2	0.2	152.8	0.9
72	721022	280-700	47.4	0.4	189.4	1.6
72	721020	300-700	41.2	0.4	164.7	1.4
143	14310201	290-700	40.7	0.3	162.8	1.0
143	1431029	290-700	43.9	0.3	175.8	1.0
143	14392998	250-700	35.6	0.3	142.5	1.3
333	333080598	300-700	36.3	0.3	145.2	1.0
333	333080698	290-700	36.9	0.2	147.7	0.9

The formation enthalpy of $NbAl_3$ was determined from DSC runs obtained from 1Nb/3Al-0.5 wt.% Cu films that yielded satisfactory baselines. An average value of 40.8 ± 0.5 kJ/g-atom was determined considering the independent measurements. The results of the individual film measurements are listed in Table 4. XIII.

Table 4. XIII: Table of values for the enthalpy of formation of $NbAl_3$ determined by DSC measurements of free standing multilayer films with 1Nb/3Al-0.5 wt. % Cu.

Period [nm]	Run ID	Range [°C]	ΔH (Ave) [kJ g-atom^{-1}]	ΔH (σ) [kJ g-atom^{-1}]	ΔH (Ave) [kJ mol^{-1}]	ΔH (σ) [kJ mol^{-1}]
143	110698b2	200-700	40.8	0.5	163.3	1.8
333	111998b1	200-700	40.8	0.6	163.3	2.2

Finally, the enthalpy of formation of $NbAl_3$ was determined for several 1Nb/3Al-1.0 wt.% Cu multilayers with various periodicities. An average value of 41.2 ± 1.6 kJ/g-

atom was obtained from four separate measurements. Data from the individual runs are listed in Table 4.XIV.

Table 4.XIV: Table of values for the enthalpy of formation of $NbAl_3$ determined by DSC measurements of free standing multilayer films with 1Nb/3Al-1.0 wt.% Cu.

Period [nm]	Run ID	Range [°C]	ΔH (Ave) [kJ g-atom^{-1}]	ΔH (σ) [kJ g-atom^{-1}]	ΔH (Ave) [kJ mol^{-1}]	ΔH (σ) [kJ mol^{-1}]
30	101598a1	200-700	40.8	0.8	163.1	3.1
143	101798b2	200-700	40.5	0.8	161.8	3.1
143	101798b4	200-700	40.7	0.4	162.9	1.6
333	010699c1	200-700	40.0	0.6	160.1	2.3

4.5 Discussion: Nb/Al

For film with varying layer bilayer thicknesses both peak A and B shifted to higher temperatures as Λ increased as shown in Figure 4. 28. This was previously observed by Ball and Todd (1987) during their survey of thin film transition metal reactions. Later, this effect was addressed in more detail during a study of Ni/Al multilayers. As with $NbAl_3$, $NiAl_3$ forms by a similar two-stage mechanism as evidenced by DSC experiments (Ma et al. 1991). As in Nb/Al, peak B will shift to higher temperatures due to the increase in the amount of reactants i.e., the reaction requires more time to reach completion. In a constant heating rate experiment, this translates into increased temperatures. The explanation for the shift of peak A, on the other hand, was not related to the amount of reactants, since it had been identified as a nucleation and growth event.

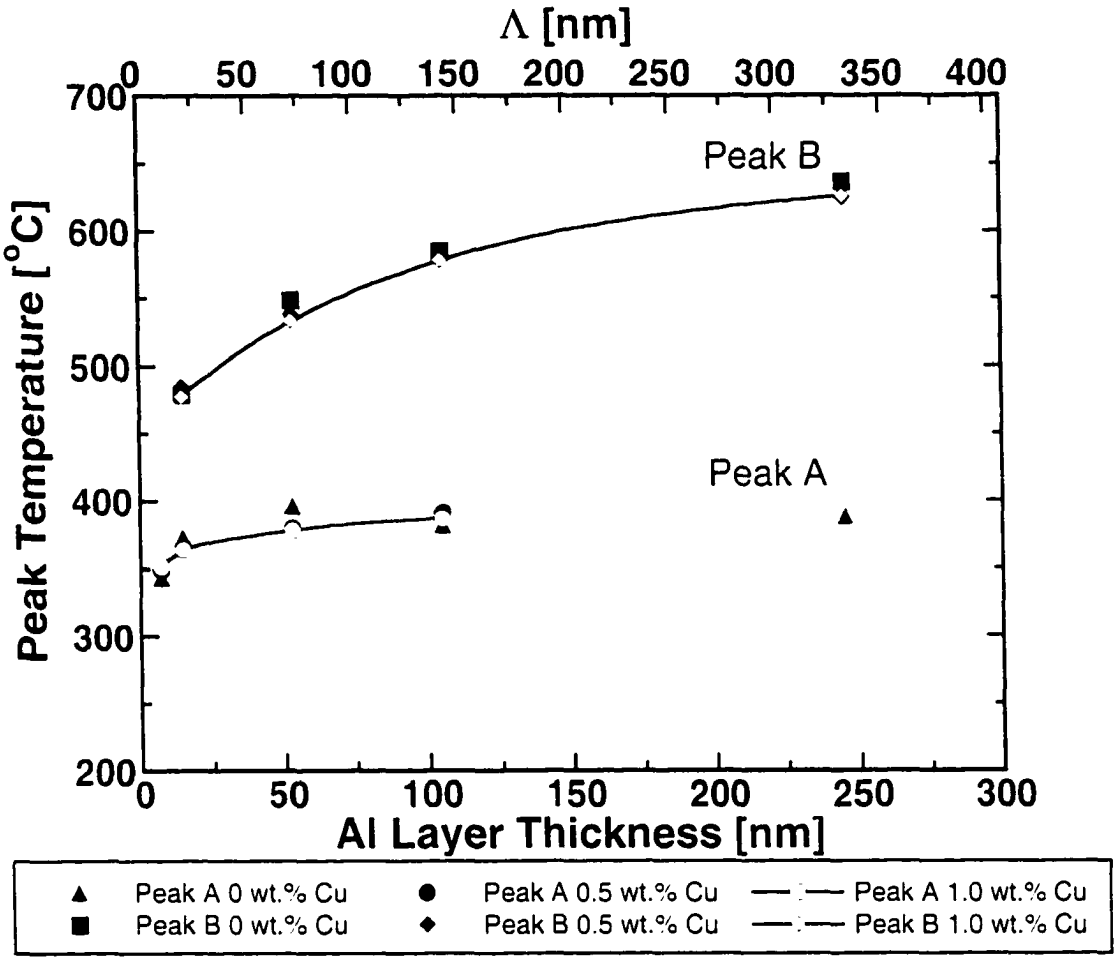

Figure 4. 28: Variation in peak temperatures as a function of deposited Al layer thickness and bilayer periodicity for constant-heating-rate DSC traces for 1Nb/3Al, 1Nb/3Al-0.5 wt.% Cu, and 1Nb/3Al-1.0 wt.% Cu.

More information was necessary to address the reason for the shift to higher temperatures. In the Ni/Al study, cross-sectional TEM investigations revealed that the $NiAl_3$ penetrated into the Al layer at grain boundary intersections at the interlayer interface (Ma et al. 1992, 1993). The authors postulated that this was evidence for the potency of grain boundary triple junctions as preferable nucleation sites for intermetallic phase formation. Since the number of triple junctions will scale with the grain size and generally the grain size scales with the layer thickness, thicker layers will have

proportionally fewer nucleation sites than thinner ones. If there was a lower density of possible nucleation sites then, if the phase nucleated predominantly at these sites, then more time would be required for the interfacial regions to be consumed (for a constant growth rate) which would explain the peak shift. A similar explanation was used in the description of peak shift in sputtered Nb/Al films with various thicknesses (Barmak et al. 1998). Again, cross-sectional TEM micrographs taken at the early stages of the reaction showed that $NbAl_3$ penetrated into the Al grain boundaries.

For the Nb/Al system, constant heating rate DSC experiments showed that the addition of 0.5 or 1.0 wt.% Cu to the Al did not have a measurable effect on the peak-shift behavior. Qualitatively, this would indicate that the reaction kinetics were not strongly affected by the addition of Cu. As shown in Figure 4. 28, the data for 0, 0.5 and 1.0 wt.% Cu multilayers effectively overlap for the range of periods investigated. This finding is in contrast with results reported by Ball and Todd (1987) where the temperature of peak A was shifted to higher temperatures with the addition of 4 wt.% Cu. This difference in the peak shift behavior might be attributed to $CuAl_2$ precipitates that formed in their samples. Extensive precipitation was not expected in the samples used in this study due to the small amounts of Cu present in the Al and the short annealing times.

The idea that the reaction kinetics in $NbAl_3$ formation was not affected by Cu additions was borne out by the activation energy measurements. When plotted versus Cu concentration, values for peak A and B cannot be distinguished when considering the errors in individual data points as shown in Figure 4. 29. A similar finding was reported by Ball and Todd (1987), although the data presented from their study was not as

extensive. For comparison, activation energies for Nb/Al-0 wt.% Cu samples obtained from DSC measurements by Barmak et al. (1998) are also included in the plot.

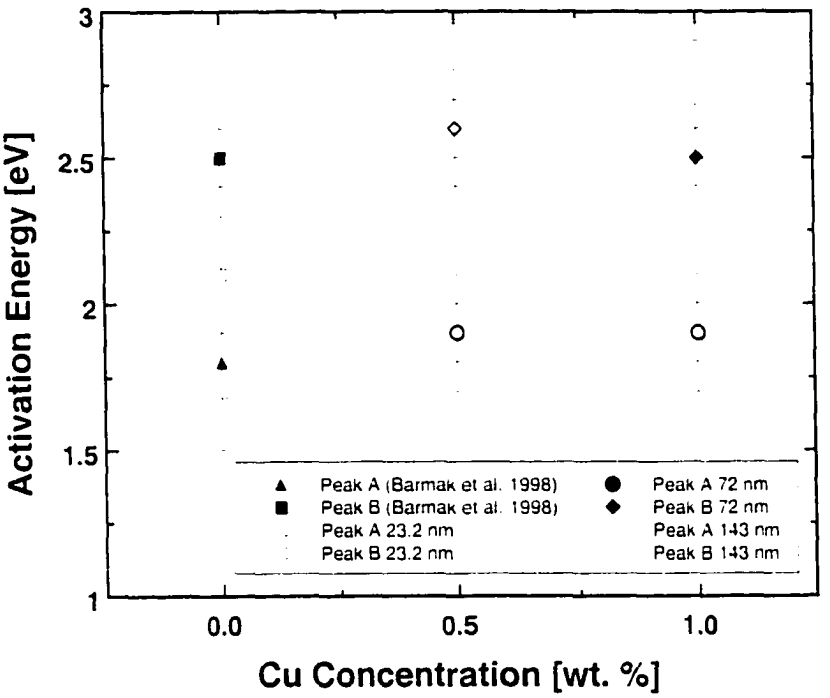

Figure 4. 29: Activation energies for peaks A and B obtained from the Kissinger analysis of 1Nb/3Al, 1Nb/3Al-0.5 wt.% Cu, and 1Nb/3Al-1.0 wt.% multilayer films plotted as a function of Cu concentration. Thicker lines around points indicate an overlap of the data points.

For the multilayers with Al-0 wt.% Cu, the results from the current work are in good agreement with earlier data for peak A. The values obtained for peak B are slightly lower than that reported by Barmak et al. (1998). However, note that the current measurement was taken from one film whereas the measurements of the work of Barmak et al. (1998) are averages of several measurements from films with different Λ. The aim of this experiment was not to completely replicate the previous results, but to provide a means of comparing present results with those from similar studies. DSC results indicate that the reaction is relatively insensitive to deposition or DSC equipment provided the multilayers are prepared and analyzed under similar conditions.

The physical interpretation of the activation energies is non-trivial. Since the values may not be ascribed to a unique reaction process (e.g., diffusion, nucleation, grain growth, etc.) an unambiguous description may not be possible. Some insight might be gained through examination of relevant diffusion data available in the literature for Nb/Al in Table 4. XV.

Table 4. XV: Relevant diffusion data for the Nb/Al system.

System	D_0 [cm^2/s]	Q [eV]	Temp. Range [°C]	References
Nb in Nb	8×10^{-3}	3.62 ± 0.09	1080 – 2420	Smithells (1992)
	3.7	4.54 ± 0.01		
Al in Nb	450	4.46	1427 – 1727	Smithells (1992)

Clearly, activation energies for both peaks A and B are lower than diffusion of Al in Nb or Nb in Nb as measured at relatively high temperatures. The measured activation energy for peak A is closer to either the activation energy for Al self diffusion or Al diffusion through $NbAl_3$ approximated by the early studies of Slama and Vignes (1972) and Ogurtani (1972). However, these values are significantly lower than activation energy obtained for peak B where large amounts of $NbAl_3$ would have formed. This draws attention to the differences between reaction kinetics in artificially modulated thin film structures as compared to bulk systems. Such differences could most likely be attributed to the smaller microstructural and diffusion length scales present both in the as-deposited state and during the reaction. Given the high value of the activation energy for Al diffusion in Nb one can deduce that Nb in Al might be considerably lower, thus providing a reason for the observed enhanced growth of $NbAl_3$ into the Al layer.

The effect of Cu on the transformation of the Λ = 10 nm films was also investigated by constructing a plot of n vs. Cu concentration in Figure 4. 30. The data indicated that, the presence of Cu reduced the value of n from 2.8 to ~2.5.

Note, however, that the values for the Avrami exponent obtained in this study are slightly higher than the values reported by Barmak et al. (1996) and Barmak et al. (1998). In those studies n was ~ 2 for 1Nb/3Al multilayers with Λ = 10 nm. In this work the value of n is ~ 2.8. This difference may be a result of different deposition conditions that would effect the structure of the interfacial region such as the number of tri-junctions or grain boundaries. The nucleation conditions determining the Avrami exponent may be sensitive to these changes in microstructure which could depend on the particular sputtering conditions and could influence transformation kinetics. Further DSC experiments involving a larger number of samples might be useful to determine the run-to-run reproducibility of the peak shapes.

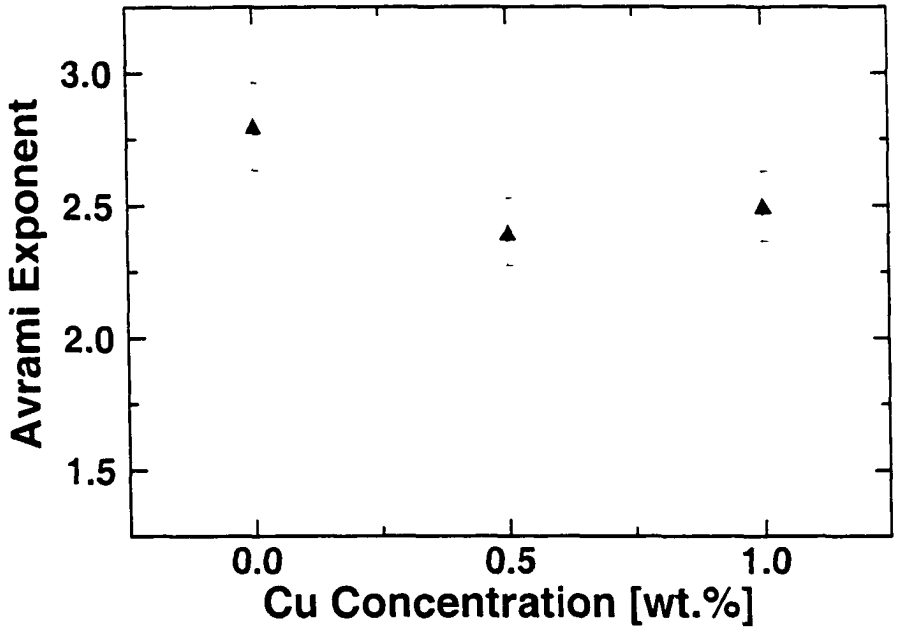

Figure 4. 30: Plot of the Avrami exponent determined from fits to peak A for 1Nb/3Al multilayer thin-films with Λ = 10 nm vs. Cu concentration.

A discussion of the enthalpy values determined from the Nb/Al and Nb/Al(Cu) films begins with an comparison with the current values available in the literature.

Table 4. XVI summarizes the enthalpy associated with the formation of $NbAl_3$ from current and previous measurements.

Table 4. XVI: Summary of the values of the formation enthalpy of $NbAl_3$ obtained from the literature.

Sample Type	Method	ΔH (average) [kJ/g-atom]	# of meas.	Ref.
Nb-Al alloy	Knudsen Cell Effusion	32.6 ± 2.1		Shilo et al. (1989)
Evaporated Nb-Al multilayers (Cu underlayers)	Calibrated DTA	42.5 ± 7.5		Coffey et al. (1992)
Nb and Al powders	Direct Synthesis Calorimetry	40.5 ± 0.6		Meschel and Kleppa (1992)
N/A	FP-LMTO(a)	41.5		Colinet et al. (1997)
Sputtered Nb/Al-0 wt.% Cu multilayers (Cu underlayer)	DSC	40.0 ± 4.1	8	This work
Sputtered Nb/Al-0.5 wt.% Cu multilayers (Cu underlayer)	DSC	40.8 ± 0.5	2	This work
Sputtered Nb/Al-1.0 wt.% Cu multilayers (Cu underlayer)	DSC	40.5 ± 0.6	6	This work
All multilayers combined	DSC	40.6 ± 2.9	16	This work

(a) The linear-muffin-tin-orbital (LMTO) method in the full potential (FP) approximation.

Note that the current measurements reported in the table were determined from several samples with different Λ. The number of samples used to determine the average enthalpy also varied depending on the quality of the baselines. The error on an individual measurement was never more than 0.8 kJ/g-atom due primarily to the error in weighing the sample. The larger scatter in the data is, in part, due to deviations from stoichiometry. Taking the heat of formation as 40 kJ/mol and a deviation of ±4 at.%, could account for

measured values as low as 36 kJ/mol. The larger scatter in the Nb/Al samples as compared to Nb/Al(Cu) is expected to be a consequence of the longer exposure of these samples to acid, and thus possible incorporation of hydrogen into the Nb layers. This further highlights the importance of the type and method of preparation of the sacrificial underlayer.

Considering the other past and present measurements, the enthalpy of formation of $NbAl_3$ obtained from the Knudsen cell effusion measurement is clearly low in comparison. The values obtained from DTA experiments, while accurate, exhibit larger errors. The errors in these measurements, in addition to run-to-run variations, are due to the errors in the calibration constant K and C that must be determined to account for the heat capacity and thermal conductivity of the DTA apparatus, respectively (Coffey et al. 1992). The calibration constants K and C are required to convert the temperature difference measured in the DTA to power in order to calculate the heat released by the reaction. In contrast, DSC measurements eliminate these errors by directly measuring power evolved in an exothermic reaction resulting in a more precise value. The formation enthalpy data obtained in our study also compares favorably to that of Meschel and Kleppa (1992) measured by direct synthesis calorimetry. It is also worth noting that all of the experimental measurements, except the Knutsen cell effusion measurement, agree well with the value calculated using first principles.

By plotting the heat of formation values versus bilayer period or layer thickness, the extent of interdiffusion or compound formation prior to phase formation can be ascertained. Figure 4. 31 shows such a plot for the Al/Nb samples. The values for the heat of formation are observed to be relatively constant within the error, this indicates

that significant interdiffusion does not occur in this system. This result differs from systems such as Al/Ni where the formation of a compound during deposition causes a pronounced decrease in the total heat of the reaction (Barmak et al. 1995, Barmak et al. 1997).

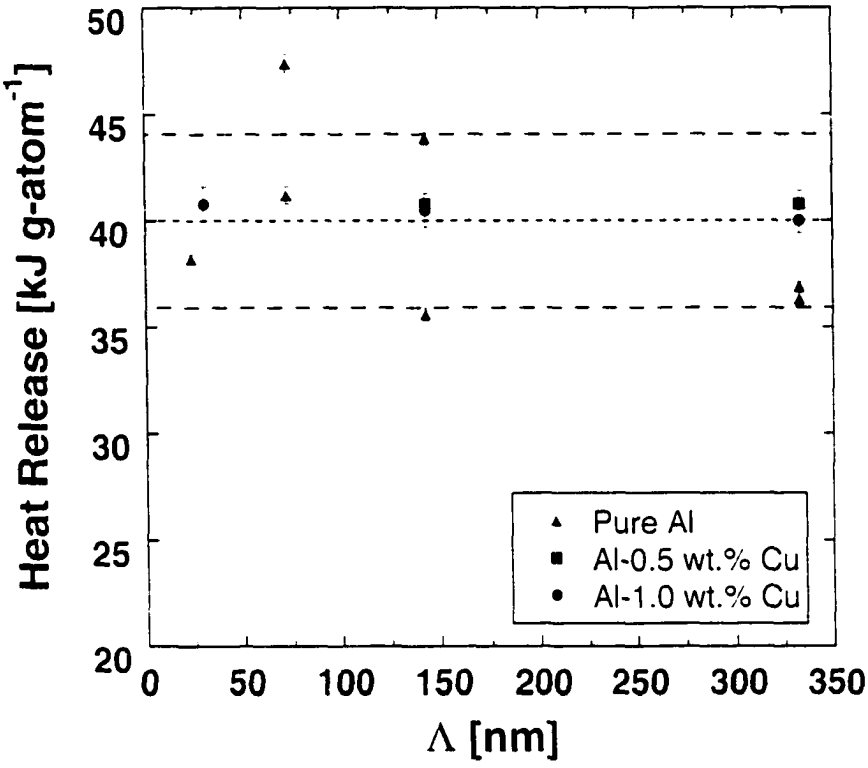

Figure 4. 31: Plot of reaction enthalpy (ΔH) vs. bilayer period (Λ) for a series of 1Nb/3Al, 1Nb/3Al-0.5 wt.% Cu, and 1Nb/3Al-1.0 wt.% Cu. The constant value of ΔH indicates that intermixing does not occur in significant amounts in this system. The dashed line indicates the average ΔH obtained for the films with pure Al.

The effect of intermixing on the heat of formation of $NbAl_3$ was then investigated in more detail. Another multilayer film was deposited with a 10 nm-thick co-deposited alloy layer with a composition of $Nb_{42}Al_{58}$, as estimated from the relative deposition rates of Nb and Al at 250 W. X-ray diffraction of this alloy revealed a broad diffraction peak indicative of an amorphous, disordered, or nanocrystalline phase. This sample simulated

the effect of a 10 nm intermixed layer at each of the reactant interfaces. The DSC trace showed a marked difference from the 1Nb/3Al, Λ = 72 nm film shown in Figure 4.18 and reaction enthalpy was measured as 33.1 ± 0.5 kJ/g-atom (Figure 4. 32). The heat release between Peak A and B was believed to be a result of the superposition of the crystallization of the amorphous or disordered NbAl layer to the equilibrium $NbAl_3$ phase and the simultaneous solid state reaction process.

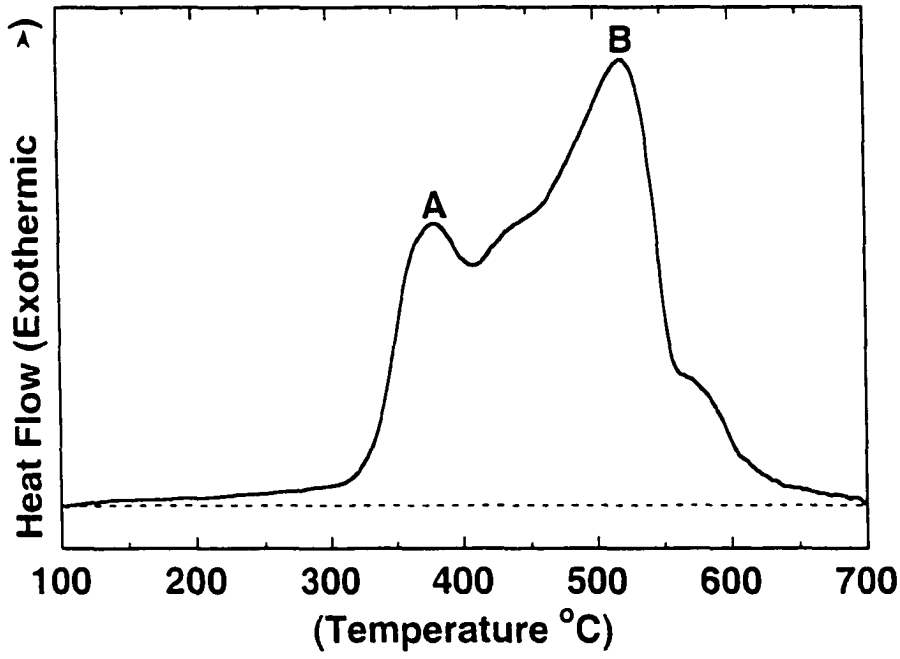

Figure 4. 32: Baseline-subtracted, constant heating rate DSC trace of a 1Nb/$Nb_{48}Al_{52}$/3Al multilayer film with an Λ_{eff} = 92 nm heated at 40 °C/min to 700 °C.

The relationship between heat of reaction (ΔH) of a sample and the heat of formation for a compound (ΔH_f) for a certain amount of intermixing is given by (Weihs et al. 1996, Michaelsen et al. 1997),

$$\Delta H = \Delta H_f \left(1 - \frac{4\omega}{\Lambda_{eff}} \right) \qquad (4.11)$$

where ω is the half-thickness of the intermixed layer and Λ is the bilayer thickness. This equation assumes an intermixed region with a sharp composition profile.

In a multilayer sample, with an interleaved co-deposited layer, an effective period, Λ_{eff}, is defined as,

$$\Lambda_{eff} = \Lambda + 2t_{NbAl} \qquad (4.12)$$

This is shown schematically in Figure 4. 33.

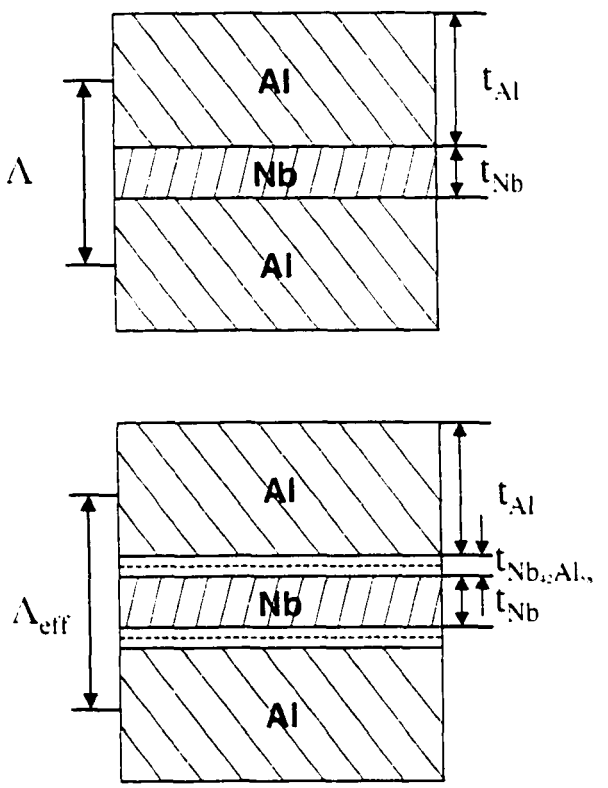

Figure 4. 33: Schematic illustration of the definition of Λ_{eff} for multilayers with an interleaved co-deposited layer.

For a multilayer with Λ =72 nm, Λ_{eff} = 92 nm. Substituting the values for Λ, ω (10 nm) and using the values measured from DSC for ΔH_f, eq. 4.11 yields a heat of reaction (ΔH) of 31.3 ± 3.1 kJ/g-atom. This value is close to the heat of reaction of $NbAl_3$ measured directly from calorimetry for the samples with the co-deposited layers.

Conversely, if the heat of formation measured from the DSC is substituted for ΔH, ω can be calculated. This yields a value of 8 ± 3 nm in reasonable agreement with the co-deposited layer thickness.

Quantitative analytical electron microscopy experiments have also shown that the interface width in a $\Lambda = 333$ nm Nb/Al multilayer was < 5 nm with a sharp interlayer transition (Lucadamo et al. 1999). The apparent lack of significant intermixing or reaction in the Nb/Al films may result from the small atom size difference (~3 %) between Al and Nb, resulting in the presence of granular epitaxy in these films. This is evident in the as-deposited microstructures where "macrograins" aligned in similar orientations are observed to propagate through several bilayers (discussed in Chapter 5). Previous studies have indeed indicated that a large atom size difference can lead to increased intermixing or the formation of disordered interfaces (Hufnagel et al. 1992, Clemens and Hufnagel 1993). The fiber texture of the Nb and Al layers is also evident in X-ray diffraction measurements which indicate the predominance of the Nb(110) and Al (111) peaks (Barmak et al. 1998). At sufficiently low Λ (< 10 nm) superlattice peaks have been observed in Nb/Al multilayers (McWhan et al. 1983, Baumann et al. 1992, Barmak et al. 1998).

4.5.1 Ti/Al-0 wt.%, Ti/Al-0.5 wt.% Cu, and Ti/Al-1.0 wt.% Cu

There are relatively few previous studies that have used calorimetry to investigate the formation of $TiAl_3$ (Wölhert 1995, Michaelsen et al. 1994, Michaelsen et al. 1996, Federspiel et al. 1999). The study of the $TiAl_3$ formation requires careful investigation since this phase can also exist in two metastable structures. As mentioned earlier, a detectable heat release is associated with the formation of the first metastable and second metastable structure ($L1_2$ and DO_{23}) that can be resolved at low bilayer thicknesses. However, the transformation of the DO_{23} phase to the equilibrium DO_{22} phase was not detected by DSC measurements (Michaelsen et al. 1996). Additional complexity results from the formation of $L1_2$ occurring in two-stages (as with $NbAl_3$ formation) and the shift to higher temperatures of the first peak and second peak of $L1_2$ formation with increasing Al layer thickness or Λ. This shift eventually causes the $L1_2$ peak B peak to merge with and eventually overshadow the exotherm resulting from DO_{23} formation. Because of this behavior, the choice of Λ for the DSC study is critical to measure the appropriate transitions. Three peaks are visible in a narrow range of thicknesses of films with Λ ~ 20-30 nm. The first peak of $L1_2$ formation (Peak A) and the peak associated with the transformation of $L1_2$ to DO_{23} formation (Peak C) are observed in films with $\Lambda < 30$. However, a 10 nm film was used to determine the activation energies for $L1_2$ peak A and the $L1_2$ to DO_{23} transformation for the formation of $TiAl_3$. The activation energy of $TiAl_3$ formation for the $L1_2$ and DO_{23} was also *independently* determined in films with dilute Cu additions. In this present study, films with Λ = 10 and 20 nm were investigated. The results of the calorimetry studies of the Ti/Al and Ti/Al(Cu) films are reported in the following sections.

4.5.1.1 Effect of Film Thickness on Overall Reaction Kinetics

A plot of 1Ti/3Al multilayers heated at 40 °C/min to 600 °C is shown in Figure 4. 34. For the Ti/Al experiments, films with $\Lambda < 30$ nm were used due to the overlap of the exothermic reaction peaks that occurs as the layer thicknesses increase. The superposition of the peaks prevents accurate and unique identification of the different phase transformations.

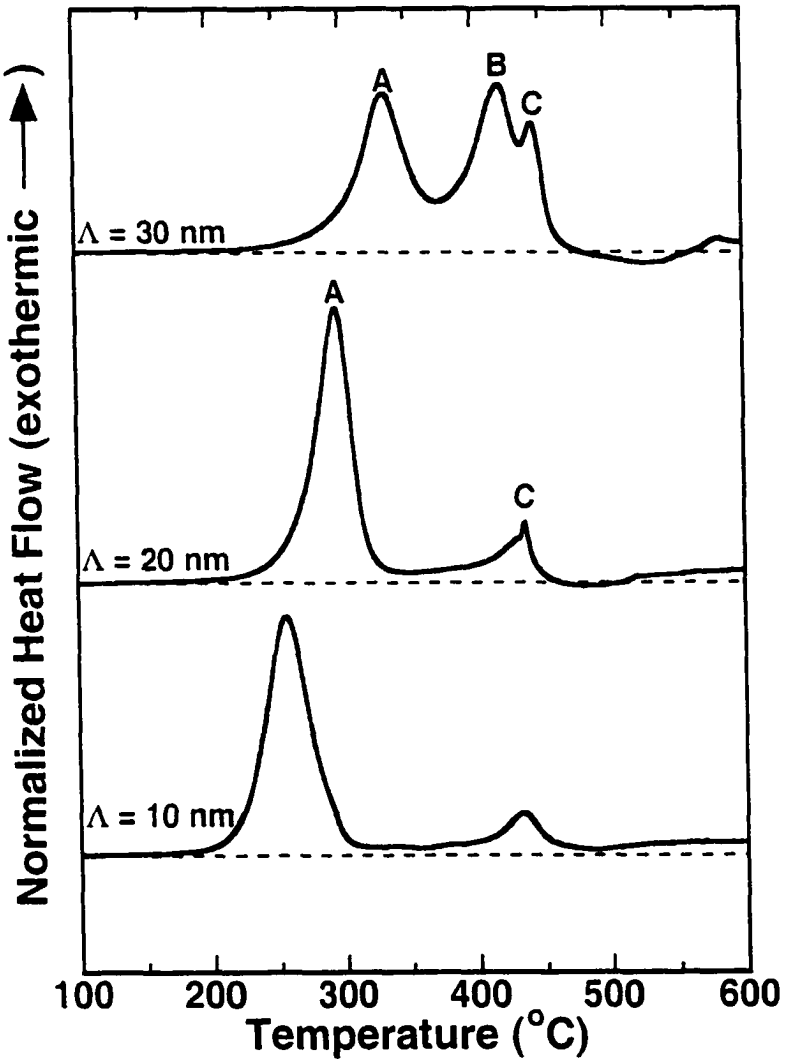

Figure 4. 34: Baseline-subtracted, constant heating rate DSC traces obtained from a series of 1Ti/3Al 0 wt.% Cu multilayers heated at 40 °C/min to 600 °C. Peaks A, B, and C corresponds to the formation of $TiAl_3$.

The constant heating rate traces shown in Figure 4. 34 clearly show the lower reaction temperatures that are present in the Ti/Al system. For this heating rate the formation of the $L1_2$ $TiAl_3$ begins at ~250 °C. The peak temperatures of the two exothermic peaks are summarized in Table 4. XVII.

Table 4. XVII: DSC peak temperatures for 1Ti/3Al-0.0 wt.% Cu multilayers heated at 40 °C/min to 700 °C.

sample ID	Λ [nm]	Peak A [°C]	Peak B [°C]	Peak C [°C]
121198a4	10	267	-	448
121498a1	20	296	-	437
1Ti3Al040698	30	335	420	445

The 10 and 20 nm period multilayers indicated some heat release following peak A. A second exothermic peak (peak C) then occurs at ~425 °C. Previous studies by Michaelsen (1996) have identified this as the formation of DO_{23} superlattice structure of $TiAl_3$. The reaction is not completed until ~600-700 °C when the equilibrium DO_{22} structure of the $TiAl_3$ phase is formed. Due to the low enthalpy associated with this transformation it is not observed in the DSC. Note that if thicker Al or Ti layers are used, the formation of the metastable structures of $TiAl_3$ will be obscured. Thus, much of the literature extant on $TiAl_3$ formation does not describe the formation of $L1_2$ and DO_{23} $TiAl_3$ because these phases could not be resolved in calorimetric investigations using thick bilayers or in RBS studies which are insensitive to such changes in crystal structure.

In order to assess the effects of dilute Cu concentrations on the formation of the $TiAl_3$ phase, a series of multilayers was deposited with nominally the same bilayer thickness and composition as the 0 wt.% Cu samples. The results from the 10 nm, 20 nm, and 30 nm samples are shown in Figure 4. 35.

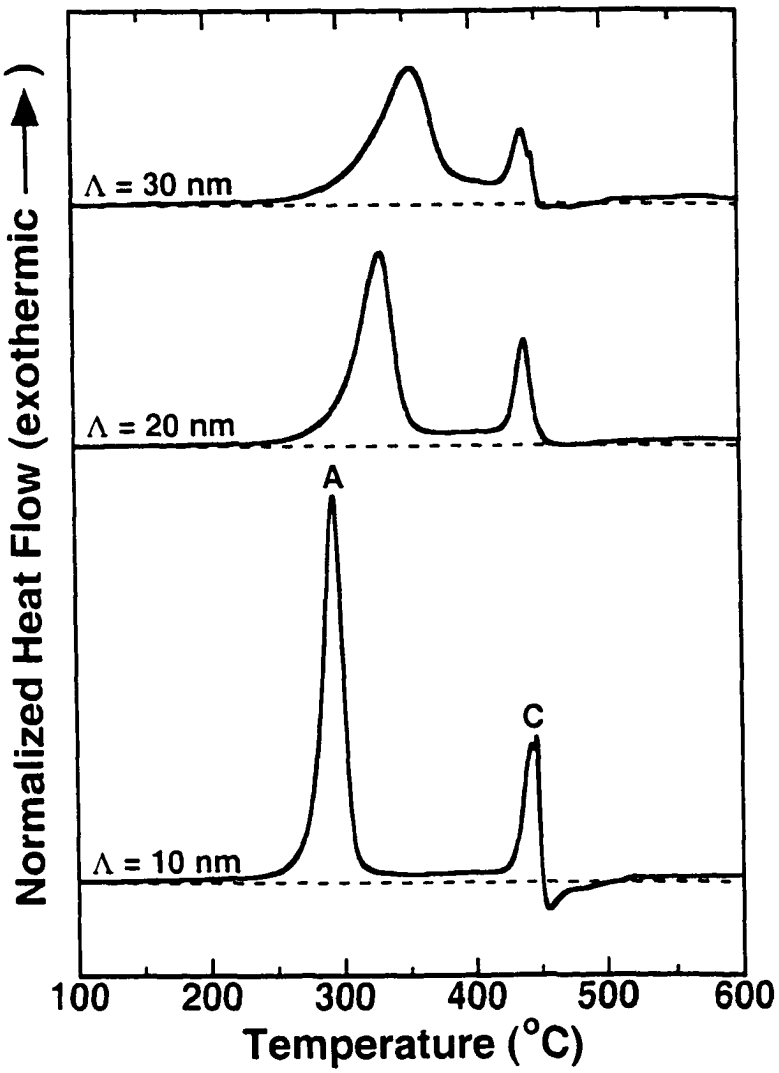

Figure 4. 35: Baseline-subtracted, constant heating rate DSC traces obtained from a series of 1Ti/3Al-0.5 wt.% Cu multilayers heated at 40 °C/min to 600 °C. Peaks A, B, and C correspond to the formation of $TiAl_3$

As with the 0 wt.% Cu samples, these traces exhibit two peaks (labeled A and C) that correspond to the formation of the $L1_2$ and DO_{23} metastable $TiAl_3$ structures. Systematic changes in peak shape or height were not observed when compared with the traces from samples without Cu, however, the second peak associated with $L1_2$ formation (peak B) was notably absent from the DSC trace of the 30 nm film. Peak A was considerably narrower in this set of samples and broadened with increasing period. Peak

A also shifted to higher temperatures with increasing bilayer thickness. The slight heat release after the completion of the DO_{23} transformation could be caused by DO_{22} formation or the growth of $TiAl_3$ grains. The summary of the peak temperatures for this series of multilayers is listed in Table 4.XVIII.

Table 4.XVIII: DSC peak temperatures for 1Ti/3Al-0.5 wt.% Cu multilayers heated at 40 °C/min to 700 °C.

sample ID	Λ [nm]	Peak A [°C]	Peak B [°C]	Peak C [°C]
102898a1	10	294	-	444
110698a2	20	332	-	440
110598a1	30	356	-	440

As with the 0 wt.% Cu and 0.5 wt.% Cu samples, Ti/Al-1.0 wt.% Cu samples were deposited with 10, 20, and 30 nm periodicities. Again, no distinct differences were observed between the multilayers containing Cu and the multilayers without Cu. However, like the 0.5 wt.% Cu sample the Λ = 30 nm sample did not exhibit peak B associated with the formation of the $L1_2$ phase. The results from the calorimetry experiments are shown in Figure 4.36. Unlike the 0.5 wt.% Cu samples, the heat signal did not cross below the baseline after the formation of the DO_{23} phase. Peak A shifted to higher temperatures with increasing period while peak C remained at a constant temperature. The peak temperatures for the 1Ti/3Al-1.0 wt.% Cu multilayers are listed in Table 4. XIX.

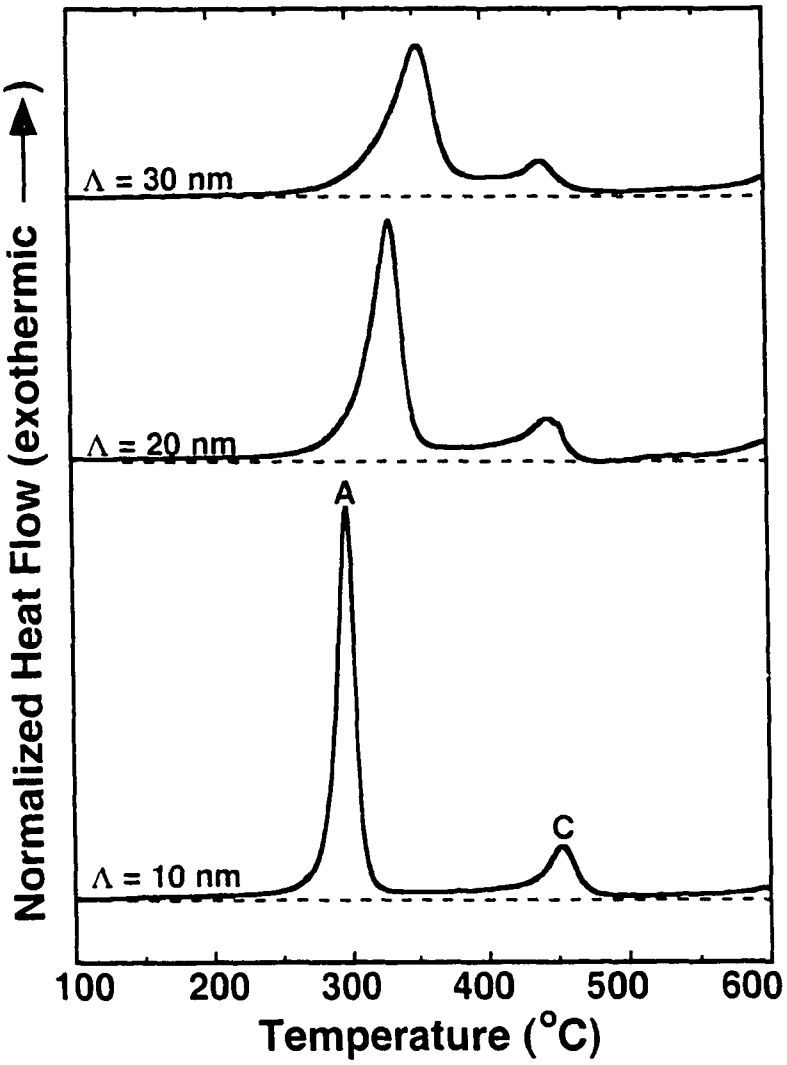

Figure 4.36: Baseline-subtracted, constant heating rate DSC traces obtained from a series of 1Ti/3Al-1.0 wt.% Cu multilayers heated at 40 °C/min to 600 °C. Peaks A and C correspond to the formation of $TiAl_3$.

Table 4. XIX: DSC peak temperatures for 1Ti/3Al-1.0 wt.% Cu multilayers heated at 40 °C/min to 700 °C.

sample ID	Λ [nm]	Peak A [°C]	Peak B [°C]	Peak C [°C]
101398b1	10	298	-	452
101398a1	20	330	-	444
101598b1	30	354	-	441

4.5.1.2 Activation Energy

Using the Kissinger analysis, activation energies were determined for peaks A and C in a 10 nm 1Ti/3Al multilayer. This experiment was performed to provide a comparison between the current films and those deposited elsewhere in addition to providing a control sample to compare with samples containing Cu. The results from the Kissinger analysis are shown in Figure 4. 37. As with the Nb/Al films, three heating rates (20, 40, 80 °C/min) were used to assess the magnitude of the shift in position of the peaks.

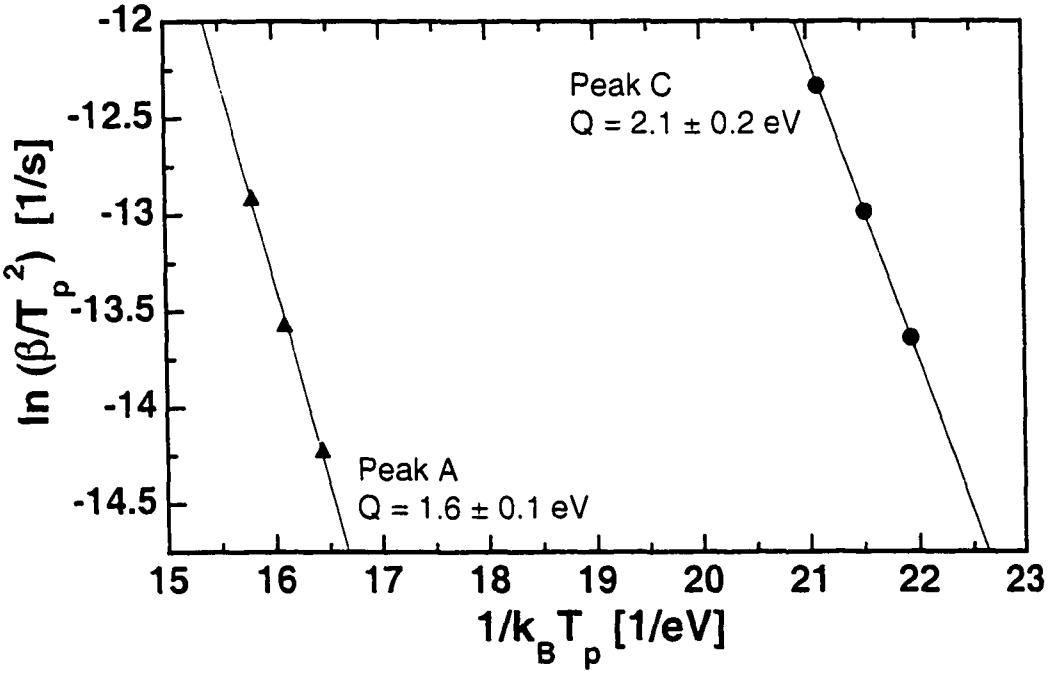

Figure 4. 37: Kissinger plot showing activation energies for peaks A and C from a 1Ti/3Al-0 wt.% Cu, Λ = 10 nm multilayer thin-film.

The results from the linear fit used to determine the activation energies for peak A and C and the value of the frequency factor, v, calculated from eq. 4.9 are listed in Table 4. XX.

Table 4. XX: Results from Kissinger analysis of DSC data for a 1Ti/3Al multilayer film with Λ = 10 nm.

Peak	Q [eV]	Error (98% conf.)	y-int. [$K^{-1}s^{-1}$]	Error (98% conf.)	Freq. Factor (v) [s^{-1}]
1Ti/3Al- 0 wt.% Cu; Λ = 10 nm (121198a)					
A	1.6	0.1	20.84	0.70	2.04×10^{13}
C	2.1	0.1	20.11	4.08	1.31×10^{13}

As can be seen from the resulting data, the values of 1.6 ± 0.1 eV and 2.1 ± 0.2 eV for the activation energies of peak A and C are in remarkable agreement with values of 1.6 ± 0.1 and 2.0 ± 0.2 reported in the literature (Michaelsen et al. 1996).

Activation energies for the processes associated with peaks A and C were again obtained by a Kissinger analysis of the peak position data for a 10 nm and 20 nm 1Ti/3Al-0.5 wt.% Cu multilayer and are shown in Figure 4. 38. The parameters obtained from the linear fit to the data are listed in Table 4. XXI. The values of activation energies for both samples agree within measurement error for both peaks. At this level of Cu concentration, the values of the activation energies are not significantly different from the activation energies measured for the sample without Cu.

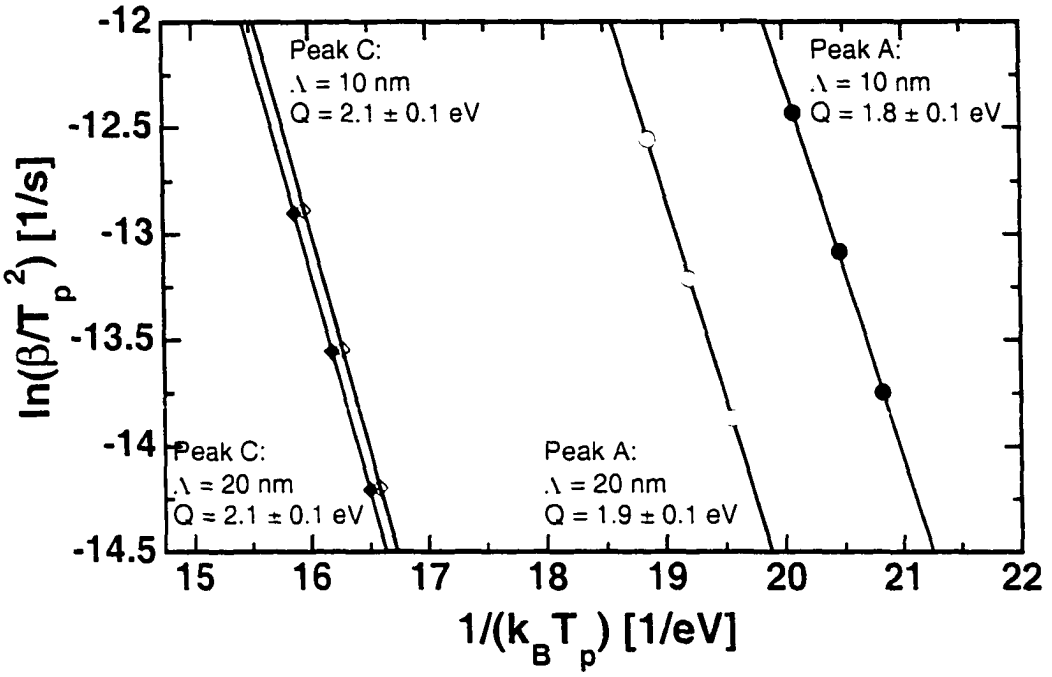

Figure 4. 38: Kissinger plot showing activation energies for peaks A and C from 1Ti/3Al-0.5 wt.% Cu, Λ = 10 nm and Λ = 20 nm multilayer thin-films.

Table 4. XXI: Results from Kissinger analysis of DSC data for a 1Ti/3Al-0.5 wt.% Cu multilayer films with Λ = 10 nm and Λ = 20 nm.

Peak	Q [eV]	Error (98% conf.)	y-int. [$K^{-1}s^{-1}$]	Error (98% conf.)	Freq. Factor (ν) [s^{-1}]
1Ti/3Al- 0.5 wt.% Cu; Λ = 10 nm (102898a)					
A	1.8	0.1	23.09	2.6	$2.19x10^{14}$
C	2.1	0.1	20.03	0.60	$1.20x10^{13}$
1Ti/3Al-0.5 wt.% Cu; Λ = 20 nm (110698a)					
A	1.9	0.1	23.06	2.52	$2.27x10^{14}$
C	2.1	0.1	20.36	0.56	$1.69x10^{13}$

Finally, using the Kissinger analysis with three heating rates, activation energies were determined for peaks A and C in 10 and 20 nm 1Ti/3Al-1.0 wt.% Cu multilayers. The results are shown in Figure 4. 39.

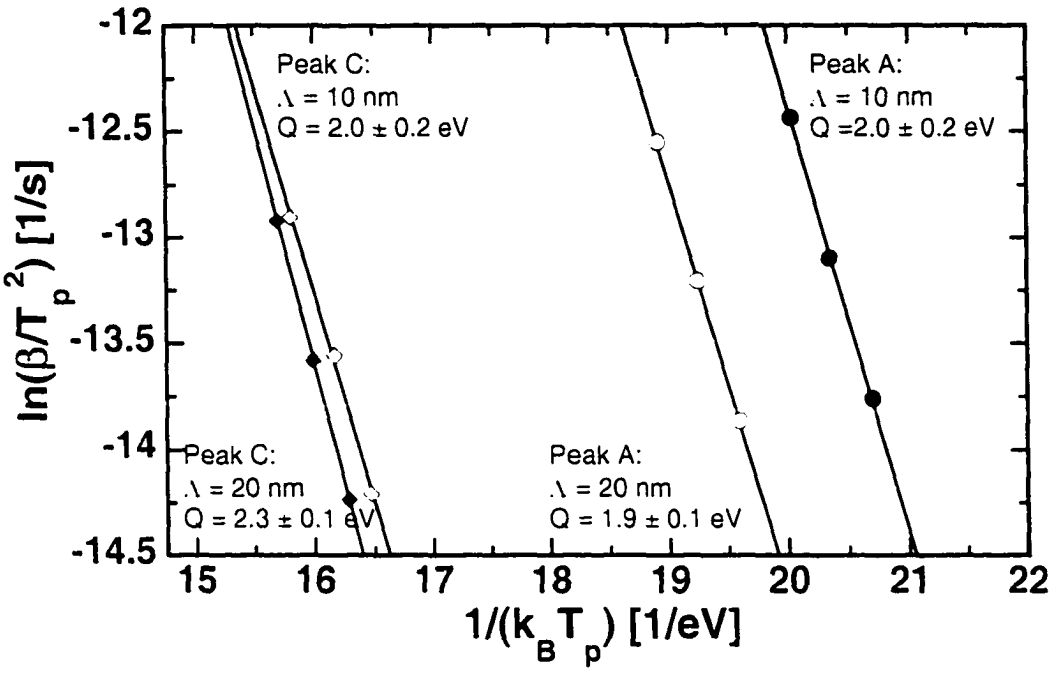

Figure 4. 39: Kissinger plot showing activation energies for peaks A and C from 1Ti/3Al-1.0 wt.% Cu, Λ = 10 nm and Λ = 20 nm multilayer thin-films.

The results obtained from the linear fit to the data are shown in Table 4. XXII.

Table 4. XXII: Results from Kissinger analysis of DSC data for a 1Ti/3Al-1.0 wt.% Cu multilayer films with Λ = 10 nm and Λ = 20 nm.

Peak	Q [eV]	Error (98% conf.)	y-int. [$K^{-1}s^{-1}$]	Error (98% conf.)	Freq. Factor (ν) [s^{-1}]
1Ti/3Al- 1.0 wt.% Cu; Λ = 10 nm (101398b)					
A	2.0	0.2	27.45	3.22	$1.93x10^{16}$
C	2.3	0.2	22.34	0.12	$1.32x10^{14}$
1Ti/3Al-1.0 wt.% Cu; Λ = 20 nm (101398c)					
A	1.9	0.1	23.60	0.64	$3.95x10^{14}$
C	2.0	0.1	18.15	2.76	$1.73x10^{12}$

4.5.1.3 Reaction Order (Avrami Exponent)

The analysis proposed by Michaelsen and Dahms (1996) was also used to determine the Avrami exponents associated with the $TiAl_3$ formation. Constant heating

rate DSC traces from a 10 nm 1Ti/3Al multilayer taken at 20, 40, and 80 °C/min were fit using eq. 4.9. A representative result of a film annealed at 40 °C/min is shown in Figure 4. 40. Activation energies and frequency factors were obtained from the Kissinger analysis of the DSC data presented in Table 4. XVII. The only fit parameters were the Avrami exponent, n, and a multiplicative scaling factor that was ~1 in all cases. The fit resulted in an Avrami exponent of ~1.0. This low value resulting from a somewhat poor fit to the data is probably due to the more symmetrical, bell-shape of the heat signal. Typically, the signal would have a steeper slope on the high temperature side of the peak.

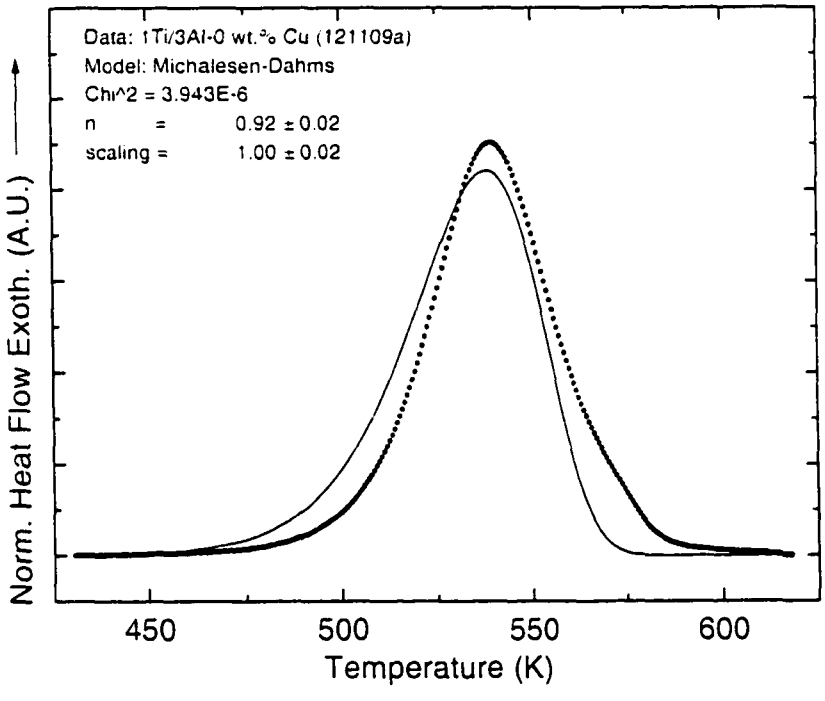

Figure 4. 40: DSC trace of a 1Ti/3Al multilayer film with Λ = 10 nm, taken at a heating rate of 40 K/min. The full line is the best fit of a JMA process to the measurement using eq. 4.8.

Table 4. XXIII: Results obtained from a non-linear least-squares fit to the experimental DSC trace obtained from a 1Ti/3Al-0 wt.%Cu multilayer with Λ = 10 nm.

Run	P1 (scaling)	fit error	P2 (n)	fit error	fit error (est)
121198a2	0.999	0.013	0.900	0.014	
121198a1	0.996	0.017	0.914	0.018	
121198a4	0.987	0.016	0.908	0.018	
121198a3			0.952	0.024	
Average	0.99	0.02	0.92	0.02	0.14
Stdev	0.01	0.00	0.02	0.004	

Constant heating rate DSC traces from three 1Ti/3Al-0.5 wt.% Cu films with Λ = 10 nm were also fit using eq. 4.8. A representative trace is shown in Figure 4. 41. The average Avrami exponent, n, for the three traces was 2.0 ± 0.1. The fit for these traces was substantially improved over the 1Ti/3Al-0 wt.% Cu samples. A summary of the fitting parameters from the different traces is listed in Table 4. XXIV.

Table 4. XXIV: Results obtained from a non-linear least squares fit to experimental DSC data obtained for a 1Ti/3Al-0.5 wt.% Cu multilayer with Λ = 10 nm.

Run	P1 (scaling)	error	P2 (n)	error	fit error (est)
102809a2	0.937	0.004	1.952	0.010	
102898a1	0.952	0.005	2.006	0.012	
102898a3	0.911	0.007	1.995	0.019	
Average	0.93	0.01	1.98	0.01	0.11
Stdev	0.02	0.00	0.03	0.005	

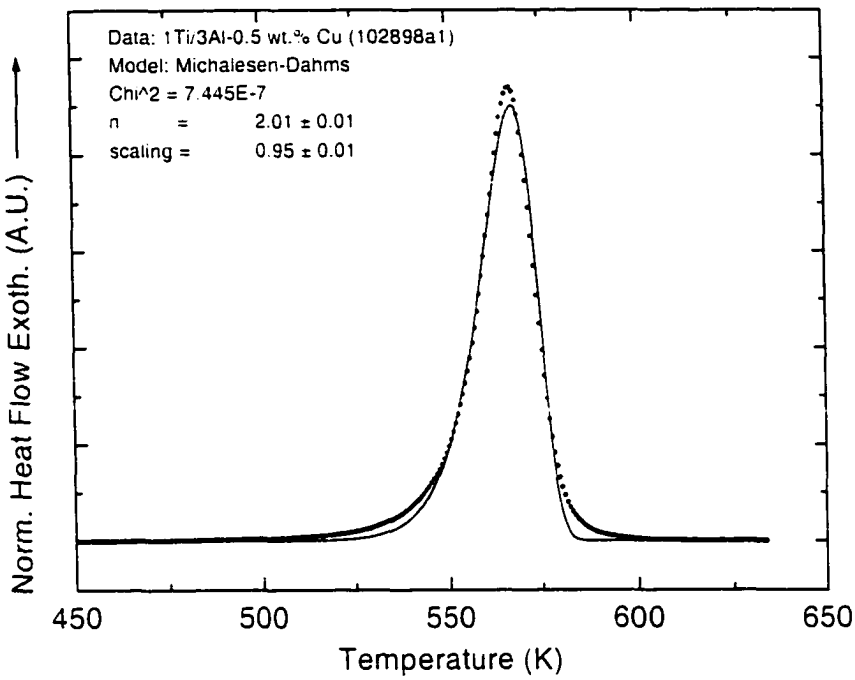

Figure 4. 41: DSC trace of a 1Ti/3Al-0.5 wt.% Cu multilayer film with Λ = 10 nm, taken at a heating rate of 40 °C/min. The full line is the best fit of a JMA process to the measurement using eq. 4.8.

The same procedure was employed to fit the data from 1Ti/3Al-0.5 wt.% Cu multilayers with Λ = 20 nm. A representative trace from these results is shown in Figure 4. 42. The fitting produced an average value of the Avrami exponent of 1.2 ± 0.1.

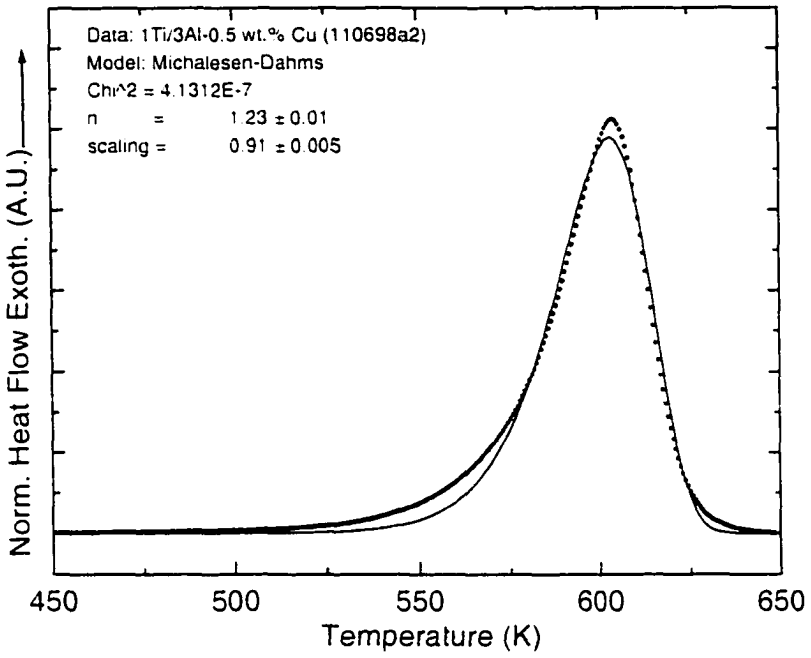

Figure 4. 42: DSC trace of a 1Ti/3Al-0.5 wt.% Cu multilayer film with Λ = 20 nm, taken at a heating rate of 40 °C/min. The full line is the best fit of a JMA process to the measurement using eq. 4.8.

The results of the individual fits to the experimental DSC data are listed in Table 4. XXV.

Table 4. XXV: Results obtained from a non-linear least squares fit to experimental DSC data obtained for a 1Ti/3Al-0.5 wt.% Cu multilayer with Λ = 20 nm.

Run	P1 (scaling)	error	P2 (n)	error	fit error (est)
110698a1	0.89	0.0004	1.284	0.007	
110698a2	0.90	0.005	1.227	0.00853	
110698a3	0.87	0.006	1.185	0.00954	
Average	0.89	0.00	1.23	0.01	0.07
Stdev	0.02	0.00	0.05	0.001	

The Avrami exponent was determined from the DSC traces from 1Ti/3Al-1.0 wt.% Cu multilayers with Λ = 10 and 20 nm. Figure 4. 43 shows a representative result

for a 10 nm film annealed at 40 °C/min. The average of fits to three different traces was found to be 2.0 ± 0.2.

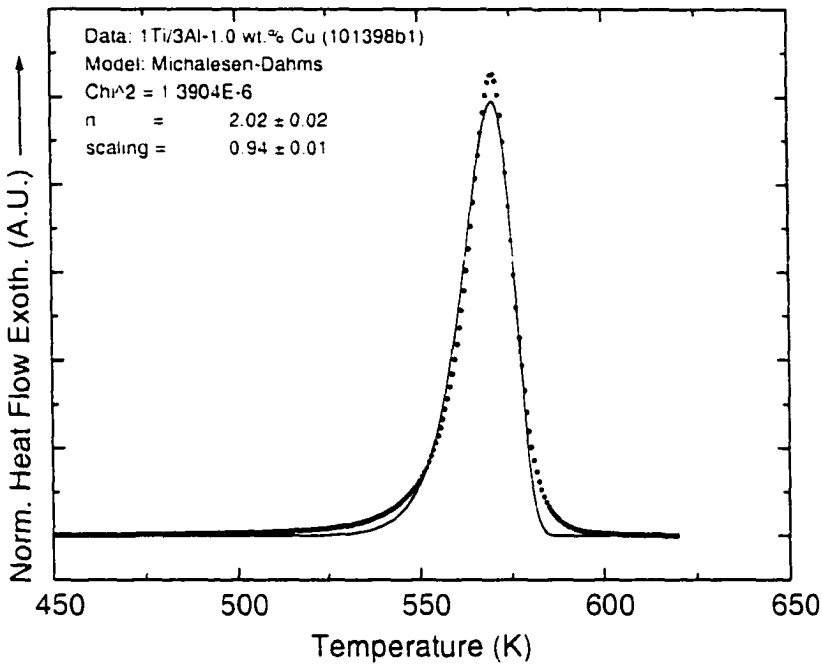

Figure 4. 43: DSC trace of a 1Ti/3Al-1.0 wt.% Cu multilayer film with Λ = 10 nm, taken at a heating rate of 40 °C/min. The full line is the best fit of a JMA process to the measurement using eq. 4.8.

The output of the non-linear least squares fitting routine for samples annealed at three different heating rates is summarized in Table 4. XXVI.

Table 4. XXVI: Results obtained from a non-linear least squares fit to experimental DSC data obtained for a 1Ti/3Al-1.0 wt.% Cu multilayer with Λ = 10 nm.

Run	P1 (scaling)	error	P2 (n)	error	fit error (est)
101398b3	0.905	0.004	2.004	0.009	
101398b1	0.940	0.007	2.009	0.017	
101398b2	0.921	0.011	2.112	0.029	
Average	0.92	0.01	2.04	0.02	0.20
Stdev	0.02	0.00	0.06	0.010	

A representative trace from a Λ = 20 nm film is shown in Figure 4. 43. The average from fits to three separate runs was 1.4 ± 0.1.

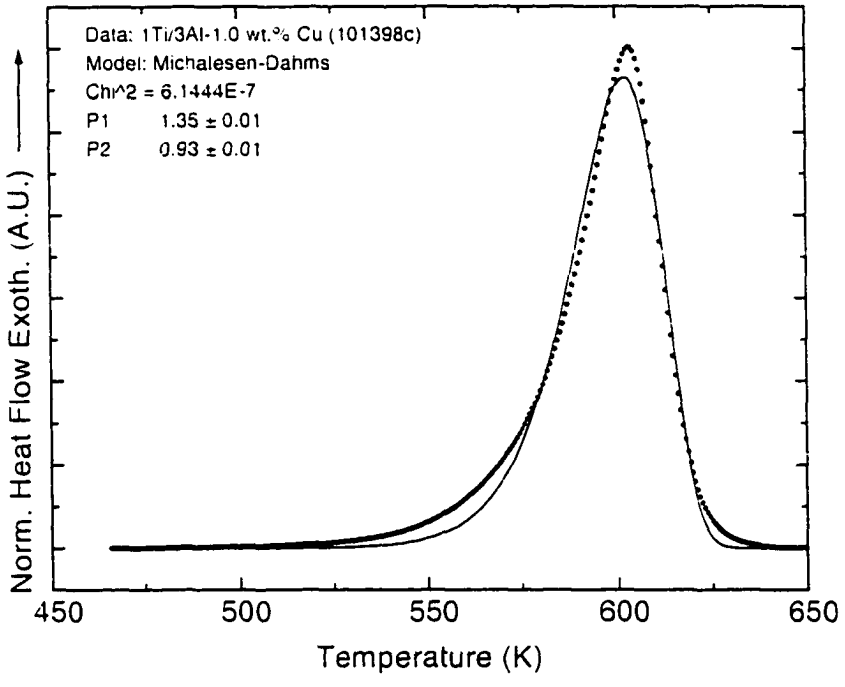

Figure 4. 44: DSC trace of a 1Ti/3Al-1.0 wt.% Cu multilayer film with Λ = 20 nm, taken at a heating rate of 40 °C/min. The full line is the best fit of a JMA process to the measurement using eq. 4.8.

A summary of the output from the non-linear least squares fitting routine for samples annealed at three different heating rates is provided in Table 4. XXVII.

Table 4. XXVII: Results obtained from a non-linear least squares fit to experimental DSC data obtained for a 1Ti/3Al-1.0 wt.% Cu multilayer with Λ = 20 nm.

Run	P1 (scaling)	error	P2 (n)	error	fit error (est)
101398c4	0.907	0.005	1.449	0.009	
101398c1	0.923	0.006	1.367	0.010	
101398c5	0.886	0.008	1.377	0.015	
Average	0.91	0.01	1.40	0.01	0.07
Stdev	0.02	0.00	0.04	0.003	

4.5.1.4 Reaction Enthalpy: $TiAl_3$

Due to difficulties obtaining a matching baseline at the high temperature part of the DSC trace, the reaction enthalpy was determined from only one DSC run for a 1Ti/3Al multilayer with Λ = 10 nm heated to 700 °C at 40 °C/min. The results from this measurement are listed in Table 4. XXVIII.

Table 4. XXVIII: Enthalpy measurement obtained from a 1Ti/3Al-0 wt.% Cu multilayer film annealed to 700 °C at 40 °C/min

Period [nm]	Run ID	Range [°C]	ΔH (Ave) [kJ g-atom^{-1}]	ΔH (σ) [kJ g-atom^{-1}]	ΔH (Ave) [kJ mol^{-1}]	ΔH (σ) [kJ mol^{-1}]
10	121198a2	170-488	25.5	0.4	102.1	1.6

As with the 1Ti/3Al-0 wt.% Cu samples, the 1Ti/3Al-0.5 wt.% Cu samples did not exhibit consistent baselines that matched at the high temperature portion of the reaction. However, two runs provided acceptable baselines enabling the determination of the reaction enthalpy. The results are listed in Table 4. XXIX. The average of the two measurements yielded an enthalpy of 32.3 ± 0.6 kJ/g-atom.

Table 4. XXIX: Enthalpy measurements obtained from 1Ti/3Al-0.5 wt.% Cu multilayer films annealed to 700 °C at 40 °C/min.

Period [nm]	Run ID	Range [°C]	ΔH (Ave) [kJ g-atom^{-1}]	ΔH (σ) [kJ g-atom^{-1}]	ΔH (Ave) [kJ mol^{-1}]	ΔH (σ) [kJ mol^{-1}]
20	110698a1	150-447	32.3	0.4	129.1	1.7
20	110698a2	150-493	32.3	0.9	129.1	3.5

As with the previous two enthalpy measurements, experimental inconsistencies in the baseline determination did not permit comprehensive determination of the reaction enthalpies for the 1Ti/3Al-1.0 wt.% Cu films. However, runs obtained from a Λ = 10 nm multilayer exhibited acceptable baselines and were used to calculate a reaction enthalpy.

The results of the calculation are listed in Table 4. XXX. The average of the two measurements yielded a reaction enthalpy of 26.8 ± 0.6 kJ/g-atom.

Table 4. XXX: Enthalpy measurements obtained from 1Ti/3Al-1.0 wt.% Cu multilayer films annealed to 700 °C at 40 °C/min.

Period [nm]	Run ID	Range [°C]	ΔH (Ave) [kJ g-atom^{-1}]	ΔH (σ) [kJ g-atom^{-1}]	ΔH (Ave) [kJ mol^{-1}]	ΔH (σ) [kJ mol^{-1}]
10	101398b1	158-690	25.5	0.3	102.1	1.3
10	101398b2	150-512	28.2	0.8	112.7	3.1

4.6 Discussion: Ti/Al

Some characteristics of the reaction of the Ti/Al multilayers are similar to the reaction of Nb/Al. As in Nb/Al, peak A is found to shift to higher temperatures as a function of Λ as seen in Figure 4. 45. Similar explanations of non-random nucleation mediated by the as-deposited grain sizes of the Al layers can explain the shift. The peak temperature associated with the formation of the DO_{23} superlattice structure of $TiAl_3$ was observed to stay essentially constant as a function of Λ. This clearly indicates that there are differences in details of he nucleation and growth processes that lead to the formation of this phase as compared to the $L1_2$ phase. Although, not explicitly observed in this study, it is expected that peak B will also shift in a similar manner to peak B in the Nb/Al films. The reaction mechanism is again fundamentally identical.

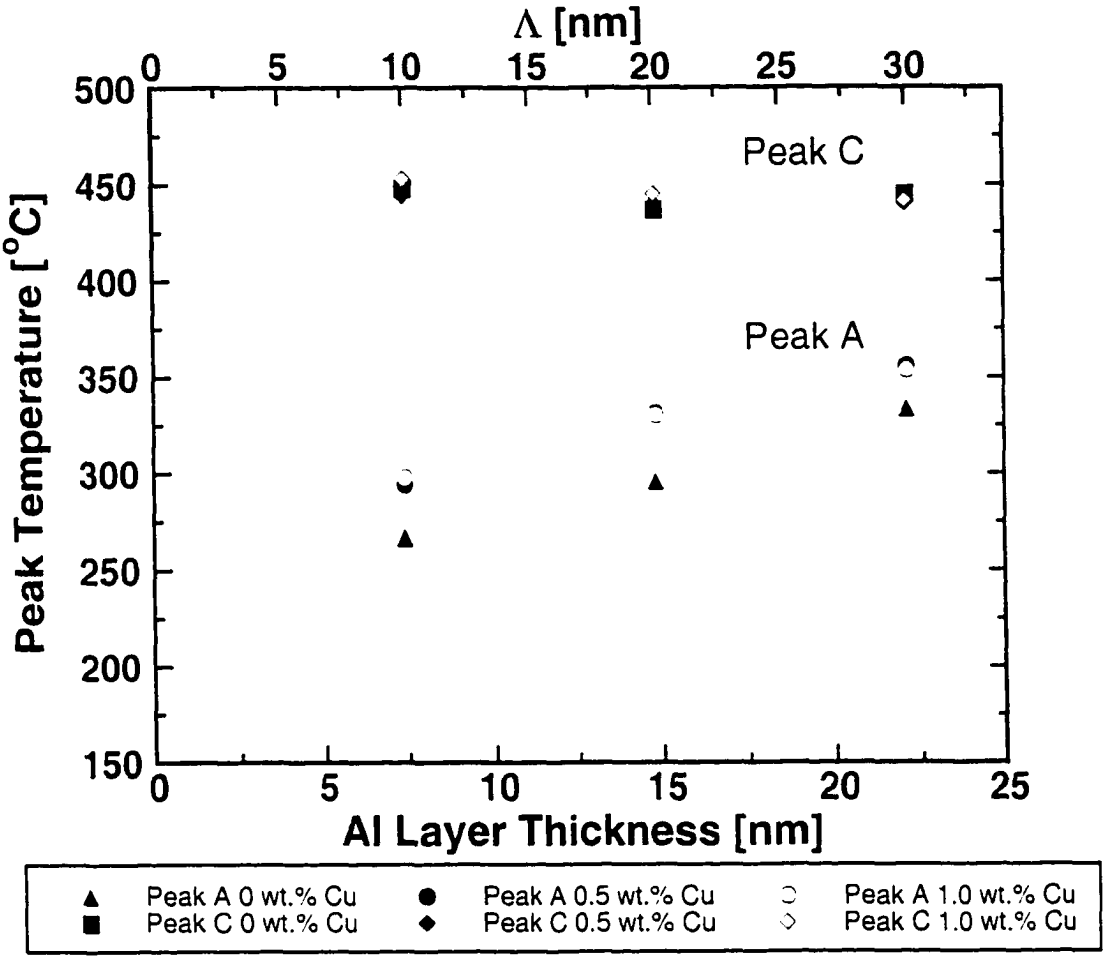

Figure 4. 45: Plot of peak temperatures for reactions associated with Peak A and Peak C for 1Ti/3Al, 1Ti/3Al-0.5 wt.% Cu, and 1Ti/3Al-1.0 wt.% Cu as a function of Al layer thickness.

The presence of Cu was found to influence the temperature of the first reaction peak for the Ti/Al multilayers. In the case of the films with 0.5 and 1.0 wt.% Cu in solution with the Al, the peak temperature is ~50 °C higher than the samples without Cu, as seen in Figure 4. 45. This behavior would be consistent with higher activation energies associated with the formation of $TiAl_3$ as reported by other authors (Wittmer and Huang 1984; Tardy and Tu 1985; Wittmer et al. 1985; Krivanek et al. 1992). Based on preliminary microstructural evidence, the increase in activation energy was initially

attributed to the reduction in Al diffusion by Cu that had segregated to the Al grain boundaries or reacting interfaces.

Measurements of activation energies in previously studied reports precludes discussion in the context of the current data. This is primarily due to the fact that earlier reports did not distinguish among the various $TiAl_3$ structures that formed and were limited by the techniques used to obtain kinetic data. Given the somewhat large variability in the activation energies reported in the literature, it is likely that the reported values are effectively some combination of the activation energies associated with $L1_2$, DO_{23}, Ti_9Al_{23}, or DO_{22} formation. Furthermore given that the majority of the studies report activation energies of ~1.8-2.0 eV, it appears likely that these studies are primarily measuring the energy associated with the $L1_2 \rightarrow DO_{23}$ transformation. This transformation occurs at ~ 400 °C, the temperature where many of the studies were conducted. By contrast to the majority of existing studies, the investigations of Michaelsen et al. (1996) distinguish between the different phases when obtaining the activation energies.

Despite the differences in the data existing in the literature, it is worthwhile to consider the available activation energy regarding the diffusion of Ti and Al summarized in Table 4. XXXI.

Table 4. XXXI: Summary of available diffusion data on the Ti-Al system.

System	D_0 [cm^2/s]	Q [eV]	Temp. Range [°C]	References
Al in $TiAl_3$	0.14	1.81 ± 0.04	350 – 500	Tardy and Tu (1985)
Ti in $TiAl_3$	0.210	1.68 ± 0.05	350 – 500	Tardy and Tu (1985)
Al in $TiAl_3$ w/ 0.56 wt.% Cu	0.64	1.88 ± 0.02	350 – 500	Tardy and Tu (1985)
Ti in $TiAl_3$ w/ 0.56 wt.% Cu	15	2.17 ± 0.04	350 – 500	Tardy and Tu (1985)
Al in Al	2.25	1.5	300 –700	Smithells (1992)
Ti in Ti	6.6×10^{-5}	1.75	740 – 876	Smithells (1992)
Al in Ti	7.4×10^{-7}	1.62	600 – 850	Smithells (1992)

For the samples prepared with pure Al layers, the activation energy for the first peak is closest to the diffuison of Al in Ti (and presumably Ti in Al) which would be consistent with compound formation. Peak B or peak C which have activation energies of 1.8-2.0 eV most closely match the activation energy for diffusion of Al in $TiAl_3$. These interpretations of the effective activation energies appear reasonable in light of the experimental evidence.

The effect of Cu was found to be significant only on the diffusion of Ti in $TiAl_3$ (Tardy and Tu 1985). This would be most easily seen in changes in activation energy of peak B or peak C (after a contiguous layer of $TiAl_3$ had formed). Because of the errors in the measurement, a definitive correlation between the current measurements and the reported activation energies could not be made. However, the activation energies of peak C for the Λ = 10 and 20 nm samples with and without Cu are in the range that would correspond to the values of activation energy of Ti in $TiAl_3$ or Al in $TiAl_3$ as reported by Tardy and Tu (1985).

To determine the effect of Cu additions on activation energy, a plot of Q vs. Λ was constructed for the Λ = 10 and Λ = 20 nm films. Figure 4. 46 shows the results for the Λ = 10 nm samples. The first observation that can be made is the excellent agreement with previous measurements of the activation energies for peaks A and C at 0 wt.% Cu. This would seem to indicate that the reaction is relatively insensitive to changes in deposition conditions, i.e., geometry, sputtering pressure, power, etc. The activation energies are not significantly different for the samples with Al-0.5 wt.% Cu suggesting that the Cu may not have a measurable effect at this low concentration level. For the samples with Al-1.0 wt.% Cu, the activation energy for peak C does not change within the error of the measurement, however, the activation energy for peak A is ~0.4 eV larger than that for the 0 wt.% Cu sample. This could be attributed to the increased Cu additions in the sample that are beginning to effect reaction kinetics at this concentration as observed by other researchers.

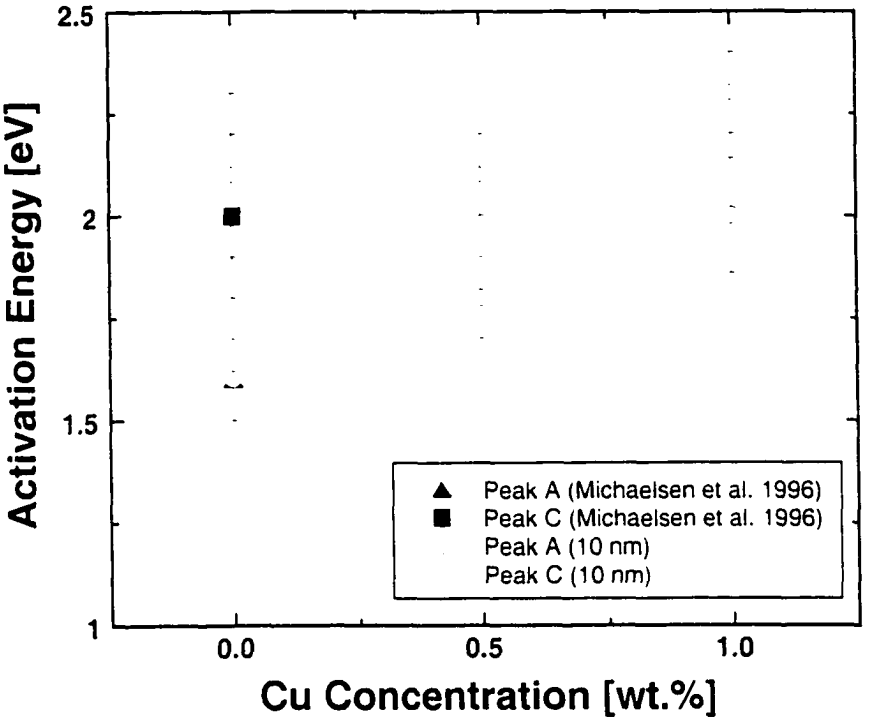

Figure 4. 46: Activation energies for peaks A and C obtained from the Kissinger analysis of 1Ti/3Al, 1Ti/3Al-0.5 wt.% Cu, and 1Ti/3Al-1.0 wt.% multilayer films with Λ = 10 nm plotted as a function of Cu concentration.

A similar plot was constructed for the 20 nm samples and is shown in Figure 4. 47. Activation energies were not determined for an Al-0 wt.% Cu sample. However, the measurements of Michaelsen et al. (1996) are included for comparison since these provide a representative activation energy for the Ti/Al averaged over several periodicities. As with the 10 nm samples, no observable difference in activation energies for peaks C was detected between the Al-0.5 wt.% Cu and Al 1.0 wt.% Cu samples. No difference in activation energy was measured between peak A for the 0.5 wt.% and 1.0 wt.% Cu samples. However, the activation energy for the Al-1.0 wt.% Cu sample was slightly higher (including error bars) than that reported for Michaelsen et al. (1996) with pure Al samples. This again suggests that at the higher Cu concentration levels, the reaction was affected by the presence of Cu. A mentioned earlier, the proposed

mechanism for this interaction is the segregation of Cu to Al grain boundaries and interphase interfaces where it retards the diffusion of the Al atoms (Wittmer et al. 1985). The work of Tardy and Tu (1985) also determined that Cu affects the diffusion of Ti in $TiAl_3$ significantly more than the diffusion of Al in $TiAl_3$. This was explained by the preference of Cu to sit on Al lattice sites in the $TiAl_3$ compound, thus hindering the motion of Ti because of a stronger binding energy between Ti-Cu than Al-Cu.

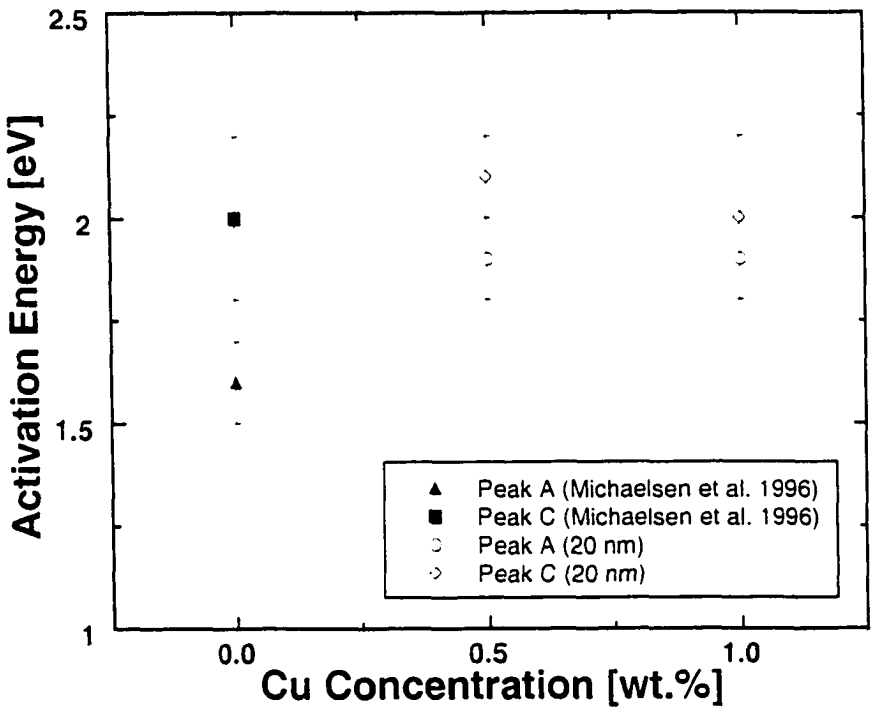

Figure 4. 47: Activation energies for peaks A and C obtained from the Kissinger analysis of 1Ti/3Al, 1Ti/3Al-0.5 wt.% Cu, and 1Ti/3Al-1.0 wt.% multilayer films with Λ = 20 nm plotted as a function of Cu concentration.

As a means of assessing the effect of Cu on the Avrami exponent of peak A associated with the formation of $TiAl_3$ with the $L1_2$ structure, a plot was constructed showing the variation of n as a function of Cu concentration and is shown in Figure 4. 48.

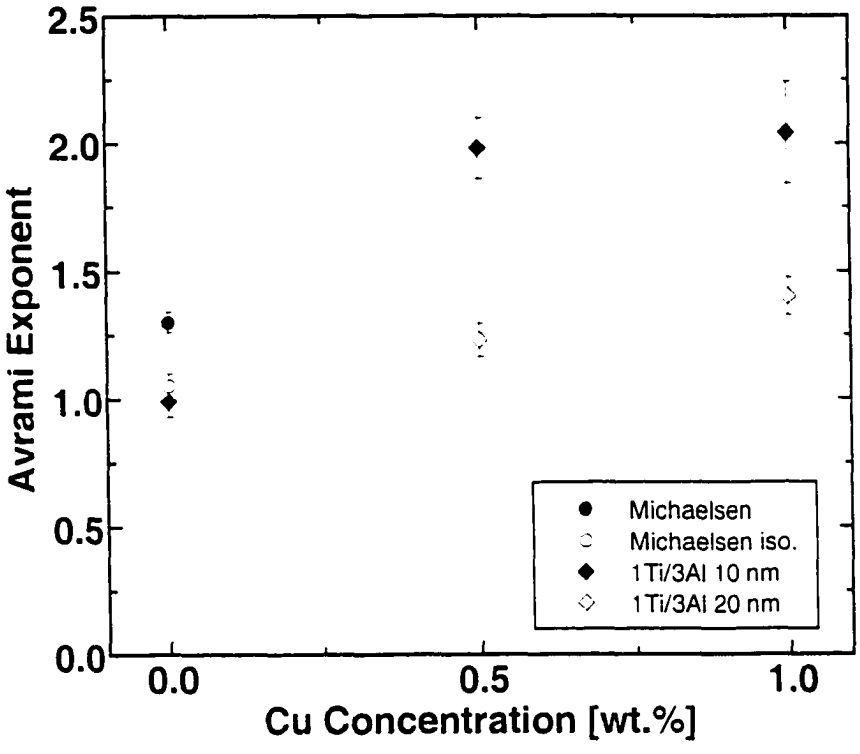

Figure 4. 48: Plot of Avrami exponent obtained from constant heating rate DSC scans of Ti/Al multilayer thin-films vs. Cu concentration.

The plot indicates an increase in n to a value of ~2 for the 10 nm films composed of Al(Cu) layers as compared to the measurements of Michaelsen et al. (1996) for films with pure Al. No change in n was observed between the Al-0.5 wt.% Cu and Al-1.0 wt.% Cu samples. The value of n was found to decrease with increasing bilayer thickness as seen from the 20 nm samples. These results indicate a value close to 1.25 for n and could signify a change in the nucleation behavior associated with $TiAl_3$ formation. An increasing Avrami exponent could mean an increase in the spatial randomness of nucleation sites or in the dimensionality of the growth (i.e., 2-D to 3-D). A change in n could also indicate a change in the rate of nucleation (i.e., fixed population of pre-existing nuclei to constant nucleation rate). For the case of the 20 nm film, the

increase in n by the addition of Cu is offset with the decrease in n caused by the intervention of peak B.

The effect of Cu on the Avrami exponent of Nb/Al films with Λ = 10 nm was not as strong and serves to highlight possible differences in the details of the nucleation behavior in these two systems.

A plot of the Avrami exponent vs. the Al layer thickness is show in Figure 4. 49. This graph highlights the decrease in n with increasing layer thickness, as suggested from the previous figure.

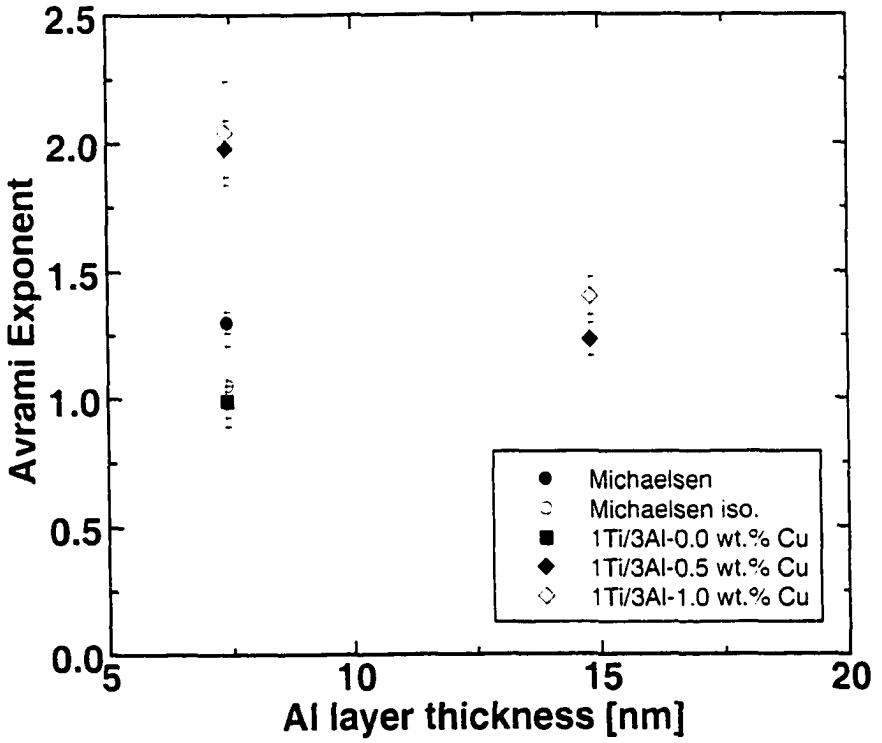

Figure 4. 49: Plot of Avrami exponent obtained from constant-heating-rate DSC traces taken at 40 °C/min for Ti/Al multilayer thin films vs. Al layer thickness.

One possible explanation for the trends observed in the value of the Avrami exponent relies on the recent simulation results of Rickman et al. (1996). If the nucleation of the $TiAl_3$ phase occurred primarily heterogeneously at Al grain boundaries

in the interface, this could result in a low value of the Avrami exponent. As will be shown in Chapter 6, the addition of Cu to the Al produces a refined Al grain structure. The higher volume fraction of grain boundaries in the interface would produce a larger number of heterogeneous nucleation sites and appear more "homogeneous" over a given area. According to the simulation results, a more random (homogeneous) nucleation event would produce a narrower transformation peak, corresponding to a higher Avrami exponent. This is what was observed experimentally in Figure 4. 48 as Cu was added to the Al. As the Al layer thickness increased, the grain size would also increase, thus the Λ = 20 nm film will always have a relatively larger grain size than the 10 nm film. An increase in the grain size would place an additional restriction on the spatial distribution of nuclei in the interface and cause the nucleation to appear more heterogeneous. Again, according to the simulation results, this would *reduce* the Avrami exponent as seen in Figure 4. 49.

Despite the lack of a large volume of data regarding the enthalpy of the Ti/Al reaction leading to the formation of $TiAl_3$, the available data suggest several conclusions. The data can be compared with literature values determined by a large number of independent measurements using a range of bilayer periods obtained by Michaelsen (1996). These results indicated an enthalpy of 34.7 ± 0.3 kJ/g-atom. This value is close to the bulk heat of formation of $TiAl_3$, 35.6 kJ/g-atom (Smithells 1992) and suggests that little or no intermixing occurs at the interfaces during deposition. Furthermore, results obtained from a multilayer with a bilayer period of 5 nm indicated a reaction enthalpy of 21.6 kJ/g-atom (Michaelsen et al. 1996). In this case, the authors concluded that, during

deposition, a reaction had consumed a significant fraction of the multilayer reducing the total enthalpy.

In the present results, both the Al-0 wt.% Cu and Al-1.0 wt.% Cu samples with Λ = 10 nm have nearly identical enthalpies. This suggests that, as in Nb/Al, the addition of Cu does not influence the overall reaction enthalpy. However, the enthalpies obtained from these Ti/Al films are lower than the bulk heat of formation of $TiAl_3$. This suggests that some intermixing has occurred during deposition. Note that the amplitude of peak C was much lower in the traces from the present study as compared to the results of Michaelsen et al. (1996), especially for the 10 nm films. This could be due to deviations from stoichiometry (Michaelsen 1998) and could also result in a decrease in the measured enthalpy.

Enthalpy results from the Al-0.5 wt.% Cu samples support the possibility of intermixing in the 10 nm samples. Here the measured enthalpy was relatively close to that obtained by Michaelsen et al. (1996) as well as being larger than that obtained from both sets of 10 nm samples. Peak C is also larger for these runs. Therefore, the available data suggest that the addition of Cu had no measurable effect on the reaction enthalpy of $TiAl_3$ while some intermixing could have occurred in the 10 nm films. Further experiments would be necessary to assess the reasons for the decrease in peak C and its effect on the total reaction enthalpy.

4.7 Summary and Conclusions

Phase formation in Nb/Al and Ti/Al multilayer thin-films has been investigated by constant-heating-rate DSC experiments. The data from the present studies are generally consistent with earlier investigations. In addition, new information has been

provided concerning the effect of dilute Cu additions on the reaction kinetics. This has been particularly of use in the study of Ti/Al where the formation of metastable modifications to the crystal structure of $TiAl_3$ was not explicitly addressed when reporting activation energies for the formation of the $TiAl_3$ in the majority of previous reported studies.

In Nb/Al multilayers, the presence of Al-0.5 or Al-1.0 wt.% Cu layers was not found to systematically affect the peak temperatures associated with the formation of $NbAl_3$. In addition, the effective activation energies of $NbAl_3$ formation were also not influenced by the presence of Cu. The values of the activation energies were ~1.8 eV for peak A and ~2.6 eV for peak B in agreement with previous studies of sputter-deposited multilayer thin-films. The Avrami exponents associated with $NbAl_3$ formation as measured from constant-heating-rate scans from Λ = 10 nm films with Al-0 wt.% Cu, Al-0.5 wt.% Cu and Al-1.0 wt.% Cu decreased from ~2.8 to 2.4 with increasing Cu concentration. Finally, the enthalpy of formation of $NbAl_3$ was found to be independent of Cu concentration or bilayer thickness and resulted in an average value 40.6 ± 2.9 kJ/g-atom.

By contrast, the addition of 0.5 and 1.0 wt.% Cu was found to increase the temperature of the DSC peak attributed to $L1_2$ $TiAl_3$ formation in Ti/Al multilayers by ~25 °C. No significant difference in the temperature of the peak was found between the 0.5 and 1.0 wt.% Cu samples. Finally, Cu did not affect the peak temperature associated with DO_{23} formation.

The activation energies of peak A increased from 1.6 ± 0.1 eV to 2.0 ± 0.2 with the addition of 1.0 wt.% Cu. This finding is in qualitative agreement with the trends

reported in the literature. As with the peak temperature, no trend was evident in the activation energy of peak C with the addition of Cu. The value of the effective activation energy for DO_{23} formation was ~2.1 eV corroborating previous reports.

A definitive physical description of the activation energies was not possible given the errors in the measurement. However, the values were in agreement with reported activation energies for diffusion in the Al-Ti system. Peak A most close matched the elemental diffusion of Al in Ti (or Ti in Al) while peak C corresponded to the diffusion of Al or Ti in $TiAl_3$.

The decrease of the measured Avrami exponents with increasing Cu concentration was explained in light of computer simulation results which indicated that increasing "randomness" in the nucleation site density would result in a higher value of n. It was postulated that the increase in nucleation site density in the multilayers could be related to the decrease in as-deposited grain size, observed in electron microscopy studies, caused by the presence of Cu in the Al layers. This would lead to a more spatially random distribution of nucleation sites, as compared to a microstructure composed of fewer grain boundaries. This explanation was also consistent with the *decrease* in the Avrami exponent with increasing Al layer thickness. In this case, the Al grains would be larger and place further constraints on the spatial distribution of the nuclei. Simulation indicated that such limitations on the spatial distribution of nucleation sites could result in lower values of n.

The enthalpy of $TiAl_3$ formation obtained for 10 nm films with 0 and 1.0 wt.% Cu was less than the bulk heat of formation of $TiAl_3$, but were similar in magnitude (~26 kJ/g-atom). This suggested that the addition of Cu did not have a strong effect on the

enthalpy and that some intermixing might have occurred during deposition. The enthalpy obtained from a 0.5 wt.% Cu sample with $\Lambda = 20$ nm (~32 kJ/g-atom) was closer to the bulk heat of formation of $TiAl_3$ and supported the idea of intermixing in the lower period films. However, variation in the height of peak C may have influenced the measured enthalpy obtained for these measurements.

5 X-ray Diffraction

5.1 Introduction

X-ray diffraction (XRD) studies of the multilayer films provided complementary information that was used to quantify various aspects of the solid-state reactions in Nb/Al and Ti/Al multilayers. In addition, XRD was used to quantitatively assess of the texture of the as-deposited multilayer films as a function of reactant layer thickness and Cu additions.

Kinetic information concerning aluminide formation for both Nb/Al and Ti/Al multilayers was obtained at the National Synchrotron Light Source (NSLS) located at Brookhaven National Laboratory (BNL) in Upton, NY. The experiments were conducted on IBM/MIT beamline X20C. The high photon flux provided by synchrotron radiation provided a means to detect the small volumes of product phase present during the initial stages of the phase formation. The diffraction measurement was made using a specialized setup incorporating a hot stage and a position-sensitive linear detector. Thus, specific diffraction peaks could be monitored as a function of temperature (or time), but only over a 10^{0} angular range. Assuming that the derivative of the intensity of these peaks is proportional to the volume fraction transformed as a function of time, the *in situ* XRD data could be used study the kinetics of the reaction as in calorimetry. The XRD data could then be used determine activation energies using the Kissinger method. Unlike calorimetry, which provides no information concerning the composition or structure of the reaction products, XRD has yielded new information concerning the kinetics of the metastable phase formation observed in the Ti/Al system. The *in situ*

XRD experiments have also provided supporting evidence for the two-stage reaction mechanism proposed for both the Nb/Al and Ti/Al reactions.

5.2 Background

5.2.1 Thin Film Texture Theory and Measurement

In general, a polycrystalline material will be composed of substructure of individual grains. Each grain will possess a particular crystallographic orientation with respect to its neighbors. If all of the grains in a material had different orientations with respect to each other, the material is described as having a random orientation. However, often, a particular crystallographic orientation is preferred. This results in a subset of grains possessing a specific orientation. When the fraction of this similarly oriented population of grains becomes detectable above the other randomly oriented crystals, the material is "textured". Many factors have been identified that contribute to the formation of crystallographic texture. Initial quantification of orientation correlated the particular form of texture with a material process. The nomenclature for describing the main classes of texture is derived from the particular process that induced the texture i.e., "sheet" or "fiber".

The texture of polycrystalline thin-films has been and continues to be the subject of a significant amount of study. Initially, experiments focused primarily on studying the texture of polycrystalline Al thin-films given to their use in semiconductor metallization schemes. A commonly reported result was that Al deposited from the vapor would form a microstructure composed of grains that were oriented with the (111) planes parallel to the substrate surface with no in-plane orientation (Vaidya and Sinha 1981; Knorr 1991; Thompson 1993). This produced a rotational symmetry about the [111] axis of the film

and was often called "fiber" texture due to is resemblance to the texture found in drawn wire (in this case the axis of symmetry is along the drawing direction). Early experiments to quantify the texture in the films relied on comparisons of the relative heights of the (111) peaks obtained from conventional θ-2θ scans (Vaidya and Sinha 1981). When electromigration studies were performed on these sets of films, the results revealed that films with stronger (111) fiber texture had the largest resistance to electromigration failures. Subsequent studies involved determining the origins of the fiber texture and applying more sophisticated techniques to better quantify thin-film texture.

The primary techniques that have emerged as means of quantifying the texture of materials are rocking curve analysis and pole figure analysis. Rocking curves are obtained by setting a fixed θ-2θ condition and tilting the sample surface normal towards and away from the incident beam axis by several degrees shown schematically in Figure 5. 1. The relative full-width at half-maximum (FWHM) of the diffracted intensity profile provides a measure of the "spread" of the texture in the specimen. A small FWHM would imply that the sample contained grains that were oriented within a few degrees of the particular axis being probed. A perfect crystal would produce a delta function, while a completely random sample would produce a very low signal. The rocking curve scan samples orientation space along one dimension and cannot, for instance measure in plane orientations or determine the fractions of oriented and random grains.

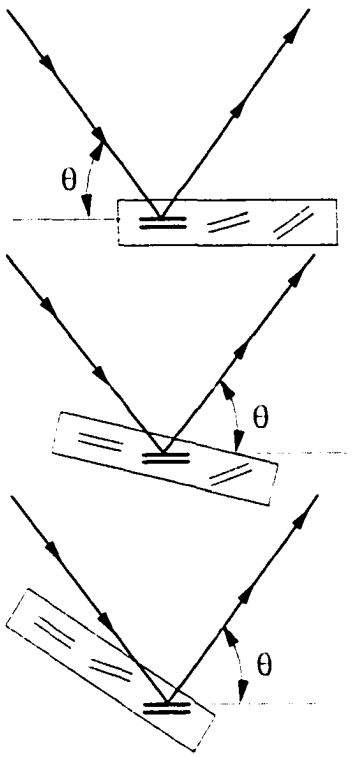

Figure 5. 1: Schematic illustration of a rocking curve measurement in a polycrystalline sample (Courtesy of C. Lavoie-IBM Corp.)

Although rocking curves can provide a relative comparison of the texture between different samples, the technique has a number of shortcomings. Rocking curves cannot determine if a sample has relatively strong fiber texture about the surface normal, but with a systematic offset of the texture axis (so called "near fiber"). Rocking curves also cannot determine if a sample is textured with a pole that is not commensurate with the sample surface normal (so called "annular" texture). A schematic illustration of these different texture archetypes is shown in Figure 5. 2. For the most accurate means of quantifying the texture of a sample, pole figure measurements are necessary.

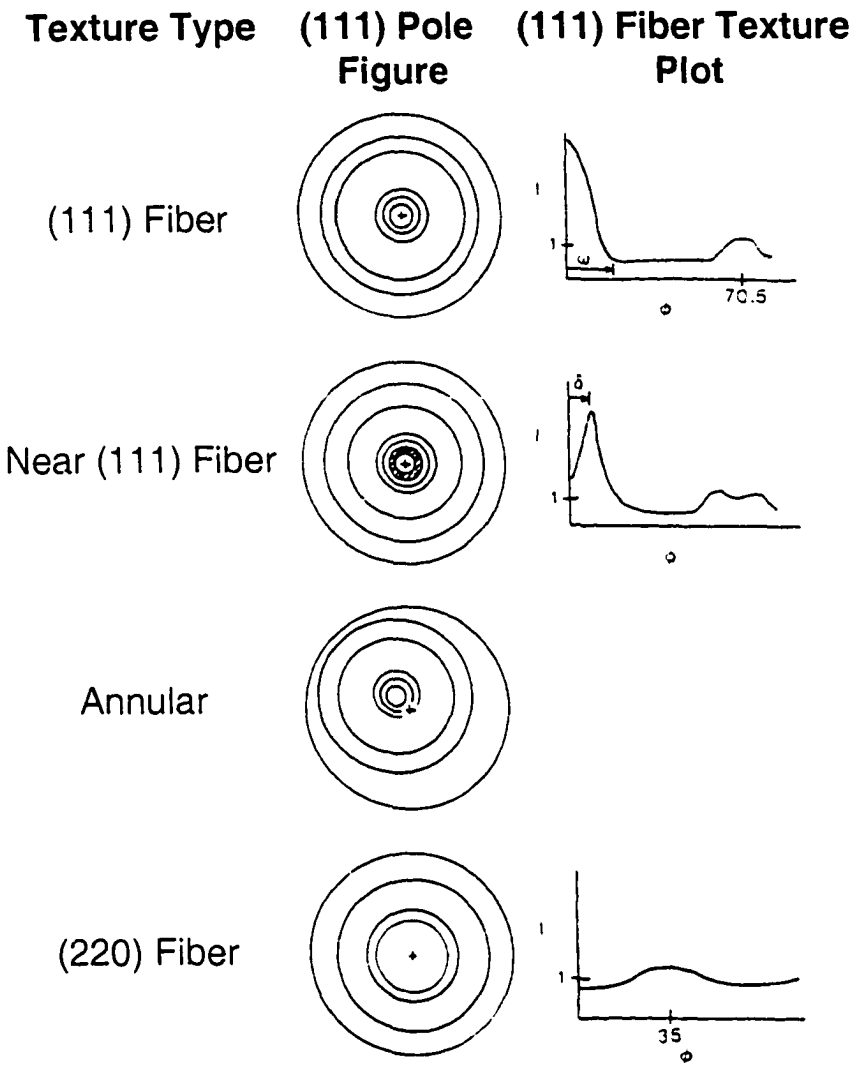

Figure 5. 2: Texture archetypes in Al-based metallurgies (from Knorr and Rodbell 1992).

A pole figure is obtained by setting the source and detector at a particular diffraction condition corresponding to the pole of interest and rotating the sample about its surface normal (0-360°) while tilting it about an axis in the plane of the sample (typically 0-80°). The Schultz reflection geometry is commonly employed in determining a pole figure as shown in Figure 5. 3.

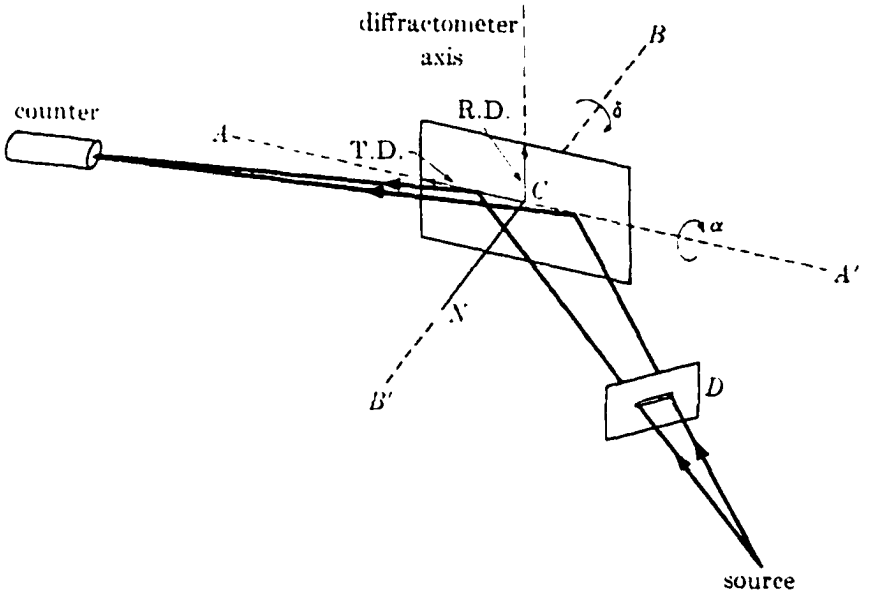

Figure 5. 3: The Schultz reflection method for determining the pole figure of the material. Typically δ will vary from 0 – 360° as α is rocked from 0 – 85° (from Cullity 1978).

The pole figure contains information about the offset of the texture as well as the volume fractions of textured and random material, and whether any preferred in-plane orientations are present. Pole figure data is typically reported in a three dimensional surface plot. If the film in fiber textured with no in-plane texture, the data can be represented in a two-dimensional form called a pole plot. The pole plot is obtained by integrating the intensity at each tilt angle for the entire 360° of rotation or by slicing through the pole figure at one value of ϕ. The plot can be normalized to the total diffracted intensity. A schematic of a pole plot for a (111)-oriented film is shown in Figure 5. 4.

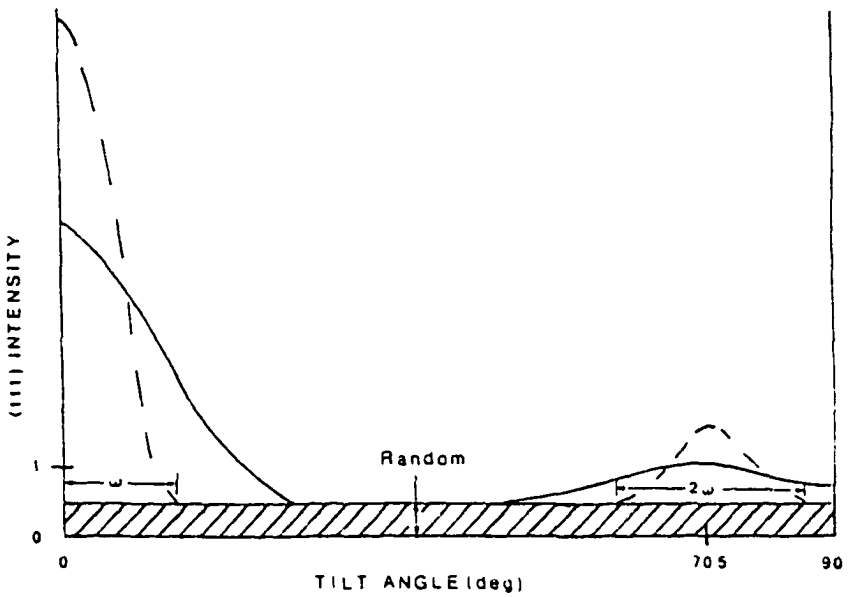

Figure 5. 4: Schematic representation of a typical <111> fiber texture showing two components. The two quantities that define this texture are the half width of the <111> fiber component, ω, and the volume fraction of randomly oriented grains (from Knorr and Rodbell 1992).

The pole plot is sufficient to describe the texture in a sample that contains no preferred in-plane orientation or that is fiber or near-fiber oriented. Since all of the films examined in this study indicated no preferred in plane texture, the results obtained have been plotted in the form of a pole plot. These plots will also simplify discussions of the relevant measurements. For a consistent definition of the quality of the texture, ω_{95} will be used. This is defined as the angle containing 95% of the (111) intensity.

In summary, the objectives of the following XRD experiments were as follows:

1) To determine the effect of bilayer thickness on multilayer texture.
2) To determine the effect of multilayer composition (i.e., Nb/Al vs. Ti/Al) on multilayer texture.
3) To determine the effects of Cu additions on multilayer texture.

4) To study aluminide formation *in situ* in order to provide a more detailed and accurate description of reaction kinetics, and where possible, to determine activation energies for the formation of specific phases.

5.2.2 Nb/Al XRD

As-deposited XRD studies of sputtered Nb/Al multilayers have been reported recently by Barmak et al. (1998). The results from θ-2θ scans taken from 1Nb/3Al samples revealed the variation in diffracted intensity with periodicity as shown in Figure 5. 5.

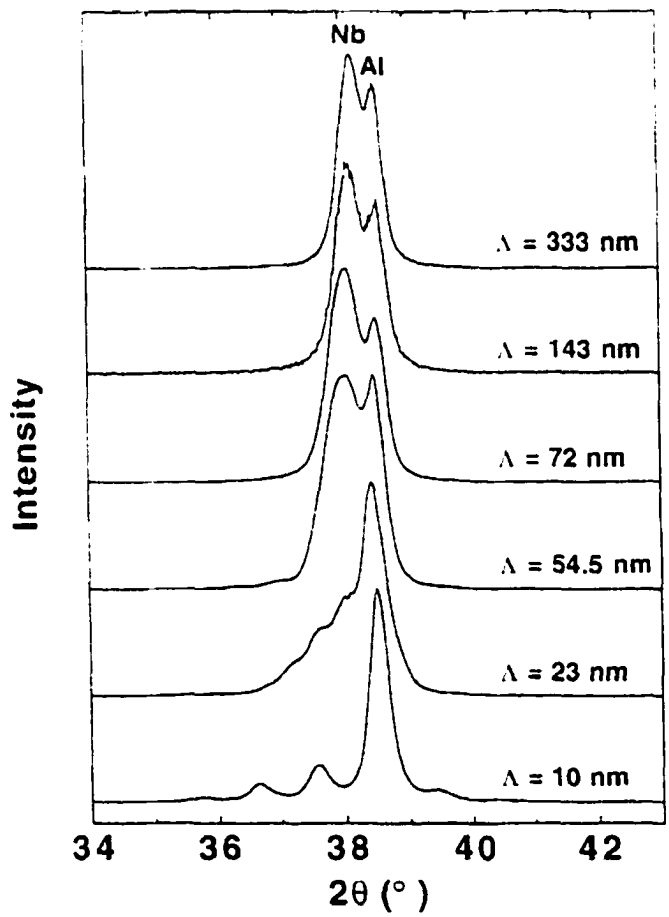

Figure 5. 5: Theta-two theta scans of sputter deposited 1Nb/3Al multilayers with various periodicities. Note the satellite reflections in the Λ = 10 and 23 nm samples present to the left of the intense Al(111)/Nb (110) peak at ~38.4° (from Barmak et al. 1998).

The traces were dominated by the Al (111) and Nb (110) peaks, signifying the presence of fiber texture in the growth direction for these films. The results showed two peaks for films with $\Lambda > 54.5$ nm. The Al (111) peak was found to be in the bulk position, however, the Nb (110) peak was shifted to lower angles. This result and other transmission XRD measurements confirmed an orthorhombic distortion of the Nb unit cell resulting from a lattice expansion of Nb in the plane of the film and lattice compression in the plane of the film.

For films with $\Lambda < 54.5$ nm, a single peak corresponding to an average lattice spacing was observed. In these samples, satellite peaks due to the formation of a coherent superlattice were visible. Superlattices had also been reported by McWhan et al. (1983) and Baumann et al. (1992) in sputter-deposited and evaporated Nb/Al multilayers, respectively.

Previously, *ex situ* XRD has been used successfully in conjunction with TEM investigations to identify the sequence of phase formation in annealed Nb/Al multilayers. Initially, *ex situ* studies were conducted using controlled annealing experiments on evaporated Nb/Al multilayers (Coffey et al. 1992). The results of this study are shown in Figure 5. 6. They indicate the formation of $NbAl_3$ starting at ~435 °C. For multilayers with Nb in excess of the tri-aluminide composition, the formation of $NbAl_3$ was followed by the A15 Nb_3Al phase starting at ~800 °C. Above 900 °C, diffraction peaks belonging to σ-Nb_2Al were also observed.

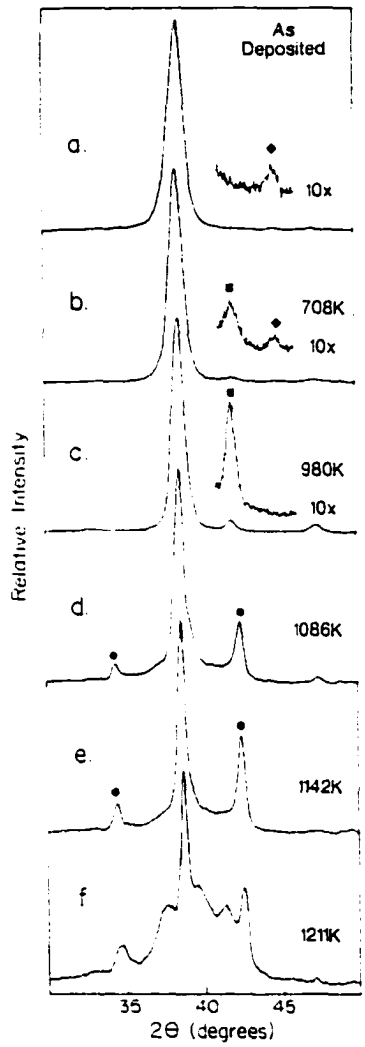

Figure 5. 6: XRD patterns for 3Nb/1Al multilayer samples (d_{Al} = 45 nm, d_{Nb} = 98 nm) annealed to the indicated temperatures at 20 K/min. The insets for the traces (a), (b), and (c) are a 10 × magnification to display the weaker peaks of the Al rich phases. The diffraction lines unique to the different phases are identified by the symbols ● for A15, ■ for the $NbAl_3$, and ◆ for the Al. The major peak a 2θ = 38° is primarily Nb in partially reacted samples, although the strongest diffraction lines of Al, $NbAl_3$, and Nb_3Al overlap as well. The additional peaks near the central peak in trace (f) are due to Nb_2Al (from Coffey et al. 1992).

Recall that the multilayers in the present work were deposited with a fixed stoichiometry of 1Nb/3Al so that the reactants were completely consumed in the formation of the tri-aluminide. Therefore, the phases richer in Nb (σ and A15) were not

observed in these experiments. Since some of the samples had excess Al, in some cases melting and recrystallization of the Al was observed.

An *in-situ* heating experiment was also conducted on a conventional diffractometer equipped with a hot-stage and position sensitive detector. A sputtered 1Nb/3Al multilayer with Λ = 72 nm was heated at 1 °C/s in 10° increments to 700 °C. At each temperature step a θ–2θ scan was taken that covered the position of the Al (111) and Nb (110) peak as shown in Figure 5. 7. The results indicate a drop in intensity beginning at ~ 350 °C and ending at ~400 °C. This was interpreted to be the reaction associated with peak A in the DSC experiments. Simultaneously, a peak began to develop at the position of the primary diffracting peak of $NbAl_3$. Note that unique identification of $NbAl_3$ was not possible at this time due to the limited width of the window and the absence of other $NbAl_3$ peaks. Further heating resulted in a second pronounced drop in the reactant peak intensity at starting ~450 °C. This was labeled as reaction B.

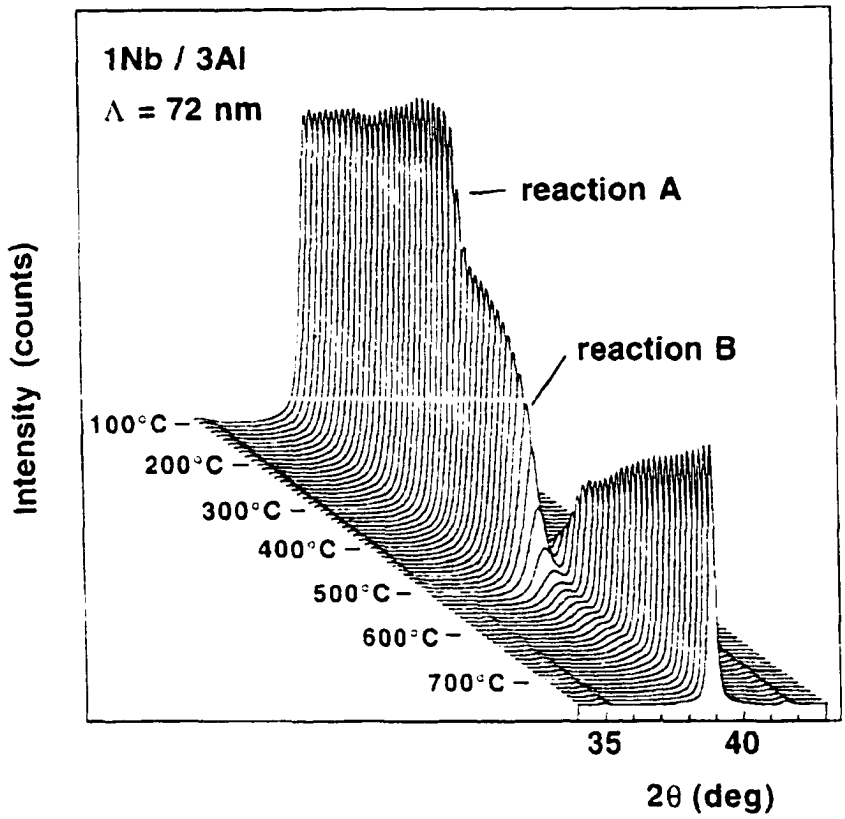

Figure 5. 7: Hot stage XRD measurements for a 1Nb/3Al multilayer film with Λ = 72 nm (from Barmak et al. 1998).

5.2.3 Ti/Al XRD

XRD studies of Ti/Al thin-film texture are more common than Nb/Al due to the use of these materials in microelectronics metallization. Many of the earlier studies of Ti/Al and Ti/Al(Cu) dealt with relatively thick (500 nm) Al layers deposited on thin (<100 nm) Ti layers. Fiber texture was observed in all cases with Al possessing a <111> orientation and Ti a <0002> orientation (Tracy et al. 1994, Knorr et al. 1998). Results also indicated that the texture of the Al layers varied with the texture of the Ti underlayer and led to "texture inheritance" (Tracy et al. 1994). Other recent studies have shown that the strength of the fiber texture is sensitive to the thickness of the Ti underlayer (Adamik

et al. 1998) shown in Figure 5. 8, and the number of Al/Ti bilayers in a multilayer (Adamik et at. 1997, Adamik et al. 1998) as shown in Figure 5. 9.

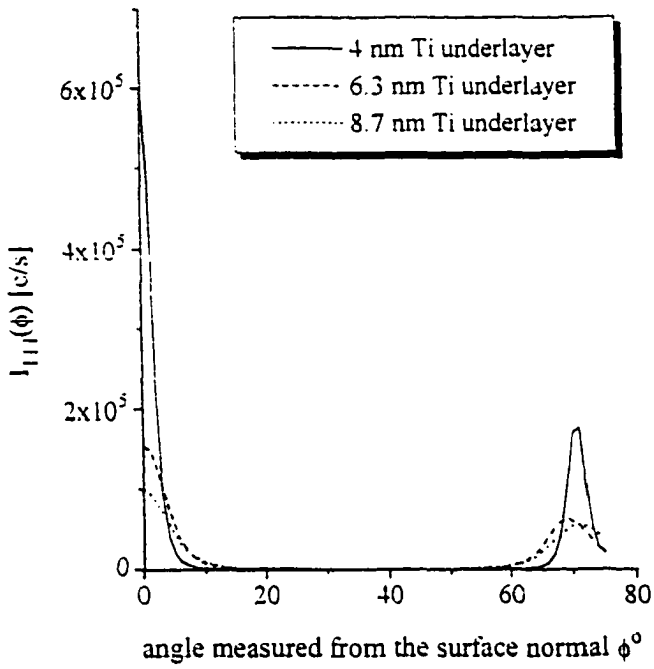

Figure 5. 8 <111> pole figures of Al films deposited onto Ti underlayers of different thickness (from Adamik et al. 1998).

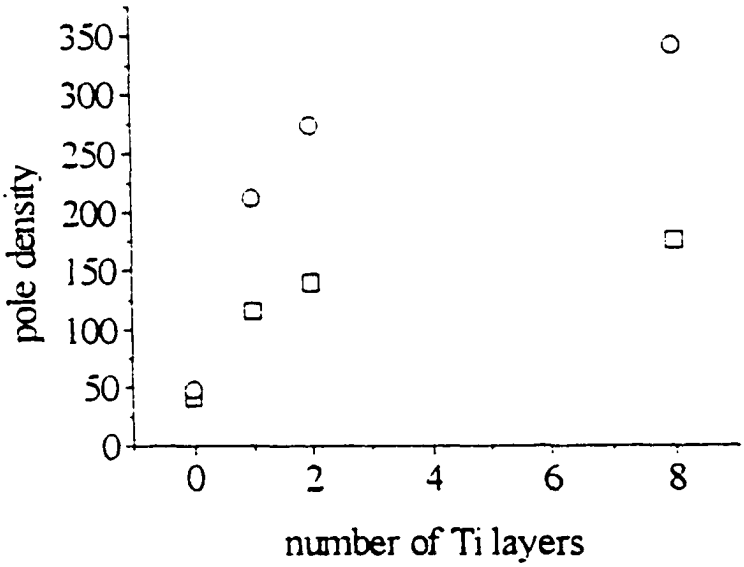

Figure 5. 9: <111> (□) and <222> (○) pole densities as a function of the number of Ti layers for stratified Al/Ti films (from Adamik et al. 1997).

The crystal structure of the underlayer was also shown to affect the development of <111> texture in the Al (Kamijo and Mitsuzuka 1995). Other studies of Ti/Al(Cu) films found that the substrate surface roughness influenced the fiber texture of the deposited films with smoother substrate surfaces leading to improved texture as shown in Figure 5. 10 (Rodbell et al. 1996a).

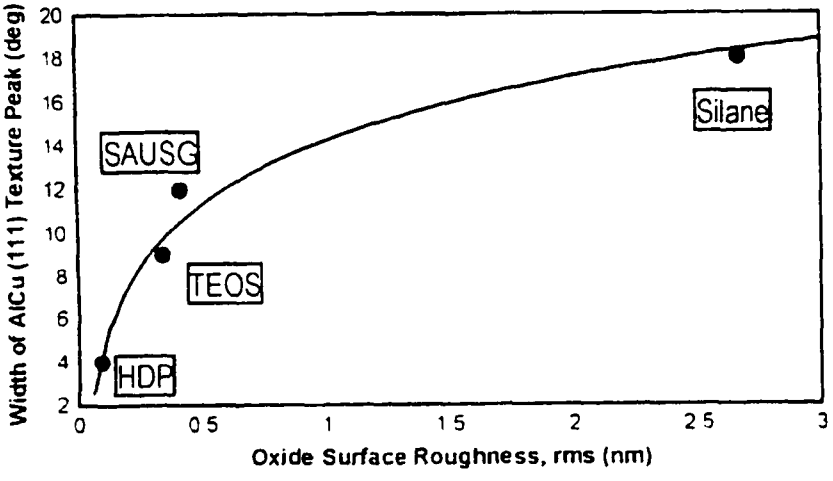

Figure 5. 10: Al(Cu) (111) texture peak width (ω) versus substrate roughness for 20 nm collimated Ti (150 °C)/750 nm Al-0.5 wt.% Cu (550 °C) blanket films deposited on Silane, TEOS, HDP, and SAUSG oxides (from Rodbell et al. 1996a).

X-ray diffraction measurements of Ti/Al multilayers sputtered onto sapphire substrates with an overall composition of $Ti_{56}Al_{44}$ and Λ = 50 nm showed evidence of an initially strong fiber texture in the XRD pattern being dominated by the Ti (0002)/Al (111) reflection (Michaelsen et al. 1994) as seen in Figure 5. 11. The authors reported a FWHM from rocking curve measurements that was nearly equal to that of the sapphire substrate.

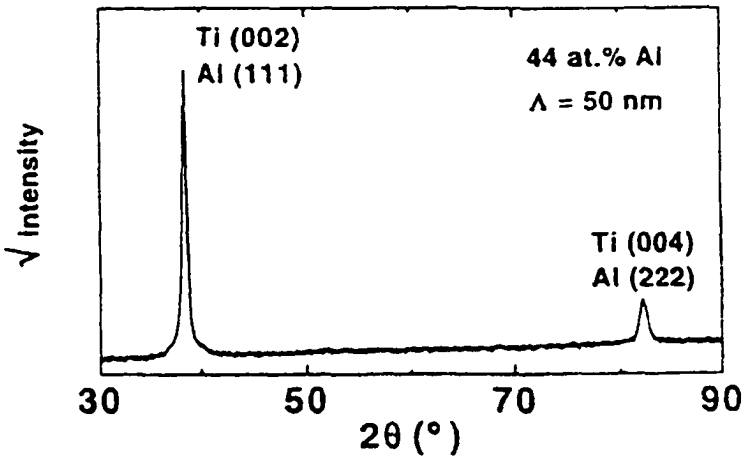

Figure 5. 11: Theta-two theta scan of Ti/Al multilayer film with overall composition $Ti_{56}Al_{44}$ with Λ = 50 nm. Note the square root intensity scale.

An *in situ* heating experiment was conducted on this sample. XRD peak intensities were measured over the range of 2θ = 37-40° as the sample was heated at 40 °C/min shown in Figure 5. 12. At 400 °C, a shift in the Ti (0002) Al (111) peak position was observed, simultaneously, a shoulder developed on the high angle side of the peak. These effects were later attributed to $TiAl_3$ formation with the cubic, $L1_2$ structure. Further heating produced the expected equilibrium phase, TiAl, based on the multilayer stoichiometry. This experiment produced the first evidence that the initial Ti/Al intermetallic forms coherently with the parent layers maintaining a high degree of fiber texture.

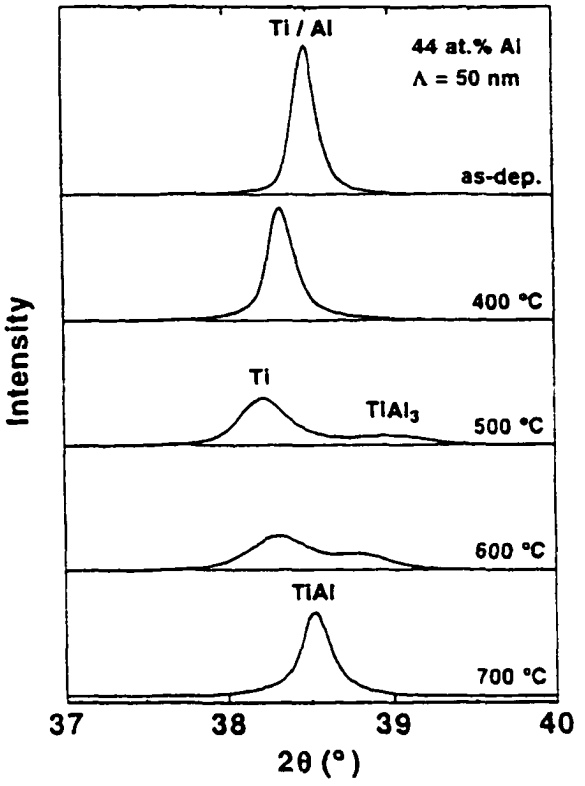

Figure 5. 12: X-ray patterns in the range $37^{\circ} \leq 2\theta \leq 40^{\circ}$ of a Ti/Al multilayer with an overall composition $Ti_{56}Al_{44}$ and a modulation period of 50 nm, taken *in situ* during heating at a rate of 40 °C/min. Note the peak shift that is due to thermal lattice expansion. All measurements are displayed with the same intensity scale.

A subsequent study focussed on the formation of metastable structures of $TiAl_3$ that occurred during annealing (Michaelsen et al. 1996). *Ex situ* XRD experiments were conducted on a sputter deposited 1Ti/3Al multilayer with Λ = 10 nm and are shown in Figure 5. 13. At 377 °C (650 K), the (100) superlattice reflection for the $L1_2$ phase was observed. Further annealing resulted in a splitting of the (200) reflection and the formation of $TiAl_3$ with a DO_{23} structure at 527 °C (800 K). A θ-2θ scan taken at ~700 °C (1000 K) indicated a slight increase in tetragonality due to the formation of $TiAl_3$ with the equilibrium DO_{22} structure.

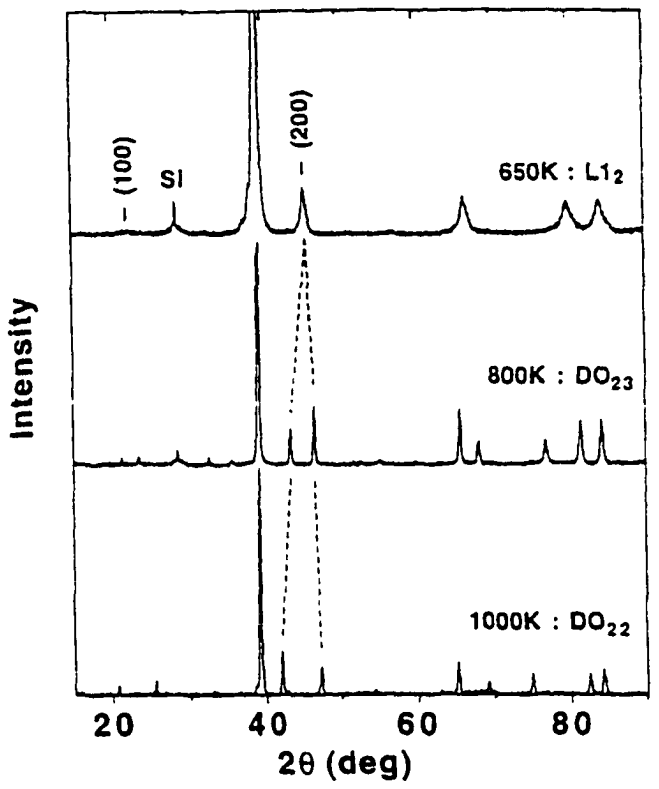

Figure 5. 13: XRD patterns of a Λ = 10 nm sample after heating to different temperatures. The peak at $2\theta = 28^{\circ}$ is due to the Si wafer used as a substrate for the XRD measurements. The (100) superlattice reflection of the $L1_2$ phase is indicated in the uppermost curve. The dashed lines indicate the increase of tetragonality (from Michaelsen et al. 1996).

The DO_{23} metastable modification of the $TiAl_3$ phase closely resembles the crystal structure of the Ti_9Al_{23} phase reported during annealing of evaporated Ti/Al(Cu) thin film bilayers (Rodbell et al. 1991; Rodbell 1992). In these studies, additional peaks due to the presence of Ti_9Al_{23} were evident in the evaporated films, but were absent from films that were sputtered as seen in Figure 5. 14.

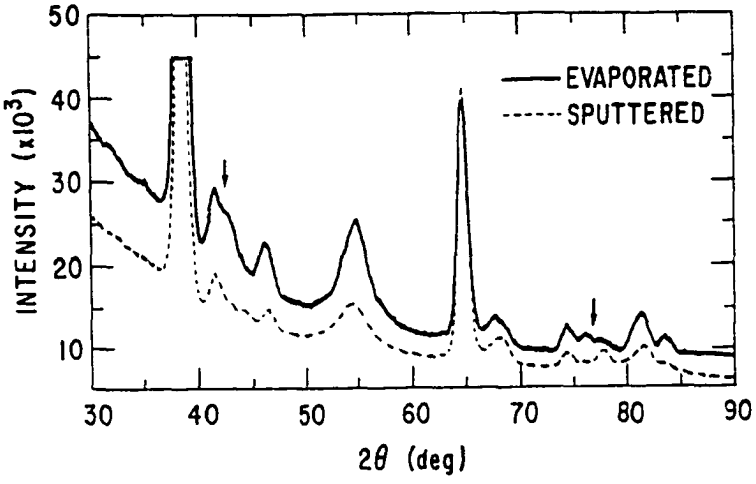

Figure 5. 14: XRD intensity vs. 2θ plots for annealed, 400 °C for 1 hour in 90% N_2-10% H_2 (a) sputtered Al-0.5 wt.% Cu and (b) evaporated Al-0.67 wt.% Cu 4-layered samples. Note the presence of extra diffraction peaks in the evaporated film which correspond to the superlattice phase Ti_9Al_{23} (from Rodbell et al. 1991).

Another interesting observation made in this study was that the formation of the Ti_9Al_{23} phase in evaporated samples was suppressed by the presence of Cu in the Al layers. This was evident in a series of multilayer samples deposited with a range of Cu concentrations as shown in Figure 5. 15.

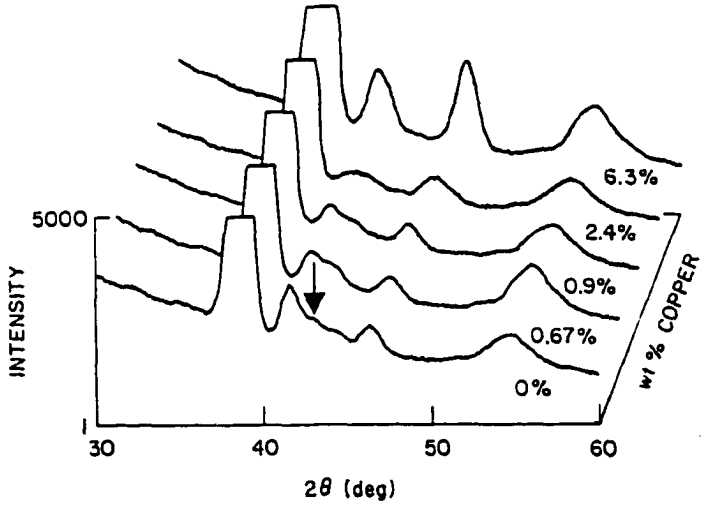

Figure 5. 15: XRD intensity vs. 2θ plots for a series of annealed (400 °C for 1 hour in 90% N_2-10% H_2) evaporated 4-layered samples as a function of wt.% Cu (a) 0, (b) 0.67, (c) 0.9, (d) 2.4, and (e) 6.3 wt.% Cu. Note the magnitude of the extra diffraction peaks (which correspond to the superlattice phase Ti_9Al_{23}) decrease as the Cu concentration increases (from Rodbell et al. 1991).

5.3 Experiment

5.3.1 Rocking Curve Measurements

X-ray rocking curve measurements were conducted by Dr. Carsten Michaelsen at the Institute for Materials Research, GKSS Research Center, Geesthacht, Germany. A Siemens D5000 Bragg-Brentano powder diffractometer with a 200 mm radius was used for the measurements. Cu K_α radiation at 40 kV and 30 mA was used along with a graphite secondary monochromator using variable slits that provide an illuminated area with a constant width of 6 mm. Rocking curves were conducted with $2\theta = 38.5^\circ$at the position of the Al (111)/Nb (110) peak and the Al(111)/Ti(0002) peak. To generate the rocking curve, the angle between the X-ray tube and the detector was kept constant. The X-ray tube was then moved from 0° to 38.5° while the detector moved from 38.5° to 0°. The figure of merit used to compare the rocking curve scans was the FWHM of the peak as determined from a Gaussian fit to the data. Note that due to the similar spacing of the close-packed planes, the peaks corresponding to the close packed planes of Ti (0002) or Nb (110) and Al (111) could not be separated. Since Al is the majority constituent of the multilayers and is the alloyed element, it is expected that changes in the width of the rocking curves are primarily due to microstructure changes attributable to the Al layers. This assumption is supported by TEM investigations showing changes in the Al grain structure with the additions of Cu and will be addressed in detail in Chapter 6. Due to variations in sample thicknesses resulting in variation of absolute peak intensities, the rocking curves were normalized by the total area beneath the peak.

5.3.2 Pole Figure Measurements

Pole figure measurements of as-deposited multilayers were conducted by Dr. Kenneth P. Rodbell and performed IBM Technology Division in East Fishkill, NY. Samples ~ 1 cm x 1cm were used for the analysis. Pole figure measurements were conducted in a Rigaku RU 300 unit with a rotating anode generator and a Bruker Histar area detector allowing evaluation from Debye rings in a 55° 2θ range using a 6 cm sample-to-detector distance. The setup is illustrated schematically in Figure 5. 16.

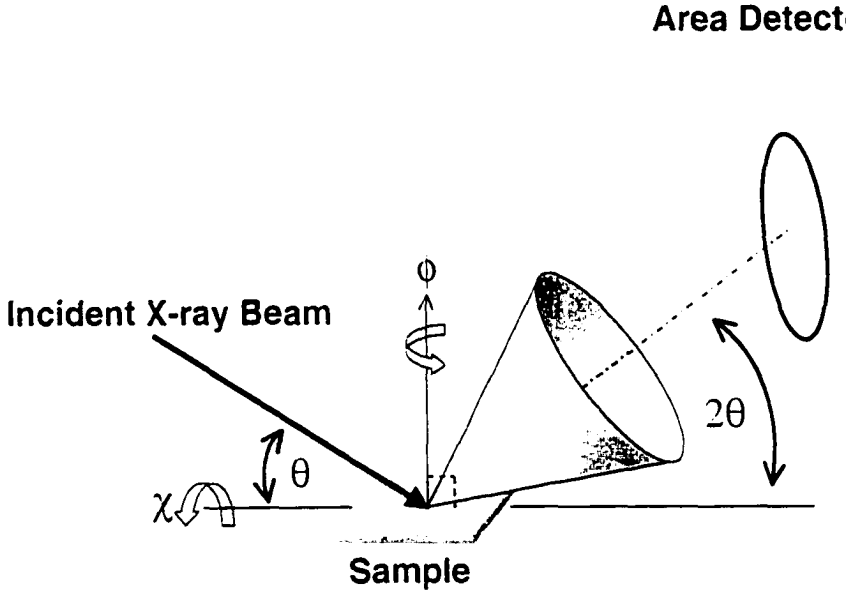

Figure 5. 16: Schematic illustration of the use of the diffractometer/area detector setup used to determine the pole figures.

Scans were obtained at 40 keV at 100 mA using a pair of matched Gobel mirrors that produced monochromatic Cu K_α radiation and concentrated the flux into a 800 μm diameter pinhole collimator. The positions of the Debye rings were calibrated using a corundum sample prior to analysis. For the Al (111)/Ti (0002) pole figure 2θ was set to 40° and θ was set to 28° (note exact Bragg conditions were not necessary due to the use of the area detector). These angles were chosen to place the (111) pole near the top of the

area detector. Following data acquisition, each frame was corrected for the flat surface of the area detector and a pole figure was generated. For comparison of film texture, fiber plots were used since in all cases the samples showed rotational symmetry about the fiber axis. A background was selected on the low angle and high angle side of the primary diffraction ring. The average of this background value was subtracted to obtain the net intensity in the peak. Pole figures were collected for ϕ = 0-360°. The tilt angle, χ, was varied from 0 to 55° at 0.1° increments. A complete pole figure scan was acquired in ~ 20 min. To generate the pole plot the intensity of the Debye rings was integrated for each value of χ at a ϕ value of 60°. The diffracted intensity was normalized by the average (111) intensity in the pole plot. The (111) peak offset (δ) and $\omega_{0.5}$ of the peak were then determined.

5.3.3 *In situ* Synchrotron X-ray Diffraction

As mentioned earlier, intermetallic compound formation was studied using the IBM/MIT beam line X20C at the Brookhaven National Laboratory National Synchrotron Light Source (Stephenson, 1988, Stephenson et al. 1989). A multilayer monochromator provided an average photon flux of $3x10^{12}$ photons/sec with an energy resolution of the 1.5% at 6.9 keV (0.1797 nm). The diffraction data were acquired in a Bragg-Brentano (θ-2θ) geometry every 0.5 s (1.5 °C) using a position-sensitive detector using a linear array of 1024 photodiodes. To prevent saturation of the detector, for most runs the incident intensity was attenuated by inserting a Cu foil into the beam path. The foil was typically 2 mil (~50 μm) thick. In the Ti/Al films, increased sensitivity to product phase formation was accomplished by tilting the sample up to 11.5° away from the exact Bragg

condition for the intense Al(111)/Ti (0002) peak. This decreased the diffracted intensity of the strongly textured, high intensity Al (111)/Ti (0002) peak.

Samples were heated in purified He ($O_2 < 10^{10}$ ppm) at ramp rates of 60 -1620 °C/min (1-27 °C/s) from 100 to ~700 °C while X-ray diffraction, sheet resistance, and roughness were measured simultaneously shown schematically in Figure 5. 17. The majority of the ramped runs were conducted at 180 °C/s. The actual temperature of the sample stage was calibrated using a series of eutectic melting point materials providing an accuracy of ± 3 °C. The ramp rate was accurate to within ~ ± 3% of the set value.

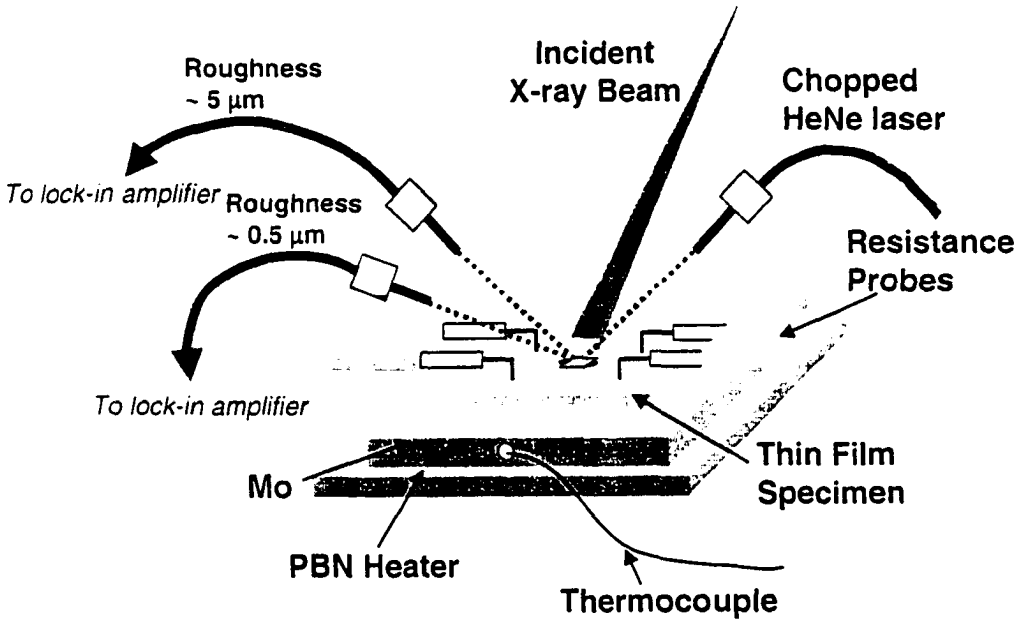

Figure 5. 17: Schematic illustration of the sample stage used during the *in situ* XRD measurements. The entire assembly was housed in a turbo-pumped vacuum chamber. The PBN heater was mounted on a thick Cu cooling block.

Typical acquisitions contained 600 frames (5 min) of data. The diodes were binned into groups of 8 to produce a scan containing 128 pixels. The physical size of the diode array provided an angular detection window of ~10°. *In situ* sheet resistance was

measured using a four-point probe method. A constant current of 25 mA was passed through the sample and the corresponding voltage drop was measured.

Surface roughness data was probed on 0.5 μm and 5 μm length scales by measuring the intensity of two reflected laser beams positioned at different incident angles. The lasers were chopped at a fixed frequency allowing detection at high temperatures where radiation of similar wavelengths was emitted. The reflected laser signal passed through a lock-in amplifier before being sent to the A/D converter.

The sample chamber was turbo-molecular pumped and attained a typical vacuum level of 10^{-7} Torr. Before a run was commenced, a θ-2θ scan was acquired. The detector and sample were then positioned at the selected θ-2θ angles. The chamber was purged once with purified He and evacuated. The He was then allowed to flow continuously and the run was started. After data acquisition was complete, a second θ-2θ scan was taken before removing the sample.

All of the data was subsequently processed on an IBM RS/6000 workstation using specialized routines written for use with the Matlab® software package. The routines enabled contour plots of X-ray intensity versus 2θ and temperature or time as well as integrated intensity plots to be created. The software programs also determined transition temperatures based on maxima or minima in the first derivatives of the integrated intensity, resistance, or light scattering data.

5.4 Results and Discussion

5.4.1 As-Deposited Films

5.4.1.1 Film Texture of Nb/Al and Nb/Al(Cu)

5.4.1.1.1 Rocking Curve Analysis

Rocking curves for as-deposited Nb/Al multilayers with varying periodicity are shown in Figure 5. 18. The peaks were Gaussian-shaped and had a FWHM of ~ 3°.

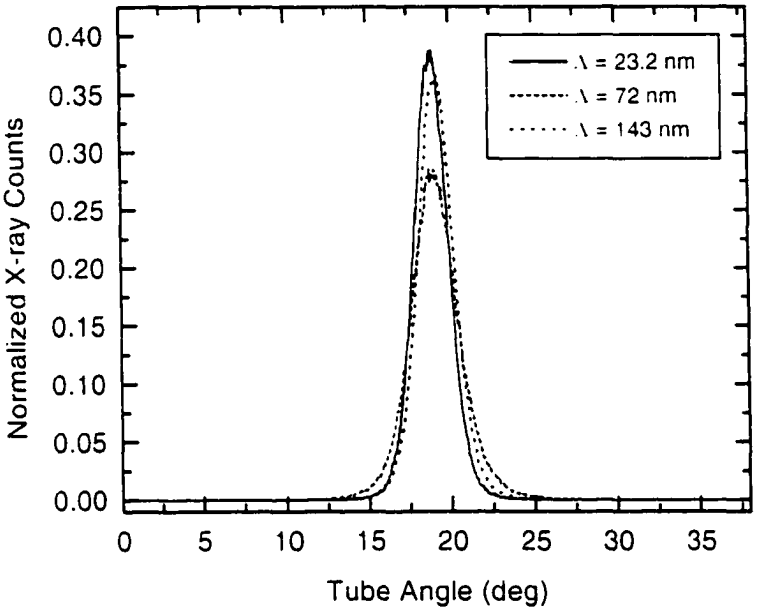

Figure 5. 18: Rocking curves obtained for as-deposited 1Nb/3Al samples with Λ = 23.2, 72, and 143 nm.

The multilayers with Λ = 20 nm did not exhibit double peaked rocking curves for any of the Al(Cu) alloy samples as shown in Figure 5. 19. The results show a broadening of the rocking curve as the Cu concentration was increased. The FWHM increased to ~7° for the 0.5 wt.% sample and ~9° for the 1.0 wt.% sample. Furthermore, the intensity of the peak was reduced by approximately 75% for the samples containing Cu. The rocking curve results for the 1Nb/3Al multilayers are summarized in Table 5. I.

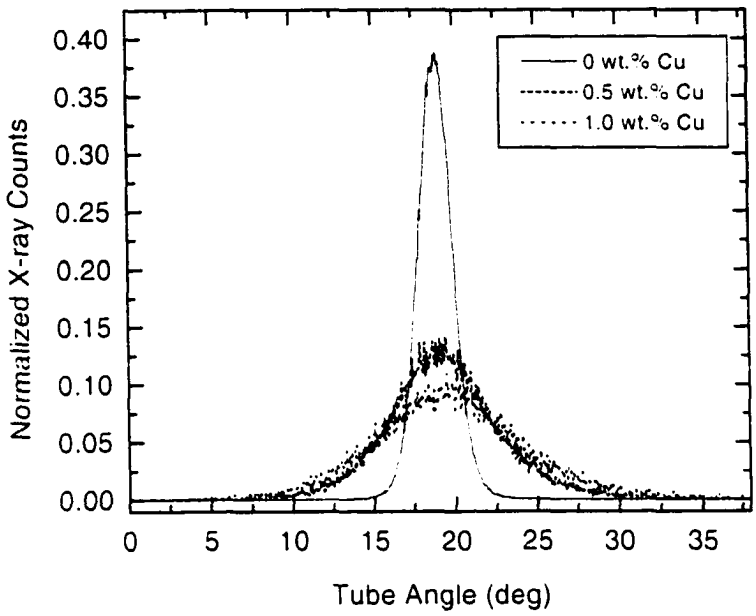

Figure 5. 19: Rocking curve scans obtained from as-deposited 1Nb/3Al Λ = 20 nm multilayers with Al-0 wt.% Cu, Al-0.5 wt.% Cu, and Al-1.0 wt.% Cu.

Table 5. 1: Results from rocking curve analysis of 1Nb/3Al and 1Nb/3Al(Cu) samples.

Λ [nm]	Cu Conc. [wt.%]	FWHM [deg]
23.2*	0.0	2.41
20*	0.5	7.08
20*	1.0	9.77
72	0.0	3.28
143	0.0	2.53

* Indicates satellite (superlattice) peaks were visible.

5.4.1.1.2 Pole Figure Analysis

A pole plot was obtained for 1Nb/3Al-0 wt.% Cu multilayers with Λ = 23.2 and Λ = 333 nm. As seen from Figure 5. 20, both multilayers indicated texturing of the Al and Nb. The offset was considerably less for the 23.2 nm sample as compared to the 333 nm multilayer. The values for ω_{95} were within 1^{o} of each other.

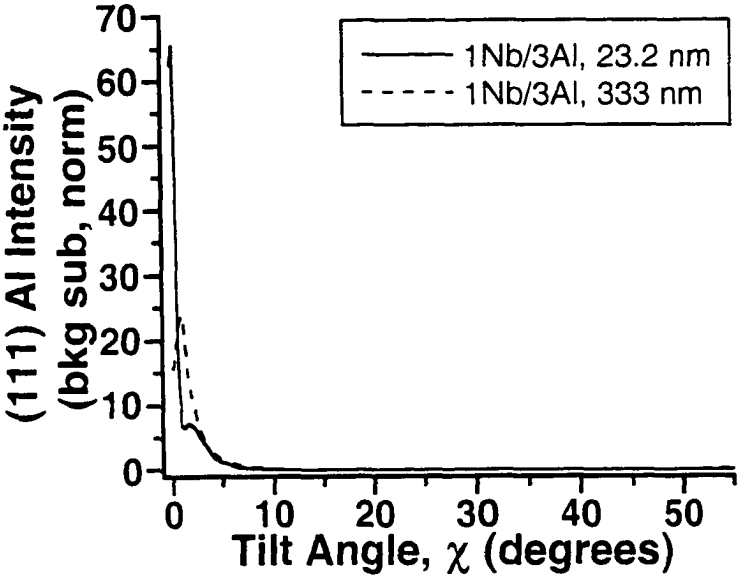

Figure 5. 20: Pole plot of Al (111) Nb(110) intensity for 1Nb/3Al multilayers with Λ = 23.2 and 333 nm.

Figure 5. 21 shows the effect of 1 wt.% Cu on the multilayer texture. A sharp decrease in intensity was evident. The offset increased from 0.1 to 0.6° and the $\omega_{1/2}$ increased from 4.5 to 8.8° in the Al(Cu) sample.

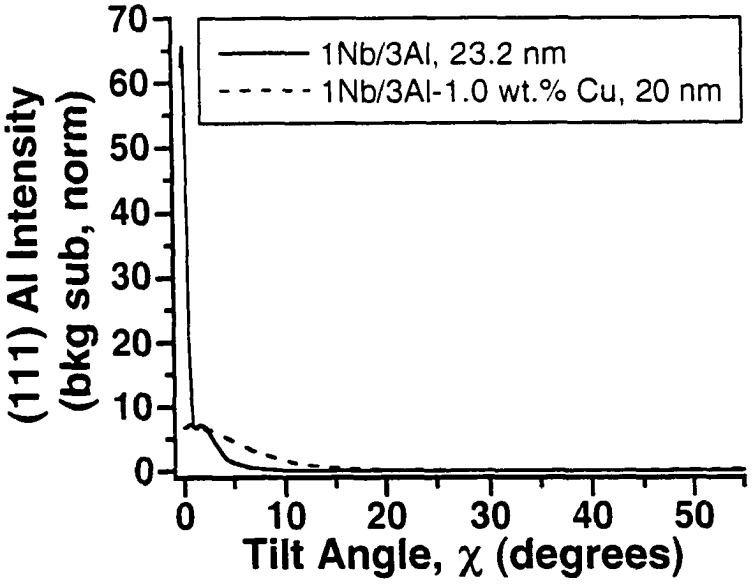

Figure 5. 21: Pole plot showing the effect of 1 wt.% Cu on the texture of 1Nb/3Al multilayers with Λ = 23.2 and 20 nm.

Figure 5. 22 shows the results from a pole plot of 1Nb/3Al multilayers with Λ = 333 nm both with and without Al(Cu) layers. Again, an increase in the offset (δ) was observed from 0.9° to 8.4°. The ω_{95} value nearly doubled from 5.4° to 9.8°.

The results of the δ and ω_{95} measurements for the 1Nb/3Al samples have been summarized in Table 5. II.

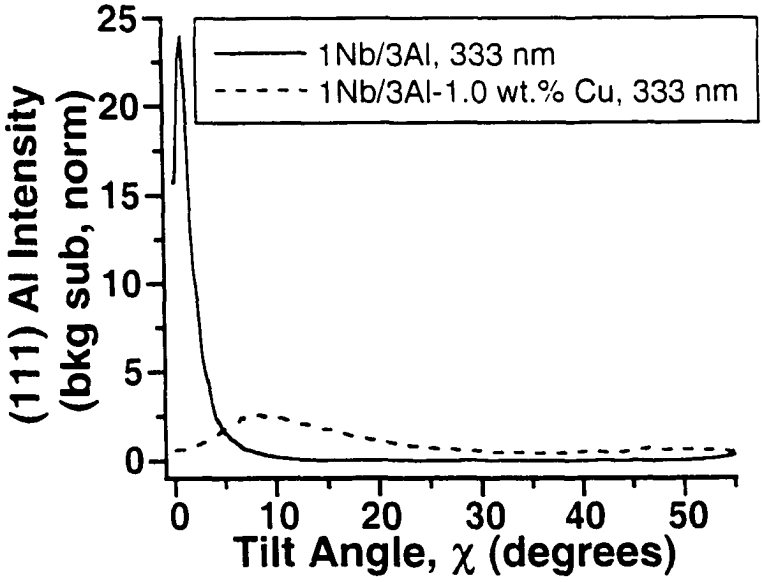

Figure 5. 22: Pole plot showing the effect of 1 wt.% Cu on the texture of 1Nb/3Al multilayers with Λ = 333 nm.

Table 5. II: Summary of offset (δ) and ω_{95} results obtained from pole plots of 1Nb/3Al and 1Nb/3Al-1.0 wt.% Cu samples.

Λ/Al Thickness [nm]	Cu conc. [wt.%]	Offset (δ) [deg]	ω_{95} [deg]
23.2	0	0.1	4.5
20	1.0	0.6	8.8
333/245	0	0.9	5.4
333/245	1.0	8.3	9.8

5.4.1.2 Film Texture of Ti/Al and Ti/Al(Cu)

5.4.1.2.1 Rocking Curve Analysis

As with the Nb/Al samples, rocking curves were used to assess the texture of the Ti/Al multilayers. Figure 5. 23 shows a comparison of four as-deposited 1Ti/3Al multilayers with periods ranging from 10 nm to 333 nm. Unlike the Nb/Al multilayers, the FWHMs increase as the period decreases. Also, the peak shifts to slightly higher angles with decreasing Λ. The Λ = 333 nm sample has the smallest FWHM of 3.08°.

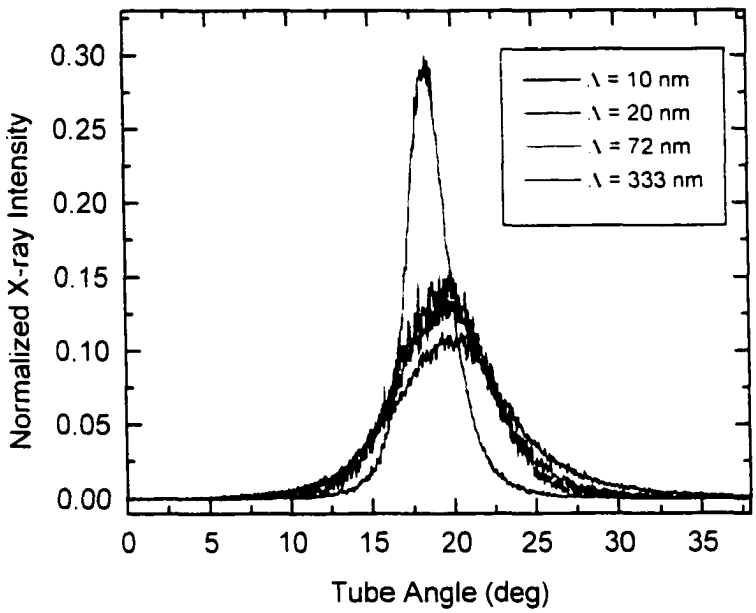

Figure 5. 23: Rocking curves obtained for as-deposited 1Ti/3Al samples with Λ = 10, 20, 72, and 333 nm.

The effects of Cu additions were assessed for all periods and two Cu concentrations, since the splitting of the diffraction peak was not observed in the Ti/Al samples. Figure 5. 24 shows the results obtained from Λ = 10 nm 1Ti/3Al multilayers with 0, 0.5, and 1.0 wt.% Cu. The FWHM appeared independent of Cu concentration for this case.

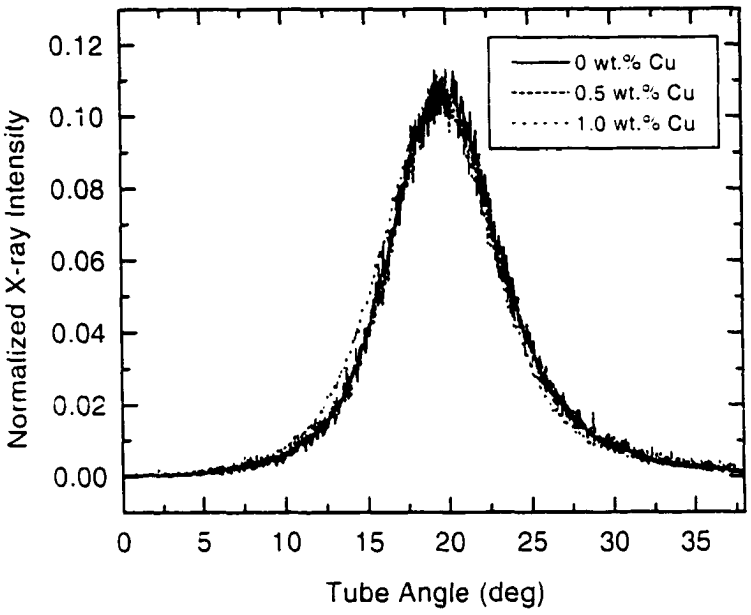

Figure 5. 24: Rocking curve showing the effect of Cu additions on the texture of 1Ti/3Al multilayers with Λ = 10 nm.

The FWHM of the rocking curve was again found to be independent of Cu concentration for the Λ = 20 nm multilayers. A slight decrease in X-ray intensity was evident in the samples containing the Al(Cu) alloy layers as seen in Figure 5. 25.

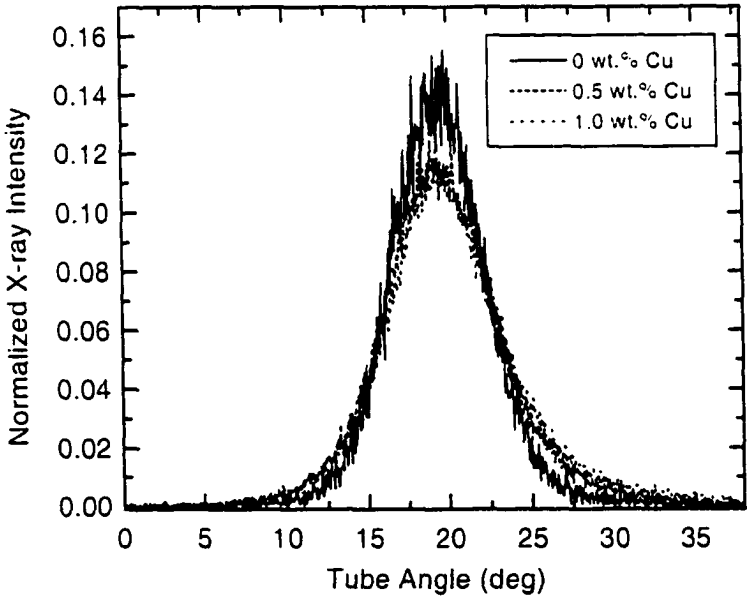

Figure 5. 25: Rocking curve showing the effect of Cu additions on the texture of 1Ti/3Al multilayers with Λ = 20 nm.

As the bilayer thickness increased, the effect of Cu became more pronounced. This was evident in the Λ = 72 nm samples where the FWHM increased by 3-4° for the samples containing Cu as shown in Figure 5. 26. The diffraction peaks for the samples also appeared asymmetric. This may be indicative of an offset in the texture or strain effects as observed in some of the Nb/Al samples.

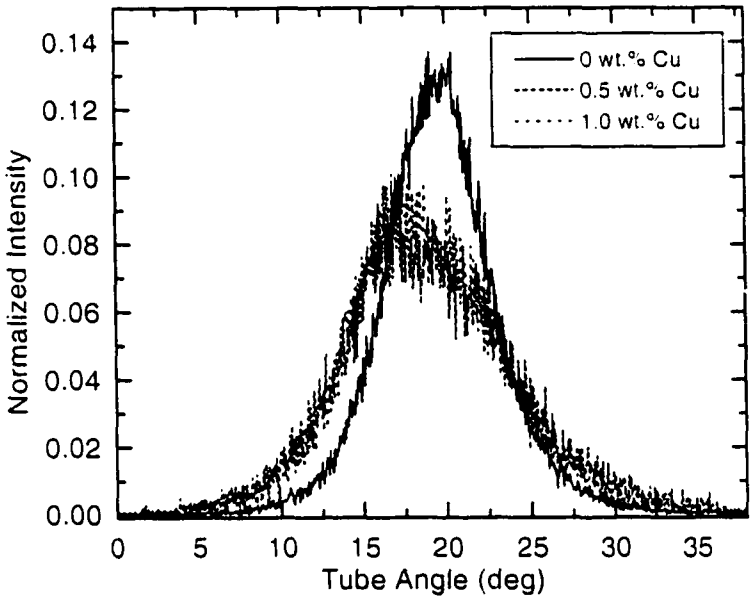

Figure 5. 26: Rocking curve showing the effect of Cu additions on the texture of 1Ti/3Al multilayers with Λ = 72 nm.

Finally, rocking scans were obtained for 1Ti/3Al multilayers with Λ = 333 nm. These samples indicated the highest sensitivity to the presence of Cu with the FWHM of the Al(Cu) multilayers nearly three times the value of the 0 wt.% Cu sample as seen in Figure 5. 27. A significant drop in the diffracted intensity was also observed. These results showed a decrease in Al (111)/Ti (0002) texture with increasing Cu content. Note that a significant difference was not observed between the 0.5 and 1.0 wt.% Cu samples.

The results of the rocking curve measurements are summarized in Table 5. III.

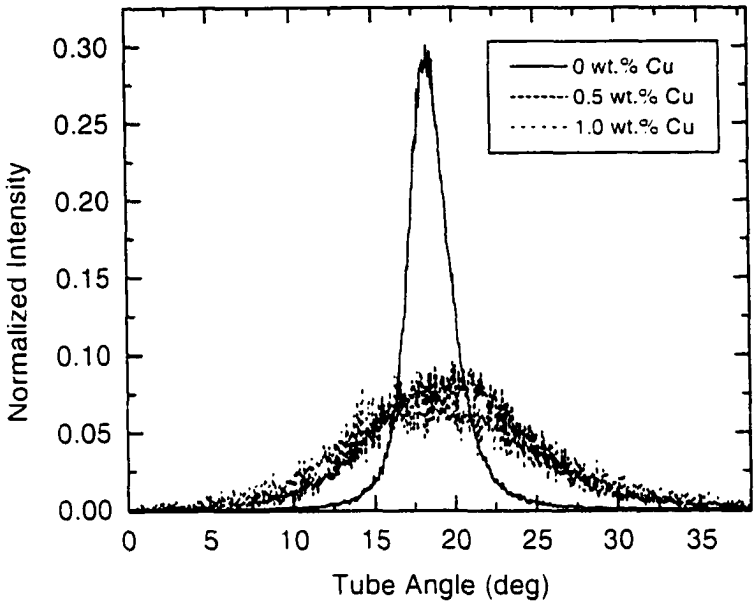

Figure 5. 27: Rocking curve showing the effect of Cu additions on the texture of 1Ti/3Al multilayers with Λ = 333 nm.

Table 5. III: Summary of results obtained from rocking curves of 1Ti/3Al multilayer films with 0, 0.5 and 1.0 wt.% Cu.

Λ [nm]	Cu conc. [wt.%]	FWHM [deg]
10*	0.0	8.16
10*	0.5	8.14
10*	1.0	8.51
20	0.0	6.53
20	0.5	7.72
20	1.0	7.79
72	0.0	7.04
72	0.5	11.07
72	1.0	10.18
333	0.0	3.08
333	0.5	10.89
333	1.0	13.34

* Indicates weak satellite (superlattice) reflections were observed.

5.4.1.2.2 Pole Figure Analysis

As with the Nb/Al samples, pole plots were measured to supplement the information obtained from the rocking curve scans. Figure 5. 28 shows a comparison of as-deposited 1Ti/3Al multilayers with Λ = 20 and 333 nm. As implied by the rocking curves, the offset was nearly identical (0.5-0.6) for the two samples while the ω_{95} value was slightly greater for the 20 nm sample as compared with the 333 nm sample 10° versus 7.8°, respectively.

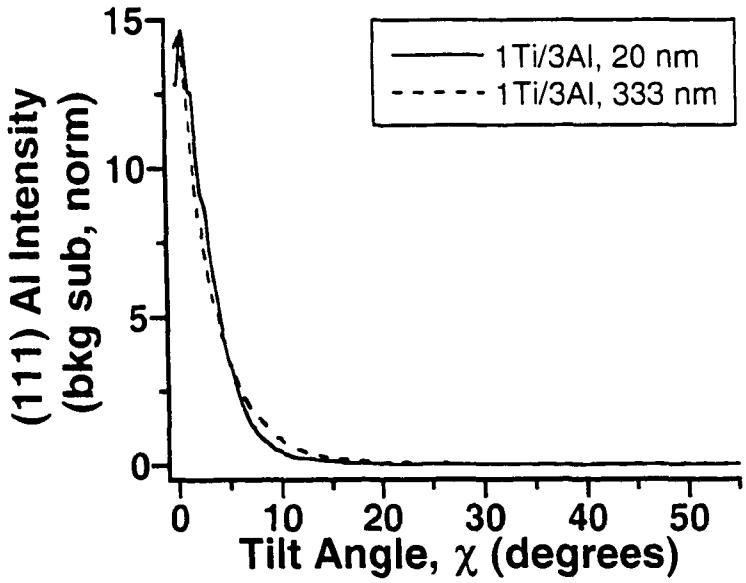

Figure 5. 28: Pole plot of Al (111)/Ti(0002) intensity for 1Ti/3Al multilayers with Λ = 20 and 333 nm.

The effect of 1 wt.%Cu on the texture of the Ti/Al multilayers was also measured for Λ = 20 and Λ = 333 nm films. Figure 5. 29 shows the results of a pole figure of 1Ti/3Al multilayers with Λ = 20 nm. Besides a small drop in diffracted intensity, the effect of Cu on the offset or ω_{95} was negligible.

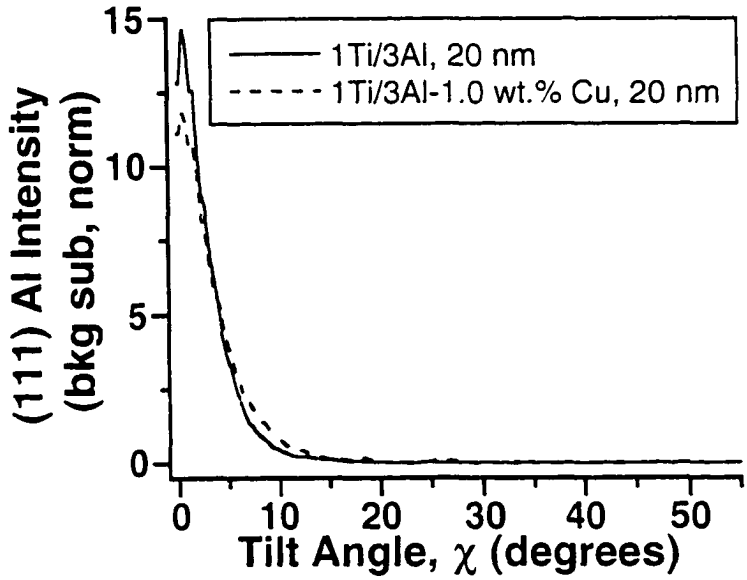

Figure 5. 29: A pole plot showing the effect of Cu on 1Ti/3Al multilayer films with Λ = 20 nm containing 0 and 1.0 wt.% Cu.

Pole figures were also generated for 1Ti/3Al samples with Λ = 333 nm and are shown in Figure 5. 30. In this case, the effect of adding Cu was more apparent. The offset increased from 0.5 to 1.6° and the $\omega_{1/2}$ increased from 7.8 to 9.5°. The samples containing the Al(Cu) also have a much lower intensity.

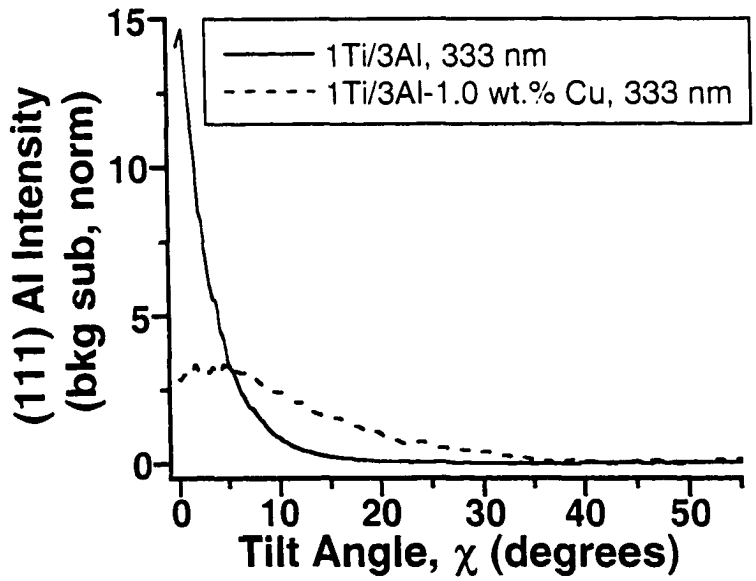

Figure 5. 30: A pole plot showing the effect of Cu on 1Ti/3Al multilayer films with Λ = 333 nm containing 0 and 1.0 wt.% Cu.

The results of the pole plots of the 1Ti/3Al and 1Ti/3Al(Cu) multilayers are summarized in Table 5. IV.

Table 5. IV: Summary of the results obtained from the pole plots of 1Ti/3Al and 1Ti/3Al(Cu) multilayers.

Λ [nm]	Cu conc. [wt.%]	Offset [deg]	ω_{95} [deg]
20	0	0.6	10
20	1.0	0.5	9.9
333	0	0.5	7.8
333	1.0	1.6	9.5

5.4.1.3 Discussion

In order to explain the rocking curve and pole figure results, the mechanisms leading to fiber texture in thin-film multilayers must be understood. Texture development can occur through the process of grain growth where high energy grain boundaries are replaced by lower energy boundaries. In addition, texture can also be determined by surface energies, especially in the early stages of film coalescence (Harper and Rodbell 1997). This results in the formation of a <111> fiber texture. Experiments of Al film growth have found that the <111> texture is established between 100 nm-200 nm of film growth (Lita and Sanchez 1999). Thereafter, the texture increases gradually as the grain size increases.

In addition to surface energy effects, grains can acquire a preferred orientation through the minimization of strain energy (Sanchez 1994, Zielinski, et al. 1995, Thompson and Carel 1996). For Al films, this mechanism was shown to be prominent at relatively high temperatures (> ~400 ^{o}C) and at thicknesses > 0.5 μm (Thompson and

Carel 1996). For the deposition conditions and films studied in this work, strain energy minimization was not expected to be the dominating mechanism of texture formation.

Interface roughness can also influence the texture of the deposited film. This effect was also believed to be a factor for the Nb/Al and Ti/Al multilayers. Cross-sectional TEM results will show that the Nb and Ti with their low adatom and grain boundary mobilities result in a rough interface. The deposition of the next Al layer on top of the previous Nb layer was affected by this roughness. The magnitude of the roughness was also a function of layer thickness, with the thicker Nb or Ti layers forming the roughest interfaces. In the thicker bilayers, the "underlayer" will develop a rougher surface and cause a decrease in texture as observed by Adamik et al. (1998). In this case the authors attributed the increase in texture with thinner layers to the presence of FCC Ti (Ahuja, et al. 1994; Banerjee et al. 1996). However, several studies have provided convincing evidence that FCC Ti was merely an artifact of TEM sample preparation (Shechtman, et al. 1994; Bonevich et al.1999). Therefore, the results of Adamik et al. (1998) are more likely due to surface or granular roughness introduced during deposition of thicker Ti layers.

The addition of Cu affects the texture evolution by interfering with the Al grain growth. The films with Cu still maintain a columnar structure, but have much smaller aspect ratios. The larger number of Al(Cu) grains per unit length produces a "granular roughness" at the interface due to the varying surface facets and disrupts the texture inheritance between successively deposited layers. The cumulative effect is an increase in the offset and weakening of the fiber texture. The combined grain growth-roughness mechanism was present in the 333 nm films and probably occurs for films with Λ as low

as 30 nm where superlattice formation has not been observed or reported. The role of solute Cu is less clear in the low period samples (< ~20 nm) where significant lateral grain growth was not expected to have occurred, although the Al grains are still columnar (see Chapter 6). In this case, the effect may be to inhibit superlattice formation by influencing the interfacial strain between the layers through changes in the Al lattice parameter. This would lead to a more random orientations and the observed decrease in pole intensity.

Figure 5. 31 compares the texture of a 23 nm film of Nb/Al and a 20 nm film of Ti/Al. The small peak immediately adjacent to the primary peak of the (111) reflection is a result of the superlattice formed in the Nb/Al multilayer. Clearly, the presence of the superlattice has a strong effect on the texture with the (111) Al intensity in Nb/Al being more than four times that of the Ti/Al film with a similar periodicity. The offset and $\omega_{1/2}$ are also less for the Nb/Al film.

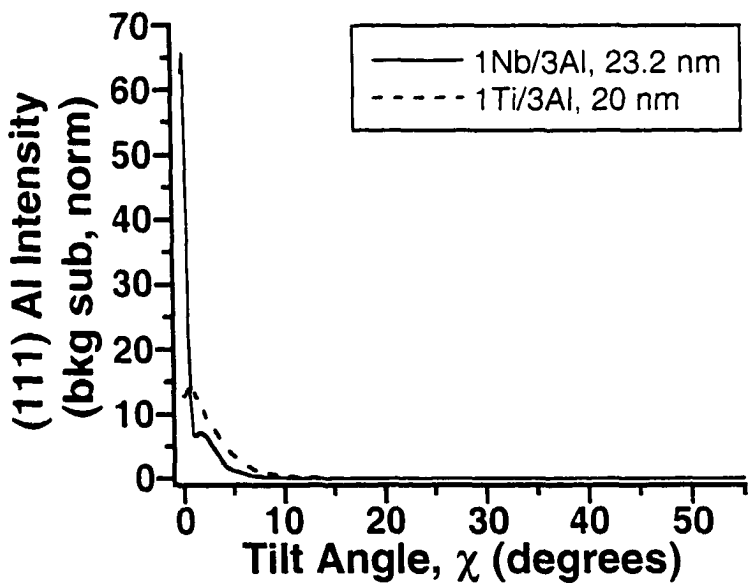

Figure 5. 31: Pole plot comparing 1Nb/3Al and 1Ti/3Al multilayers with Λ = 20 nm.

Figure 5. 31 shows a similar plot made with 333 nm Nb/Al and Ti/Al multilayers. In this case the Ti/Al offset is nearly half that of the Nb/Al presumably due to the interface roughness effects discussed earlier. The Nb/Al ω_{95} value is still smaller than the Ti/Al by ~3° indicating a slightly higher degree of fiber texture in this sample.

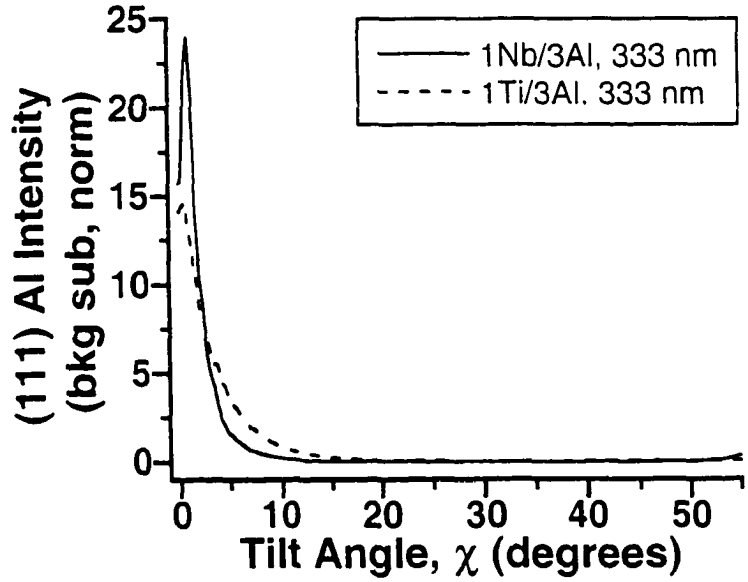

Figure 5. 32: Pole plot comparing 1Nb/3Al and 1Ti/3Al multilayers with Λ = 333 nm.

A comparison of pole plots was made to provide insight into how the addition of Cu could affect the texture in Nb/Al multilayers compared to Ti/Al multilayers. A pole plot showing the results previously obtained for Λ = 20 nm films is shown in Figure 5. 33. Although both set of films contain an offset of ~0.5°, the results indicated that the Ti/Al(Cu) films maintained a slightly better texture evidenced by a lower ω_{95} value and higher pole intensity.

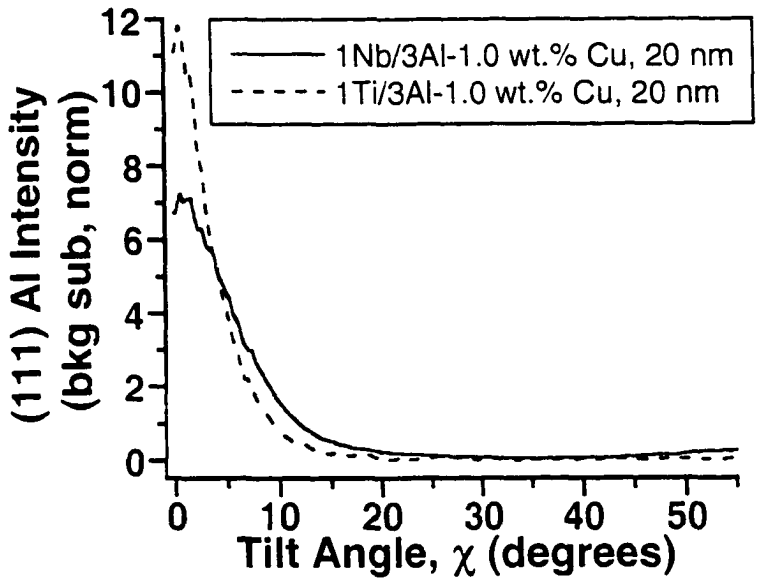

Figure 5. 33: Pole plot showing the differences between 1Nb/3Al-1.0 wt.% Cu and 1Ti/3Al-1.0 wt.% Cu multilayers with Λ = 20 nm.

A similar plot was constructed for the Al-1.0 wt.% Cu 333 nm films, shown in Figure 5. 34. Results were consistent with those for the 20 nm films. In this case, the offset was significantly less for the Ti/Al(Cu) sample as compared to the Nb/Al(Cu) sample. The pole intensity was also greater for the Ti/Al(Cu) sample, however, the $\omega_{0.5}$ value was nearly identical for the two multilayers. This difference in offset was possibly due to lower interfacial or granular roughness present in the Ti layers. This will be examined in the next chapter.

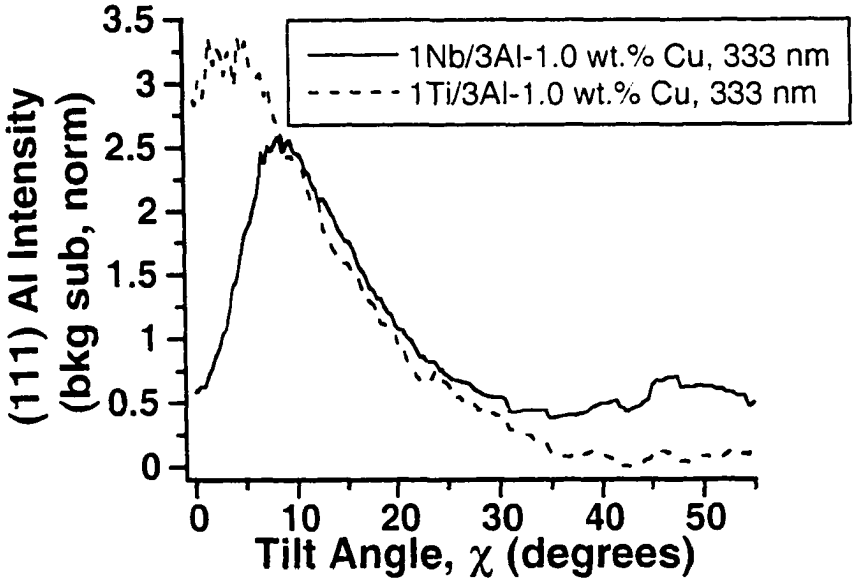

Figure 5. 34: Pole plot showing the differences between 1Nb/3Al-1.0 wt.% Cu and 1Ti/3Al-1.0 wt.% Cu multilayers with Λ = 333 nm.

5.4.1.4 Summary and Conclusions

The previous set of experiments has provided insight into the mechanisms of texture formation in multilayer thin-film structures and the effects of different materials and solute additions on this texture. In the Nb/Al and Ti/Al systems, several driving forces exist for texture formation. At lower layer thicknesses, the formation of epitaxial, coherent superlattices orients the depositing material through the thickness of the multilayer and leads to the formation of "macrograins". Due to the low temperatures and short deposition times per layer, grain growth during deposition is negligible and surface and interfacial energy minimization drives texture formation. However, above a certain thickness, grain growth during deposition begins to dominate texture formation. During this process, the high-energy grain boundaries are replaced by low energy boundaries and by grains with low surface energy orientations (i.e., Al (111)). Increased strain caused by the larger layer thickness, means that coherency may not be maintained across all layer

interfaces (although granular epitaxy may be present). However, the increased volume fraction of larger, oriented grains, results in an overall improvement in the texture as in the case of the 333 nm Ti/Al film.

Here it is worth noting that, Ti/Al metallurgy has been employed for nearly two decades in the microelectronics industry. Ti was chosen as the underlayer material due to the relatively low resistance of the intermetallic phase $TiAl_3$ that was inevitably formed during processing and the ability of the Ti to introduce strong fiber texture in the Al. The current experiments provided supplemental information concerning the ability of an underlayer to strengthen the texture of a subsequently deposited layer. The present results showed that for the processing conditions employed, Nb introduced a significant offset when used as an underlayer for Al(Cu) metallurgy while Ti maintained fiber texture without producing a substantial offset in the Al(Cu) overlayer.

Despite the large amount of research that has been conducted on Al/Ti thin films, a correlation between Cu concentration and fiber texture has not yet been reported. The effect of Cu in a thin film structure consisting of a thin Ti underlayer and a relatively thick Al(Cu) film would most likely be negligible. However, the use of a multilayer structure sometimes consisting of 50 layers (Λ = 10nm) or a minimum of 7 layers (Λ =333 nm), has amplified a slight effect resulting from changes in the microstructure of a constituent layer. Although, similar multilayers are not found in commercial thin-film metallizations, these studies showed that they provided an innovative means of observing subtle, but detectable phenomena in thin-films.

5.4.2 *In situ* Synchrotron X-ray Diffraction Results (Annealed Films)

5.4.2.1 Nb/Al and Nb/Al(Cu)

A θ–2θ scan obtained from a 1Nb/3Al, Λ = 72 nm multilayer annealed to 700 °C at 180 °C/min is shown in Figure 5. 35.

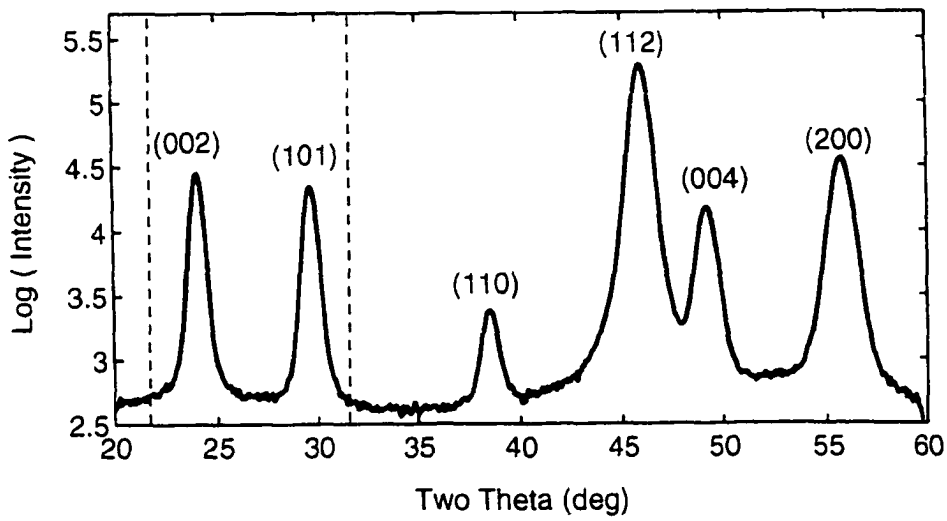

Figure 5. 35: *Ex situ* θ-2θ scan from a 1Nb/3Al, Λ = 72 nm multilayer heated from 100 to 700 °C at 180 °C/min. Peaks identified correspond to the equilibrium $NbAl_3$ phase. The dashed lines indicate the approximate window selected for the *in situ* runs (λ = 0.1797 nm).

The *in situ* diffraction analysis requires three values to be plotted: two-theta, temperature and X-ray intensity. The data can be represented in three-dimensions forming a surface of X-ray intensities as a function of temperature (for constant-heating-rate scans) as shown in Figure 5. 36.

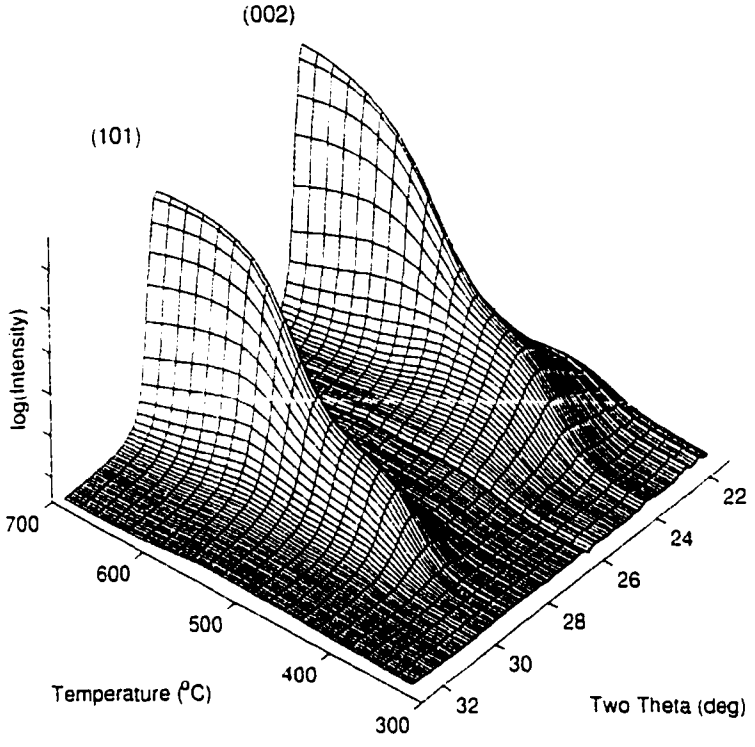

Figure 5. 36: A three-dimensional representation of the data obtained from the position-sensitive detector. XRD intensity is plotted as a function of temperature and two-theta for a 1Nb/3Al, Λ = 72 nm multilayer annealed at 180 °C/min from 100 °C to 700 °C.

Although the three dimensional plot provides an intuitive display of the data, a more convenient representation involves a two dimensional plot with XRD intensity represented by a color scale with contours demarcating areas of equal intensity. Such a plot is shown in Figure 5. 37 along with the windows used to determine the intensity of the different peaks. For the Nb/Al and Nb/Al(Cu) multilayers, windows were set to measure the intensity of the (002) and (101) peaks of $NbAl_3$. These peaks were chosen because they did not overlap with any elemental Al or Nb peaks, thus simplifying interpretation of the results and providing direct observation of product phase formation. The (002) peak is located at $2\theta = 24.065^{\circ}$ for the incident radiation used. The

corresponding window was set from 22.6 to 24.7°. The (101) peak was located at 29.664°. The window was set from 28.1 to 30.2°.

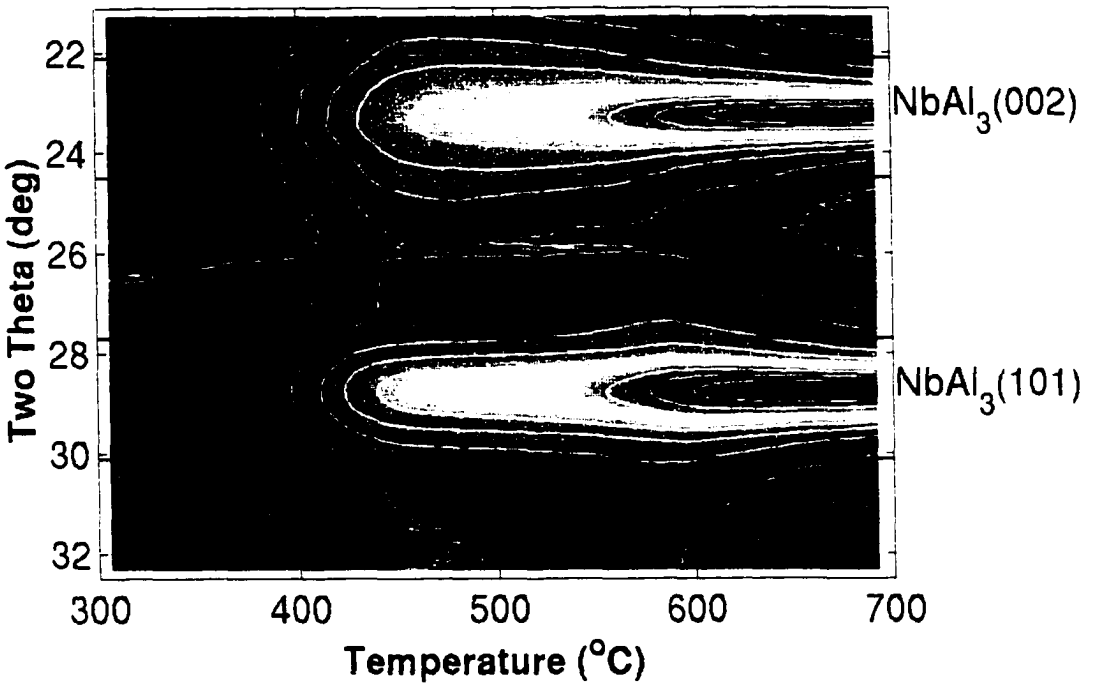

Figure 5. 37: Plot of X-ray intensities as a function of 2θ and temperature obtained for a 1Nb/3Al multilayer with Λ = 72 nm showing the position of the windows (black horizontal lines) used to determine the integrated intensities for the peaks attributed to the $NbAl_3$ phase.

5.4.2.1.1 Nb/Al-0 wt.% Cu

5.4.2.1.1.1 Effect of Layer Thickness on Reaction Kinetics

A series of 1Nb/3Al multilayers with Λ ranging from 10-333 nm were annealed in the *in situ* apparatus as described in the experimental section. The plots of XRD intensity as a function of 2θ and annealing temperature are shown in Figure 5. 38.

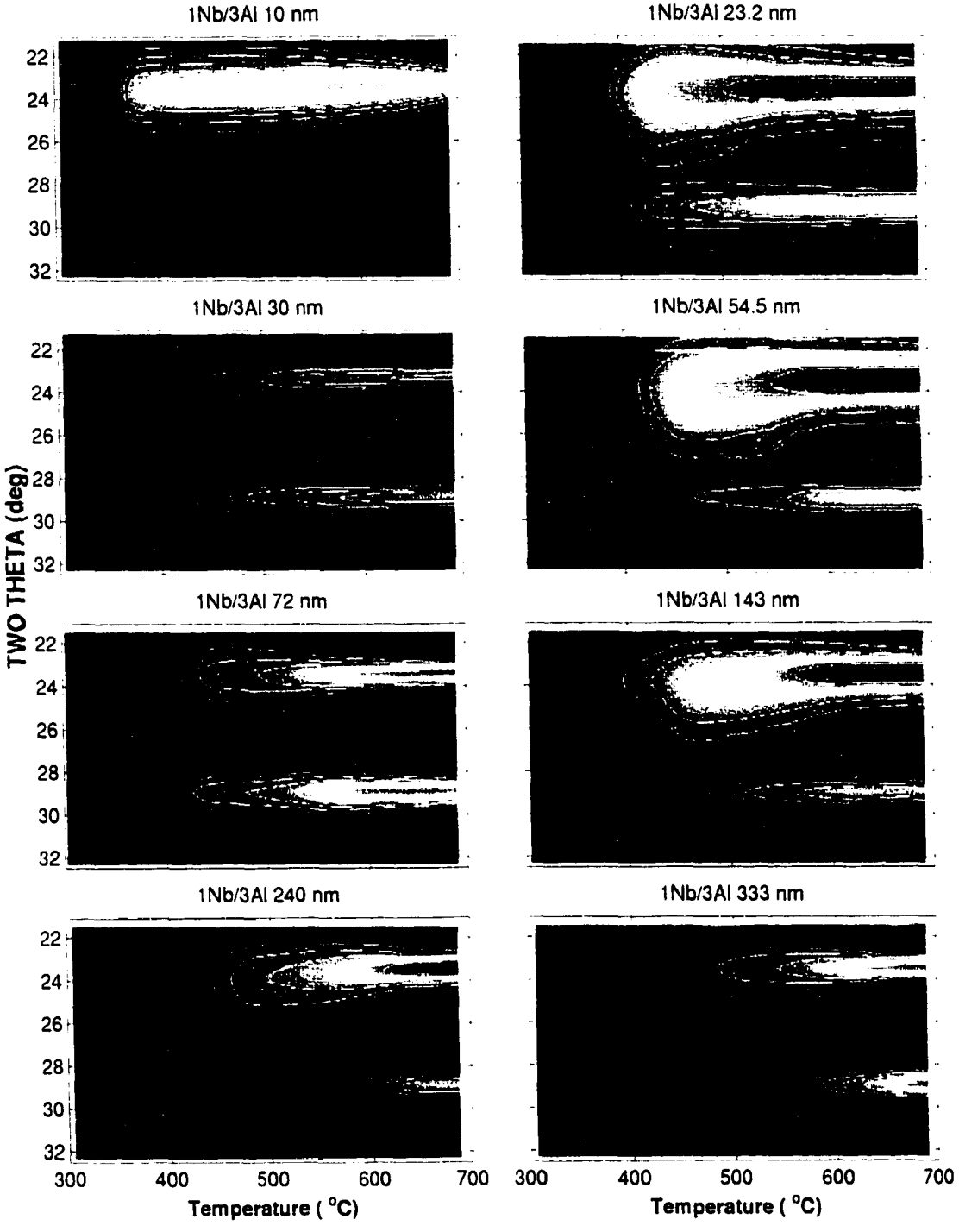

Figure 5. 38: Diffracted X-ray intensity as a function of 2θ and temperature for 1Nb/3Al-0 wt.% Cu multilayers with Λ ranging from 10 nm to 333 nm heated at 180 °C/min from 100-700 °C in purified He. (Blue is the lowest intensity, red represents high intensity).

Beginning with the Λ = 10 nm film in the upper left corner of the figure, the results indicated the formation of the $NbAl_3$ (002) peak with increasing temperature. The absence of the neighboring (101) peak could indicate that the product phase has formed with a particular texture. The texture of the product phase may be a result of the texture of the as-deposited films. As observed in the 23 nm film, the <111> texture was sharp in both rocking curves and pole plots. For the thicker films the texture was weaker and tended to develop an offset presumably due to interface roughness. The 10 and 23 nm samples also showed multiple satellite reflections adjacent to the Al(111)/Nb (110) peak in the θ-2θ scans prior to annealing (faintly visible in the lower left corner of the plots). These satellites could be attributed to the formation of coherent superlattices as discussed earlier.

The (101) reflection was visible for films with Λ > 23 nm and paralleled formation of the (002) peak in all of the periods studied. The (101) peak was also lower in relative intensity with the exception of the Λ = 30 nm and 72 nm samples. The reason for the different behavior of these samples is unknown, but could be a result of run-to-run differences in deposition. The lower intensity of the (002) and (101) peaks in the 30 nm sample was probably a result of the lower total thickness of this sample (0.5 μm) compared with 1 μm for the other samples. In all of the films studied, the width of the diffraction peaks decreased as the temperature increased. This was especially evident in the (002) $NbAl_3$ reflections. This was presumably due to rapid grain growth and coarsening of $NbAl_3$ during heating. In the 23 nm, 54.5 nm, 143 nm, and 240 nm samples, a low shoulder was present on the high angle side of the peak. This could be a result of strain during the initial stages of phase formation. Strain could have developed

if the $NbAl_3$ phase formed coherently with the Al and Nb. Note that the (103)/(112) d-spacing of $NbAl_3$ (~2.30Å) is close to that of both Nb (110) and Al (111) 2.336 Å and 2.338 Å, respectively. Once the layer grew to a sufficient thickness, the interfaces would be unable to maintain coherency and the d-spacings would relax to the equilibrium values. In general, the formation temperature of $NbAl_3$ increased with increasing Λ from ~ 350 °C for the 10 nm to ~450 °C for the 333 nm film.

To examine the kinetics of phase formation in more detail and to provide a means of comparing the XRD kinetic data with DSC results, the integrated intensities within each window were determined as a function of temperature for each film as shown in Figure 5. 39. The integrated intensity was assumed to be proportional to the volume of $NbAl_3$ formed during the reaction.

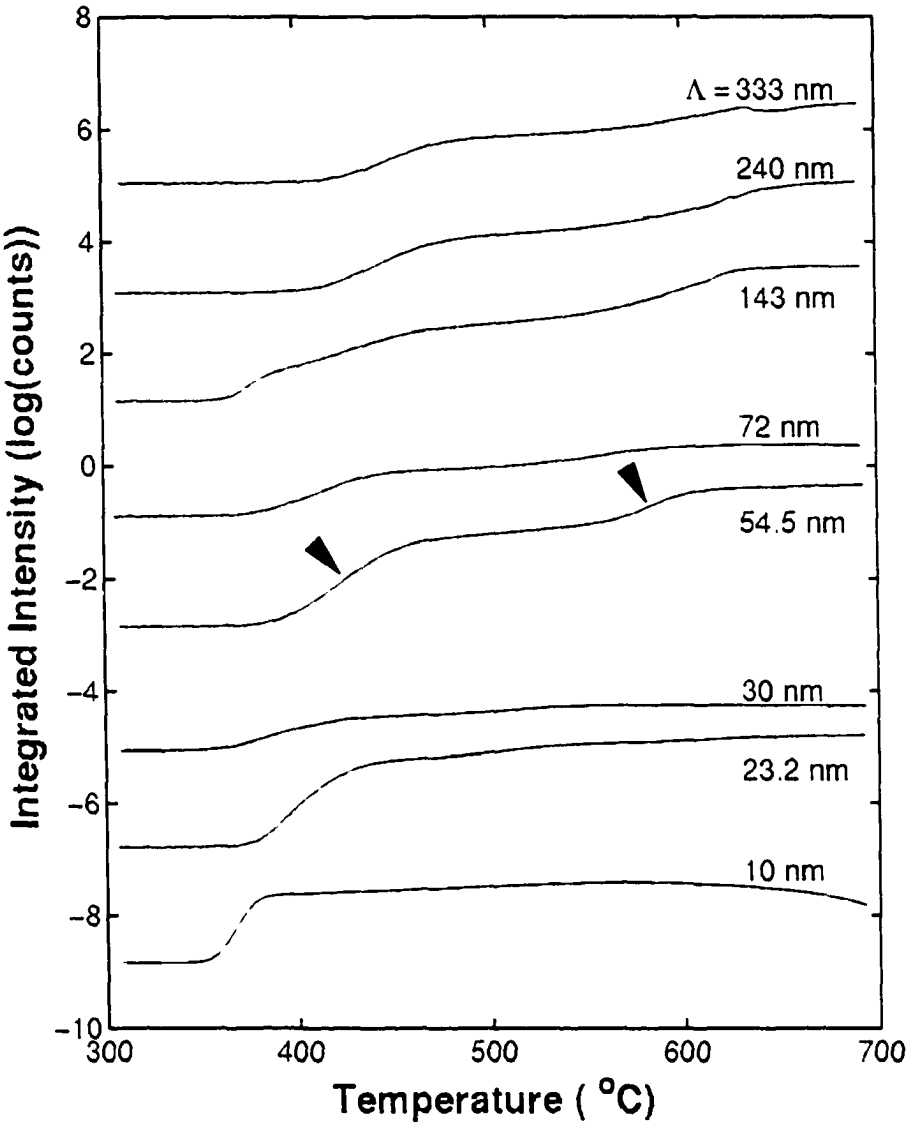

Figure 5. 39: Integrated XRD intensity as a function of temperature for the $NbAl_3$ (002) peak in 1Nb/3Al-0 wt.% Cu multilayers.

In all of the multilayers, the integrated intensity increased with temperature as expected for the transformation of Nb and Al to $NbAl_3$. In films with $\Lambda > \sim 23$ nm, two inflection points were observed in the trace indicating a reduction in the rate of formation of $NbAl_3$. The 143 nm film exhibited an additional inflection at slightly less than 400 °C.

These transitions in the integrated intensity became clearer by smoothing the integrated intensities and differentiating them with respect to temperature. This result provided the *rate* of change of the integrated intensity (volume transformed) as a function of temperature as shown in Figure 5. 40. In the plot shown, the heights of the peaks were normalized so that the maximum value of the curve was equal to one. Another advantage to this approach was that the differentiated results were analogous to a constant heating rate DSC traces where the rate of heat (or enthalpy) release was measured as a function of temperature. In the DSC measurement, the amount of *heat evolved* was assumed to be proportional to the volume fraction transformed. Similar to the DSC results, the first derivative of the integrated intensity of the *in situ* XRD results produced two separated peaks and suggested an intermediate reduction in the reaction rate. The behavior held for both the $NbAl_3$ (002) and (101) diffraction peaks.

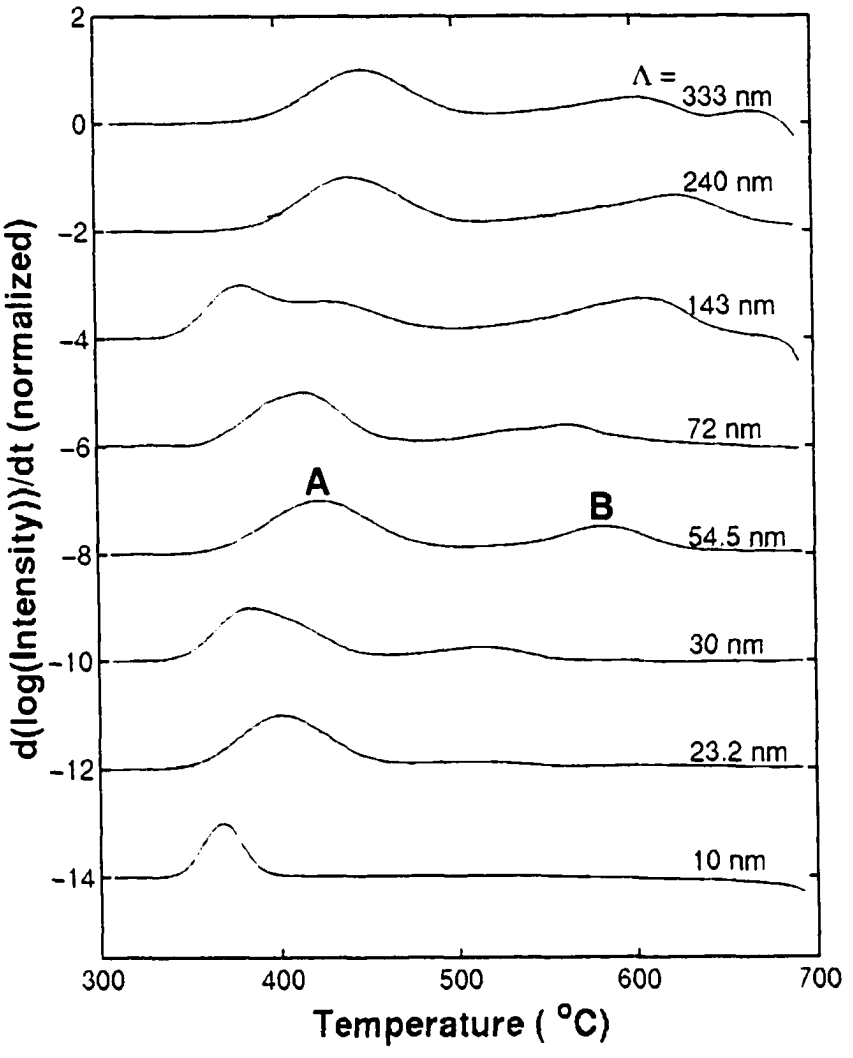

Figure 5. 40: The first derivative of the integrated intensity as a function of temperature for the NbAl$_3$ (002) diffraction peak in 1Nb/3Al-0 wt.% Cu multilayers.

As with the DSC results presented in Chapter 4, the 10 nm film produced only one peak signifying the consumption of the reactants during the first stage of product phase growth. In the other samples, the two peaks were attributed to a two-stage mechanism of phase formation as proposed in the model of Coffey et al. (1989). The peak temperatures are listed in Table 5. V.

Table 5. V: XRD peak temperatures for $NbAl_3$ formation in 1Nb/3Al-0 wt.% Cu multilayers annealed at a heating rate of 180 °C/min obtained from the plots of the first derivative of the integrated intensity of the $NbAl_3$ (002) peak.

Sample ID	Λ [nm]	Peak A [°C]	Peak B [°C]
112998a	10	367.1	
021098a	23.2	400.4	506.6
120898b	30	383.3	513.6
020998a	54.5	423.3	582.3
020798a	72	419.0	589.2
021098b	143	427.9	615.7
020898a	240	443.4	622.3
080798a/100597a	333	441.7	

A similar approach was followed for the analysis of the $NbAl_3$ (101) peaks. The integrated intensities as a function of temperature are shown in Figure 5. 41. Again, two inflections were observed in the curves with $\Lambda > 23$ nm. Note in this case, minimal intensity was observed for the 10 nm diffraction peak.

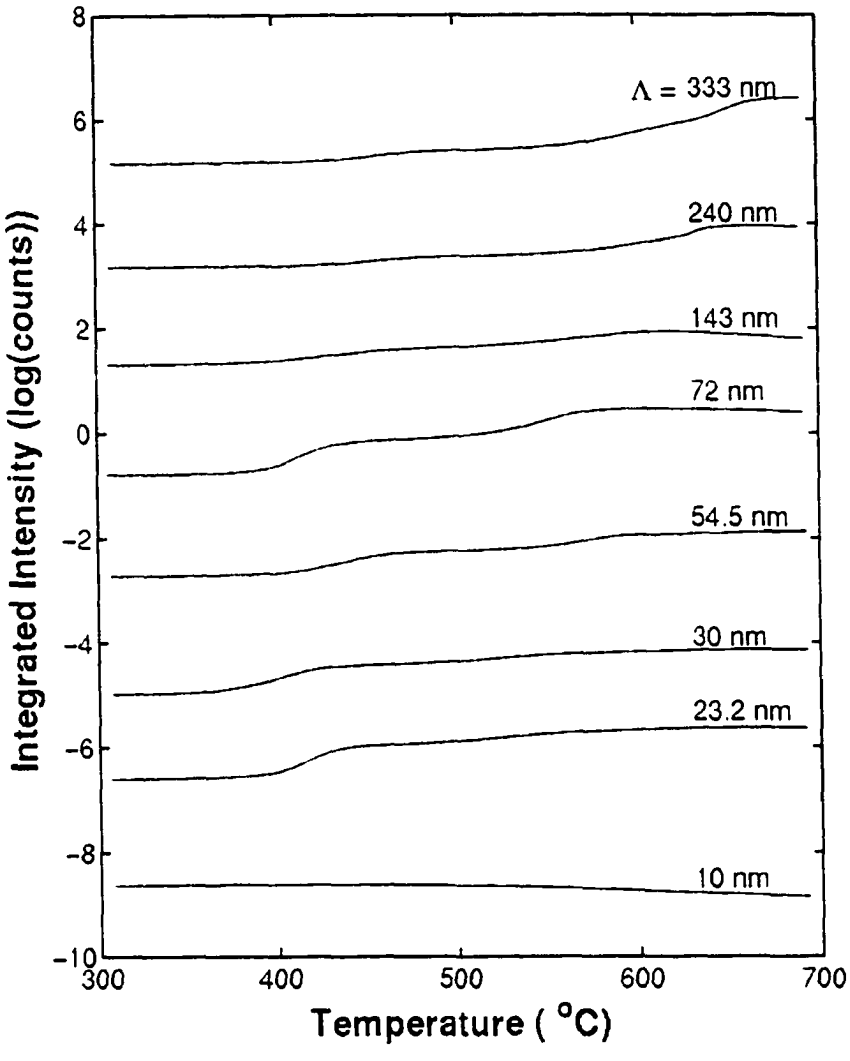

Figure 5. 41: Integrated XRD intensity as a function of temperature for the $NbAl_3$ (101) peak in 1Nb/3Al-0 wt.% Cu multilayers.

Transitions were identified readily in the first derivative of the XRD intensity as shown in Figure 5. 42. The additional peak present in 143 nm film was absent in this plot suggesting that it was related to the $NbAl_3$ (002) reflection and could be a result of texturing. Although the first peak appeared symmetrical, the second peak was broader and possessed an asymmetric shape that was evident in the films with $\Lambda > 143$ nm. This behavior was also similar to the DSC results.

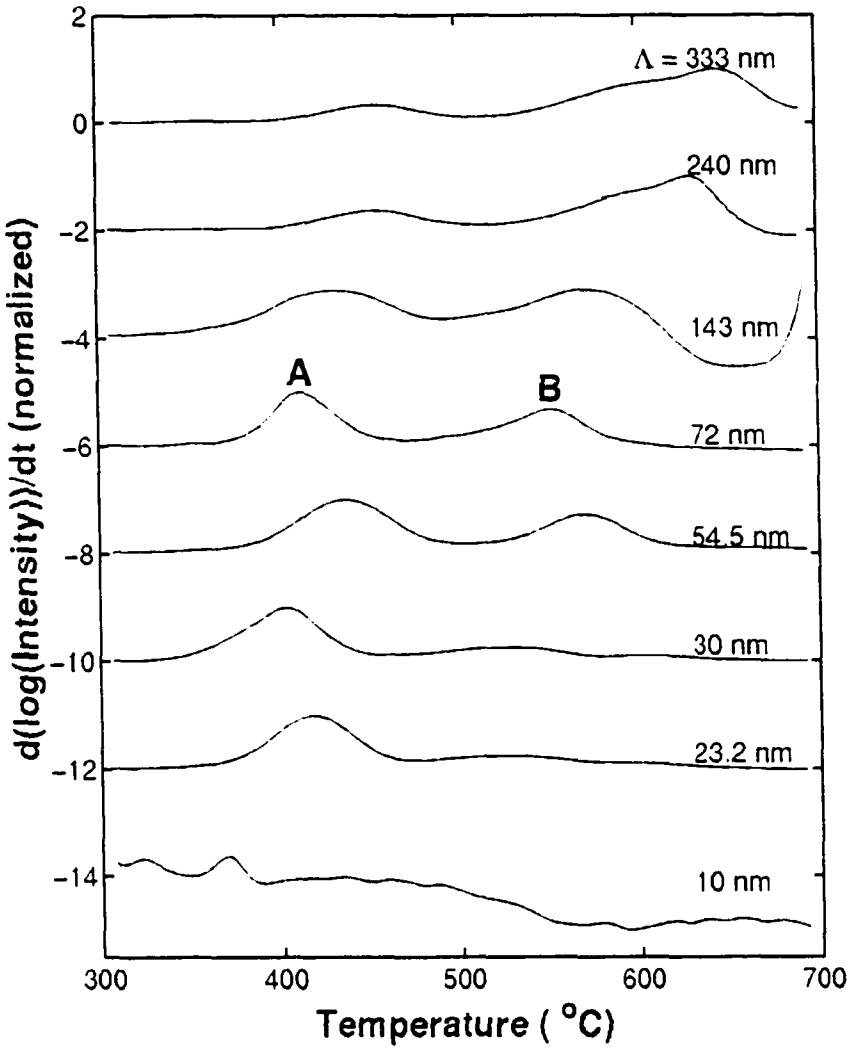

Figure 5. 42: First derivative of the integrated XRD intensity as a function of temperature for the curves for the $NbAl_3$ (101) peak in 1Nb/3Al-0 wt.% Cu multilayers.

The peak temperatures determined from the curves in Figure 5. 42 are listed in Table 5. VI.

Table 5. VI: XRD peak temperatures for $NbAl_3$ formation for in 1Nb/3Al-0 wt.% Cu multilayers annealed at a heating rate of 180 °C/min obtained from the plots of the first derivative of the integrated intensity of the $NbAl_3$ (101) peak.

Sample ID	Λ [nm]	Peak A [°C]	Peak B [°C]
112998a	10		
021098a	23.2	416.1	526.3
120898b	30	401.7	523.8
020998a	54.5	435.9	569.7
020798a	72	419.9	578.5
021098b	143	429.4	567.4
020898a	240	454.5	626.3
080798a/100597a	333	445.6	631.8

Although the shapes of the peaks were replicated in most cases, one notable difference between the DSC and XRD results was in the relative heights of the two peaks.

5.4.2.1.1.2 Activation Energy

The previous section indicated that discrete stages of phase growth could be identified by differentiating the integrated intensity curves for the analyzed peaks. To further assess the validity of this approach to the study of the reaction kinetics, a Λ = 72 nm sample was annealed at heating rates of 60, 180, 540, and 1620 °C/min. The peak temperatures were obtained as before and a Kissinger plot was constructed shown in Figure 5. 43. Errors were taken into account from the linear regression fit routine as well as a graphical method that calculated the slopes of various linear fits through an iterative process accounting for the range of error in each point. The larger of the errors (at 98% confidence = 2σ) was taken as the experimental error. This procedure was employed for all of the activation energies determined from the *in situ* XRD measurements.

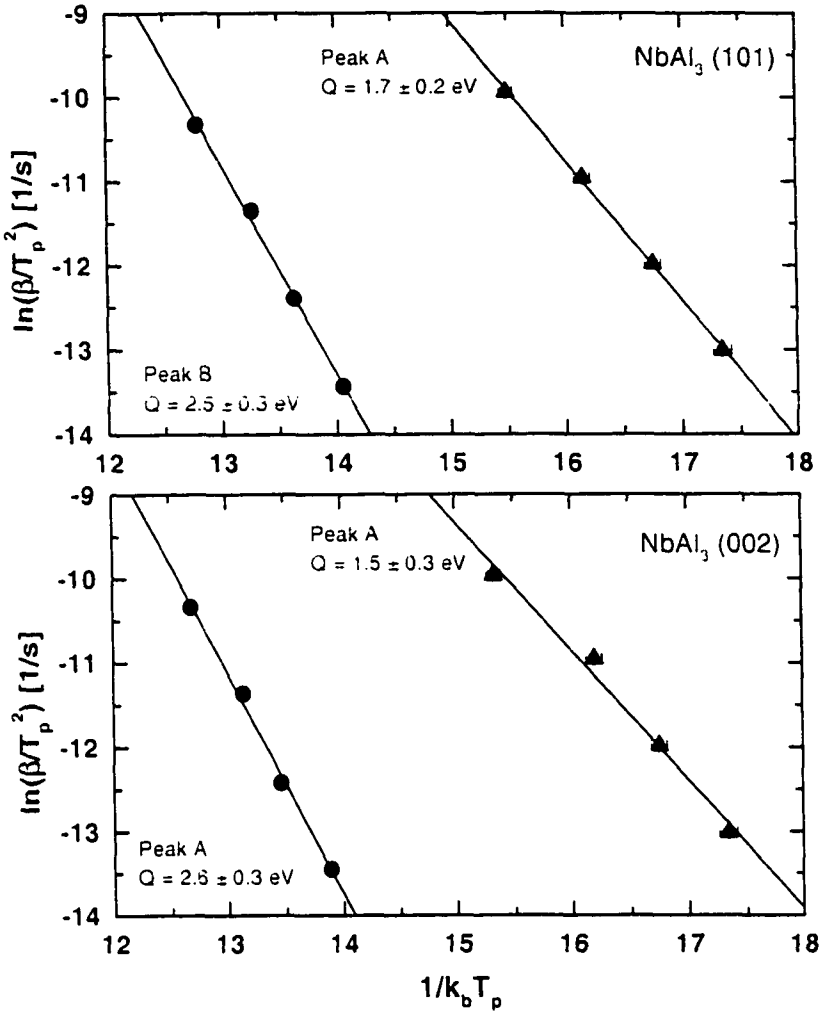

Figure 5. 43: Kissinger plot showing activation energies for peaks A and B from a 1Nb/3Al-0 wt.% Cu multilayer with Λ = 72 nm.

The output from the linear regression analysis used to fit the data for the Kissinger analysis is listed in Table 5. VII.

Table 5. VII: Results from Kissinger analysis of XRD data for a 1Nb/3Al-0 wt.% Cu multilayer film with Λ = 72 nm.

1Nb/3Al- 0 wt.% Cu; Λ = 72 nm (020798a)					
Peak	Q [eV]	Error (98% conf.)	y-int. [$K^{-1}s^{-1}$]	Error (98% conf.)	Freq. Factor (ν) [s^{-1}]
A (101)	1.7	0.2	15.94	1.07	1.65E+11
B (101)	2.5	0.3	21.60	2.88	7.00E+13
A (002)	1.5	0.3	13.55	4.16	1.36E+10
B (002)	2.6	0.3	22.92	3.20	2.72E+14

The activation energies determined from the Kissinger analysis for peak A and B in both the (101) and (002) $NbAl_3$ reflections were in excellent agreement with and corroborated those determined from DSC experiments. These results provided further proof of the validity of this approach to the study of the reaction kinetics in thin-film multilayers and encouraged application of this technique to other material systems.

5.4.2.1.2 Nb/Al-0.5 wt.% Cu

5.4.2.1.2.1 Effect of Layer Thickness on Reaction Kinetics

A subset of multilayers with Al-0.5 wt.% Cu were examined using the synchrotron apparatus to investigate the effects of Cu additions on the formation of $NbAl_3$. XRD intensity plotted as a function of 2θ and temperature for samples heated at 180 °C/min are shown in Figure 5. 44. As with the Al-0 wt.% Cu samples, the two diffraction peaks are evident in all of the traces. Satellite peaks were present in the as-deposited 20 nm sample indicative of a coherent superlattice. During annealing, significant narrowing of the peak width was evident in the Λ = 20 nm film, however, the larger periods did not indicate a significant decrease in peak width with temperature.

Shoulders were not evident on the low angle side of the peaks suggesting that strain might not play as prominent of a role in the transformation.

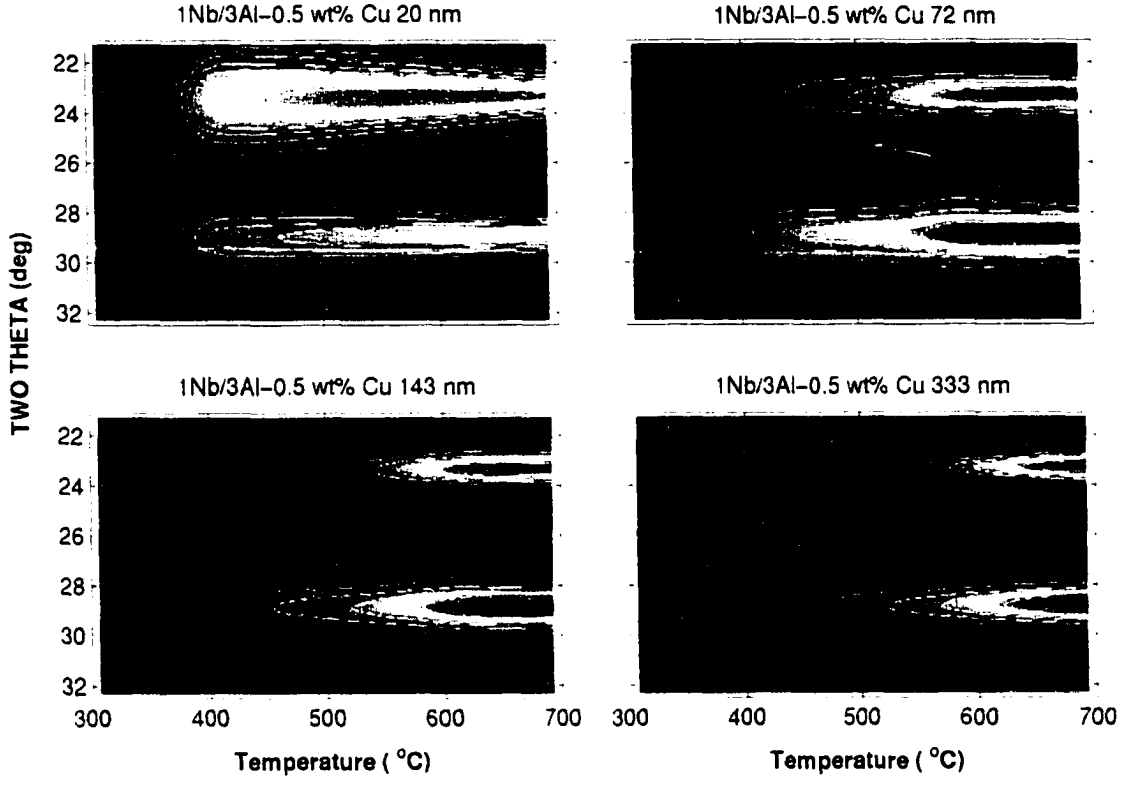

Figure 5. 44: XRD intensity as a function of 2θ and temperature for 1Nb/3Al-0.5 wt.% Cu multilayers with Λ ranging from 20 - 333 nm annealed from 100-700 °C at 180 °C/min in purified He.

The temperature of the appearance of the $NbAl_3$ (002) peak increased with increasing periodicity while the temperature of the $NbAl_3$ (101) peak exhibited less of a shift to higher temperatures with increasing bilayer thickness.

The integrated intensities were determined for the two reflections and are shown in Figure 5. 45. As with the 0 wt.% Cu samples. two inflections in the curves were observed for films with $\Lambda > 20$ nm.

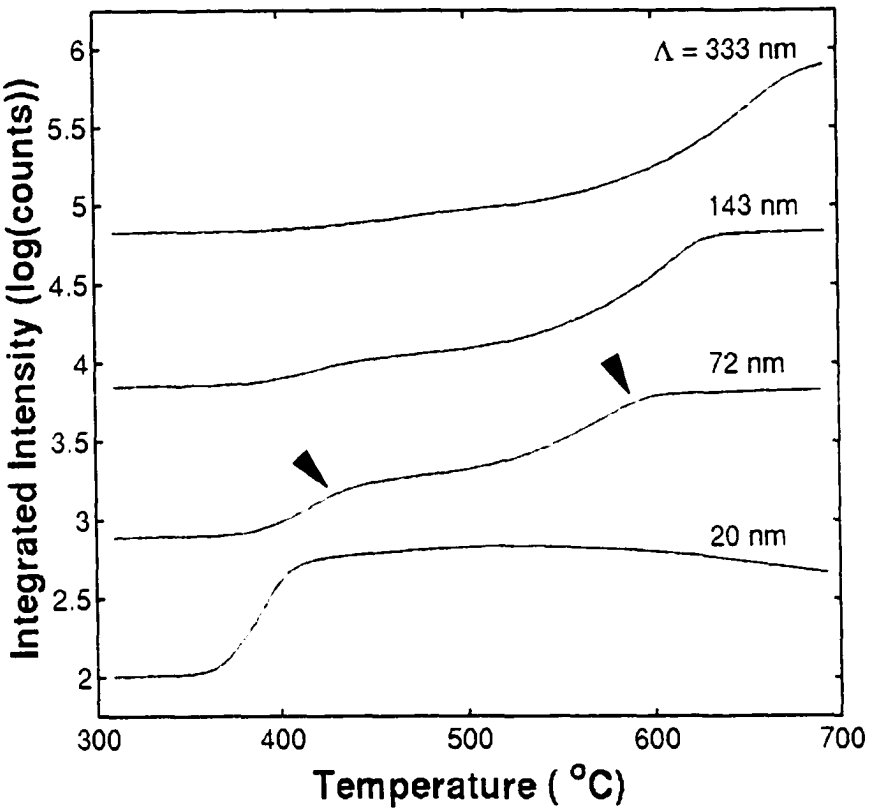

Figure 5. 45: Integrated XRD intensity as a function of temperature for the Nb_3Al (002) peak in 1Nb/3Al-0.5 wt.% Cu multilayers.

The normalized first derivatives of the smoothed integrated XRD intensity data yielded two separated peaks as before. The symmetry of the first peak (Peak A) was evident as well as the asymmetry of the second (Peak B). The relative peak heights for a given period did not compare directly with the DSC results, however, in general peak B did increase in intensity relative to peak A with increasing period.

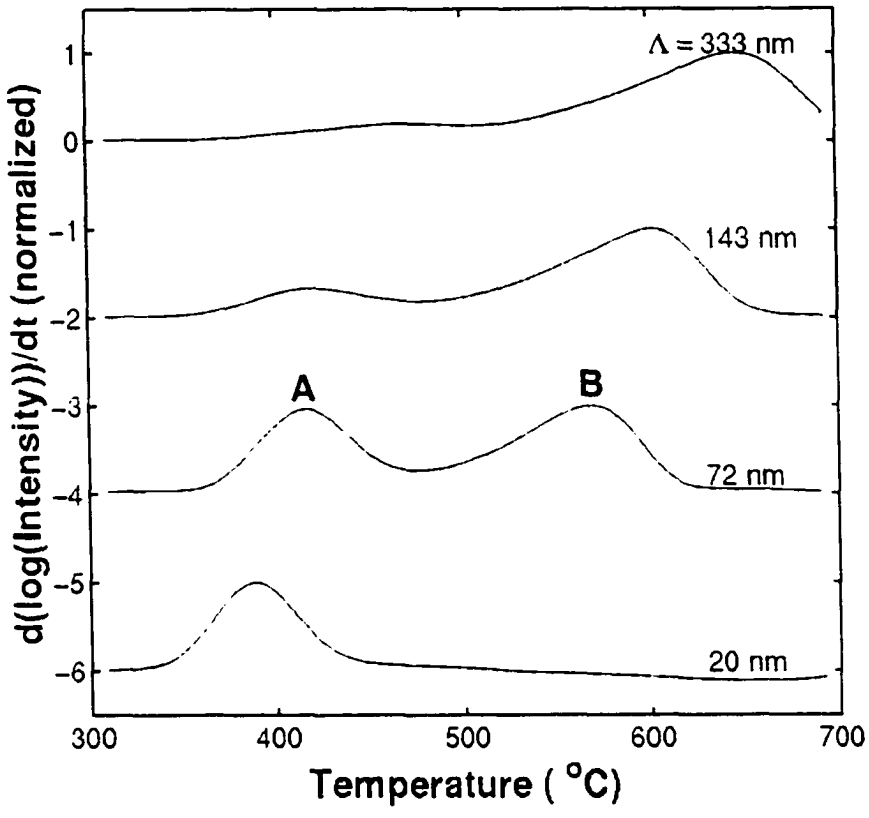

Figure 5. 46: Normalized first derivative of the integrated XRD intensity as a function of temperature for the $NbAl_3$ (002) reflection in 1Nb/3Al-0.5 wt.% Cu multilayers.

Peak temperatures were determined from the plot of the first derivative and are listed in Table 5. VIII.

Table 5. VIII: XRD peak temperatures for $NbAl_3$ formation in 1Nb/3Al-0.5 wt.% Cu films annealed at a heating rate of 180 °C/min determined from the first derivative of the integrated intensity of the $NbAl_3$ (002) peak.

Sample ID	Λ [nm]	Peak A [°C]	Peak B [°C]
111698a	20	388.4	476.2
102798a	72	417.2	565.8
111298a	143	420.5	601.7
103098a	333	472.2	645.9

A plot of the integrated intensities of the (101) peaks yielded results that were similar to those obtained from the (002) peak is shown in Figure 5. 47. Again, two inflections were evident for films with $\Lambda > 20$ nm.

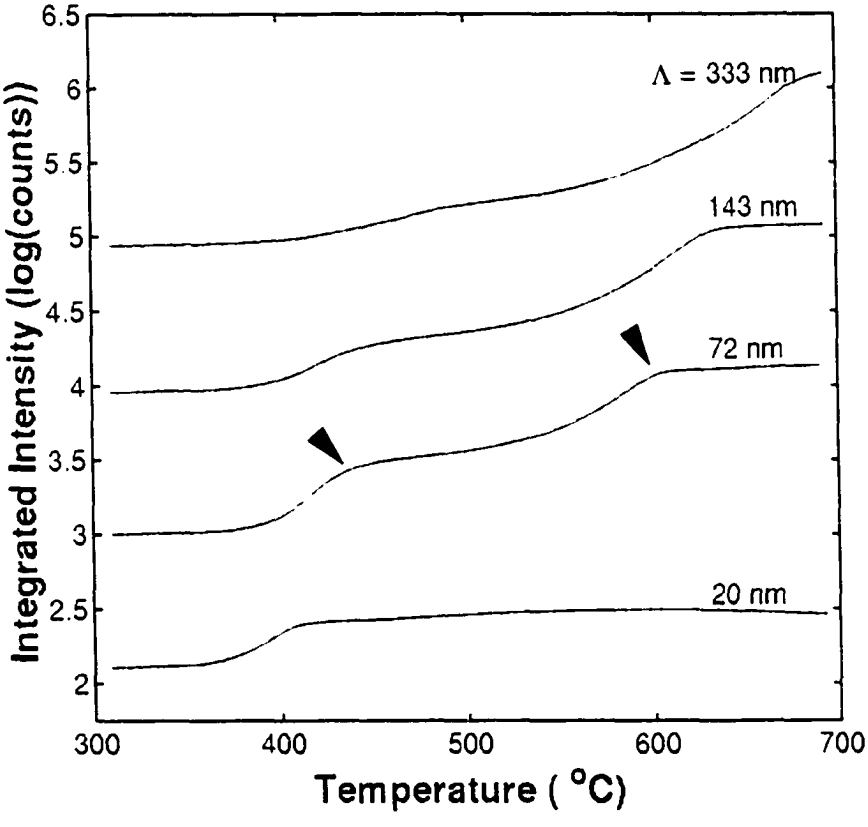

Figure 5. 47: Integrated intensity as a function of temperature for the $NbAl_3$ (101) peak in 1Nb/3Al-0.5 wt.% Cu multilayers.

The first derivatives of the integrated XRD intensities are shown in Figure 5. 48. The results were nearly identical with the $NbAl_3$ (002) peaks. One notable difference was the increase in the amplitude of peak A in the $NbAl_3$ (101) curves.

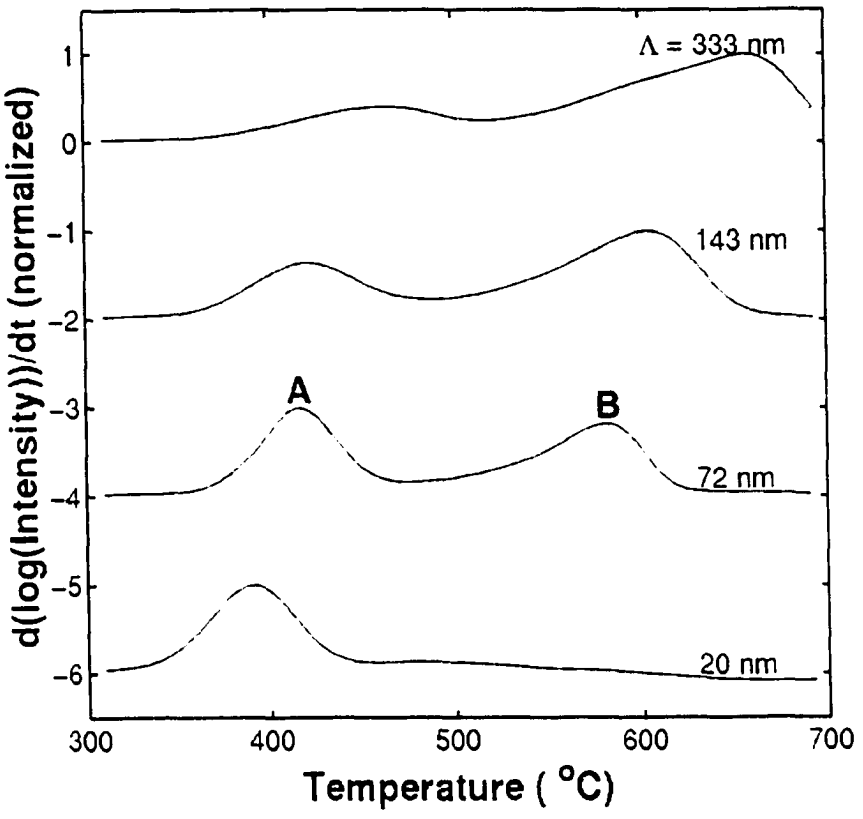

Figure 5. 48: Normalized first derivative of XRD as a function of temperature for the $NbAl_3$ (101) reflection in 1Nb/3Al-0.5 wt.% Cu multilayers.

The peak temperatures obtained from the derivatives of the integrated intensity curves are listed in Table 5. IX.

Table 5. IX: XRD peak temperatures for $NbAl_3$ formation in 1Nb/3Al-0.5 wt.% Cu films annealed at a heating rate of 180 °C/min determined from the first derivative of the integrated intensity of the $NbAl_3$ (101) peak.

Sample ID	Λ [nm]	Peak A [°C]	Peak B [°C]
111698a	20	391.8	--
102798a	72	417.2	577.8
111298a	143	420.5	602.9
103098a	333	464.5	655.4

5.4.2.1.2.2 Activation Energy

Activation energies for the two peaks were determined using the Kissinger analysis Figure 5. 49. The results were in good agreement with the previous results obtained by DSC yielding average values of ~1.8 eV for peak A and ~2.8 eV for peak B.

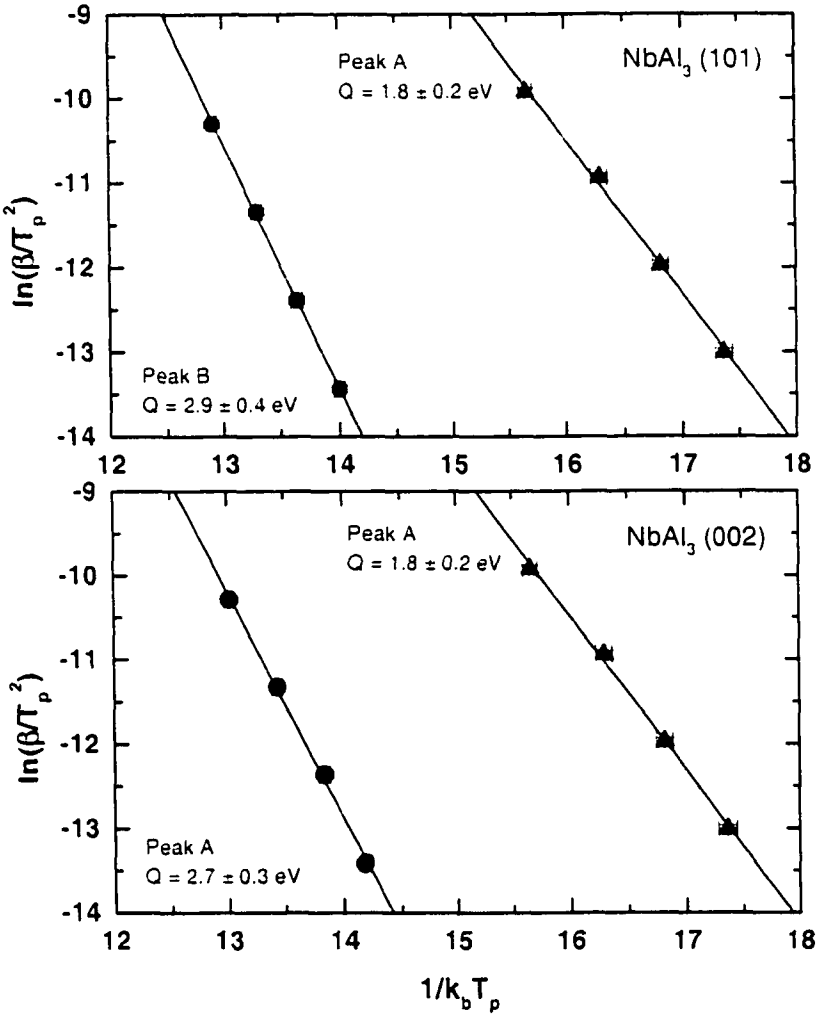

Figure 5. 49: Kissinger plots showing the activation energies determined from XRD data for peaks A and B from a 1Nb/3Al-0.5 wt.% Cu. Λ = 72 nm multilayer thin-film.

A summary of the results of the linear regression analysis used in the Kissinger plots are listed in Table 5. X.

Table 5. X: Results from Kissinger analysis of XRD data for a 1Nb/3Al-0.5 wt.% Cu multilayer film with Λ = 72 nm.

1Nb/3Al- 0.5 wt.% Cu; Λ = 72 nm (102798a)					
Peak	Q [eV]	Error (98% conf.)	y-int. [$K^{-1}s^{-1}$]	Error (98% conf.)	Freq. Factor (v) [s^{-1}]
A (101)	1.8	0.2	18.70	2.04	2.80E+12
B (101)	2.9	0.4	27.17	1.21	2.12E+16
A (200)	1.8	0.2	18.67	2.08	2.70E+12
B (200)	2.7	0.3	24.434	2.28	4.65E+14

5.4.2.1.3 Nb/Al-1.0 wt.% Cu

5.4.2.1.3.1 Effect of Layer Thickness on Reaction Kinetics

A set of samples with the same periodicity as the Al-0.5 wt.% Cu, but containing layers of Al-1.0 wt.% Cu were also examined. The plots of XRD intensity versus 2θ and temperature for samples annealed at a constant heating rate of 180 °C/min are shown in Figure 5. 50. A 10 nm sample was also included in the analysis for this composition. Satellite reflections were present in the as-deposited 10 nm and 20 nm samples. Some satellites are visible in the lower left corner of the 10 nm peak. They disappeared upon heating at ~375 °C coinciding with the formation of the $NbAl_3$ (002) diffraction peak. In comparing this sample with the 10 nm sample without the Cu additions, similarities in the absence of the (101) peak and a significant decrease of the (002) peak width are evident. However, the Al-1.0 wt.% Cu sample initially began with a greater width and appeared to sharpen at a higher rate. Also, the peak intensity decreased abruptly at ~650 °C. The other samples yielded similar behavior to the Al-0.5 wt.% runs.

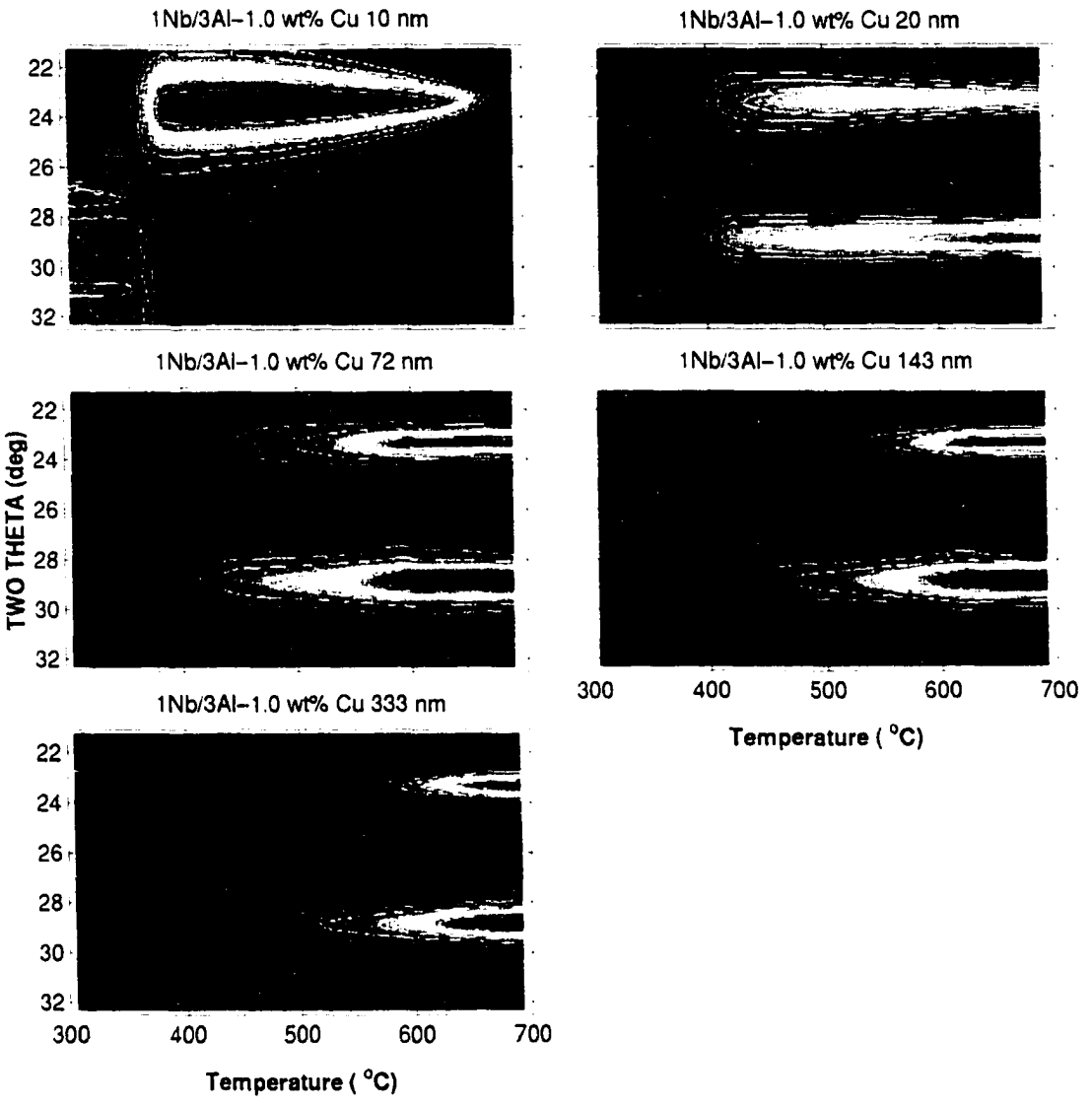

Figure 5. 50: XRD intensity as a function of 2θ and temperature for 1Nb/3Al-1.0 wt.% Cu multilayers with Λ ranging from 10 - 333 nm heated from 100 to 700 °C at 180 °C/min in purified He.

The peak widths of both the $NbAl_3$ (002) and (101) peaks of films with $\Lambda > 20$ nm did not decrease significantly with temperature. The appearance of the (002) reflection occurred at higher temperatures as Λ increased while the (101) reflection remained nearly constant in temperature. All samples exhibited peaks identified with the equilibrium $NbAl_3$ DO_{22} phase following the anneal.

The integrated intensities determined from the $NbAl_3$ (002) window are plotted as a function of temperature in Figure 5. 51. Two inflections were evident in curves with Λ > 20 nm. The inflections are most prominent in the Λ = 72 nm film.

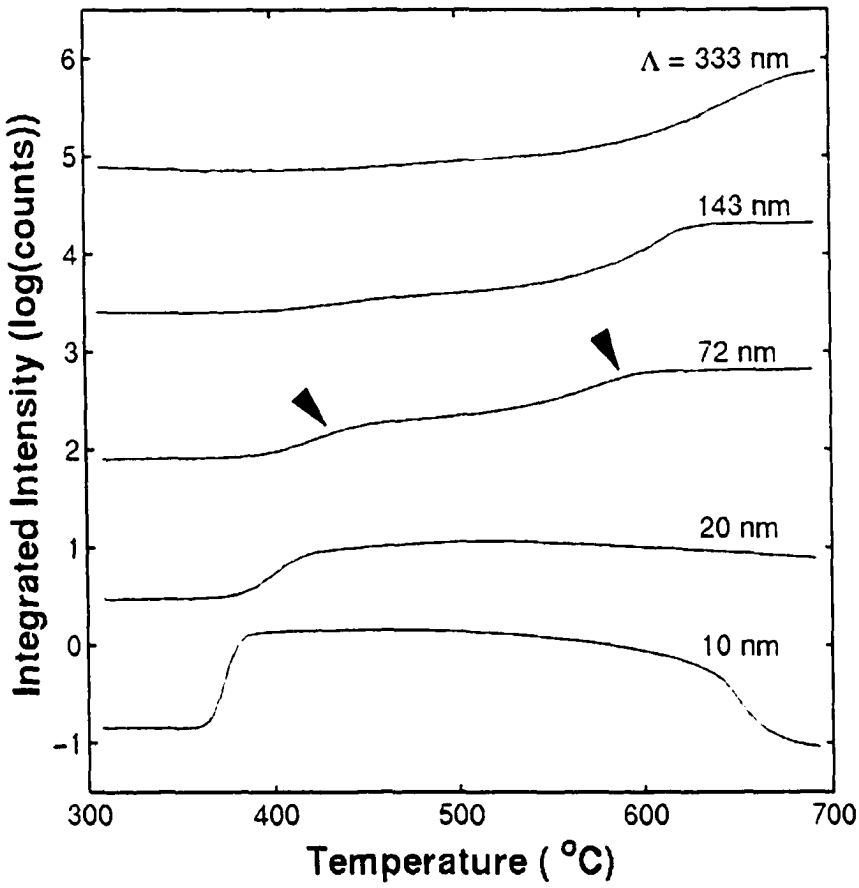

Figure 5. 51: Integrated XRD intensity as a function of temperature for the $NbAl_3$ (002) reflection in 1Nb/3Al-1 wt.% Cu multilayers.

The normalized first derivative of the integrated intensity is plotted as a function of temperature in Figure 5. 52.

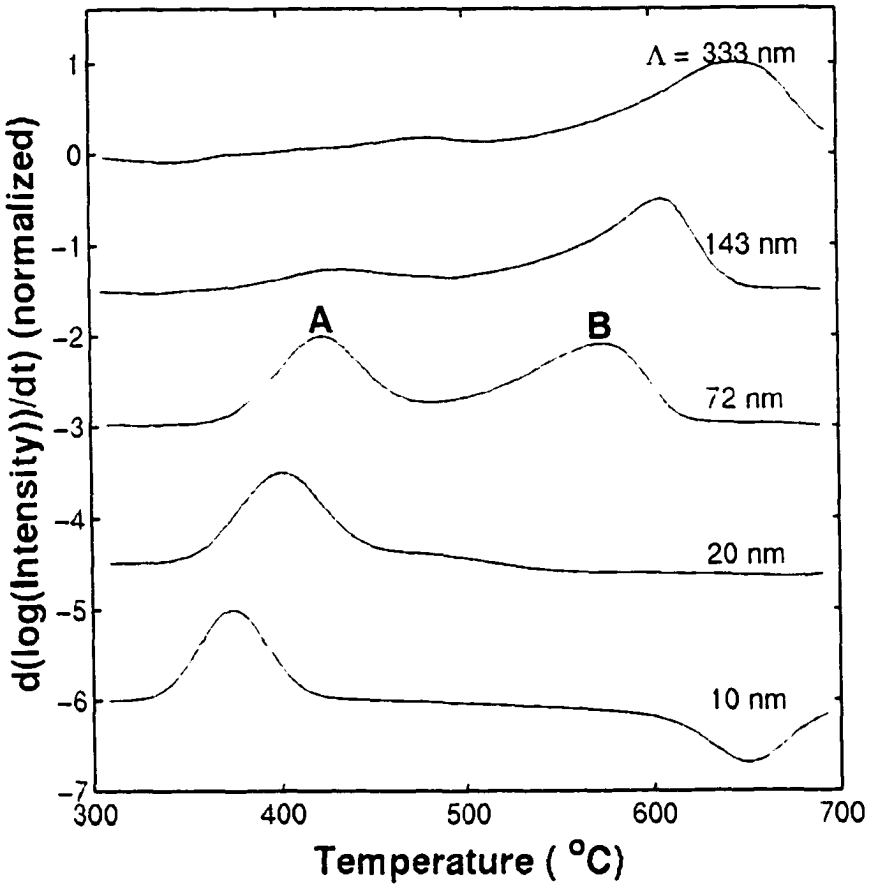

Figure 5. 52: Normalized first derivative of the integrated intensity of the $NbAl_3$ (002) peak as a function of temperature in 1Nb/3Al-1.0 wt.% Cu multilayers.

Two, separated peaks were observed for $\Lambda > 20$ nm, although a small shoulder was evident on the high temperature side of the 20 nm film. The first peak was again found symmetrical and bell-shaped. The second peak was asymmetric and increased in height relative to the first peak for a given period. Compared with the 0 wt.% Cu samples, the first peak for the 333 nm film was drawn out over a larger temperature range producing a less distinct shape. Note the negative peak in the 10 nm sample where the intensity decreased. A summary of the peak temperatures is provided in Table 5. XI.

Table 5. XI: XRD peak temperatures for $NbAl_3$ formation in 1Nb/3Al-1.0 wt.% Cu films annealed at a heating rate of 180 °C/min determined from the first derivative of the integrated intensity of the $NbAl_3$ (002) peak.

Sample ID	Λ [nm]	Peak A [°C]	Peak B [°C]
010499b	10	374	--
010699a	20	400.2	453.2
101698d	72	421.8	573.3
100798a	143	453.1	605.4
101298a	333	478.1	646.9

The integrated intensity of the $NbAl_3$ (101) peaks is shown in Figure 5. 53.

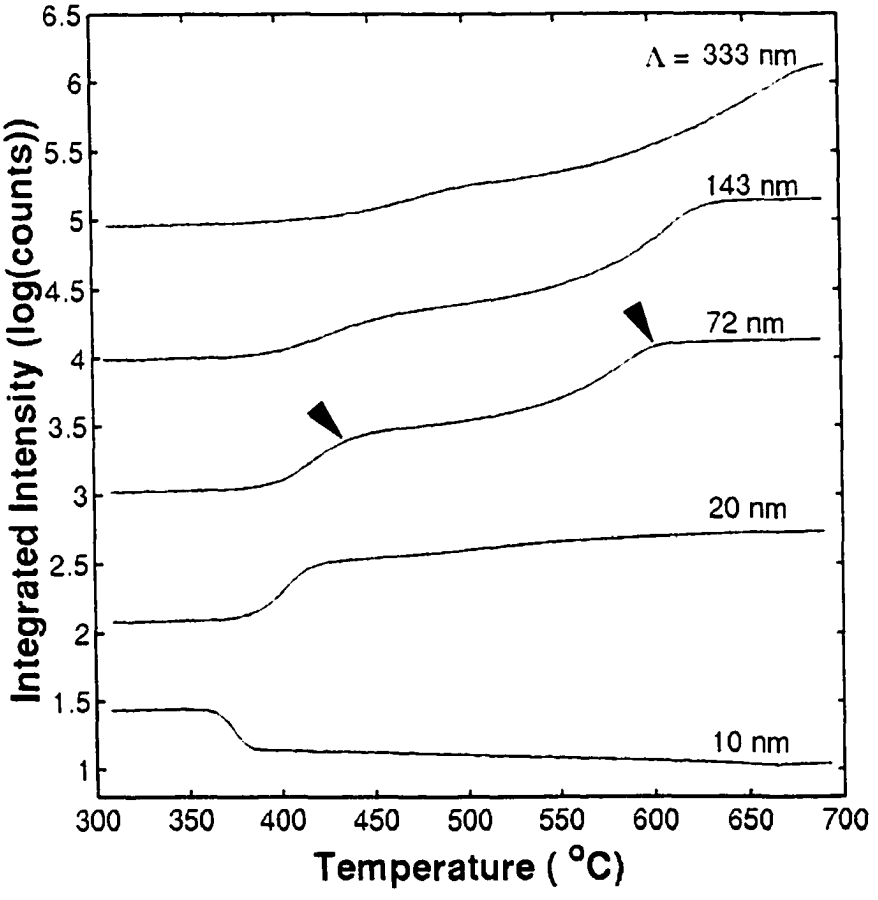

Figure 5. 53: Integrated intensity as a function of temperature for the $NbAl_3$ (101) peak in 1Nb/3Al-1.0 wt.% Cu multilayers.

The results essentially replicate the (002) peak data. The initial decrease observed in the 10 nm film resulted from the disappearance of intensity associated with the satellite reflections of the as-deposited films. The (101) intensity remained virtually absent for the remainder of the anneal.

The normalized first derivative was calculated from the smoothed integrated intensity data and is shown in Figure 5. 54. Consistent with earlier findings, the results produced two peaks of similar shapes and relative heights to the (002) data and previous results for the 1Nb/3Al multilayers.

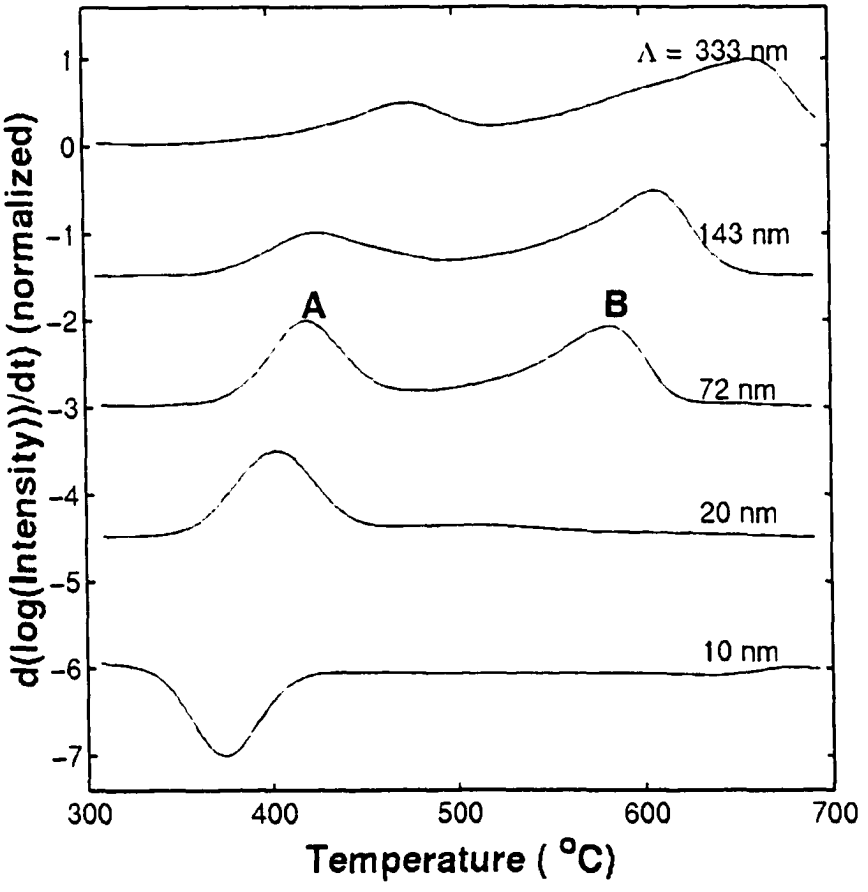

Figure 5. 54: Normalized first derivatives of the integrated XRD intensity of the $NbAl_3$ (101) reflection in 1Nb/3Al-1.0 wt.% Cu multilayers.

Peak temperatures determined from the derivative curves are listed in Table 5. XII.

Table 5. XII: XRD peak temperatures for $NbAl_3$ formation in 1Nb/3Al-1.0 wt.% Cu films annealed at a heating rate of 180 °C/min determined from the first derivative of the integrated intensity of the $NbAl_3$ (101) peak.

Sample ID	Λ [nm]	Peak A [°C]	Peak B [°C]
010499b	10	--	--
010699a	20	401.6	453.5
101698d	72	418.5	582.6
100798a	143	453.1	606.8
101298a	333	473.7	658.3

5.4.2.1.3.2 Activation Energy

Activation energies were determined for the two peaks in the (002) and (101) reflections using a 1Nb/3Al-1.0 wt.% Cu film annealed at four heating rates. The corresponding Kissinger plots are shown in Figure 5. 55.

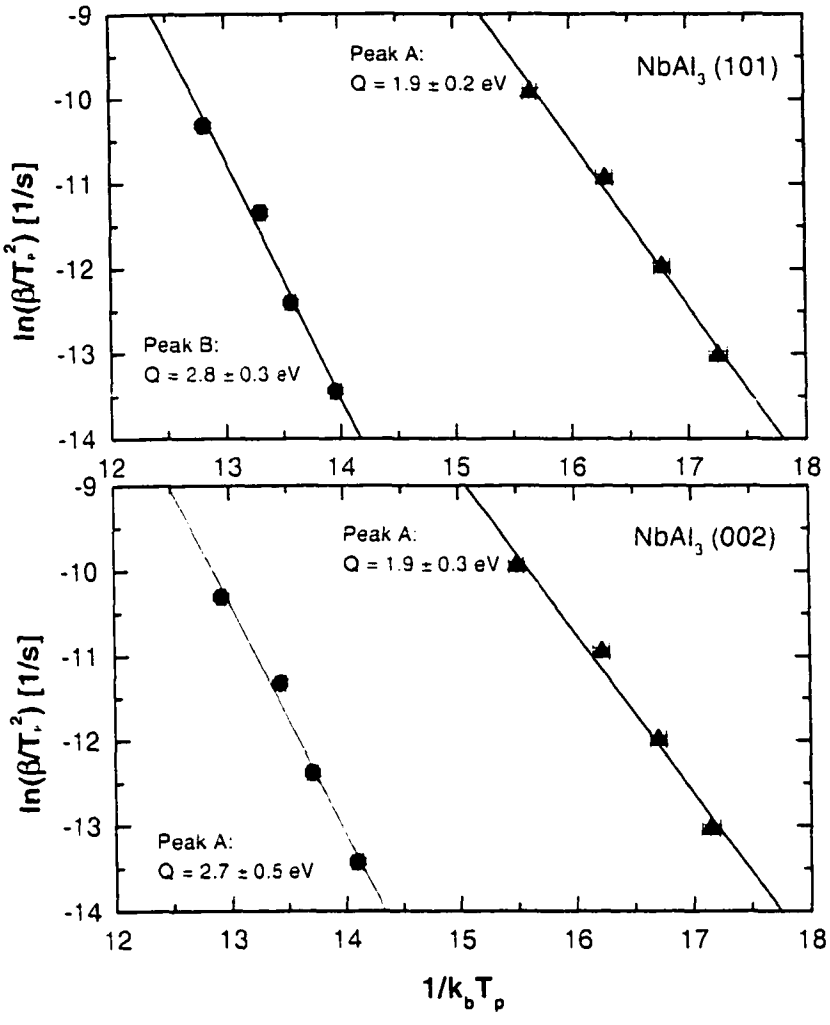

Figure 5. 55: Kissinger plots showing activation energies for peak A and B from a 1Nb/3Al-1 wt.% Cu. Λ = 72 nm multilayer thin-film.

Results yielded average values of ~2 eV and ~2.8 eV for peaks A and B, respectively. These values were consistent with the previous observations. A summary of the linear regression analysis used to calculate the activation energies for the two peaks is provided in Table 5. XIII.

Table 5. XIII: Results from the Kissinger analysis of XRD data for a 1Nb/3Al-1.0 wt.% Cu film with Λ = 72 nm.

1Nb/3Al- 1.0 wt.% Cu; Λ = 72 nm (101698d)					
Peak	Q [eV]	Error (98% conf.)	y-int. [$K^{-1}s^{-1}$]	Error (98% conf.)	Freq. Factor (v) [s^{-1}]
A (101)	1.9	0.2	20.60	3.58	1.98E+13
B (101)	2.8	0.3	25.57	6.2	4.12E+15
A (200)	1.9	0.3	19.20	5.52	4.72E+12
B (200)	2.7	0.5	24.69	6.26	1.65E+15

5.4.2.2 Discussion: Nb/Al

To assess the effect of bilayer thickness on the formation of $NbAl_3$ as monitored by *in situ* XRD, peak positions were plotted as a function of Al layer thickness/bilayer thickness as shown in Figure 5. 56. The Al layer thickness was chosen as the ordinate axis because of existing and new microstructural evidence that indicated enhanced growth of $NbAl_3$ along the Al grain boundaries that intersect the Nb/Al interface. Therefore, the available data suggests that the initial stages of phase formation may be in fact influenced primarily by the Al microstructure. This point will be discussed further in the next chapter. The results indicated a behavior similar to that observed in the DSC results in the current work and previously published work by Barmak et al. (1998). Both peaks A and B shifted to higher temperatures with increasing Al layer thickness. Peak A shifted gradually to higher temperatures from 7-100 nm and was nearly independent of temperature for $t_{Al} > 100$ nm. Peak B initially exhibited a more rapid increase in temperature with increasing Al thickness, however, as with Peak A, the rate decreased appreciably after $t_{Al} \sim 100$ nm. Both the $NbAl_3$ (101) and (002) diffraction peaks followed the same trend.

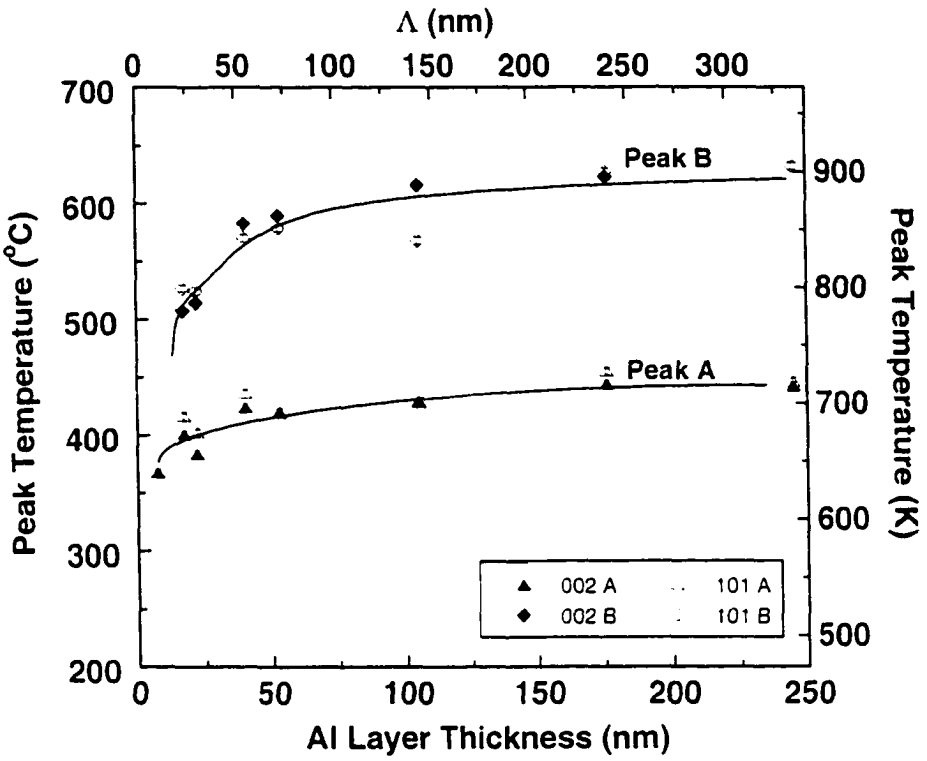

Figure 5. 56: Temperatures of peaks A and B as a function of Al layer thickness for 1Nb/3Al-0 wt.% Cu film annealed from 100 to 700 °C at 180 °C/min. Lines drawn to guide the eye.

Although not providing direct proof, these results were again consistent with the mechanism of phase formation proposed in Chapter 4. In this case, the temperature of peak A depended on the nucleation site density and was mediated by heterogeneities such as grain boundaries and grain boundary tri-junctions in the interface. The temperature of peak B was determined by the amount of reactants that were present in the as-deposited film. Peaks A and B would increase in temperature as the nucleation site density decreased, and the thickness of the reactants (Λ) increased.

A similar plot of peak temperature vs. Al layer thickness was constructed for the Al-0.5 wt.% Cu samples using the peak temperatures derived from the derivative XRD plots as shown in Figure 5. 57.

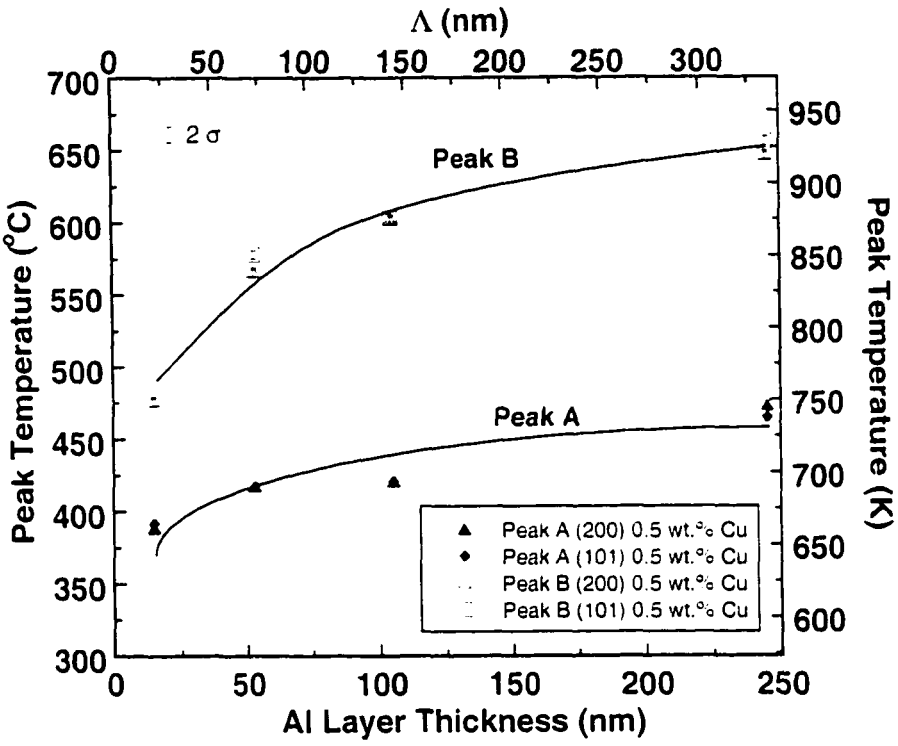

Figure 5. 57: Temperatures of peaks A and B as a function of Al layer thickness for 1Nb/3Al-0.5 wt.% Cu film annealed from 100 to 700 °C at 180 °C/min. Lines drawn to guide the eye.

The trend of increasing peak temperature with Al layer thickness still held for both peaks. The $NbAl_3$ (101) and (002) peaks showed nearly identical behavior.

The peak positions of the Al-1.0 wt.% Cu samples are shown as a function of temperature for the (101) and (002) reflections in Figure 5. 58. Again, similar trends were evident in the peak temperatures. These results paired with the previous set obtained from the 0.5 wt.% samples indicated that the presence of Cu does not strongly influence the peak temperatures associated with the formation of $NbAl_3$ from Nb/Al thin-films.

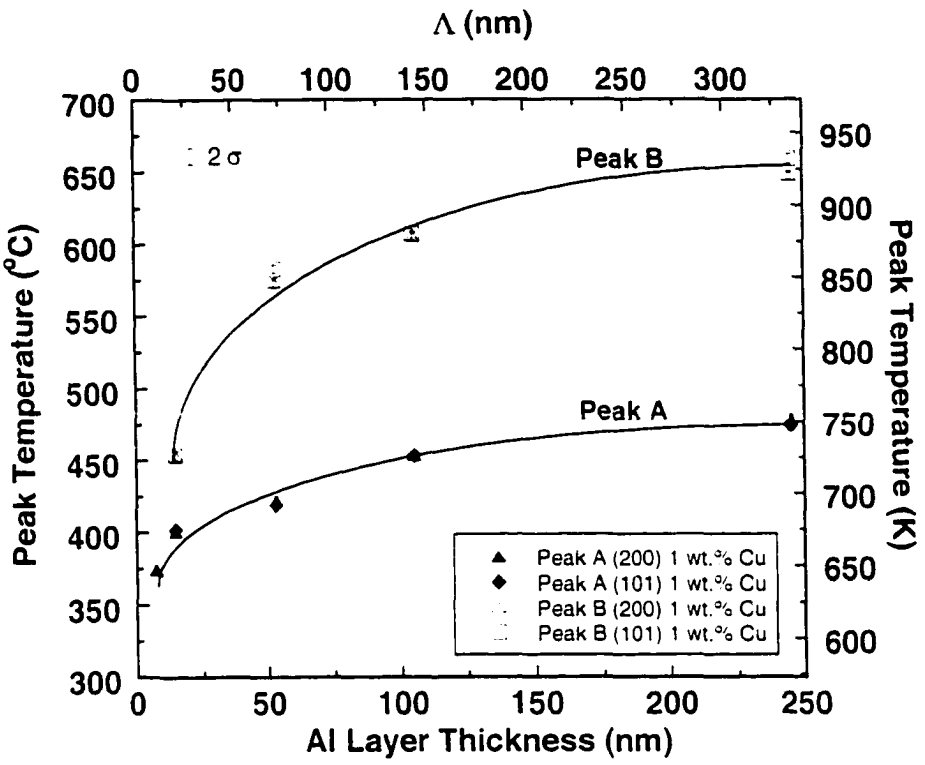

Figure 5. 58: Temperatures of peaks A and B as a function of Al layer thickness for 1Nb/3Al-1.0 wt.% Cu film annealed from 100 to 700 °C at 180 °C/min. Lines drawn to guide the eye.

To provide a clearer comparison of the samples with and without Cu, the peak temperature plots for the $NbAl_3$ (002) reflection were combined in Figure 5. 59. As described above, the plots essentially cover the same shift in temperature for both peak A and peak B. In addition, systematic changes in peak temperature were not evident for either peak.

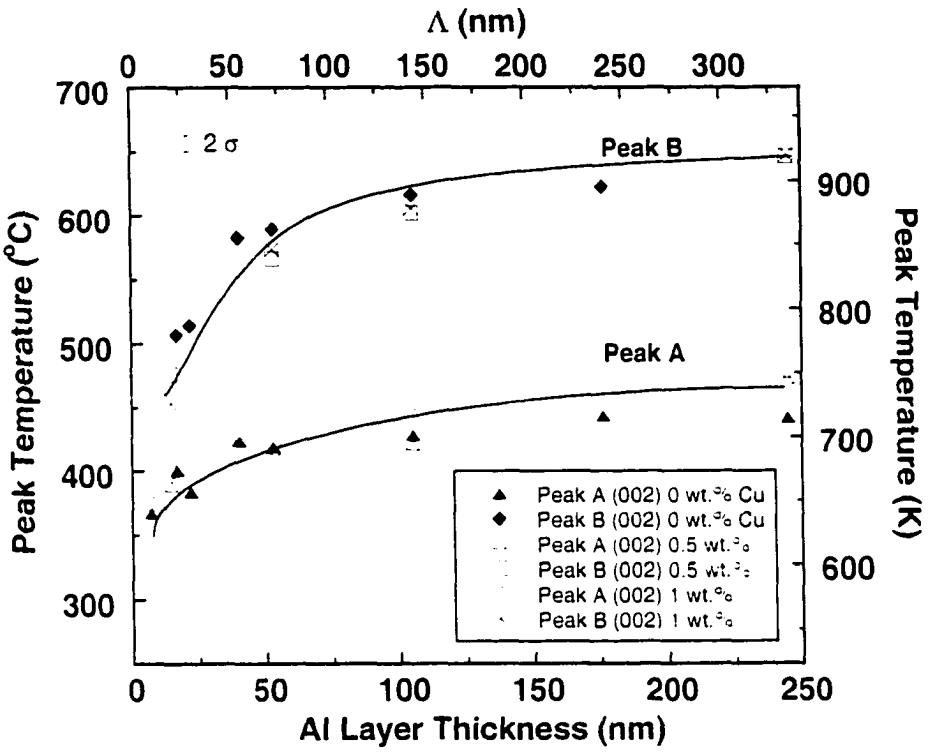

Figure 5. 59: Comparison of the temperatures of peaks A and B determined from the $NbAl_3$ (002) reflection as a function of Al layer thickness for 1Nb/3Al-0.0, 0.5, and 1.0 wt.% Cu films annealed from 100 to 700 °C at 180 °C/min. Lines drawn to guide the eye.

When the peak temperatures from the $NbAl_3$ (101) reflections of the different films were plotted, no systematic trends were evident with respect to the different Cu concentrations. An increase in temperature for peaks A and B for both the 0.5 and 1.0 wt.% Cu samples was observed for the sample with t_{Al} = 245 nm (Λ = 333 nm). These results are shown in Figure 5. 60.

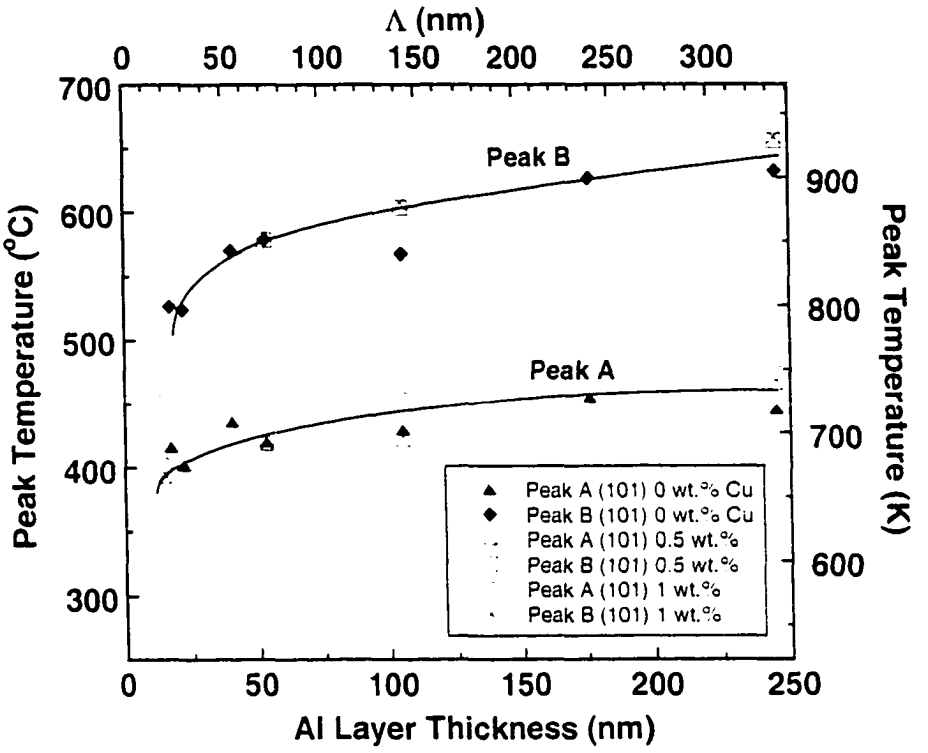

Figure 5. 60: Comparison of the temperatures of peaks A and B determined from the $NbAl_3$ (101) reflection as a function of Al layer thickness for 1Nb/3Al-0.0, 0.5, and 1.0 wt.% Cu films annealed from 100 to 700 °C at 180 °C/min. Lines drawn to guide the eye.

To assist in the assessment of the effects of Cu additions on the reaction, XRD intensities plotted as a function of 2θ and temperature were also compared for the different periodicities and Cu concentrations. Figure 5. 61 shows a series of plots for 1Nb/3Al films with Λ = 20 and 72 nm with 0, 0.5 and 1.0 wt.% Cu. Some trends were evident. Focusing first on the 20 nm samples, a distinct drop in intensity with increasing Cu concentration was noted. This was primarily due to the difference in total thickness for the samples 1 μm for 23 nm and 0.5 μm for the 20 nm samples with Al(Cu). The other main observations involved the position and shape of the diffraction peaks. The (002) peak initially formed with a broad high-angle shoulder. This was an indication of a small $NbAl_3$ grain size present during the early stages of compound formation.

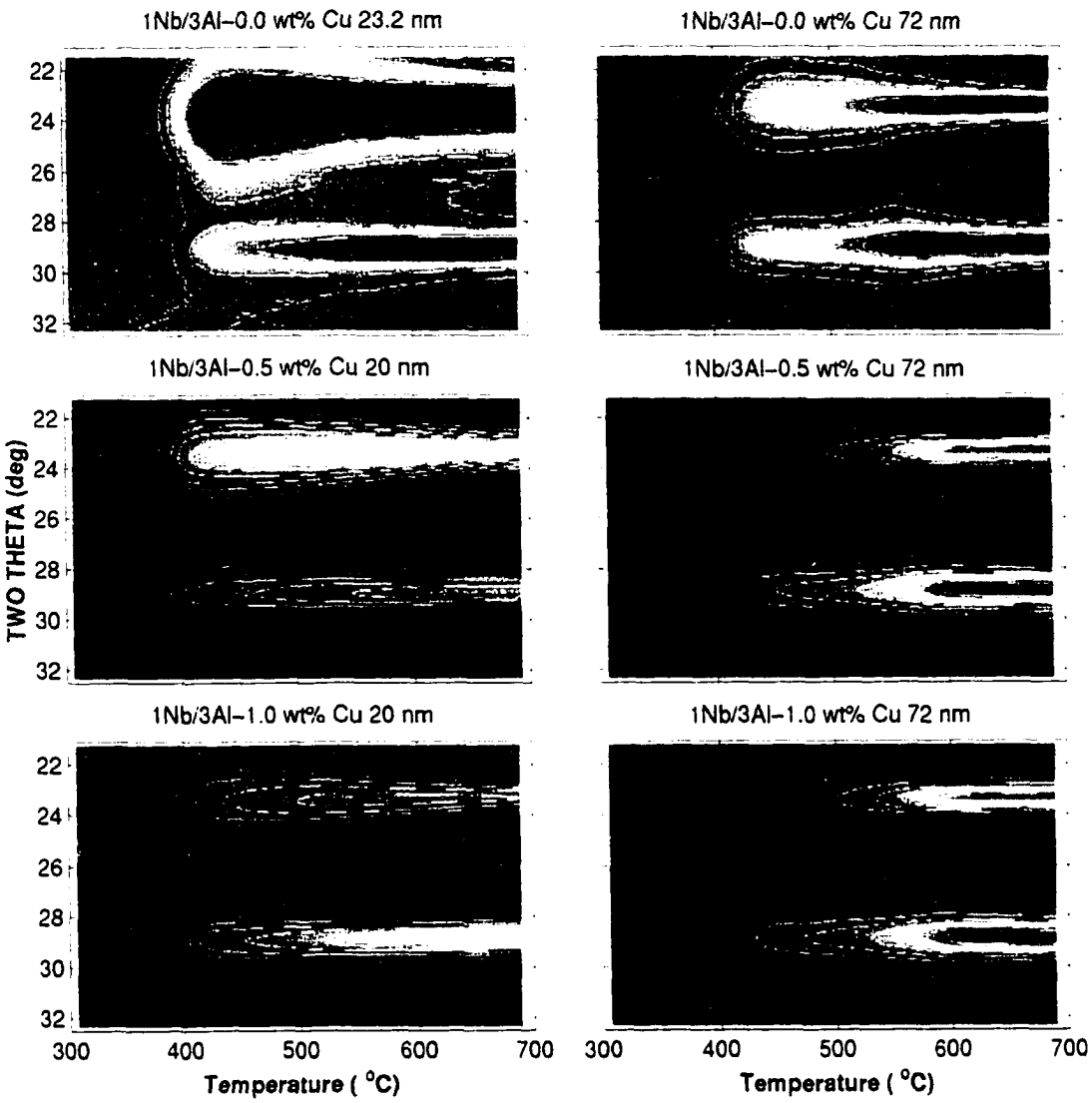

Figure 5. 61: XRD intensity as a function of 2θ and temperature comparing the effects of Cu on the formation of $NbAl_3$ for 1Nb/3Al multilayers with Λ = 20 and 72 nm.

The (002) peak also shifted towards slightly higher angles indicative of strain in the newly formed layer. Peak widths decreased as the sample was annealed indicating grain growth simultaneous with phase formation. The relative intensities of the (002) and (101) peaks also appeared to change for the different Cu concentrations. This could be a result of the effect of the as-deposited texture (strongest for the 0 wt.% Cu samples)

influencing the texture of the product phase. The (002) peak decreases in intensity relative to the (101) peak as the Cu concentration increased. Recall that the Al (111)/Nb(110) fiber texture also decreased substantially for the 20 nm 1Nb/3Al sample with pure Al layers as compared to Al-1.0 wt.% Cu multilayer film.

Examining the plots prepared from the Λ = 72 nm film revealed that the peak shift was not observed for any of the samples, although peak width did appear broader in the 0 wt.% Cu sample. The peak widths were again observed to decrease during annealing suggesting grain growth commensurate with phase formation. Although both the (101) and (002) peaks attained the same intensity levels at the end of the anneal (all samples were 1 μm thick), the 0 wt.% Cu samples appeared to reach the maximum ~50 °C lower in temperature than the samples containing Cu. This could be indicative of a reduction in reaction rate caused by the presence of Cu. Also, the (002) peak was observed to decrease slightly in intensity relative to the (101) peak in the samples containing Cu. From the available texture information, it would be expected that, as with the 23 nm sample, the multilayers without Cu would possess a higher degree of texture.

Figure 5. 62 compares slightly thicker films with Λ = 143 nm and 333 nm with different Cu concentrations. The 143 nm film with 0 wt.% Cu again exhibited a high-angle shoulder that shifted to lower angles as the sample was heated. The (002) peak was higher in intensity that the (101) peak for this sample and the width of both peaks decreased as the heating progressed, although this was more evident in the (002) reflection. Consistent with the 20 nm and 72 nm films, the intensity of the (002) and (101) peaks decreased with the addition of Cu to the Al layers with the (002) reflection becoming progressively weaker (all multilayers were 1 μm thick).

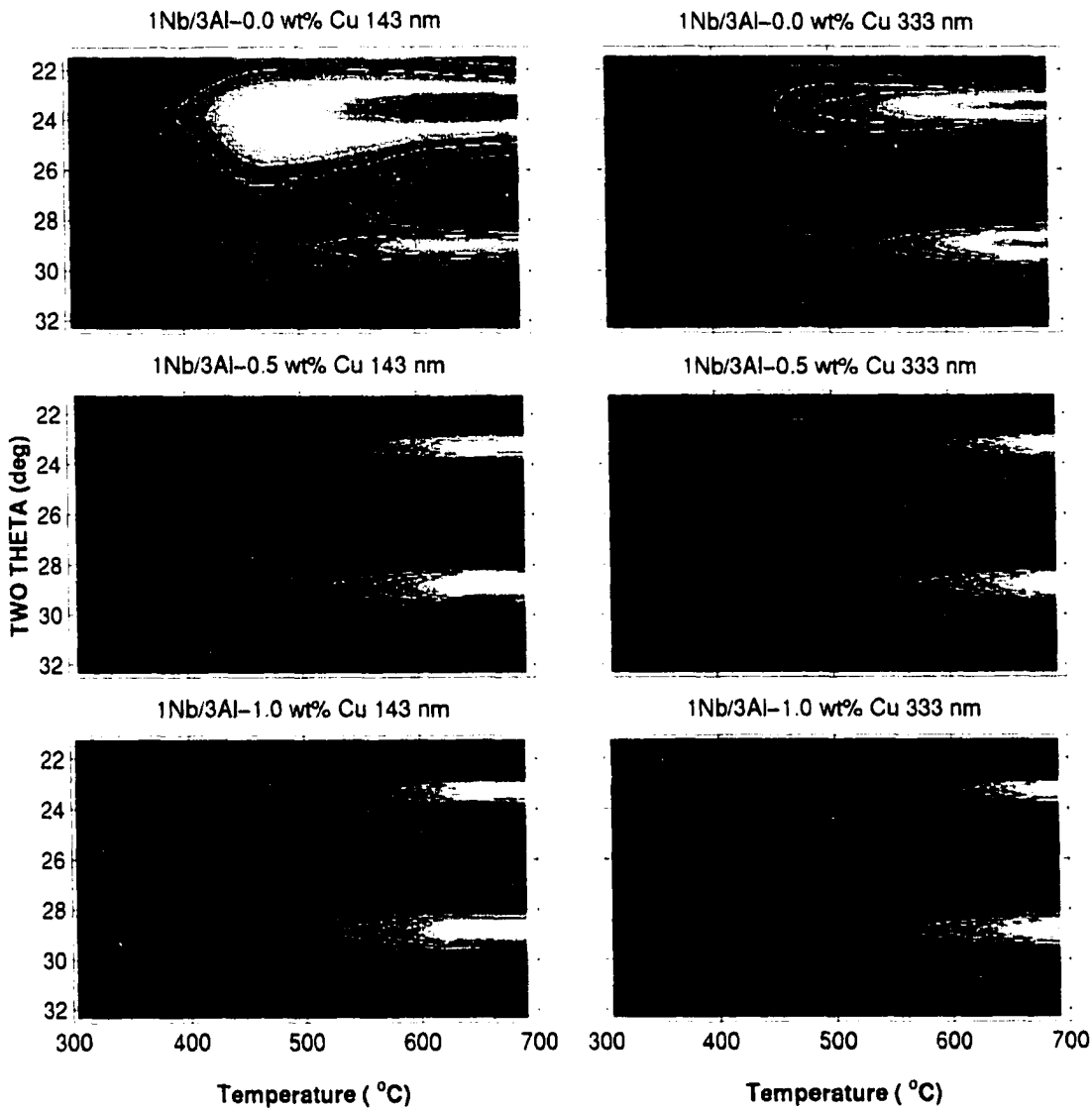

Figure 5. 62: XRD intensity as a function of 2θ and temperature comparing the effects of Cu on the formation of $NbAl_3$ for 1Nb/3Al multilayers with Λ = 143 and 333 nm.

The results from the 333 nm sample essentially duplicated the 143 nm findings. The 0 wt.% Cu sample does not exhibit a shoulder on the (002) peak, although the width of the peak was significantly larger than either the 0.5 or 1.0 wt.% Cu samples. The (002) and (101) peaks decreased in intensity with the addition of Cu and the maximum intensity seemed to have shifted to higher temperatures.

The interpretation of the *larger* width of the (002) peak in the samples *without* Cu was difficult to reconcile with the proposed mechanism of phase formation. A smaller initial grain size of $NbAl_3$ would indicate a higher density of nucleation sites or a higher nucleation rate. The former explanation appeared unlikely, however, since the addition of Cu was observed to lower the grain size of the as-deposited films (shown in the next chapter). A smaller as-deposited grain size would produce more tri-junctions and thus, more potential nucleation sites. This should result in a smaller coalesced grain size of the $NbAl_3$ and a broadened XRD peak in the samples containing Cu as compared to the samples without Cu. A decrease in the peak width during annealing was evident for the $\Lambda = 20$ samples with and without Cu. In the thicker samples, the diffraction peaks of the Al(Cu) multilayers *did not* exhibit narrowing associated with grain growth. Therefore, the evidence suggests that the initial grain size of the $NbAl_3$ layer was relatively independent of the as-deposited grain size for the thinner bilayer periods. However, for the thicker films, the nucleation site density of the $NbAl_3$ phase could have been reduced by the presence of Cu. This would have resulted in a larger coalesced grain size that possesses a smaller driving force for further growth. The diffracted peak width would then be constant with annealing temperature. Quantification of the peak widths and corresponding microstructural observations would be necessary to clarify this point.

A comparison was made between the activation energies determined by the *in situ* XRD experiments and those determined by DSC for peaks A and B. As can be seen from Table 5. XIV, excellent agreement was found between the two techniques.

Table 5. XIV: Comparison of activation energies for $NbAl_3$ formation from *in situ* XRD measurements and DSC experiments calculated using the Kissinger approach. For the XRD measurements, the top value is from the (101) peaks and the bottom value is from the (002) peaks. All measurements were taken from samples with Λ = 72 nm except where noted.

Cu conc.	XRD		DSC	
[wt.%]	Peak A [eV]	Peak B [eV]	Peak A [eV]	Peak B [eV]
0	1.7 ± 0.2 1.5 ± 0.3	2.5 ± 0.3 2.6 ± 0.3	1.7 ± 0.1 (Λ = 23 nm)	2.1 ± 0.2 (Λ = 23 nm)
0.5	1.8 ± 0.2 1.8 ± 0.2	2.9 ± 0.4 2.7 ± 0.3	1.9 ± 0.1	2.6 ± 0.2
1.0	1.9 ± 0.2 1.9 ± 0.3	2.8 ± 0.3 2.7 ± 0.5	1.9 ± 0.1	2.5 ± 0.1

Figure 5. 63 shows the activation energies determined from the (101) XRD data for a 1Nb/3Al multilayer with Λ = 72 nm plotted as a function of Cu concentration. As with the DSC results, no significant change in the activation energy was observed for peak A or B as Cu was added to the Al layers.

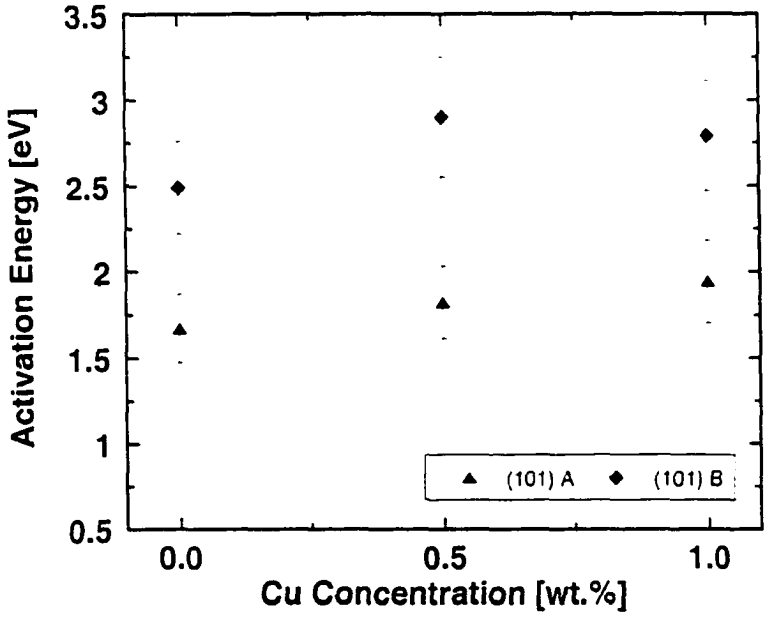

Figure 5. 63: Activation energies for peaks A and B of $NbAl_3$ formation determined from the $NbAl_3$ (101) reflections plotted as a function of Cu concentration for a Λ = 72 nm film.

A similar result was found for the (002) XRD peaks. Figure 5. 64 shows the activation energies determined from a series of 1Nb/3Al multilayers with Λ = 72 nm having 0.5 and 1.0 wt.% Cu in the Al. The activation energies again appeared similar within experimental error.

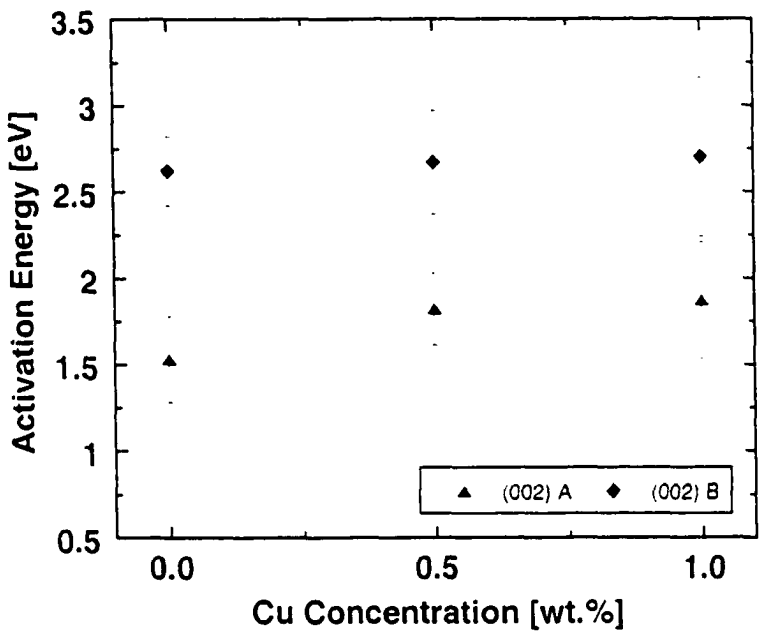

Figure 5. 64: Activation energies for peaks A and B of $NbAl_3$ formation determined from the $NbAl_3$ (002) reflections plotted as a function of Cu concentration for a Λ = 72 nm film.

In summary, results from *in situ* XRD experiments conducted at a constant heating rate provided quantitative information regarding the kinetics of $NbAl_3$ formation. In addition, some insight was gained into effects of as-deposited microstructure and the presence of Cu in solution on the microstructure of $NbAl_3$. When the XRD peak temperatures were plotted versus Al layer thickness, a trend similar to that first reported in DSC studies of Nb/Al multilayers was observed. Examination of the diffracted XRD intensities also revealed that the as-deposited texture might influence the texture of the $NbAl_3$. The *in situ* XRD contour plots brought to light interesting differences in the

microstructure of the reacted layer depending on initial bilayer thickness and Cu concentration. Finally, activation energies determined by applying the Kissinger analysis were found to be comparable to those found by the DSC experiments (~1.8 eV for peak A and 2.5 eV for peak B) and did not show a strong dependence on Cu concentration for the bilayer period and compositions investigated.

5.4.2.3 Ti/Al and Ti/Al(Cu)

The reaction of the Ti/Al and Ti/Al(Cu) films was more complex than Nb/Al. This was evident in a three-dimensional plot of XRD intensity vs. two theta and temperature for a 1Ti/3Al, Λ =72 nm sample annealed at 180 °C/min shown in Figure 5. 65.

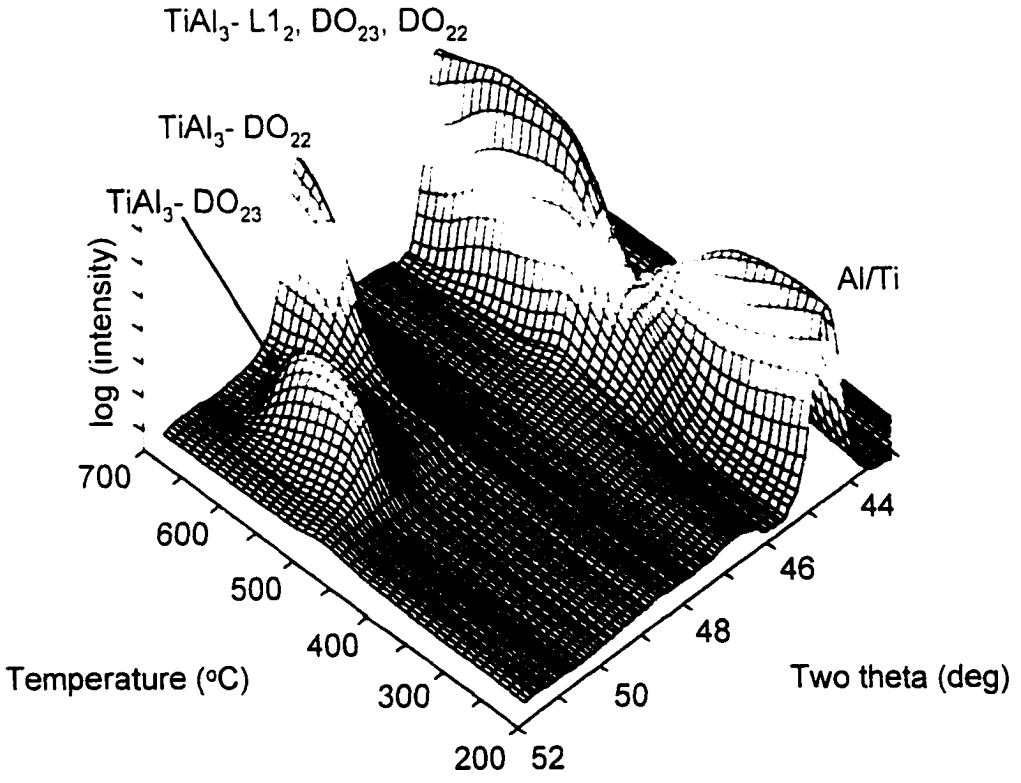

Figure 5. 65: Three-dimensional plot of XRD intensity plotted as a function of temperature and 2θ for a 1Ti/3Al, Λ = 72 nm multilayer film annealed at 180 °C/min from 100 °C to 700 °C.

A two-dimensional contour plot of XRD intensity versus 2θ and temperature for a 1Ti/3Al, Λ = 72 nm multilayer annealed at 180 °C/min is shown in Figure 5. 66. Scans were typically conducted with the sample tilted away from the exact Bragg condition in order to reduce the intensity of the Al(111)/Ti (0002) peak and increase sensitivity to the product phase peaks. For the majority of the results θ was set to 35° while 2θ was set at 47°. The resulting angular window included the elemental Al (111) and Ti (0002) reflections as well as peaks attributed to two metastable superlattice structures of $TiAl_3$ and the equilibrium $TiAl_3$ structure (Table 5. XV).

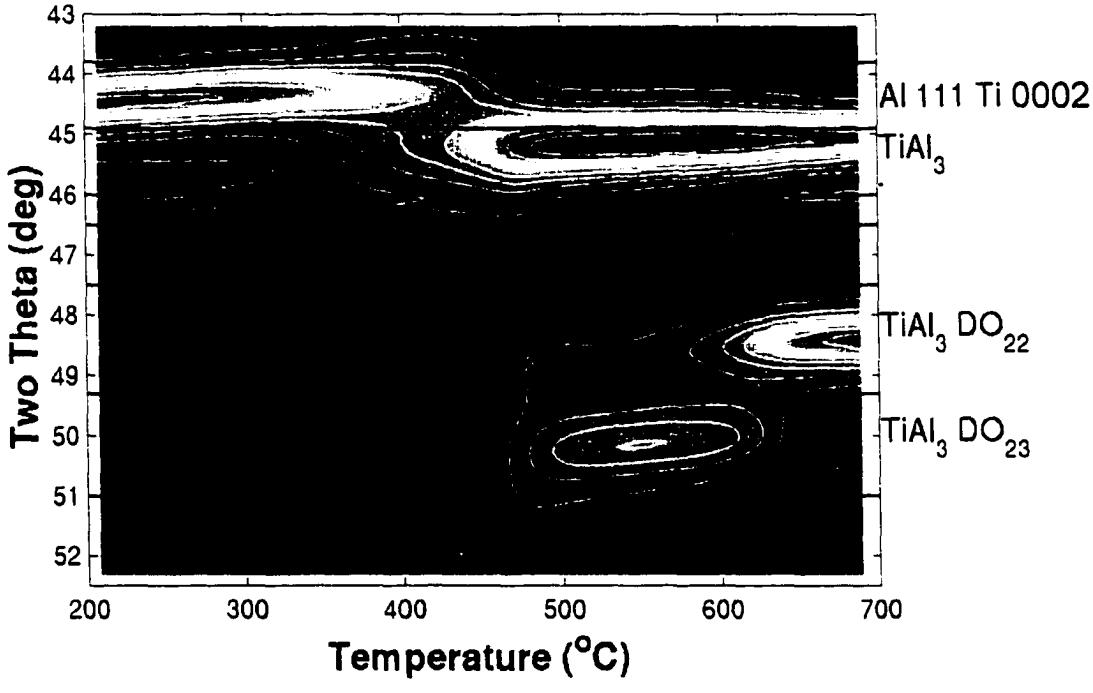

Figure 5. 66: XRD intensity as a function of 2θ and temperature for a 1Ti/3Al, Λ = 72 nm multilayer thin-film annealed at 180 °C/min to 700 °C showing the ranges used for the four windows.

Table 5. XV: Selected 2θ ranges used to monitor XRD peaks during formation of $TiAl_3$.

Peak(s)	2θ range [deg]
Al (111) Ti (0002)	43.8 – 44.9
$TiAl_3$-$L1_2$ (111) ≤ ~450 °C $TiAl_3$-DO_{23} (114) ≥ ~450 °C Ti_9Al_{23} (118) ≥ ~450 °C $TiAl_3$-DO_{22} (112/103) ≥ ~450 °C	44.9 – 46.0
$TiAl_3$-DO_{23} (008) Ti_9Al_{23} (0 0 16)	49.3 – 51.0
$TiAl_3$-DO_{22} (004)	47.5 – 49.3

Several prominent features were evident in the *in situ* XRD data of the Ti/Al reaction. First a peak appeared at 2θ = ~45.5° at temperatures of 350 – 400 °C, as the temperature increased a second peak became evident at 2θ = ~50°. This peak subsequently diminished in intensity while a third peak grew in intensity at 2θ = ~ 48°. As mentioned earlier, the formation of metastable superlattice structures of $TiAl_3$ have been reported to precede the equilibrium structure. In order to identify the peaks in the window selected for the ramped heating experiments, a series of *ex situ* θ-2θ scans were performed at the beamline. A series of 72 nm samples were heated at 180 °C/min to different temperatures and quenched to room temperature. A θ-2θ scan was then acquired from 20 to 60°. The angular range was limited by physical constraints imposed by the XRD apparatus (water lines, cables, etc.). The results for the as-deposited film and five anneal temperatures are plotted in Figure 5. 67.

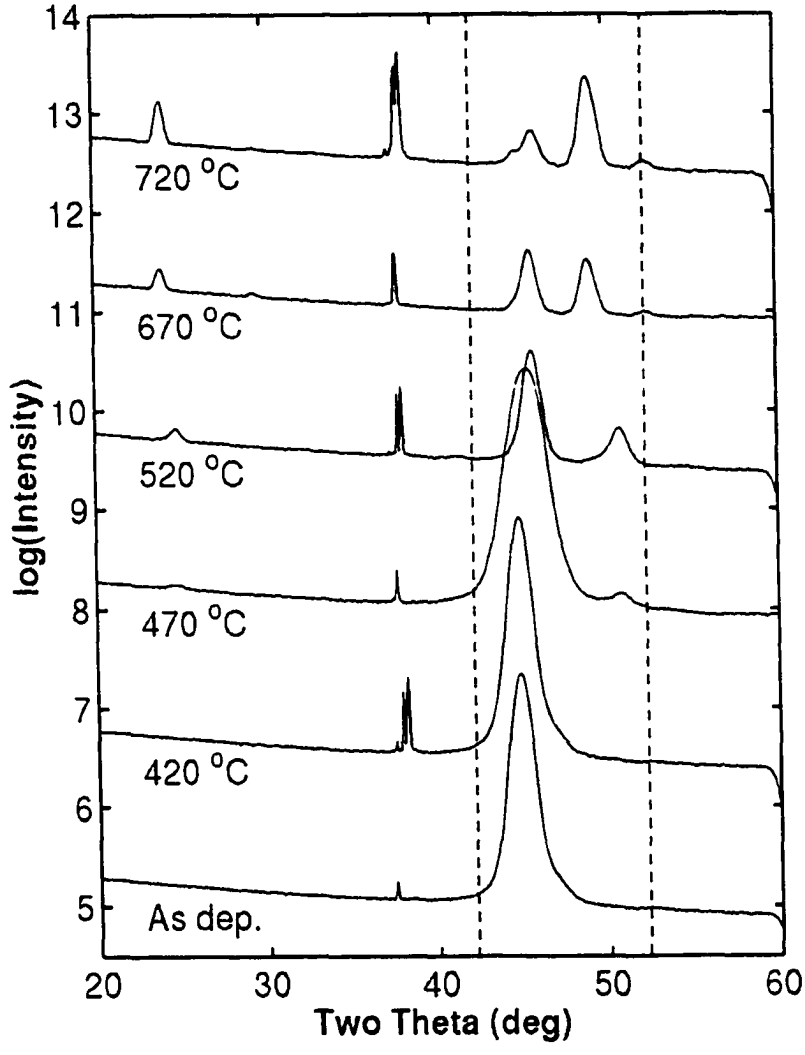

Figure 5. 67: Series of *ex-situ* θ–2θ XRD scans of a 1Ti/3Al, Λ = 72 nm multilayer thin-film annealed to the indicated temperature at 180 °C/min and quenched. The sharp peak at 2θ = 38° is from the Si substrate. The dashed lines indicate the approximate window selected for the *in situ* measurements with λ = 0.1797 nm. Note the logarithmic scale for the diffracted intensity.

In the as-deposited film, a single strong peak was visible and attributed to the Al (111)/Ti (0002) planes. A second, less intense peak at ~53° was indexed as Al (200). The absence of the other peaks of Al and Ti agreed with the previous texture measurements and TEM investigations that indicated the presence of fiber texture in these samples. At 400 °C the peak at ~45° shifted slightly towards a higher angle. No

other peaks were evident in the scan, however, *ex situ* TEM investigations of planview samples annealed to 420 °C have indicated that the cubic, $L1_2$ superlattice structure of $TiAl_3$ began to form at this temperature. As mentioned in the background section, this phase has been observed to form coherently with the Ti and Al layers (see Figure 5. 12) and does not result in the formation of additional peaks. The sheet resistance (not shown) also began to increase rapidly at this temperature, another indication of intermetallic phase formation.

At 470 °C, the primary peak at ~ 45° has shifted to higher angles and has broadened. Also visible are a small peaks identified with the high temperature superlattice structures of $TiAl_3$. Due to the multiple overlapping reflections and the absence of additional peaks, a unique identification was not possible. Some $L1_2$-$TiAl_3$ may also remain at this temperature and may be contributing to the intensity of the primary diffraction peak.

Annealing to 520 °C placed the sample in the middle of the diffraction peak in the *in situ* scan associated with the high temperature superlattice phase of $TiAl_3$. The large central peak in the *ex situ* trace has decreased substantially in height and the superlattice reflections at ~25° and 51° have increased in intensity. This could indicate a loss of fiber texture in the product phase or the dissolution of the $L1_2$-$TiAl_3$ structure.

After annealing the sample to 670 °C, the superlattice peak at 51° had disappeared. Several new peaks at 24°, 29°, and 49° appeared and were indexed as the equilibrium tetragonal DO_{22} structure of $TiAl_3$. A faint peak at ~52° also appeared. This was presumably due to recrystallized excess Al that had melted during heating.

At 720 °C, the peaks for the DO_{22} phase have grown in intensity, again signifying possible loss of texture or additional transformation of unreacted areas of film. A small peak was visible on the low angle side of the (112)/(103) peak of $TiAl_3$. This peak was at the position of the original Al (111)/Ti (0002) peak and is believed to have resulted from further recrystallization/grain growth of the unconsumed Al. The diffraction peaks identified from the series of θ-2θ scans are listed in Table 5. XVI.

The probable identities of the diffraction peaks were determined from the *ex situ* results. Although, unique indexing of the peaks from the metastable superlattice structure was not possible in all cases, the results from previous work were consistent with the possible identities of the phases.

Table 5. XVI: Summary of the XRD peaks identified in *ex situ* θ-2θ scans of a 1Ti/3Al, Λ = 72 nm film annealed at 180°C/min to the indicated temperatures.

Measured Angle	Identity	2θ [deg]	Reference
As-Deposited			
44.8	Al (111)	45.201	JCPDS: 04-0787
	Ti (0002)	45.140	JCPDS: 44-1294
~53.0	Al (200)	52.709	JCPDS: 04-0787
420 °C @ 180 °C/min			
44.9	Al (111)	45.201	JCPDS: 04-0787
	Ti (0002)	45.140	JCPDS: 44-12940
	$TiAl_3$ $L1_2$ (111)	~46.1	Hong et al. 1988, Srinivasan et al. 1991
~53.0	Al (200)	52.709	JCPDS: 04-0787
470 °C @ 180 °C/min			
24.7	$TiAl_3$-DO_{23} (004)	24.7	Srinivasan et al. 1991
	Ti_8Al_{24}-(008)	24.527	JCPDS: 26-0038
	Ti_9Al_{23}-(008)	24.705	JCPDS: 18-0069
45.4	$TiAl_3$ $L1_2$ (111)	~46.1	Hong et al. 1988, Srinivasan et al. 1991
	$TiAl_3$-DO_{23}-(114)	45.9	Srinivasan et al. 1991
	Ti_8Al_{24}-(118)	45.969	JCPDS: 26-0038
50.8	$TiAl_3$ DO_{23}-(008)	50.6	Srinivasan et al. 1991
	Ti_9Al_{23}-(0 0 16)	50.871	JCPDS: 18-0069
520 °C @ 180 °C/min			
24.6	$TiAl_3$-DO_{23} (004)	24.7	Srinivasan et al. 1991
	Ti_8Al_{24}-(008)	24.527	JCPDS: 26-0038
	Ti_9Al_{23}-(008)	24.705	JCPDS: 18-0069
41.5	$TiAl_3$-DO_{23} (105)	41.4	Srinivasan et al. 1991
	Ti_9Al_{23} (114)	40.994	JCPDS: 18-0069
45.7	$TiAl_3$-DO_{23}-(114)	45.9	Srinivasan et al. 1991
	Ti_8Al_{24}-(118)	45.959	JCPDS: 26-0038
50.8	$TiAl_3$ DO_{23}-(008)	50.6	Srinivasan et al. 1991
	Ti_9Al_{23}-(0 0 16)	50.871	JCPDS: 18-0069
670 °C @ 180 °C/min			
23.8	$TiAl_3$-DO_{22} (002)	24.179	JCPDS: 37-1449
29.5	$TiAl_3$-DO_{22} (101)	29.621	JCPDS: 37-1449
45.7	Al (111)	46.201	JCPDS: 04-0787
	$TiAl_3$-DO_{22} (112)/(103)	45.964	JCPDS: 37-1449
49.0	$TiAl_3$-DO_{22} (004)	49.503	JCPDS: 37-1449
52.4	Al (200)	52.709	JCPDS: 04-0787
720 °C @ 180 °C/min			
23.9	$TiAl_3$-DO_{22} (002)	24.179	JCPDS: 37-1449
29.3	$TiAl_3$-DO_{22} (101)	29.621	JCPDS: 37-1449
38.3	$TiAl_3$-DO_{22} (110)	38.504	JCPDS: 37-1449
~44.9	Al (111)	45.201	JCPDS: 04-0787
45.9	$TiAl_3$-DO_{22} (112)/(103)	45.964	JCPDS: 37-1449
49.1	$TiAl_3$-DO_{22} (004)	49.503	JCPDS: 37-1449
52.2	Al (200) 52.709	52.709	JCPDS: 04-0787

5.4.2.3.1 Ti/Al-0 wt.% Cu

5.4.2.3.1.1 Effect of Layer Thickness on Reaction Kinetics

A series of 1Ti/3Al multilayer films with various Λ were annealed at 180 °C/min in purified He while XRD data was acquired. The results from this experiment are shown in Figure 5. 68. Beginning with a description of the 10 nm film, the XRD results indicated the formation of a peak at $2\theta = 45^{o}$ beginning at ~ 300 °C, while the elemental Al and Ti peak simultaneously disappeared (the faint peak in the lower left corner of the plot was due to the Al (200) reflection that also disappears). This was indicative of compound formation. At such low temperatures, it seemed likely that the new peak was due to the formation biaxially strained layer of $L1_2$ $TiAl_3$. This strain was approximated by a simple calculation. For the observed angle, the lattice spacing of the $L1_2$ (111) plane would be ~2.35 Å. The resulting lattice parameter was ~4.07 Å, which was slightly larger than the experimentally determined value of 3.92 Å. This would produce a compressive strain in the $TiAl_3$ layer of ~4%. This could be due to thermal expansion differences between the film and substrate. The peak position did not shift appreciably with further annealing until ~475 °C, where another peak appeared at a slightly higher angle.

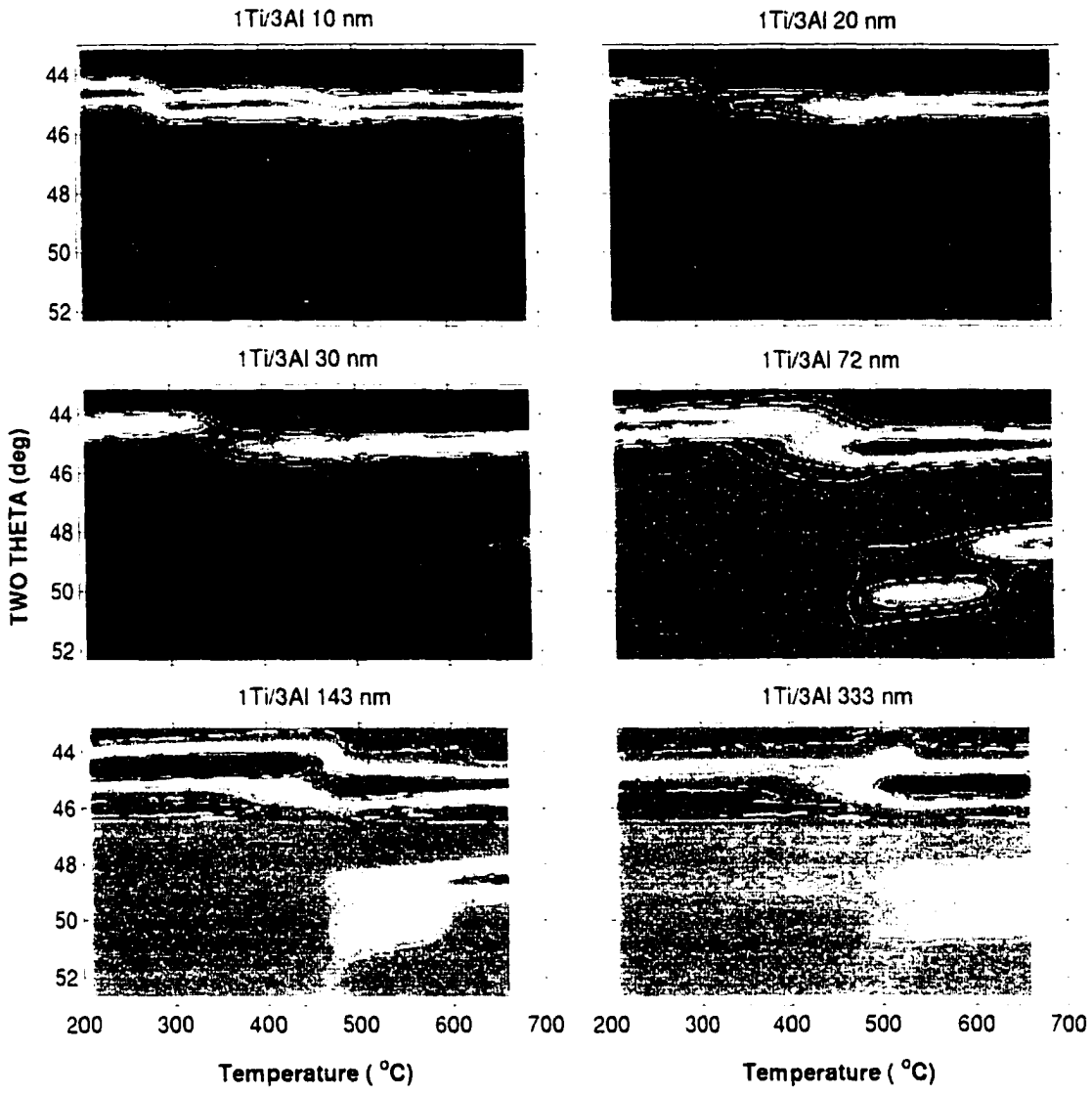

Figure 5. 68: XRD intensity as a function of 2θ and temperature for 1Ti/3Al multilayers with Λ ranging from 10 to 333 nm heated from 100 °C to 700 °C at 180 °C/min.

Simultaneously, a third peak evolved at ~51 °C (faint on this plot). These peaks were believed to correspond to the formation of the high temperature metastable superlattice phase. As mentioned previously, the peaks at ~45 and 51° can be attributed to the DO_{23} structure of $TiAl_3$ observed by Michaelsen et al. (1996) and Srinivasan et al. (1991). However, the peak at ~44° most closely matches the (1 0 11) peak in the Ti_9Al_{23}

phase first reported by Raman and Schubert (1965) and later observed by Rodbell et al. 1991 and Rodbell (1992) in thin-film reactions. The peaks at 44° and 51° disappear upon further annealing at ~650 °C. At this point in the reaction, a fifth peak was observed at ~49° and attributed to the (004) reflection of equilibrium DO_{22} structure of the $TiAl_3$ phase as expected from multilayer stoichiometry and confirmed by the *ex situ* XRD measurements. Some narrowing of the intense peak at ~45° was evident at temperatures above ~500 °C indicative of product phase grain growth.

For the films with larger periodicities, similar peaks attributable to the metastable and equilibrium phases discussed above were visible. Several trends were noted in the formation of these phases. First, the temperature of the appearance of the first $TiAl_3$ peak at ~45° and the disappearance of the Al and Ti peak occurred at successively higher temperatures. The tetragonal, metastable phase peak present at 44° diminished in relative intensity and was not visible in samples with Λ > ~30 nm. Conversely, the peak at 51° increased in relative intensity as Λ increased. This peak remained constant in temperature as the layer thickness increased. However, the peak at ~49° attributed to the equilibrium structure decreased in formation temperature with increasing periodicity. For the samples with Λ = 143 nm and 333 nm, the formation of the metastable tetragonal form of $TiAl_3$ and the equilibrium structure appeared simultaneously. Due to the strong fiber texture in the 333 nm sample, the Al (111)/Ti (0002) intensity was reduced considerably by tilting further away from the Bragg condition, and therefore does not appear in this plot. Recall from the pole plots and rocking curve data that this sample, in fact, had the highest degree of texturing of the Ti/Al multilayers investigated.

Applying the same methodology used to interpret the XRD results of the Nb/Al multilayers, the integrated intensities were determined from the different X-ray windows. Figure 5. 69 shows the intensities obtained from the window monitoring the Al (111) and Ti (0002) peak. In the films with $\Lambda < 30$ nm three distinct drops were evident in the integrated intensity plots: the first occurred between 300-400 °C, the second occurred between 400 and 500 °C, and the third drop was observed at ~650 °C. For the films with $\Lambda > 72$ nm one drop in intensity was observed. The apparent *increase* in integrated intensity for the 333 nm film resulted from the lower intensity (absence) of the Al (111)/Ti (0002) peak followed by the appearance of the intermetallic peak with a higher intensity. The window for the elemental Al/Ti peak overlapped a portion of the intermetallic peak causing an increase in the integrated intensity. This was an artifact due to the diffraction conditions and window positions.

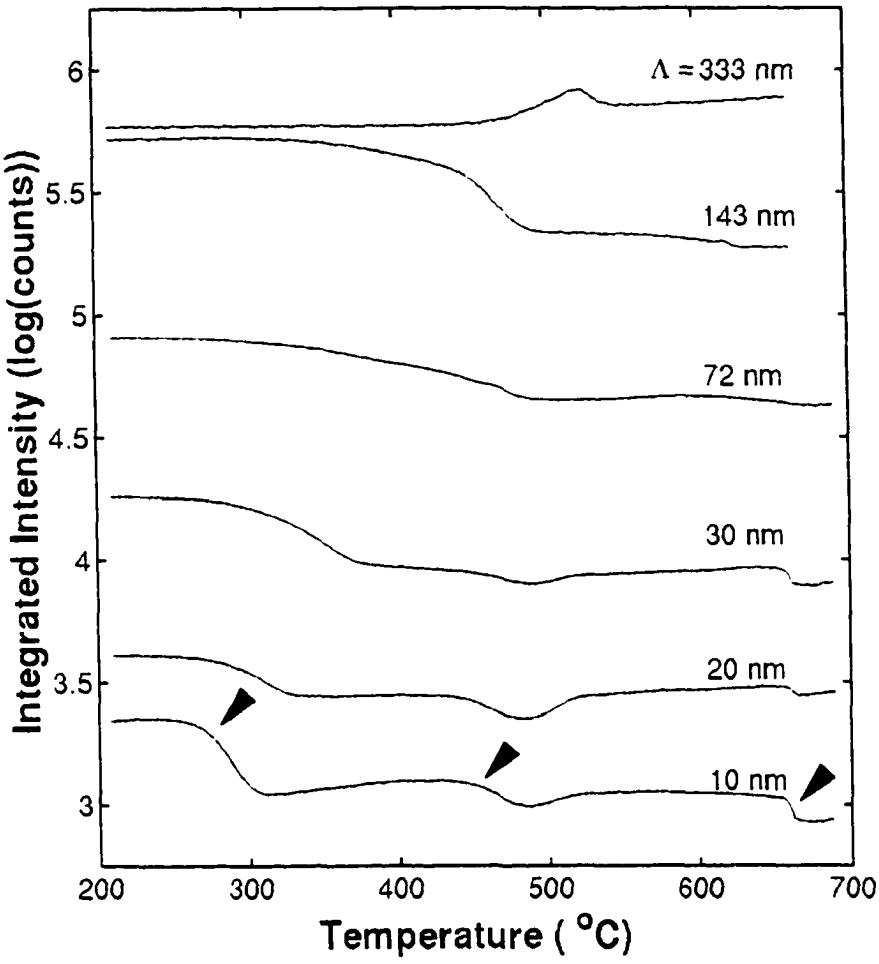

Figure 5. 69: Integrated XRD intensity as a function of temperature for Al (111)/Ti (0002) peaks in 1Ti/3Al-0 wt.% Cu multilayers.

To further investigate the nature of the transitions, the normalized first derivatives of the integrated intensity were determined for each of the curves and are plotted in Figure 5. 70. Since the exact nature of the peaks in the derivative curves was not known *a priori*, they are labeled as peak 1, peak 2, peak 3 and peak 4 to differentiate them from peak A and peak B (or C) as described in the DSC results from the Ti/Al multilayers.

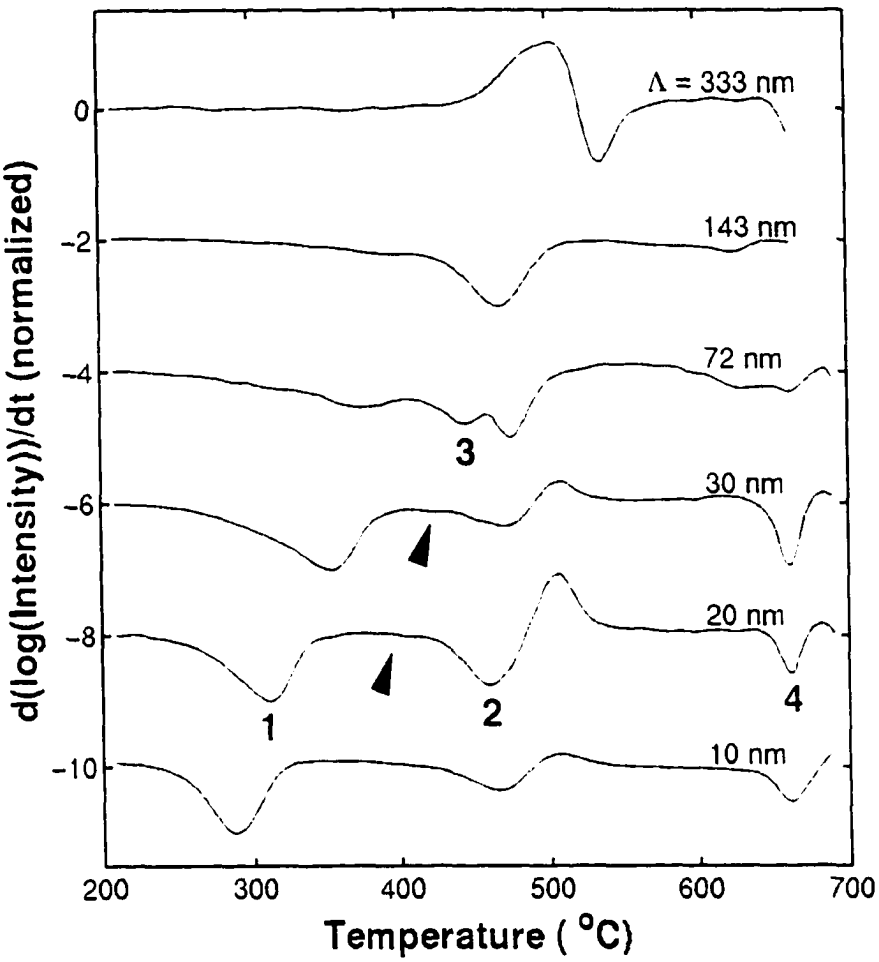

Figure 5. 70: Normalized first derivative of the integrated XRD intensity as a function of temperature in 1Ti/3Al-0 wt.% Cu multilayers. Note the peak at ~660 °C due to the melting of Al in some of the samples.

The drops in intensity were represented by peaks in the derivative plots. The first peak (peak 1) was observed to shift to higher temperatures and broaden as the periodicity increased. Given the temperature range of this peak, the decrease in XRD intensity was most likely due to the formation of the $TiAl_3$ phase with the cubic $L1_2$ structure. The temperature of the peak 2 was independent of the multilayer period and corresponded with the formation of the metastable tetragonal Ti/Al phases. The behavior of these two

peaks was quite similar to peaks A and C found in the constant-heating-rate DSC traces of the 1Ti/3Al multilayers (Chapter 4). In the DSC results, the first peak (peak A) shifted to higher temperatures while the second peak (peak C) remained constant as the period increased. A third peak, between the first and second peaks of the XRD data, was slightly visible in the 20, 30 and 72 nm samples. This could be the second peak (peak B) of $TiAl_3$ $L1_2$ formation that was previously observed in DSC traces for films with $\Lambda > 30$ nm. Finally, the peak at 660 °C (peak 4) was attributed to the melting of unreacted Al present in the samples. Note that as indicated by the DSC results, the first peak of $L1_2$ formation and the peak associated with the formation of the tetragonal metastable structure merge, forming one peak in the 143 nm sample. A summary of the observed peak temperatures is given in Table 5. XVII.

Table 5. XVII: Peak temperatures determined from the plots of the first derivative of the integrated intensity of the Al(111)/Ti (0002) peaks in 1Ti/3Al-0 wt.% Cu multilayers.

		Al (111)/Ti (0002)		
Sample ID	**Λ [nm]**	**Peak 1 [°C]**	**Peak 2 [°C]**	**Peak 4 [°C]**
120698a	10	286.8	465.4	661.2
120798a	20	310.1	459.5	661.1
120898a	30	352.4	469.4	660.5
052198a	72	373.7	473.5	
052298a	143		466.4	660.2
052498a	333		535.0?	

The integrated intensities for the second window were plotted in Figure 5. 71. These results were generally the inverse of the previous integrated intensity plot. Instead of decreases in XRD intensity, a stepped increase in intensity was observed.

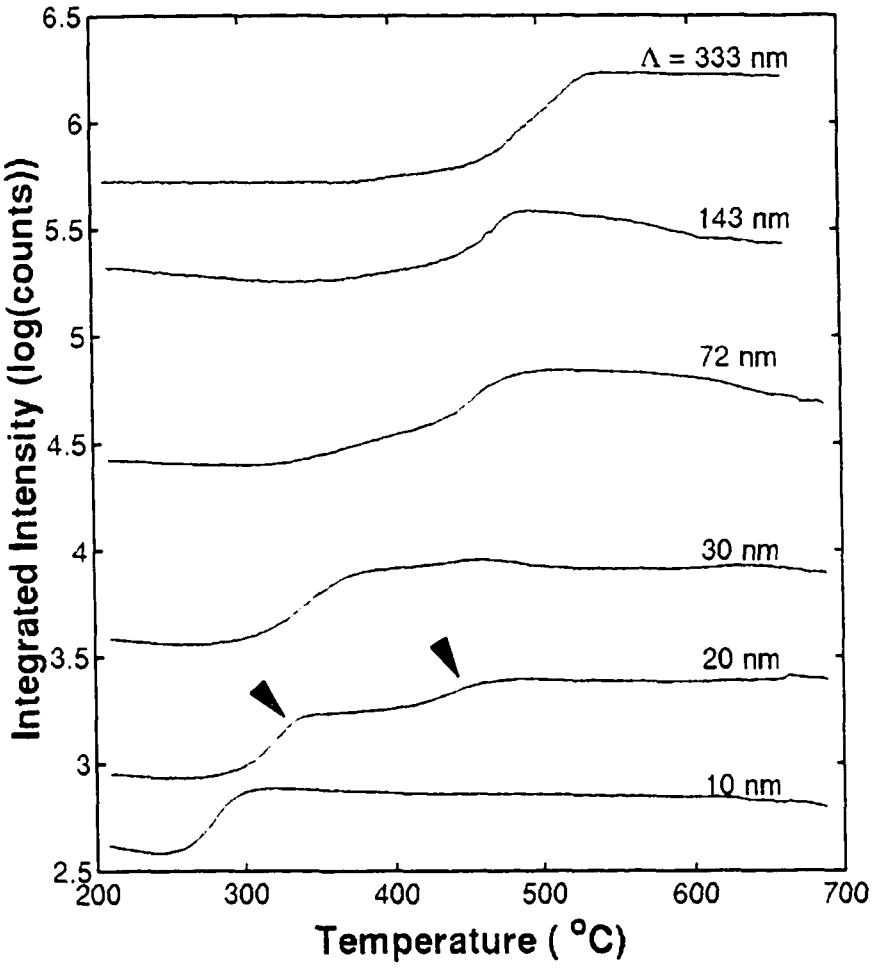

Figure 5. 71: Integrated XRD intensity for the peak associated with several $TiAl_3$ phases as a function of temperature in 1Ti/3Al-0 wt.% Cu multilayers. The $L1_2$ phase is stable to ~500 °C.

The normalized first derivatives produced peaks associated with phase formation as shown in Figure 5. 72. The first peak was again attributed to $L1_2$ formation based on temperature, shape, and the characteristic shift and decrease in relative intensity with increasing Λ. The second peak was attributed to the formation of the metastable tetragonal modification of $TiAl_3$ based primarily on the temperature and associated peaks visible in other windows of the scan. Note that the second peak of the 333 nm has saturated due to the high intensity. The presence of a second peak associated with $L1_2$

formation was not as obvious in this window. However, the intensity between peak 1 and 2 in the 72 nm sample does not decrease substantially possibly indicating the superposition of another peak.

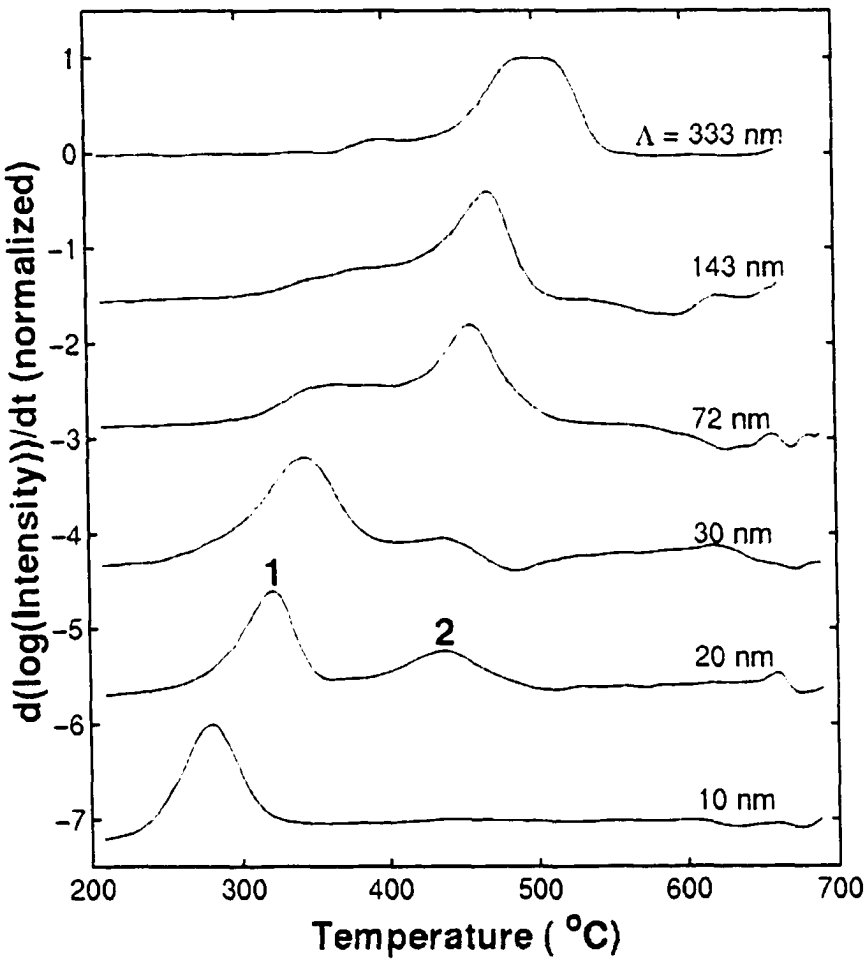

Figure 5. 72: Normalized derivative of the integrated XRD intensity as a function of temperature in 1Ti/3Al-0 wt.% Cu multilayers. Note the presence of two peaks for $\Lambda > 20$ nm.

The peak temperatures determined from the derivative plots are listed in Table 5. XVIII.

Table 5. XVIII: Peak temperatures determined from the plots of the first derivative of the integrated intensity of the $TiAl_3$ peak in 1Ti/3Al-0 wt.% Cu multilayers.

Sample ID	Λ [nm]	Peak 1 [°C]	Peak 2 [°C]
120698a	10	279.4	
120798a	20	319.5	436.1
120898a	30	343.0	435.2
052198a	72	367.2	456.0
052298a	143	468.4	465.3
052498a	333	399.3	500.0

The next peak investigated, in terms of the temperature of its appearance, belonged to the tetragonal, metastable structure of $TiAl_3$ (the highest angle window in Figure 5. 66). The location of this peak matched structures proposed by Srinivasan et al. (1991) and Raman and Schubert (1965) so an exact identification was not possible. The plot of integrated intensity vs. temperature indicated an increase in diffracted intensity that reached a plateau and gradually decayed to the original value as seen in Figure 5. 73. The width of the plateau was nearly constant over the range of periodicities studied. However, the height of the plateau was lower for the 10 and 20 nm films and larger for the 30, 72, 143 nm films.

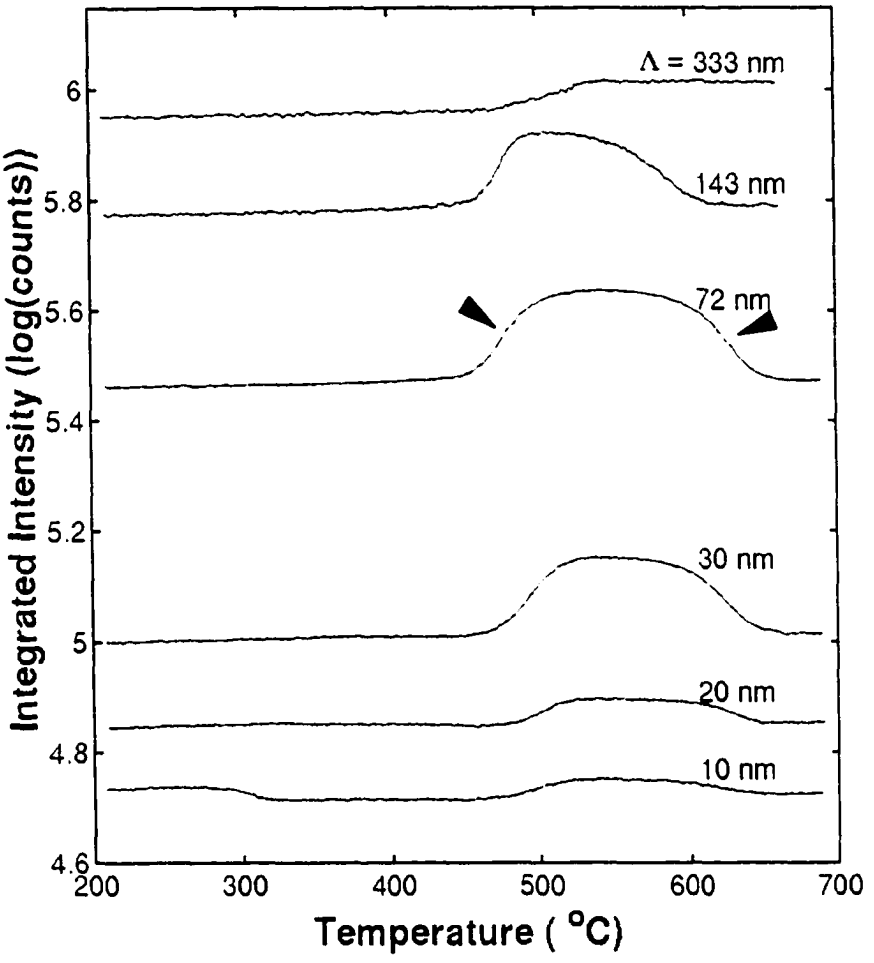

Figure 5. 73: Integrated XRD intensity as a function of temperature for the metastable tetragonal $TiAl_3$ peak in 1Ti/3Al-0 wt.% Cu multilayers.

The normalized first derivatives of the integrated intensity curves are shown in Figure 5. 74. As expected, two peaks result from the change in slope associated with the formation (positive) and disappearance (negative) of the diffraction peak. The negative peak at 300 °C in the 10 nm sample was due to the disappearance of the adjacent Al (200) peak. The curves showed that the transformation to the high temperature superlattice was consistent in temperature and rate as a function of Λ. The duration of the peak was essentially constant for the 10, 20, and 30 nm films. The range increased slightly for the

72 nm film then decreased by ~40 °C in the 143 nm film. The behavior measured from the 333 nm sample was somewhat irregular as the disappearance of the peak was not observed.

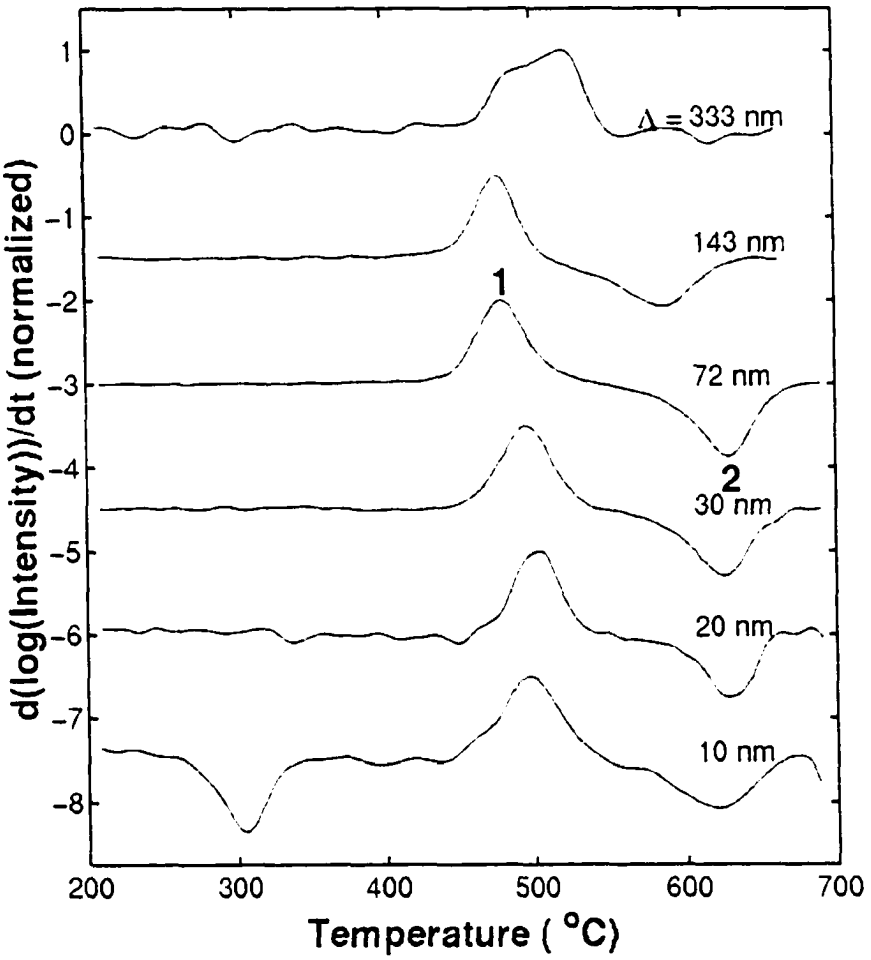

Figure 5. 74: Normalized first derivatives of integrated XRD intensity for the metastable tetragonal $TiAl_3$ peak as a function of temperature in 1Ti/3Al-0 wt.% Cu multilayers.

A summary of the peak temperatures obtained from the derivative plots is listed in Table 5. XIX.

Table 5. XIX: Peak temperatures determined from the plots of the first derivative of the integrated intensity of the metastable tetragonal superlattice of $TiAl_3$ in 1Ti/3Al-0 wt.% Cu multilayers.

		$TiAl_3$ (superlattice)		
Sample ID	**Λ [nm]**	**Peak 1 [°C]**	**Peak 2 [°C]**	**Temp. Range**
120698a	10	496.6	620.3	124
120798a	20	500.7	627.5	127
120898a	30	495.2	624.4	129
052198a	72	477.3	627.8	150
052298a	143	475.5	586.2	111
052498a	333	520.8		

The final phase that was tracked by *in situ* measurements was the equilibrium structure of $TiAl_3$ at ~49°. Note that no other reported $TiAl_3$ metastable structures have peaks in this range. The integrated intensity plots shown in Figure 5. 75 indicated a gradual increase in intensity beginning at ~500 °C and lasting until the end of the heating program.

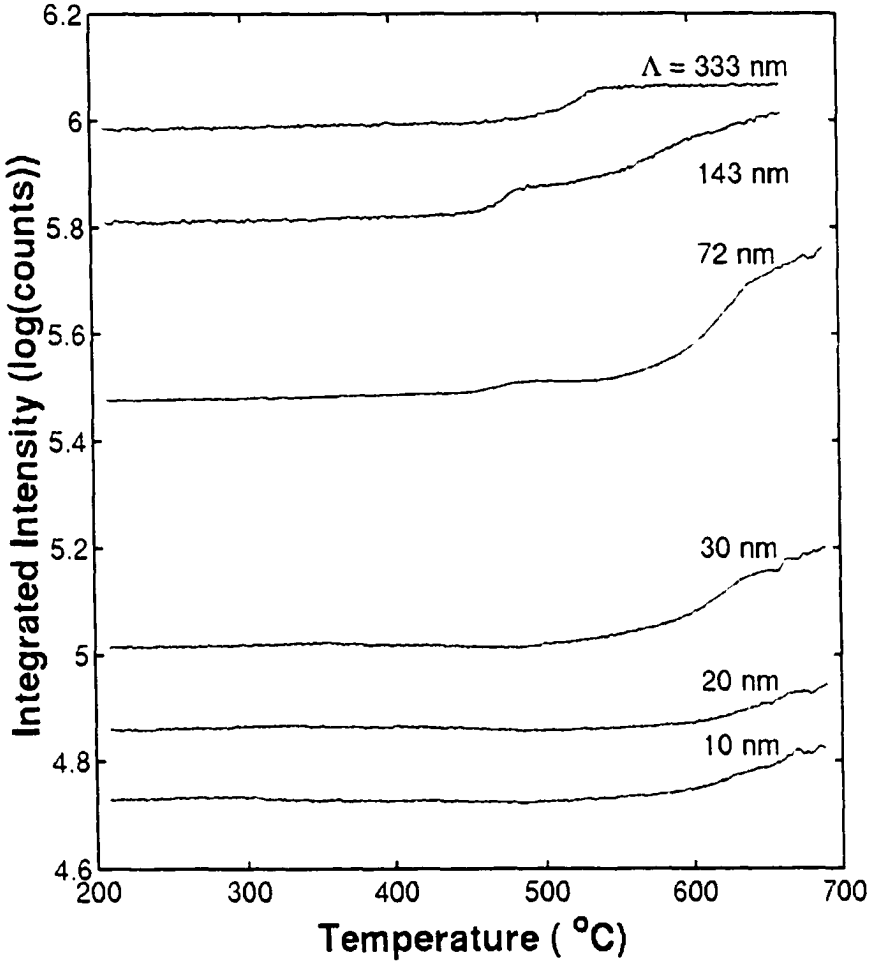

Figure 5. 75: Integrated XRD intensity as a function of temperature for $TiAl_3$-DO_{22} (004) peaks in 1Ti/3Al-0 wt.% Cu multilayers.

Plots of the normalized first derivative of the integrated intensity again proved to be a useful means of enhancing the transitions in XRD intensity that occurred during phase formation. The curves indicated a large peak at ~600 °C as seen in Figure 5. 76. For the films with $\Lambda > 30$ nm, a second peak formed at ~450 °C commensurate with the formation of the metastable tetragonal $TiAl_3$ phase. This low temperature peak varied in temperature and relative height (intensities are normalized among periodicities).

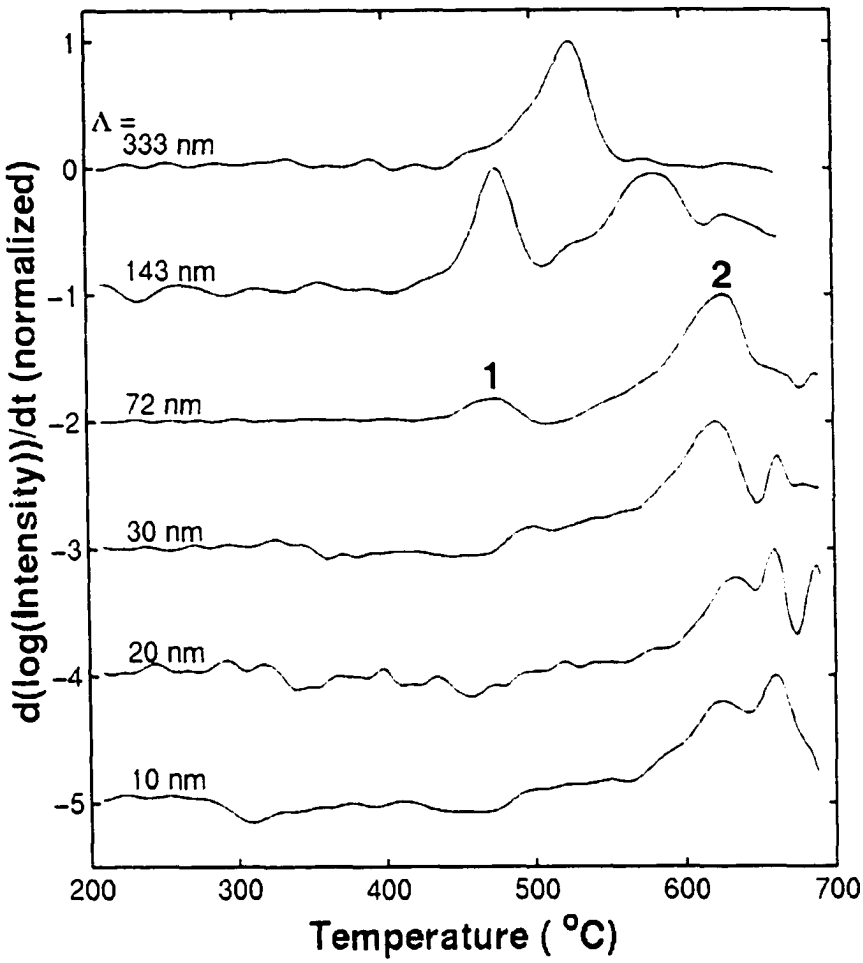

Figure 5. 76: Normalized first derivatives of the integrated XRD intensity $TiAl_3$-DO_{22} (004) peaks as a function of temperature in 1Ti/3Al-0 wt.% Cu multilayers.

The temperatures determined from the integrated intensity curves are listed in Table 5. XX.

Table 5. XX: Peak temperatures determined from the plots of the first derivative of the integrated intensity of the $TiAl_3$-DO_{22} (004) reflection in 1Ti/3Al-0 wt.% Cu multilayers.

		$TiAl_3$ DO_{22} (004)	
Sample ID	**Λ [nm]**	**Peak 1 [°C]**	**Peak 2 [°C]**
120698a	10		623.5
120798a	20		632.2
120898a	30	498.5	621.4
052198a	72	474.4	626.2
052298a	143	476.8	581.8
052498a	333		525.0

5.4.2.3.1.2 Activation Energy

A 1Ti/3Al, Λ = 72 nm sample was chosen to represent the different stages of phase formation in the Ti/Al multilayers. The peaks of the different metastable phases, as well as the elemental Ti/Al peaks and the equilibrium $TiAl_3$ phase were well-defined in the integrated intensity plots. As with the Nb/Al multilayers, four heating rates were employed 60, 180, 540, and 1620 °C/min to perform a Kissinger analysis on the peaks identified in the subsections listed above. Figure 5. 77 shows the results obtained from the Kissinger plots based on the two peaks found in the Al (111) / Ti (0002) diffraction windows.

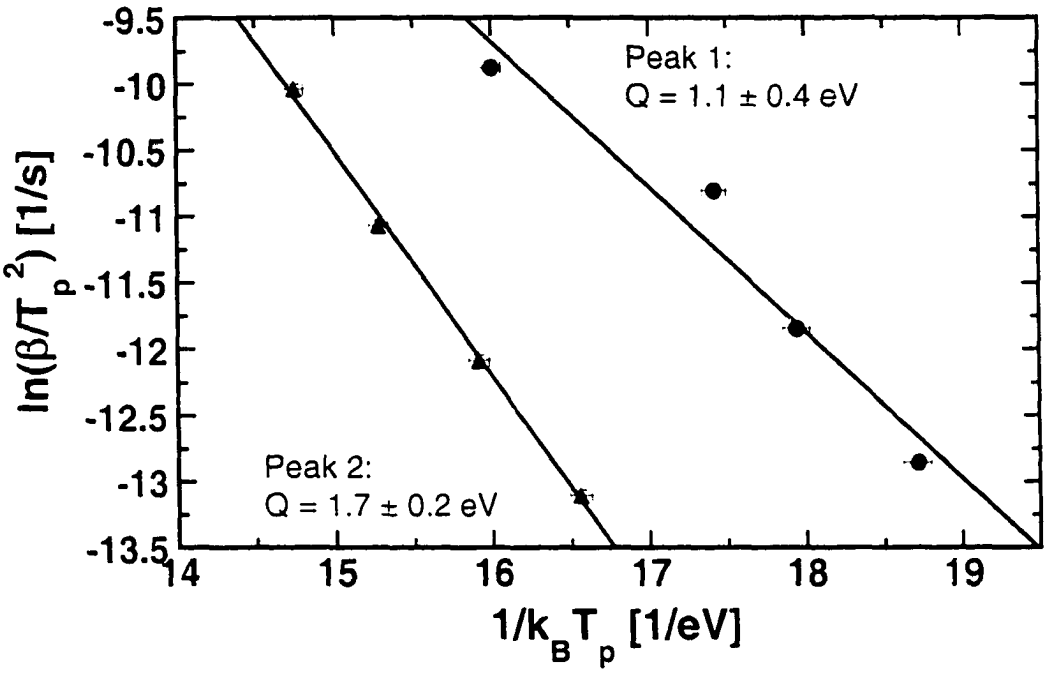

Figure 5. 77: Kissinger plot showing activation energies determined from *in situ* XRD measurements of the Al(111)/Ti (0002) peak for a 1Ti/3Al multilayer thin-film.

The results of the linear regression analysis used to determine the activation energy are listed in Table 5. XXI.

Table 5. XXI: Results of the Kissinger analysis of XRD data for a 1Ti/3Al multilayer thin-film with Λ = 72 nm found by monitoring the intensity changes of the Al and Ti peak.

1Ti/3Al-0 wt.% Cu, Λ =72 nm Al(111)/Ti(0002)					
Peak	Q [eV]	Error (98% conf.)	y-int. [K^{-1} s^{-1}]	Error (98% conf.)	Freq. Factor (ν) [s^{-1}]
1	1.1	0.4	7.89	6.44	3.41E+07
2	1.7	0.2	14.64	1.80	4.46E+10

Activation energies were also determined for the changes in the peak attributed to the metastable cubic and tetragonal $TiAl_3$ superlattices. The corresponding Kissinger plot is shown in Figure 5. 78.

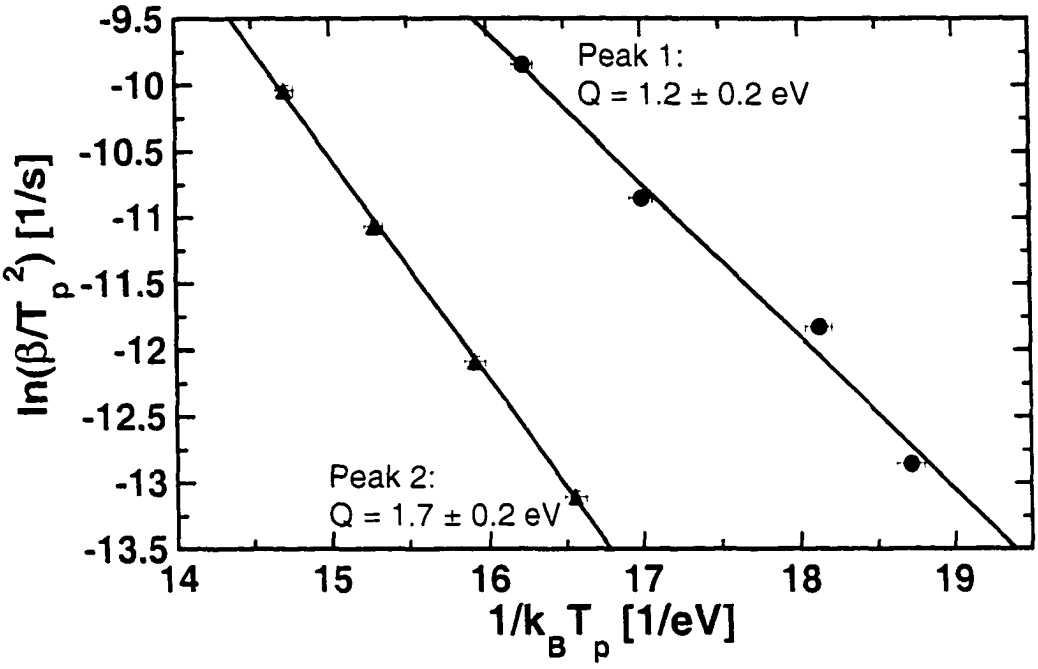

Figure 5. 78: Kissinger plot showing the activation energies for peaks 1 and 2 of the $TiAl_3$ superlattices in a 1Ti/3Al, Λ = 72 multilayer thin-film.

The results of the linear regression analysis used to determine the activation energies are listed in Table 5. XXII.

Table 5. XXII: Results of the Kissinger analysis of XRD data for the $TiAl_3$ superlattice peaks in 1Ti/3Al multilayer films with Λ = 72 nm.

1Ti/3Al-0 wt.% Cu, Λ =72 nm $TiAl_3$-metastable superlattices					
Peak	Q [eV]	Error (98% conf.)	y-int. [K^{-1} s^{-1}]	Error (98% conf.)	Freq. Factor (v) [s^{-1}]
1 (cubic)	1.2	0.2	8.79	3.60	8.73E+07
2 (tetra)	1.7	0.2	14.15	1.10	2.66E+10

Figure 5. 79 is a plot of the activation energies obtained for the positive and negative peaks associated with the metastable tetragonal superlattice of $TiAl_3$.

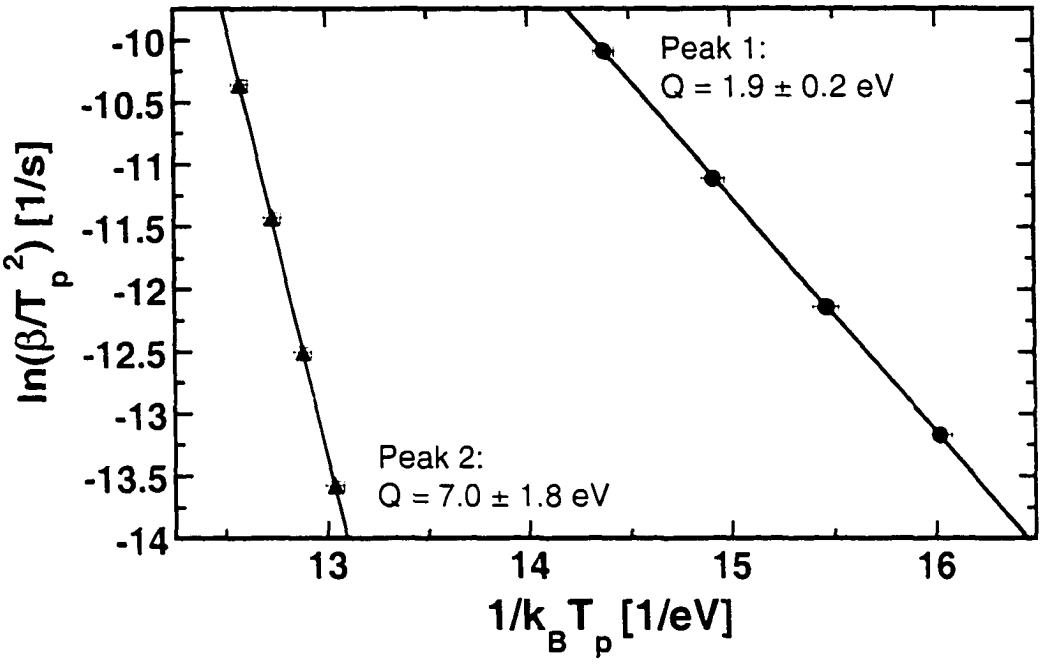

Figure 5. 79: Kissinger plot showing activation energies for peaks 1 and 2 of metastable tetragonal form of $TiAl_3$ from 1Ti/3Al multilayer thin film with Λ = 72 nm.

A summary of the linear regression analysis used to fit the data in the Kissinger analysis is listed in Table 5. XXIII.

Table 5. XXIII: Results of Kissinger analysis of a 1Ti/3Al multilayer thin-film with Λ = 72 nm for the $TiAl_3$-metastable tetragonal superlattice peaks.

1Ti/3Al-0 wt.% Cu, Λ =72 nm $TiAl_3$-metastable tetragonal superlattice					
Peak	Q [eV]	Error (98% conf.)	y-int. [K^{-1} s^{-1}]	Error (98% conf.)	Freq. Factor (ν) [s^{-1}]
1	1.9	0.2	16.89	0.26	4.71E+11
2	7.0	1.8	77.98	1.60	6.01E+38

Finally, activation energies were determined for the two peaks that were assigned to the formation of the equilibrium structure of $TiAl_3$. The Kissinger plot is shown in Figure 5. 80. Note that these values represent the first attempts to directly quantify the activation energy associated with the formation of this particular structure of $TiAl_3$

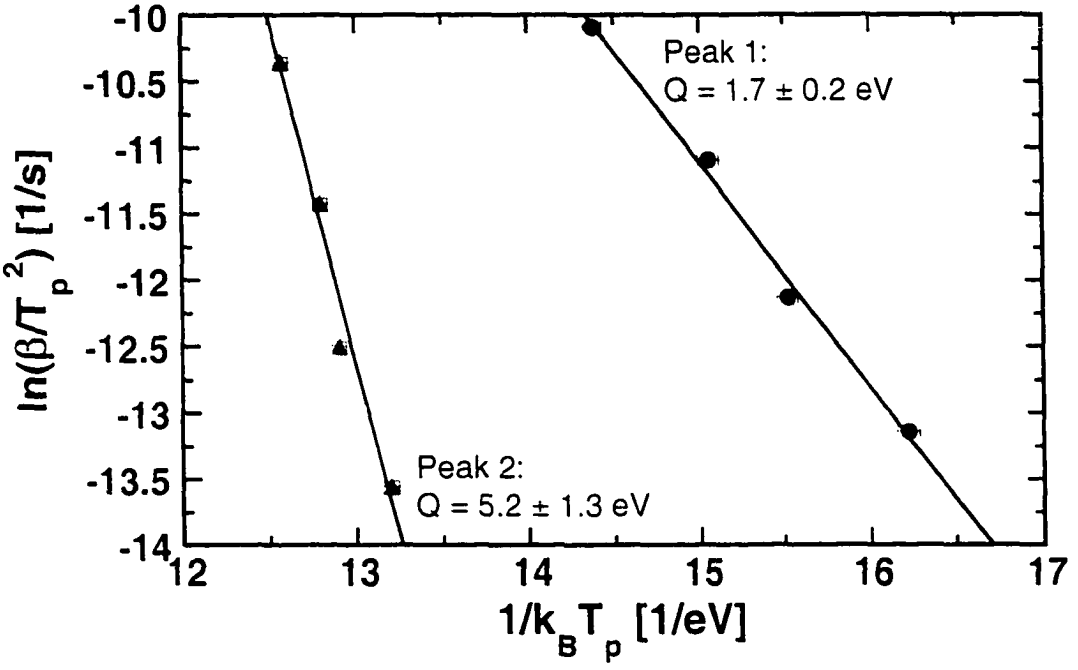

Figure 5. 80: Kissinger plot showing activation energies for $TiAl_3$-DO_{22} (004) in 1Ti/3Al multilayer thin-films with Λ = 72 nm.

The results of the linear regression analysis used to determine the activation energies in the Kissinger plots are listed in Table 5. XXIV.

Table 5. XXIV: Results of Kissinger analysis of XRD data of $TiAl_3$-DO_{22} (004) peaks in a 1Ti/3Al multilayer thin-film with Λ = 72 nm.

1Ti/3Al-0 wt.% Cu, Λ =72 nm $TiAl_3$-DO_{22} (004)					
Peak	Q [eV]	Error (98% conf.)	y-int. [K^{-1} s^{-1}]	Error (98% conf.)	Freq. Factor (ν) [s^{-1}]
1	1.7	0.2	16.89	0.26	4.71E+11
2	5.2	1.3	77.98	1.60	6.01E+38

5.4.2.3.2 Ti/Al-0.5 wt.% Cu

5.4.2.3.2.1 Effect of Layer Thickness on Reaction Kinetics

To assess the effects of Cu on the formation of the $TiAl_3$ intermetallic compound formation, a series of films was deposited containing Al layers containing 0.5 wt.% Cu. Figure 5. 81 shows contour plots of XRD intensity as a function of 2θ and temperature for a series of multilayers with various Λ heated at 180 °C/min to 700 °C in He.

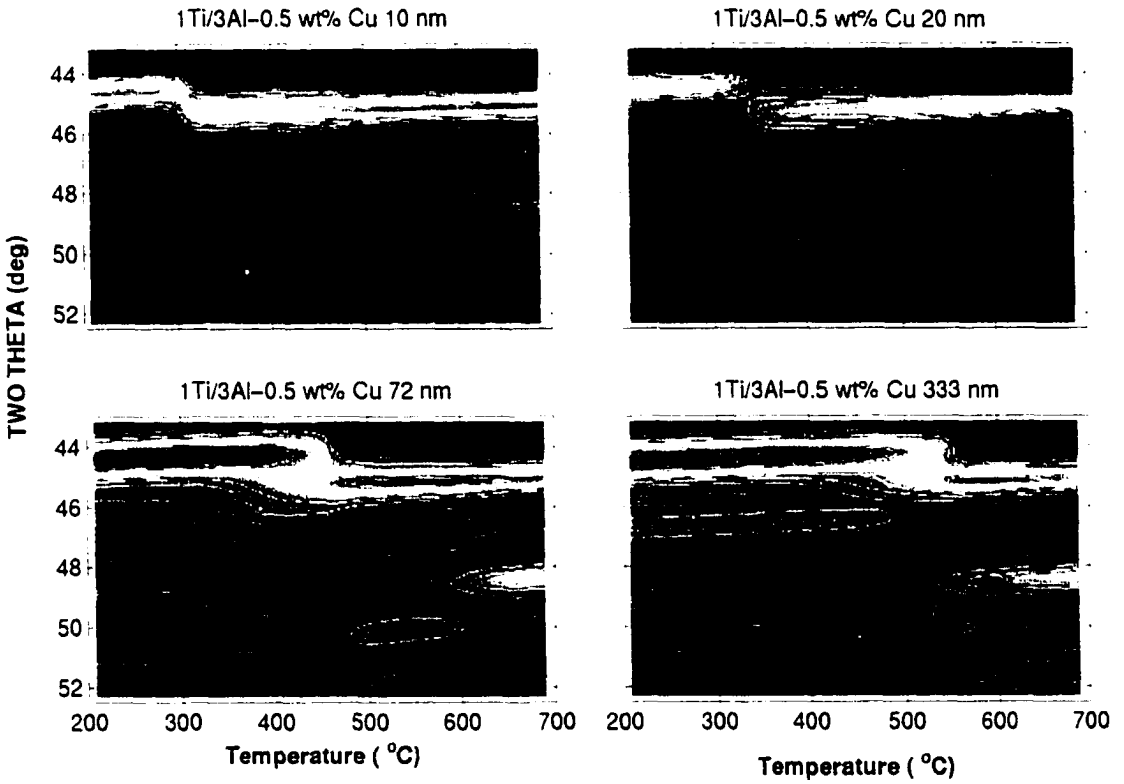

Figure 5. 81: XRD intensity as a function of 2θ and temperature for 1Ti/3Al-0.5 wt.% Cu multilayers with Λ ranging from 10 to 333 nm and annealed from 100 to 700 °C at 180 °C/min.

Overall, the results closely resemble the data obtained from the samples without the Cu additions. For the 10 nm samples, a decrease in the Al (111)/ Ti (0002) intensity was again observed beginning at ~ 300 °C. The Al (002) reflection was also faintly

visible at ~52°. The only diffraction peak visible in the selected window was the one located at ~45°, again believed to correspond to the formation of the $TiAl_3$ phase with the metastable cubic $L1_2$ superlattice structure. The peak narrowed and increased with intensity at ~480 °C while a second peak appeared at ~50.8° signifying the formation of the metastable tetragonal superlattice form of $TiAl_3$. However, the peak previously observed at ~44° was notably absent in this and the other XRD scans for this set of samples. The diffraction peak associated with the equilibrium, tetragonal DO_{22} structure was obvious by ~600 °C at which the metastable superlattice phase had been transformed.

Increasing the periodicity did not change the overall form of the diffraction peaks. The obvious changes were an extension of the temperature range where the elemental Al and Ti peaks were visible and, in another variation from the previous set of samples, the appearance of the Ti (101) peak at ~47°. This was likely due to texture changes in the microstructure initiated by the presence of the Cu (this point will be addressed in more detail in the following chapter). Considering the XRD texture measurements of the as-deposited films, Cu was found to reduce the fiber texture of the Al (111) and Ti (0002) planes. As a results other orientations (such as Al (200) or Ti (101)) would become visible in the θ-2θ scans. A small degree of peak narrowing was visible in the intense $TiAl_3$ diffraction peak at ~45° indicating grain growth. As a final, general observation, the $TiAl_3$ DO_{22} peak at ~49° appeared to form at lower temperatures as the periodicity increased while the peak at ~51° corresponding to the high temperature, superlattice structure of $TiAl_3$ became smaller.

Applying the same approach as in the previous analyses of the Nb/Al and Ti/Al multilayers, the integrated intensities were determined for the various windows in the *in*

situ XRD scans. Figure 5. 82 shows the integrated intensity for the Al (111)/Ti (0002) peaks as a function of temperature. As with the 0 wt.% Cu samples, two distinct decreases in intensity were observed for the 10 and 20 nm films. The first drop shifted to higher temperatures with increasing Λ and eventually the transition between the two became indistinct.

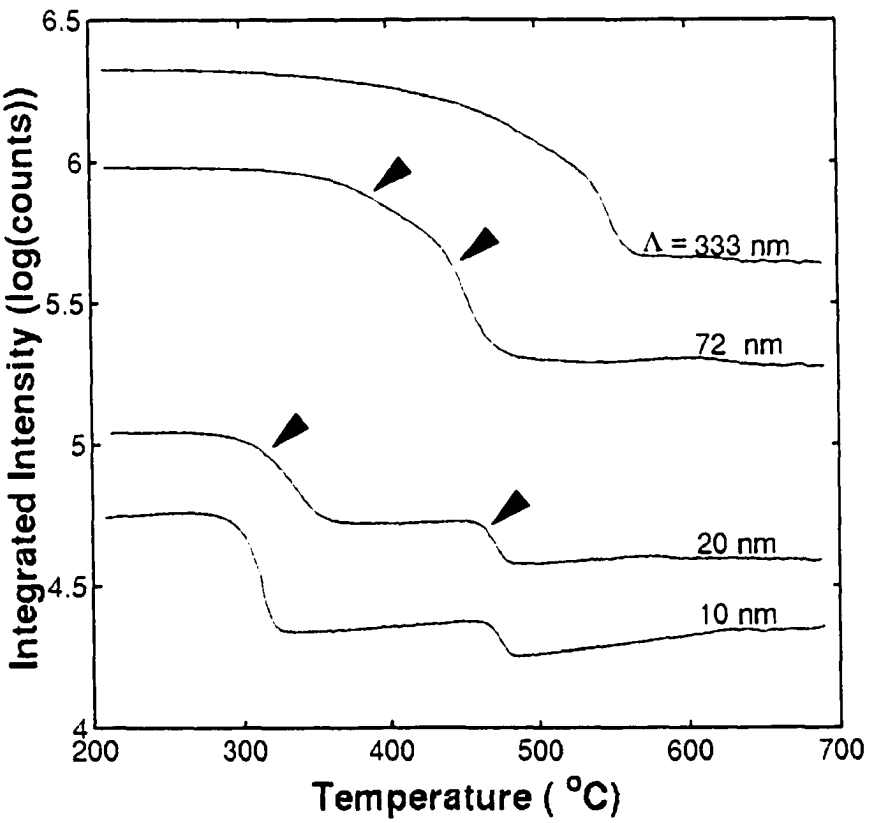

Figure 5. 82: Integrated XRD intensity as a function of temperature for the Al (111)/Ti (0002) peak in 1Ti/3Al-0.5 wt.% Cu multilayers.

The normalized first derivative of the integrated intensity is shown in Figure 5. 83. Two peaks were again evident in the curves. Based on peak temperature and relationship to Λ, Peak 1 was believed to correspond to the formation of the metastable cubic $L1_2$ superlattice of $TiAl_3$. The temperature of the second peak correlated with the

appearance of the superlattice peaks for the metastable tetragonal form of $TiAl_3$ (DO_{23} or Ti_9Al_{23}). The second peak associated with the formation of the $L1_2$ structure was absent in this set of samples as in the DSC results. This further supports the notion that the Cu has affected the formation mechanism of the $TiAl_3$ phase. Also, like the DSC results peak 1 and 2 ("A" and "C" merge into a single peak at $\Lambda > 72$ nm). Peak 1 shifted to higher temperatures and broadened as Λ increased.

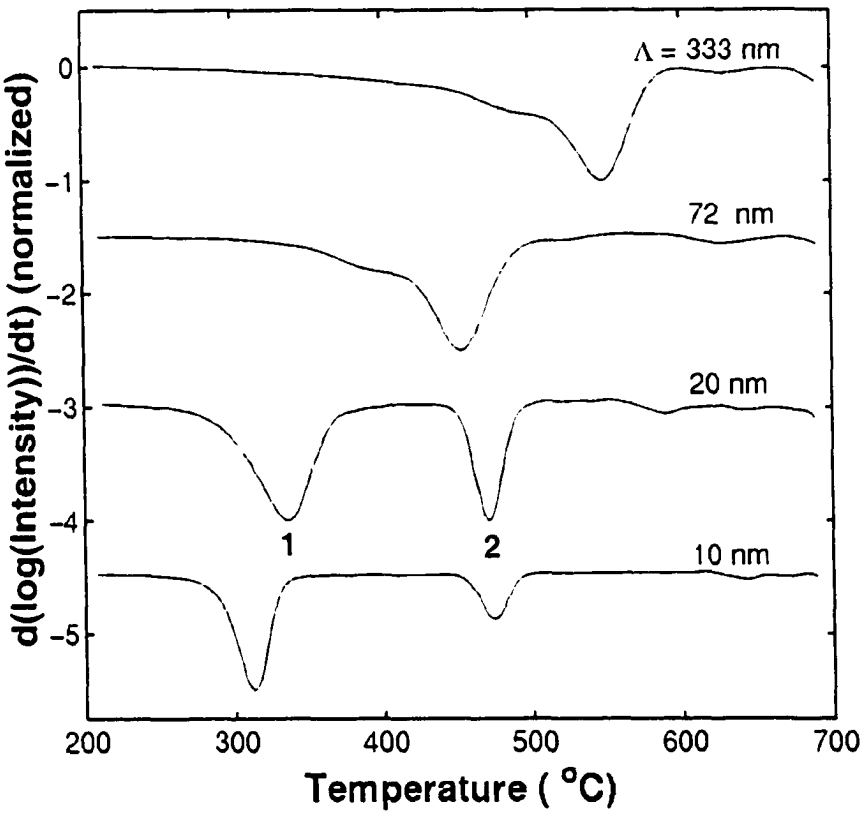

Figure 5. 83: Normalized first derivative of the integrated intensity of the Al(111)/Ti (0002) peaks as a function of temperature for 1Ti/3Al-0.5 wt.% Cu multilayers.

The peak temperatures determined from the derivative plots for peaks 1 and 2 are listed in Table 5. XXV.

Table 5. XXV: Peak temperatures determined from XRD data for Al (111)/Ti (0002) reflections in 1Ti/3Al-0.5 wt.% Cu multilayers.

		Al (111)/Ti (0002)	
Sample ID	**Λ [nm]**	**Peak 1 [°C]**	**Peak 2 [°C]**
111398a	10	311.8	473.5
111698b	20	335.7	469.3
110998b	72	389.8	453.7
110998a	333	485.7	547.5

Figure 5. 84 shows the integrated intensity of the window encompassing the $TiAl_3$ peaks belonging to the cubic and tetragonal metastable superlattice phases and the equilibrium tetragonal structure. The behavior of the curves does not mirror the results from the Al suggesting the relationship between consumption of the reactants and formation of the products was not straightforward in this case. Two distinct stages of growth were evident in the 72 nm trace, however, in the 10 and 20 nm films, only a single increase in diffracted intensity was observed.

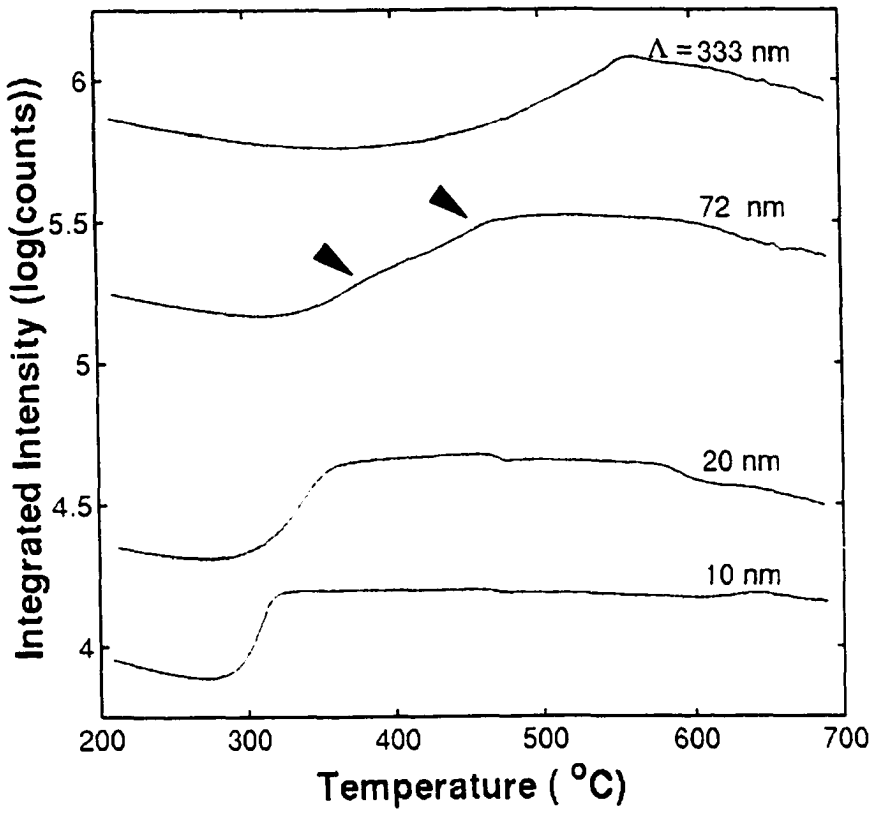

Figure 5. 84: Integrated XRD intensity as a function of temperature for $TiAl_3$ cubic and tetragonal superlattices and DO_{22} (112)/(103) reflections in 1Ti/3Al-0.5 wt.% Cu multilayers.

Calculation of the normalized derivatives confirmed the behavior of the integrated intensity curves and showed only a single peak for the 10 and 20 nm films as seen in Figure 5. 85. This peak did exhibit the characteristic temperature shift with increasing period, however, the relative height did not decrease with increasing Λ.

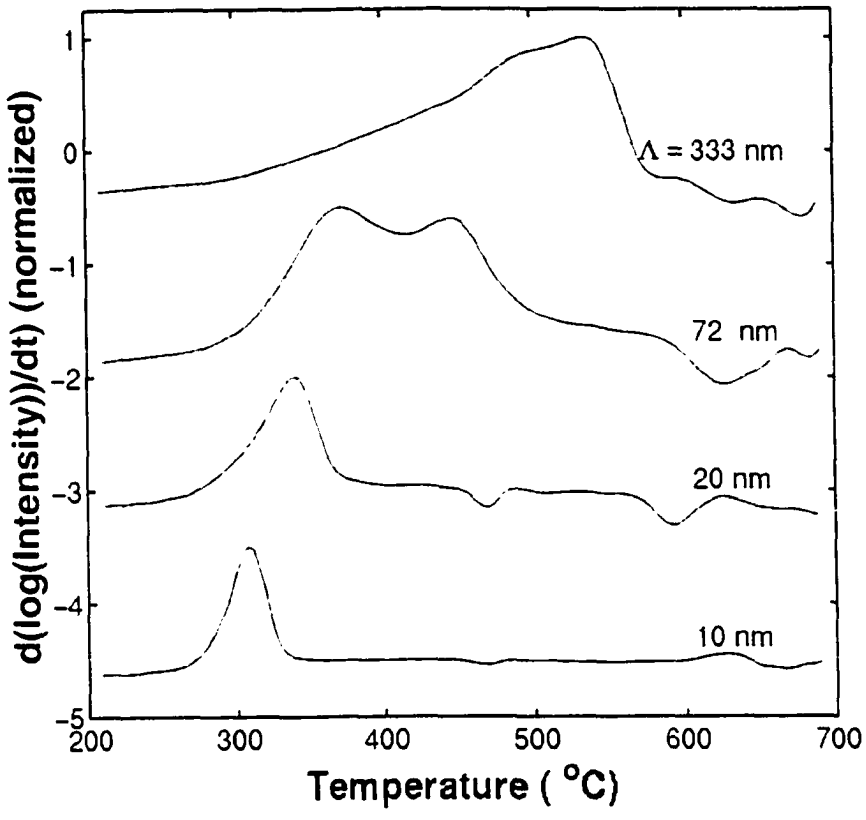

Figure 5. 85: Normalized first derivative of XRD integrated intensities for $TiAl_3$ cubic and tetragonal superlattices and DO_{22} (112)/(103) reflections in 1Ti/3Al-0.5 wt.% Cu multilayers.

The peak temperatures obtained from the derivative plots are listed in Table 5. XXVI.

Table 5. XXVI: Peak temperature determined from XRD data for the metastable cubic and tetragonal forms of $TiAl_3$ and the DO_{22} (112)/(103) reflections in 1Ti/3Al-0.5 wt.% Cu multilayers.

Sample ID	Λ [nm]	Peak 1 [°C]	Peak 2 [°C]
111398a	10	307.0	--
111698b	20	338.5	--
110998b	72	370.6	448.9
110998a	333	500.0	539.2

The formation of the metastable tetragonal superlattice peak was examined in Figure 5. 86. The integrated intensity was seen to increase at ~475 °C and form a plateau of constant intensity with the exception of the 333 nm film.

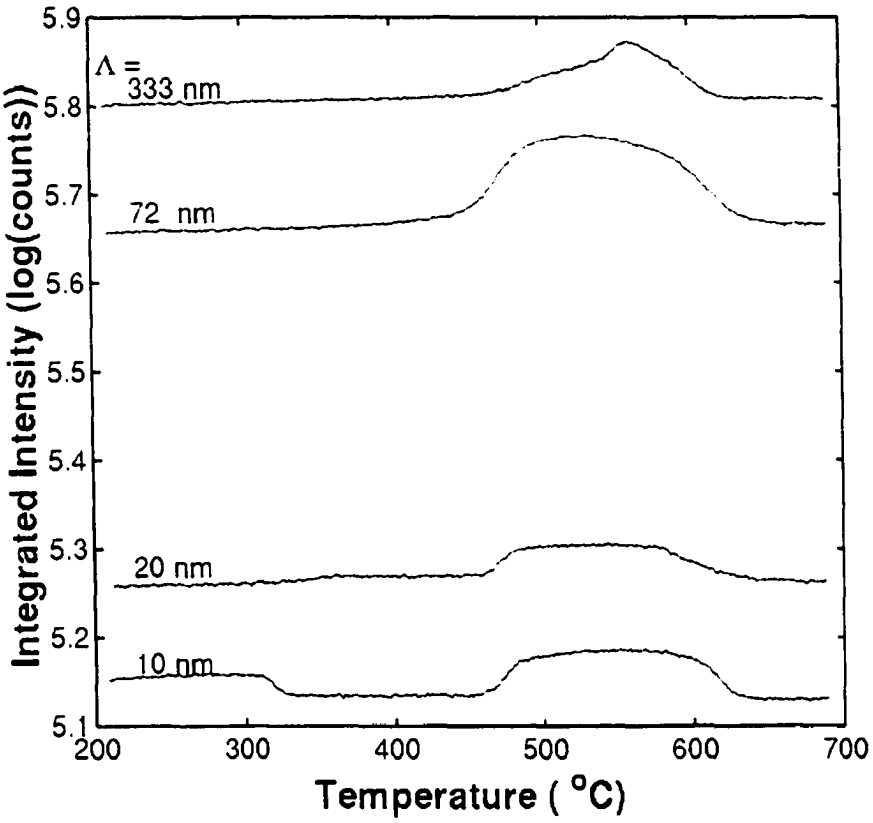

Figure 5. 86: Integrated XRD intensities as a function of temperature for the metastable tetragonal superlattice peak of $TiAl_3$ in 1Ti/3Al-0.5 wt.% Cu multilayers.

The normalized derivative of the curves produced a trace with positive and negative peaks corresponding to the formation and disappearance of the diffraction peak as shown in Figure 5. 87. The second peak appears to gradually shift to lower temperatures, from ~625 °C to ~600 °C as Λ increased.

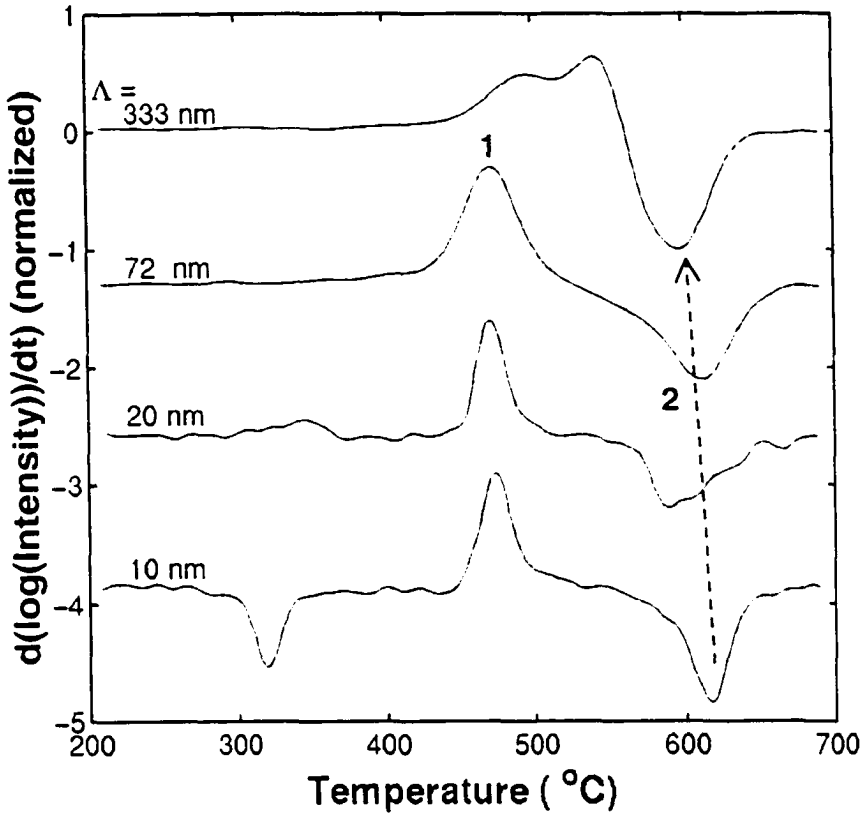

Figure 5. 87: Normalized first derivative of the integrated XRD intensity of the metastable tetragonal superlattice peak as a function of temperature in 1Ti/3Al-0.5 wt.% Cu multilayers.

The peak temperatures and temperature range between the maximum and minimum of the derivatives are listed in Table 5. XXVII.

Table 5. XXVII: Peak temperatures determined from XRD intensities for metastable tetragonal form of $TiAl_3$ in 1Ti/3Al-0.5 wt.% Cu multilayers.

Sample ID	Λ [nm]	Peak 1 [°C]	Peak 2 [°C]	Peak Range
111398a	10	473.4	616.5	143
111698b	20	471.3	589.4	118
110998b	72	472.0	610.6	139
110998a	333	495.4	596.5	101

Figure 5. 88 shows the integrated intensity associated with the formation of the equilibrium structure of $TiAl_3$ occurring at relatively high temperature. For the 10, 20, and 333 nm films a single increase in intensity was observed beginning at ~600 °C and lasting until the end of the run. The 72 nm again showed another peak preceding the high temperature increase in intensity.

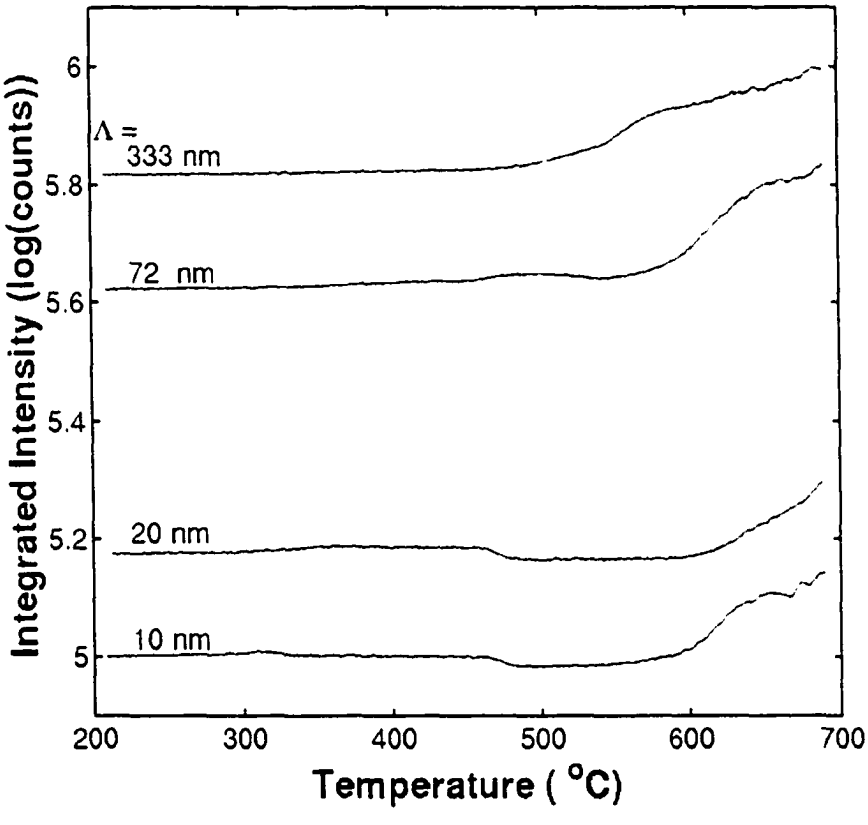

Figure 5. 88: Integrated XRD intensity as a function of temperature for the $TiAl_3$-DO_{22} (004) peak in 1Ti/3Al-0.5 wt.% Cu multilayers.

This intensity transitions were readily identified in the normalized derivative traces as shown in Figure 5. 89. The small, negative peak in the 10 and 20 nm films was attributable to a fluctuation in the background intensity and was not related to phase formation. The 72 nm film was the only sample in the thickness range where two peaks

were visible. The results from the other films were in agreement with the previous sets of samples. The 333 nm sample may also possess double-peaked formation, however, the peaks appear as though they have merged.

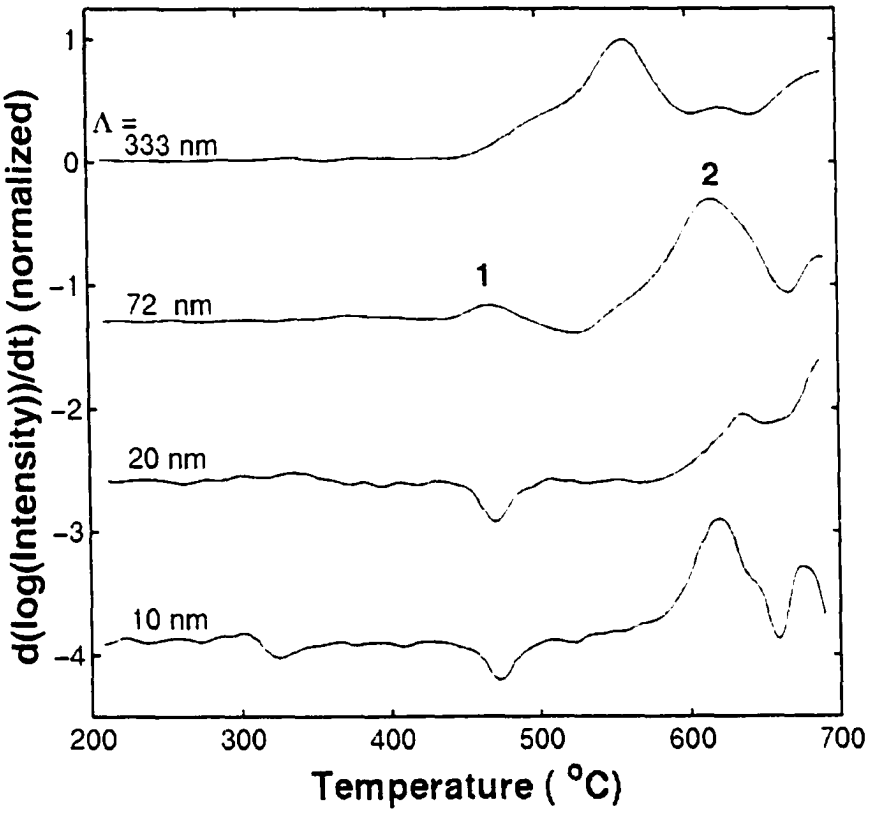

Figure 5. 89: Normalized first derivative of the curves for the $TiAl_3$-DO_{22} (004) peak 1Ti/3Al-0.5 wt.% Cu multilayers.

The peak temperatures obtained from the derivative plots showing the formation of the (004) peak of the DO_{22} structure of $TiAl_3$ are listed in Table 5. XXVIII.

Table 5. XXVIII: Peak temperatures determined from XRD data for the $TiAl_3$-DO_{22} (004) reflection in 1Ti/3Al-0.5 wt.% Cu multilayers.

Sample ID	Λ [nm]	Peak 1 [°C]	Peak 2 [°C]
111398a	10	--	619.7
111698b	20	--	634.6
110998b	72	465.7	614.0
110998a	333	516.0 (est.)	557.6

5.4.2.3.2.2 Activation Energy

The Kissinger analysis was used to determine the activation energies associated with the reproducible peaks in a 1Ti/3Al-0.5 wt.% Cu sample with Λ = 72 nm. Because peak 1 was not separable from the peak 2 of the Al (111)/Ti (0002) intensities, only the activation energy for the second peak could be reliably determined. The resulting Kissinger plot is shown in Figure 5. 90.

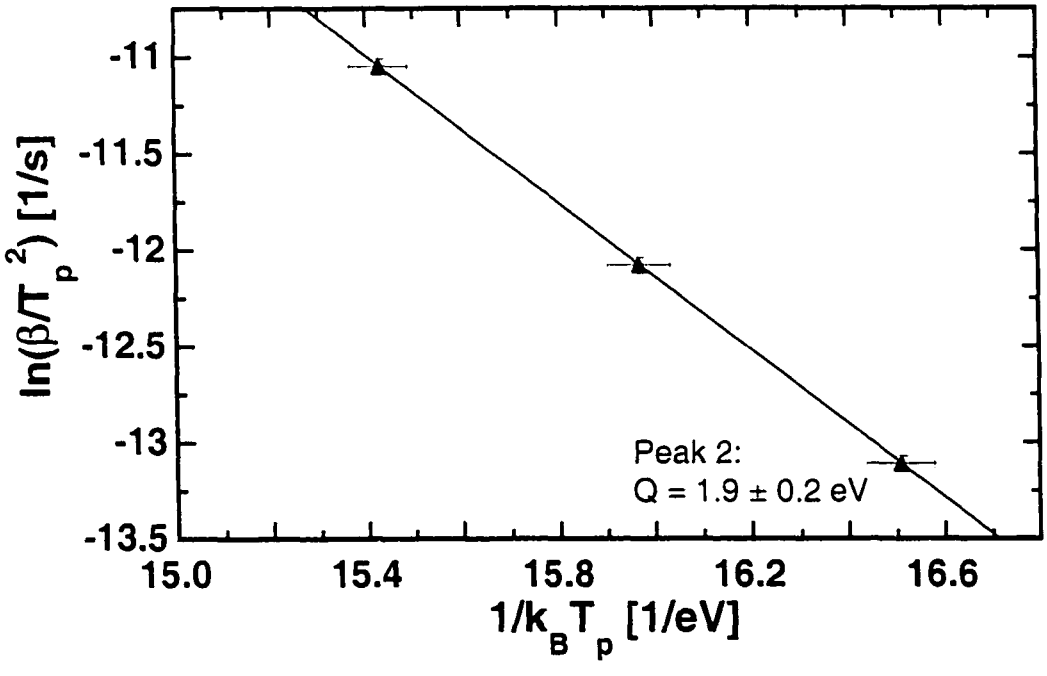

Figure 5. 90: Kissinger plot showing activation energies for Al (111)/Ti (0002) in 1Ti/3Al-0.5 wt.% Cu multilayer thin-films with Λ = 72 nm.

The output of the linear regression analysis used to calculate the activation energy of the peak 2 is listed in Table 5. XXIX.

Table 5. XXIX: Results from Kissinger analysis for the Al (111)/Ti (0002) reflections in 1Ti/3Al-0.5 wt.% Cu multilayer thin-films with Λ = 72 nm.

1Ti/3Al-0.5 wt.% Cu, Λ =72 nm Al (111)/Ti (0002)					
Peak	Q [eV]	Error (98% conf.)	y-int. [K^{-1} s^{-1}]	Error (98% conf.)	Freq. Factor (ν) [s^{-1}]
2	1.9	0.2	18.39	0.02	2.15E+12

Activation energies were also determined for the peaks associated with the formation of metastable cubic and tetragonal superlattice forms of $TiAl_3$. The Kissinger plot is shown in Figure 5. 91.

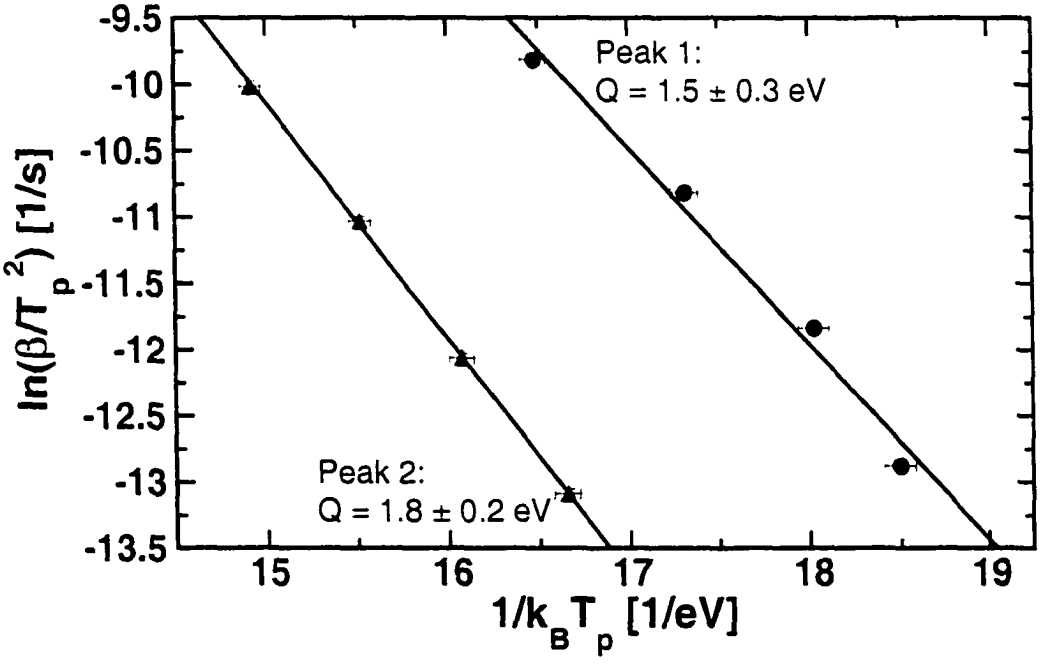

Figure 5. 91: Kissinger plot showing activation energies for $TiAl_3$ metastable superlattice peaks in 1Ti/3Al-0.5 wt.% Cu multilayer thin-films with Λ = 72 nm.

The results from the linear regression analysis used to determine the activation energies are summarized in Table 5. XXX.

Table 5. XXX: Results of Kissinger analysis for $TiAl_3$ metastable superlattices in 1Ti/3Al-0.5 wt.% Cu multilayer thin-films with Λ = 72 nm.

1Ti/3Al-0.5 wt.% Cu, Λ =72 nm $TiAl_3$-metastable cubic and tetragonal superlattices					
Peak	Q [eV]	Error (98% conf.)	y-int. [$K^{-1} s^{-1}$]	Error (98% conf.)	Freq. Factor (v) [s^{-1}]
1	1.5	0.3	14.64	4.80	3.92E+10
2	1.8	0.2	16.56	0.8	3.20E+11

The activation energies were determined for the formation of the two peaks belonging to the $TiAl_3$ metastable tetragonal superlattice reflection at ~51°. The Kissinger plot is shown in Figure 5. 92. The second peak corresponds to the disappearance of the phase.

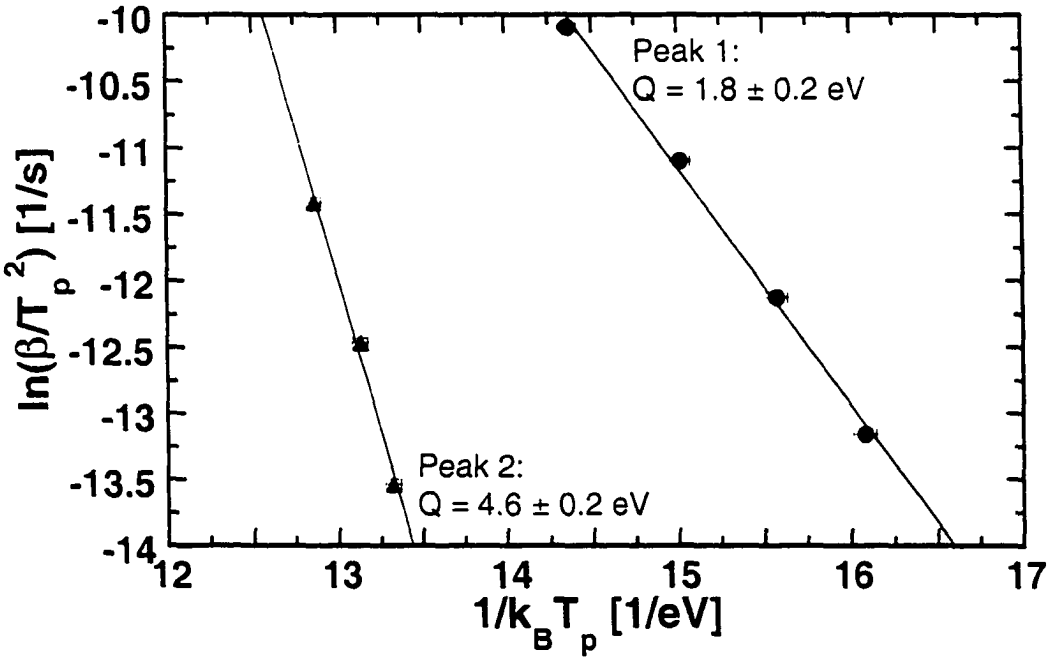

Figure 5. 92: Kissinger plot showing activation energies for $TiAl_3$ metastable tetragonal superlattice phase in 1Ti/3Al-0.5 wt.% Cu multilayer thin-films with Λ = 72 nm.

The results revealed and activation energy of ~1.8 eV for the peak 1 and ~4.6 eV for peak 2. The output of the linear regression analysis is listed in Table 5. XXXI.

Table 5. XXXI: Kissinger plot showing activation energies for $TiAl_3$-metastable tetragonal superlattice peak in 1Ti/3Al-0.5 wt.% Cu multilayer thin-films with Λ = 72 nm.

1Ti/3Al-0.5 wt.% Cu, Λ =72 nm $TiAl_3$-metastable tetragonal superlattice					
Peak	Q [eV]	Error (98% conf.)	y-int. [K^{-1} s^{-1}]	Error (98% conf.)	Freq. Factor (ν) [s^{-1}]
1	1.8	0.3	15.55	2.60	1.17E+11
2	4.6	0.2	47.68	12.40	2.71E+25

Finally, the activation energy was determined for the two transitions in XRD intensity associated with the equilibrium tetragonal DO_{22} structure of $TiAl_3$. The Kissinger plot is formed from the intensity evolution of the (004) peak is shown in Figure 5. 93.

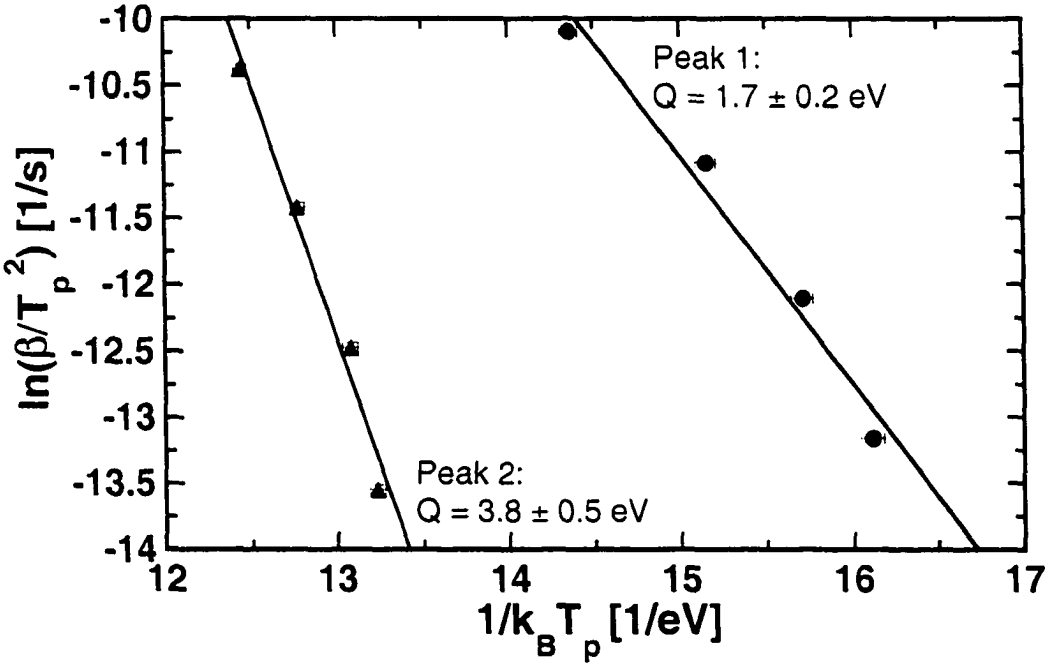

Figure 5. 93: Kissinger plot showing activation energies for $TiAl_3$-DO_{22} (004) in 1Ti/3Al-0.5 wt.% Cu multilayer thin-films with Λ = 72 nm.

The results indicated an activation energy of 1.7 eV for the first peak and 3.8 eV for the second peak. The output of the linear regression analysis is summarized in Table 5. XXXII.

Table 5. XXXII: Results of Kissinger analysis for $TiAl_3$-DO_{22} (004) in 1Ti/3Al-0.5 wt.% Cu multilayer thin-films with Λ = 72 nm.

1Ti/3Al-0.5 wt.% Cu, Λ =72 nm $TiAl_3$-DO_{22} (004)					
Peak	Q [eV]	Error (98% conf.)	y-int. [K^{-1} s^{-1}]	Error (98% conf.)	Freq. Factor (v) [s^{-1}]
1	1.7	0.2	14.73	6.20	4.96E+10
2	3.8	0.5	37.39	11.40	7.71E+20

5.4.2.3.3 Ti/Al-1.0 wt.% Cu

Given that large changes in the kinetic behavior between samples with 0.5 wt.%Cu and 1.0 wt.% Cu were not observed in the constant-heating-rate DSC results, a single 1.0 wt.% Cu sample was chosen for *in situ* XRD analysis. In order to provide a basis for comparison with the previous two sample sets, a 1Ti/3Al-1.0 wt.% Cu, Λ = 72 nm sample was selected to determine the activation energies associated with the different metastable phases and the equilibrium phase. The XRD intensity vs. 2θ and temperature is shown in Figure 5. 94.

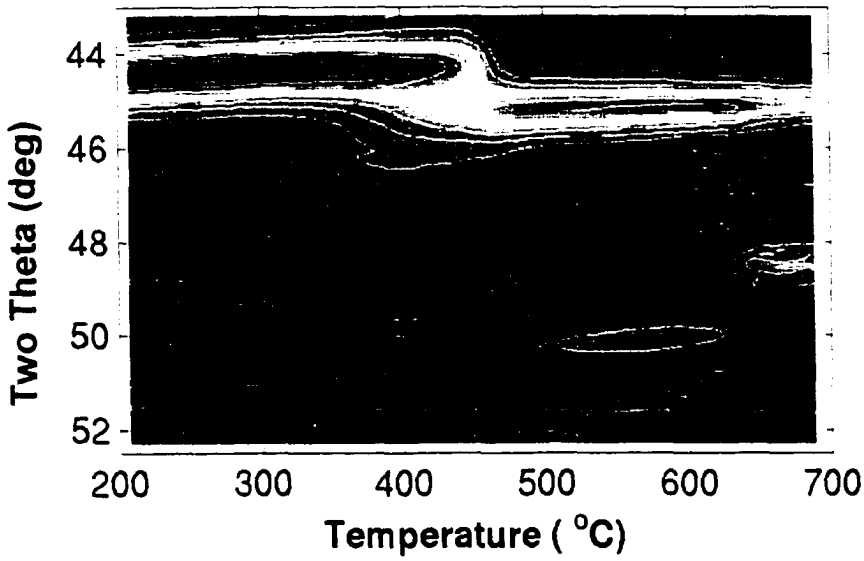

Figure 5. 94: XRD intensity as a function of 2θ and temperature for a 1Ti/3Al-1.0 wt.% Cu multilayer thin-film with Λ = 72 nm annealed at 180 °C min from 100 °C to 700 °C in purified He.

5.4.2.3.3.1 Activation Energy

A series of four heating rates was again used to determine the activation energies associated with the different structures of the $TiAl_3$ phase using the 1Ti/3Al-1.0 wt.% Cu, Λ = 72 nm sample. The resulting Kissinger plot obtained from the second peak of the Al (111)/Ti (0002) reflection is shown in Figure 5. 95.

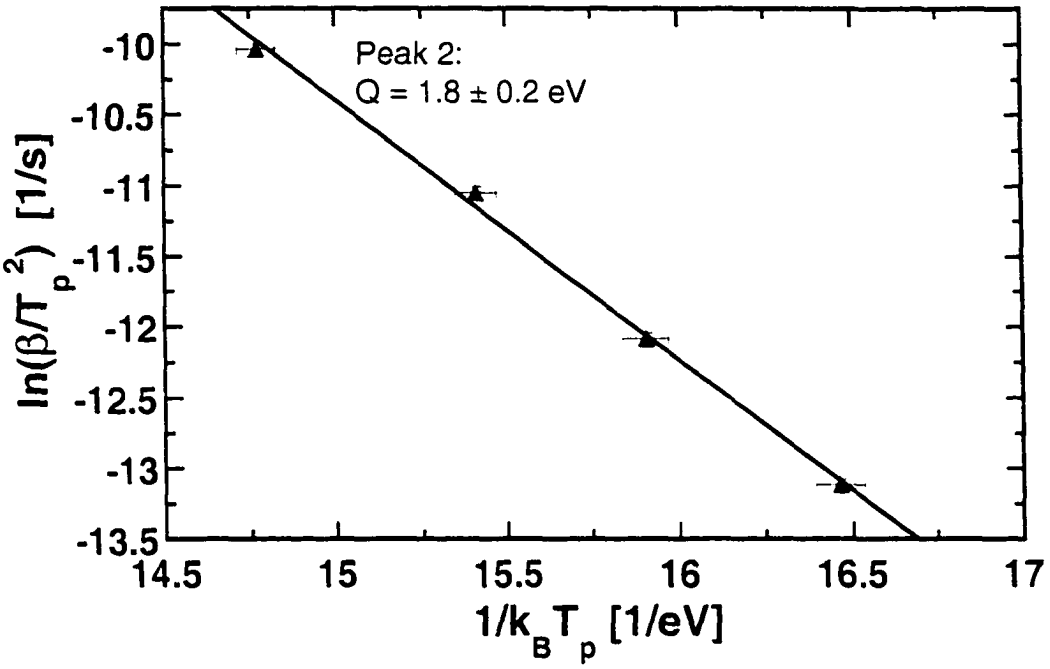

Figure 5. 95: Kissinger plot showing activation energy from Al(111)/Ti (0002) in a 1Ti/3Al-1.0 wt.% Cu multilayer thin-film with Λ = 72 nm.

The linear regression fit to the data yielded an activation energy of ~1.8 eV. The output of the fit analysis is summarized in Table 5. XXXIII.

Table 5. XXXIII: Results of Kissinger analysis of Al(111)/Ti (0002) in a 1Ti/3Al-1.0 wt.% Cu multilayer thin-film with Λ = 72 nm.

1Ti/3Al-1.0 wt.% Cu, Λ =72 nm Al (111)/Ti (0002)					
Peak	Q [eV]	Error (98% conf.)	y-int. [K^{-1} s^{-1}]	Error (98% conf.)	Freq. Factor (v) [s^{-1}]
2	1.8	0.2	17.17	2.20	6.10E+11

The activation energies associated with the transitions belonging to the metastable superlattice phases of $TiAl_3$ were also determined by the Kissinger analysis as shown in Figure 5. 96.

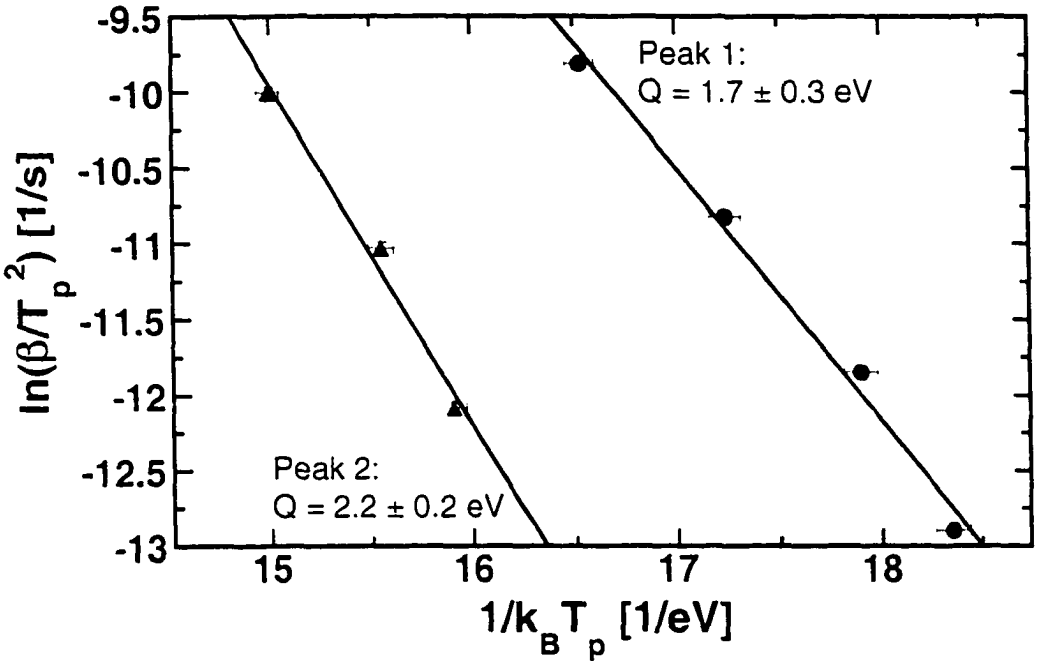

Figure 5. 96: Kissinger plot showing activation energy for formation of the metastable cubic and tetragonal superlattice structures of $TiAl_3$ in a 1Ti/3Al-1.0 wt.% Cu multilayer thin-film with Λ = 72 nm.

The results revealed activation energies of ~1.2 eV for the first peak (cubic $L1_2$) and ~1.7 eV for the second peak (high temperature-tetragonal). The output of the linear regression analysis is listed in Table 5. XXXIV.

Table 5. XXXIV: Results of Kissinger analysis of the metastable cubic and tetragonal superlattice phases in a 1Ti/3Al-1.0 wt.% Cu multilayer thin-film with Λ = 72 nm.

1Ti/3Al-1.0 wt.% Cu, Λ =72 nm $TiAl_3$ – metastable cubic and tetragonal superlattices					
Peak	Q [eV]	Error (98% conf.)	y-int. [K^{-1} s^{-1}]	Error (98% conf.)	Freq. Factor (v) [s^{-1}]
1 (cubic)	1.2	0.2	17.74	4.40	9.72E+11
2 (tetra)	1.7	0.2	23.57	9.40	4.48E+14

Figure 5. 97 is the Kissinger plot of the activation energy of the second high temperature superlattice peak visible in the two theta scans at ~51°. As before, the first

peak in the derivative plots was due to the formation of the diffraction peak, while the second was due to the disappearance of the diffraction peak.

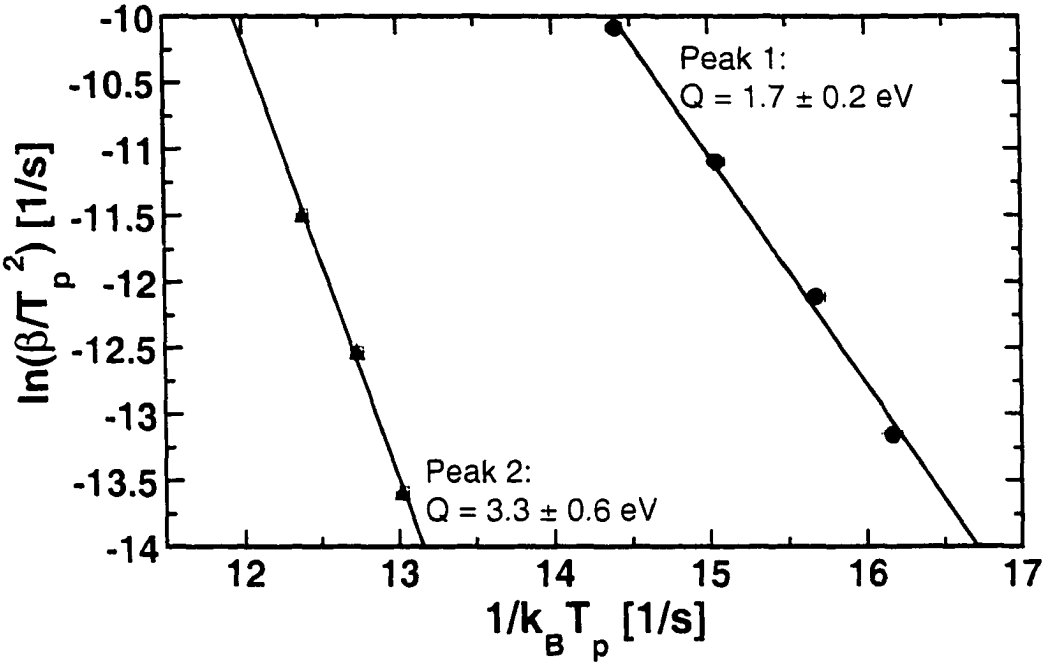

Figure 5. 97: Kissinger plot showing activation energies for metastable tetragonal $TiAl_3$ peaks in a 1Ti/3Al-1.0 wt.% Cu, Λ = 72 nm multilayer thin-film.

The results of the Kissinger analysis revealed an activation energy of 1.7 eV for the formation of the peak and 3.3 eV for the disappearance of the peak. The output of the linear regression fit is listed in Table 5. XXXV.

Table 5. XXXV: Results of Kissinger analysis of $TiAl_3$-metastable tetragonal superlattice peaks in a 1Ti/3Al-1.0 wt.% Cu, Λ = 72 nm multilayer thin-film.

1Ti/3Al-1.0 wt.% Cu, Λ =72 nm $TiAl_3$-metastable tetragonal superlattice					
Peak	Q [eV]	Error (98% conf.)	y-int. [K^{-1} s^{-1}]	Error (98% conf.)	Freq. Factor (v) [s^{-1}]
1	1.7	0.2	14.77	2.60	5.19E+10
2	3.3	0.6	29.36	5.40	2.16E+17

Finally, equilibrium $TiAl_3$ phase with the DO_{22} structure was observed to form at temperatures higher than ~600 °C. The (004) diffraction peak again contained two separated peaks. The effective activation energies for these peaks were determined from the Kissinger plot shown in Figure 5. 98.

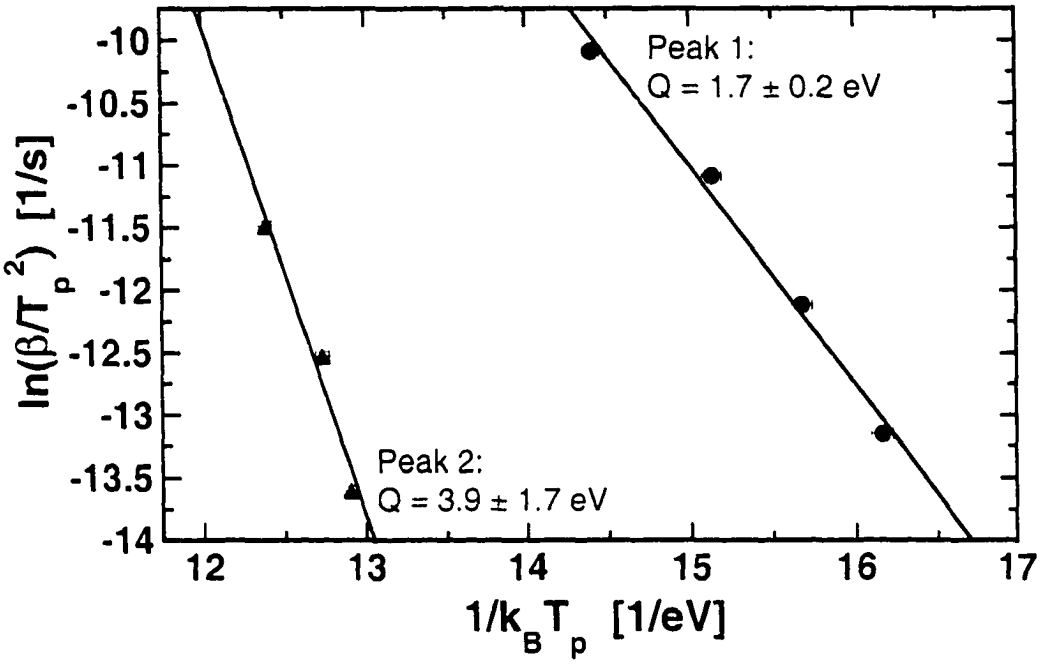

Figure 5. 98: Kissinger analysis of the $TiAl_3$-DO_{22} (004) peak from a 1Ti/3Al-1.0 wt.% Cu, Λ = 72 nm multilayer thin-film.

The regression output resulted in values of ~1.7 eV for the first peak and 3.9 eV for the second peak, summarized in Table 5. XXXVI.

Table 5. XXXVI: Results of Kissinger analysis for the TiAl3-DO_{22} (004) peak from a 1Ti/3Al-1.0 wt.% Cu, Λ = 72 nm multilayer thin-film.

1Ti/3Al-1.0 wt.% Cu, Λ =72 nm $TiAl_3$-DO_{22} (004)					
Peak	Q [eV]	Error (98% conf.)	y-int. [K^{-1} s^{-1}]	Error (98% conf.)	Freq. Factor (v) [s^{-1}]
1	1.7	0.2	15.09	4.00	7.20E+10
2	3.9	1.7	36.96	21.00	5.09E+20

5.4.2.4 Discussion: Ti/Al

Based on the temperatures of the phase formation and the results from the DSC experiments as well as electron diffraction results presented in the next chapter. The peaks in the window containing the Al (111)/Ti (0002) peak were associated with the formation of the metastable cubic, $L1_2$ structure of $TiAl_3$ (peak 1) and DO_{23} $TiAl_3$ or Ti_9Al_{23} (peak 2), depending on the temperature. These peaks were plotted as a function of Al layer thickness for the various periodicities studied at a heating rate of 180 °C/min as shown in Figure 5. 99.

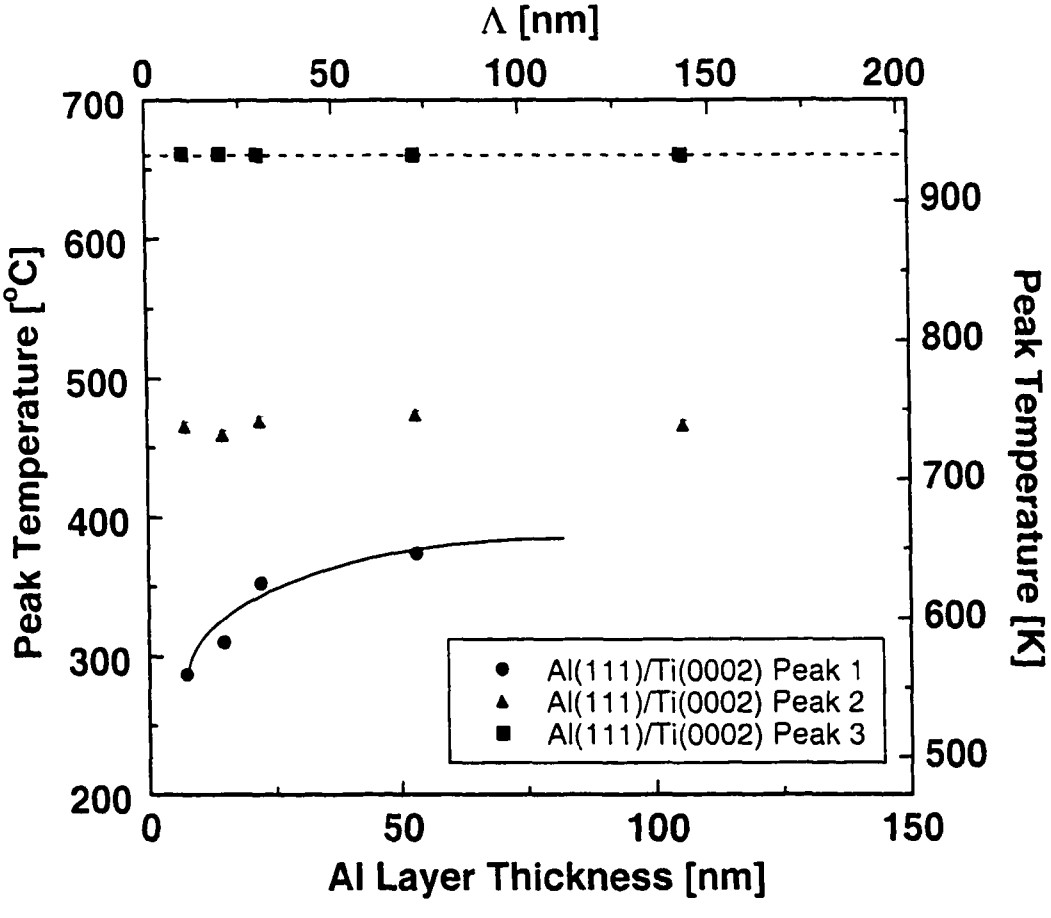

Figure 5. 99: Plot of peak temperatures obtained from XRD data as a function of Al layer thickness for the Al(111)/Ti(0002) peak for 1Ti/3Al-0 wt.% Cu multilayers heated at 180 °C/min from 100 °C to 700 °C. Dashed line indicates the melting point of Al (660 °C). Line drawn to guide the eye.

As with the XRD results, the peak associated with $L1_2$ formation shifted to higher temperatures with increasing Λ indicating a potential dependence on as-deposited grain size. On the other hand, the peak associated with the metastable tetragonal superlattice phase was independent of Λ with a small degree of scatter in the data. This suggested that the transformation of metastable cubic $TiAl_3$ to metastable tetragonal $TiAl_3$ occurred via different mechanism than for the $L1_2$ formation. Finally, the peak at 660 °C was found to be independent of layer thickness as would be expected for a melting transition.

Figure 5. 100 shows a similar plot for the XRD peak containing reflections of the cubic and tetragonal metastable structures as well as the contributions from the equilibrium tetragonal structure of $TiAl_3$. The transitions in XRD intensity found in this peak were expected to mirror the results from the Al and Ti peaks. This was observed for the first peak, assigned to (111) peak of the metastable cubic $L1_2$ phase. Peak 2 was again believed to result from the formation of the high temperature metastable structure of $TiAl_3$. Peak 2 exhibited an apparent shift to higher temperatures with increasing Λ. However, the peak position for the 333 nm film could not be accurately determined because of detector saturation.

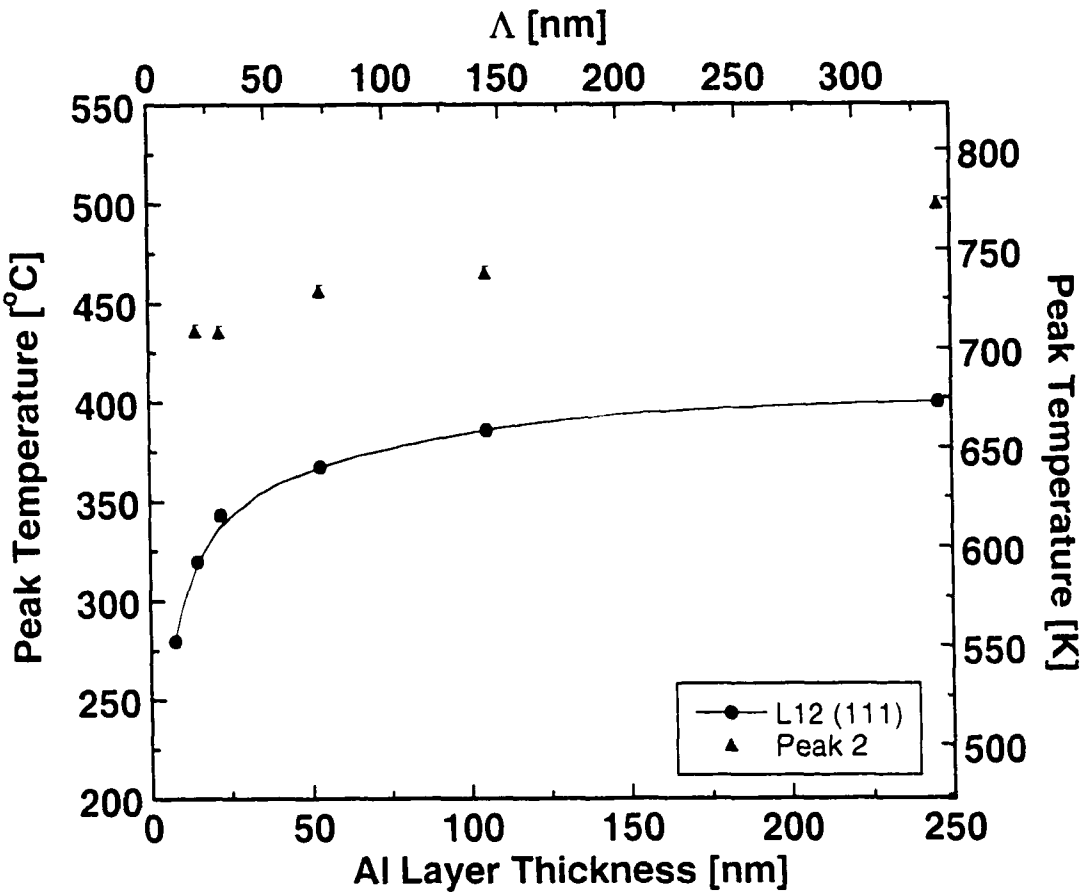

Figure 5. 100: Plot of peak temperatures obtained from XRD data as a function of Al layer thickness for the $TiAl_3$-metastable cubic and tetragonal superlattices and DO_{22} (103)/(112) peaks for 1Ti/3Al-0 wt.% Cu multilayers heated at 180 °C/min from 100 °C to 700 °C. Line drawn to guide the eye.

Figure 5. 101 is a plot of the minimum and maximum derivative temperatures for the peak at ~51° associated with the high temperature superlattice phase of $TiAl_3$. The temperatures were constant for peaks 1 and 2 in the 10, 20, and 30 nm films. Above ~50 nm there was significant scatter in the peak temperatures. Peak 2 was not observed for the 333 nm sample, because the phase had not entirely transformed to the equilibrium structure by 700 °C. The temperature range between the maximum and minimum temperatures was ~100 – 150 °C for this heating rate.

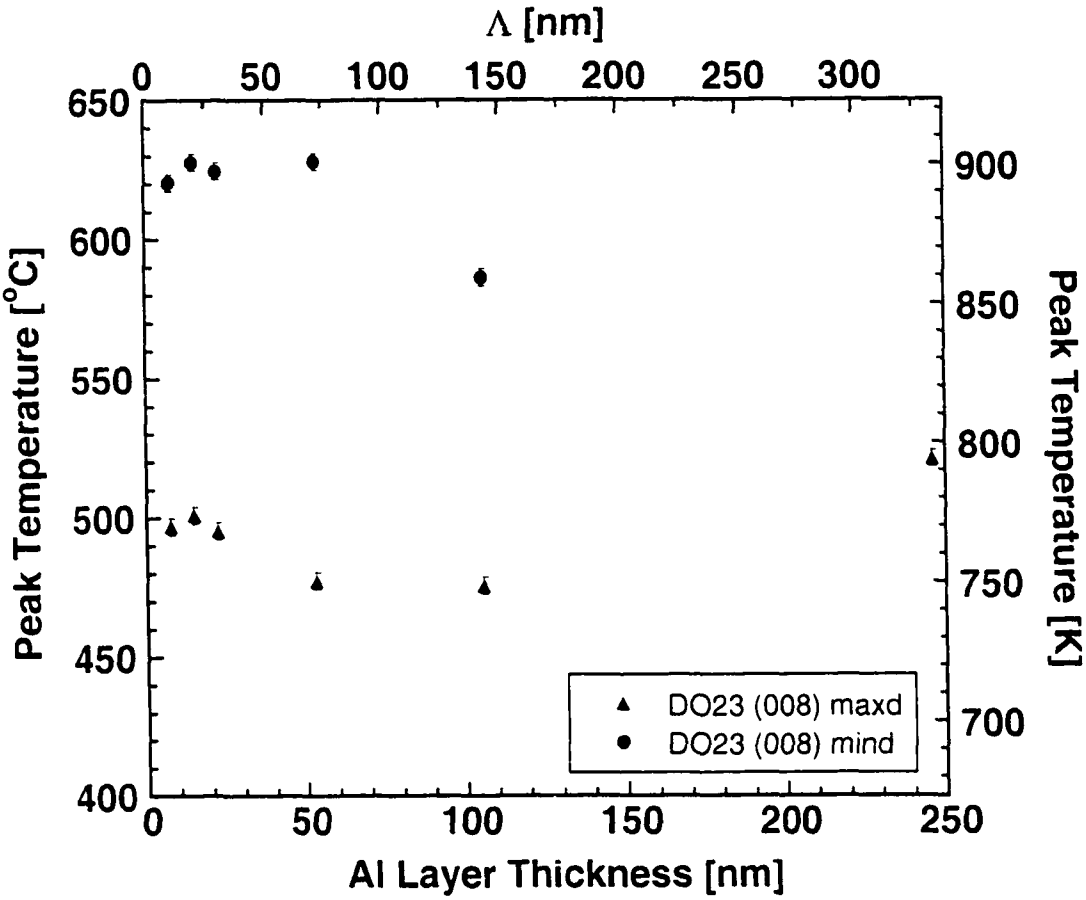

Figure 5. 101: Plot of peak temperatures obtained from XRD data as a function Al layer thickness for the $TiAl_3$-metastable tetragonal superlattice peak for 1Ti/3Al-0 wt.% Cu multilayers heated at 180 °C/min from 100 °C to 700 °C.

The peak positions of the equilibrium DO_{22} structure are plotted as a function of Al layer thickness in Figure 5. 102. Some fluctuation was evident in the temperature of peak 1. Peak 2 was constant in temperature until approximately ~100 nm. A substantial drop in peak temperature was observed for thicker Al layers. Thus, the mechanism for the double-peaked formation of the DO_{22} phase might be different from that found for the formation of the cubic $L1_2$ structure of $TiAl_3$ or $NbAl_3$ in the Nb/Al system (i.e., Coffey et al. 1989). The metastable cubic superlattice → metastable tetragonal superlattice transitions is also not well understood.

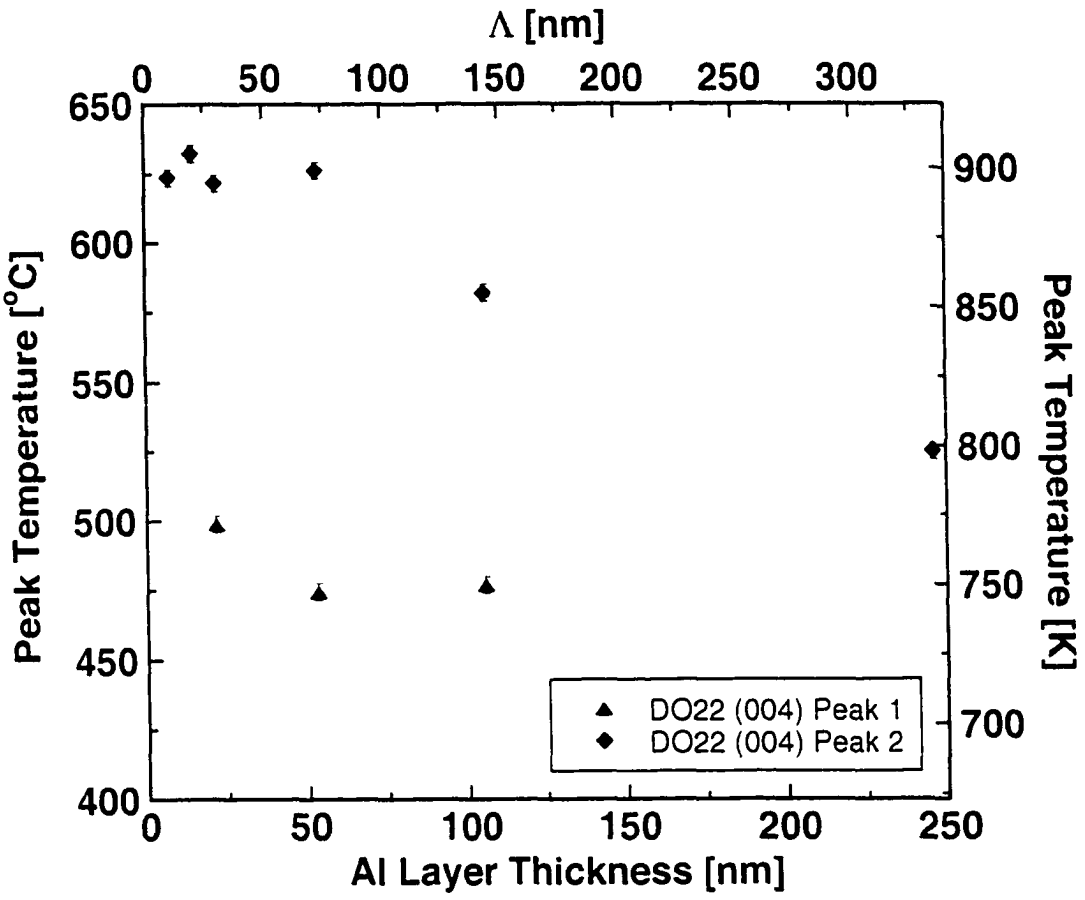

Figure 5. 102: Plot of peak temperatures obtained from XRD data as a function of Al layer thickness for the $TiAl_3$-DO_{22} (004) peak for 1Ti/3Al-0 wt.% Cu multilayers heated at 180 °C/min from 100 °C to 700 °C.

Figure 5. 103 shows the peak shift behavior for the 1Ti/3Al-0.5 wt.% samples for the Al (111)/ Ti (0002) reflections. Peak 1 was again observed to have a fairly strong dependence on Al layer thickness or Λ, and increased at a decreasing rate for the range of layer thicknesses investigated. The second peak was approximately constant in temperature for the films with $\Lambda < 72$ nm. The peak shifted to a higher temperature for the $\Lambda = 333$ nm sample. It was possible, however, that the peak for the tetragonal metastable phase was overshadowed by the second peak of $L1_2$ formation. If this was the case, the temperature of peak 2 could be inaccurate.

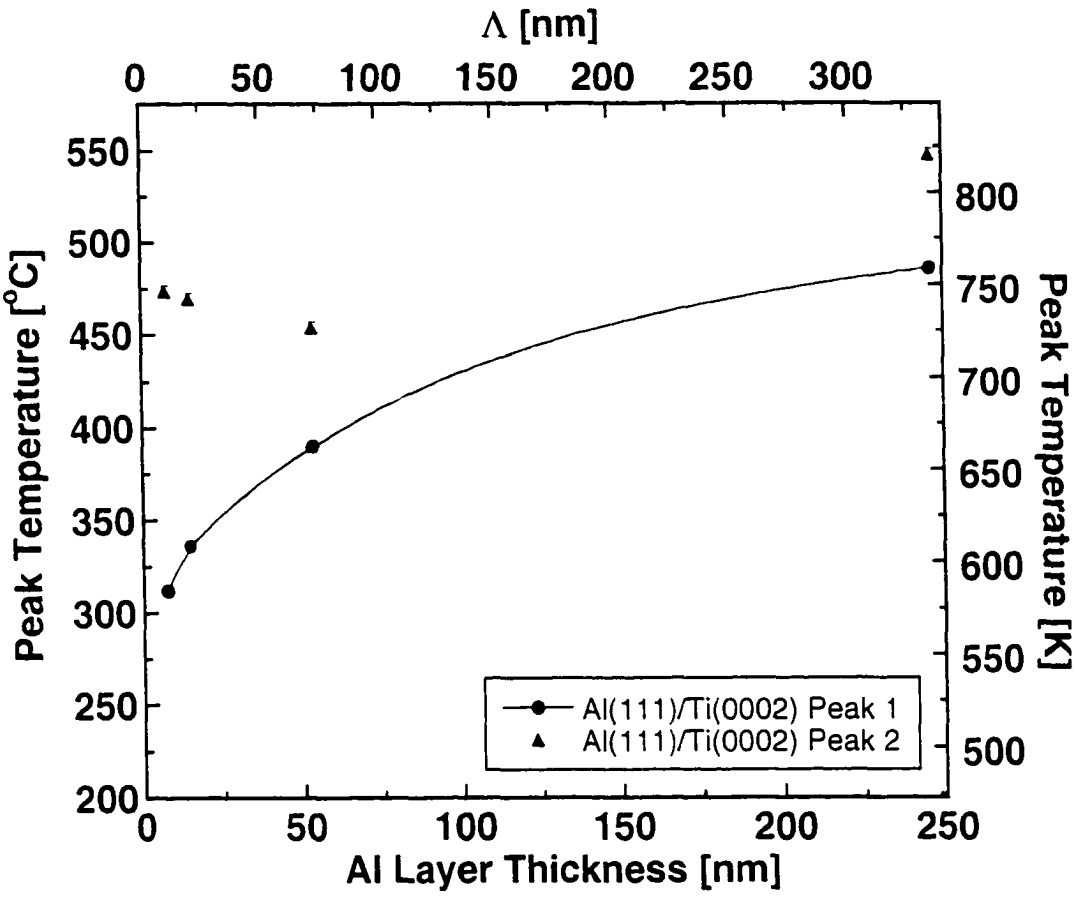

Figure 5. 103: Plot of peak temperatures obtained from XRD data as a function of Al layer thickness for Al(111)/Ti(0002) peak for 1Ti/3Al-0.5 wt.% Cu multilayers heated at 180 °C/min from 100 °C to 700 °C. Line drawn to guide the eye.

Figure 5. 104 shows the results from the diffraction peak of the superlattice reflections belonging to the metastable cubic and tetragonal structures (peak 2)of $TiAl_3$ in a plot of peak temperature vs. Al layer thickness.

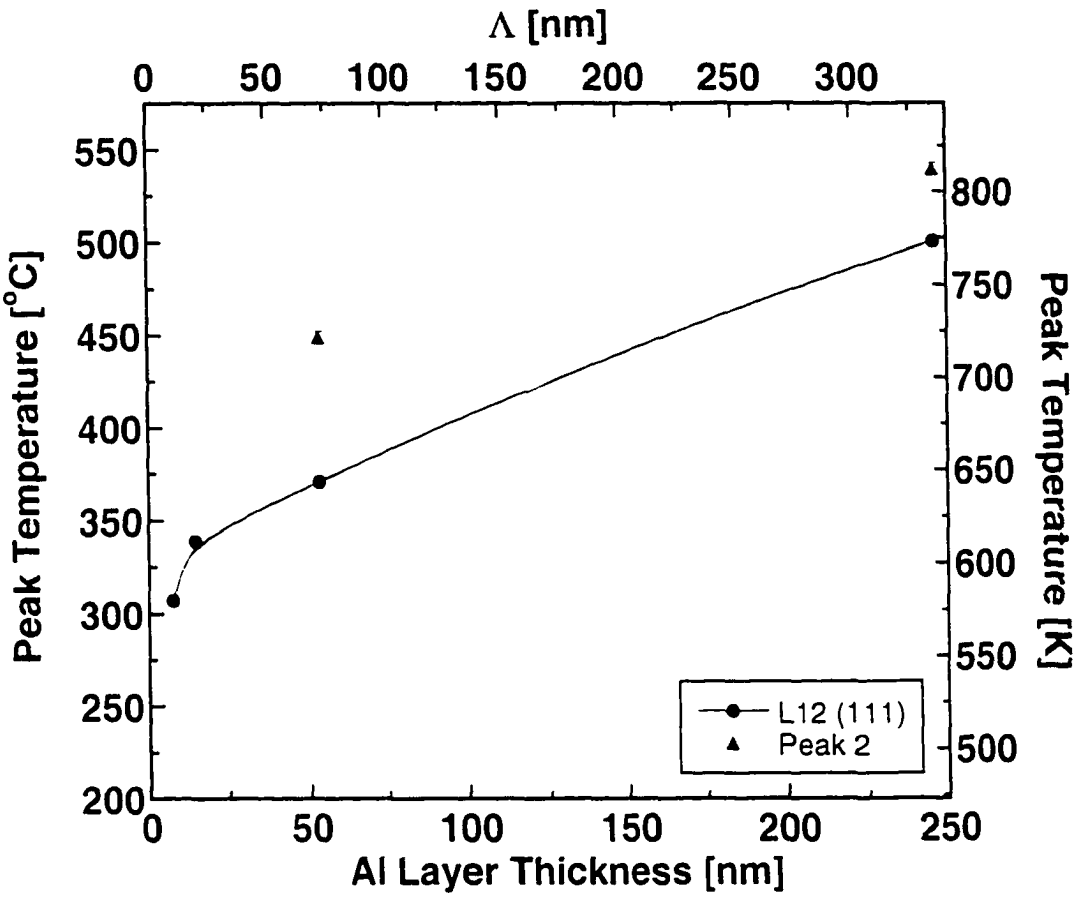

Figure 5. 104: Plot of peak temperatures obtained from XRD data as a function of Al layer thickness for $TiAl_3$-metastable cubic (Peak 1) and metastable (Peak 2) transitions for 1Ti/3Al-0.5 wt.% Cu multilayers heated at 180 °C/min from 100 °C to 700 °C. Line drawn to guide the eye.

As in the previous graph, the first peak was also attributed to the (111) peak of the metastable $L1_2$ phase. Again, a pronounced shift was observed with layer thickness suggesting a relationship between the as-deposited microstructure and formation kinetics. Unfortunately, only two films showed discernable peaks for the second transition assumed to belong to the formation of the metastable tetragonal phase. The peak at t_{Al} = 50 nm was consistent with the temperatures of peak 2 in Figure 5. 100. The temperature of peak 2 at t_{Al} = 250 nm was significantly higher, but was difficult to determine accurately due to the apparent overlap of two peaks.

Figure 5. 105 shows the results from the metastable tetragonal superlattice peak at ~51°. As before. Peak 1 is due to the onset of the diffracted intensity while peak 2 was from the decrease in diffracted intensity. Both peaks were relatively constant in temperature, independent of layer thickness although Peak 2 exhibited more scatter in temperature.

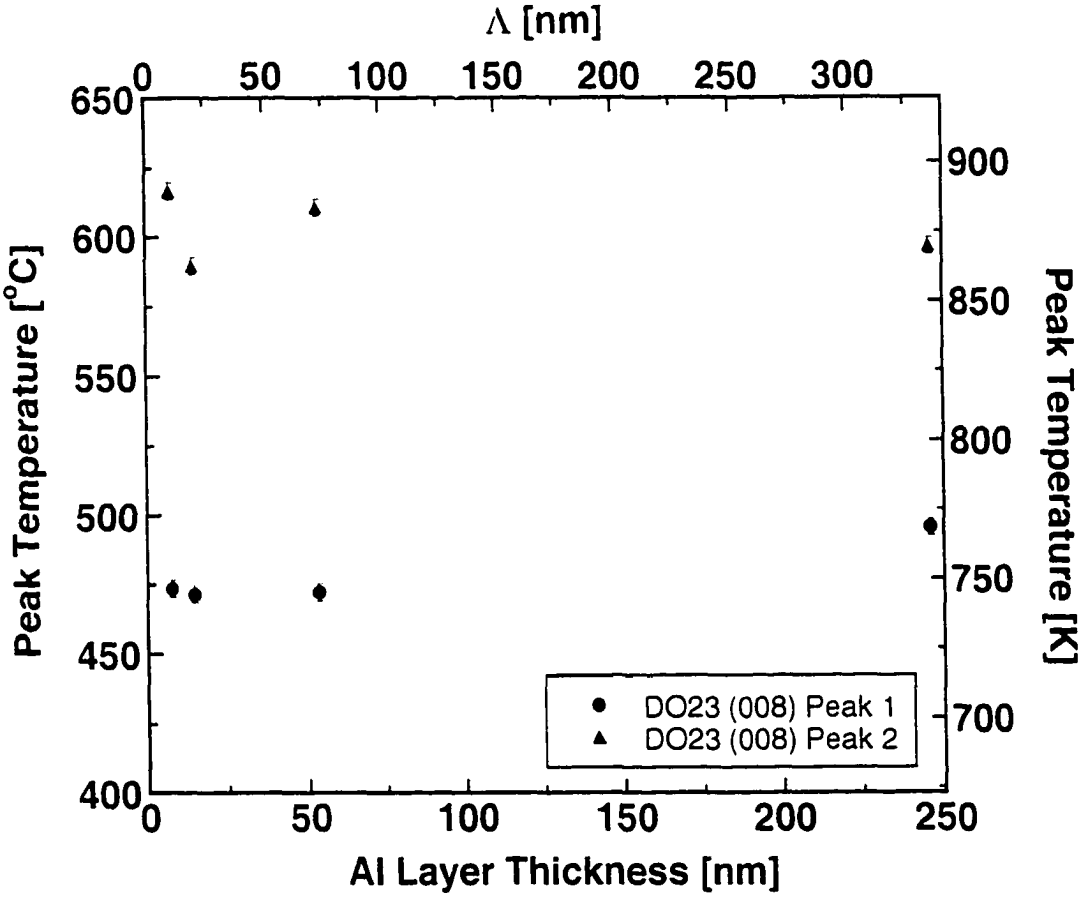

Figure 5. 105: Plot of peak temperatures obtained from XRD data as a function of Al layer thickness for the $TiAl_3$-metastable tetragonal superlattice peak for 1Ti/3Al-0.5 wt.% Cu multilayers heated at 180 °C/min from 100 °C to 700 °C.

The separation between the peaks also remained between 100-150 °C as with the 0 wt.% Cu samples.

Figure 5. 106 shows the peak positions for the (004) reflection of the equilibrium DO_{22} structure. Data for peak 1 was relatively sparse and the data did not indicate a clear trend. However, it appeared as though temperature for peak 2 was constant then shifted to lower temperatures in the Λ = 333 nm sample.

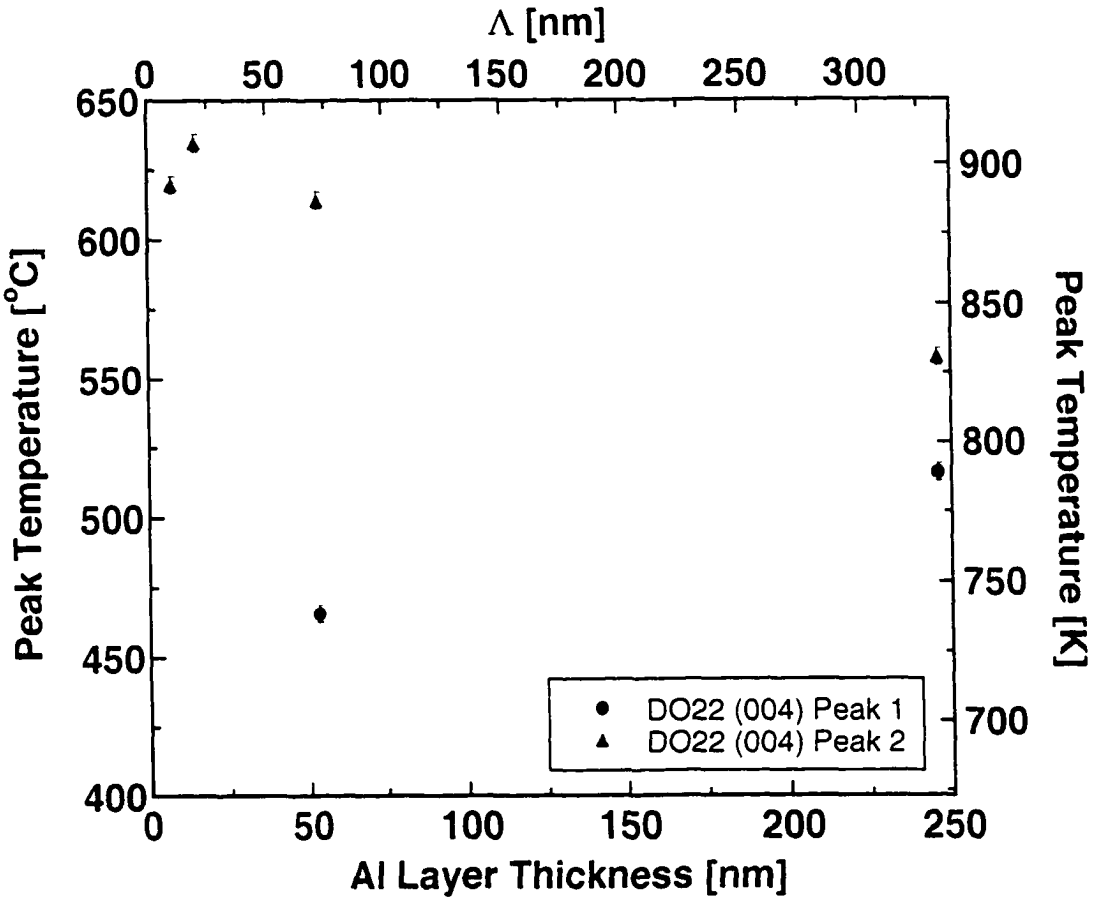

Figure 5. 106: Plot of peak temperatures obtained from XRD data as a function of Al layer thickness for the $TiAl_3$-DO_{22} (004) peak for 1Ti/3Al-0.5 wt.% Cu multilayers heated at 180 °C/min from 100 °C to 700 °C.

Figure 5. 107 plots the peak temperatures of the two transitions evident in the Al (111)/Ti (0002) diffraction peak for the 0 and 0.5 wt.% Cu samples. Recall that the first peak corresponded to the formation of cubic $TiAl_3$ while the second peak was attributed to the formation of the metastable tetragonal structure of $TiAl_3$. For films with the

identical layer thicknesses, the peak temperatures for peak 1 were ~25° C higher in the films containing Cu. The addition of Cu did not appear to have a systematic effect on the temperature of peak 2.

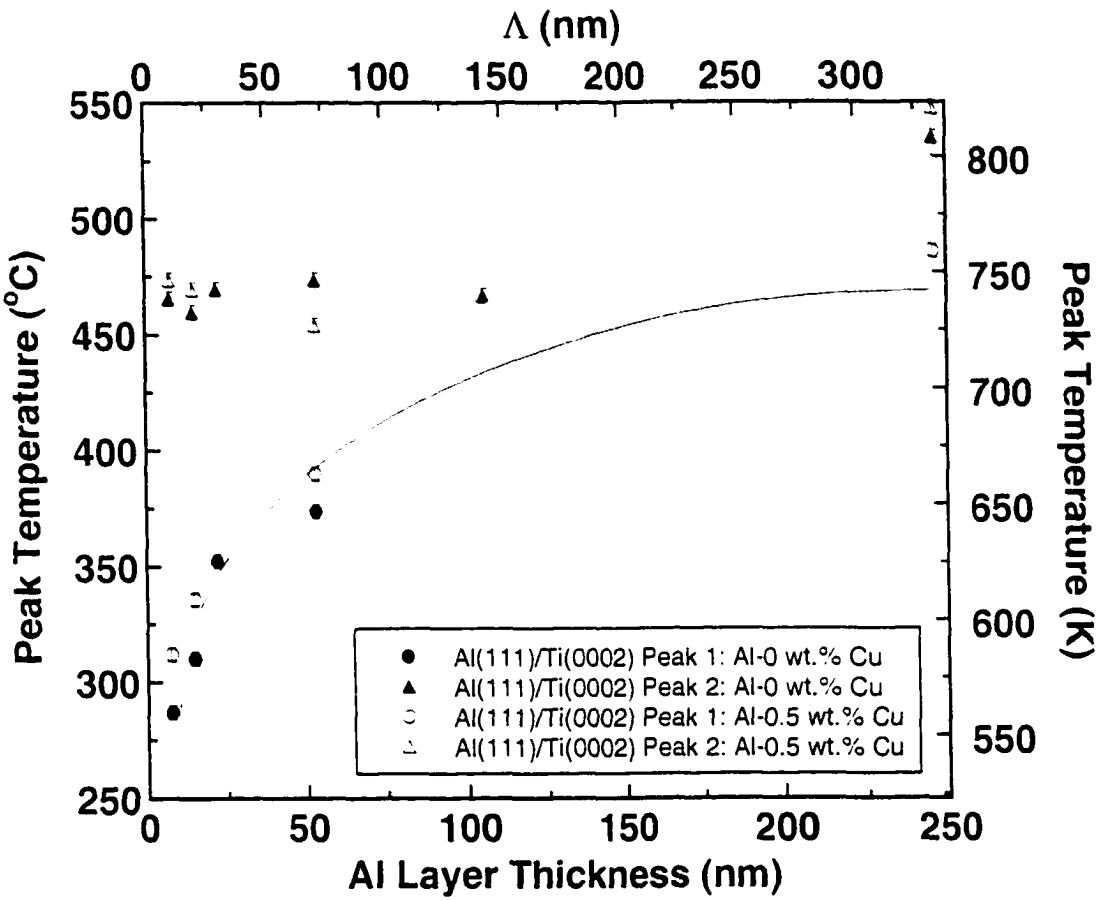

Figure 5. 107: Comparison of the peak temperatures for the transitions found in the Al(111)/Ti (0002) peak as a function of Al layer thickness for 1Ti/3Al multilayers with 0 and 0.5 wt.% Cu. Line drawn to guide the eye.

Figure 5. 108 compares peak 1 associated with the formation of the cubic $L1_2$ phase in the 0 wt.% and 0.5 wt.% Cu samples. At all bilayer periods, the peak temperature was ~25 °C higher for the samples containing Cu. This increase in peak temperature corroborates the DSC results and demonstrates that the addition of Cu retards the formation of the $L1_2$ structure in the Ti/Al multilayers.

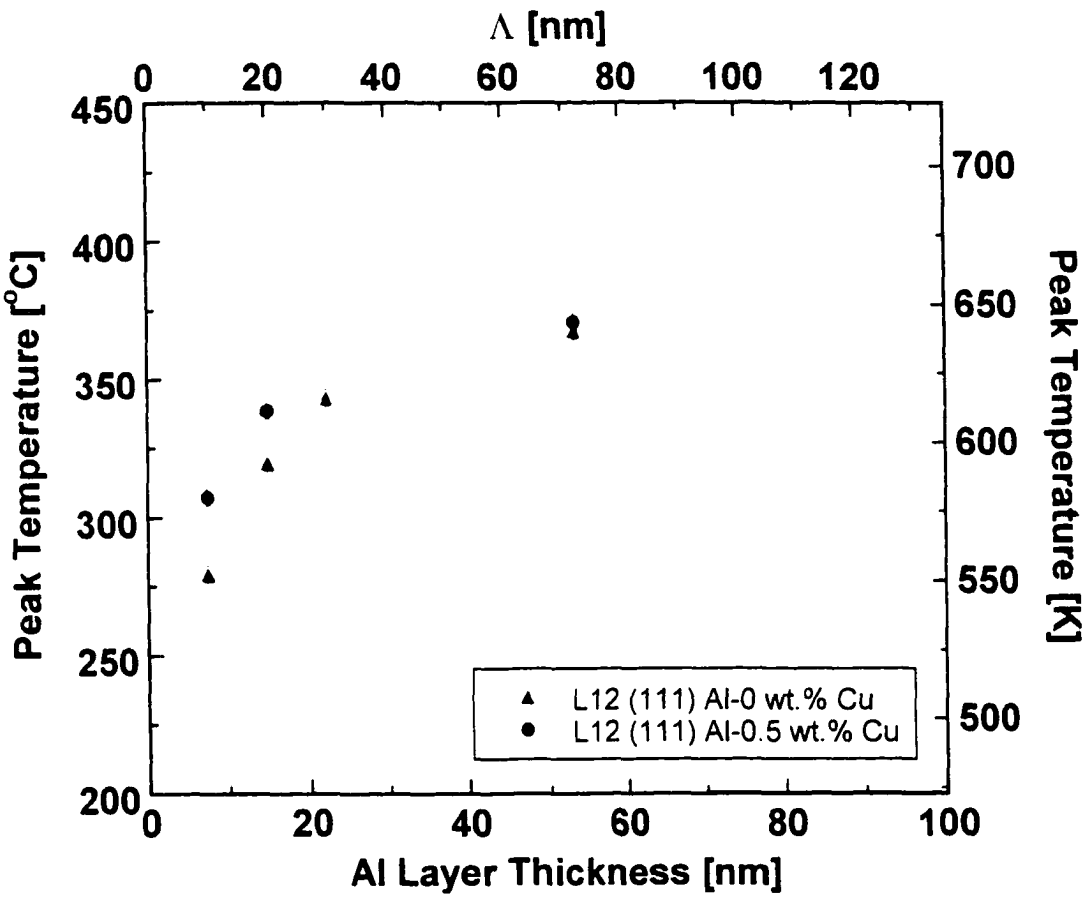

Figure 5. 108: Comparison of the peak temperatures for the $TiAl_3$-$L1_2$ (111) peaks as a function of Al layer thickness for 1Ti/3Al multilayers with 0 and 0.5 wt.% Cu.

Figure 5. 109 compares the temperatures of peaks 1 and 2 associated with the formation of the metastable, tetragonal $TiAl_3$ phase as a function of layer thickness for two Cu concentrations. The scatter in the data with Λ did not permit a consistent description of the effect of Cu on the formation of this metastable phase. In some cases the presence of Cu appeared to lower the temperature of the metastable phase formation and disappearance. This was opposite to the effect of Cu on the formation temperature of the $L1_2$ structure. In other words, the Cu might be affecting the formation of the various

phases in different ways -- in one case hindering formation while in the other promoting the formation of the metastable phase.

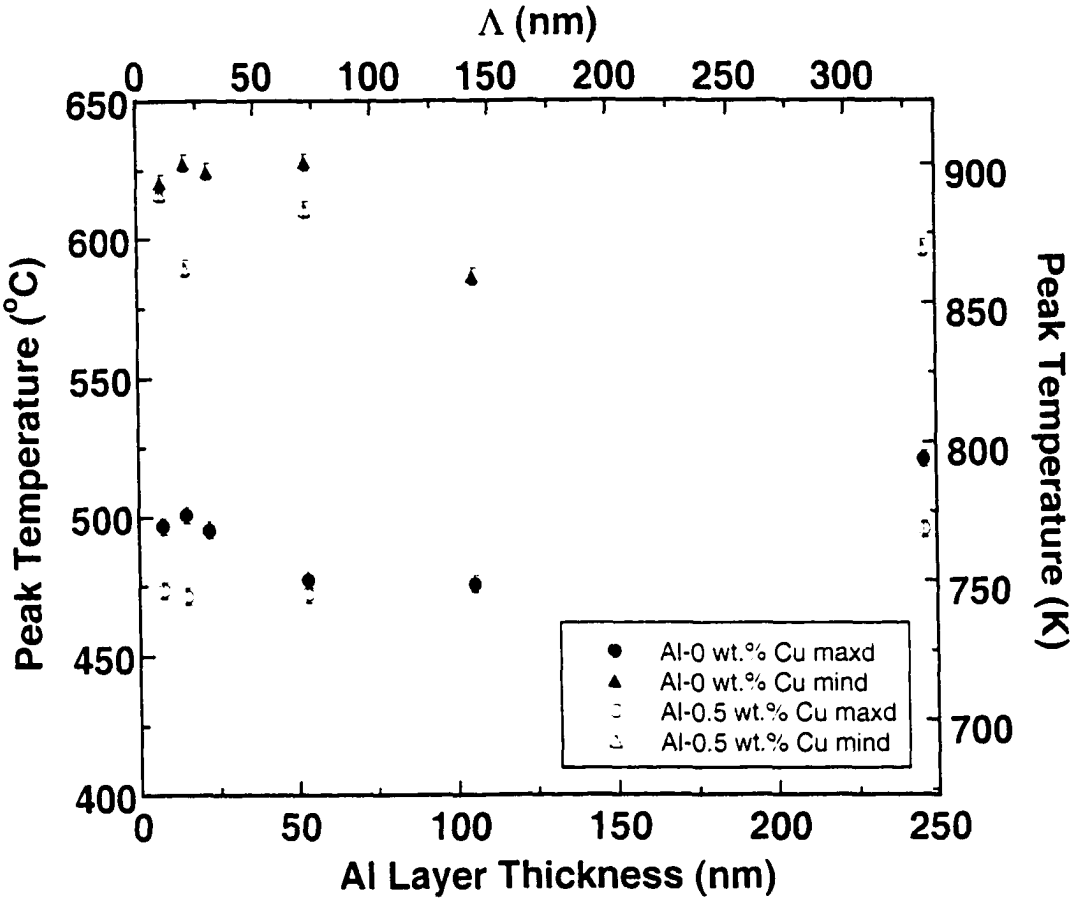

Figure 5. 109: Comparison of the peak temperatures for the $TiAl_3$-metastable tetragonal phase from the XRD data as a function of Al layer thickness for 1Ti/3Al multilayers with 0 and 0.5 wt.% Cu.

Figure 5. 110 is a plot of the peak temperatures for the equilibrium DO_{22} $TiAl_3$ phase obtained from the *in situ* XRD data of the (004) peak as a function of Al layer thickness for 0 and 0.5 wt.% Cu. Again, a clear dependence on peak temperature was not observed for either peak 1 or peak 2 partly due to the scatter in the data and also because of the absence of peaks at certain layer thicknesses.

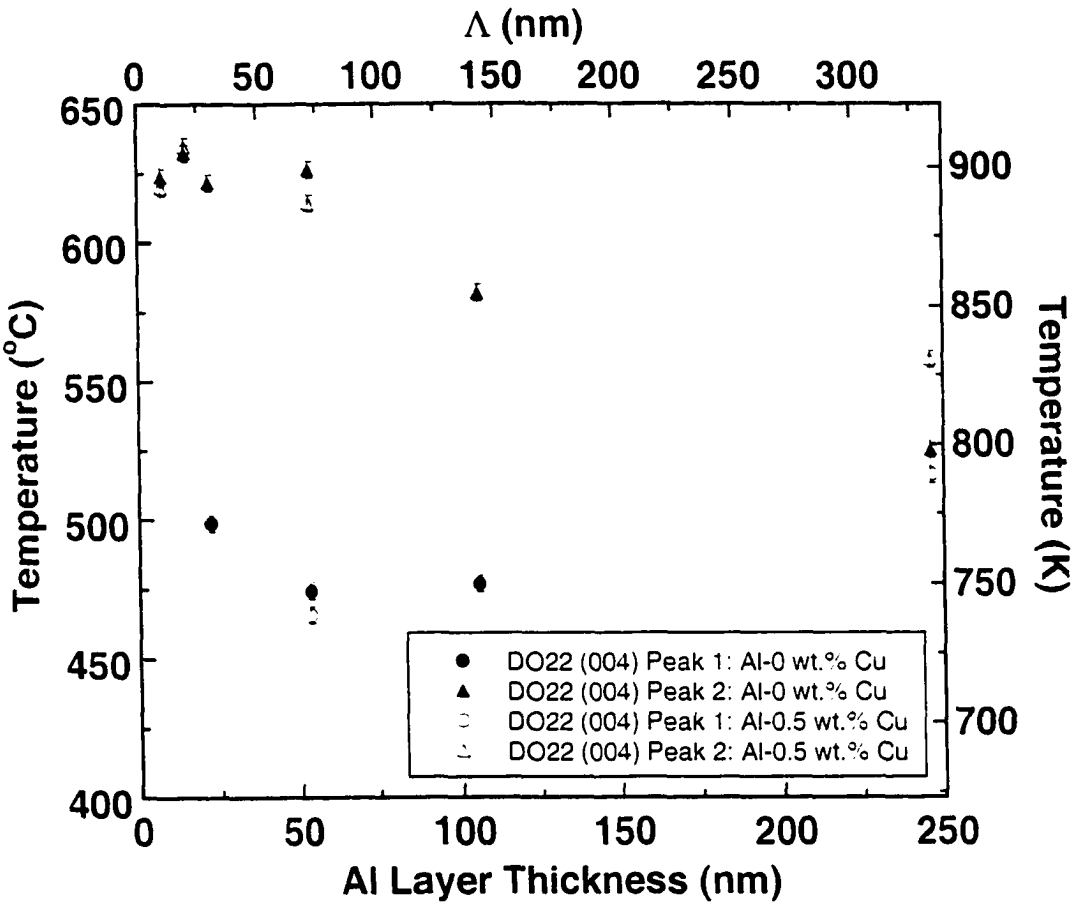

Figure 5. 110: Comparison of the peak temperatures for the $TiAl_3$-DO_{22} (004) peaks as a function of Al layer thickness for 1Ti/3Al multilayers with 0 and 0.5 wt.% Cu.

Figure 5. 111 shows the XRD intensity contour plots of 10 and 20 nm 1Ti/3Al multilayers with 0 at 0.5 wt.% Cu as functions of 2θ and temperature. The main difference associated with the addition of Cu in both samples was the disappearance of the peak at 44° previously attributed to the Ti_9Al_{23} phase, and an increase in relative intensity of the metastable tetragonal phase and the equilibrium DO_{22} phases.

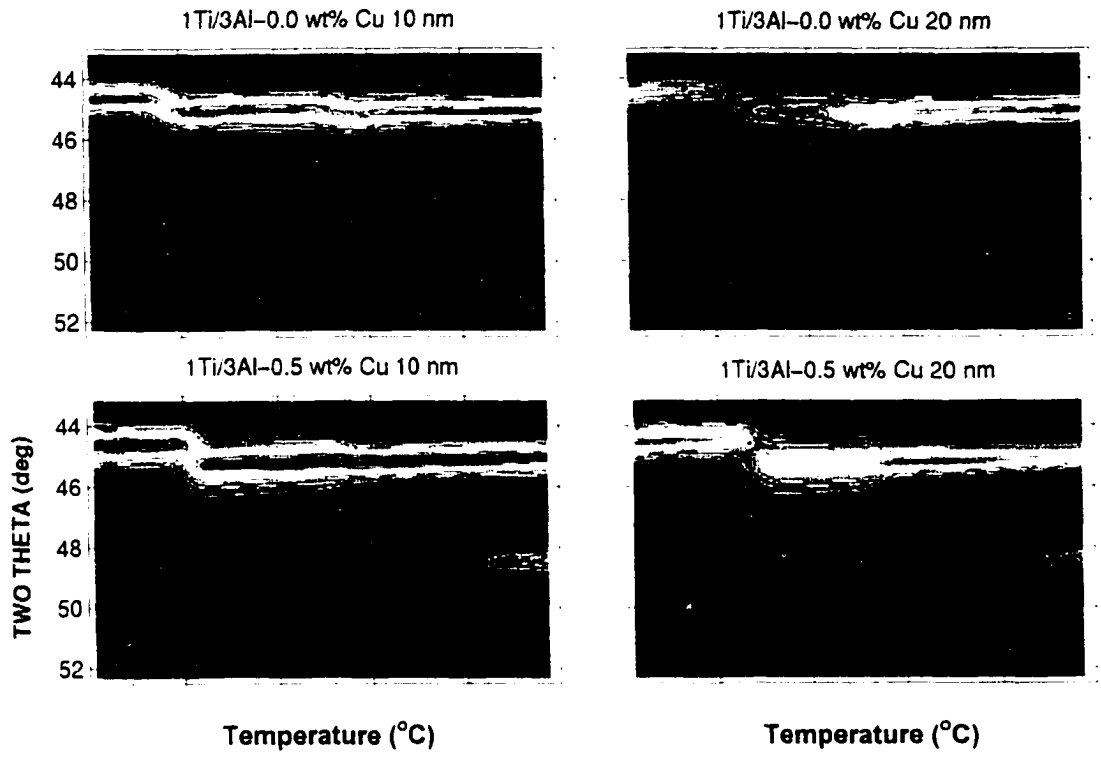

Figure 5. 111: Comparison of XRD intensity as a function of 2θ and temperature for 1Ti/3Al multilayers with 0 and 0.5 wt.% Cu with Λ = 10 and 20 nm heated at 180 °C/min.

Figure 5. 112 shows a similar series of plots comparing films with 1Ti/3Al, Λ = 72 nm containing 0, 0.5, and 1.0 wt.% Cu. Although the derivatives of the integrated intensities are more useful for determining the onset of phase formation, several observations can be made regarding the nature of phase formation. In this case the disappearance of the Al (111)/Ti (0002) peak occurs at lower temperatures for the 0 wt.% Cu sample as does the appearance of the DO_{22} $TiAl_3$ peak. A trend in the metastable tetragonal phase was not obvious from these plots, but it would appear that Cu delays the formation of the cubic and equilibrium form of $TiAl_3$.

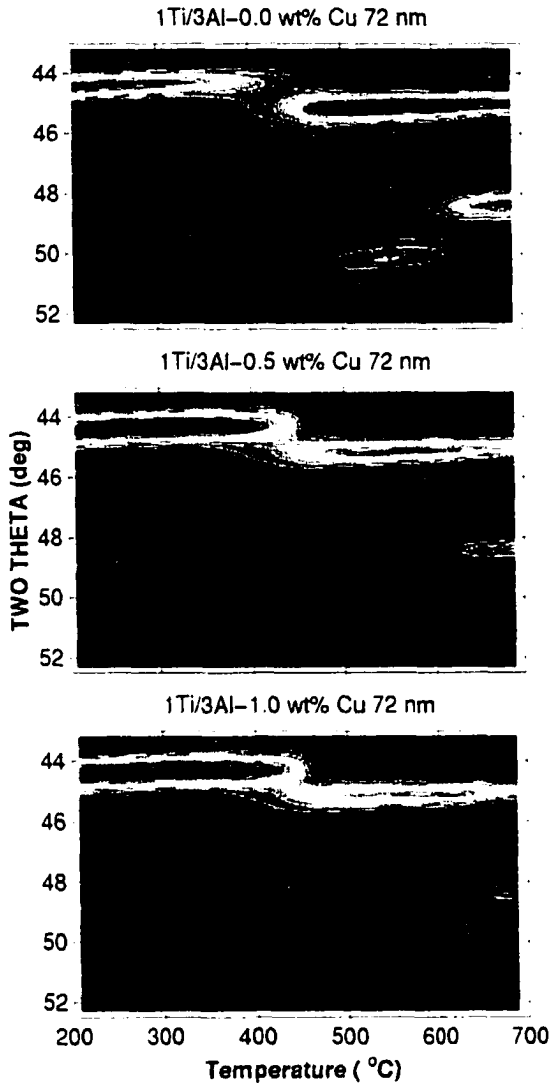

Figure 5. 112: Comparison of XRD intensity as a function of 2θ and temperature for 1Ti/3Al multilayers with 0. 0.5, and 1.0 wt.% Cu with Λ = 72 nm.

In order to more easily compare the effects on the Cu additions on the 72 nm films the normalized derivatives of the integrated intensity were plotted on one graph. Figure 5. 113 is such a plot and shows the Al (111)/Ti (0002) window for the 0. 0.5 and 1.0 wt.% Cu samples. The 0 wt.% Cu sample show three well-defined peaks at ~375 °C. 400 °C and 475 °C.

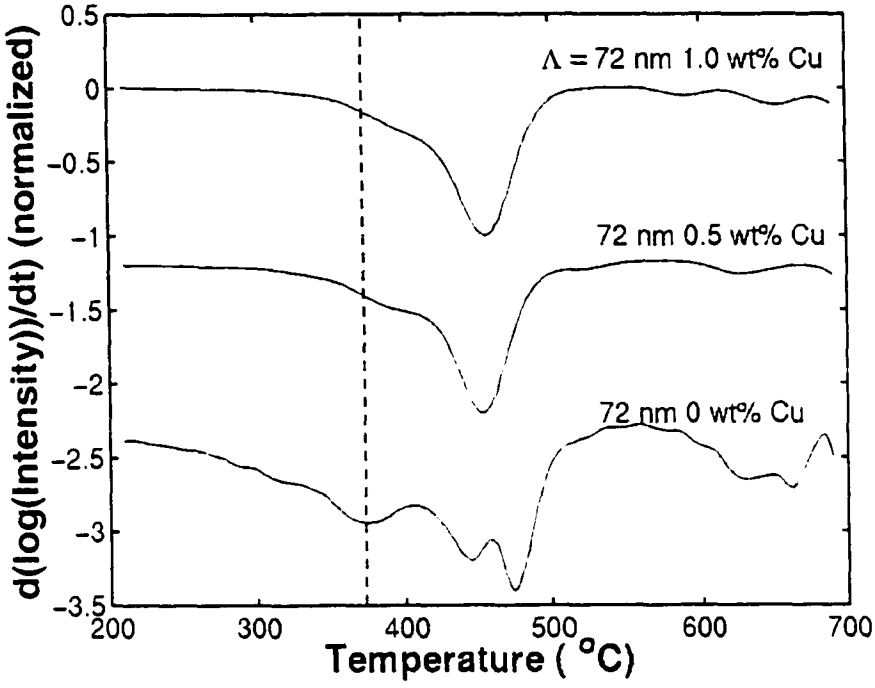

Figure 5. 113: Normalized first derivative of the integrated intensity of the Al (111)/Ti (0002) peak for 1Ti/3Al multilayers with Al-0, 0.5, and 1.0 wt.% Cu and Λ = 72 nm heated at 180 °C/min from 100 °C to 700 °C in purified He.

The first peak decreased in height when Cu was added to the Al, shifted slightly to the right, and eventually appeared as a shoulder on the second peak. Either the second or third peak has disappeared. The increase in temperature of the first peak indicated a lag in the consumption of the Al/Ti caused by the presence of the Cu.

Figure 5. 114 compares the derivative of the integrated intensity for the window encompassing the metastable cubic and tetragonal $TiAl_3$ phases and the equilibrium $TiAl_3$ structures for the 72 nm films with 0, 0.5 and 1.0 wt.% Cu. The peak shift was not as prominent in these curves, however, the relative heights of the peaks has changed, possibly due to changes in the rate of phase formation as a result of the presence of the Cu. In this case the first peak, initially half the height of the second peak, was nearly

equal in height at 0.5 wt.% Cu and exceeded the height of the second peak in the 1.0 wt.% Cu sample.

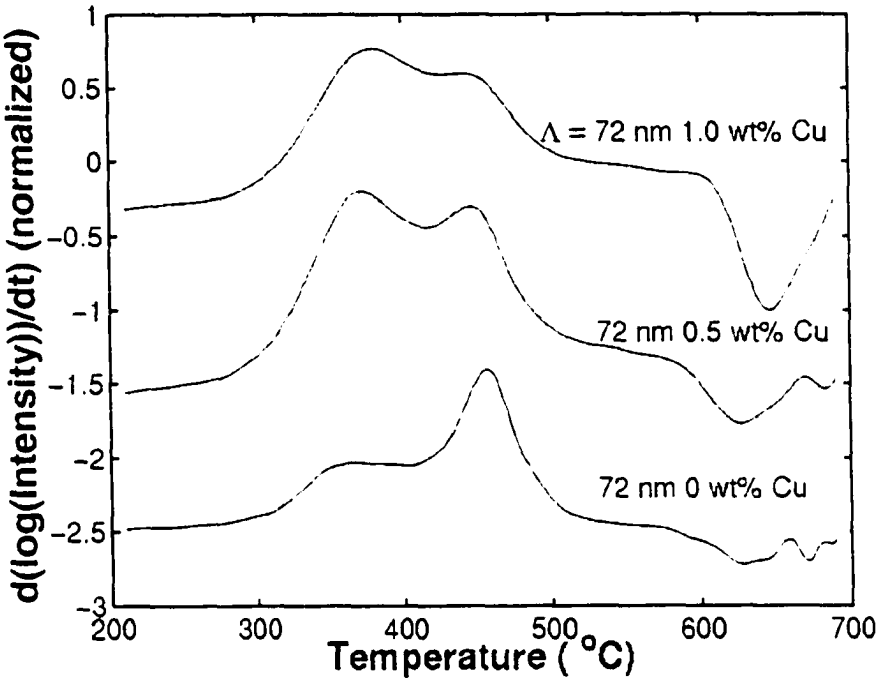

Figure 5. 114: First derivative of integrated intensity of the peak for $TiAl_3$ metastable structures and equilibrium structure for 1Ti/3Al multilayers with Al-0, 0.5, and 1.0 wt.% Cu and Λ = 72 nm heated at 180 °C/min from 100 °C to 700 °C in purified He.

Figure 5. 115 shows the peaks arising from the derivative of the integrated intensity of the XRD peak resulting from the formation the tetragonal superlattice structure of $TiAl_3$ and its transformation (and hence disappearance) to the equilibrium structure. The temperatures for both transformations were equal within measurement errors for all three samples indicating that the additions of Cu did not strongly affect the temperatures associated with the formation of this phase.

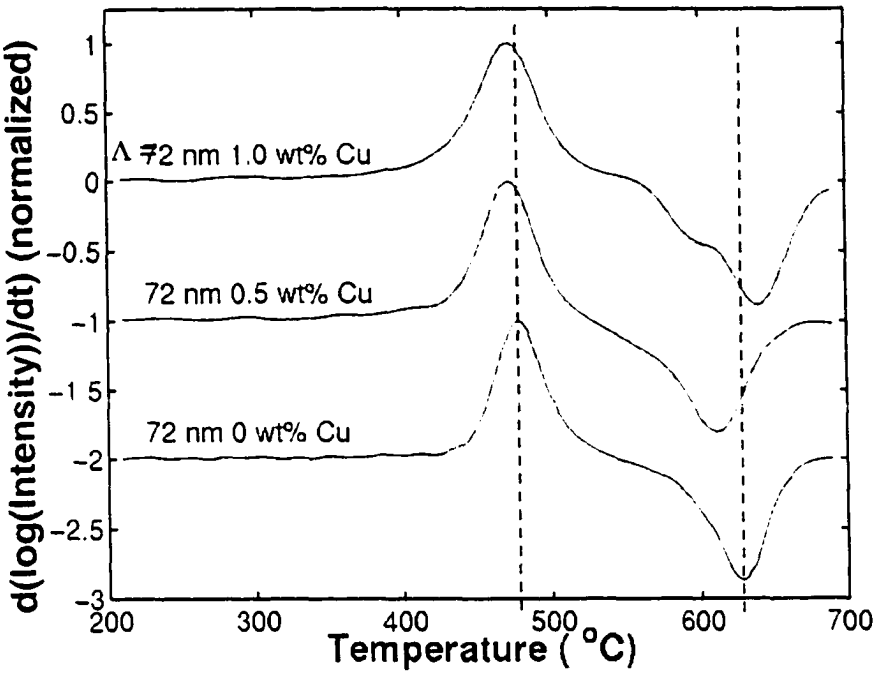

Figure 5. 115: First derivative of integrated intensity of the peak for $TiAl_3$-metastable tetragonal phase for 1Ti/3Al multilayers with Al-0, 0.5, and 1.0 wt.% Cu and Λ = 72 nm heated at 180 °C/min from 100 °C to 700 °C in purified He.

The values of the maximum and minimum of the derivatives are plotted in Figure 5. 116. This shows the relative constancy of the temperatures as well as the consistency of the temperature over which the metastable phase was forming.

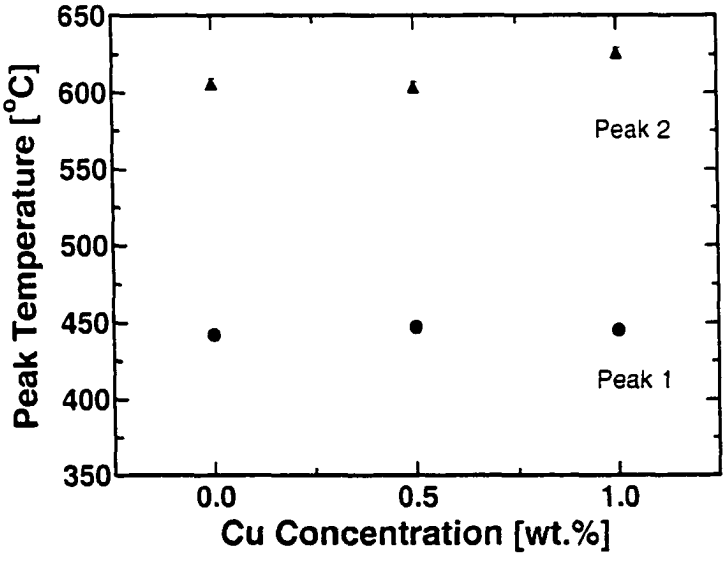

Figure 5. 116: Peak temperature determined from XRD plotted as a function of Cu concentration for the $TiAl_3$-metastable tetragonal phase of a Λ = 72 nm annealed at 180 °C/min.

Lastly, the peak transition temperatures obtained from the derivative of the integrated intensity of the equilibrium DO_{22} $TiAl_3$ (004) diffraction peak were plotted for the 72 nm multilayers with 0, 0.5, and 1.0 wt.% Cu as shown in Figure 5. 116. Peak 1 varied in shape and relative height among the three samples and shifted to slightly lower temperatures with the addition of Cu. The second peak did not show a consistent trend and varied in temperature from ~615-640 °C.

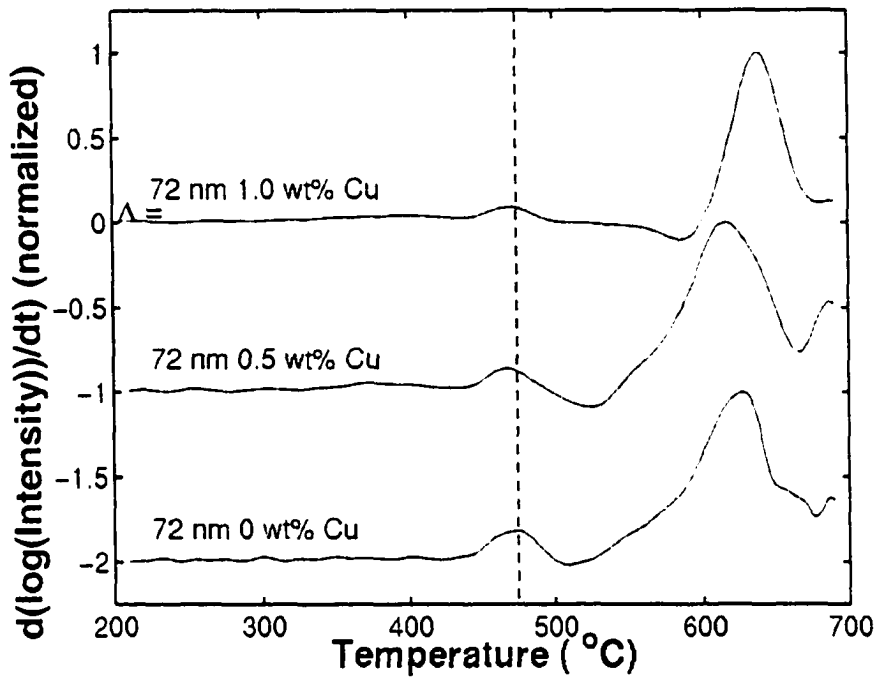

Figure 5. 117: First derivative of integrated intensity of the peak for $TiAl_3$-DO_{22} (004) for 1Ti/3Al multilayers with Al-0, 0.5, and 1.0 wt.% Cu and Λ = 72 nm heated at 180 °C/min from 100 °C to 700 °C in purified He.

The peak positions are plotted as a function of Cu concentration in Figure 5. 118. This shows the behavior outlined in the above description.

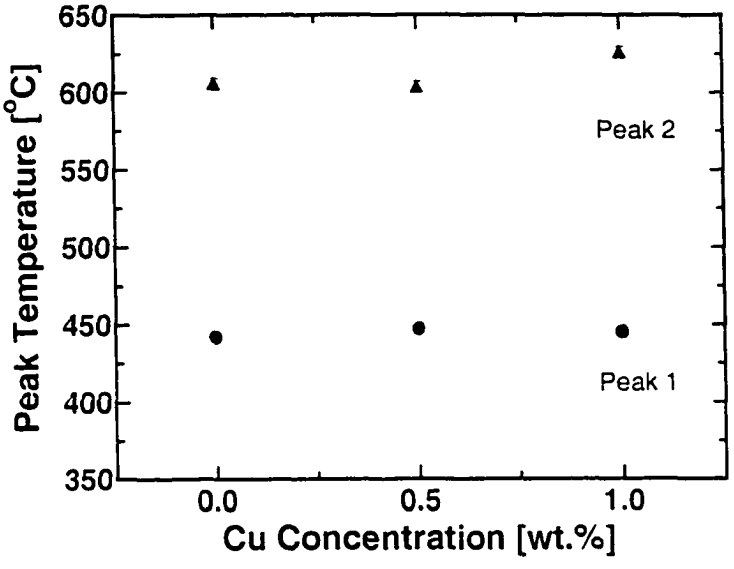

Figure 5. 118: Peak temperature determined from XRD plotted as a function of Cu concentration for the $TiAl_3$-DO_{22} (004) peak of a Λ = 72 nm annealed at 180 °C/min.

The final comparison that was made from the measurements performed using the 72 nm films was to ascertain if there was any effect on the activation energies caused by the addition of Cu. This was accomplished by creating a series of graphs that plot the activation energies determined by the Kissinger analysis as a function the Cu concentration. The first of such graphs is shown in Figure 5. 119 and contains the activation energies determined from the peaks in the Al(111)/Ti (0002) reflections. Only one measurement was made for the first peak for the 0 wt.% Cu sample, however, it is included for comparison. The second peak does not exhibit significant variation within the limits of the error bars.

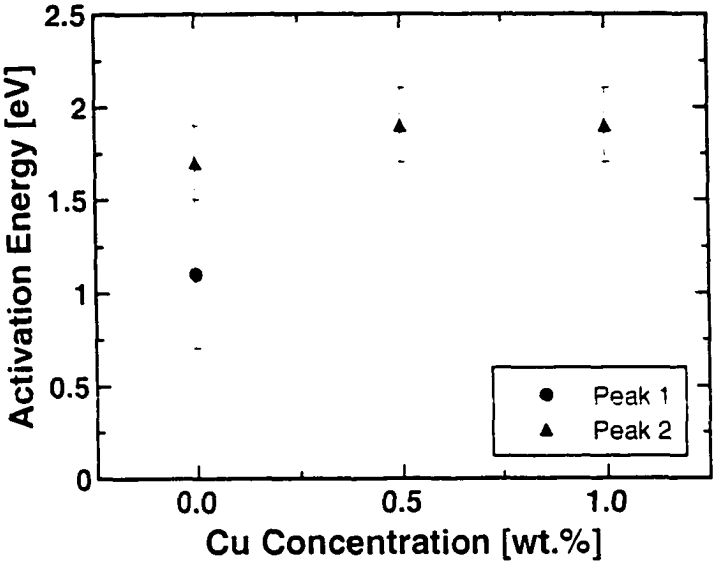

Figure 5. 119: Activation energies for peaks 1 and 2 determined from XRD data plotted as a function of Cu concentration for the Al(111)/Ti(0002) peak of a Λ = 72 nm multilayer. Note error bars are 2σ.

The second in the series of graphs contains the activation energies obtained from the two peaks corresponding to the formation of the metastable phases indicated by peak 1 (cubic, $L1_2$) and peak 2 (tetragonal) as shown in Figure 5. 120. Again, no trends were evident in the activation energies and the values were similar within measurement error.

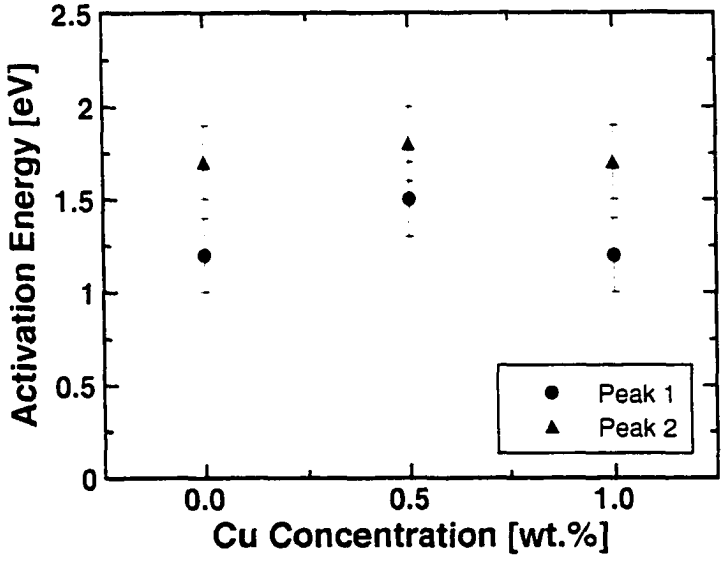

Figure 5. 120: Activation energies for peaks 1 and 2 determined from XRD data plotted as a function of Cu concentration for the $TiAl_3$ cubic (peak 1) and tetragonal (peak 2) superlattice peaks of a Λ = 72 nm multilayer. Note error bars are 2σ.

The third graph plots the activation energies determined from the metastable tetragonal structure of $TiAl_3$ and is shown in Figure 5. 121. The onset peak for the formation of this phase maintained a constant activation energy similar to peak 2 of the Al (111)/Ti (0002) peak and the second peak determined from superlattice reflection at ~45°. The decay peak, however, showed a marked drop in activation energy as Cu concentration increased, despite the large errors on the 0 wt. % Cu data point.

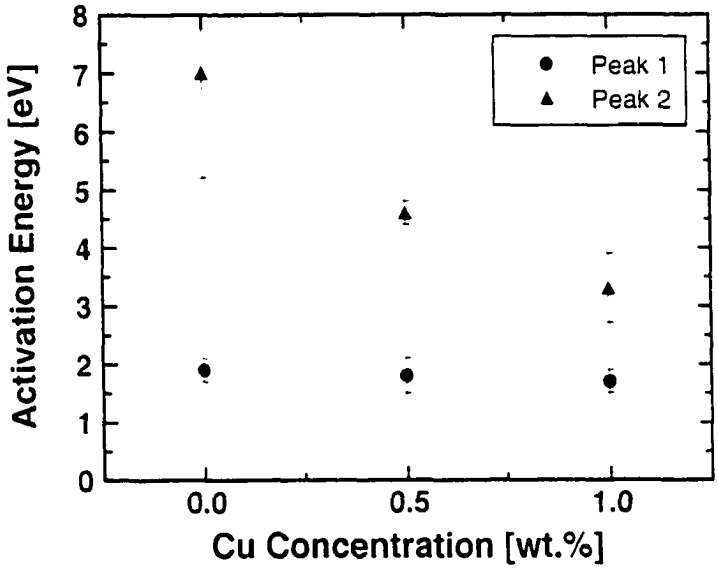

Figure 5. 121: Activation energies for peaks 1 and 2 determined from XRD data plotted as a function of Cu concentration for the $TiAl_3$-metastable tetragonal superlattice peak of a Λ = 72 nm multilayer.

Finally, the activation energies of the first and second peaks of the equilibrium DO_{22} phase were plotted as a function of Cu concentration in Figure 5. 122. Peak 1 was constant over the range of Cu concentrations investigated. The second peak, at much higher activation energy, showed significant variation with Cu concentration, but due to the larger error bars, a consistent trend could not be identified. As a final comparison of the XRD and DSC techniques, the activation energies for the different structures of $TiAl_3$ are listed in Table 5. XXXVII.

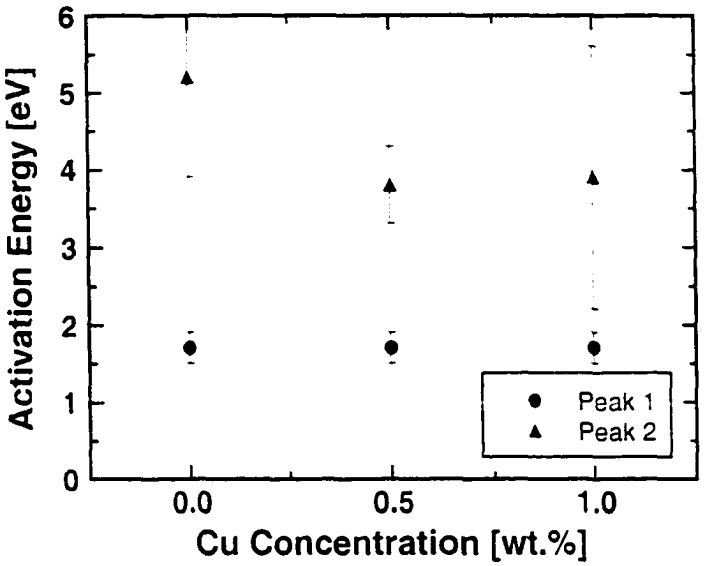

Figure 5. 122: Activation energies for peaks 1 and 2 determined from XRD data plotted as a function of Cu concentration for the $TiAl_3$-DO_{22} (004) peak of a Λ = 72 nm multilayer.

Table 5. XXXVII: Comparison of activation energies determined by DSC and *in situ* XRD for 1Ti/3Al multilayers. (*) Indicates metastable modification

$TiAl_3$ Structure	Cu Conc. [wt.%]	Λ-DSC [nm]	Q-DSC [eV]	Λ-XRD [nm]	Q-XRD [eV]
cubic*	0 wt.%	10	1.6 ± 0.1	72	1.1 ± 0.4 1.2 ± 0.2
tetragonal*	0 wt.%	10	2.1 ± 0.2	72	1.7 ± 0.2 1.7 ± 0.2 1.9 ± 0.2
tetragonal	0 wt.%	--	N/A	72	Peak 1: 1.7 ± 0.2 Peak 2: 7.0 ± 1.8 Peak 2: 5.2 ± 1.3
cubic*	0.5 wt.%	10	1.8 ± 0.1	72	1.5 ± 0.2
tetragonal*	0.5	10	2.1 ± 0.1	72	1.9 ± 0.2 1.8 ± 0.2 1.8± 0.3
tetragonal	0.5 wt.%	--	N/A	72	Peak 1: 1.7 ± 0.2 Peak 2: 4.6 ± 0.2 Peak 2: 3.8 ± 0.5
cubic*	1.0	10	2.0 ± 0.2	72	1.2 ± 0.2
tetragonal*	1.0	10	2.3 ± 0.2	72	1.8 ± 0.2 1.7 ± 0.2 1.7 ± 0.2
tetragonal	1.0	--	N/A	72	Peak 1: 1.7 ± 0.2 Peak 2: 3.3 ± 0.6 Peak 2: 3.9 ± 1.7

5.5 Summary and Conclusions

The use of the *in situ* synchrotron XRD has proven to be an effective technique for monitoring reactions in thin-film multilayers. The peak shape and peak shift behavior were analogous to the constant heating rate DSC results in most respects, with the exception of the absolute peak heights. The use of the DSC results that have been well characterized in other investigations highlighted the overall sensitivity of the *in situ* XRD technique to the analysis of thin film reaction kinetics.

The measurements of kinetics in the relatively less complex Nb/Al system also facilitated the assessment of the XRD technique to obtain quantitative kinetic information in the form of activation energies regarding the formation of $NbAl_3$. The XRD results compared favorably with DSC results in the present work. In addition, the *in situ* XRD confirmed the DSC results by showing that the addition of 0.5 or 1.0 wt.% Cu did not significantly affect the activation energy associated with $NbAl_3$ formation.

In addition to providing quantitative kinetic information, the XRD approach also revealed some information regarding the microstructure of the as-deposited and product phases. Peak widths and locations provided a rough estimate of the size of coherently diffracting regions (i.e., grain sizes) and whether the material exhibited any uniform strain, respectively.

Quantification of the Ti/Al reaction proved to be more difficult experimentally even with the use of the *in situ* XRD technique. This additional complication arose from the multiplicity of metastable phases that have been reported in numerous thin film studies of this system and the observation that some of these phases form coherently. Therefore, a distinguishing peak (as in the case for the cubic $L1_2$ structure) was not

visible in the *in situ* XRD window nor in the θ-2θ scan for the samples investigated. Based on the DSC results in this investigation and previous studies, the absence of peaks from other $TiAl_3$ structures/compounds, and TEM evidence to be presented, the presence of the low temperature $L1_2$ superlattice structure of $TiAl_3$ was thus inferred. Although a unique peak was visible for the metastable tetragonal phase, its exact identity was also ambiguous despite the observation of several peaks in the *ex situ* θ-2θ scans. Previous experiments have reported three different tetragonal metastable modifications of $TiAl_3$. The reflections of the DO_{23} structure (Wöhlert 1995, Michaelsen et al. 1996, Wöhlert and Bormann 1999), Ti_8Al_{24} (van Loo and Rieck 1973), and the Ti_9Al_{23} phase (Raman and Schubert 1965, Rodbell et al. 1991, Rodbell 1992) are very similar. The Ti_9Al_{23} phase was first reported to form during long anneals at relatively high temperatures (Raman and Schubert 1965), so it was unclear as to why it would form at temperatures < 500 °C in thin-films. However, the one peak at 44° in the low period 0 wt.% Cu samples was most closely matched by this phase and therefore it could not be unequivocally dismissed. Therefore, they were collectively referred to as "metastable tetragonal $TiAl_3$" (as opposed to the metastable *cubic* $TiAl_3$). The exact crystal structure has little bearing on the conclusions of this work.

The effect of the layer thickness on the reaction kinetics was as expected. Thicker reactant layers required longer reaction times and "compressed" the transition between the various metastable phases (since the temperature was ramped during the anneal). The peak shift behavior as a function of Al layer thickness was also consistent with the present and existing DSC results. The first peak found in the Al(111)/Ti (0002) reflection or the metastable $TiAl_3$ peak at ~45°, shifted to higher temperatures as the film

thickness increased. With experimental proof still lacking the existing interpretation, although an oversimplification, provides a suitable framework in which to view these results. If heterogeneously catalyzed nucleation and growth to impingement occurred in this system, and the density of nucleation sites was dependent on the parent microstructures, then a peak shift to higher temperature would be expected.

Despite the numerous activation energies determined for the nearly eight peaks revealed by the derivative of the integrated intensity, no observable trend as a function of Cu concentration was found. The possible exception was the activation energy of the decaying peak of the high temperature metastable tetragonal $TiAl_3$ phase which correlated with the second peak of the equilibrium DO_{22} phase.

The activation energies corroborated the DSC results in terms of the metastable tetragonal form of $TiAl_3$ and the initial cubic structure of $TiAl_3$. The *in situ* XRD results produced a slightly lower activation energy for the formation of $L1_2$ $TiAl_3$. This could be due to a breakdown in the initial assumption that XRD intensity is proportional to the volume fraction of the phase that had formed. Also, the DSC results suggested an increase in the activation energy for peak A of the 0 wt.% Cu sample and the 1.0 wt.% Cu sample that was not observed in the XRD experiments.

The most important finding to develop from the *in situ* XRD experiments was the determination of the activation energies associated with the formation of the DO_{22} phase. The discovery of a "two-stage" behavior (although the exact mechanism may be different than the proposed model of Coffey et al. (1989)) was also unexpected. Previous attempts to determine the activation energy were unsuccessful due to the lack of a significant signal in DSC experiments (Michaelsen et al.1996). The new results indicated an

activation energy for the first peak of DO_{22} that is similar to that of the metastable tetragonal phase. The activation energy of the second peak was considerably higher and also had substantial errors. Other than the *in situ* XRD setup few techniques (if any) would be able to access this information experimentally. However, the very high values of the activation energies again address the validity of the assumption made on the direct correspondence of diffraction intensity and volume fraction formed.

In summary, this chapter has explored the use of X-ray diffraction measurements to assess effects of bilayer thickness and Cu concentration on the initial texture of the multilayer microstructure. The effects of these variables on the kinetics of compound formation were also investigated. Compound formation was followed using the IBM/MIT beamline setup at Brookhaven National Laboratory. Due to the high incident photon flux, phase formation could be monitored in real time. This enabled relative measures of phase formation temperatures, and, using different heating rates, determination of activation energies. This technique proved invaluable in examination of the kinetics of the Ti/Al system where several structural variants of the $TiAl_3$ phase formed. Although the phases could not be identified using the DSC, the changes in structure produced distinctly different diffraction peaks. This ultimately allowed the (previously unknown) activation energy for the formation of the equilibrium $TiAl_3$ DO_{22} phase to be quantified.

The next chapter presents transmission electron microscopy studies that examine the grain structure of as-deposited and annealed films of Nb/Al and Ti/Al. The chapter also describes analytical electron microscopy experiments and grain size measurements.

6 Transmission Electron Microscopy (TEM)

6.1 Introduction

Due to the small dimensions inherent in the multilayers in this study, transmission electron microscopy (TEM) was required to characterize the microstructure of the as-deposited and annealed Nb/Al and Ti/Al multilayers. The use of conventional TEM instruments under bright field (BF) and centered dark-field (CDF) imaging conditions provided qualitative information on grain morphology (size and shape). In addition, selected area electron diffraction (SAD) was used to assess texture of the different films and to ascertain the identity of the various intermetallic phases. Finally, analytical electron microscopy (AEM) was performed using a dedicated, field-emission scanning transmission electron microscope (STEM) to investigate diffusion during the early stages of the Nb/Al reaction.

6.2 Background

6.2.1 Thin-Film Microstructures

6.2.1.1 As-deposited Microstructures

In the study of vapor deposited, thin-films as a function of different processing parameters, the pre-eminent description of the evolved microstructure is the "Structure Zone Model" (SZM) or simply the "Zone Model" of thin-film growth. This model has been refined and expanded over the past three decades to describe the different structure archetypes that arise from the vacuum deposition of single element or alloy films.

Initial development of the SZM was conducted using thick (up to 2 mm) thermally evaporated films of Ni, Ti, W, Al_2O_3 and ZrO_2 under nominally high-vacuum

conditions (Movchan and Demchishin 1969). Cu and Nb were used as substrate materials. The three elements and oxides were deposited on substrates with temperatures ranging from 150 – 1600 °C. The authors reported the formation of three zones depending on the homologous deposition temperature (T_{sub}/T_m) for the different materials as shown in Figure 6. 1.

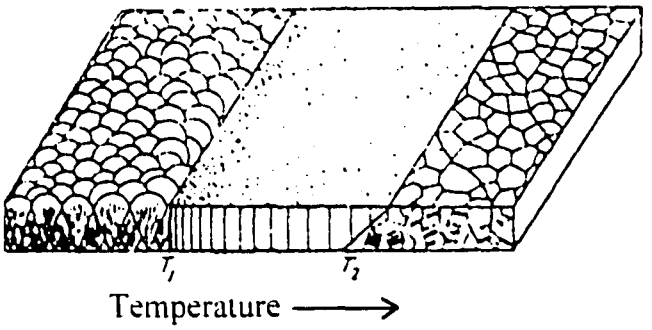

Figure 6. 1: Diagram of structural zones of evaporated films base on the temperature of the substrate (from Movchan and Demchishin 1969).

Differentiation among the three zones was made through metallographic examination of the surface and cross-sections of the samples. The first zone was characterized by tapered crystals that increased in size during growth. Zone II was comprised of columnar (through-thickness) grains that gradually became coarser with increasing substrate temperature. Zone III according to the reported observations, consisted of equiaxed grains. The cause of the formation of three regimes of growth behavior was attributed to "surface recrystallization" processes mediated by surface diffusion.

The development of the zone model was revisited by Thornton (1977). Thornton expanded the zone model to include sputtered films and favored an interpretation based on underlying physical processes. High deposition rates (50 – 20,000 Å/min) were used

in the deposition of thick (25 –250 μm) coatings of Ti, Cr, Fe, Cu, Mo, and Al on metal and glass substrates. The result was a description of microstructure that developed from process variables such as substrate temperature and sputtering pressure combined with shadowing, surface diffusion, and bulk diffusion (including grain growth) phenomena as shown in Figure 6. 2.

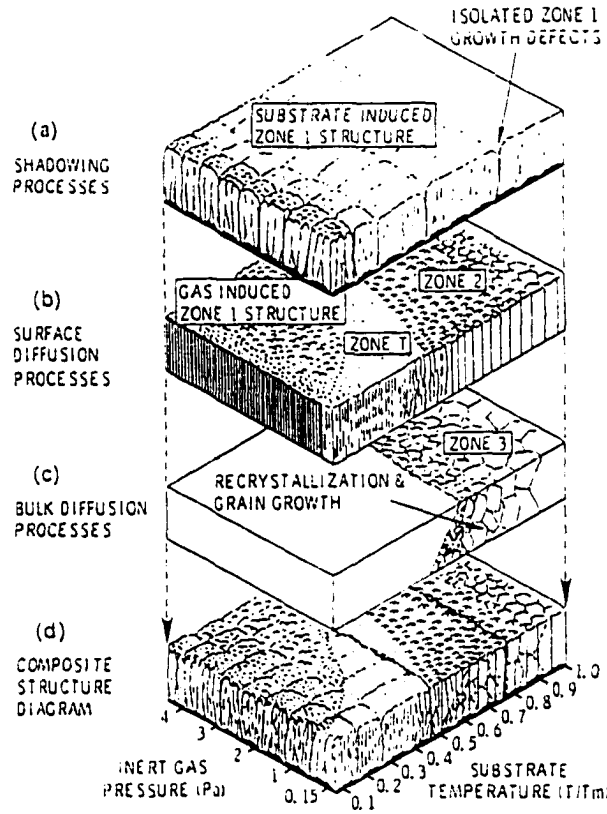

Figure 6. 2: Schematic representation showing the superposition of physical processes that establish structural zones (from Thornton 1977).

The result of this approach was a model capable of describing a larger variety of thin-film microstructures. The homologous temperature boundaries between the three zones were essentially the same as those proposed by Movchan and Demchishin (1969). The grains in Zone II were observed to have highly faceted surfaces. An additional zone (Zone T) was also incorporated into the model to account for the dense, fibrous

microstructure observed in sputtered films at deposition conditions between Zone I and Zone II.

The zone model was later re-evaluated by Grovenor et al. (1984) Smith et al. (1993) and Smith et al. (1994). These studies described a different phenomenological approach based on bulk processes, especially grain growth, in determining the structure of thin-films. The model was based on variations in individual grain boundary mobilities that cause certain boundary types to become more mobile than others as temperature increases. In Zone I the grain boundaries were immobile, producing a dense, equiaxed structure. Zone T was reinterpreted as a region where some fraction of grain boundaries are mobile, while others are not, producing a bimodal grain size distribution. As the homologous temperature increased, a larger fraction of the grain boundaries became mobile resulting in grains with an increasing aspect ratio d/h (where d is the grain diameter and h is the film thickness). In Zone II all grain boundaries were mobile forming columnar grains. Zone III was characterized by lateral grain growth and essentially resulted in an increase in aspect ratio of the grains. The authors also noted that the microstructural Zone also depended on the relative rate of grain growth and deposition flux. Finally, any factors that influenced grain boundary mobility, such as dissolved solute or inert particles, would influence the resulting Zone.

The model was developed by studying the microstructures of thick Ni and Ni-Al films and 9 other thin metal films with hcp, fcc, and bcc crystal structures. Film thicknesses ranged from 100 nm to 14 μm. Substrate temperatures ranged from -193 – 600 °C. All of the films were electron beam deposited in 10^{-8} torr background pressures.

Conclusions were based on extensive quantification of the mean, maximum, and minimum grain size of the films.

The model of Movchan and Demchishin (1969) with contributions by Thornton (1977) is compared with the model of Grovenor et al. in Figure 6. 3.

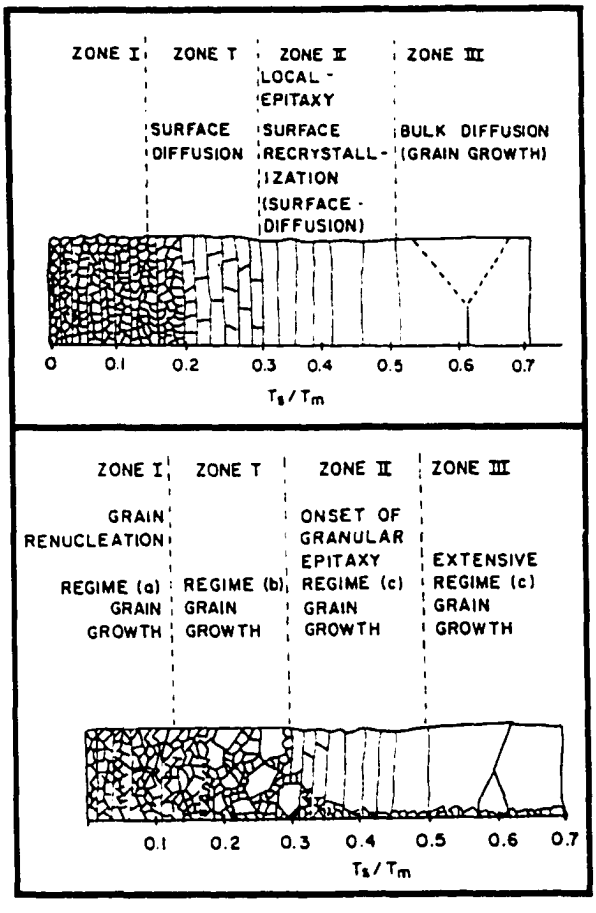

Figure 6. 3: (Top) Zone model of the grain structure of vapor deposited metal films (after Movchan and Demchishin 1969 and Thornton 1977). (Bottom) Zone model for the grain structure of vapor deposited metal films modified to include the bimodal grain size distribution in zone T, and also including the mechanisms that are proposed to control the grain structure in each of the zones (from Grovenor et al. 1984).

Recent work has favored an approach based on fundamental structure forming phenomena for a particular set of deposition conditions to determine the microstructure of vapor deposited metal films. (Adamik et al. 1994; Barna and Adamik 1995; Barna et al.

1998, Adamik et al. 1998b). Like the previous models, a description of the microstructure was derived from the homologous temperature of the material. In this case, all of the microstructures were expected to be columnar with only the width and shape of the columns varying with T_s/T_m. The changes in the width of the columns was attributed to decreasing nucleation density with increasing T_s. In Zone T, surface diffusion was again postulated to lead to competitive growth of neighboring crystals through the minimization of surface energies. For $T_s/T_m > 0.3$ (zones II and III) the microstructure evolves by restructuration. This is depicted schematically in Figure 6. 4.

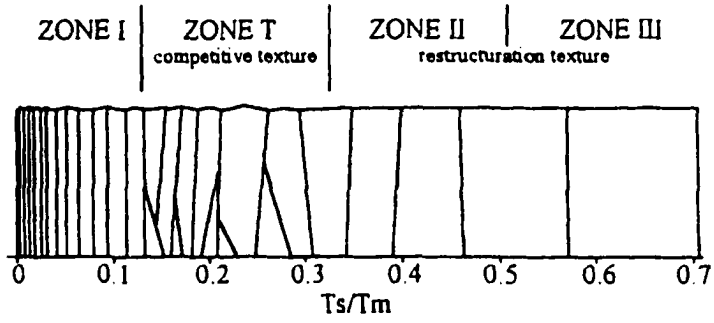

Figure 6. 4: The ideal structure zone model showing the effect of homologous temperature on microstructure and the associated structure forming phenomena (from Barna and Adamik 1995).

In addition to reevaluating the dependence of microstructure on the homologous temperature, Barna and Adamik (1995) further investigated the influence of impurities on the deposited microstructure. This resulted in a description of film structure based on the coupled effects of impurity level of the film (corroborated by experiments that controlled the O_2 partial pressure during the deposition of Al) and the texture of the deposited layer. Figure 6. 5 shows the effect of increasing impurity content on a vapor deposited thin film microstructure. Different zones were clearly differentiated, however, the changes between zones was defined by increasing the impurity content not by increasing the

substrate temperature. The results were interpreted within the framework of the form of the SZM presented by Grovenor et al. 1984) based on texture developed through a grain mechanism.

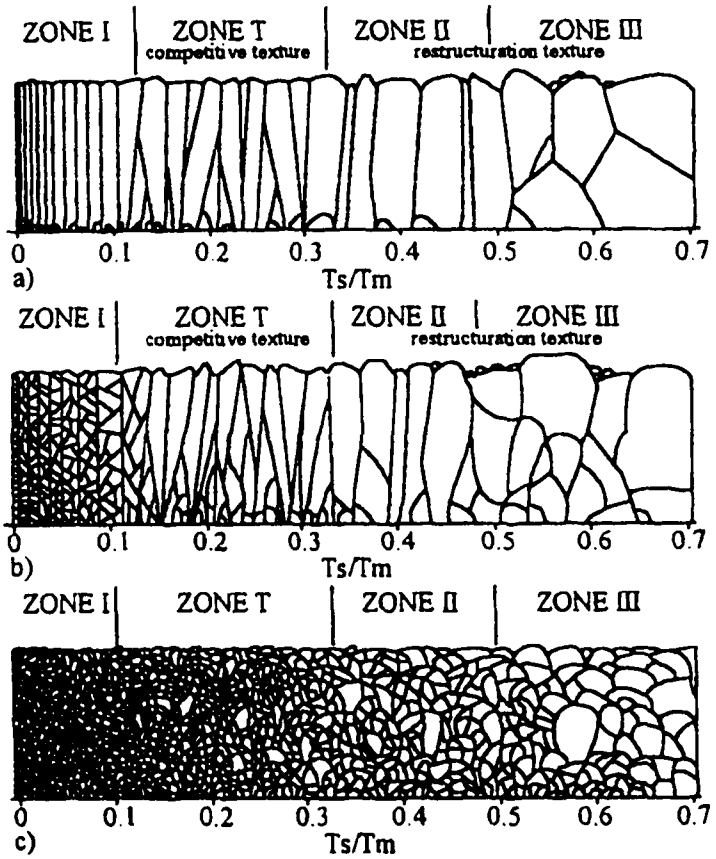

Figure 6. 5: Real structure zone models for thin film growth at: a) low, b) medium, and c) high impurity content (from Barna and Adamik 1995).

The approach proposed by Barna and Adamik 1995 can classify a broader range of experimentally observed microstructures. This is because, as with the model proposed by Thornton 1977, it does not depend solely on the homologous temperature as a process variable for a given sputtering gas pressure.

The homologous temperature transitions of the different structure zone models are summarized in Table 6. I.

Table 6. I: Comparison of homologous temperature ranges defining the different zones in the structure zone model of thin-film growth.

Reference	Zone I	Zone T	Zone II	Zone III
Movchan and Demchishin (1969)	$T_s/T_m < 0.3$		$0.3 < T_s/T_m < 0.5$	$0.5 < T_s/T_m < 1$
Thornton (1977)	$T_s/T_m < 0.15$	$0.15 < T_s/T_m < 0.3$	$0.3 < T_s/T_m < 0.5$	$T_s/T_m > 0.5$
Grovenor et al. (1984)	$T_s/T_m < -0.12$	$0.12 < T_s/T_m < 0.3$	$0.3 < T_s/T_m < 0.5$	$T_s/T_m > 0.5$
Barna and Adamik (1998)	$0 < T_s/T_m < 0.1$	$0.12 < T_s/T_m < 0.3$	$0.3 < T_s/T_m < 0.5$	$T_s/T_m > 0.5$

6.2.1.2 Reacted Microstructures

As discussed in Chapter 1, thin film reactions are prevalent and necessary in many areas of microelectronics technology. However, a systematic definition of the classes of microstructures that form during the reaction of two (or more) elements or alloys to form a third phase with a different structure and/or composition was not yet accomplished. Recently, a model has been proposed to describe the evolution the microstructure in terms of nucleation and growth kinetics along with the morphology of the product phases (Barmak et al. 1997b). Analogous to the four zones of the structure zone model, but based on the product grain microstructure, four *types* of morphology were proposed. Experimental microstructure data was provided by evaporated and sputtered Nb/Al and sputtered Ti/Al multilayers that were annealed to different temperatures, and hence, different stages of the respective reactions.

A Type 1 microstructure was defined as having a morphology with the product phases present along reactant grain boundaries (i.e., non-planar formation of the product phase). Type T corresponded to an equiaxed grain structure arising, for example, from re-nucleation of product phase grains. This was observed for the formation of $TiAl_3$

grains from a thick Ti/Al film. Type II described a structure where lateral coarsening rates were slow and resulted in grain aspect ratios <1. Finally, a type III microstructure developed when the lateral coarsening rate of the product phase was significant and resulted in product grains with aspect ratios greater than one. Examples of the three types from Nb/Al thin film reactions are shown in Figure 6. 6.

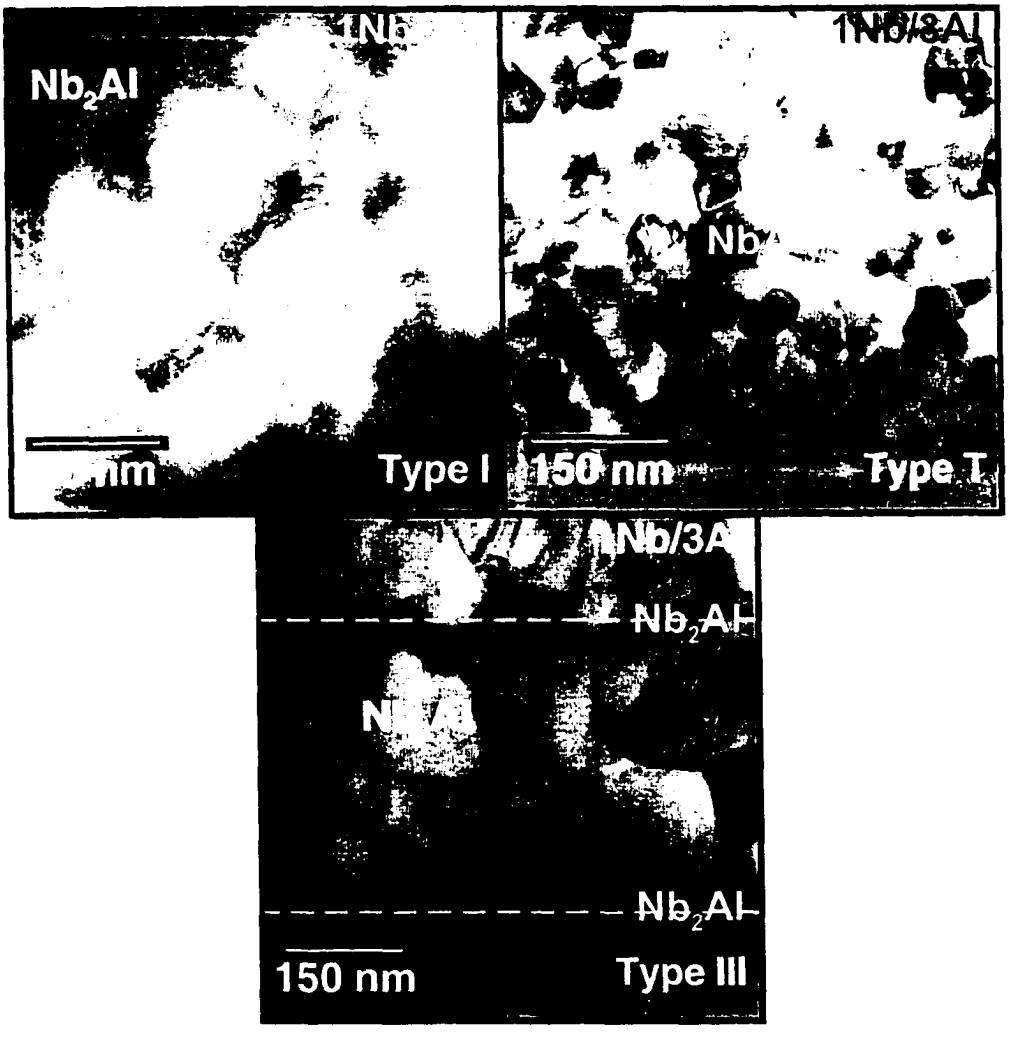

Figure 6. 6: Example microstructures from the type model proposed by Barmak et al. 1997b. Clockwise from top: TEM cross section of a partially reacted 3Nb/1Al multilayer with Λ = 500 nm showing the growth of the σ phase, Nb_2Al, along the grain boundaries of the tri-aluminide phase, cross section of a 1Nb/3Al multilayer fully reacted to yield $NbAl_3$, and a TEM cross-section of a fully reacted 3Nb/1Al multilayer with Λ = 333 nm; note the grains size of Nb_3Al is ~0.5× the original period (dashed lines).

6.2.2 Nb/Al Microstructures

Several studies have investigated the microstructures of vapor deposited Nb/Al multilayered films. The experiments focused primarily on the formation of Nb-rich compounds, since these were of interest for their superconducting properties. A study conducted by Im et al. 1988 and Im and Morris 1988b investigated two bilayer thicknesesses of Nb and Al (38 nm and 127 nm) with 23 at.% Al and 77 at.% Nb. Si wafers, niobium, and quartz plates were used as substrates, although only results from the Si and Nb substrates were reported. A 200 nm-thick Nb layer was first deposited on all of the substrates prior to multilayer deposition. The samples were then isothermally annealed at 600 °C for 100 hrs followed by an anneal at 900 °C for 20 min.

The images of the as-deposited films did not provide much information concerning the microstructure of the individual layers. This was due to difficulties in thinning the Nb layers. After the 600 °C anneal, a layer of $NbAl_3$ ~35 nm thick was visible at the position of the original Al layers. Following the 900 °C anneal the layers in both samples transformed to the A15 Nb_3Al phase. These grains were found to be equiaxed and approximately 100-200 nm in size (i.e., larger than the original period). The authors reported no evidence of the Nb_2Al (σ) phase and postulated that it had been bypassed due to the stoichiometry of the multilayer.

A more systematic approach to the evolution of the microstructure in evaporated Nb/Al multilayers was conducted by Barmak et al. (1990). In this study, several multilayers with more than one composition and several bilayer thicknesses were examined. This work also used the results obtained by calorimetry and XRD to aid in selecting the different annealing conditions.

Due to sample preparation difficulties, the microstructure of the as-deposited films remained unclear. However, the Nb layers appeared to have a zone I or zone T morphology based on the most recent versions of the zone model. Through a series of carefully controlled *ex situ* annealing experiments, the sequence of phases formed during the reaction of the multilayers was ascertained. The identity of the phases was determined by XRD and AEM experiments. Results showed that contrary to the previous thin film studies, Nb_2Al phase formation was not suppressed or bypassed in either 33 at.% Al films or 25 at.% Al films. Instead, at intermediate stages of the reaction, a layered structure developed consisting of $NbAl_3$, Nb_2Al, Nb_3Al, and unreacted Nb.

This study also presented results that had important implications for the evolution of grain structure during thin-film reactions. The first was the consumption of $NbAl_3$ by Nb_2Al via penetration along the $NbAl_3$ grain boundaries (see Figure 6. 6). The second result indicated a correspondence of the final, transformed microstructure (in this case Nb_3Al) to the parent structure. When a 25 at.% Al film was reacted to near completion the Nb_3Al grains were nearly equiaxed and columnar forming rows parallel to the original interfaces and creating a new interface at the midpoint between the original layers (see Figure 6. 6). The reaction sequence incorporating the evolution of the microstructure is depicted schematically in Figure 6. 7.

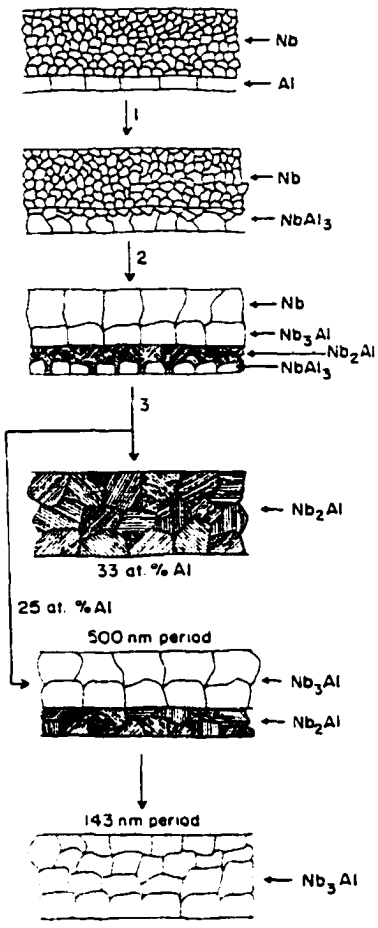

Figure 6. 7: Schematic representation of the phase formation sequence for the reaction of Nb and Al multilayer thin films (from Barmak et al. 1990).

The most relevant study in the context of the present work that involved electron microscopy studies of the Nb/Al solid state reaction also was conducted by Barmak et al. (1998). A series of UHV sputter-deposited multilayers with various bilayer thicknesses and compositions were studied, however, a significant fraction of these samples were deposited with 75 at.% Al. This enabled a more detailed study the formation of the first phase, $NbAl_3$. The cross-sectional TEM results of the as-deposited 1Nb/3Al multilayers indicated a zone II structure with approximately equiaxed grains of Al and a dense fibrous array, columnar Nb grains for the thinner films. The aspect ratio of Al grains for the thicker films was < 1 . Although only two as-deposited microstructures were

presented, they highlighted the simultaneous effects of deposition rate vs. grain growth in determining resulting microstructure. The micrographs also showed evidence of granular epitaxy where grains of a newly deposited layer grew with a similar orientation as the previous layer. This formed large "macrograins" of similarly oriented domains that extended through the entire thickness of the multilayer.

The work also reported a study of the initial and final stages of the reaction of a 75 at.% Al multilayer with Λ = 72 nm. After annealing the sample isothermally for 15 min at 377 °C, diffraction rings of $NbAl_3$ were visible. This temperature was chosen to examine the reaction mechanism at peak A in the DSC traces. By imaging a diffraction spot from one of the diffraction rings indexed as $NbAl_3$, triangular-shaped grains of the tri-aluminide were revealed to protrude into the Al grain boundaries as seen in Figure 6. 8.

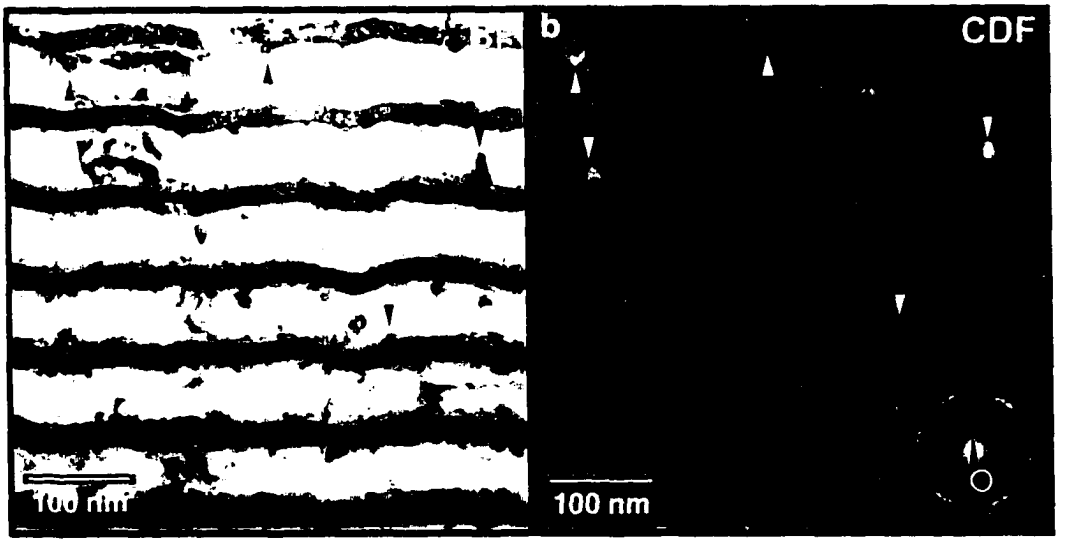

Figure 6. 8: TEM micrograph of the cross-section of a 1Nb/3Al multilayer with Λ = 72 nm annealed for 15 min at 377 °C: (a) CDF image using the inner diffraction rings unique to $NbAl_3$, indicated by a circle in the diffraction pattern in the inset. The arrows in the micrographs indicate the preferential growth of the tri-aluminide along the grain boundaries of the Al layer (after Barmak et al. 1998).

This result suggested that the slower diffusing Nb controlled the rate of the reaction in the early stages of phase formation. A similar sample was annealed to 752 °C at 50 °C/min. Recall from the DSC results that the reaction for a 72 nm film was completed at ~ 700 °C (see Figure 6. 6). The results showed an equiaxed microstructure with a grain size of ~50 nm - i.e., less than the original period. The obvious effects of starting from a multilayer structure were the nanoscale grain size and the presence of "partial grains" that had nucleated above the substrate and stopped abruptly at the substrate film interface.

6.2.3 Ti/Al Microstructures

As with XRD, significantly more microscopy experiments have been conducted on Ti/Al reactions and the corresponding microstructures due to the application of these materials in interconnections for integrated circuit applications.

Howard et al. (1978) made one of the first observations of the reacted microstructure of the reaction between Ti and Al thin films. Trilayer samples were prepared from thin-films of Al-4 wt.% Cu (500 nm), co-evaporated from elemental sources, followed by a layer of Ti (20-60 nm) and capped by another layer of Al(Cu). The samples were annealed isothermally in an inert atmosphere at 400 °C for 1-4 hours. The authors presented planview TEM results from one of the annealed samples. A region near the Al-$TiAl_3$ interface was selected and revealed a continuous layer of fine-grained $TiAl_3$ (~40 nm) and significantly larger Al grains (700-800 nm). This result, although somewhat preliminary, suggested that there was a large density of $TiAl_3$ nucleation sites.

The microstructure and kinetics of the Ti/Al reaction were again examined in a more systematic experiment conducted by Wittmer et al. (1985). In this study, bilayers

were e-beam evaporated on oxidized Si substrates with 150 nm Ti followed by 640 nm of Al or Al(Cu). The authors studied Cu concentrations from 0 to 4.5 wt.%, although microstructures were shown only for the Al-1.0 wt.% Cu samples. Cross-sectional TEM micrographs were presented showing Ti/Al samples annealed at 450 °C for 30 min and 4 hours and Ti/Al-1 wt.% Cu samples annealed under the same conditions. The micrographs showed that in the samples without Cu, the thickness of the $TiAl_3$ layer was larger and the interphase interface between the Al and $TiAl_3$ was rougher. The pure Al samples also revealed $TiAl_3$ penetration along the Al grain boundaries. In the 1 wt.% samples the interphase interface between Al and $TiAl_3$ was notably smoother and the growth of the $TiAl_3$ was not influenced by the presence of Al grain boundaries. Finally, the images indicated that the Al grain size was larger in the annealed 1 wt.% Cu samples. The reduction in interface roughness was attributed to two causes: the reduction of Ti diffusion along Al grain boundaries caused by Cu segregation to the Al grain boundaries and the enhanced Al grain growth (producing smoother interfaces) caused by the presence of Cu. In both cases the $TiAl_3$ layer was polycrystalline and appeared to consist of several grains through-thickness. The authors also noted a 3 to 4-fold *increase in the size of the $TiAl_3$ grains* in the presence of Cu. The TEM results also showed that the $TiAl_3$ layer was thinner in the samples containing 1 wt.% Cu. The authors proposed that Cu segregation to the $TiAl_3$ grain boundaries reduced diffusion *through* the intermetallic layer, and in conjunction with a lower volume fraction of grain boundaries caused by increased $TiAl_3$ grain size, resulted in the slower growth of the layer.

The growth of $TiAl_3$ was also studied by Michaelsen et al. (1994). In this work, a sputter-deposited film of Ti/Al with each layer 1 μm thick was annealed for 20 h at 400

°C. The cross-sectional TEM results clearly showed the microstructure of the Al and Ti layers and the growing $TiAl_3$ layer. The Al grains had diameters equivalent to the layer thickness (Zone III) while the Ti grains were columnar (Zone II) and had diameters of ~ 100 nm. The results showed that the $TiAl_3$ layer consisted of several grains through thickness with the grain size decreasing from the Al/$TiAl_3$ interface to the Ti/$TiAl_3$ interface. The intermetallic grains at the latter interface were ~ 10 nm in diameter. The gradient in grain diameters indicated that grain growth/coarsening occurred during phase formation and the new grains continuously nucleated at the Ti/$TiAl_3$ interface. Thus, non-equilibrium conditions were maintained at this location via rapid grain boundary diffusion. These results support the assumption made by Wittmer et al. (1985) indicating that the grain boundaries of $TiAl_3$ provided rapid diffusion paths that can sustain the reaction through intermetallic layer thicknesses of at least ~350 nm. No other Ti-Al intermetallic phases were observed indicating the high stability of the $TiAl_3$ phase in the presence of unreacted Ti and Al.

Kinetic experiments involving detailed studies of the growth rates of the various Ti-Al intermetallic phases and the relative stability of the $TiAl_3$ phase were conducted by Wöhlert (1995), Wöhlert et al. (1997) and Wöhlert and Bormann (1999). Samples were prepared in a tri-layer configuration by UHV magnetron sputtering. A 1 μm layer of Ti was deposited followed by a 200 nm thick layer of Ti_3Al or equiatomic TiAl deposited from alloy targets. The final layer was ~ 1 μm of Al. Samples were then encapsulated in evacuated quartz tubes and annealed at 400 °C for different times. In both cases, the Ti_3Al and TiAl layers were replaced by a layer of $TiAl_3$. In this case, the $TiAl_3$ was observed to form with a DO_{23} structure. The microscopy results demonstrated that the

Ti_3Al and TiAl phases were kinetically unstable with respect to $TiAl_3$ formation. Based on a competitive growth model, this was concluded to be a result of the diffusion flux through $TiAl_3$ that was several orders of magnitude higher than the other Ti-Al intermetallic compounds. Since the formation of metastable compounds with the $L1_2$ and DO_{23} structures was not predicted by the competitive growth model (Gösele and Tu 1982), the presence of these modifications was believed to result from differences in interface energies producing differing nucleation rates.

The microstructures of the Nb/Al and Ti/Al multilayers were examined in the context of the previous work classifying the as-deposited and reacted microstructures. Specifically, samples were prepared to investigate the effects of layer thickness on the as-deposited grain structure and the temporal evolution of the microstructure under constant heating rate conditions. The as-deposited microstructures were compared to the different SZM's. For the annealing experiments, samples were reacted to different stages in the reaction using the calorimeter to try to match as closely as possible the conditions used to obtain the calorimetry data. The resulting microstructures would then be used to further clarify the changes associated with the two stages of phase formation modeled by Coffey et al. (1989).

To simplify the experiments, films with molar ratios of XAl_3 were used. This would preclude the formation of more Nb or Ti rich phases at the end of the initial reaction. Further, the microstructural studies focused on the Nb/Al system, since this was the system used to develop the model and does not form metastable phases during the reaction to form $NbAl_3$.

6.3 Experiment

6.3.1 TEM Sample Preparation

6.3.1.1 Plan View

Plan view samples were prepared from the free standing films used in DSC analysis. Small squares ~ 3 mm × 3 mm were cut from the films using a razor blade. M-bond 610 (M-line Accessories, Raleigh, NC) was applied to standard Cu TEM grids with a 1 mm diameter circular hole. The free-standing multilayer film was then placed onto the grid and the epoxy was allowed to cure overnight. The samples were thinned to electron transparency in the Model 691 PIPS (Gatan Inc., Pleasanton, CA) using one gun from the film surface to prevent re-sputtering of the Cu grid. The beam energy was set to 2-3 keV at an angle of 3-4°. Ion polishing was stopped when small holes were visible in the film.

Grain sizes were measured by manually tracing the visible grain boundaries from 8" x 10" prints to transparency film using a fine-point, permanent marker. The tracings were then digitized using a flatbed scanner and imported into NIH (Scion) Image. Small gaps in the lines in the tracings were filled using a pixel dilation function. The image was then skeletonized to reduce the linewidth to 1 pixel and dilated again to produce a final linewidth of 2 pixels. The areas of the grains were then determined and tabulated automatically by the software. The area comprised by the lines was subsequently added back into the measured areas.

6.3.1.2 Cross-section

Cross-sectional samples for transmission electron microscopy were prepared using a technique first proposed by Bravman and Sinclair (1984). Two rectangular (~3

mm × ~5 mm) pieces were cleaved from the processed wafers. Four additional pieces of a similar size were cleaved from bare Si. These four pieces were ultrasonically cleaned in acetone followed by ethanol and allowed to dry. Next, G-1 epoxy (Gatan Inc., Pleasanton, CA) was applied to the film surfaces of the processed wafers and they were glued together face-to-face. Then a stack was constructed by adding two pieces of bare Si on either side of the film-film interface. The stack was placed in a small, metal clamp with teflon covering the jaws to prevent adhesion. The clamp was tightened until finger-tight with care taken to prevent the layers of the stack from sliding relative to each other. The assembly was then placed into an oven at 85 °C; any left over epoxy was also placed in the oven. When the epoxy had cured (~15-30 min), the samples were removed and allowed to cool. Due to the large amount of epoxy that was prepared, 2-4 stacks were prepared simultaneously to reduce waste.

The bonded stack was removed from the clamp. One side of the stack (perpendicular to the glue lines) was ground flat using a 15 mm diamond paper. The stack was then bonded to a rectangular block of Al using a cyanoacrylate cement commercially known as "Krazy Glue ®" or "super glue". When the glue had dried, the Al block was placed in a Buehler Isomet low speed diamond saw. Slices ~500 mm thick were cut from the stack as shown in Figure 6. 9. Typically, 5 – 8 slices could be obtained from one stack.

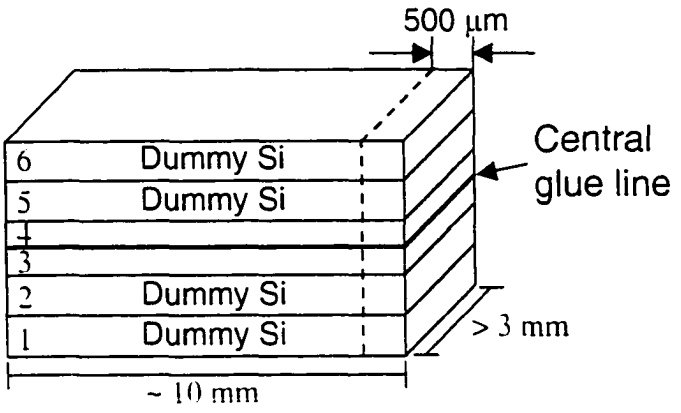

Figure 6. 9: Approximate dimensions for the composite after the Si pieces have been epoxied together; the dotted line indicates where one slice will be cut (after Bravman and Sinclair (1984).

If the slices were not detached from block during cutting, the block and sliced sample were placed in a beaker of acetone until the Krazy Glue® was dissolved. The pieces were then ultrasonically cleaned in tap water. The slices ~ 4 mm x 3 mm were then glued flat onto a glass slide. Using a Gatan Model 601 Ultrasonic Disc Cutter with the supplied SiC cutting grit, 3 mm disks were drilled from the slices as shown in Figure 6. 10.

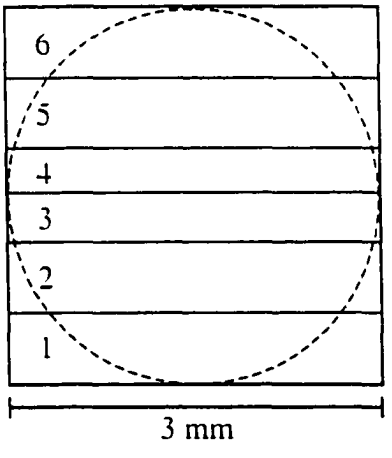

Figure 6. 10: Diagram of the 3 mm disk cut from the slices made by the diamond saw.

Care was taken to align the central glue line along the diameter of the cutting tool. The cut pieces were soaked off the slide in a beaker or petri dish containing acetone.

The thickness of a circular piece was measured to the nearest 0.001 mm with a micrometer and recorded. For all of the grinding steps used to prepare the TEM sample, a tripod-polisher (Klepeis et al. 1988) designed for flat-polishing samples was employed (Figure 6. 11).

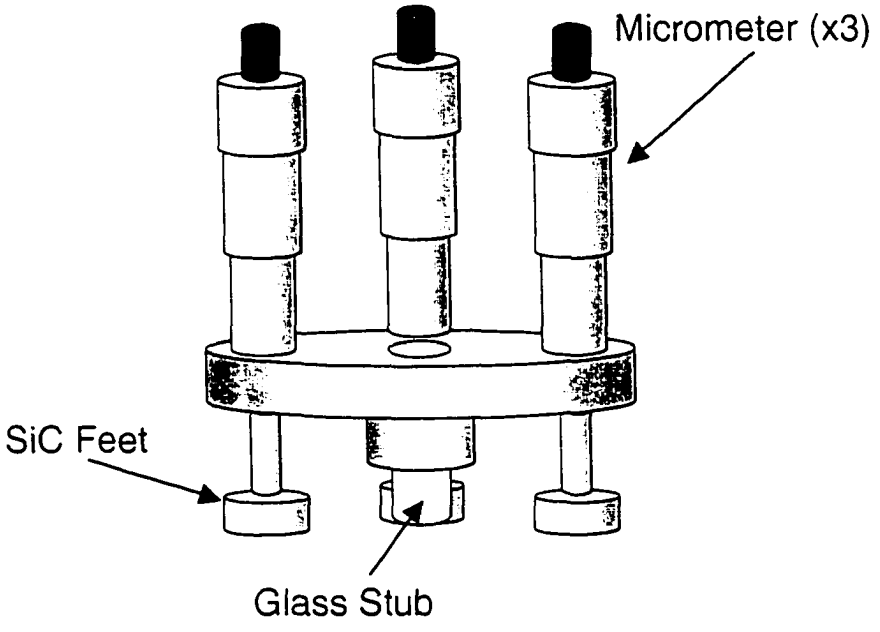

Figure 6. 11: Schematic of the tripod polishing assembly used to parallel polish the cut discs.

A Pyrex ® tripod polishing stub was prepared by co-planarizing the legs using a glass plate as a reference "flat surface". A glass stub was inserted and co-planarized with the legs by grinding ~500 μm away using 15 μm diamond paper. The TEM sample was bonded to the stub using Krazy Glue ®. The sample was ground and polished using a series of diamond papers obtained from Allied High Tech Products (Rancho Dominguez, CA). The first side was ground and polished to a target thickness of ~200 μm. Diamond papers with several different grit sizes were used with the amount removed determined

by the rule of thumb that the depth of polishing damage is approximately equal to 3 times the grit size of the polishing media. Note that the finest division of the micrometers on the tripod polisher was 10 μm. The thinning of the sample was determined using the following sequence of steps in reverse order: 10 μm in 10 μm steps with the 1 μm paper, 30 μm in 10 μm steps with the 3 μm paper, 90 μm in 30 μm steps with the 9 μm paper, and the balance with 50 μm steps using the 15 μm diamond paper. The grinding and polishing were done on a low speed polishing wheel with the diamond papers placed onto a glass plate. The wheel speed was 20-30 RPM during polishing. After finishing with the diamond papers, the sample was polished by hand on a felt nap pad using Syton HT50® (0.04 μm) for two minutes. The sample was then removed from the tripod polisher stub by soaking it in acetone.

Using a micrometer, the thickness of the sample was measured to the nearest ± 0.001 mm and recorded. A slotted Cu TEM grid (1 mm x 2 mm hole) was selected and its thickness measured and recorded. A small amount of M-Bond 610 epoxy was applied to the rough surface of the grid. The grid was then carefully placed on the sample with care taken to align the central glue line of the sample with the long axis of the slot and centered on the sample in a direction parallel to the glue line. The epoxy was allowed to cure for ~12 hrs at room temperature or in an oven at 85°C for 15-60 min.

The sample/grid assembly was glued, grid side down onto the same glass stub used for polishing the first side for second side polishing. The target thickness was 100 μm. Material was removed in two steps as follows: 60 μm/9 μm paper and 30 μm/3 μm paper. This assumes a starting thickness of 200 μm. The polishing amounts sometimes

needed to be adjusted to obtain a thickness of ~100 μm. When second side polishing was completed, the sample was removed from the stub by soaking in acetone.

The final grinding and polishing prior to thinning to electron transparency was achieved by using a Dimpler D500i (VCR Group, San Francisco, CA). A technique was developed based on previous conditions recommended for thinning Si (Carlino and Hidalgo 1992). For dimpling, the sample was first bonded to a sapphire flat using Crystal Bond ® or equivalent adhesive. Care was taken to ensure no air bubbles were trapped in the region of the grid slot beneath the sample. The flat was then loaded into an adjustable holder that allowed the center of the dimple (rotation) to be positioned via two orthogonal set-screws. This holder was essential ensure the region of the central glue line was in the center of the dimple and was not the same as translating the dimpler stage assembly. Dimpling was performed in three stages. The first step used the 3i dimpling tool (VCR Group Inc., San Francisco, CA) and a 3 μm diamond slurry (Allied High Tech Inc., Rancho Dominguez, CA). The force was set to 4-5 g, tool speed was set at 30-40, and damping set to ~6-7. The sample was rotated in a clockwise direction, although the rotation direction was not observed to affect the dimpling. Initially, the sample was inspected every ~2 min using a stereomicroscope to check the alignment of the dimple. The dimple was then centered on the central glue line (may or may not coincide with the center of the sample) using the two set screws on the sample holder. The 3 μm slurry was used until the sample was ~50 μm thick. The sample, flat, and tool was rinsed with water and cleaned lightly using a cotton swab to remove any remaining slurry. Then, using the same dimpling tool, the polishing media was switched to a 1 μm diamond slurry (Allied High Tech, Rancho Dominguez, CA). The sample was dimpled to a

thickness of ~ 15-20 μm and appeared red-orange to orange in transmitted light. Figure 6. 12 shows the sample dimensions at the final dimpling step. Note that the grid is actually 40-50 μm thick.

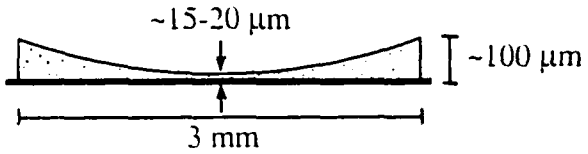

Figure 6. 12: Cross section view of a 3 mm disc after dimpling (after Bravman and Sinclair 1984).

The sample was rinsed and dried before proceeding with the final dimpling step. The final polishing step was performed using a padded wheel (4i) and Syton® HT50. Typically, 30 minutes were necessary to remove scratches in the middle of the dimple and provide a mirror finish. The thickness was monitored strictly using the transmitted light and checked at ~5 min intervals. When the sample appeared light orange to yellow in the transmitted light, dimpling was stopped. The sample was rinsed using distilled water and dried. The padded wheel was cleaned ultrasonically in distilled water. The sample was then "scrubbed" using the padded tool and distilled water for ~ 2 min. The sample was removed from the sapphire flat by dissolving the glue in a petri dish of acetone. When the sample was free of the glue, it was carefully rinsed in two separate baths of fresh acetone followed by a final rinse in ethanol. The sample was then allowed to dry in air.

Final thinning to electron transparency was accomplished using a Model 691 Precision Ion Polishing System PIPS (Gatan Inc., Pleasanton, CA) (Alani et al. 1997). The sample was mounted in the "clamp-type" holder. Single or double beam modulation was used to polish the sample in two 120° sectors that were perpendicular to the glue line.

The sample was polished only from the top (Si) side to prevent re-sputtering of the Cu grid. Additionally, a liquid nitrogen trap was used to improve the quality of the vacuum in the PIPS and reduce sample contamination. Typical polishing conditions were 3-4 keV at 4°. The sample was inspected at ~30 min intervals using the attached stereomicroscope with a supplemental high intensity light source. When the sample color changed to bright yellow the beam energy was reduced to 2 keV. Polishing was stopped when perforation of the glue line was evident. Thinning times ranged from 1 – 4 hours, depending on the starting thickness of the sample. The thinned specimen was then ready for inspection in the electron microscope.

6.3.2 Annealing

Anneals of both the planview and cross-sectional samples were conducted in a Perkin Elmer DSC 7 calorimeter under the same conditions used for the calorimetry measurements in Chapter 4. Pieces of plan view samples were placed into Cu pans lined with a piece of Pt foil. A second piece of Pt foil was placed on top of the multilayer film. The lid was then set into the pan (not sealed). After annealing to the desired temperature, the multilayer sample was easily removed from the sample pan, cut into small sections using a razor blade, and mounted on a Cu grid as described in the previous sections.

Cross-sectional samples were also annealed in the DSC. In this case, a 3 mm x 3 mm piece was cleaved from the wafer and wrapped in Pt foil. The size of the piece was limited by the size of the DSC furnace. The sample was placed film side down in the furnace and the heating program was executed. Note that because of the limited size of these samples only two or three slices were obtained for cross sectioning. All samples

were annealed in flowing ultra high purity Ar (99.9995%). The maximum temperature, limited by the DSC, was 700 °C.

6.3.3 Electron Microscopy

Electron microscopy analysis of the cross-sectional and plan view samples was conducted using a Philips 400T TEM operating at 120 kV or a JEOL 2000 FX TEM operating at 200 kV; both microscopes had LaB_6 filaments. Standard bright field and centered dark field imaging conditions were used to observe the microstructure of the as-deposited and reacted films.

Specimens were usually examined using the double-tilt specimen holder. This allowed the Si (and hence the multilayer) to be oriented perpendicular to the direction of the electron beam by tilting to a <110> zone axis.

Selected area electron diffraction patterns were used to identify the intermetallic phases that formed during annealing. The ring patterns were indexed by fitting a camera constant to the first ring of the diffraction pattern. The rings were measured to the nearest 0.1 mm using a Peak anastigmatic loupe. Relative errors were calculated for each ring by assuming a maximum error in the measurement of 0.1 mm.

Qualitative chemical analysis was performed on a Vacuum Generators HB603 dedicated scanning transmission electron microscope operating at 300 kV. Microscope conditions were set to obtain a nominal probes size (d_p) of ~1.5 nm and a probe current (i_p) of ~0.5 nA. Qualitative chemical maps were generated using Nb-Kα (16.614 keV) and Al-Kα (1.487 keV) characteristic X-rays. The maps were acquired with sizes of 64 × 64 pixels and 128 × 128 pixels at magnifications 500 kX and 1 MX, respectively. For the probe dimensions this resulted in pixel sizes of ~1.25 nm (~1.1× oversampling) for the

maps at 500 kX and ~0.9 nm (~2.2× oversampling) for the 1 MX maps. Dwell times were 200 or 300 ms per pixel. A typical frame time (t_f) for a 64 × 64 pixel map was ~20 min for a 128 × 128 pixel map t_f ~ 60 min. The elemental peak and background windows are listed in Table 6. II.

Table 6. II: Characteristic X-ray lines and the specified energy windows used to determine peak and background intensities.

Characteristic X-ray Line	Peak Window [keV]	Background Window [keV]
Nb-Kα	16.283 – 17.003	15.363 – 16.083
Al-Kα	1.283 – 1.683	0.843 – 1.243

6.4 Results

6.4.1 Nb/Al

6.4.1.1 As-deposited Films

Nb/Al multilayers with various layer thicknesses were examined in cross-section to characterize the grain structure developed during deposition. Figure 6. 13 shows the cross-sectional microstructure of a 1Nb/3Al multilayer with Λ = 23 nm.

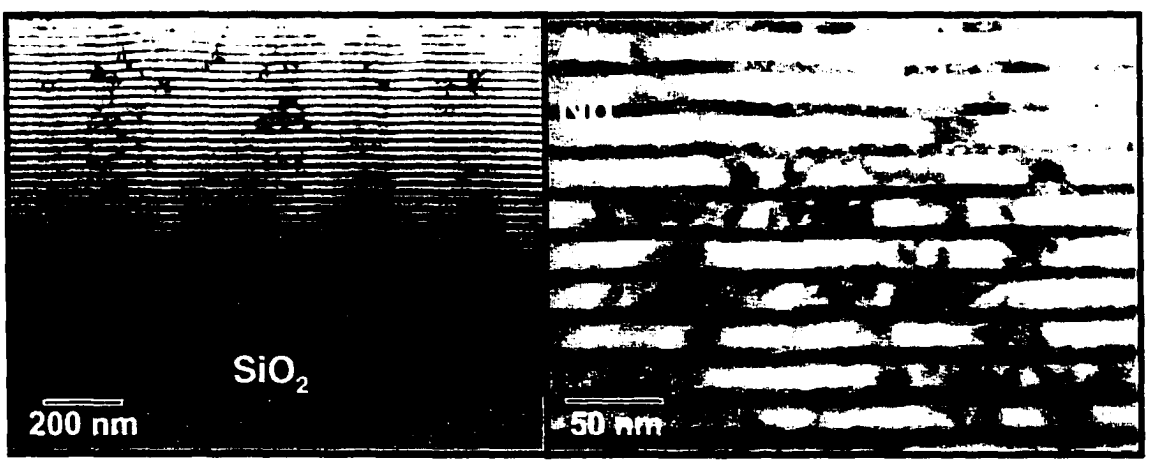

Figure 6. 13: Cross section TEM image of an as-deposited 1Nb/3Al multilayer with Λ = 23 nm.

Nearly the entire 1.5 μm thickness of the multilayer is visible in the left micrograph. The SiO_2 layer and Si substrate are also visible at the bottom of the figure. At least four columns of "macrograins" were observed to be oriented in a strong diffraction condition relative to the beam. Inspection of the selected area diffraction pattern indicated a <111> texture in agreement with the rocking curve and pole figure data. Closer inspection of the layers revealed that both the Nb and Al layers remained polycrystalline and had a columnar microstructure with the Al aspect ratios ~ 1. The Nb layers were composed of smaller crystallites that also appeared columnar with aspect ratios ~ 1.

A 1Nb/3Al multilayer with Λ = 55 nm is shown in Figure 6. 14.

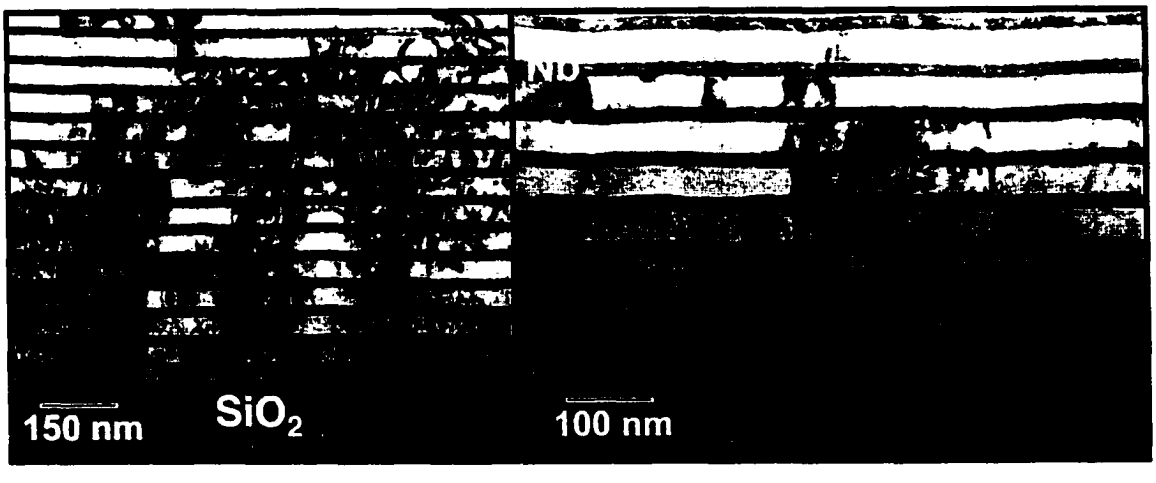

Figure 6. 14: Cross section TEM micrographs of an as-deposited 1Nb/3Al multilayer with Λ = 54.5 nm.

As with the 23 nm sample, areas of similar diffraction contrast were observed to extend through several layers. Again, both the Al and Nb layers were polycrystalline with the grain sizes proportional to the layer thickness. In some grains, the aspect ratios increased indicating lateral growth during deposition. Roughness was also evident on the

upper surfaces of some of the Nb layers. In general the Nb grains also appeared to be through-thickness, possessing an aspect ratio of ~1.

Several micrographs taken from a 1Nb/3Al, Λ = 143 nm multilayer are shown in Figure 6. 15.

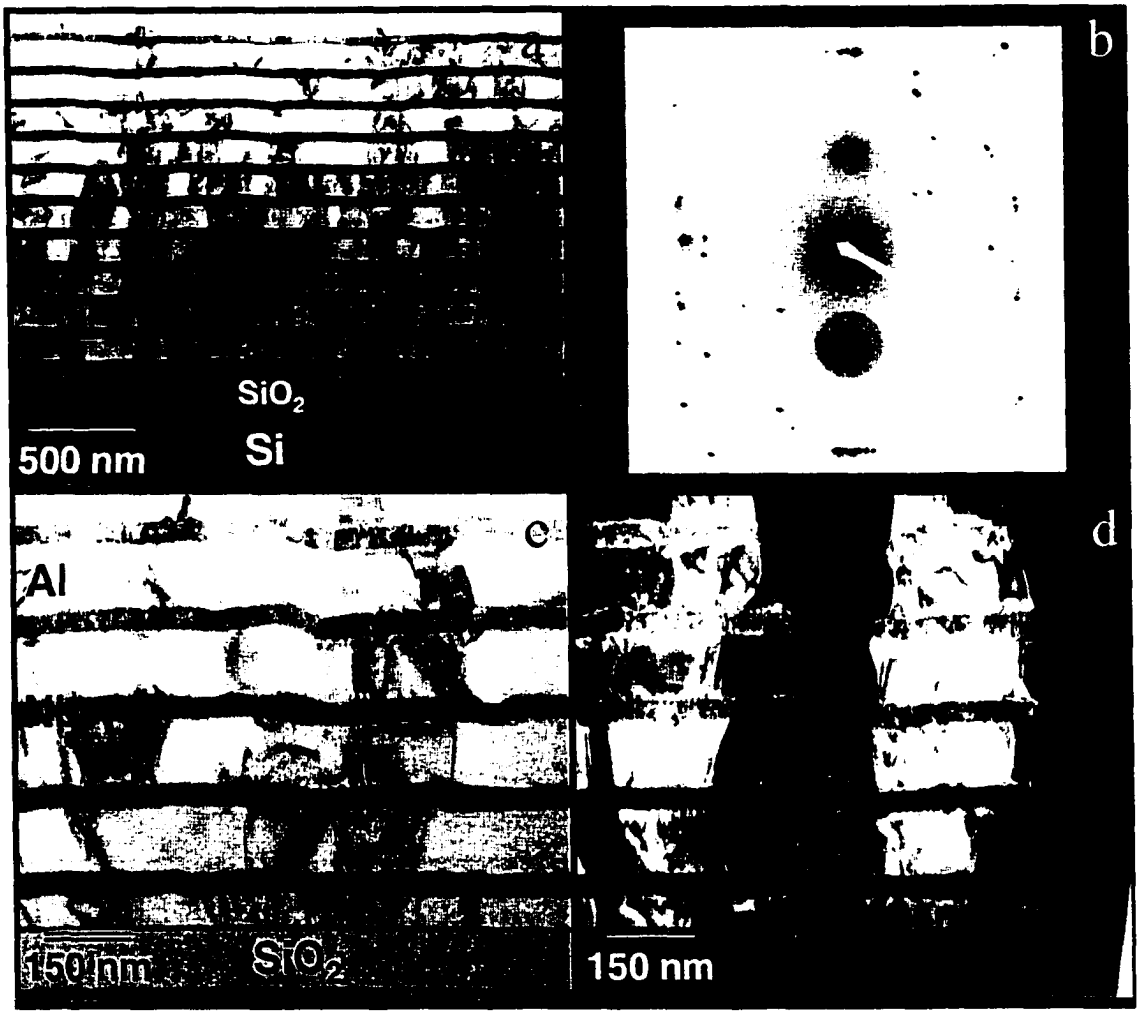

Figure 6. 15: Series of images taken from an as-deposited, 1Nb/3Al multilayer with Λ = 143 nm. a) Bright field image showing overall multilayer morphology. b) Selected area diffraction pattern showing location of Al (111)/Nb (110) spot used to form image in d). A bright field and centered dark field pair of images showing the growth of columns of similarly oriented grains. Note that both the Nb and Al layers are highlighted.

Aspect ratios of the Al grains were ≥ 1. The Nb layer was generally composed of smaller grains many of which were columnar. However, the aspect ratio of these grains

was significantly <1. Interlayer roughness was commensurate with the grain size of the Nb layers and found near the upper surfaces of the Nb layers. In addition to providing these details, the lower two micrographs comprise a bright field and centered-dark-field pair formed using the Al (111)/Nb (110) reflection. The CDF image clearly shows the similarly textured layers of Al and Nb and how this texture was preserved through the growth of sequential layers. The lateral extent of these regions was generally the width of one Al grain that spanned several Nb grains.

The variation of interlayer roughness with the film growth direction is shown in more detail in the micrographs shown in Figure 6. 16.

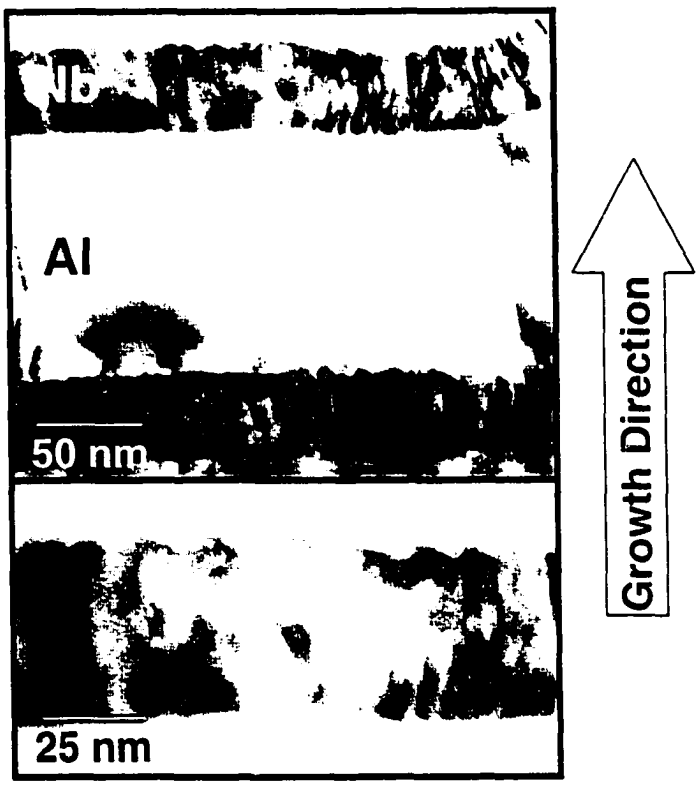

Figure 6. 16: Cross section TEM image of an as-deposited 1Nb/3Al multilayer with Λ = 143 nm showing the detail of the Nb/Al interface. The Nb layers are observed to be rougher on the top surfaces and smoother on the lower surfaces. The top surfaces of the Nb grains are faceted.

The upper micrograph shows two Nb layers and an intermediate Al layer (one grain). The lower surfaces of both Nb layers were observed to be relatively smooth with respect to their upper surfaces. This suggests that the roughness was developed in the course of the Nb layer deposition and was subsequently "smoothed" by the deposition of the Al layer. The lower micrograph shows the detail of one of the Nb layers. This indicated that the roughness was on the order of the Nb grain size and reveals the faceted surfaces of the Nb grains.

A 1Nb/3Al, Λ = 240 nm multilayer is shown in Figure 6. 17.

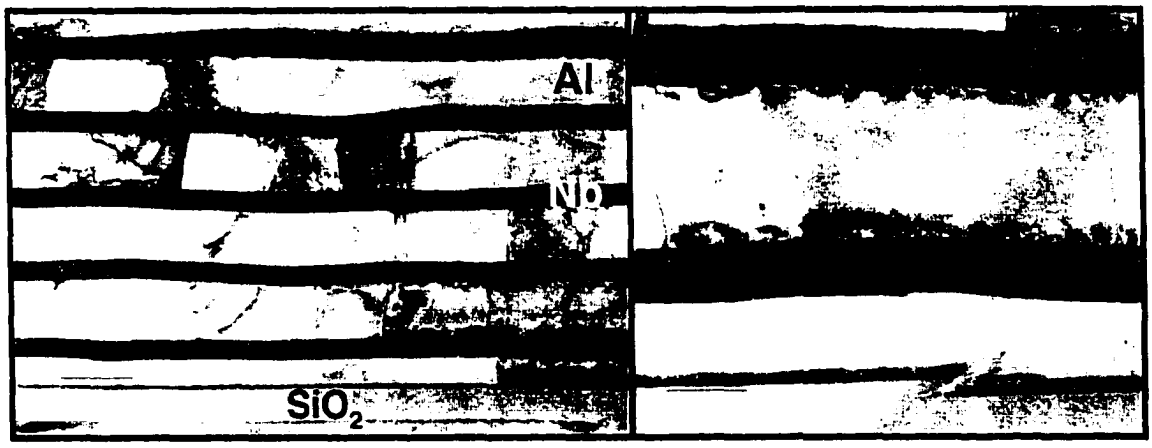

Figure 6. 17: Cross section TEM micrographs of an as-deposited 1Nb/3Al multilayer with Λ = 240 nm.

Although the microstructure of the Nb layer was not as distinct, the micrographs clearly showed the increased lateral growth of the Al grains that occurred during deposition. Most of the Al grains have aspect ratios >>1 and can span several hundred nanometers. The Nb layers were also composed of through-thickness grains, however, lateral growth was less evident with most of the grains possessing aspect ratios that were $\leq$ 1.

The corresponding diffraction patterns from the 23. 54.5, and 143 nm films are shown in Figure 6. 18.

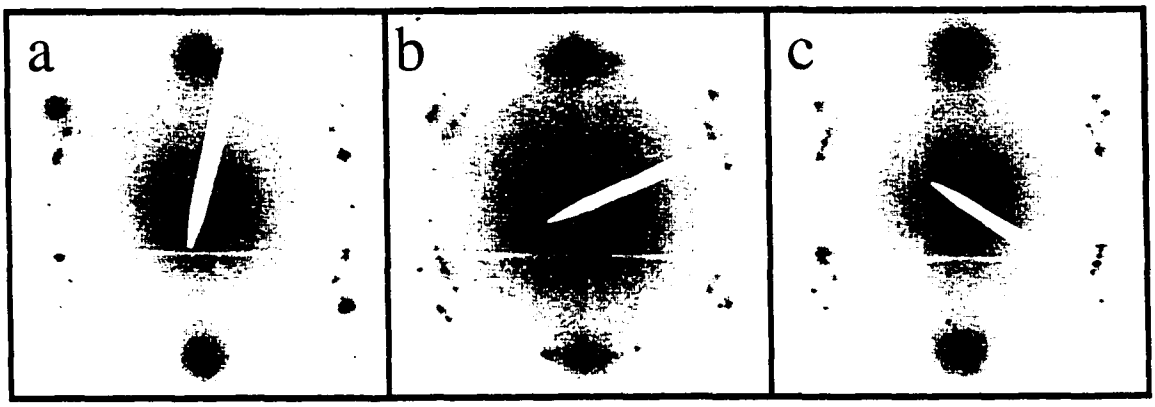

Figure 6. 18: Series of selected area electron diffraction patterns for as-deposited 1Nb/3Al multilayers. a) Λ = 23 nm, b) Λ = 54.5 nm, c) Λ = 143 nm. The selected area aperture usually covered several layers. The most intense spots are Al (111)/Nb (110).

The SAD apertures used to obtain the patters normally selected several layers, however, fewer layers were sampled as Λ increased. The SAD patterns are characterized by the textured Al (111) /Nb (110) innermost ring. This results in a pair of intense spots along the growth direction of the film. The second ring was attributed to the Al (200). The (111)/(110) "spots" develop into arcs as the period increases indicative of a decrease in fiber texture. This result was qualitatively consistent with the rocking curve and pole plot findings. The unique arrangement of the spots found in the diffraction pattern was believed to be a result of twinning between the coherent Al/Nb interfaces. This effect had been previously observed in Au/Ni multilayers using high resolution TEM (Wall and Jankowski 1989). In this case, the authors found the twinning occurred only on the Au onto Ni interfaces shown in Figure 6. 19. Besides the different elements, the other difference between those results and the present work is the much larger bilayer thickness of the Nb/Al multilayers.

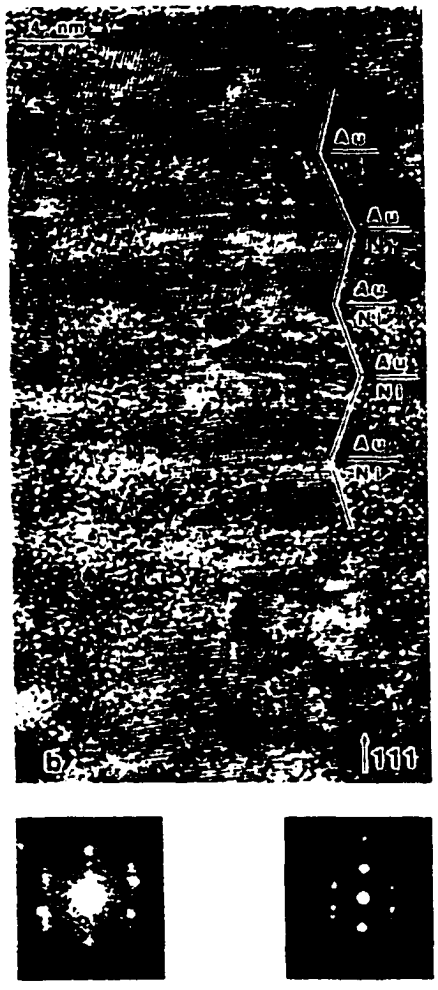

Figure 6. 19: High resolution electron micrograph along the [110] projection, with electron diffraction patterns and optical diffraction patterns showing twinning at Au onto Ni interfaces in a 4.6 nm Au/Ni multilayer sample. Compare the diffraction patterns with those shown in Figure 6. 18 and Figure 6. 20 (from Wall and Jankowski 1989).

The diffraction patterns from the Nb/Al samples can be consistently indexed as shown in Figure 6. 20 taken from a particularly well-textured region comprised of several bilayers in the 1Nb/3Al, Λ = 54.5 nm sample. The addition of some angular variation in the pattern will form the short arcs found in the higher period samples. The twin plane is marked by the horizontal line T-T. The outline of one <110> pattern is shown by the dotted white line.

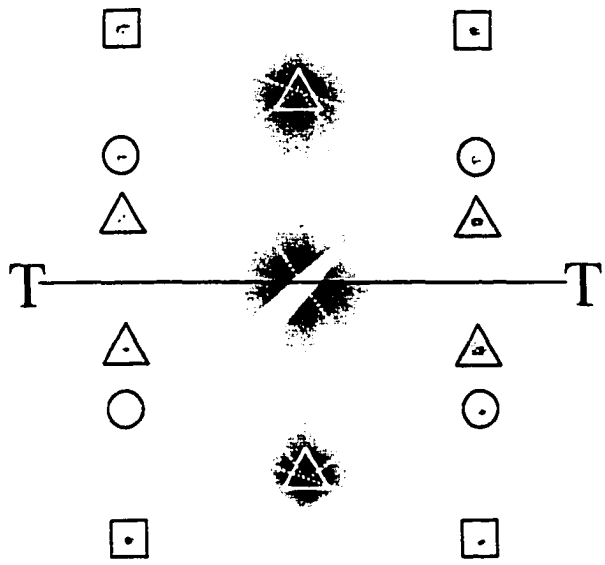

Figure 6. 20: Selected area diffraction pattern formed by twinning at the Nb/Al interfaces from a 1Nb/3Al multilayer with Λ = 55 nm. Line T-T is the twin plane. Dashed white line marks the <110> pattern. Triangle = (111), O = (200), □ = (220)

To provide insight into the effects of Cu additions on the microstructure, a 1Nb/3Al-1.0 wt.% Cu sample with Λ = 333 nm was examined in cross-section. Figure 6. 21 shows a bright field image and the corresponding electron diffraction pattern

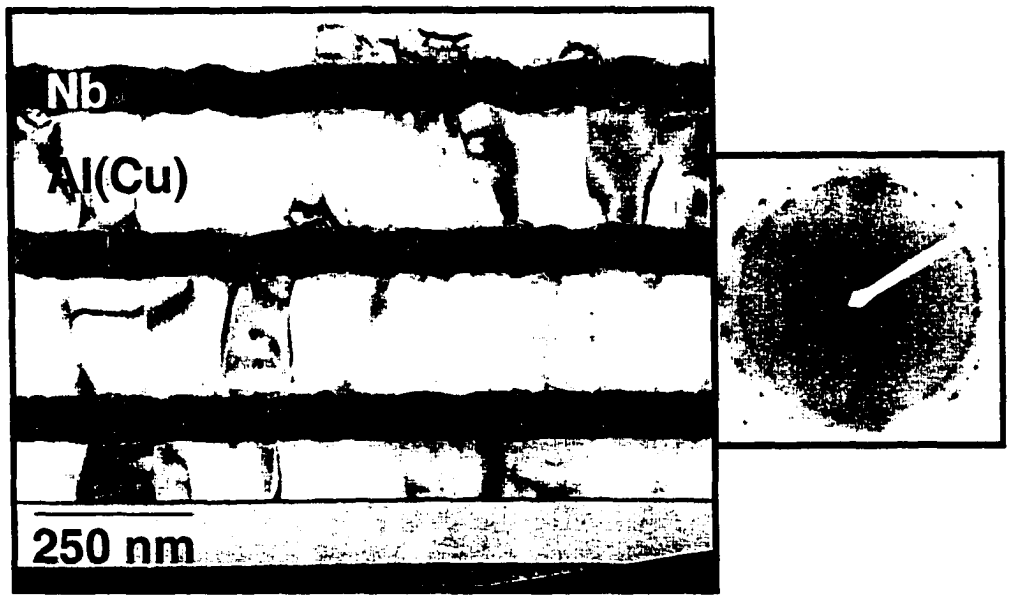

Figure 6. 21: Bright field image of an as-deposited 1Nb/3Al-1 wt.% Cu multilayer with Λ = 333 nm and the corresponding electron diffraction pattern.

The microstructure of the Al layers was significantly altered by the presence of the Cu. The aspect ratio has decreased and while the grains remain columnar, their widths have been reduced. Because of the larger number of grains per layer, the resulting interlayer interfaces have now acquired a roughness that was associated with the size of the *Al* grains. This can be seen clearly in Figure 6. 22.

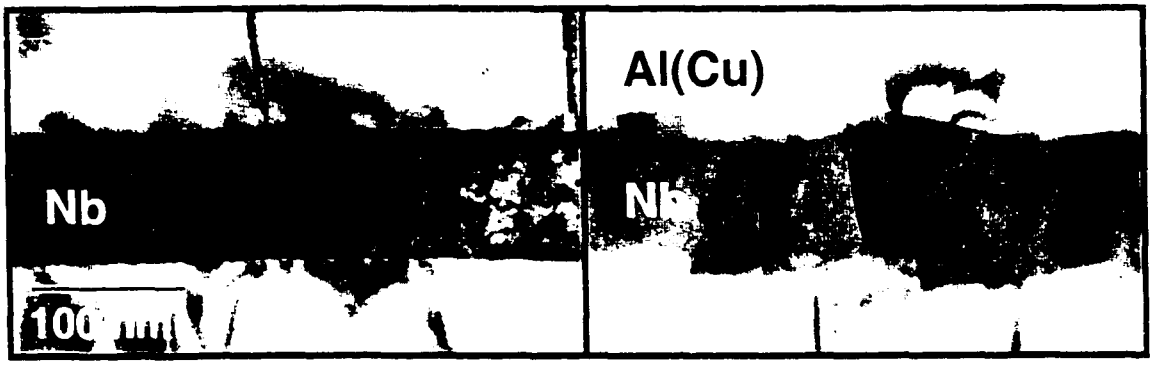

Figure 6. 22: Comparison of as-deposited 1Nb/3Al and 1Nb/3Al-1.0 wt.% Cu multilayers with Λ =333 nm showing the detail of the interlayer interface. Note the increase in roughness for the sample with the Al(Cu) layers.

The corresponding SAD indicated a nearly random texture in the growth direction for the (111) reflection in agreement with the pole figure results.

6.4.1.2 Annealed Films

Using the calorimetry data as a kinetic "map" of the reaction, *ex situ* annealing experiments were performed at three different temperatures to examine the corresponding microstructure at different stages of the reaction. Figure 6. 23 shows a representative DSC trace taken at 40 °C/min for a 1Nb/3Al Λ = 333 nm multilayer film. Cross section TEM micrographs of samples that were annealed to the various points indicated on the curve are shown in Figure 6. 23.

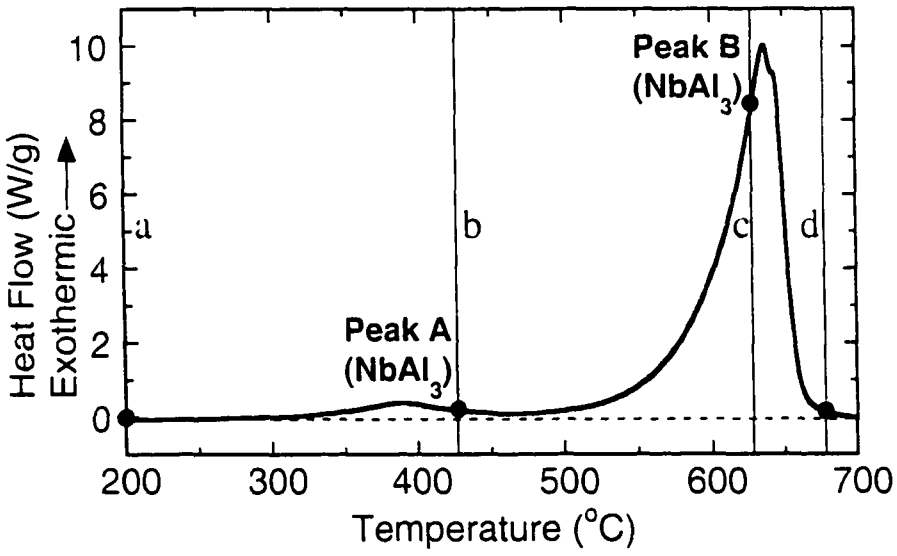

Figure 6. 23: Constant heating rate DSC trace taken at 40 °C/min for a 1Nb/3Al multilayer with Λ = 333 nm. Marked points correspond to the micrographs in Figure 6. 24.

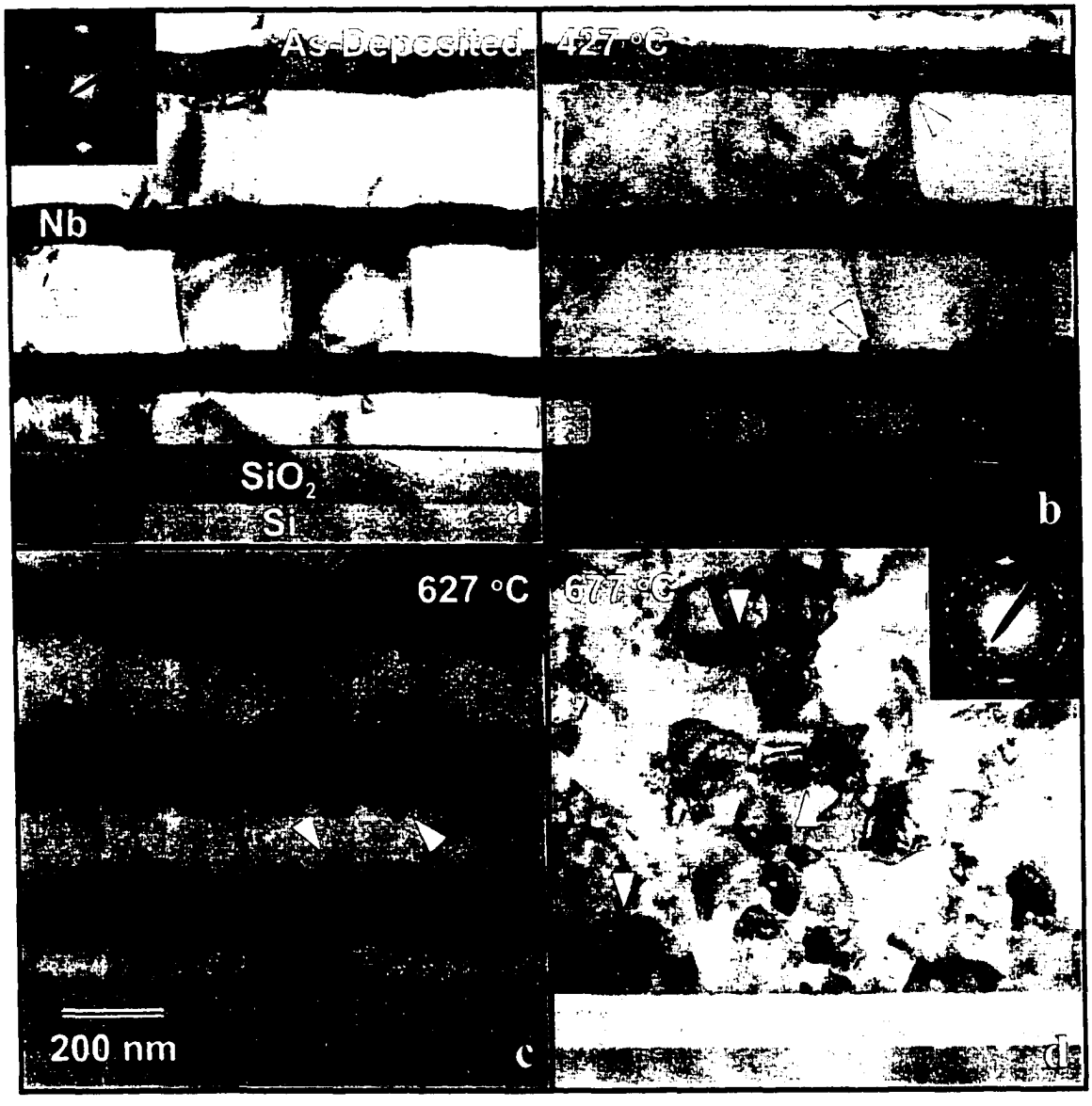

Figure 6. 24: A series of cross section TEM micrographs of a Λ = 333 nm 1Nb/3Al multilayer film annealed to the indicated temperatures at 40 °C/min in the DSC. Growth of $NbAl_3$ occurs in two stages. The first stage results in a continuous layer of $NbAl_3$ at the interface (b). Note the protrusions of $NbAl_3$ grains into the Al grain boundaries intersecting the interface (arrows). (c) During the second stage, the $NbAl_3$ grains grow and facet (arrowed) producing a rough interface; this eventually leads to an equiaxed microstructure (note unreacted Nb marked by arrows) (d).

Figure 6. 24a shows the as-deposited microstructure composed of through-thickness Al grains with most of the grains having aspect ratios >1. The Nb layers were again composed of a much higher density of through-thickness grains with some grains

having aspect ratios ~1. The majority of the Nb grains had aspect ratios <1. The electron diffraction pattern again indicated the fiber texture of the layer with the Al (111) and Nb (110) planes parallel to the substrate surface.

Upon annealing to 427 °C (immediately following the maximum of the first peak in the DSC trace), some grain growth was evident in the Al layer and a thin, polycrystalline layer of $NbAl_3$ ~10 nm thick had formed at the interlayer interfaces, as seen in Figure 6. 25. The identity of this layer was confirmed by electron diffraction.

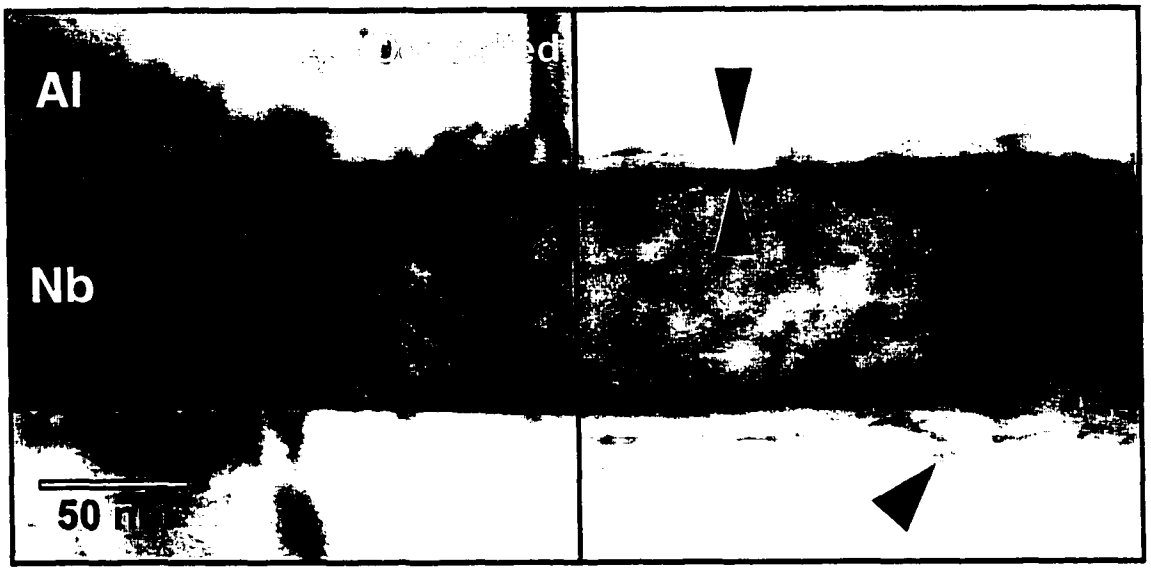

Figure 6. 25: Comparison of the Nb/Al interface in an as-deposited 1Nb/3Al multilayer with Λ = 333 nm and a specimen from the same multilayer annealed to 427 °C at 40 °C/min. Note the formation of an intermediate layer with a relatively uniform thickness between the Nb and Al. The layer was observed to protrude into the Al grain boundaries.

The $NbAl_3$ grains were observed to protrude into the Al grain boundaries where they intersected the interface suggesting accelerated growth facilitated by increased diffusivity at these regions.

To investigate this possibility further, high spatial resolution XEDS mapping was performed on areas surrounding the Al grain boundary intersections with the interface.

Since the thickness of this sample was not known, the absorption correction could not be accurately applied to the measured Al-Kα intensities. Consequently, the composition maps are qualitative in nature. Figure 6. 26 contains a bright field image obtained from an area containing an Al grain boundary that was nearly perpendicular to the Nb layer. The Al grain boundary fades into the center of a triangular-shaped region as it approaches the Nb/Al interface. A 64 x 64 pixel XEDS map taken at 1 MX revealed that this feature contained Nb as well as Al. The Nb had penetrated ~ 25 nm into the Al layer. Presumably, some Al has also diffused into the Nb as well, but this could not be detected. The relatively constant Al intensity in the Nb could also result from re-sputtering of the adjacent Al layers during ion polishing as was seen in studies of as-deposited Nb/Al multilayers (Lucadamo et al. 1999).

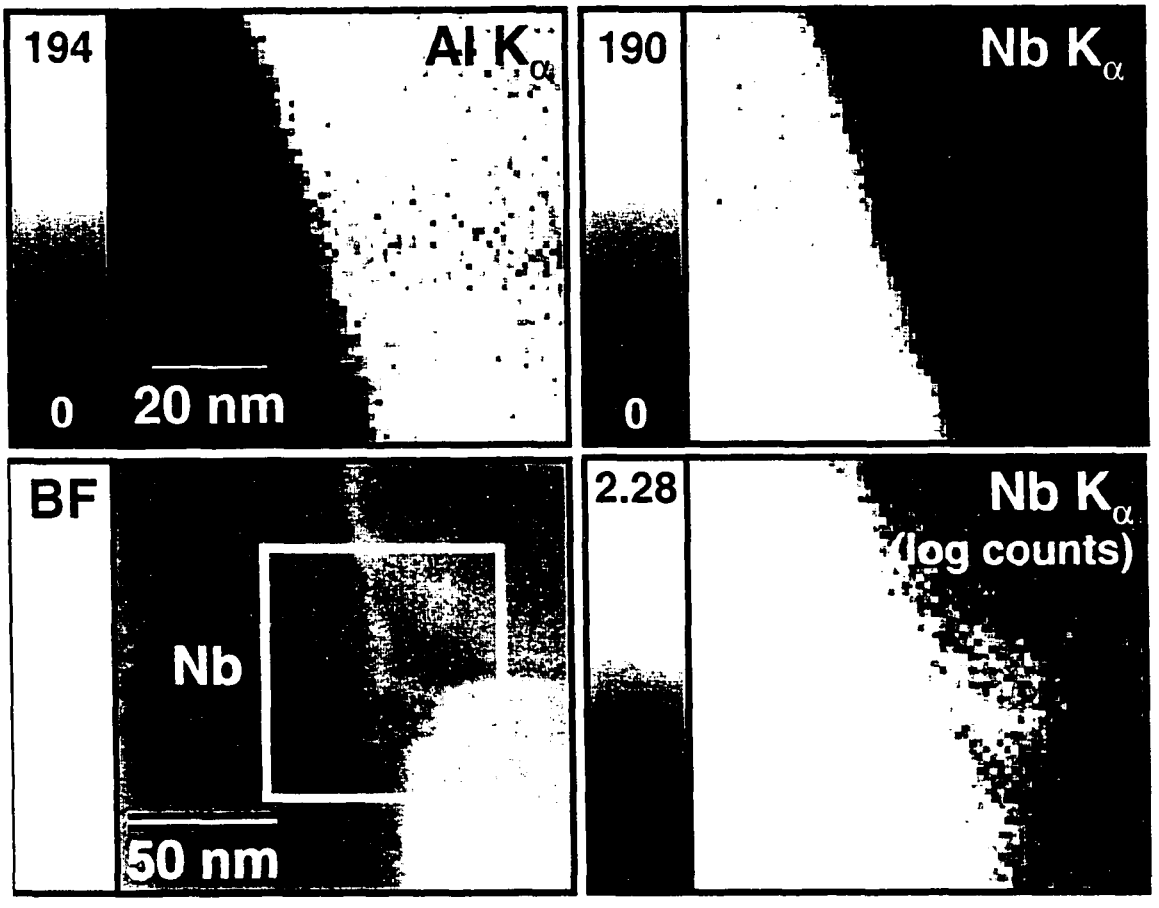

Figure 6. 26: Series of qualitative 64 x 64 pixel, EDX intensity maps showing the distribution of Al and Nb in the area surrounding an Al grain boundary in a 1Nb/3Al multilayer with Λ = 333 nm annealed to 427 °C at 40 °C/min. A log scale was used to enhance the contrast in the Nb map. The white box in the bright field image indicates the boundary of the analysis area.

Another map taken at 500 kX of a Nb layer and its associated interfaces is shown in Figure 6. 27. A triangular feature was again visible near the intersection of the Al grain boundary with the Nb layer. A second region protruding into the Al layer also was observed on the lower left side of the Nb layer. In both cases, the Nb was seen to have diffused into the Al layer with further penetration in regions near Al grain boundaries.

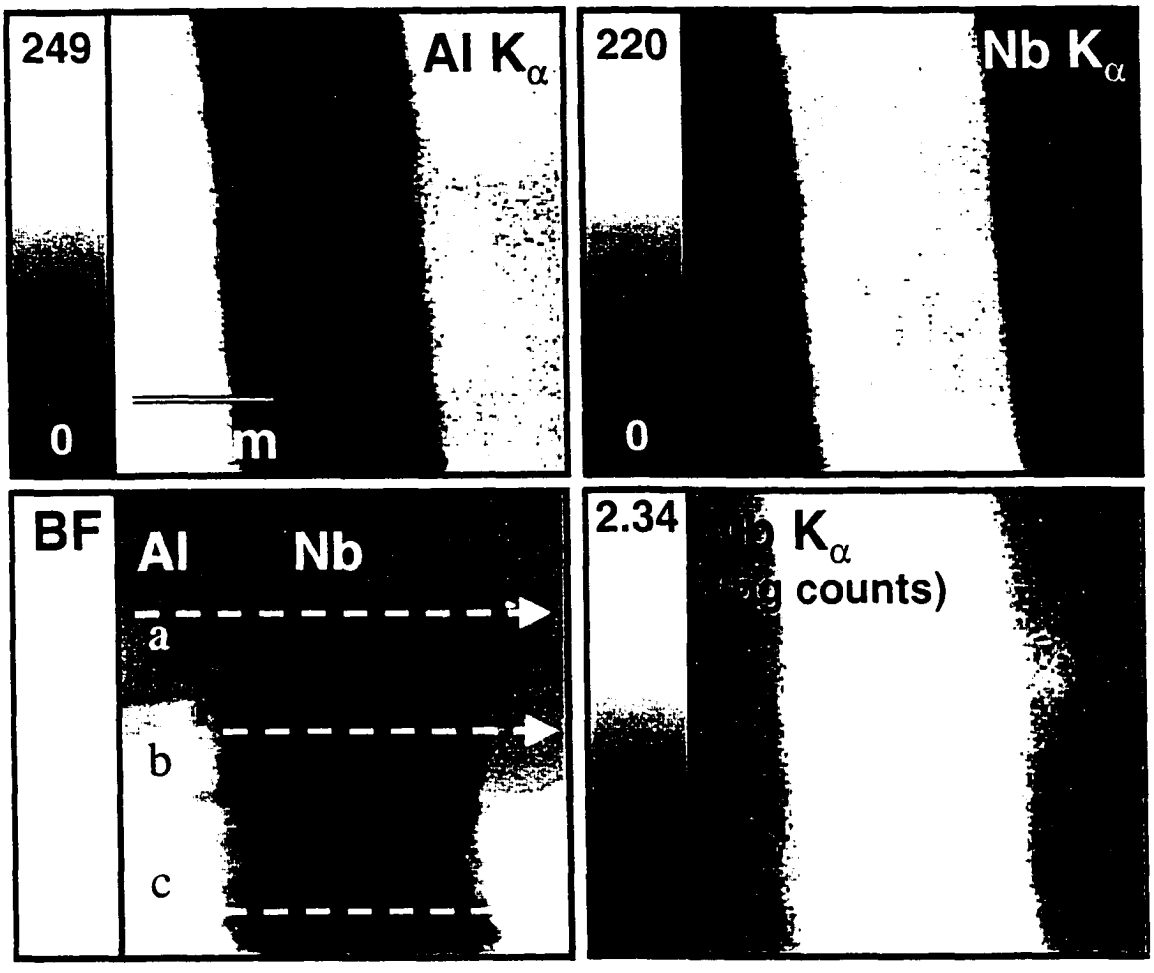

Figure 6. 27: Qualitative, 128 x 128 pixel EDX intensity maps of Al and Nb in the region surrounding a Nb layer from a 1Nb/3Al multilayer sample with Λ = 333 nm annealed to 427 °C at 40 °C/min. A triangularly-shaped feature containing Nb was observed to grow into the Al layer. Numbers indicate the net counts in each pixel. Arrows in the bright field image indicate the line profiles plotted in Figure 6. 28.

A series of line profiles was extracted from the maps at the positions indicated by the arrows and is shown in Figure 6. 28. The average net XRD intensity was plotted as a function of distance starting from the Nb layer and moving into the Al layer. To improve counting statistics, characteristic X-ray counts were averaged over a 10 pixel width for the length of the line scan. The region of enhanced Nb diffusion was clearly seen in a comparison of line profiles taken on either side of the grain boundary and directly over

the grain boundary. The middle line scan showed a narrow plateau in the Nb concentration. This could indicate formation of the stoichiometric $NbAl_3$ phase.

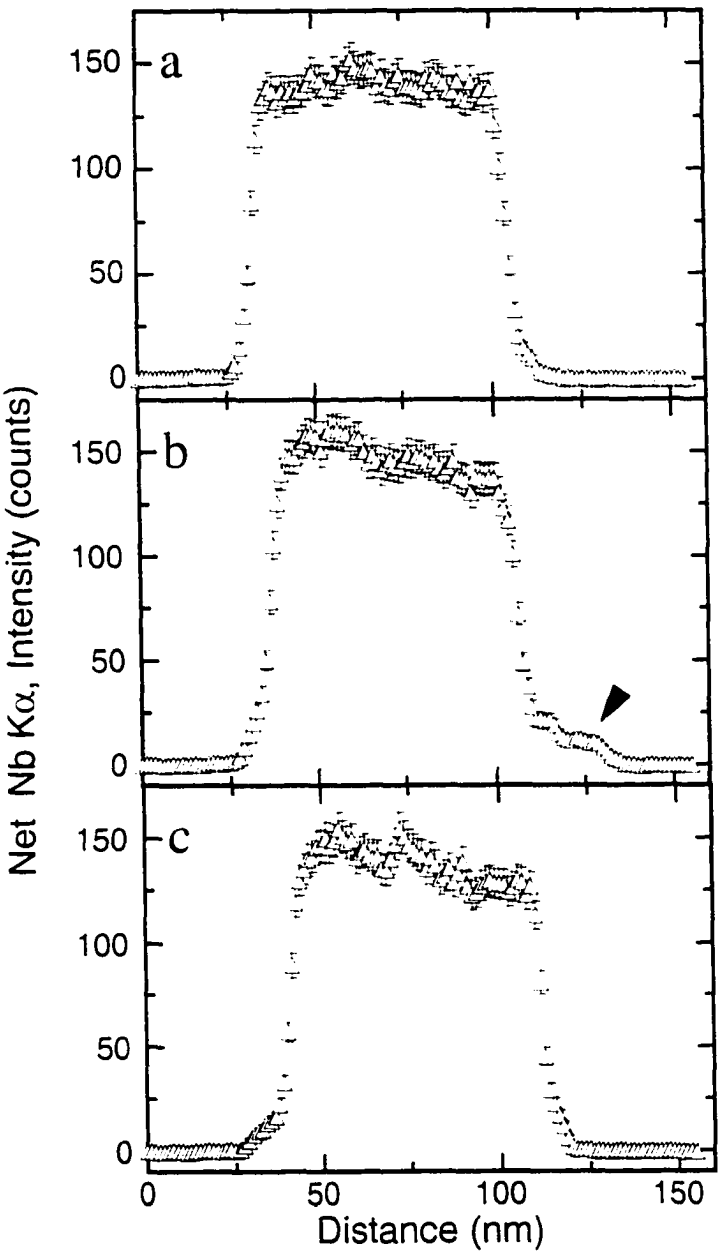

Figure 6. 28: Net Nb Kα intensity plotted vs. distance for a series of linescans extracted from the map in Figure 6. 27. The arrow marks the region of increased Nb signal in the Al layer corresponding to the triangularly-shaped feature. Error bars were determined at the 95% confidence level.

Further annealing of the 333 nm sample to 627 °C resulted in growth of the nucleated $NbAl_3$ grains and the formation of facets on many of the intermetallic grains at

the $NbAl_3$/Al interface (Figure 6. 24c). The reaction layer was ~100 nm wide as estimated from bright-field images noting that the product layer interface was not planar. Figure 6. 29 shows the detail of one faceted grain of $NbAl_3$ formed near the intersection of an Al grain boundary with the interface between layers.

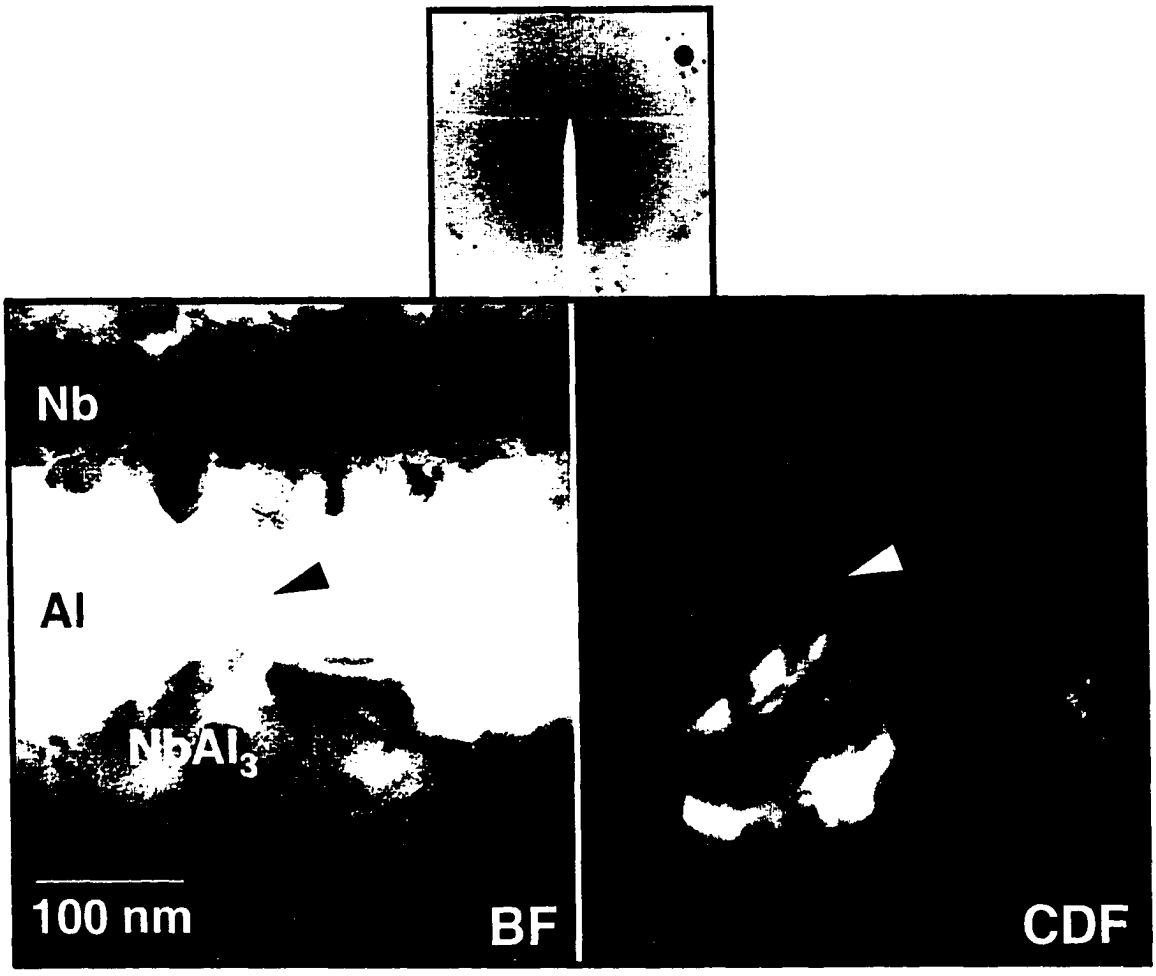

Figure 6. 29: Detail of the interface in a 1Nb/3Al multilayer with Λ = 333 nm heated to 627 °C at 40 °C/min (bottom left). Centered dark field image using a $NbAl_3$ (114) reflection (top) illuminated a faceted grain protruding into the Al layer along a grain boundary (bottom right).

The CDF image formed using a spot from the (114) ring of the $NbAl_3$ phase, indicated the facets of the product phase grains at the Al interface. Note that the grain also extends into the Nb layer, but this interface does not have well defined facets.

By 677 °C the Al layers were indistinguishable, although some remnants of the Nb layers were visible (Figure 6. 24d). The grains of $NbAl_3$ had continued to grow or coarsen and had become equiaxed with sizes less than the original period of the multilayer. At this point in the reaction, the diffraction pattern could be consistently indexed to $NbAl_3$ as shown in Figure 6. 30. Some texturing was evident in the (112) ring.

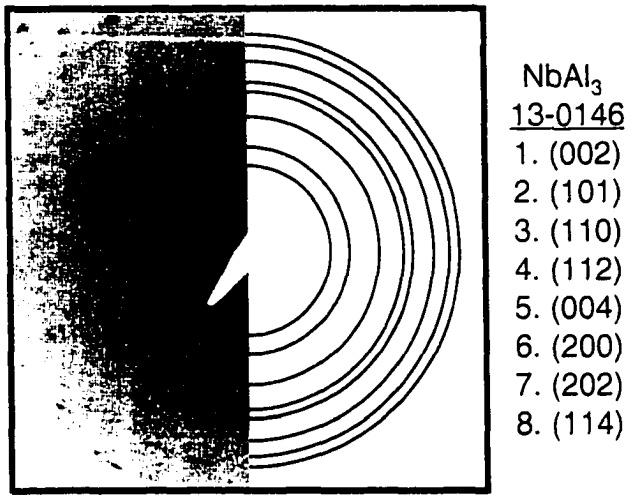

Figure 6. 30: Selected area diffraction pattern taken from the 1Nb/3Al, Λ = 333 nm multilayer annealed to 677 °C at 40 °C/min and corresponding diffraction rings for the $NbAl_3$ phase (Innermost ring = #1).

Another set of experiments was designed to study the influence of the layer thickness on microstructure evolution during product phase formation. Instead of using a series of *ex situ* anneals on several samples with different bilayer thicknesses, a novel sample architecture was developed. A multi-period sample was prepared that was comprised of several bilayers of varying thickness ranging from 10 nm to 333 nm that varied through the thickness of the multilayer (~1.2 μm). Therefore, by conducting *ex situ* annealing experiments on one sample, the effects of layer thickness on the transformed microstructure could be observed in *one* sample. The as-deposited microstructure is shown in Figure 6. 31.

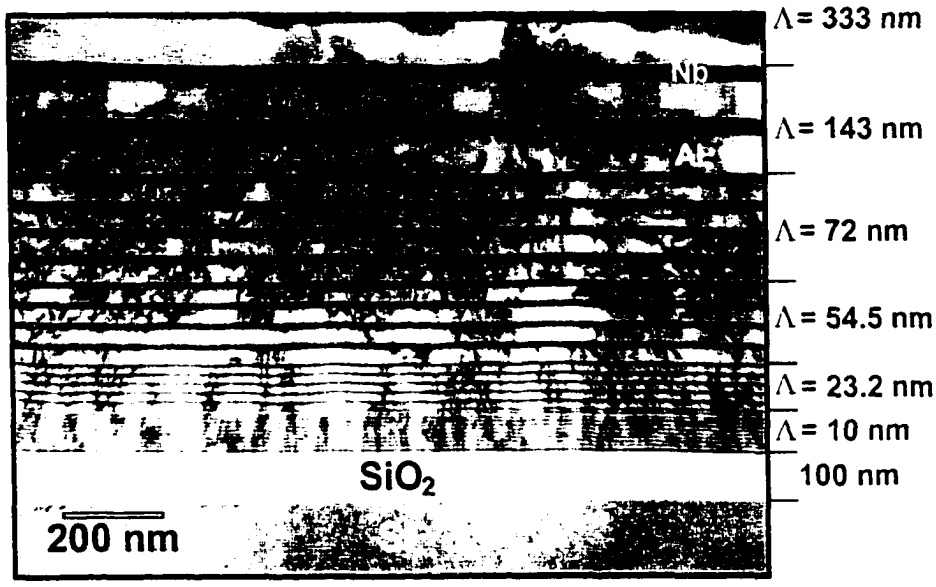

Figure 6. 31: Cross section TEM micrograph of an as-deposited 1Nb/3Al multiple-period sample with Λ ranging from 10 to 333 nm.

This sample clearly shows the increase the lateral dimension of the Al grains as well as the formation of regions with similar orientations propagating through the entire thickness of the multilayer. Figure 6. 32 shows this sample after annealing to 627 °C at 40 °C/min in the DSC.

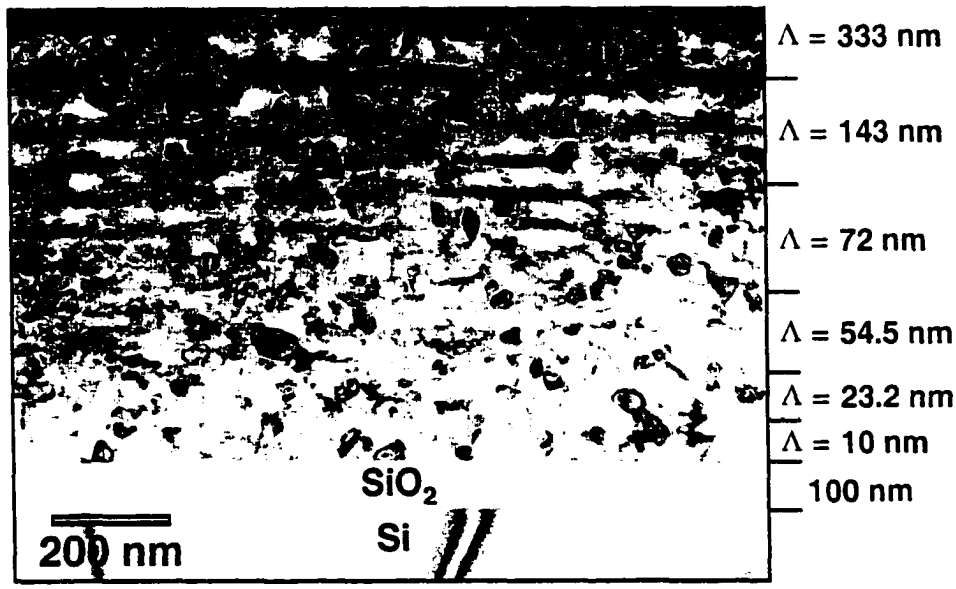

Figure 6. 32: Cross section TEM micrograph of a 1Nb/3Al multiple period sample annealed to 627°C at 40 °C/min.

The observed microstructure concurred with the calorimetry results. While layers < ~72 nm are completely transformed, there are still large amounts of unreacted Al and Nb in the bilayers with Λ = 143 and 333 nm. In addition, the $NbAl_3$ grains of the smaller bilayers have grown to span the thickness of several bilayers. No evidence of the original layered structure was preserved. In the regions composed of bilayers with Λ > 72 nm, some isolated, unreacted sites remain surrounded by regions that have transformed. Also, as was seen in the previously described 333 nm sample, faceted grains of $NbAl_3$ were observed to grow into the Al layers.

Another piece of the multi-period multilayer was annealed to 720 °C. This sample exhibited dramatic changes in the microstructure as seen in Figure 6. 33.

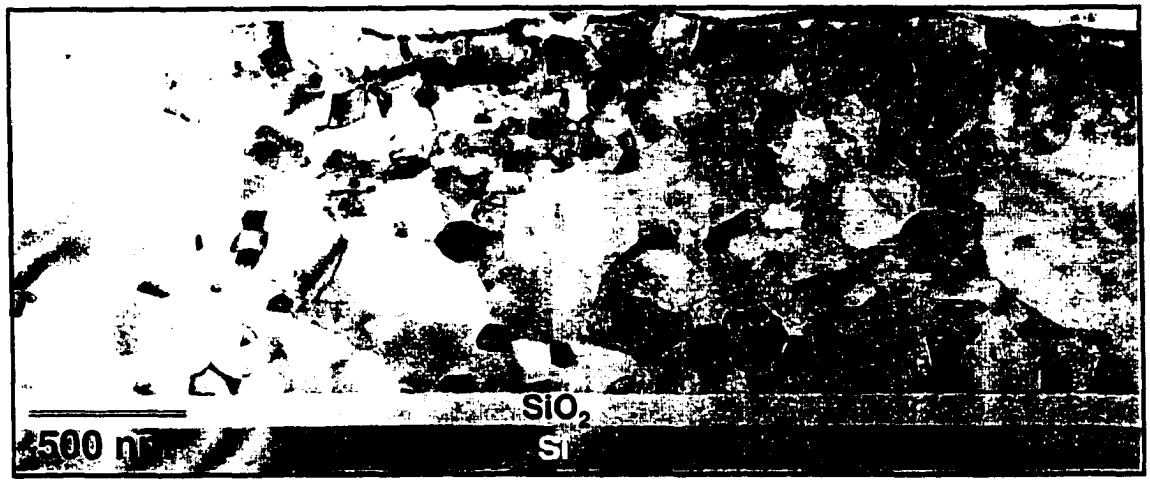

Figure 6. 33: Cross-section TEM micrograph of a multiple-period multilayer heated to 720 °C at 40 °C/min. Note the substantial growth of the grains as compared to the previous figure.

Coarsening processes resulted in fewer, larger grains throughout the microstructure especially noticeable near the bottom of the film. The presence of "half-grains" that have stopped growing due to the presence of the substrate were also observed in this region. Some unreacted Nb was still visible near the top of the film although the layer was fragmented and varied in thickness.

To further quantify the relationship between the as-deposited and fully-reacted microstructure, the grain size of several reacted samples was measured from planview TEM images. Free-standing films were annealed in the DSC to a temperature of 700 °C at 40 °C/min. Grains areas were measured from bright-field images taken from several fields of view for each sample. In all cases > 500 grains were counted in order to accurately describe the distribution (Carpenter 1998, Carpenter et al. 1998). The areas were then converted to an effective diameter by approximating the grain shape as a circle. The resulting probability distributions were fit using a gamma distribution and a log normal distribution. The gamma distribution had previously been used to fit grain size data in computer simulations designed to determine the coalesced grain sizes resulting from various spatial distributions of nucleation sites (Tong et al. 1997). The equation describing the gamma distribution is given by

$$f(x) = \frac{1}{\beta^{\alpha}\Gamma(\alpha)} x^{\alpha-1} e^{-x/\beta} \qquad 6.1$$

where,

$$\Gamma(\alpha) = \int_0^{\infty} x^{\alpha-1} e^{-x} dx \qquad 6.2$$

and α and β are the median and log of the standard deviation, respectively. The corresponding first (μ) and second (σ) moments of the distribution can then be calculated by

$$\mu = \alpha\beta$$
$$\text{and} \qquad 6.3a,b$$
$$\sigma = \sqrt{\alpha\beta^2}$$

The results of the gamma fit to several experimentally measured distributions are listed in Table 6. III.

Table 6. III: Summary of grain size data obtained for 1Nb/3Al multilayers heated at 40 °C/min to the indicated temperature. Grain size distributions were fit using a gamma distribution described by eq. 6.1.

Λ [nm]	Temperature [°C]	No. of grains	μ_d [nm]	σ_d [nm]	μ_d/Λ
23.2	700	752	25.3	10.0	1.1
72	700	1026	71.7	27.3	1.0
143	700	913	62.3	19.9	0.44
240	700	804	48.5	18.2	0.20
333	720	619	65.4	24.4	0.20

The same grain size data were fit using a log-normal distribution described by

$$f(x) = \frac{1}{\sqrt{2\pi}\beta} x^{-1} e^{-(\ln x - \alpha)/2\beta^2} \qquad 6.4$$

where

$$\mu = e^{\alpha+\beta^2/2}$$

and 6.5a,b

$$\sigma = \sqrt{e^{2\alpha+\beta^2}(e^{\beta^2}-1)}$$

The results from the fit to the log-normal distribution are listed in Table 6. IV.

Table 6. IV: Summary of grain size data obtained for 1Nb/3Al multilayers heated at 40 °C/min to the indicated temperature. Grain size distributions were fit using a log-normal distribution described by eq. 6.4.

Λ [nm]	Temperature [°C]	No. of grains	μ_d [nm]	σ_d [nm]	μ_d/Λ
23.2	700	752	28.0	12.3	1.2
72	700	1026	74.8	30.7	0.96
143	700	913	64.1	21.7	0.45
240	700	804	50.4	20.4	0.21
333	720	619	68.2	27.4	0.21

The results for the mean and standard deviation of grain sizes from the two different fits were found to be nearly identical. As shown in Figure 6. 34 the shape of the fit to the grain size distributions is nearly identical. The main difference is the presence of a longer tail for the log-normal fit.

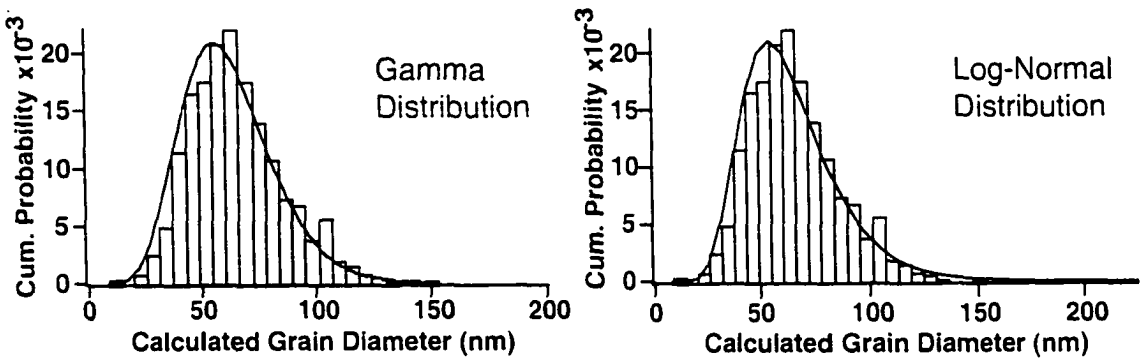

Figure 6. 34: Comparison of the fit of the gamma and log-normal probability distributions to the grains sizes measured from 1Nb/3Al multilayer films with Λ = 143 nm that were annealed to 700 °C at 40 °C/min.

6.4.2 Ti/Al

6.4.2.1 As-deposited Films

A cross section TEM micrograph of a 1Ti/3Al, Λ = 72 nm multilayer film is shown in Figure 6. 35.

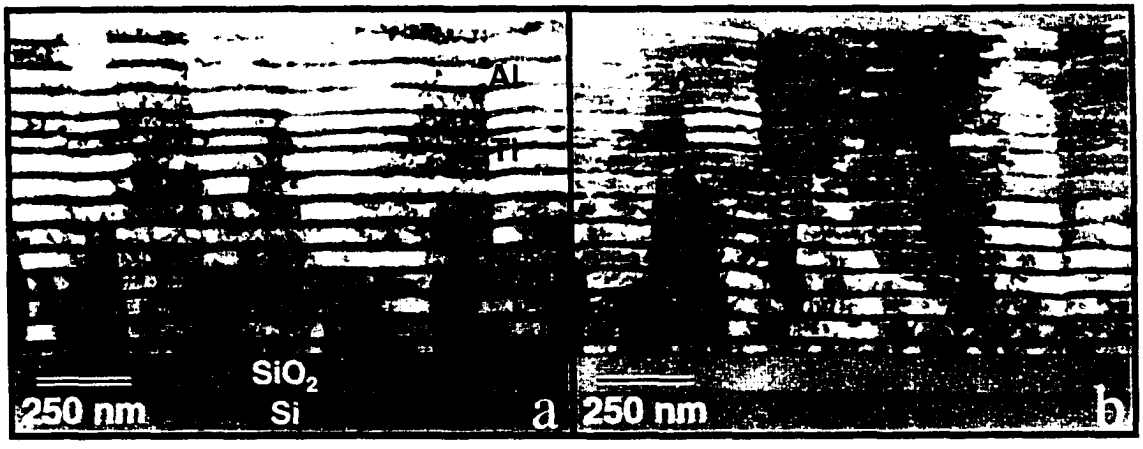

Figure 6. 35: Cross section TEM micrographs of an as-deposited 1Ti/3Al multilayer with Λ = 72 nm a) bright field b) centered dark field using the Al (111)/Ti (0002) spots.

As with the Nb/Al multilayers, the Ti/Al films contained regions of similar orientation. Several such areas are visible in CDF images formed using the Al (111) and Ti (0002) reflections (Figure 6. 35b). The "macrograins" were composed of alternating Al and Ti layers and could grow through the entire thickness of the multilayer. One Al layer that appears thinner than the others was likely due to a processing problem, such as a malfunctioning shutter. The individual grains of Al had aspect ratios that appeared to be ~ 1. In many cases the aspect ratios were > 1. The grain size of the Ti also appeared columnar with heights approximately equal to the layer thickness.

A portion of a 1Ti/3Al Λ = 143 nm multilayer is shown in Figure 6. 36.

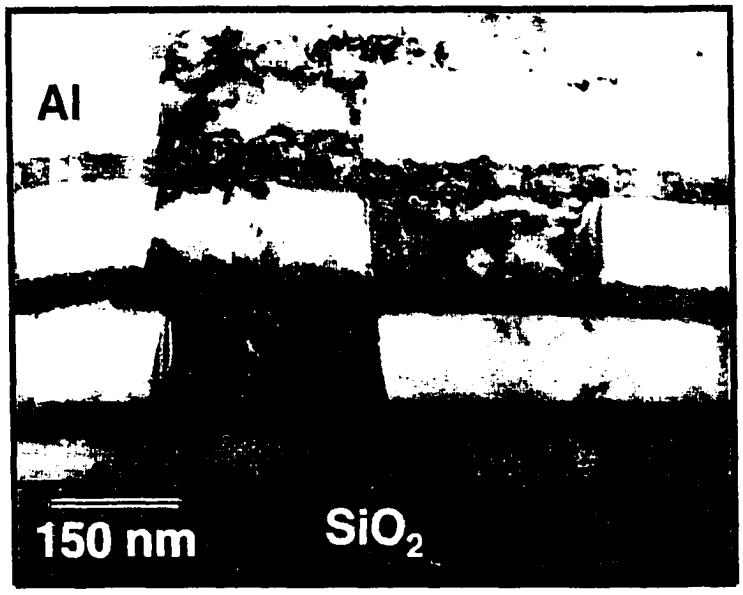

Figure 6. 36: Cross section TEM image of an as-deposited 1Ti/3Al multilayer with Λ = 143 nm.

As with the 72 nm sample, certain grains appear to grow with the same orientation through multiple layers. In this sample, the width of the "macrograins" corresponds to the size of ~1 Al grain. These grains have grown laterally and have aspect

ratios > 1. Some interfacial roughness was observed on the upper surfaces of the Ti layers. A magnified view of this effect is shown in Figure 6. 37.

Figure 6. 37: Cross section TEM micrograph of an as-deposited 1Ti/3Al multilayer with Λ = 143 nm showing the detail of the Ti/Al interface. Note significant roughness on the upper surface of the Ti layer, as compared with the lower surface.

The roughness appeared to correlate with the Ti grain size. The Ti grain structure was fairly indistinct although it was finer and had some indications of through-thickness grains.

A 1Ti/3Al multilayer with Λ = 333 nm is shown in Figure 6. 38.

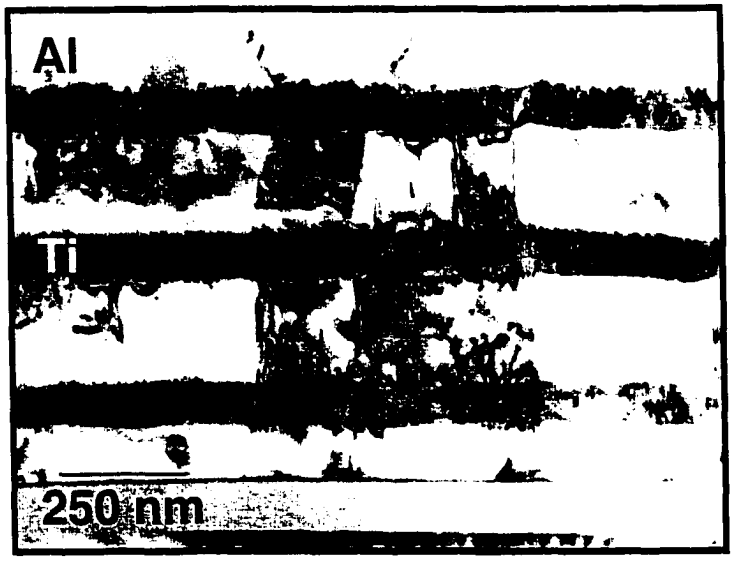

Figure 6. 38: Cross section TEM micrograph of a 1Ti/3Al multilayer with Λ = 333 nm.

The grain structure of the multilayer follows the same trends observed with the Nb/Al films. The propagation of the texture through the layers was still evident at this layer thickness. The Al grains have also increased in the lateral dimension. As with the lower period samples, the Ti layer appears to consist of a dense array of fibrous grains. The interlayer roughness was visible on the upper surfaces of most of the layers as seen in Figure 6. 39.

Figure 6. 39: Cross section TEM micrograph of a 1Ti/3Al multilayer with Λ = 333 nm showing detail of the Ti/Al interface. Note the faceted upper surface of the Ti layer. The facets are on the order of the grain size.

The selected area electron diffraction patterns from the three as-deposited Ti/Al multilayers are shown in Figure 6. 40.

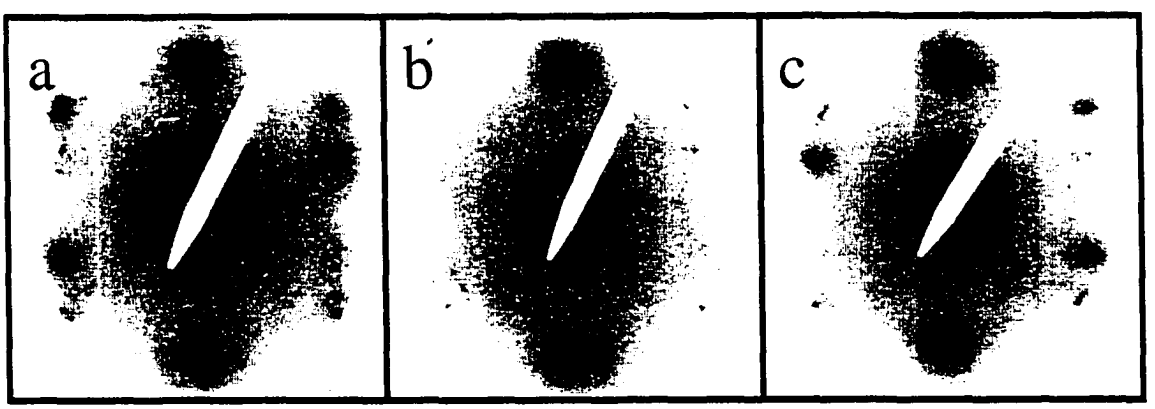

Figure 6. 40: Selected area electron diffraction patterns obtained from the as-deposited 1Ti/3Al multilayers. a) 72 nm b) 143 nm c) 333 nm. The bright spots correspond to Al (111)/Ti (0002).

The diffraction patterns appeared very similar to those obtained from the Nb/Al multilayers. The strongly textured Al (111)/Ti (0002) spots were clearly visible. The interlayer twinning phenomenon found in Nb/Al also appeared in the patterns.

A Ti/Al-1 wt.%Cu sample with Λ = 333 nm was examined to determine the effects of Cu additions on the as-deposited grain structures. The bright field image and electron diffraction pattern are shown in Figure 6. 41.

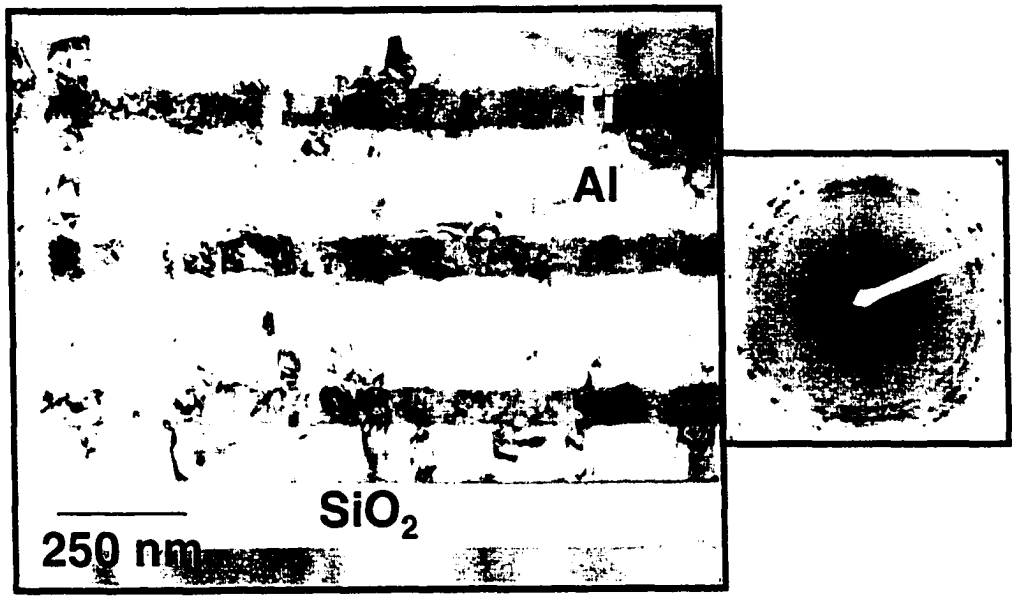

Figure 6. 41: Bright field image and selected area diffraction pattern for an as-deposited 1Ti/3Al-1.0 wt.% Cu sample with Λ = 333 nm. Compare the SAD with the one in the previous figure.

As observed in the Nb/Al sample, the addition of Cu reduced the aspect ratio of the Al grains by reducing their width appreciably. This again led to an interlayer roughness dominated by the Al grains and not the Ti grains, as was the case with the Nb/Al(Cu) sample. The Ti grains maintained a similar structure as before with some columnar grains an others that were not through-thickness. The corresponding SAD pattern does not indicate strong fiber texture, and the rings of Al and Ti were more complete.

6.4.2.2 Annealed Films

A study of the microstructure evolution of $TiAl_3$ formation proved more challenging than the study of $NbAl_3$ formation. This was due to the simultaneous presence of metastable and stable superlattice structures of the $TiAl_3$ as well as the lower reaction temperatures. Because of these effects, unambiguous phase identification was difficult especially due to the reduced number of spots in the cross-sectional pattern due to the texture of the products and reactants. The lower reaction temperatures allowed for significant product and reactant grain growth and interdiffusion to occur at low temperatures, thus obscuring the underlying microstructural changes due to the formation of the new phase. An example of this behavior is shown for a $\Lambda = 333$ nm sample annealed to 477 °C at 40 °C/min shown in Figure 6. 42. A substantial portion of the Ti layer has already been consumed while the layer of $TiAl_3$ exhibited an extremely rough interface with grains that extend approximately 1/3 of the way through the Al layers. Faceting of the grains did not seem as pronounced as it was in the Nb/Al multilayers.

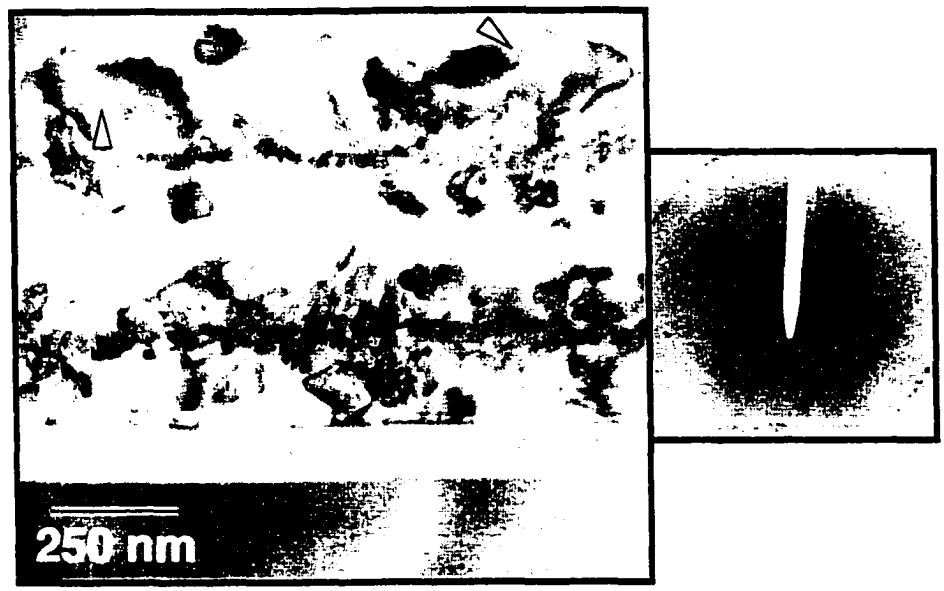

Figure 6. 42: Cross section TEM bright field micrograph and corresponding electron diffraction pattern of a 1Ti/3Al multilayer with Λ = 333 nm annealed to 477 °C at 40 °C/min. Some untransformed Al is indicated by the arrows.

As a result of the difficulty in determining the evolution of the phases from electron diffraction of cross-sectional samples, the focus was shifted to determining which phases were actually present at a given temperature for the samples deposited in this study. A series of plan view samples was prepared in order to provide a direct comparison with the *in situ* XRD results. The planview orientation provided significantly more diffracted intensity since the films had no in-plane orientation and revealed complete rings for indexing measurements. Free-standing 1Ti/3Al films with Λ = 72 nm were annealed in the DSC to 400, 525, and 700 °C corresponding to the formation of the $L1_2$, $DO_{23}/Ti_9Al_{23}/Ti_8Al_{24}$, and DO_{22} structures of $TiAl_3$, respectively. The films were heated at 60 °C/min in order to correspond directly with *in situ* XRD data obtained from the *in situ* XRD studies. The XRD intensity plotted as a function of 2θ and temperature for the 1Ti/3Al sample annealed at 60 °C/min is shown in Figure 6. 43.

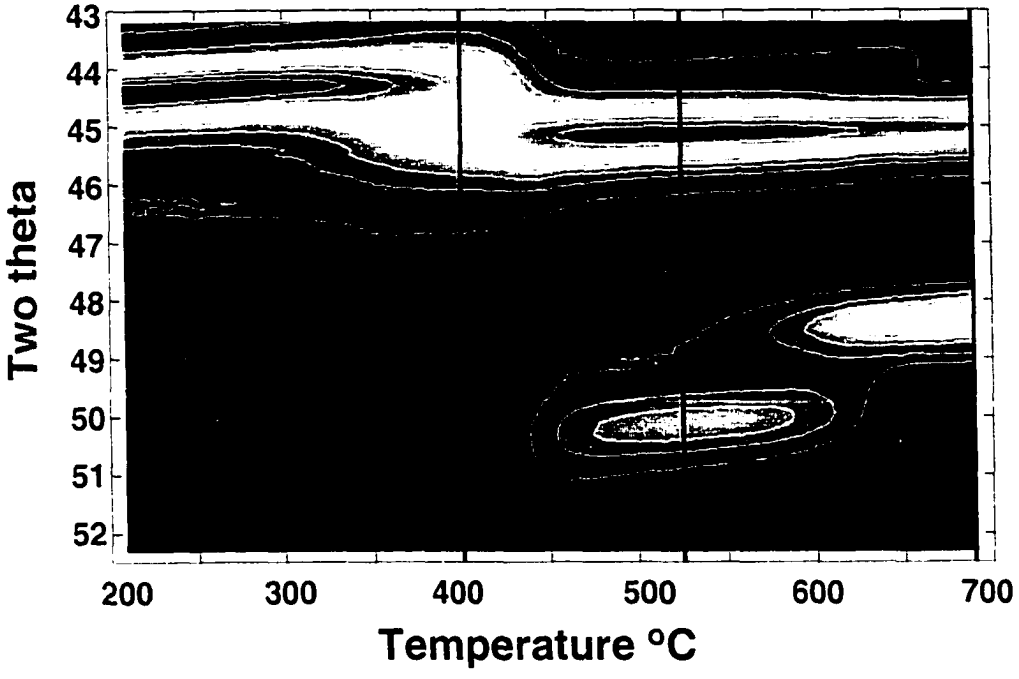

Figure 6. 43: Diffracted XRD intensity as a function of 2θ and temperature for a 1Ti/3Al multilayer film with Λ = 72 nm annealed at 60 °C/min to 700 °C in He. Black vertical lines denote temperatures selected for *ex situ* electron diffraction analysis.

The vertical lines mark the temperatures chosen for electron diffraction analysis. At each of the chose temperatures a "linescan" of XRD intensity vs. 2θ was extracted from *in situ* plot. The resulting SAD patterns, XRD curves, and indexing data for both diffraction patterns is shown in Figure 6. 44.

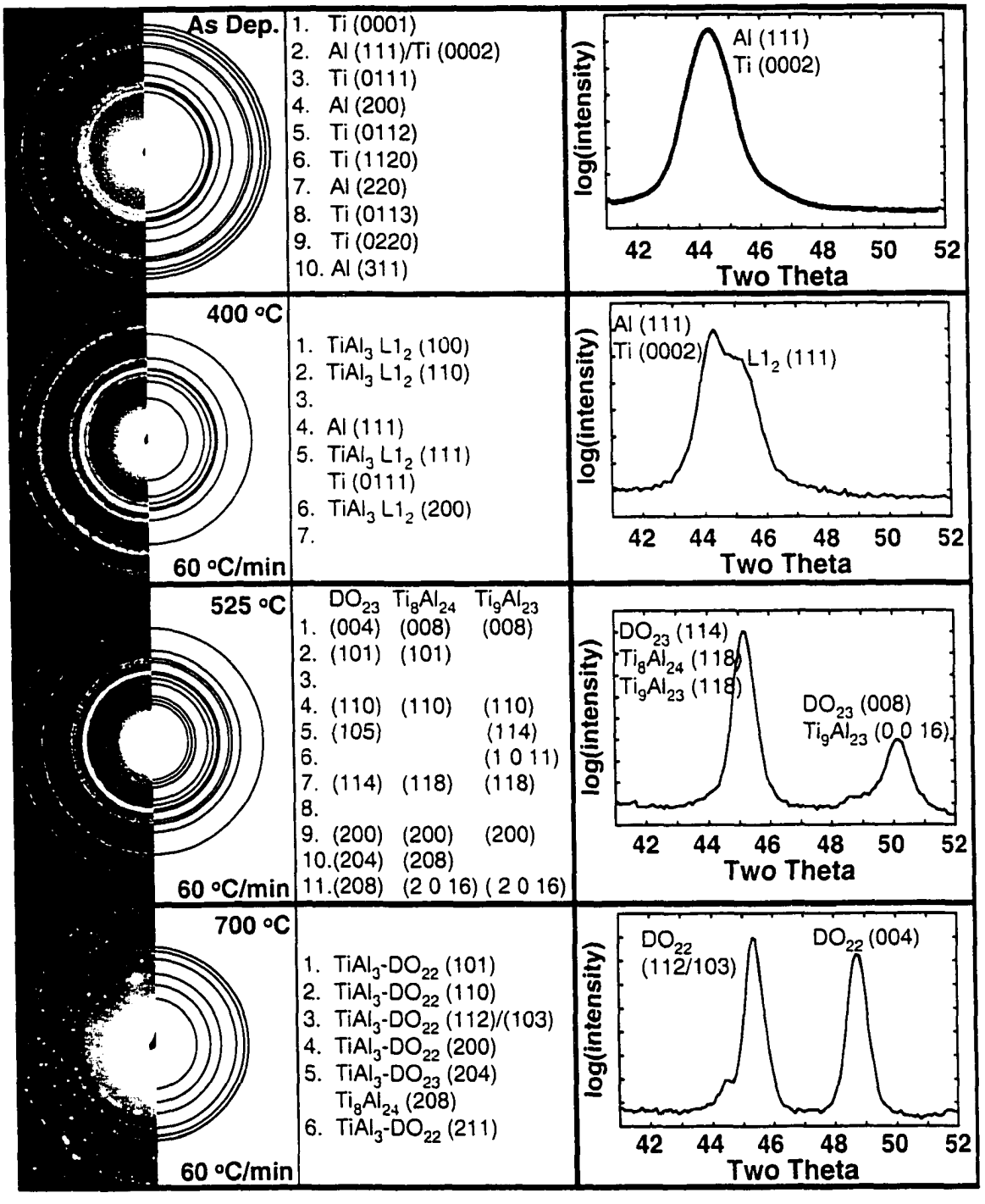

Figure 6. 44: Series of electron diffraction patterns, XRD patterns, and ring indices for 1Ti/3Al multilayers with Λ = 72 nm annealed at 60 °C/min to the indicated temperatures. Results reveal the formation of two metastable phases prior to the equilibrium structure (innermost ring = #1).

In the as-deposited state, only the rings corresponding to fcc Al and hcp Ti were visible. The indexing results are listed in Table 6. V.

Table 6. V: Measured radii from the selected area diffraction pattern taken from an as-deposited 1Ti/3Al multilayer with Λ = 72 nm. Camera constant = 25.29 mm-Å.

r (meas) [mm]	d (calc) [Å]	rel. error [Å]	Al 04-0787	Ti 44-1294
9.9	2.555	0.026		100
10.85	2.331	0.021	111	002
11.3	2.238	0.020		101
12.5	2.023	0.016	200	
14.6	1.732	0.012		102
17.2	1.470	0.009		110
17.7	1.429	0.008	220	
19.1	1.324	0.007		103
19.9	1.271	0.006		200
20.7	1.222	0.006	311	

Upon annealing to 400 °C the electron diffraction result clearly showed that the peak that developed on the high angle side of the Al (111)/Ti (0002) peak was due to the formation of $TiAl_3$ with the $L1_2$ structure. The indexed peaks are listed in Table 6. VI.

Table 6. VI: Measured radii from the selected area diffraction pattern taken from a 1Ti/3Al multilayer with Λ = 72 nm annealed to 400 °C at 40 °C/min. Camera constant = 37.3 mm-Å.

r (meas) [mm]	d (calc) [Å]	rel. error [Å]	$TiAl_3$-$L1_2$	Al 04-0787	Ti 44-1294
9.4	3.968	0.042	100		
13.4	2.784	0.021	110		
14.9	2.503	0.017			
16.1	2.317	0.014		111	
16.5	2.261	0.014	111		101
18.8	1.984	0.011	200		
24.5	1.522	0.006			

As with the XRD θ-2θ curves, the feature that appeared at 50.8 °C when the sample was heated to 525 °C could not be uniquely indexed to a particular $TiAl_3$ phase. The structure with the DO_{23} prototype appeared to have the largest number of indexed rings, however, other rings were present that best matched one (or both) of the other reported structures. The measurements from the electron diffraction pattern are listed in Table 6. VII.

Table 6. VII: Measured radii from the selected area diffraction pattern taken from a 1Ti/3Al multilayer with Λ = 72 nm annealed to 525 °C at 40 °C/min. Camera constant = 37.85 mm-Å.

r (meas) [mm]	d (calc) [Å]	rel. error [Å]	$TiAl_3$- DO_{23} 48-1385*	Ti_9Al_{23} 18-0069	Ti_8Al_{24} 26-0038	$TiAl_3$-DO_{22} 37-1449
9.0	4.206	0.047	004	008	008	
9.9	3.823	0.039	101		101	
10.7	3.537	0.033				101
13.7	2.763	0.020	110	110	110	
14.9	2.540	0.017	105	114		
16.0	2.366	0.015		1 0 11		
16.4	2.308	0.014	114	118	118	112/103
18.6	2.035	0.011				
19.4	1.951	0.010	200	200	200	
21.3	1.777	0.008	204		208	
26.5	1.428	0.005	208	2 0 16	2 0 16	

* Structure prototype, lattice constants from Srinivasan et al. (1991)

Finally, following the anneal to 700 °C, the rings and XRD pattern was best matched by equilibrium $TiAl_3$ with the DO_{22} structure. The measurements taken from the diffraction pattern are listed in Table 6. VIII. This experiment corroborates the interpretation of the XRD results in the previous chapter and confirms the identity of the different peaks.

Table 6. VIII: Measured radii from the selected area diffraction pattern taken from a 1Ti/3Al multilayer with Λ = 72 nm annealed to 700 °C at 60 °C/min. Camera constant = 37.3 mm-Å.

r (meas) [mm]	d (calc) [Å]	rel. error [Å]	$TiAl_3$-DO_{22} 37-1449	$TiAl_3$-DO_{23} 48-1385*	Ti_9Al_{23} 18-0069	Ti_8Al_{24} 26-0038
10.6	3.519	0.033	101			
13.8	2.703	0.020	110		110	
16.3	2.288	0.014	112/103		118	118
19.7	1.893	0.010	200			
21.5	1.735	0.008		204		
22.5	1.658	0.007	211	213		

* Structure prototype, lattice constants from Srinivasan et al. (1991)

6.5 Discussion

The as-deposited films were comprised of microstructures that could be best interpreted using the zone model first introduced by Grovenor et al. (1984) and later investigated by Barna and Adamik (1995). The homologous temperature of the materials and deposition temperatures used in this study are shown in Table 6. IX. An estimated substrate temperature of ~40 – 80 °C was used in the calculation.

Table 6. IX: Estimated homologous temperatures for the films deposited in this study based on the zone models of Grovenor et al. (1984) and Barna and Adamik (1995)

Element	T_s/T_m	Predicted Zone (Grovenor et al. 1984)	Predicted Zone (Barna and Adamik 1995)
Al	0.06 – 0.12	I, T	II
Al(Cu)	0.06 – 0.12	I,T	T
Ti	0.024 – 0.048	I	I
Nb	0.026 – 0.032	I	I

The ratios alone would predict a nominally zone I grain structure for both the Al, Nb, and Ti layers. Although zone I structure may accurately describe the microstructure

of the Nb and Ti layers , the TEM images indicated that the grains in the layers Al resembled a zone II/zone III microstructure.

Despite the low homologous temperature, significant grain growth had occurred. This apparent discrepancy could be explained by considering the effect of deposition rate on the zone model. A lower incoming flux of atoms will naturally require a longer amount of time to deposit a layer of a given thickness. During this time, grains could grow in a lateral direction driven by surface and interface energy minimization. This would also lead to the development of the <111> fiber texture. The processing conditions used in this study resulted in deposition rates of ~0.1 nm/s or less. The differences in grain structure for a 1Nb/3Al multilayer films sputter-deposited at nominally room temperature in different UHV systems are shown in Figure 6. 45. The increased deposition rate reduced the in-plane grain size and aspect ratio.

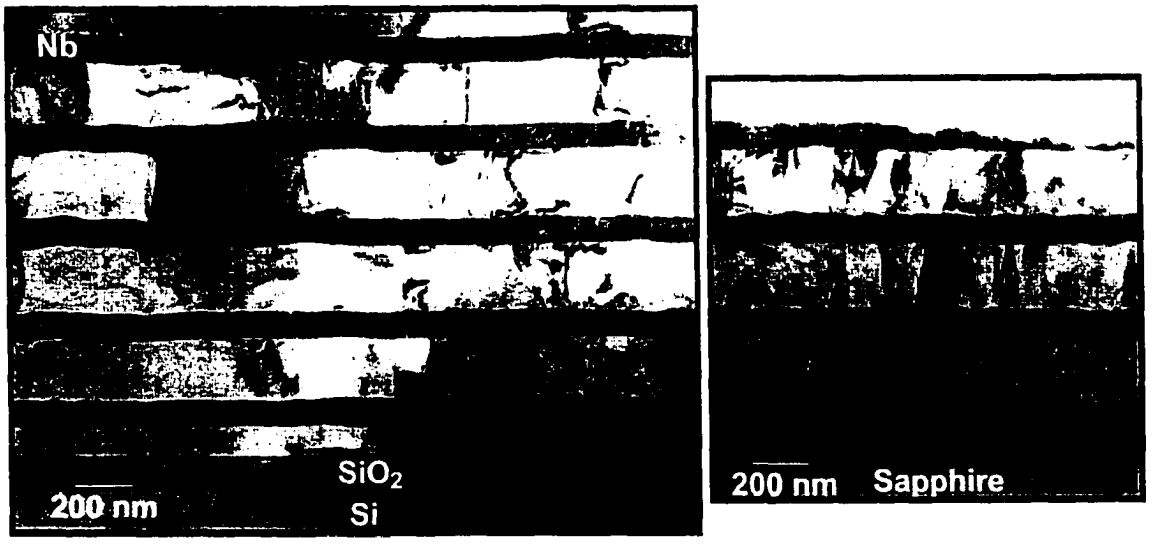

Figure 6. 45: Comparison of two 1Nb/3Al multilayers with Λ = 333 nm deposited in different UHV systems at nominally identical substrate temperatures, but with different deposition rates. The sample on the right had a higher deposition rate producing a columnar structure composed of grains with lower aspect ratios (Barmak et al. 1998; Lucadamo et al. 1999).

For a constant rate of deposition and lateral grain growth, the aspect ratio of the grains will be determined by the thickness of the layer. This is shown schematically in Figure 6. 46.

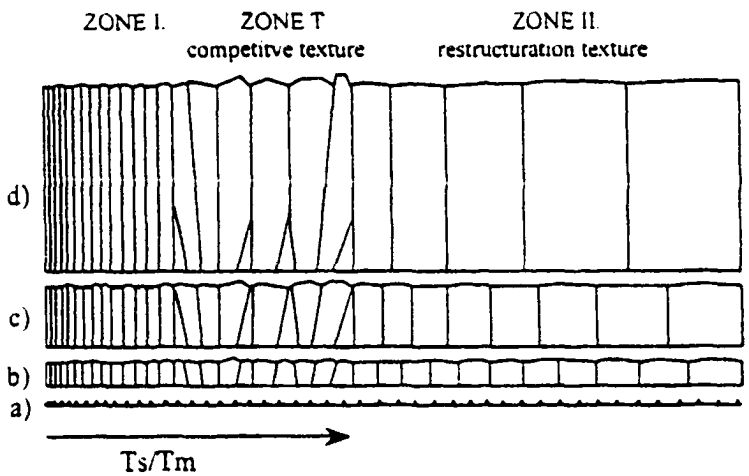

Figure 6. 46: Schematic illustration of the structure of different zones at varying layer thicknesses. Note the increase in aspect ratio with thickness. Note also the variation in surface roughness with the width of the grains (from Barna and Adamik 1998).

The structure zone model that is based on the substrate temperature also cannot accurately predict the microstructure of the as-deposited multilayers with the Cu additions. However, as predicted by Grovenor et al. (1984) and later shown by Barna and Adamik (1995, 1998), the purity of the deposited film will also affect the microstructure. The partial pressure of O_2 was controlled for a series of sputter-deposited Al films (Adamik et al. 1997b). The result was a decrease in grain aspect ratio with increasing O_2 pressures. In addition, a drop in the <111> pole intensity was observed as shown in Figure 6. 47.

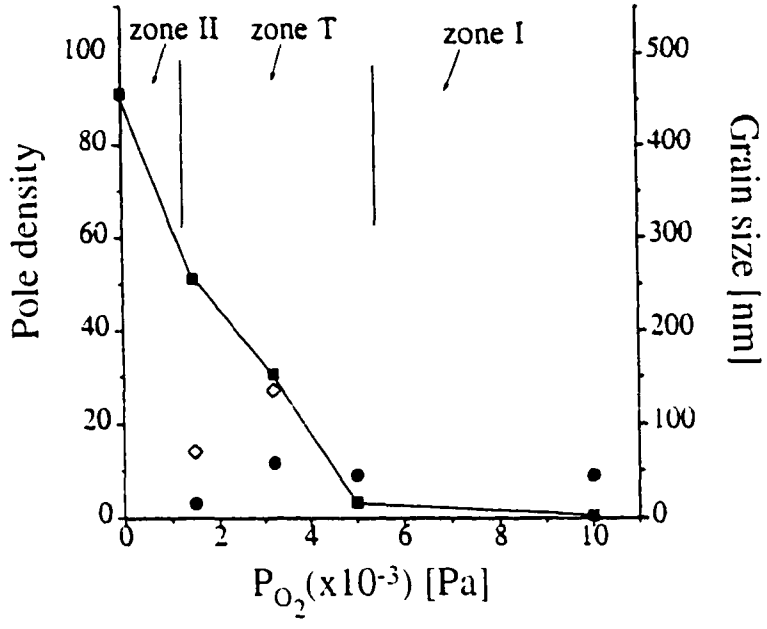

Figure 6. 47: Microstructural characteristics of an Al film as a function of oxygen pressure during deposition (■) P_{111} pole density; (●) P_{200} (×10) pole density; (◆) P_{311} (x10) pole density (adapted from Adamik et al. 1998b).

The addition of 1 wt.% Cu was found to similarly affect the as-deposited Al grain size. This was most likely due to a change in the Al grain boundary mobility caused by the interaction of Cu atoms. A mechanism such as solute drag was the probable cause for the reduced Al grain boundary mobility. A model by Cahn (1962) showed that the velocity of a grain boundary would decrease with increasing concentrations of solute in the bulk.

The formation of interlayer roughness may also have affected the observed texture results. As was shown by Rodbell et al. (1996) the formation of interfacial roughness can also increase the width and offset of the <111> texture. Interlayer roughness was observed in both the Nb/Al and Ti/Al samples at top surfaces of the Nb and Ti layers. This indicated that this roughness developed during growth of these layers by shadowing or the formation of low energy facets. Based on the data of Rodbell et al.

(1996) it is believed that the magnitude of this roughness (several nm) would be sufficient to cause the observed degradation of texture when the film period increased.

To summarize, the grain size in the Nb and Ti layers was influenced primarily by the nucleation density with evidence of subsequent grain growth in thicker layers. The microstructure of these layers appeared to fit the structure zone model in the form proposed by Grovenor et al. (1984) or Barna and Adamik (1995). For the Al layers, the grain size was determined by grain growth during deposition and was described by the model of Grovenor et al. (1984) and Barna and Adamik (1995). The addition of Cu was found to reduce the grain size of the Al. This could also be qualitatively understood by considering the experimental work of Barna and Adamik (1995).

For the study of microstructure evolution in reacted films, constant-heating-rate DSC data provided a means of identifying key points for *ex situ* observations during the Nb/Al reaction. Specific anneals were chosen to examine the validity of the assumptions of the model of Coffey et al. (1989). Although direct observation of the microstructure during the coalescence stage of peak A was not attained, the morphology after coalescence was characterized. The formation of a ~10 nm thick layer of $NbAl_3$ was clearly observed in bright-field micrographs and confirmed by electron diffraction. This value was in good agreement with the estimate of 8 nm made from DSC measurements by determining the half-period where peak B disappears (Barmak et al. 1998). Enhanced growth was observed at the intersections of Al grain boundaries with the interface. Aluminide growth along the Al grain boundaries was also observed in evaporated Hf/Al (Lever et al. 1977; Wittmer et al. 1986), Ti/Al (Wittmer et al. 1985), Ni/Al (Ma et al.

1991,1992), Zr/Al (Mingard and Cantor 1993), and in other sputter deposited Nb/Al films (Barmak et al. 1998).

The presence of Nb in these regions was confirmed by qualitative EDX mapping experiments. This supported the idea that the kinetics of the initial stages of the reaction are controlled by diffusion of the Nb atoms as proposed by Barmak et al. 1998.

The observation of a rough growing interface following the anneal to 627 °C clearly showed that the reaction proceeded by non-planar growth. This irregular reaction front could lead to the slight slope observed at the end of peak B as suggested modifications made by Barmak et al. (1996) to the model of Coffey et al (1989). Figure 6. 48 shows the effect of the addition of interfacial roughness term for films with different values of z_{max} (product layer thickness).

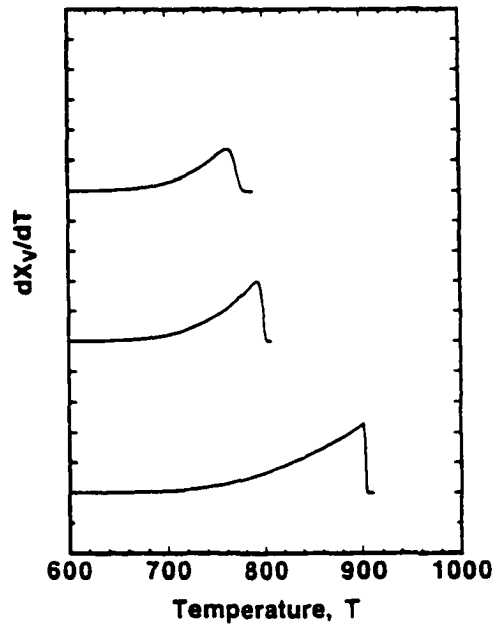

Figure 6. 48: Impact of the maximum product layer thickness, z_{max}, on the termination of the diffusional growth stage. From top to bottom of the figure, z_{max} is 45, 60, and 210 nm respectively (Barmak et al. 1996).

Note that the addition of the roughness parameter led to a more gradual termination of peak B especially in the thinner bilayer films. This agreed qualitatively with the experimental results from constant heating rate DSC experiments.

The presence of "pockets" of untransformed reactants was also seen in the multiple-period sample annealed 627 °C at 40 °C/min. At this temperature, the pockets were only observed in the films with $\Lambda > 72$ nm. The transformation of these regions could lead to the presence of the "foot" evident in the 1Nb/3Al samples with $\Lambda = 72$ and 143 nm. The multiple-period sample also confirmed that the reaction reached completion more rapidly in the lower period multilayers as seen in the constant heating rate DSC experiments. The resulting microstructure continued to evolve during heating through grain growth and coarsening processes.

At 677 °C the reaction was near completion as evidence by the small amounts of remaining reactants. As with the previously reported results of the transformation of a 72 nm film (Barmak et al. 1997; Barmak et al. 1998), the product grain sizes were less than the original period. No abnormal grain growth was observed. This was corroborated by grain size measurements conducted on planview samples. For the Λ =333 nm film, the measured grain diameters were ~0.2 Λ. The multiple-period sample annealed to 720 °C at 40 °C/min revealed significant differences as compared to the 333 nm sample annealed to 677 °C. This was evident in the large intermetallic grains that grew near the center of the film cross-section. This indicated rapid coarsening of the $NbAl_3$ grains following the reaction.

Other measurements of product phase grain sizes from multilayers with a range of Λ provided some new information regarding the relationship of the as-deposited and

fully-reacted microstructures. Results obtained from fits of the gamma and log-normal distributions to the experimental data suggested that for $\Lambda < \sim 72$ nm the product grain size corresponded to the bilayer period. However, for the films with $\Lambda > 72$ nm the ratio of the measured grain diameter to the original multilayer decreased to $\sim 0.2\ \Lambda$. This indicated that the length scales associated with the nucleation and growth of $NbAl_3$ might have been smaller than the reactant grain sizes. Another possibility is that nucleation of new product phase grains had re-occurred at the advancing interphase interface after a critical thickness of $NbAl_3$ had formed. Recall that this had been observed previously for $TiAl_3$ formation in relatively thick Ti/Al films (Michaelsen et al. 1994).

In comparison with the Nb/Al multilayers, significant changes in the evolved microstructure were evident at low temperatures for the Ti/Al films. In the case of a 333 nm sample annealed to 477 °C, the reaction interface was observed to be rough, consistent with previous observations (Wittmer et al. 1985; Michaelsen et al. 1994). The growing $TiAl_3$ layer was composed of many equiaxed grains. The structural form of the $TiAl_3$ could not be determined from the limited information provided by electron diffraction. However, from calorimetry and *in situ* XRD data, the phase would probably be composed of a mixture of the metastable cubic and tetragonal modifications.

The study of planview TEM foils of 1Ti/3Al multilayers annealed *ex situ* provided valuable information about the formation of the metastable structures. The information obtained from electron diffraction was used to confirm the results obtained from *in situ* XRD studies of $TiAl_3$ formation.

6.6 Summary and Conclusions

The previous chapter has sought to provide microstructural evidence to supplement the results from the DSC and XRD results obtained from Nb/Al and Ti/Al multilayer thin films. Several key observations have been made:

1.) The as-deposited grain structures follow the zone model as proposed by Grovenor et al. (1984) and Barna and Adamik (1995). The Al grains exhibited a zone II morphology while the Ti and Nb grains exhibited a zone I or zone T morphology. In both cases, layers were composed of columnar grains. The grain growth was driven through interface surface energy minimization producing a <1 1 1> fiber texture. The aspect ratio of the Al grains increased with increasing layer thickness. The aspect ratios of the Ti and Nb grains were generally < 1 and were relatively constant with layer thickness. Some Ti and Nb grains had aspect ratios that were ~1.

2.) Interlayer roughness was observed to correlate with the grain sizes of the Ti or Nb grains. The top surfaces of the grains appeared to have distinct facets in the thicker films (Λ > 143 nm).

3.) The addition of 1 wt.% Cu to the Al decreased the lateral grain sizes in the Al layers for both the Nb/Al and Ti/Al multilayers resulting in a zone T microstructure as defined by Barna and Adamik (1995) This was presumably due to the reduction in grain boundary mobility by a solute drag mechanism. The smaller grains resulted in a rougher interlayer interface than the films without Cu.

4.) The reaction associated with peak A in the DSC traces produced a continuous layer of $NbAl_3$ in 1Nb/3Al multilayers. Growth of this phase along the Al grain

boundaries intersections at the Nb/Al interface was observed using X-ray mapping in an AEM. Further reaction into peak B of the constant-heating-rate DSC traces resulted in the formation of a non-planar $NbAl_3$/Al interface. Some of the $NbAl_3$ grains acquired facets. Further reaction past peak B produced a nominally equiaxed microstructure with grain sizes less than the original period of the films.

4.) The diameters of the $NbAl_3$ grains immediately following consumption of the reactants are approximately equal to the bilayer period for films with $\Lambda < 72$ nm. However, the grain size was found to be independent of the original bilayer period for films with $\Lambda > 72$ with a diameter of ~0.2 Λ.

5.) For similar heating rates, the reaction of Ti/Al films exhibited rapid changes in grain structure commensurate with phase formation. For a $\Lambda = 333$ nm multilayer heated to 477 °C at 40 °C/min, non-planar growth of $TiAl_3$ was observed as found in previous studies. The $TiAl_3$ layer was composed of equiaxed grains with diameters smaller than the layer thickness.

6.) *Ex situ* anneals of free-standing plan view TEM samples of a $\Lambda = 72$ nm 1Ti/3Al multilayer identified the presence of $L1_2$ $TiAl_3$ after annealing to 400 °C at 60 °C/min. Further reaction to 525 °C converted this phase to the metastable tetragonal phase with a DO_{23} structure, although rings identified with Ti_8Al_{24} and Ti_9Al_{23} were also found in the diffraction pattern. Upon annealing to 700 °C the majority of the diffraction rings were identified as the equilibrium DO_{22} $TiAl_3$.

7 Summary and Conclusions

Experiments utilizing the complementary analytical techniques of DSC, XRD, and TEM, provided new information regarding the relationship of kinetics and microstructure evolution in thin-film reactions. In addition, the underlying trends in as-deposited film microstructure and kinetics of $NbAl_3$ and $TiAl_3$ formation were elucidated and quantified. This was accomplished through the characterization of a series of multilayer films deposited and analyzed under identical conditions. To determine the effects of dilute Cu additions on the reaction kinetics, multilayers composed of pure Al layers as well as Al-0.5 wt.% Cu and Al-1.0 wt.% Cu were prepared. The use of the multilayer architecture increased the volume fraction of interfaces and provided increased sensitivity to the early stages of phase formation in both DSC and diffraction (TEM and XRD) measurements. The use of the multilayer samples also amplified the effect of Cu on the development of texture during film growth. The results from these experiments augmented previous work regarding the two-stage reaction mechanism proposed by Coffey et al. (1989) and further clarified the effect of dilute Cu additions on phase formation kinetics; however, the formation of $TiAl_3$ was found to be more complex than previously reported.

In detail, sputter-deposited 1Nb/3Al multilayer films with $\Lambda = 10 - 333$ nm and total thicknesses of 0.5-1.5 μm have been investigated. Activation energies determined from DSC were consistent with previous studies of the two-stage formation of $NbAl_3$. In constant-heating-scans a single, exothermic peak was observed for $\Lambda < \sim 20$ nm (peak A).

For films with larger periods, two peaks were present with the second peak (peak B) increasing in relative height with increasing Λ. *In situ* synchrotron XRD studies confirmed that, over the temperature range studied, no phases other than $NbAl_3$ formed. In both DSC and *in situ* XRD studies of $NbAl_3$ formation, peak A initially exhibited a slight shift to higher temperatures with increasing bilayer period until $\Lambda \sim 100$ nm. As with earlier studies, this was attributed to heterogeneous nucleation occurring at preferential sites in the interface. The nucleation sites were believed to correspond to a microstructural length scale that varied appreciably with the parent microstructure (i.e., Al grain boundaries or tri-junctions). Further evidence supporting this idea was provided by EDX intensity maps that showed enhanced diffusion of Nb at Al grain boundaries intersecting the interlayer interface. Also, measurements of grain size of free-standing multilayer samples annealed to the end of the reaction (700 °C) showed a linear variation of product grain size with Λ (or Al layer thickness). This also suggested a relationship between the reactant and product microstructural length scales. For films with $\Lambda > 72$ nm the grain size was found to be $\sim 0.2\Lambda$ indicating that the correspondence between reactant and product microstructures was more complex in these samples.

Cross-sectional, TEM observations have provided support for the model of Coffey et al. (1989). *Ex situ*, cross-sectional TEM studies of the microstructure of a Λ = 333 nm sample that had been annealed at a constant heating rate in the DSC indicated that after the first peak, a continuous, relatively planar layer of $NbAl_3$ had formed. The thickness of this layer was 8-10 nm, consistent with the calculated thickness from constant-heating-rate DSC measurements. Annealing into peak B resulted in the formation of faceted $NbAl_3$ grains and a non-planar interphase interface. Preferential

growth of $NbAl_3$ along Al grain boundaries was observed in the microstructure. Finally, annealing past peak B resulted in the formation of mostly equiaxed $NbAl_3$ grains that appeared to be smaller than the original bilayer thickness, consistent with the prior grain size measurements. Thus, although somewhat of an oversimplification of the microstructural evolution during phase formation, the approach of the Coffey model appears to be somewhat consistent with the observed microstructures.

XRD pole plots showed that all of the as-deposited multilayers were Al <111>/Nb <110> fiber textured. The films with Λ = 333 nm had a lower pole intensity and a slightly larger offset than films with Λ = 23.2 nm. This stronger texture in the 23.2 nm films was attributed to the formation of a coherent superlattice of Nb and Al layers. For thicker Nb and Al layers, coherency may not be maintained across all interfaces. These results indicated that film texture resulted from the formation of a superlattice for the films with Λ = 23.2 nm, and by grain growth for films with Λ = 333 nm. In all films, "macrograins" of similarly oriented grains were observed to propagate through the thickness of the multilayer.

The increase in the offset of the Al <111>/Nb <110> peak appeared consistent with an interface roughening mechanism. Specifically, the Nb layers acquired a "granular roughness" on the upper surfaces due to lower adatom mobilities and shadowing effects during deposition. This effect was expected to be prominent in the films with thicker Nb layers (i.e., larger Λ). Cross-sectional TEM analysis using selected-area diffraction qualitatively confirmed the decrease in the fiber texture of the films with increasing Λ and revealed that the layers exhibited a twin-like structure at the Nb/Al interfaces of the multilayer.

The addition of 0.5 and 1.0 wt.% Cu was not found to significantly alter the activation energies (peak A ~1.8 eV, peak B ~2.5 eV) for the formation of $NbAl_3$ or the overall shape of the DSC scans. The addition of Cu also did not affect the value of the formation enthalpy of $NbAl_3$, which was found to be ~40 kJ/g-atom. XRD pole plots showed that the presence of Cu decreased the Al <111>/Nb <110> pole intensity in as-deposited multilayers and led to a significant increase in the offset for films with Λ = 333 nm. The presence of Cu also caused a decrease in the growth of Al grains during deposition, therefore, leading to a substantial decrease in texture for thicker films where the fiber texture was developed by a grain growth mechanism. The smaller diameters of the Al grains led to an increase in the interlayer roughness that could explain the higher texture offset in these samples.

Sputter-deposited 1Ti/3Al multilayers with total thicknesses of 0.5 or 1 μm were also investigated for Λ in the range of 10 –333 nm. Constant-heating-rate DSC studies of $TiAl_3$ formation revealed up to three exothermic peaks corresponding to the formation of $TiAl_3$. As was previously observed, these peaks were associated with the formation of metastable superlattice structures with cubic (peaks A and B) or tetragonal (peak C) unit cells. The activation energies for peaks A and C were found to be ~1.6 eV and ~2.0 eV, respectively. *In situ* XRD also revealed two peaks for the formation of the metastable cubic structure, as confirmed by electron diffraction. As in the Nb/Al samples, the DSC and *in situ* XRD results showed that peak A shifted to higher temperatures with increasing Λ. These results suggested that, as with Nb/Al thin films, the nucleation of the metastable cubic structure of $TiAl_3$ was affected by the underlying microstructure. This conclusion was based on the Avrami exponents obtained from fits to the constant-

heating-rate DSC results. The Avrami exponent for the transformation of Λ = 10 and 20 nm films *increased* from ~1 to ~2 in multilayers with Al(Cu). In addition, the Avrami exponent *decreased* with increasing Λ. As with the Nb/Al samples, electron microscopy observations of as-deposited films indicated that the Al(Cu) grain size was smaller than the pure Al grain size. The interpretation of the Avrami exponents was facilitated by results from computer simulations that addressed the effect of the spatial distribution of nuclei on transformation kinetics. These results showed that nucleation occurring from sites restricted to an underlying lattice network resulted in a lower Avrami exponent. The present exponents suggest that, if nucleation occurred primarily at sites along Al grain boundaries, the increase in the Avrami exponent in the Al(Cu) samples would result from the more random appearance of the underlying Al microstructure, assuming a fixed population of initial nuclei. Conversely, the larger Al layer thicknesses (grains) will place further restrictions on the locations of nucleation sites and lead to a decrease in the Avrami exponent, as observed experimentally.

XRD pole figure measurements showed that the as-deposited Ti/Al multilayers were Al <111>/Ti <0002> fiber textured. The pole intensity, offset, and ω_{95} of a Λ = 20 nm sample were nearly equal to that of a Λ = 333 nm sample, indicating that superlattice formation does not strongly influence the texture in this system as it does in Nb/Al. Also, the texture of the 1Ti/3Al, Λ= 20 nm sample had a larger offset and ω_{95} than the 23.2 nm 1Nb/3Al sample. The 1Ti/3Al, Λ =333 nm multilayer was found to have a slightly lower offset than its 1Nb/3Al counterpart. The microstructure of the as-deposited films revealed "macrograins" extending through multiple layers as in the Nb/Al films.

The effects of Al(Cu) on the formation of $TiAl_3$ was also studied. DSC results found that activation energy of the formation of the metastable cubic structure ($L1_2$) of $TiAl_3$ (peak A) increased by ~0.1-0.2 eV in the presence of Al-1.0 wt.% Cu. The addition of 0.5 or 1.0 wt.% Cu also led to an increase in the formation temperature of $TiAl_3$ by ~ 25 °C of peak A. The temperature of formation of the metastable tetragonal form of $TiAl_3$ was not affected by the presence of Cu or changes in Λ. These results were corroborated by *in situ* XRD measurements. The *in situ* XRD measurements also provided a direct measurement of the formation of the metastable tetragonal form of $TiAl_3$ and the formation of the equilibrium tetragonal form of $TiAl_3$. The activation energy determined from the *in situ* XRD scans was ~1.8 eV in good agreement with the DSC measurements of peak C (~2 eV). Several metastable phases with slightly different lattice parameters were visible in this temperature range. Overlaps of the diffraction peaks in XRD or rings in electron diffraction often prevented a unique identification. The electron diffraction pattern obtained from a Λ = 72 nm sample most closely matched that of a DO_{23} structure, as reported in other studies of sputter-deposited films. However, *in situ* XRD revealed peaks in films with Λ < 30 nm that most closely matched the Ti_9Al_{23} phase, which has also been reported previously in evaporated films. Some findings suggested that metastable phase formation was affected by sample stoichiometry. The magnitude of this effect is still unknown and despite significant efforts to accurately control the multilayer composition, slight run-to-run variations (up to ~ 4 at.% for either element) were possible. In all of the samples studied, formation of the equilibrium structure (DO_{22}) of the $TiAl_3$ phase was indexed unambiguously. Formation occurred in two stages with the activation energy of the first peak ~1.7 eV. The

activation energy of the second peak was much higher (several eV) and may have resulted from the limitations of this application of the *in situ* XRD technique. Nevertheless, this study represents the first attempt to independently quantify the activation energies for the formation of the metastable and equilibrium structures of $TiAl_3$ formation. Studies of the microstructure evolution of $TiAl_3$ were complicated by the formation of the metastable structures and the rapid changes in grain structure upon annealing. Cross-sectional TEM observation of a Λ = 333 nm sample annealed to 477 °C revealed the presence of a polycrystalline $TiAl_3$ layer with a non-planar interphase interface.

The enthalpy of formation of $TiAl_3$ from a 20 nm film (~32 kJ/g-atom) was found to be close to the reported bulk value (~37 kJ/g-atom) and, as with $NbAl_3$, appeared independent of Cu concentration. Films with Λ = 10 nm exhibited a slightly lower value of the formation enthalpy (~26 kJ/g-atom) suggesting that during deposition some intermixing had occurred at the interfaces. Due to fluctuations in the height of peak C for the different multilayers, further measurements would be required to verify this point.

The texture of the Ti/Al multilayers was also observed to decrease with the addition of 1 wt.% Cu. However, the effect was not as pronounced as the results from the Nb/Al multilayers. The increase in offset was again attributed to increased interlayer roughness caused by the reduction in Al lateral grain size. This was especially evident in the Λ = 333 nm films. To summarize, the dominant roughness present during multilayer deposition changed from the top surfaces of the Ti layers to the Al layers. The fiber texture of the Ti/Al multilayers also appeared to be less sensitive to the additions of Cu than the Nb/Al films.

8 Future Work

Several opportunities exist for furthering the research presented in this study. A broader range of solute additions can be investigated to determine if there is, in fact, a critical concentration where the activation energies of either of the two-stages of the formation of $NbAl_3$ or $TiAl_3$ are strongly influenced. Higher Cu concentrations will eventually result in the formation of Al_2Cu precipitates given sufficient annealing time and complicate interpretation of the results. A range of elements with varying amounts of solubility in Al might also clarify the effects of solute on reaction kinetics.

A more detailed investigation of the Avrami exponent involving some samples with $\Lambda < 10$ may also be useful for further classification of the solid state reactions of different systems. Unfortunately, the constant heating approach is only applicable for samples of Nb/Al Ti/Al with $\Lambda <$ ~20 nm due to the interference of peak B. Further analysis of thicker films would require isothermal studies. The values of Λ studied might be limited by the evolved signal will be reduced by the lower volume fraction of interfaces.

Quantification of the interlayer roughness could provide a better understanding of the relationship to texture development in the multilayers. A series of experiments could be conducted in which the surface roughness of a deposited film is quantified by AFM or profilometry for a series of thicknesses. This experiment could then be extended to bilayers to determine what effect the thickness (roughness) of the underlayer has on the second layer (see Rodbell et al. 1997). These results could then be complemented by pole figure XRD.

The relationship between as-deposited and product phase texture was not clearly explained. However, some of the TEM and XRD results suggested that a highly textured parent microstructure may impart a greater degree of texture to the product phase, particularly if the product phase can maintain some coherence (such as in Ti/Al) during its formation. The texture of the product phase could be quantified by pole figure XRD measurements and compared with the results from the as-deposited films.

Factors that influence the grain structure such as deposition rate and solute concentration could be further examined and quantified through systematic grain size measurements of the as-deposited films. Grain sizes of as-deposited layers could be measured from bilayer planview samples if the underlayer was sufficiently thin or if it could be selectively removed by ion polishing. Grain size quantification of reacted films would be more challenging due to the possibility of coarsening during reaction and the ability to prepare electron-transparent samples from brittle, intermetallic compounds. These difficulties might be surmounted by carefully chosen and controlled annealing conditions and sample configurations.

Experiments to study the evolution of composition profiles across layer interfaces in thin-film reactions could be performed using the multiple period sample architecture. As an example, a specimen could be deposited and reacted to transform the layers with the lower bilayer thickness. AEM could then be performed using the fully reacted layers to determine a k-factor. Then, linescans or maps could be taken from the layers with higher values of Λ (that have not completely reacted) to determined the evolution of the concentration profile of a particular element during the reaction.

High resolution TEM (HRTEM) of the as-deposited multilayers would confirm the nature of the granular epitaxy suggested by the electron diffraction and XRD experiments. HRTEM would also could also provide new information concerning the interface between the parent and product layers in the initial stages of the reaction, such as whether coherency is maintained at small product layer thicknesses. The use of energy-filtered TEM to investigate partially reacted multilayers in cross section or planview orientations may also provide information about the elemental distributions at different stages of the reaction. Finally, it might be useful to attempt an *in situ* heating experiment in the TEM using a cross-sectional sample to see if the initial stages in grain structure could be observed directly. Such an experiment might provide critical proof of the validity of the model of Coffey et al. (1989).

The evolution of stress during multilayer deposition or reactions would also comprise an interesting study. There are very few studies in the literature that have examined the stress evolution that occurs during phase formation. Experiments involving isothermal and constant heating-rate anneals could be conducted using equipment such as a Tencor Flexus. A preliminary survey on the Ti/Al and Nb/Al systems indicated a qualitative similarity of the stress behavior with the DSC behavior. For films with $\Lambda > 72$ nm ramped at 10 ^{o}C/min, two separated, tensile stress transitions were found in the stress signature. A similar experiment conducted on Ti/Al revealed a trace that also resembled the constant-heating-rate DSC results with essentially one tensile transition for the thinner and thicker bilayers. These results could then be correlated with the kinetics and microstructure. The initial findings and the relative absence of data in this area mark this as a potentially rich area for further discoveries.

9 References

Adamik, M., Barna, P.B., Tomov, I., and Biro, D. (1994) "Problems of structure evolution in polycrystalline thin films," phys. stat. sol., **A145**, 275-280.

Adamik, M., Tomov, I., and Barna, P.B. (1997) "Texture evolution in stratified Al thin films," Solid State Phenom., **56**, 213-218.

Adamik, M., Barna, P.B., and Tomov, I. (1998) "Ultrasharp textures in Al/Ti layered structures," Surf. Coat. Technol., **100-101**, 333.

Adamik, M, Barna, P.B., and Tomov, I. (1998a) "Columnar structures in polycrystalline thin films developed by competitive growth," Thin Solid Films, **317**, 64-68.

Ahuja, R. and Fraser, H.L. (1994) "Microstructural transitions in titanium-aluminum thin film multilayers," J. Elect. Mater., **23**, 1027-1034.

Alani, R., Mitro, R.J., and Swann, P.R., (1997) "An updated ion polishing system for TEM specimen preparation of materials," Mat. Res. Soc. Proc., **Vol. 480**, 263-292.

Ames, I., d'Heurle, F.M., and Horstmann, R.E. (1970) "Reduction of electromigration in aluminum films by copper doping," IBM J. Res. and Develop., **14**, 461-463.

ASM Handbook (1992) Alloy Phase Diagrams, Vol. 3, H. Baker ed., ASM International, Metals Park, OH.

Asta, M., de Fontaine, D., van Schilfgaarde, M., Sluiter, M, and Methfessel, M. (1992) "First-principles phase-stability study of fcc alloys in the Ti-Al system," Phys. Rev. B, **46**, 5055-5072.

Avrami, M. (1939) "Kinetics of phase change," J. Chem. Phys., **7**, 1103-1112.

Baglin, J.E.E., d'Heurle, F.M., and Hammer, W.N. (1978) "The interaction process for Ag-Al polycrystalline thin-film couples," J. Appl. Phys., **50**, 266-275.

Ball, R.K. and Todd, A.G. (1987) "The formation of titanium, chromium, niobium, and zirconium aluminides in thin films for interconnections," Thin Solid Films, **149**, 269-282.

Banerjee, R., Ahuja, R., and Fraser, H.L. (1996) "Dimensionally induced structural transformations in titanium-aluminum multilayers," Phys. Rev. Lett., **76**, 3778-

Barmak, K., Coffey, K.R., Rudman, D.A., and Foner, S. (1990) "Phase formation sequence for the reaction of multilayer thin films of Nb/Al," J. Appl. Phys., **67**, 7313-7322.

Barmak, K. and Coffey, K.R. (1993) "Grain boundary diffusion controlled precipitation as a model for thin film reactions," Mat. Res. Soc. Proc., **Vol. 311**, 51-56.

Barmak, K., Michaelsen, C., Bormann, R., and Lucadamo, G. (1995) "Reactive phase formation in sputter-deposited Ni/Al thin films," Mat. Res. Soc. Proc., **Vol. 382**, 33-38.

Barmak, K, Michaelsen, C., Rickman, J.M., and Dahms, M. (1996) "Reactive phase formation in thin-films: Evolution of grain structure," Mat. Res. Soc. Proc., **Vol. 403**, 51-62.

Barmak, K., Michaelsen, C., and Lucadamo, G. (1997) "Reactive phase formation in sputter-deposited Ni/Al multilayer thin films," J. Mater. Res., **12**, 133-146.

Barmak, K., Rickman, J.M., and Michaelsen, C. (1997b) "Evolution of grain structure in thin film reactions," J. Elect. Mater., **26**, 1009-1020.

Barmak, K., Michaelsen, C., Vivekanand, S., Ma, F. (1998) "Formation of the first phase in sputter-deposited Nb/Al multilayer thin-films," Phil. Mag. A., **77**, 167-185.

Barna, P.B. and Adamik, M. (1995) "Growth mechanisims of polycrystalline thin films," in *The Science and Technology of Thin Films* eds. I.C. Matacotta and G. Ottoviani, World Scientific, N.J., 1-28.

Barna, P.B. and Adamik, M. (1998) "Fundamental structure forming phenomena of polycrystalline films and the structure zone models," Thin Solid Films, **317**, 27-33.

Baumann, J.R., Liebemann, E.K., Simon, M., and Bucher, E. (1992) "Growth, structural study, and thermal stability of metallic Al/Nb superlattice," Phys. Rev. B, **45**, 3778-3783.

Beyers, R. and Sinclair, R. (1985) "Metastable phase formation in titanium-silicon thin films," J. Appl. Phys., **57**, 5240-5245.

Bonevich, J., van Heerden, D., and Josell, D. (1999) "Face-centered-cubic titanium: An artifact in titanium/aluminum multilayers," J. Mater. Res., **14**, 1977-1981.

Bower, R.W. (1973) "Characteristics of aluminum-titanium electrical contacts on silicon," Appl. Phys. Lett., **23**, 99-101.

Bravman, J.C., and Sinclair, R. (1984) "The preparation of cross-section specimens for transmission electron microscopy," J. Elect. Mater., **1**, 53-61.

Cabral, Jr., C., Clevenger, L.A., Harper, J.M.E., Roy, R.A., Saenger, K.L., Miles, G.L., and Mann, R.W. (1997) "*In-situ* X-ray diffraction analysis of $TiSi_2$ phase formation from a titanium-molybdenum bilayer," Mat. Res. Soc. Proc., **Vol. 441**, 295-301.

Cabral, Jr., C., Clevenger, L.A., Harper, J.M.E., d'Heurle, F.M., Roy, R.A., Saenger, K.L., Miles, G.L., and Mann, R.W. (1997a) "Lowering the formation temperature of the C54-TiSi2 phase using a metallic interfacial layer," J. Mater. Res. **12**, 304-307.

Cabral, Jr., C., Clevenger, L.A., Harper, J.M.E., d'Heurle, F.M., Roy, R.A., C. Lavoie, Saenger, K.L., Miles, G.L., Mann, R.W., and J.S. Nakos (1997b) "Low temperature formation of C54-$TiSi_2$ using titanium alloys," Appl. Phys. Lett., **71**, 3531-3533.

Cahn, J.W. (1962) "The impurity-drag effect in grain boundary motion," Acta Met., **10**, 789-798.

Carlino, V.L. and Hidalgo, A.J. (1992) "Advancements in dimpling technique for automatically and repeatably thinning TEM samples to near electron transparency," Mat. Res. Soc. Proc., **Vol. 254**, 99-108.

Carpenter, D.T. (1998) Ph.D. Thesis, Lehigh University, Bethlehem, Pennsylvania.

Carpenter, D.T., Rickman, J.M., and Barmak, K. (1998) "A methodology for automated quantitative microstructural analysis of transmission electron micrographs," **84**, 5843-5854.

Clemens, B.M. and Hufnagel, T.C. (1993) "Amorphous alloys formed by solid state reaction," J. Alloys Compounds, **194**, 221- 227.

Clevenger, L.A., Thompson, C.V., Cammarata, R.C., and Tu, K.N. (1988) "Reaction kinetics of nickel/silicon multilayer films," Appl. Phys. Lett., **52**, 795-797.

Clevenger, L.A. and Thompson, C.V. (1990) "Nucleation-limited phase selection during reactions in nickel/amorphous silicon multilayer thin films," J. Appl. Phys., **67**, 1325-1333.

Clevenger, L.A., Thompson, C.V., de Avillez, R.R., and Ma, E. (1990a) "Nucleation controlled phase selection in vanadium/amorphous-silicon multilayer thin films," J. Vac. Sci. Technol., **A8**, 1566-1571

Coffey, K.R., Clevenger, L.A., Barmak, K., Rudman, D.A., and Thompson, C.V. (1989) "Experimental evidence for nucleation during thin-film reactions", Appl. Phys. Lett., **55**, 852-854.

Coffey, K.R., Barmak, K., Rudman, D.A., and Foner, S. (1992) "Thin film reaction kinetics of niobium/aluminum multilayers," J. Appl. Phys., **72**, 1341-1349.

Coffey, K.R. and Barmak, K. (1994) "A unified approach to grain boundary diffusion and nucleation in thin film reactions," Mat. Res. Soc. Proc., **Vol. 343**, 193-204.

Coffey, K.R. and Barmak, K. (1994b) "A new model for grain boundary diffusion and nucleation in thin film reactions," Acta Metall. Mater., **42**, 2905-2911.

Colgan, E.G. (1990) "A review of thin-film aluminide formation," Mater. Sci. Rep., **5**, 1-44.

Colinet, C., Pasturel, A., Manh, D.N., Pettifor, D.G., and Miodownik, P. (1997) "Phase stability study of the Al-Nb system," Phys. Rev. B, **56**, 552-565.

Corcoran, Y.L., King, A.H., de Lanerolle, N., and Kim, B. (1990) "Grain boundary diffusion and growth of titanium silicide layers on silicon," J. Elect. Mater., **19**, 1177-1183.

Cullity, B.D. (1978) Elements of X-ray Diffraction 2nd Ed., Addison-Wesley, Reading Mass.

Emeric, E., Bergman, C., Glugnet, G., Gas, P., and Audier, M. (1998) "Formation of a decagonal quasicrystalline film by reactive diffusion in Al/Co multilayers," Phil. Mag. Lett., **78**, 77-85.

Estabil, J.J., Rathore, H.S., and Levine, E.N. (1991) "Electromigration improvements with titanium underlay and overlay in Al(Cu) metallurgy," Proc. of the 8th annual VLSI Multilevel Interconnection Conference, IEEE, 242-248.

Federspiel, X., Voiron, F., Ignat, M., Marieb, T., and Fujimoto, H. (1998) "Interfacial reactions in multilayers intended for microelectronics devices," Mat. Res. Soc. Proc., **Vol. 514**, 547-552.

Federspiel, X. (1999) "Role of grain boundaries in $TiAl_3$ growth," Unpublished.

Fujimura, N. Nishida, N., Ito, T., and Nakayama, Y. (1989) "Effects of texture in the titanium layer on solid state reactions for Al/Ti/Si and Al/TiN/Ti/Si systems". Mat. Sci. Engr., **A108**, 153-157.

Gösele, U. and Tu, K.N. (1982) "Growth kinetics of planar binary diffusion couples: 'Thin-film case' versus 'bulk cases'." J. Appl. Phys., **53**, 3252-3260.

Gösele, U. and Tu, K.N. (1989) " 'Critical thickness' of amorphous phase formation in binary diffusion couples." J. Appl. Phys., **66**, 2619-2626.

Grovenor, C.R.M., Hentzell, H.T.G., and Smith, D.A. (1984) "The development of grain structure during growth of metallic films," Acta Metall., **32**, 773-781.

Gupta, D., Vieregge, K., Rodbell, K.P., and Tu, K.N. (1993) "Microelectronic applications of thin films of $TiAl_3$," in Diffusion in Ordered Alloys B. Fultz, R.W. Cahn, and D. Gupta eds. The Minerals Metals and Materials Society, 247-259.

Guthrie, W.L., Patrick, W.J., Levine, E., Jones, H.C., Mehter, E.,A., Houghton, T.F., Chiu, G.T., and Fury, M.A. (1992) "A four-level VLSI bipolar metallization design with chemical-mechanical planarization," IBM J. Res. Develop., **36**, 845-856.

Han, C.C. and Bene, R.W., "Variations in interface compound nucleation for Ti-Al ultrathin films on Si substrates," Appl. Phys. Lett., **47**, 1077-1079.

Harper, J.M.E. and Rodbell, K.P. (1997) "Microstructure control in semiconductor metallization," J. Vac. Sci. Technol. B, **15**, 763-779.

Henderson, D.W. (1979) "Experimental analysis of non-isothermal transformations involving nucleation and growth," J. Thermal Anal., **15**, 325-331.

Hong, Q.Z., Lilienfeld, D.A., and Mayer, J.W. (1988) "Thermal and ion-induced, metastable-cubic Al_3M phases in Al-Ti and Al-Hf thin films," J. Appl. Phys. **64**, 4478-4483.

Howard, J.K., Lever, R.F., Smith, P.J., and Ho, P.S. (1976) "Kinetics of compound formation in thin film couples of Al and transition metals," J. Vac. Sci. Technol., **13**, 68-71.

Howard, J.K., White, J.F., and Ho, P.S. (1978) "Intermetallic compounds of Al and transitions metals: Effect of electromigration in 1-2-μm-wide lines," J. Appl. Phys., **49**, 4083-4093.

Huang, H.-C.W. and Wittmer, M. (1984) "Effect of Cu on Al-transition metal reaction kinetics," Mat. Res. Soc. Proc., **Vol. 25**, 157-162.

Hufnagel, T.C., Brennan, S., Payne, A.P., and Clemens, B.M. (1992) "Observation of a rapid amorphization reaction," J. Mater. Res., **7**, 1976-1979.

Hurd, J.L., Rodbell, K.P., Gignac, L.M., Clevenger, L.A., Iggulden, R.C., Schnabel, R.F., Weber, S.J., and Schmidt, N.H. (1998) "Linewidth and underlayer influence on texture in submicrometer-wide Al and AlCu lines," Appl. Phys. Lett., **72**, 326-328.

Im, Y., Johnson, P.E., McKnelly Jr., L.T., and Morris Jr., J.W. (1988) "Nb_3Al formation in sputter-deposited Nb/Al multilayer samples," J. of Less-Common Met., **139**, 87-95.

Im, Y., and Morris Jr., J.W. (1988b) "Sequence of phase formation in Nb/Al multilayered samples," J. Appl. Phys., **64**, 3487-3491.

Johnson, W.A. and Mehl, R.F. (1939) "Reaction kinetics in processes of nucleation and growth," Trans. AIME, **135**, 416-458.

Joint Committee on Powder Diffraction Standards (1998) Powder Diffraction File, Inorganic Index (Swarthmore, Pennsylvania: International Center for Diffraction Data).

Jorda, J.L., Flükiger, R., and Muller, J. (1980) "A new metallurgical investigation of the niobium-aluminum system," J. of Less-Common Met., **75**, 227-239.

Kamijo, A. and Mitsuzuka, T. (1995) "A highly oriented Al [111] texture developed on ultrathin metal underlayers," J. Appl. Phys., **77**, 3799-3804.

Keller, R.R., Kalnas, C.E., and Phelps, J.M. (1999) "Local crystallography and stress voiding in Al-Si-Cu versus copper interconnects," J. Appl. Phys., **86**, 1167-1169.

Kissinger, H.E. (1957) "Reaction kinetics in differential thermal analysis," Anal. Chem., **29**, 1702-1706.

Kittl, J.A., Gribelyuk, M.A., and Samavedam, S.B. (1998) "Mechanism of low temperature C54 $TiSi_2$ formation bypassing C49 $TiSi_2$: Effect of Si microstructure and Mo impurities on the Ti-Si reaction path," Appl. Phys. Lett., **73**, 900-902.

Klepeis, S.J., Benedict, J.P., and Anderson, R.M. (1988) "A grinding/polishing tool for TEM sample preparation," Mat. Res. Soc. Proc., **115**, 179-183.

Knorr, D.B. (1991) "Texture and microstructure effects on electromigration behavior of aluminum metallization," Mat. Res. Soc. Proc., **Vol. 225**, 21-26.

Knorr, D.B. (1993) "The role of texture on the relationship of aluminum-based interconnects," Mat. Res. Soc. Proc., **Vol. 309**, 75-86.

Knorr, D.B. and Rodbell, K.P. (1992) "Effects of texture, microstructure, and alloy content on electromigration of aluminum-based metallization," SPIE, **1805**, 210-221.

Knorr, D.B. and Rodbell, K.P. (1996) "The role of texture in the electromigration behavior of pure aluminum lines," J. Appl. Phys., **79**, 2409-2417.

Knorr, D.B., Tracy, D.P., and Rodbell, K.P. (1991) "Correlation of texture with electromigration behavior in Al metallization," Appl. Phys. Lett., **59**, 3241-3243.

Knorr, D.B., Merchant, S.M., and Biberger, M.A. (1998) "Development of texture in interconnect thin film stacks," J. Vac. Sci. Technol. B, **16**, 2734-2744.

Krafcsik, I., Gyulai, J., Palmström, C.J., and Mayer, J.W. (1983) "Influence of Cu as an impurity in Al/Ti and Al/W thin-film reactions," Appl. Phys. Lett., **43**, 1015-1017.

Lasky, J.B., Nakos, J.S., Cain, O.J., and Geiss, P.J. (1991) "Comparison of transformation to low-resistivity phase and agglomeration of $TiSi_2$ and $CoSi_2$," IEEE Trans. Electron Devices, **38**, 262-269.

Lever, R.F., Howard, J.K., Chu, W.K., and Smith, P.J. (1977) "Anomalous growth of $HfAl_3$ in thin films," J. Vac. Sci. Technol., **14**, 158-161.

Licata, T.J., Colgan, E.G., Harper, J.M.E., and Luce, S.E. (1995) "Interconnect fabrication processes and the development of low-cost wiring for CMOS products," IBM J. Res. and Develop., **39**, 419-435.

Lita, A. and Sanchez Jr., J. (1999) "Charaterization of surface structure in sputtered Al films: Correlation to microstructure evolution," J. Appl. Phys., **85**, 876-882.

Lucadamo, G., Watanabe, M., Barmak, K., Michaelsen, C., Williams, D.B., and Alani, R. (1999) "High-resolution quantitative X-ray microanalysis of Nb/Al multilayer thin films using the z-factor approach," Phil. Mag. A, **79**, 1423-1442.

Lucadamo, G., Barmak, K., Hyun, S., Cabral, Jr., C., and Lavoie, C. (1999a) "Evidence of a two-stage reaction mechanism in sputter deposited Nb/Al multilayer thin-films studied by *in situ* synchrotron X-ray diffraction," Mater. Lett., **39**, 268-273.

Lundin, C.E. and Yamamoto, A.S. (1963) "The equilibrium phase diagram, niobium (columbium)-aluminum," Trans. Metall. Soc. AIME, **236**, 863-872.

Ma, E., Thompson, C.V., and Clevenger, L.A. (1991) "Nucleation and growth during reactions in multilayer Al/Ni films: The early stage of Al_3Ni formation," J. Appl. Phys. **69**, 2211-2218.

Ma, E., Clevenger, L.A., and Thompson, C.V. (1992) "Nucleation of an intermetallic at thin-film interfaces: VSi_2 contrasted with Al_3Ni," J. Mater. Res., **7**, 1350-1355.

Ma, Z., Allen, and L.H., Allman, D.D.J. (1995) "Microstructural aspects and mechanism of the C49-to-C54 polymorphic transformation in titanium disilicide," J. Appl. Phys., **77**, 4384-4388.

Ma, Z., Xu, Y., Allen, L.H., Lee, S. (1993) "Nucleation and growth in the initial stage of metastable titanium disilicide formation," J. Appl. Phys., **74**, 2954-2956.

Mann, R.W. and Clevenger, L.A. (1994) "The C49 to C54 phase transformation in $TiSi_2$ thin films," J. Electrochem. Soc., **141**, 1347-1350.

Mann, R.W., Clevenger, L.A., Agnello, P.D., and White, F.R. (1995) "Silicides and local interconnections for high-performance VLSI applications," IBM J. Res. Develop., **39**, 403-416.

Mann, R.W., Miles, G.L., Knotts, T.A., Rakowski, D.W., Clevenger, L.A., Harper, J.M.E., d'Heurle, F.M., Cabral, Jr., C. (1995) "Reduction of the C54-$TiSi_2$ phase transformation temperature using refractory metal ion implantation," Appl. Phys. Lett., **67**, 3729-3731.

McWhan, D.B., Gurvich, M., Rowell, J.M., and Walker, L.R. (1983) "Structure and coherence of NbAl multilayer films," J. Appl. Phys., **54**, 3886-3891.

Meschel, S.V and Kleppa, O.J. (1993) "Standard synthesis of formation of 4d aluminides by direct synthesis calorimetry," J. Alloy Compounds, **191**, 111-116.

Michaelsen, C., Wöhlert, S. Bormann, R. (1994) "Phase formation and microstructural development during solid-state reactions in Ti-Al multilayer films" Mat. Res. Soc. Proc., **343**, 205-210.

Michaelsen, C., Wölhert, S., Bormann, R., and Barmak, K. (1996) "The early stages of solid-state reactions in Ti/Al multilayer films," Mat. Res. Soc. Proc., **398**, 245-250.

Michaelsen, C., and Dahms, M. (1996) "On the determination of nucleation and growth kinetics by calorimetry," Thermochim. Acta, **288**, 9-27.

Michaelsen, C., Barmak, K., and Weihs, T.P. (1997) "Investigating the thermodynamics and kinetics of thin film reactions by differential scanning calorimetry," J. Phys. D., **30**, 3167-3186.

Michaelsen, C. (1998) private communication.

Mingard, K.P. and Cantor, B. (1993) "microstructural characterization of reactions in Al-Zr thin film couples," J. Mater. Res., **8**, 274-285.

Mouroux, A. and Zhang, S.-L. (1999) "Alternative pathway for the formation of C54 TiSi2," J. Appl. Phys., **86**, 704-706.

Mouroux, A., Zhang, S.-L., Kaplan, W., Nygren, S., Ostling, M., and Petersson, C.S. (1996) "Enhanced formation of the C54 phase of $TiSi_2$ by an interposed layer of molybdenum," Appl. Phys. Lett., **69**, 975-977.

Movchan, B.A. and Demchishin, A.V. (1969) "Study of the structure and properties of thick vacuum condensates nickel, titanium, tungsten, aluminum oxide, and zirconium dioxide," Fiz. Metal. Metalloved., **28**, 653-660.

Nahar, R. K., Devashrayee, N.M., and Khokle, W.S. (1988) "Diffusivity of Al in Ti and the effect of Si doping for very large scale integrated circuit metallization," J. Vac. Sci. Technol., **B6**, 880-883.

Nahar, R.K. and Devashrayee, N.M. (1987) "Effect of Si on the reaction kinetics of Ti/AlSi bilayer structures," Appl. Phys. Lett., **50**, 130-131.

Nakamura, K., Lau, S.S., Nicolet, M-A., and Mayer, J.W. (1976) "Ti and V layers retard interaction between Al films and polycrystalline Si," J. Appl. Phys., **28**, 277-280.

Ogurtani, T. (1972) "Kinetics of diffusion in the Nb/Al system," Met. Trans., **3**, 421-425.

Privitera, S., La Via, F., Grimaldi, M.G., and Rimini, E. (1998) "Effect of linewidth reduction on the characteristic time spread in C49-C54 phase transition," Appl. Phys. Lett., **73**, 3863-3865.

Raman, A., and Schubert, K. (1965) "On the constitution of some alloy series related to $TiAl_3$," Z. Metallkde., **56**, 44-52.

Rickman, J.M., Tong, W.S., and Barmak, K. (1997) "Impact of heterogeneous boundary nucleation on transformation kinetics and microstructure," Acta. mater., **45**, 1153-1166.

Rodbell, K.P., DeHaven, P.W., and Mis, J.D. (1991) "Electromigration behavior in layered Ti/AlCu/Ti films and its dependence on intermetallic structure," Mat. Res. Soc. Proc., **225**, 91-97.

Rodbell, K.P. (1992) "Electromigration behavior of multilayered Al/Hf and Al/Ti fine lines and its dependence on Cu and Pd solute additions," Microelectron. Reliab., **32**, 1521-1526.

Rodbell, K.P., Hurd, J.L., and DeHaven, P.W. (1996) "Blanket and local crystallographic texture determination in layered Al metallization," Mat. Res. Soc. Proc., **403**, 617-626.

Rodbell, K.P., Svilan, V., Gignac, L.M., Dehaven, P.W., Murphy, R.J., and Licata, T.J. (1996a) "Film crystallographic texture and substrate surface roughness in layered aluminum metallization," Mat. Res. Soc. Proc., **428**, 261-271.

Roy, R. and Sen, S.K. (1992) "Calorimetric and other studies of intermetallic phase formation in Ag/Al bilayer thin films," J. Mater. Sci., **27**, 6098-6104.

Sanchez, J.E. (1994) "Effects of crystallographic orientation on film morphological evolution," Mat.Res. Soc. Proc., **Vol. 343**, 641-652.

Schechtman, D., van Heerden, D., and Josell, D. (1994) "fcc titanium in Ti-Al multilayers," Mat. Lett., **20**, 329-334.

Shilo, I., Franzen, H.F., and Schiffman, R.A. (1982) "Enthalpies of formation of niobium aluminides as determined by the Knudsen effusion method," J. Electrochem. Soc., **129**, 1608-1613.

Slama, G. and Vignes, A. (1972) "Diffusion dans les aluminiures de niobium," J. Less-Common Metals, **29**, 189-202.

Smith, D.A., Small, M., and Stanis, C. (1993) "Electron microscopy of the grain structure of metal films and lines," Ultramicroscopy, **51**, 328-338.

Smith, D.A. and Ibrahim, A. (1994) "Zone descriptions of film structure – A rationale," Mat. Res. Soc. Proc., **Vol. 317**, 401-412.

Smithells Metals Reference Book 7th ed. (1992) Edited by E.A. Brandes and G.B. Brook, Butterworth-Heinemann Ltd., New York.

Srinivasan, S., Desch, P.B., and Schwartz, R.B. (1991) "Metastable phases in the Al_3X (X = Ti, Zr, and Hf) intermetallic system," Scripta Met., **25**, 2513-2516.

Stephenson, G.B. (1988) "Time-resolved X-ray scattering using a high-intensity multilayer monochromator," Nucl. Inst. Meth., **A266**, 447-451.

Stephenson, G.B., Ludwig, K.F., Jordan-Sweet, J.L., Brauer, S., Mainville, J., Yang, Y.S., and Sutton, M. (1989) " Instrumentation for millisecond-resolution scattering studies" Rev. Sci. Instrum., **60**, 1537-1540.

Tardy, J. and Tu, K.N. (1985) "Solute effect of Cu on interdiffusion in Al_3Ti compound films," Phys. Rev., **32**, 2070-2081.

The National Technology Roadmap for Semiconductors, Semiconductor Industry Association, San Jose, CA 1997.

Thompson, C.V. (1993) "Texture evolution during grain growth in polycrystalline thin films," Scripta Met., **28**, 167-172.

Thompson, C.V. and Carel, R. (1995) "Texture development in polycrystalline thin films," Mat. Sci. Engr., **B32**, 1995.

Thompson, C.V. and Carel, R. (1996) "Grain growth and texture evolution in thin films," Mater. Sci. Forum, **204-206**, 83-89.

Thornton, J.A. (1977) "High rate thick film growth," Ann. Rev. Mater. Sci., **7**, 239-260.

Tong, W.S., Rickman, J.M., and Barmak, K. (1997) "Impact of boundary nucleation on product grain size distribution," J. Mater. Res., **12**, 1501-1507.

Tracy, D.P., Knorr, D.B., and Rodbell, K.P. (1994) "Texture in multilayer metallization structures," J. Appl. Phys., **76**, 2671-2680.

Uhilg, H.H. and Revie, R.W. (1985) Corrosion and Corrosion Control 3rd ed., John Wiley and Sons, New York, 350.

Vaidya, S., Sheng, T.T., and Sinha, A.K. (1980) "Linewidth dependence of electromigration in evaporated Al-0.5 % Cu," Appl. Phys. Lett., **36**, 464-466.

Vaidya, S. and Sinha, A.K. (1981) "Effect of texture and grain structure on electromigration in Al-0.5 wt.% Cu thin films," Thin Solid Films, **75**, 253-259.

van Loo, F.J.J. and Rieck, G.D. (1973) "Diffusion in the titanium-aluminum system – I. Interdiffusion between solid Al and Ti or Ti-Al Alloys," Acta Met., **21**, 61-71.

Wall, M.A. and Jankowski, A.F. (1989) "Atomic imaging of Au/Nb multilayers," Thin Solid Films, **181**, 313-321.

Williams, D.B, Watanabe, M., and Carpenter, D.T. (1998) "Thin film analysis and chemical mapping in the analytical electron microscope," Mikrochim. Acta [Suppl], **15**, 49.

Wittmer, M., Le Goues, F., and Huang, H.-C.W. (1985) "Effect of Cu on the kinetics and microstructure of Al_3Ti formation," J. Electrochem. Soc., **132**, 1450-1455.

Wittmer, M., Huang, H.-C.W., and LeGoues, F. (1986) "Interdiffusion and precipitation in Al-Hf thin-film couples," Phil. Mag. A, **53**, 687-707.

Wöhlert, S. (1995) "Fruhstadien der phasenbildung im system titan-aluminum," Ph.D. thesis, Technical University of Hamburg-Harburg, Hamburg, Germany.

Wöhlert, S., Michaelsen, C., and Bormann, R. (1997) "Phase selection by competitive growth in Ti/Al thin film diffusion couples," Mat. Res. Soc. Proc., **Vol. 441**, 15-20.

Wöhlert, S., and Bormann, R. (1999) "Phase selection governed by different growth velocities in the early stages of the Ti/Al phase reaction," J. App. Phys., **85**, 825-832.

Zielinski, E.M., Vinci, R.P., and Bravman, J.C. (1995) "The influence of strain energy on abnormal grain growth in copper thin films," Appl. Phys. Lett., **67**, 1078-1080.

Zhang, S.-L. C. Lavoie, Cabral, Jr., C., Harper, J.M.E., d'Heurle, F.M., and Jordan-Sweet, J. (1999) "*In situ* characterization of titanium silicide formation: The effect of Mo interlayer, temperature ramp-rate, and annealing atmosphere," J. Appl. Phys., **85**, 2617-2626.

Zhao, X.-A., So, F.C.T., and Nicolet, M.-A. (1988) "$TiAl_3$ formation by furnace annealing of Ti/Al bilayers and the effect of impurities," J. Appl. Phys., **63**, 2800-2807.

VITA

Gene Anthony Lucadamo was born on September 23, 1972 to Eugene (Gene) and Maryann Lucadamo in Allentown, Pennsylvania. After graduating from Emmaus High School, he was gained admission to Lehigh University and began his undergraduate study in the fall of 1990. He earned a Bachelor of Science degree (with Honors) in Materials Science and Engineering in June 1994. He then to pursue graduate studies in the same department. Working with former Lehigh faculty member, Prof. Katayun (Katy) Barmak (currently at Carnegie Mellon University), he was awarded a Master of Science degree in January 1997. After receiving the Master's degree, Gene immediately began doctoral studies again under the guidance of Prof. Katy Barmak. Prior to completing his Ph.D., Gene had authored or co-authored ten refereed journal articles and five conference articles. He also participated in internship programs at Sandia National Laboratories, Albuquerque, NM and at the IBM T. J. Watson Research Center, Yorktown Heights, NY. For his research accomplishments, Gene was inducted into Sigma Xi, the Research Honor Society, in 1997.